

✓ VOLUME 81

MARCH 10, 1977

NUMBER 5

JPCA_x

THE JOURNAL OF
PHYSICAL
CHEMISTRY



PUBLISHED BIWEEKLY BY THE AMERICAN CHEMICAL SOCIETY

THE JOURNAL OF PHYSICAL CHEMISTRY

BRYCE CRAWFORD, Jr., Editor
STEPHEN PRAGER, Associate Editor
ROBERT W. CARR, Jr., C. ALDEN MEAD, Assistant Editors

EDITORIAL BOARD: C. A. ANGELL (1973-1977), F. C. ANSON (1974-1978), V. A. BLOOMFIELD (1974-1978), J. R. BOLTON (1976-1980), L. M. DORFMAN (1974-1978), W. FALCONER (1977-1978), H. L. FRIEDMAN (1975-1979), H. L. FRISCH (1976-1980), W. A. GODDARD (1976-1980), E. J. HART (1975-1979), W. J. KAUZMANN (1974-1978), R. L. KAY (1977-1981), D. W. McCLURE (1974-1978), K. MYSELS (1977-1981), R. M. NOYES (1973-1977), R. G. PARR (1977-1979), W. B. PERSON (1976-1980), J. C. POLANYI (1976-1980), S. A. RICE (1976-1980), F. S. ROWLAND (1973-1977), R. L. SCOTT (1973-1977), W. A. STEELE (1976-1980), J. B. STOTHERS (1974-1978), F. A. VAN-CATLEDGE (1977-1981), B. WEINSTOCK (1977)

Published by the
AMERICAN CHEMICAL SOCIETY
BOOKS AND JOURNALS DIVISION

D. H. Michael Bowen, Director
Marjorie Laflin, Assistant to the Director

Editorial Department: Charles R. Bertsch,
Head; Marianne C. Brogan, Associate
Head; Celia B. McFarland, Joseph E.
Yurvati, Assistant Editors

Magazine and Production Department:
Bacil Guiley, Head

Research and Development Department:
Seldon W. Terrant, Head

Advertising Office: Centcom, Ltd., 50 W.
State St., Westport, Conn. 06880.

Editorial Department at the ACS Easton
address.

Page charges of \$60.00 per page may be
paid for papers published in this journal.
Ability to pay does not affect acceptance or
scheduling of papers.

Bulk reprints or photocopies of indi-
vidual articles are available. For information
write to Business Operations, Books and
Journals Division at the ACS Washington
address.

Requests for **permission to reprint**
should be directed to Permissions, Books and
Journals Division at the ACS Washington
address. The American Chemical Society and
its Editors assume no responsibility for the
statements and opinions advanced by con-
tributors.

Subscription and Business Information

1977 Subscription rates—including surface
postage

	U.S.	PUAS	Canada, Foreign
Member	\$24.00	\$33.00	\$34.00
Nonmember	96.00	105.00	106.00
Supplementary material	15.00	19.00	20.00

Air mail and air freight rates are avail-
able from Membership & Subscription Ser-
vices, at the ACS Columbus address.

New and renewal subscriptions should
be sent with payment to the Office of the
Controller at the ACS Washington address.

Changes of address must include both old
and new addresses with ZIP code and a recent
mailing label. Send all address changes to the
ACS Columbus address. Please allow six
weeks for change to become effective. **Claims
for missing numbers** will not be allowed if
loss was due to failure of notice of change of
address to be received in the time specified:

if claim is dated (a) North America—more
than 90 days beyond issue date, (b) all other
foreign—more than 1 year beyond issue date;
or if the reason given is "missing from files".
Hard copy claims are handled at the ACS
Columbus address.

Microfiche subscriptions are available
at the same rates but are mailed first class to
U.S. subscribers, air mail to the rest of the
world. Direct all inquiries to Special Issues
Sales, at the ACS Washington address or call
(202) 872-4554. **Single issues** in hard copy
and/or microfiche are available from Special
Issues Sales at the ACS Washington address.
Current year \$4.75. Back issue rates available
from Special Issues Sales. **Back volumes** are
available in hard copy and/or microform.
Write to Special Issues Sales at the ACS
Washington address for further information.
Microfilm editions of ACS periodical pub-
lications are available from volume 1 to the
present. For further information, contact
Special Issues Sales at the ACS Washington
address. **Supplementary material** men-
tioned in the journal appears in the microfilm
edition. Single copies may be ordered directly
from Business Operations, Books and Jour-
nals Division, at the ACS Washington ad-
dress.

	U.S.	PUAS, Canada	Other Foreign
Microfiche	\$2.50	\$3.00	\$3.50
Photocopy			
1-7 pages	4.00	5.50	7.00
8-20 pages	5.00	6.50	8.00

Orders over 20 pages are available only on
microfiche, 4 × 6 in., 24X, negative, silver
halide. Orders must state photocopy or mi-
crofiche if both are available. Full biblio-
graphic citation including names of all au-
thors and prepayment are required. Prices
are subject to change.

© Copyright, 1977, by the American
Chemical Society. No part of this publication
may be reproduced in any form without
permission in writing from the American
Chemical Society.

Published biweekly by the American
Chemical Society at 20th and Northampton
Sts., Easton, Pennsylvania 18042. Second
class postage paid at Washington, D.C. and
at additional mailing offices.

Editorial Information

Instructions for authors are printed in
the first issue of each volume. Please conform
to these instructions when submitting man-
uscripts.

Manuscripts for publication should be
submitted to *The Journal of Physical
Chemistry*, Department of Chemistry, Uni-
versity of Minnesota, Minneapolis, Minn.
55455. Correspondence regarding **accepted
papers and proofs** should be directed to the

American Chemical Society
1155 16th Street, N.W.
Washington, D.C. 20036
(202) 872-4600

Member & Subscription Services
American Chemical Society
P.O. Box 3337
Columbus, Ohio 43210
(614) 421-7230

Editorial Department
American Chemical Society
20th and Northampton Sts.
Easton, Pennsylvania 18042
(215) 258-9111

Volume 81, Number 5 March 10, 1977

JPCHAx 81(5) 373-498 (1977)

ISSN 0022-3654

Correlation between the Inhibition of Positronium Formation by Scavenger Molecules, and Chemical Reaction Rate of Electrons with These Molecules in Nonpolar Liquids ... Béla Lévy and Ole E. Mogensen*	373
Quenching of Benzene Fluorescence in Pulsed Proton Irradiation ... M. L. West	377
Kinetic Isotope Effects and Intermediate Formation for the Aqueous Alkaline Homogeneous Hydrolysis of 1,3,5-Triaza-1,3,5-trinitrocyclohexane (RDX) ... John C. Hoffsommer*, Donald A. Kubose, and Donald J. Glover	380
Photoionization and Recombination Luminescence of <i>N,N'</i> -Disubstituted Dihydrophenazines in 3-Methylpentane at 77 K ... U. Brühlmann and J. Robert Huber*	386
3. The System HBr + (Pr) ₄ NBr + H ₂ O at 25 °C. Application of Pitzer's Equations ... Rabindra N. Roy*, James J. Gibbons, Ronald Snelling, James Moeller, and Terry White	391 ■
Monomer Concentrations in Binary Mixtures of Nonmicellar and Micellar Drugs ... D. Attwood	394
Identification and Localization of Cluster and Hydroxylated Forms of Divalent Cation Oxide in Y Zeolite ... Antoine Abou-Kais, Claude Mirodatos, Jean Massardier, Denise Barthomeuf, and Jacques C. Vedrine*	397
⁴ T ₂ State Lifetimes and Intersystem Crossing Efficiencies in Chromium(III) Complexes ... Francesco Castelli and Leslie S. Forster*	403
The Contribution of Higher Order Cluster Terms to the Activity Coefficients of the Small Ions in Polyelectrolyte Solutions ... Kunihiko Iwasa* and Jan C. T. Kwak	408
Excited State Chemistry of Indigoid Dyes. 5. The Intermediacy of the Triplet State in the Direct Photoisomerization and the Effect of Substituents ... Andree D. Kirsch and George M. Wyman*	413
Solvent-Induced Polarization Phenomena in the Excited State of Composite Systems with Identical Halves. 1. Effects of Solvent Medium on the Fluorescence Spectra of 1,2-Dianthrylethanes ... Toyoharu Hayashi, Tatsuo Suzuki, Noboru Mataga*, Yoshiteru Sakata, and Soichi Misumi	420
Solvent-Induced Polarization Phenomena in the Excited State of Composite Systems with Identical Halves. 2. Effects of Solvent Polarity upon the Fluorescence of [2.2](1,3)Pyrenophane ... Toyoharu Hayashi, Noboru Mataga*, Teruo Umemoto, Yoshiteru Sakata, and Soichi Misumi	424
Charge Transfer Triplet State of <i>p</i> -Nitroaniline ... J. Wolleben and A. C. Testa*	429
Thermodynamics of Nonpolar Mixtures Exhibiting Liquid-Liquid Phase Equilibria. Aliphatic and Aromatic Esters with Alkanes ... G. Manzini and V. Crescenzi*	431
Electron Paramagnetic Resonance of Rare Earth Ions in Zeolites ... Lennox E. Iton* and J. Turkevich	435
Electron Spin Resonance Studies of Anisotropic Ordering, Spin Relaxation, and Slow Tumbling in Liquid Crystalline Solvents. 2 ... K. V. S. Rao, Carl F. Polnaszek, and Jack H. Freed*	449
An Electron Spin-Lattice Relaxation Mechanism Involving Tunneling Modes for Trapped Radicals in Glassy Matrices. Theoretical Development and Application to Trapped Electrons in γ -Irradiated Ethanol Glasses ... Michael K. Bowman* and Larry Kevan	456
Nuclear Magnetic Resonance Relaxation Studies of Carbonic Anhydrase Derivatives in Frozen Solutions ... E. Hsi and R. G. Bryant*	462

THE JOURNAL OF PHYSICAL CHEMISTRY

Registered in U. S. Patent Office © Copyright, 1977, by the American Chemical Society

VOLUME 81, NUMBER 5 MARCH 10, 1977

Correlation between the Inhibition of Positronium Formation by Scavenger Molecules, and Chemical Reaction Rate of Electrons with These Molecules in Nonpolar Liquids

Béla Lévy¹ and Ole E. Mogensen*

Chemistry Department, Danish Atomic Energy Commission, Research Establishment Risø, DK-4000 Roskilde, Denmark
(Received March 29, 1976)

Publication costs assisted by Research Establishment Risø

o-Ps yields were determined in various liquid hydrocarbons, tetramethylsilane, and mixtures thereof as a function of C₂H₅Br and CCl₄ concentration. These molecules are known to be good electron scavengers and positronium inhibitors as well. The spur reaction model of Ps formation predicts a correlation between the inhibition coefficient and the chemical rate constant of electrons with scavenger molecules. We found that the dependence of the inhibition coefficient on the work function (V_0) of electrons in different liquids shows a very unusual behavior, similar to that recently found for the chemical rate constants of quasifree electrons with the same scavenger molecules. The inhibition coefficient as a function of V_0 had a maximum for C₂H₅Br, while it increased monotonously with decreasing V_0 for CCl₄. The inhibition coefficient for C₂H₅Br in a 1:1 molar tetramethylsilane-*n*-tetradecane mixture was found to be greater than in both of the pure components. The clear correlation found between electron scavenging rate constants and positronium inhibition constitutes the severest test to date of the spur reaction model of positronium formation. The importance of the positron annihilation method from the point of view of radiation chemistry is also emphasized.

Introduction

For many years the excess electron in liquids (e.g., the hydrated electron²) has been an important topic of research in radiation chemistry. In particular the excess electron in nonpolar liquids is studied very much at present. It is probably less known that the properties of the two other light particles, the positron and the positronium (Ps) atom³ in liquids, are strongly correlated to those of the excess electron. We shall in this article give an account of such a correlation.

The values of the Ps formation probabilities measured for different liquids, and the inhibition of Ps formation in them caused by different solutes, were little understood until very recently³ when one of the present authors (O.E.M.) proposed a new model of Ps formation: the spur reaction model.^{4,5} This model correlates the Ps yields to the results of spur research obtained in radiation chemistry. A spur formed during the interaction of an ionizing

particle with matter can be defined as a group of reactive intermediates which are so close together that there is a significant probability of their reacting with each other before diffusing into the bulk medium. The positronium is assumed to be formed by a reaction between a positron and an electron in the positron spur. The positron spur is the group of reactive species (e.g., the positron, excess electrons, positive ions, etc.), which is created around the positron when it loses the last of its kinetic energy. Ps formation competes with the recombination of the electrons and their parent positive ions ("geminate recombination"), and also with the diffusion of electrons out of the spur. Reactions of the electrons or the positrons in the spur with the solvent molecules, or with scavengers, will also decrease the probability of Ps formation.

The purpose of our work was to measure the inhibition of Ps formation by C₂H₅Br and CCl₄ in nonpolar liquids and to correlate the strength of the Ps inhibition to the

electron rate constants measured by Allen et al.⁶ The spur model of Ps formation predicts that the strength of the Ps inhibition vs. V_0 will show a maximum at the same V_0 value as the electron rate constant in the C_2H_5Br case, while a monotonously increasing inhibition strength for decreasing V_0 is expected for CCl_4 . The expected behavior of the Ps inhibition was found.

Here we present positronium inhibition measurements for the following systems: C_2H_5Br in *n*-tetradecane (*n*- C_{14}), *n*-hexane (*n*- C_6), 2,2,4-trimethylpentane (isooctane, *i*- C_8), 2,2-dimethylpropane (neo- C_5), and tetramethylsilane (TMS); CCl_4 in *n*- C_{14} , *i*- C_8 , and TMS. In addition of these systems the inhibition function for C_2H_5Br were also determined in *n*- C_{14} -TMS ($X_{TMS} = 0.49$) and *n*- C_6 -neo- C_5 ($X_{n-C_6} = 0.25$) mixtures (X represents the mole fraction of the component in the subscript).

Experimental Section

Lifetime Measurements. About 40 μCi of $^{22}NaCl$ deposited between two Kapton (Du Pont) polyimide foils of 1 mg/cm² constituted the positron source. The positron lifetimes were measured as usual by determining the time interval between the detection of a 1.28-MeV photon, emitted simultaneously with the emission of a positron (start signal) and the detection of an 0.511-MeV annihilation photon (stop signal).³ The time resolution function of our conventional lifetime spectrometer, determined by measuring the spectrum of a ^{60}Co source, could well be described as a sum of three Gaussian curves with a fwhm of 390 ps for the total curve. The lifetime spectra were analyzed by the POSITRONFIT EXTENDED⁷ computer program for three lifetimes and intensities with 8% source correction. Details of the application of this program are discussed in ref 5c.

Materials. The chemicals were of analytical grade from Merck and were used without further purification. All the liquid samples were thoroughly degassed by the freeze-thaw method and afterwards distilled under vacuum into an ampoule containing the positron source. During the recording of the lifetime spectra the source and the sample were kept in this air-tight ampoule. The necessary amounts of neopentane and tetramethylsilane solvents and of solutes added to a given volume of solvent were determined by PV technique in the same apparatus as used for degassing the samples. All measurements were performed at 20 °C.

Results

The analyses of the lifetime spectra gave the following results. The shortest lifetimes (τ_1) were found around 150 ps, the medium lifetimes (τ_2) around 500 ps, while the longest lifetimes (τ_3) for the pure solvents and mixtures were: *n*- C_{14} 3.35 ns, *n*- C_6 3.94 ns, *i*- C_8 4.11 ns, neo- C_5 5.17 ns, TMS 4.77 ns, TMS-*n*- C_{14} 3.75 ns, *n*- C_6 -neo- C_5 4.61 ns, and C_2H_5Br 3.23 ns. Through the lifetime results for their solutions, C_2H_5Br and CCl_4 proved to be practically pure inhibitors; hence, it was unnecessary to make any corrections to the intensity data due to quenching contributions. The relative Ps yield $P(c)$ is therefore

$$P(c) = I_3(c)/I_3(0) \quad (1)$$

where $I_3(c)$ is the intensity of the longest-lived component extracted from the lifetime spectrum at an inhibitor concentration c . The $I_3(0)$ values, i.e., the o-Ps yields measured in pure solvents or their mixtures were *n*- C_{14} 37.5%, *n*- C_6 41.6%, *i*- C_8 44.2%, neo- C_5 52.7%, TMS 55.5%, TMS-*n*- C_{14} 45.6%, and *n*- C_6 -neo- C_5 45.3% (C_2H_5Br 5.2%) (uncertainties $\approx \pm 0.7$ absolute %). The values of $P(c)$ calculated from the experimentally found

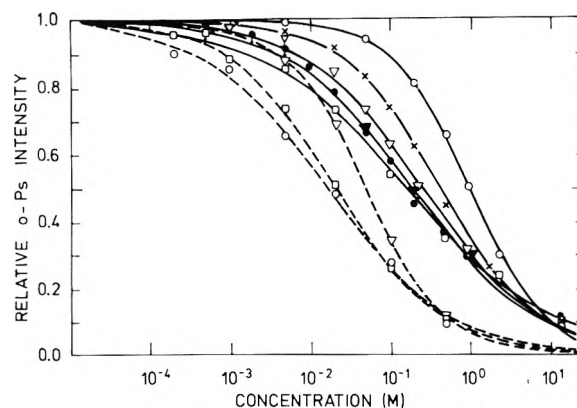


Figure 1. Relative o-Ps intensities as a function of inhibitor concentration in various solvents: (∇) *n*- C_{14} , (\bullet) *n*- C_6 , (\square) *i*- C_8 , (\times) neo- C_5 , (\circ) TMS, (∇) TMS-*n*- C_{14} mixture. Solid curves for C_2H_5Br and dashed curves for CCl_4 are fit to eq 7 with σ and α values in Table I. (The solid curve for the TMS-*n*- C_{14} mixture is omitted.)

$I_3(c)$ values by eq 1 are presented in Figure 1 with a logarithmic scale for the inhibitor concentration (in mol/dm³). Data found for C_2H_5Br in *n*- C_6 -neo- C_5 mixtures were situated on a curve almost identical with that for *n*- C_6 ; hence, they were omitted for the sake of clarity.

The relative Ps yields from right to left correspond to increasing inhibition strengths, because it is obvious that stronger inhibitors decrease the Ps yield at lower concentrations. Even if the curves are compared in only this simple, visual manner, clear qualitative agreement with electron rate constant data⁶ is immediately manifested.

Parameter Fitting of the Relative Ps Yields. A discussion of the possibilities of obtaining a theoretical expression for the relative Ps yield $P(c)$ as a function of electron scavenger concentration in the framework of the spur reaction model of Ps formation has been published elsewhere.^{5c} Here it was concluded that an application of a detailed spur diffusion theory to the positron spur problem is not promising at present. However, the Ps yield may be correlated to the electron spur results by use of the reasonable assumption that the relative electron-positron "recombination" in the positron spur (i.e., the Ps yield) is strongly correlated to the relative electron-ion recombination in the electron spur. The yield of a given product $G(p)$ of an electron reaction with a scavenger is normally described by

$$G(p) = G_{fi} + G_{gi} F(c) \quad (2)$$

Here G_{fi} denotes the yield of "free ions", while G_{gi} represents the yield of "geminate ion pairs". $F(c)$ is the scavenging function.⁸ Hence, we may assume that

$$P(c) = (G_{fi} + G_{gi} - G(p))/G_{gi} = 1 - F(c) \quad (3)$$

Thus the meaning of eq 3 is that the probability of Ps formation is proportional to the fraction of unscavenged "geminate electrons". $1 - F(c)$, i.e., formally our $P(c)$, plays an important role in Schuler's phenomenological scavenging model specifying the distribution function of the ion-pair lifetimes.^{8b}

With regard to the explicit analytical form of $F(c)$ and of the corresponding $P(c)$, three formulas have mainly been used in radiation chemistry. For very dilute solutions, several authors^{9,10} have theoretically derived the following expression:

$$F(c) = Kc^{1/2} \quad (4)$$

However, this formula is totally inapplicable in our case, since we use high solute concentrations. Another sca-

TABLE I: Summary of Results Obtained by Parameter Fitting of *o*-Ps Inhibition Functions Measured in Various Liquids and Liquid Mixture

Solvent	V_0 , eV	Inhibitor	σ , M ⁻¹	α	$\sqrt{\Delta^2}$
<i>n</i> -Tetradecane	0.21	C ₂ H ₅ Br	3.9 ± 0.4 (5.2)	0.61 ± 0.01 (0.78)	0.032 (0.012)
(<i>n</i> -C ₁₄)		CCl ₄	20.5 ± 1	0.88 ± 0.01	0.005
<i>n</i> -Hexane (<i>n</i> -C ₆)	0.00	C ₂ H ₅ Br	5.3 ± 0.5 (8.2)	0.57 ± 0.01 (0.74)	0.025 (0.005)
Isooctane (<i>i</i> -C ₈)	-0.26	C ₂ H ₅ Br	6.0 ± 0.6 (10.3)	0.48 ± 0.01 (0.62)	0.018 (0.005)
		CCl ₄	46.0 ± 1	0.67 ± 0.01	0.006
Neopentane (neo-C ₅)	-0.35	C ₂ H ₅ Br	2.4 ± 0.2 (2.8)	0.73 ± 0.01 (0.83)	0.014 (0.004)
Tetramethylsilane (TMS)	-0.51	C ₂ H ₅ Br	1.04 ± 0.1	0.94 ± 0.01	0.011
		CCl ₄	59.0 ± 1	0.58 ± 0.01	0.021
TMS + <i>n</i> -C ₁₄ ($X_{\text{TMS}} = 0.49$)	-0.14 ^a	C ₂ H ₅ Br	4.8 ± 0.5 (7.8)	0.56 ± 0.01 (0.75)	0.021 (0.002)
<i>n</i> -C ₆ + neo-C ₅ ($X_{n\text{-C}_6} = 0.25$)	-0.26 ^a	C ₂ H ₅ Br	4.3 ± 0.5 (5.5)	0.55 ± 0.01 (0.63)	0.014 (0.009)

^a Calculated values from the V_0 values of the pure solvent components, assuming a linear relationship between V_0 and the molar fraction X .

vening function that can be theoretically derived using a simple, competitive kinetic model^{8a} is

$$F(c) = \frac{\sigma c}{1 + \sigma c} \quad (5)$$

The corresponding relative Ps yield is

$$P(c) = \frac{1}{1 + \sigma c} \quad (5a)$$

Schuler and co-workers,⁸ however, found that eq 5 did not describe their scavenging results well enough in cyclohexane and *n*-hexane solvents. They proposed the use of an empirical function

$$F(c) = \frac{(\sigma c)^{1/2}}{1 + (\sigma c)^{1/2}} \quad (6)$$

The relative Ps yields corresponding to eq 6 would be

$$P(c) = \frac{1}{1 + (\sigma c)^{1/2}} \quad (6a)$$

The analyses of our Ps yield results showed that fairly good fits could be obtained by use of (5a) in some solvents and (6a) in other solvents. To improve the goodness of the fit for all solvents we therefore fitted the results with a slightly modified empirical expression using a second adjustable parameter α in the exponent:

$$P(c) = \frac{1}{1 + (\sigma c)^\alpha} \quad (7)$$

which would correspond to the following scavenging function:

$$F(c) = \frac{(\sigma c)^\alpha}{1 + (\sigma c)^\alpha} \quad (7a)$$

It will be shown that this empirical formula gives reasonable agreement with experimental data measured in solvents of high electron mobility.

It is important to realize that we cannot expect a detailed quantitative correlation between the measured properties of the positron and electron spurs.^{4,5} The positron spur, being part of a "high linear-energy-transfer" track, is very probably more dense than the normally

studied electron spurs. The distribution of electron-positron distances at thermalization probably also differs from the distribution of electron-ion distances. Several other properties of the two spurs (e.g., yields of specific ions and radicals) may be different too. The experimentally determined Ps yield might also be influenced by the reaction of Ps with the reactive species in the spur. Another point of interest is that detailed tests of (5) or (6) seem not to have been performed in some of the solvents used (see below). Hence, the fact that it was necessary to use a two-parameter formula (7) instead of the one-parameter formulas (5a) or (6a) to obtain good fits is not surprising at all.

The fitting procedure with two adjustable parameters was carried out on a programmable table calculator (EMG 666) minimizing the RMS deviation between the measured and calculated points. The results of the fitting procedure are presented in Table I. The V_0 values for pure solvents are Holroyd's latest data for 20 °C,¹¹ while for the mixtures they are calculated values assuming a linear relationship between V_0 and the mole fraction, as it was found by Holroyd and Tauchert¹² to be valid for TMS-*n*-C₆ and neo-C₅-*n*-C₆ mixtures. The last column of Table I contains the goodness of the fit expressed as the RMS deviation between the measured and calculated points. The data in parentheses represent the results when only the upper part of the total inhibition curve ($P(c) > 0.6$) was involved in the fitting procedure. In the cases of C₂H₅Br in TMS and CCl₄ in all three solvents investigated, the two fitting procedures gave practically identical results.

In the case of C₂H₅Br, one of the reasons for the difference between the two fitting procedures might be the high concentration of C₂H₅Br. At high concentrations the "solute" molecules themselves contribute considerably to the primary processes of radiolysis. The spur size and rate constants of the electrons and the positron are probably also influenced by the solute molecules in high concentration, in particular in the high electron mobility (large spur) solvents neo-C₅ and TMS.

In Figure 1 the solid curves for C₂H₅Br and the dashed curves for CCl₄ are drawn using eq 7, with σ and α values calculated from the total curve fitting (Table I). The calculated curve for C₂H₅Br in the TMS-*n*-C₁₄ mixture, which is practically identical with the *n*-C₆ curve, is omitted.

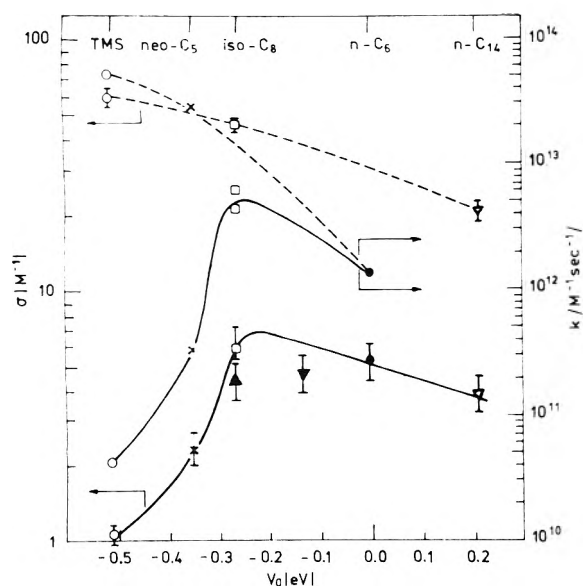


Figure 2. Ps inhibition coefficients (σ , left-hand scale) and electron rate constants (k , right-hand scale) for reactions with C_2H_5Br (solid curves) and CCl_4 (dashed curves) as a function of V_0 : (\blacktriangle) $n-C_6$ - $neo-C_5$ mixture, others symbols as in Figure 1.

Discussion

General Remarks. Although the correlation between the results of the present Ps inhibition measurements and those of the electron rate constant determinations⁶ is clear by simply looking at Figure 1, the comparison is more convincing in a figure presenting both sets of data. Figure 2 shows positronium inhibition constants (σ , left-hand scale) together with Allen, Gangwer, and Holroyd's electron rate constants⁶ (k , right-hand scale) as a function of V_0 . The solid and dashed lines are visual fits for C_2H_5Br and CCl_4 data, respectively. In both cases the curves for C_2H_5Br exhibit a maximum for the same solvent (i.e., for the same V_0), and both curves are very much steeper from the left to the maximum than from the right to the maximum. Very convincing is also the fact that the points for the solvent mixtures, the V_0 values which were adjusted to be close to the maximum, are situated reasonably well on a common curve with the pure solvents. From this point of view, one must also consider the inaccuracy in calculating the V_0 values for the mixtures. The CCl_4 curves, on the other hand, increase with decreasing V_0 in both cases.

The prediction of the spur reaction model of Ps formation proved to be valid for this very unusual case, and this seems to be the severest test of this model to date. As discussed above the reaction rate of the spur electrons is only one factor affecting the process of Ps formation, and that there are several others which may greatly modify the very complex and complicated situation in the spur. The good qualitative correlation between these two quantities (i.e., σ and k),¹³ however, demonstrates the important role of electron reaction rates in Ps formation, at least in these nonpolar liquids of high electron mobility.

With respect to the other models of Ps formation, namely, the Ore model¹⁴ and its modified version¹⁵ or the "hot-Ps" reaction model,¹⁶ these do not seem to be able to explain such unusual changes for the probability of Ps formation without the use of special assumptions and practically unavailable and unverifiable data for any system. The main problem is that all these models take into account positrons and Ps atoms of fairly large energies only, while it seems that very small changes in the work function of thermalized electrons are responsible for the

great changes in electron rate constants or Ps inhibition properties. Although the spur reaction model itself is unable to make a priori predictions of Ps formation for every special case, its great advantage lies in the fact that, for explanations and predictions, it can use general principles and experiences originating from radiation chemistry.

Comparison with Steady-State Scavenging Results. The basic idea of the spur reaction model of Ps formation is that Ps atoms are formed as a result of the scavenging of the spur electrons by the positrons. Thus any processes in which spur electrons are involved compete with Ps formation¹⁷ and a strong correlation must exist between scavenging and Ps inhibition experiments. This assumption gave the theoretical basis for using the scavenging function to fit the relative Ps yields and evaluate the inhibition coefficients (σ). Thus, in principle, the Ps inhibition coefficient has the same meaning as the relative scavenging constant in Schuler's phenomenological model for scavenging in hydrocarbons⁸ and the numerical values of these two quantities must be similar or at least comparable. Unfortunately, however, we have hardly any data with which to make this comparison. Rad and Bansal¹⁸ measured the relative scavenging constant for C_2H_5Br in isooctane and their $5 M^{-1}$ value is very close to ours: $\sigma = 6 \pm 0.6 M^{-1}$. Although Infelta and Schuler's¹⁹ value for C_2H_5Br in cyclohexane ($7.8 M^{-1}$) is not directly comparable since we have no data for this solvent, it seems to be quite reasonable because the V_0 of cyclohexane is close to that of isooctane. The agreement of these results is promising, but the data are insufficient to prove the mutual identity of the two constants.

Conclusion

For the two good Ps inhibitors, or electron scavengers, that we have studied (C_2H_5Br and CCl_4), the inhibition coefficients in nonpolar liquids can be correlated with V_0 , the energy level of the mobile conduction electrons in the various solvents. This correlation is similar to that found between V_0 and the electron reaction rate constants for the same scavengers. These Ps inhibition measurements thus seem to be the severest test to date of the spur reaction model, which predicts a strong correlation between the formation probability of Ps and the electron scavenging rates in the positron spur. The analysis of the Ps inhibition curves resulted in the use of a new empirical fitting parameter instead of the constant used so far in the concentration exponent.²⁰ In order to improve our understanding of the nature of matter, more experimental efforts are needed especially for extending the steady-state scavenging measurements to liquids of low V_0 . For this purpose, Ps inhibition measurements can provide useful and important information both for radiation chemistry and for Ps chemistry.

Acknowledgment. The authors are grateful to P. Jansen for stimulating discussions, and to R. A. Holroyd for furnishing unpublished electron work function data. They are also much indebted to N. J. Pedersen for valuable technical assistance.

References and Notes

- (1) Visiting scientist from the Department of Physical Chemistry and Radiology, Eotvos University of Budapest, Hungary.
- (2) E. J. Hart and M. Anbar, "The Hydrated Electron", Wiley, New York, N.Y., 1970.
- (3) (a) J. H. Green and J. Lee, "Positronium Chemistry", Academic Press, New York, N.Y., 1964; (b) V. I. Goldanskii, *At. Energy Rev.*, **8**, 3 (1968); (c) V. I. Goldanskii and V. G. Firsov, *Annu. Rev. Phys. Chem.*, **22**, 209 (1971); (d) "Positron Annihilation", A. T. Stewart and L. Roellig, Ed., Academic Press, New York, N.Y., 1967; (e) H. J. Ache, *Angew. Chem.*, **84**, 234 (1972); (f) R. N. West, *Adv. Phys.*, **22**, 263 (1973);

- (g) J. A. Merrigan, J. H. Green, and S. J. Tao in "Physical Methods of Chemistry", A. Weissberger and B. W. Rositter, Ed., Vol. 1, Part III. D. Wiley, New York, N.Y., 1972, p 501.
- (4) O. E. Mogensen, *J. Chem. Phys.*, **60**, 998 (1974).
- (5) (a) P. Jansen, M. Eldrup, O. E. Mogensen, and P. Pagsberg, *Chem. Phys.*, **6**, 265 (1974); (b) O. E. Mogensen, *Appl. Phys.*, **6**, 315 (1975); (c) M. Eldrup, V. P. Shantarovich, and O. E. Mogensen, *Chem. Phys.*, **11**, 129 (1975); (d) P. Jansen, M. Eldrup, B. Skytte Jensen, and O. E. Mogensen, *ibid.*, **10**, 303 (1975).
- (6) A. O. Allen, T. E. Gangwer, and R. A. Holroyd, *J. Phys. Chem.*, **79**, 25 (1975).
- (7) P. Kirkegaard and M. Eldrup, *Comput. Phys. Commun.*, **3**, 240 (1972); **7**, 401 (1974).
- (8) (a) J. M. Warman, K.-D. Asmus, and R. H. Schuler, *Adv. Chem. Ser.*, No. **82**, 25 (1968); (b) S. J. Rzed, P. P. Infelta, J. M. Warman, and R. H. Schuler, *J. Chem. Phys.*, **52**, 3971 (1970); (c) R. H. Schuler and P. P. Infelta, *J. Phys. Chem.*, **76**, 3812 (1972).
- (9) (a) A. Hummel, *J. Chem. Phys.*, **48**, 3268 (1968); (b) A. Mozumder, *ibid.*, **55**, 3026 (1971); (c) J. L. Magee and A. B. Taylor, *ibid.*, **56**, 3061 (1972).
- (10) A. Hummel, *Adv. Radiat. Chem.*, **4**, 1 (1974).
- (11) R. A. Holroyd, private communication.
- (12) R. A. Holroyd and W. Taichert, *J. Chem. Phys.*, **60**, 3715 (1974).
- (13) A reasonable linear correlation seems to exist between $\log k$ vs. σ for a given scavenger in different solutions.
- (14) A. Ore, *Univ. Bergen, Årbok, Naturvitensk. Række*, No. **9** (1949).
- (15) S. J. Tao and R. H. Green, *J. Chem. Soc. A.*, 408 (1968).
- (16) (a) L. J. Bartal, J. B. Nicholas, and H. J. Ache, *J. Phys. Chem.*, **76**, 1124 (1972); (b) L. J. Bartal and H. J. Ache, *Radiochim. Acta*, **17**, 205 (1972).
- (17) On the other hand, reactions of solvated positrons (e_s^+) can also compete with Ps formation. Thus, for instance, the reaction of e_s^+ with Br^- or Cl^- ions, which are products of the reaction of electrons with scavenger molecules (C_2H_5Br and CCl_4), will probably result in the formation of e^+Br^- or e^+Cl^- bound states, as was recently pointed out by Mogensen and Shantarovich [*Chem. Phys.*, **6**, 100 (1974)]. The rate constant of the $e^+ + Cl^-$ reaction in water was found to be $2.5 \times 10^{10} M^{-1} s^{-1}$, but rate constants for nonpolar liquids are not known.
- (18) S. J. Rzed and K. M. Bansal, *J. Phys. Chem.*, **76**, 2374 (1972).
- (19) P. P. Infelta and R. H. Schuler, *J. Phys. Chem.*, **76**, 987 (1972).
- (20) The α^{-1} vs. σ curves were found to be linear for a given scavenger in different solvents. At the same time the α^{-1} vs. V_0 curves were qualitatively similar to the σ vs. V_0 curves in Figure 2.

Quenching of Benzene Fluorescence in Pulsed Proton Irradiation[†]

M. L. West

Pacific Northwest Laboratory, Battelle Boulevard, Richland, Washington 99352 (Received July 2, 1975; Revised Manuscript Received December 2, 1976)

Publication costs assisted by Pacific Northwest Laboratory

The luminescence behavior of dilute solutions of benzene in cyclohexane is investigated for proton and ultraviolet excitation. Benzene fluorescence from proton excitation does not show the delayed component that has been reported for numerous aromatic solvents. Instead there is an initial rapid decay attributed to dynamic quenching followed by a slower decay approaching that observed for ultraviolet excitation. The initial quenching is shown to be consistent with intratrack quenching by transient species.

Introduction

The luminescence behavior of organic systems subjected to ionizing radiation can be expected to differ from that of ultraviolet excited systems whenever ionic interactions become important or whenever the effects of nonhomogeneous energy deposition must be considered. Differences in fluorescence decay obtained from these two modes of excitation can therefore give time-correlated information about events following deposition of the radiation. Previous experimental radioluminescence studies with pulsed ionizing radiation¹⁻³ have shown that aromatic solvents typically exhibit a fluorescent component which decays exponentially with a rate similar to that for ultraviolet excitation and an additional delayed fluorescence component which decays nonexponentially over several microseconds. The delayed component has been explained by a bimolecular reaction between solute anions and cations resulting from charge transfer and electron scavenging, respectively.

Our investigation of excitation and quenching mechanisms associated with ionizing radiation were conducted on dilute solutions of benzene in cyclohexane. This system is not complicated by excimer emission and has a very rapid energy transfer from solvent to solute (<1 ns). Also, because of the small electron affinity of benzene, delayed

fluorescence from long-lived benzene ion precursors should be minimized. Fluorescence time response curves have been obtained for both proton and ultraviolet excitation. For proton excitation, an initial rapid quenching is observed followed by a decay that approaches that present in ultraviolet excitation. Benzene fluorescence does not exhibit a long-lived delayed component. The dynamic quenching observed for proton excitation is postulated to be an intratrack quenching by transient species.

Experimental Section

(a) *Samples.* Benzene and cyclohexane (Mallinckrodt Nanograde) were prepared by fractional distillation followed by freeze-thaw-pump to remove oxygen. Additional samples were deaerated by helium and nitrogen purging. Lifetimes measured from ultraviolet excitation were identical for the three types of purging and agreed within experimental error with those reported in the literature.⁴ All samples for proton irradiation were prepared by helium purging.

(b) *Apparatus.* A block diagram of the experimental apparatus⁵ is shown in Figure 1. Proton pulses of <0.3 ns fwhm are available from a 2-MeV Van de Graaff accelerator using a 3.33-MHz high-voltage rf oscillator for beam chopping. A commercially available deuterium flash lamp is used for ultraviolet excitation measurements. Photons emitted from the excited sample are collected with quartz optics, passed through a scanning spectrometer, and

[†] This paper is based on work performed under United States Atomic Energy Commission Contract AT(45-1)-1830.

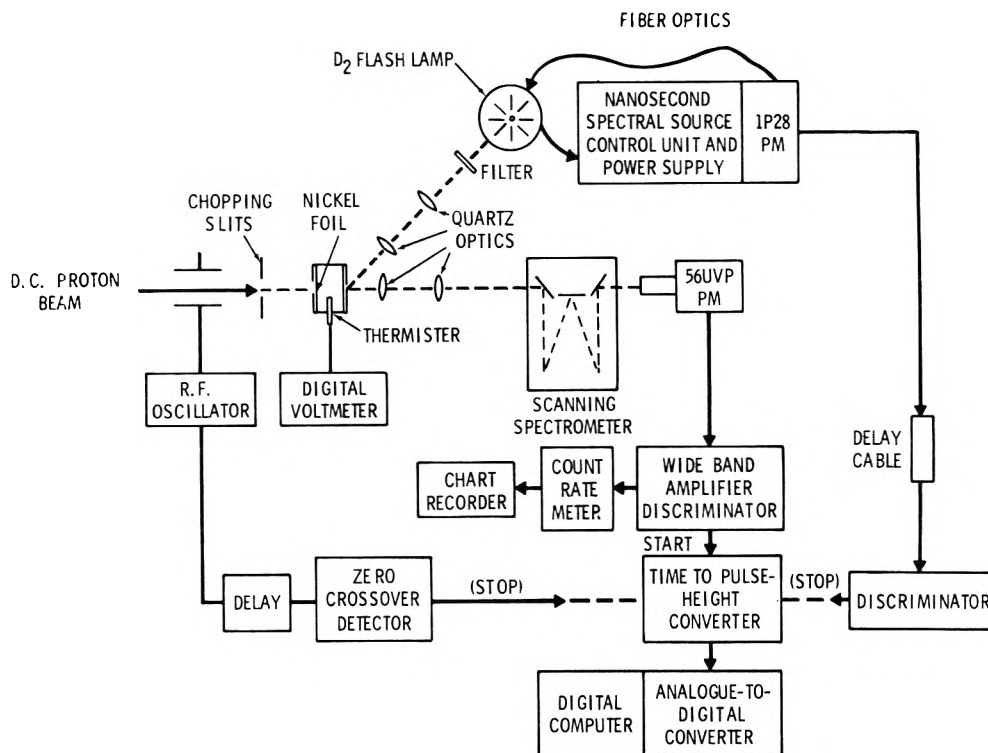


Figure 1. Delayed coincidence counting system.

focused on a cooled photomultiplier tube. A zero time marker is obtained for ultraviolet excitation by a second detector which observes the exciting light source; for proton excitation the timing marker is generated by signal derived from the rf chopper. Single photon pulses selected within the gated period of a time to pulse height converter are counted as a function of pulse delay after the zero time pulse and displayed in a multichannel analyzer that is interfaced to a small on-line digital computer.

The irradiation cell consists of a cylindrical stainless steel chamber with a 254- μm nickel foil for proton beam entrance and a quartz window for light collection. Continuous flow from a reservoir of deaerated solution replaces irradiated liquid in the target volume.

Results

Dilute solutions (0.01 M) of benzene in cyclohexane were irradiated with both protons and ultraviolet light using the same sample cell and liquid handling technique. Emission spectra appear identical under these two modes of excitation and correspond to fluorescence from the first excited singlet state of benzene. Excimer fluorescence, resulting from the interaction of excited and ground state benzene molecules, is not observed at these concentrations. Fluorescence decay was measured with the scanning spectrometer adjusted to a 4-nm bandpass and centered on the prominent vibrational peak at 278 nm. Sample temperature was monitored with a glass encapsulated thermister placed in the irradiated cell.

Decay curves of this singlet state emission for the two modes of excitation are shown in Figure 2; these curves are uncorrected for the finite time resolution of the excitation and detection systems. For proton excitation, the time response is slightly over 2 ns fwhm and largely represents time spread in the photomultiplier. For ultraviolet excitation, the flashlamp gives an asymmetrical time response of about 10 ns fwhm. Correction for scattered light from the flashlamp, which influences the results in the first 20 ns of the ultraviolet response curve, is determined from measurements on samples of neat

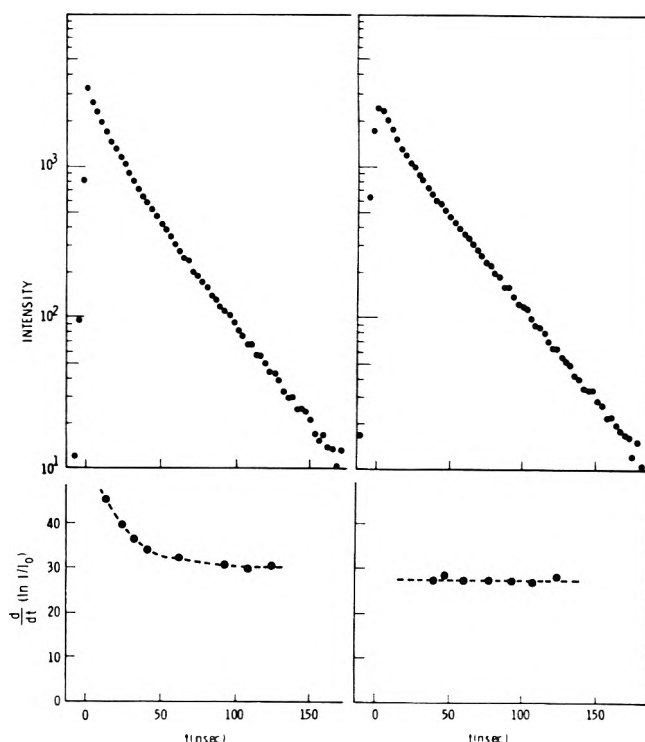


Figure 2. Fluorescence decay of benzene (0.01 M) in cyclohexane, $T = 14.5^\circ\text{C}$: (a) proton excitation (1.7 MeV); (b) UV excitation (2537 Å); (c) logarithmic derivative of intensity for proton excitation, k_p ; (d) logarithmic derivative of intensity for UV excitation, k_{uv} .

cyclohexane. Each data point in the response curves shown in Figure 2 represents a sum over 10 channels of actual data accumulation.

Fluorescence decay for ultraviolet excitation is exponential and can be properly described by a single time-independent rate constant k_{uv} . Fluorescence decay for proton excitation is not initially described by a simple exponential, but may be conveniently parameterized by a time-dependent rate parameter $k_p(t)$ defined as the

negative logarithmic derivative of intensity with respect to time. The lower curves in Figure 2 illustrate this time dependence over several orders of magnitude of fluorescence decay.

Discussion

The decay curves for proton irradiation of benzene in cyclohexane do not exhibit a delayed component as has been reported for numerous scintillator solutions excited by ionizing radiation. Ludwig and others^{1,2} have interpreted this delayed component as fluorescence from excited molecules formed from diffusion and recombination of solute anions and cations. In the case of benzene isolated molecules have a negative electron affinity and, although temporary negative ionic states have been reported⁶ for condensed systems of benzene at 77 K, stable solutions of benzene anions do not occur at room temperature. Also, Bakale et al.⁷ observed no significant scavenging by benzene of electrons in solutions of *n*-hexane at room temperature. Thus, the absence of a delayed component in solutions of benzene in cyclohexane excited by ionizing radiation is not inconsistent with Ludwig's interpretation of solute anions as precursors of delayed fluorescence.

The observed response curves for proton excitation suggest an initial rapid quenching ($t < 50$ ns) that eventually disappears to yield a decay rate equal to that for ultraviolet excitation. If we assume a dynamic quenching of excited molecules by a time dependent concentration of radiation produced quenchers, then

$$dI/dt = -k_{uv}I - k_s Q(t)I \quad (1)$$

where k_{uv} is the decay constant for ultraviolet excitation, k_s is the quenching constant of excited molecules by radiation produced quenchers, and $Q(t)$ is the time-dependent concentration of quenching molecules. Furthermore

$$\ln I/I_0 = -k_{uv}t - \int_0^t k_s Q(t) dt \quad (2)$$

$$\frac{d}{dt}(\ln I/I_0) = -k_{uv} - k_s Q(t) \quad (3)$$

This logarithmic derivative of intensity has been previously defined as κ_p , i.e.

$$\kappa_p = -\frac{d}{dt}(\ln I/I_0) = k_{uv} + k_s Q(t) \quad (4)$$

With these assumptions of dynamic quenching, the fluorescence response curves then give the time dependence of the quencher concentration. By comparing decay rates for proton and ultraviolet excitation we obtain $k_s Q(t)$.

In Figure 3, $\kappa_p - k_{uv}$ is shown as a function of inverse time. The curve is a fit to the data by the equation

$$k_s Q(t) = \kappa_p - k_{uv} = A/(1 + Bt) \quad (5)$$

with $A = 0.085 \text{ ns}^{-1}$ and $B = 0.33 \text{ ns}^{-1}$.

Any assumed mechanism of excited state quenching that is to be consistent with our experimental results must predict the time dependence of eq 5. Furthermore, values of the parameters A and B derived from this assumed mechanism of quenching should be consistent with established radiochemical data on condensed systems.

One such mechanism that would predict the correct time dependence but gives unreasonable parameters is an initial concentration of quenchers uniformly distributed throughout the solution that disappear through bimolecular recombinations, i.e.

$$dQ/dt = -k_q Q^2 \quad (6)$$

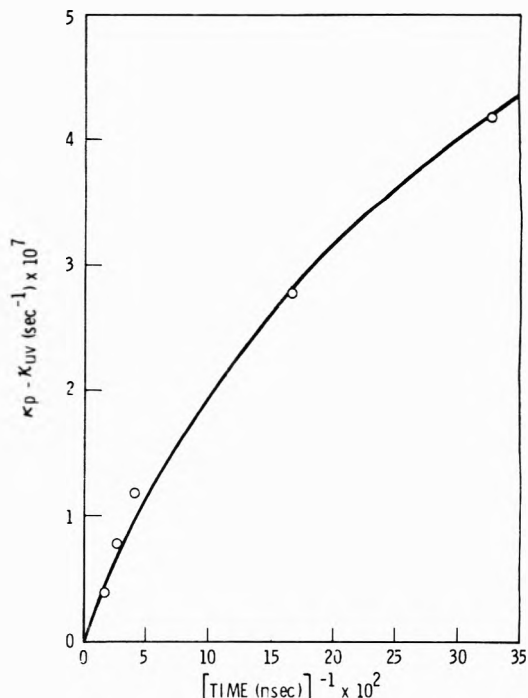


Figure 3. $\kappa_p - \kappa_{uv}$ as a function of time after excitation, 0.01 M benzene in cyclohexane, $T = 14.5^\circ \text{C}$.

and

$$Q(t) = Q_0/(1 + k_q Q_0 t) \quad (7)$$

where k_q is the second-order rate constant for disappearance by recombination and Q_0 is the concentration at $t = 0$. If such a mechanism were responsible for excited state quenching, then the initial concentration Q_0 and therefore the fluorescence decay rate would depend on proton beam intensity. However, the proton beam current was varied over three orders of magnitude in intensity with no observed change in fluorescence decay shape. Also, the initial concentration Q_0 determined from eq 7 ($k_q Q_0 = 0.33 \text{ ns}^{-1}$) is unreasonably large for the dose of ~ 1 rad used in these experiments. If k_q is diffusion limited, then $Q_0 \sim 10^{-2} \text{ M}$ and the G value for production of quenching species must exceed 10^7 . This G value is obviously unrealistic.

A more reasonable mechanism which assumes an initial high concentration of quenching species and also predicts the correct time dependence is excited state quenching by transient species within individual proton tracks. If we assume that N_0 quenching species are created along a proton track with uniform density inside a cylinder of initial radius r_0 then the radial density is expressed in terms of the temporal evolution of the track core. This track core can be expressed as

$$r^2(t) = r_0^2 + 2Dt \quad (8)$$

where D is the diffusion coefficient describing diffusion of quenching molecules in solutions of cyclohexane. The concentration is then

$$Q(t) = N_0/v = N_0/\pi l r_0^2 (1 + 2Dt/r_0^2) \quad (9)$$

By comparing eq 5 and 9 we obtain $r_0^2/2D = 3 \text{ ns}$. The initial radius r_0 can be determined if the diffusion coefficient D of the quenching species is known. If we take $D = 2 \times 10^{-5} \text{ cm}^2 \text{ s}^{-1}$, a value typical of species of molecular size in cyclohexane, then $r_0 \sim 35 \text{ \AA}$. Simplified track structure models in liquid systems predict a track core radius within a factor of 2 of this value.⁸ The G value for production of excited state quenchers can also be estimated

from eq 5 and 9. If the excited state quenching constant k_e is diffusion limited then $G \sim 0.5$.

Intratrack quenching from this distribution of quenching molecules predicts no change in decay with variation in proton beam current. Increasing the beam current merely increases the number of proton tracks and does not change the local quencher density along the track. At the maximum proton beam current, proton tracks are on the average 2000 Å apart so there is little chance for track-track interaction.

Quenching by transient species (i.e., radicals) has been previously invoked by Beriman⁹ as an explanation of low fluorescence yields from scintillator solution under α particle excitation. Our data suggest that such a mechanism is responsible for excited state quenching and, furthermore, this quenching is an intratrack phenomena. This simple theory of track expansion is consistent with

our experimental data and gives reasonable values of initial track radius and G value for production of excited state quenching species.

References and Notes

- (1) P. K. Ludwig, *Mol. Cryst.*, **4**, 147 (1968).
- (2) D. Paligoric and J. Klein, *Int. J. Radiat. Phys. Chem.*, **4**, 359 (1972).
- (3) E. L. Frankevich, T. Morrow, and G. A. Salmon, *Proc. R. Soc. London, Ser. A*, **328**, 445 (1972).
- (4) W. P. Helman, *J. Chem. Phys.*, **51**, 354 (1969).
- (5) L. L. Nichols and W. E. Wilson, *Appl. Opt.*, **7**, 167 (1968).
- (6) T. R. Tuttle, Jr., and S. L. Weissman, *J. Am. Chem. Soc.*, **80**, 5342 (1958).
- (7) G. Bakale, E. C. Gregg, and R. D. McCreary, *J. Chem. Phys.*, **57**, 4246 (1972).
- (8) R. D. Cooper and R. W. Wood, Ed., "Physical Mechanisms in Radiation Biology", Technical Information Center, Office of Information Services, U.S. Atomic Energy Commission, 1974.
- (9) I. B. Beriman, R. Grismore, and B. G. Oltman, *Trans. Faraday Soc.*, **59**, 2010 (1963).

Kinetic Isotope Effects and Intermediate Formation for the Aqueous Alkaline Homogeneous Hydrolysis of 1,3,5-Triaza-1,3,5-trinitrocyclohexane (RDX)

John C. Hoffsommer,* Donald A. Kubose, and Donald J. Glover

Naval Surface Weapons Center, White Oak Laboratory, Silver Spring, Maryland 20910 (Received October 1, 1976)

Publication costs assisted by the Naval Sea Systems Command, Washington, D.C.

The kinetics and activation parameters for the aqueous alkaline hydrolysis of hexaproteo (RDX- h_6) and hexadeuterio (RDX- d_6) 1,3,5-triaza-1,3,5-trinitrocyclohexanes with hydroxide ion concentrations between 0.020 and 0.25 M and temperatures of 25.0, 35.0, and 45.0 °C have been investigated. Both RDX- h_6 and RDX- d_6 showed good second-order rate constants for the expression, $-d(\text{RDX})/dt = k_2(\text{OH}^-)(\text{RDX}) = k_1(\text{RDX})$, where k_1 is the first-order rate constant with excess hydroxide ion. At 25.0 °C the kinetic isotope effect for k_2 (RDX- h_6)/ k_2 (RDX- d_6) = 2.4. Mass spectral evidence for two short-lived intermediates, pentaproteo (I- h_5) and pentadeuterio (I- d_5) 1,3,5-triaza-3,5-dinitrocyclohexene-1, obtained by loss of the elements of nitrous acid from RDX- h_6 and RDX- d_6 is presented. Products obtained on further hydrolysis of I- h_5 include, NO_2^- , N_2O , NH_3 , N_2 , CH_2O , and HCOO^- , the relative amounts of which depend on the hydroxide ion concentration. A novel method is presented for generating these base sensitive, short-lived intermediates with strongly basic ion-exchange resins.

Introduction

Although the initial slow reaction of secondary nitramines with base has been postulated to be the elimination of the elements of nitrous acid,^{1,2} subsequent fast reactions have prevented the isolation of any initial products closely related to the starting nitramine. Thus, Jones³ speculates that 1,3,5-triaza-3,5-dinitrocyclohexene-1 (I- h_5) would be a likely initial product formed during a slow E2 elimination of the elements of nitrous acid from 1,3,5-triaza-1,3,5-trinitrocyclohexane (RDX- h_6) during alkaline hydrolysis in methanol. If, as Jones suggests, the first step for alkaline hydrolysis of RDX- h_6 is proton abstraction from the acidic methylene hydrogens between two adjacent nitramine groups, a difference in hydrolysis rate would be expected where the methylene hydrogens of RDX- h_6 were replaced with deuterium atoms (RDX- d_6). We wish now to report our findings concerning the kinetics and intermediate formation for the alkaline homogeneous hydrolysis of RDX- h_6 and RDX- d_6 in water.

Experimental Section and Results

Materials. RDX- h_6 was recrystallized three times from acetone, dried, and checked for purity by TLC, VPC, and GC/MS. RDX- d_6 was generously obtained from S. Bulusu, Picatinny Arsenal, Dover, N.J., and checked for purity by

the same techniques used for RDX- h_6 . The isotopic purity of RDX- d_6 was 99+% by mass spectral analysis.

Analysis. Aqueous solutions of RDX- h_6 and RDX- d_6 were analyzed by vapor phase chromatography of benzene extracts using 2,4,6-trinitrotoluene (TNT) as an internal standard.⁴ In general, a Hewlett-Packard, Model 5750, research gas chromatograph was used with a 4 ft \times 0.25 in. glass column packed with 2.95% Dexsil 300 GC on Chromosorb WAWDMCS, 80/100 mesh; column temperature, 175 °C; injection port, 180 °C; carrier gas, argon/methane, 95/5; flow rate, 192 mL/min; Ni-63 detector temperature, 290 °C; pulse, 150 μ s; attenuation, \times 80. Dilutions were made so that the final concentrations were approximately 7.4×10^{-6} M RDX and 7.1×10^{-7} M TNT and retention times were approximately 200 and 80 s, respectively. Peak heights were used to calculate RDX concentrations by comparisons to standards of known concentrations.

Kinetics. Stock aqueous solutions of 1 to 2 $\times 10^{-4}$ M RDX- h_6 and RDX- d_6 were made by weighing 1 to 2 mg of each into 100-mL volumetric flasks and transferring with a small volume of acetone. The acetone was removed at 30 to 40 °C with a small suction tube with water aspiration. Distilled water was added to the dry residue and the flasks were warmed in a water bath between 50 and 60 °C to

TABLE I: Observed First-Order Rate Constants for the Aqueous Homogeneous Alkaline Hydrolysis of RDX-h₆ with Excess Base^a

% completion	Time, min ^b	RDX-h ₆ × 10 ⁵ , M ^c	10 ⁴ k ₁ , d s ⁻¹
0	0	7.6	
15.8	7.98	6.4	3.5
17.1	11.88	6.3	2.6
28.9	16.05	5.4	3.5
36.8	19.96	4.8	3.8
40.7	27.91	4.5	3.1
42.1	31.97	4.4	2.8
48.7	35.99	3.9	3.1
52.6	40.05	3.6	3.1
76.3	80.06	1.8	3.0
82.9	99.96	1.3	2.9
		Av	3.1 ± 0.2

^a OH⁻ = 8.048 × 10⁻² M. ^b Obtained with an automatic timer, Precision Scientific Co., Chicago, Ill. ^c Gas chromatographic analysis of benzene extract. ^d k₁ = 1/t ln (RDX)₀/(RDX)_t.

effect solution. These solutions were filtered through 0.4 μm millipore filters and analyzed by vapor phase chromatography.

Standard aqueous solutions of RDX-h₆ and RDX-d₆ were thermostated in either 10- or 25-mL volumetric flasks in a constant temperature bath held to ±0.05 °C at least 1 h before a run. Separate flasks containing 0.1–0.5 M aqueous sodium hydroxide were thermostated at the same time. For a given kinetic run, 1–3 mL of the standard base was pipetted into the flask containing the RDX solution. Base concentration was determined after a run by titration with standard 0.1 N hydrochloric acid solution. RDX concentration was determined at a specific time by removing 1.00-mL aliquots of the reaction mixture with a calibrated syringe and extracting immediately with 10, 5, or 3 mL of benzene depending on the extent of reaction. The distribution coefficient for RDX between benzene and water was determined to be 8.2 at room temperature. From 6 to 65 μL of a 4.43 × 10⁻⁴ M TNT solution in benzene was added to the benzene extract as internal standard so that the ratio of the peak heights for RDX and TNT was approximately unity in the chromatographic analysis. The results of one kinetic run for the hydrolysis of RDX-h₆ is shown in Table I.

The first-order rate constants, k₁, for both RDX-h₆ and RDX-d₆ were found to vary with OH⁻ concentration and indicated that the OH⁻ ion was involved in the rate-determining step. Table II shows first-order dependence for hydroxide ion for basic hydrolysis of both RDX-h₆ and RDX-d₆.

Second-order rate constants, k₂, were calculated from the first-order rate constant, k₁, using the expression, k₂ = k₁/OH⁻. The k₂ values obtained for the aqueous homogeneous alkaline hydrolysis of both RDX-h₆ and RDX-d₆ show the kinetic isotope effect as a function of temperature, Table III.

Heats of activation, ΔH[‡], for the basic hydrolyses of RDX-h₆ and RDX-d₆ calculated from these k₂ values were found to be 23.0 ± 0.2 and 24.1 ± 0.3 kcal mol⁻¹, respectively, while the corresponding entropies of activation, ΔS[‡], for these hydrolyses were calculated to be 8 ± 1 and 10 ± 1 cal deg⁻¹, respectively. Errors were estimated by the method of Purlee, Taft, and De Fazio.⁵

RDX-h₆ Intermediate (I-h₅) Formation in Water. An 1.98 × 10⁻⁴ M aqueous solution of RDX-h₆ (90 mL) was stirred vigorously with 10 mL of benzene. To this mixture was added 1.42 mL of 17.5 M sodium hydroxide to give a final OH⁻ concentration of 0.272 M in the aqueous phase.

TABLE II: Order with Respect to Hydroxide Ion for Reaction with RDX-h₆ and RDX-d₆ in Water at 25.0 °C

RDX-h ₆			RDX-d ₆		
OH ⁻ , M	10 ⁴ k ₁ , s ⁻¹	Order ^a	OH ⁻ , M	10 ⁴ k ₁ , s ⁻¹	Order ^a
0.0271	1.2		0.0279	0.37	
0.2450	9.8	0.95	0.248	3.9	1.1
0.0735	2.9		0.0667	1.2	
0.2450	9.8	1.0	0.2185	3.5	0.90
0.0735	2.9		0.0279	0.37	
0.1370	5.7	1.1	0.2015	3.0	1.1

^a Value of x from, k₁₋₁/k₁₋₂ = (OH₁₋₁⁻)/(OH₁₋₂⁻)^x, where k₁₋₁ and k₁₋₂ are first-order rate constants for the disappearance of RDX-h₆ or RDX-d₆ at a given hydroxide ion concentration.

TABLE III: Kinetic Isotope Effects for the Aqueous Alkaline Hydrolysis of RDX-h₆ and RDX-d₆^a

Temp, °C	10 ³ k ₂ ^b		k ₂ (RDX-h ₆)/k ₂ (RDX-d ₆)
	RDX-h ₆	RDX-d ₆	
25.0	3.9 ± 0.2 (6) ^c	1.6 ± 0.1 (6)	2.4
35.0	14 ± 1 (6)	6.0 ± 0.3 (4)	2.3
45.0	48 ± 3 (5)	22 ± 1 (5)	2.2

^a Numbers in parentheses indicate number of kinetic determinations. ^b Units M⁻¹ s⁻¹; second-order rate constants were calculated from first-order k₁ values obtained from at least three different OH⁻ concentrations between 0.020 and 0.25 M. ^c Ionic strength for all runs between 0.020 and 0.25; rate decreased only 17% in 1.71 M aqueous NaCl and OH⁻ = 0.0651 in a separate run.

After 5 min a gas chromatographic trace of the benzene extract showed a peak at 1.3 min (I-h₅) in addition to the RDX-h₆ peak at 3.36 min.

RDX-h₆ Intermediate (I-h₅) Formation on Basic Ion-Exchange Resins. A 1.98 × 10⁻⁴ M aqueous solution of RDX-h₆ was passed through a strongly basic ion-exchange resin⁶ at the rate of 5 resin volumes/min. The pH of this effluent was 7.78. Chromatographic analysis of a benzene extract of this effluent gave a trace with peak retention times which were identical with that found in the homogeneous hydrolysis of RDX-h₆. On standing the pH of the aqueous unbuffered effluent containing I-h₅ decreased to pH 5.68 while the peak corresponding to I-h₅ decreased 98%. No height change was noted for the RDX-h₆ chromatographic peak. A number of attempts were made to isolate I-h₅ by concentration and separation from RDX-h₆ on TLC plates. These attempts were unsuccessful apparently due to the volatility of I-h₅ as well as its hydrolytic instability. Although a wide variety of conditions was explored using the basic resin, I-h₅ was always contaminated with RDX-h₆. Finally, GC/MS techniques were employed to separate and establish the identity of I-h₅.

Mass Spectral Analysis of I-h₅ and I-d₅ Intermediates. The intermediates I-h₅ and I-d₅ were prepared by separately passing 100 mL of aqueous 8.73 × 10⁻⁵ M RDX-h₆, then 100 mL of aqueous 8.16 × 10⁻⁵ M RDX-d₆ through 10 g of Amberlite 410 basic ion-exchange resin⁷ in 12 to 13 min, respectively. In each case the effluents were extracted with 100 mL of high-purity benzene.⁸ The extracts were concentrated to approximately 1 mL by boiling, and further concentrated to 5 to 10 μL in tapered tubes under vacuum. These concentrated benzene solutions were injected directly into the GC/MS (Varian MAT 111) with the following conditions: injection port 190 °C; separator, 195 °C; inlet line, 195 °C; column, 6 ft × 1/8 in. SS packed with 3.4% Dexsil 300 GC on Chromosorb WAWDMCS, 80/100 mesh; temperature programed, 140 °C to 220 °C at 20 °C/min; ion source pressure, 5 × 10⁻⁶

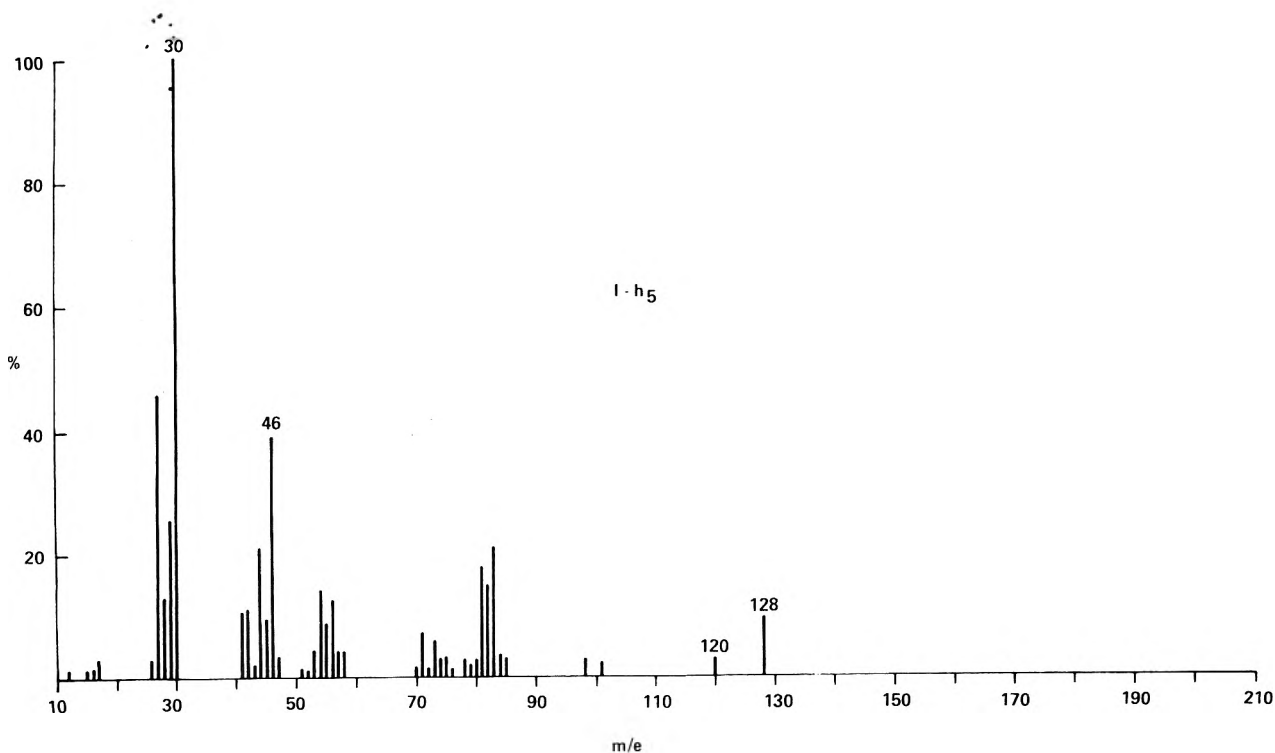
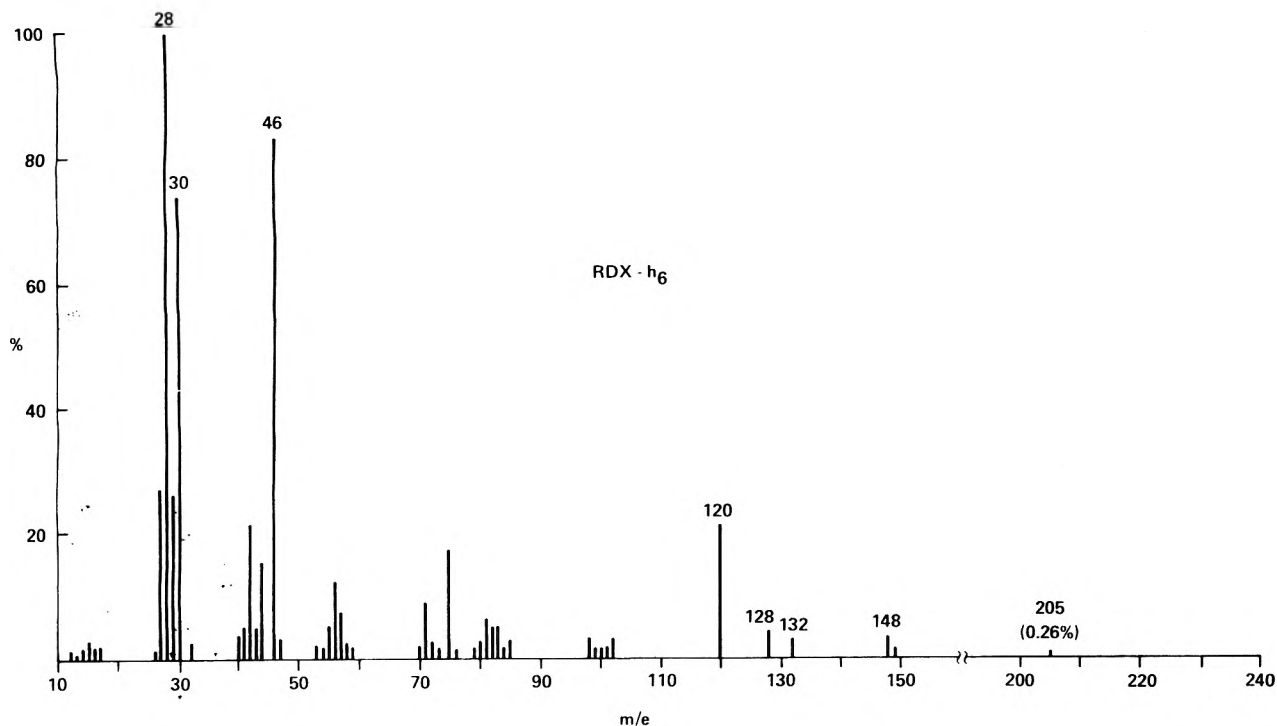
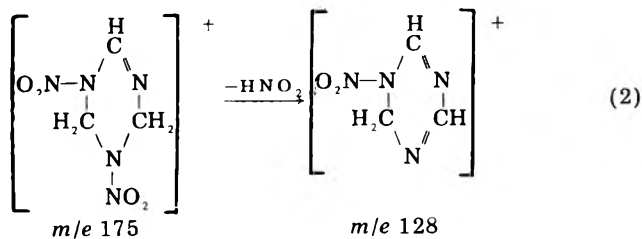


Figure 1. Mass spectra of RDX-h₆ and hydrolysis intermediate, I-h₅.



in the mass spectrum of I-h₅ can also arise by a similar mechanism.

The mass spectra of deuterium labeled RDX-d₆ and its hydrolysis intermediate, I-d₅, are shown in Figure 2. Of

the differences between the mass spectra of I-h₅ and I-d₅, the ones significant to the above discussion are increases in *m/e* of the peak at *m/e* 120 to *m/e* 122 and *m/e* 128 to *m/e* 132. This shows that the *m/e* 128 ion contains four hydrogens and that the *m/e* 120 ion contains two hydrogens. This observation is consistent with the proposed structure, I-h₅, as the intermediate hydrolysis product from RDX-h₆.

The RDX-h₆ hydrolysis intermediate, I-h₅, rapidly reacts with hydroxide ion, Table IV, to give a number of products, Table VII, indicating ring opening. The hydrolyses of both RDX-h₆ and I-h₅ show first-order dependence on hydroxide ion, Tables II and IV, while a comparison of their

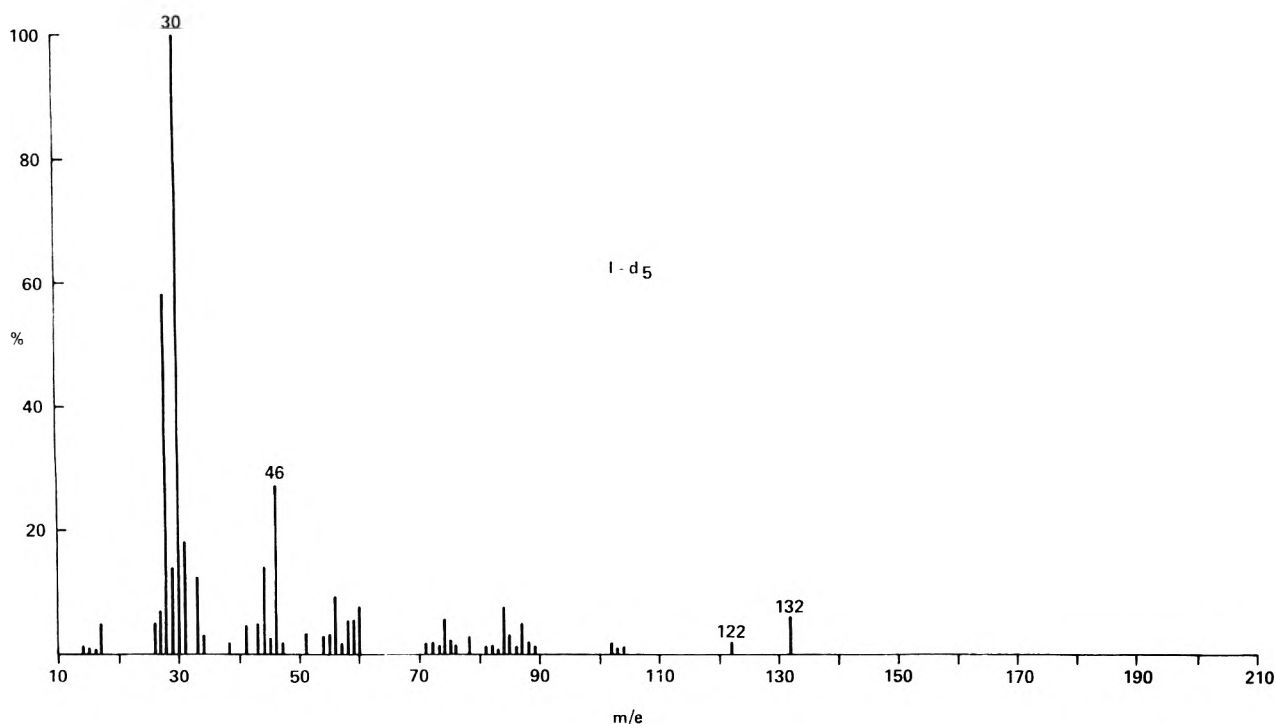
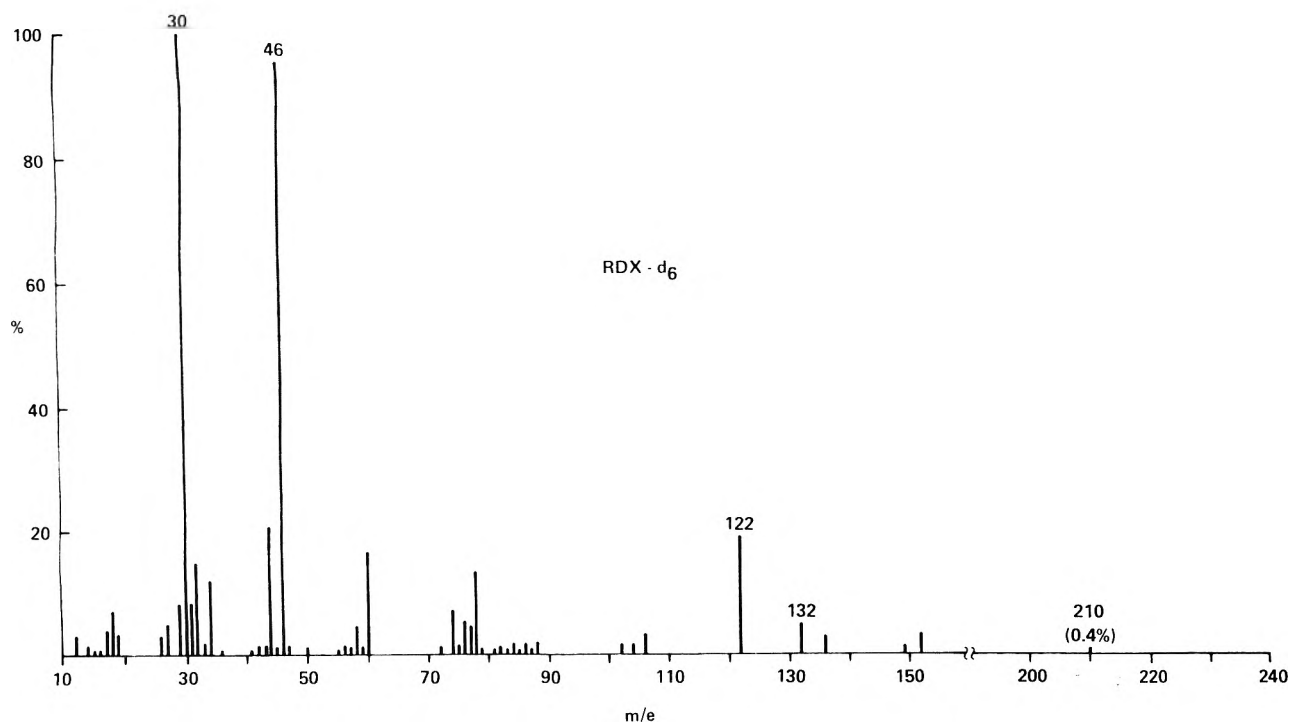


Figure 2. Mass spectra of RDX-d₆ and hydrolysis intermediate, I-d₅.

second-order rate constants show that $k_2(\text{I-h}_5)/k_2(\text{RDX-h}_6) = 1 \times 10^5$ at 25.0 °C, Tables III and IV.

It is somewhat surprising that the major hydrolysis path of I-h₅ does not appear to involve a second proton abstraction followed by loss of nitrite as has been speculated by Jones.³ Only in 50% (19 M) aqueous sodium hydroxide under heterogeneous conditions were 2 mol of nitrite ion produced, Table V. It might also be mentioned here that under all our conditions no evidence for nitrate ion formation was found as has been previously reported.¹³

The formation of both HCOO⁻ and CH₂O indicates that ring opening of I-h₅ most likely occurs by hydroxide ion attack on carbon followed by a series of complex bond

cleavages to form NH₃, N₂, and N₂O. The formation of small amounts of H₂ undoubtedly occurs by OH⁻ attack on CH₂O under Canizzaro conditions.¹⁴ Thus, the basic hydrolysis of methylenedinitramine, CH₂(NHNO₂)₂, has been reported¹⁵ to give a mixture of N₂, N₂O, and CH₂O, while the basic hydrolysis of nitramide, NH₂NO₂, to yield N₂O and H₂O is classic.¹⁶

The formation of NH₃ might arise from a small unstable molecule such as aminomethanol, [NH₂CH₂OH], which would be expected to decompose to CH₂O, NH₃, and complex polymeric products.

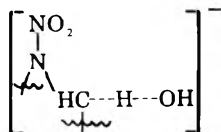
It is of interest to compare the activation parameters for RDX-h₆ basic hydrolysis in several solvents, Table VIII.

TABLE VIII: Activation Parameters for the Homogeneous Alkaline Hydrolysis of RDX-h₆ as a Function of Solvent

Solvent	ΔH^\ddagger ^a	ΔF^\ddagger ^a	ΔS^\ddagger ^b
Water ^c	22.6	20.7	+8
Methanol ^d	27.6	20.7	+23
"Wet" acetone ^e	14.1	17.3	-11

^a kcal mol⁻¹. ^b cal deg⁻¹. ^c This work. ^d Data of W. H. Jones, *J. Am. Chem. Soc.*, **76**, 829 (1954). ^e Data of S. Epstein and C. A. Winkler, *Can. J. Chem.*, **29**, 731 (1951).

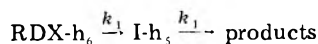
Although the rates of RDX hydrolysis are nearly the same for both water and methanol at 25.0 °C, hydrolysis proceeds over 200 times as fast in acetone. Also, the heats of activation for both water and methanol are nearly twice that with acetone as solvent. ΔH^\ddagger varies linearly with ΔS^\ddagger and gives a slope of 378 K as the isokinetic temperature. Since this temperature lies fairly near the experimental temperature (298–319 K), the formation of molecular complexes with solvent is implied.¹⁷ The large differences found in the entropies of activation for the three solvents could be rationalized in terms of differing degrees of solvation for both the OH⁻ ion as well as the RDX-h₆. The hydroxide ion would be expected to be more highly hydrogen bonded in water and methanol solvents, and, thus, more structurally ordered in the ground state than in acetone solvent. On this basis, more solvent disorientation would be expected for water and methanol solvents in passing through the activated complex than with acetone.



activated complex

Considering the transition state as a negatively charged complex, one would expect that an increase in ionic strength should have little effect on the hydrolysis rate, as found, Table III.

Finally, it is not surprising that the transient hydrolysis intermediate, I-h₅, has not previously been detected since I-h₅ hydrolyzes 10⁵ times as fast as RDX-h₆ at 25.0 °C, Tables III and IV. Viewing the kinetics as a consecutive irreversible process of the type



where k_1 and k_1' are the respective first-order hydrolysis constants in excess base, it is possible to derive an expression for the formation of a maximum concentration

of I-h₅.¹⁸ Since $k_1 = k_2(\text{OH}^-)$ for both RDX-h₆ and I-h₅, Tables II, III, and IV, the following expression may be written, $(\text{I-h}_5)_{\text{max}} = (\text{RDX-h}_6)_0 (k_2'/k_2)^{k_2/k_2-k_2'}$, where k_2' and k_2 are the hydrolysis second-order rate constants for I-h₅ and RDX-h₆, respectively, and $(\text{RDX-h}_6)_0$ is the initial concentration of RDX-h₆. From this expression it is seen that $(\text{I-h}_5)_{\text{max}} = 10^{-5}(\text{RDX-h}_6)_0$. Only by rapid removal of I-h₅ from OH⁻ ion is it possible to increase the concentration of I-h₅. This has been accomplished by allowing RDX-h₆ to react with OH⁻ in the presence of benzene, and, by rapidly flowing a solution of RDX-h₆ in water through a strongly basic ion-exchange resin where the OH⁻ reactive groups are fixed. This latter technique might well be used to form other transient intermediates with a variety of reactive nucleophiles on the ion-exchange resin.

Acknowledgment. The authors wish to thank the Naval Sea Systems Command, Washington, D.C., for their support under Task SF 57572301 for all phases of this work.

References and Notes

- (1) A. P. N. Franchimont and H. Van Erp, *Recl. Trav. Chim. Pays-Bas*, **14**, 224 (1895).
- (2) A. H. Lamberton, *Q. Rev. Chem. Soc.*, **5**, 75 (1951).
- (3) W. H. Jones, *J. Am. Chem. Soc.*, **76**, 829 (1954).
- (4) J. C. Hoffsommer, *J. Chromatogr.*, **51**, 243–251 (1970).
- (5) E. L. Purlee, R. W. Taft, and C. A. De Fazio, *J. Am. Chem. Soc.*, **77**, 837 (1955). See also L. L. Schaefer and F. A. Long in "Advances in Physical Organic Chemistry", Vol. 1, V. Gold, Ed., Academic Press, New York, N.Y., 1963, pp 7–9.
- (6) Amberlite 400 (Rohm & Haas Co., Philadelphia, Pa.), a polystyrene/divinylbenzene copolymer with trimethylammonium hydroxide functionality.
- (7) Same polymer backbone as Amberlite 400 except the functionality is the dimethylethanol-ammonium hydroxide.
- (8) Certified benzene (Fisher Scientific Co.), no glc peaks greater than that given by 0.02 ng/mL of the pesticide, heptachlor epoxide, for use with ec detectors.
- (9) R. G. Bates, "Determination of pH, Theory and Practice", Wiley, New York, N.Y., 1954, p 157.
- (10) P. Griess, *Ber. Dtsch. Chem. Ges.*, **12**, 426 (1879); given in F. D. Snell and C. T. Snell, "Colorimetric Methods of Analysis", Vol. 2, 3rd ed, Van Nostrand, New York, N.Y., 1949, pp 802–804.
- (11) J. Stals, *Trans. Faraday Soc.*, **67**, 1768 (1971).
- (12) S. Bulusu, T. Axenrod, and G. W. A. Milne, *Org. Mass Spectrom.*, **3**, 13–21 (1970).
- (13) F. Somlo, *Z. Gesamte. Schiess Sprengstoffwes.*, **35**, 175 (1940).
- (14) H. S. Fry, J. J. Uber, and J. W. Price, *Recl. Trav. Chim. Pays-Bas*, **50**, 1060–1065 (1931), as reported in J. F. Walker, "Formaldehyde", ACS Monograph Series, F. M. Beringer, Ed., Reinhold, New York, N.Y., 1964, p 214.
- (15) A. H. Lamberton, C. Lindley, and J. C. Speakman, *J. Chem. Soc.*, 1650 (1949).
- (16) J. N. Bronsted and K. J. Pedersen, *Z. Phys. Chem.*, **108**, 185 (1924); also R. P. Bell, "Advances in Catalysis", Vol. 4, Interscience, New York, N.Y., 1952, p 170.
- (17) J. E. Leffler and E. Grunwald, "Rates and Equilibria of Organic Reactions", Wiley, New York, N.Y., 1963, p 394.
- (18) S. Glasstone, "Textbook of Physical Chemistry", 2nd ed, Van Nostrand, New York, N.Y., 1946, p 1077.

Photoionization and Recombination Luminescence of *N,N'*-Disubstituted Dihydrophenazines in 3-Methylpentane at 77 K

U. Brühlmann and J. Robert Huber*

Fachbereich Chemie, Universität Konstanz, D-775 Konstanz, West Germany (Received May 7, 1976; Revised Manuscript Received December 6, 1976)

The photoionization and the isothermal recombination luminescence (ITL) of 5,10-dimethylphenazine (DMP), 5-methyl-10-phenylphenazine (MPP), and 5,10-diphenylphenazine (DPP) were investigated in a 3-methylpentane (3-MP) glass at 77 K using a nitrogen laser as the excitation source. The biphotonic nature of the ionization and the particular photophysical properties of these molecules enables one to control the amount of ionization products by simply varying the laser pulse repetition frequency. The slight deviation of the ITL spectra from those of the normal fluorescence and phosphorescence is attributed to differences in the molecular geometry. The ratio of the triplet to singlet molecules, generated following recombination of the electron with the cation, was found to be close to the statistical value of three (DMP: 2.8; MPP: 2.8; DPP: 2.3). From the decay of the ITL the spatial distribution of the trapped electrons around the cations was derived by numerically solving the Smoluchowski equation according to the method of Ichikawa, Yoshida, and Hayashi.

Introduction

Photoionization of organic molecules dissolved in a glassy matrix often leads to stationary cations and stabilized electrons with lifetimes of several minutes or even hours depending on, e.g., the matrix properties, excitation conditions, and the temperature.^{1,2} The subsequent isothermal or photostimulated recombination of the separated charges can produce electronically excited states which may decay by radiative means manifested by fluorescence and/or phosphorescence of the initial molecule. The spectral properties, the kinetics and efficiency of this recombinator luminescence contain important information not only on the photoionization process and the relaxation of the excited molecule formed upon charge recombination, but also on the spatial distribution and transport properties of trapped electrons in the matrix.^{1,3}

In a comprehensive study Albrecht and co-workers¹ investigated the photoionization of *N,N,N',N'*-tetramethyl-*p*-phenylenediamine (TMPD) in a 3-methylpentane (3-MP) matrix and, in turn, the recombination mechanism under isothermal conditions or by applying light and a high electric field as stimuli. As well as the elucidation of the photoionization mechanism these authors established important features of the 3-MP matrix with respect to electron trapping and mobility. Their results together with the findings of γ -radiolysis studies³ make 3-MP at 77 K one of the most thoroughly investigated matrices.

Photoionization and recombination luminescence experiments in polar matrices for compounds other than TMPD have recently been published for diphenylamine, carbazole, indole, and tryptophan.⁴⁻⁶ In the present communication we report on the photoionization and recombination luminescence of the *N,N'*-disubstituted dihydrophenazines 5,10-dimethylphenazine (DMP), 5-methyl-10-phenylphenazine (MPP), and 5,10-diphenylphenazine (DPP) (formula cf. Figure 3) in a 3-MP matrix at 77 K. This system proved to be very suitable for studying these processes. In particular, the spectral properties and the decay characteristics of the isothermal recombination luminescence (ITL) were investigated and the ratio of the triplet to singlet states produced following charge recombination was established.

Experimental Section

The *N,N'*-disubstituted dihydrophenazines were synthesized according to a published procedure.⁷ After recrystallization and sublimation the melting points of these compounds were 152 °C (DMP), 117 °C (MPP), and 283 °C (DPP). 3-Methylpentane was purified by three cycles of column chromatography (aluminum oxide 90, Merck). After this procedure the optical density was found to be 0.1/cm at 237 nm. Excitation of the samples and recording of transient species were performed with a laser flash apparatus. This instrument consists of a nitrogen laser (Model 100 A, Lambda Physik, Göttingen) with a pulse energy of 2 mJ and a half-width of 3 ns, a monitoring lamp (Osram XBO 250W4) with a pulsing unit (Model 410, Applied Photophysics), a high intensity monochromator (Bausch & Lomb), and a RCA 1P28 photomultiplier tube. A pulse generator (Model 1901 A, Hewlett-Packard) drives the laser at a standard frequency of 7 Hz and an electronic shutter (Compur Electronic) extracts single laser pulses. Under these conditions the energy of the selected pulses, measured with a calibrated photodiode (ITT, F-4018 UVG), was found to be very reproducible. Corrected emission spectra were recorded on a computerized luminescence spectrometer system which is described in detail elsewhere.⁸ Fluorescence lifetimes were determined with the time correlated single photon counting technique⁹ using an Ortec Model 9200 nanosecond fluorescence spectrometer with a Spex Minimate analyzing monochromator. The samples were deoxygenated either by repeated freeze-pump-thaw cycles or by bubbling nitrogen gas through the solution. To avoid formation of aggregates and/or microcrystals all experiments were performed with highly diluted samples (5×10^{-6} to 7×10^{-5} M).

Results

A recently published spectroscopic study on the DMP, MPP, and DPP molecules¹⁰ was concerned with the absorption and emission spectra, the fluorescence and phosphorescence lifetimes, and the emission quantum yields. Some of these results pertinent to the present investigation are given in Table I. Using laser flash excitation ($\bar{\nu} = 29670 \text{ cm}^{-1}$) the three amines exhibit a strong triplet-triplet (T-T) absorption around 22000 cm^{-1}

TABLE I: Fluorescence (ϕ_f), Phosphorescence (ϕ_p), and Intersystem Crossing (ϕ_{isc}) Quantum Yields, Lifetimes τ , and Ratio of the Recombination Fluorescence to Phosphorescence Quantum Yields (A_{RP}/A_{RF}) of DMP, MPP, and DPP in 3-MP at 77 K^a

Molecule	IP _g , eV		τ_f , ns	k_{isc} , s ⁻¹	τ_p , s		ϕ_f	ϕ_{isc}	ϕ_p	A_{RP}/A_{RF}	$\alpha = \phi_{RT}/\phi_{RS}$
	Vert	Adiab			298 K	77 K					
DMP	6.57	6.3	122	3.3×10^6	8×10^{-6}	1.4	0.60	0.40	0.10	1.35	2.8
MPP	6.43	6.2	80	7.0×10^6	6×10^{-6}	1.2	0.47	0.53	0.15	2.00	2.8
DPP		5.9	80	8.9×10^6	1×10^{-5}	1.2	0.35	0.65	0.26	3.37	2.3

^a The data of the normal fluorescence and phosphorescence are from ref 10. The gas phase ionization potentials IP_g of DMP and MPP are from ref 15.

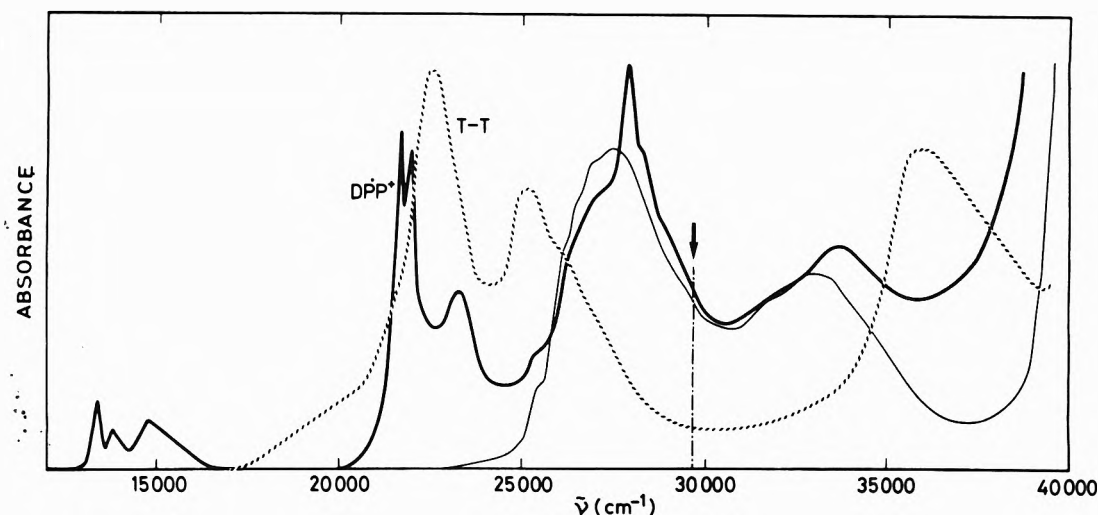


Figure 1. Ground state absorption spectrum (—) and triplet-triplet absorption spectrum (---) of DPP in 3-MP. The former was recorded at 77 K, the latter at room temperature. The absorption spectrum of the cation radical DPP^{•+} in 3-MP at 77 K (strong solid line) contains some ground state absorption above 25 000 cm⁻¹. The arrow marks the laser excitation wavelength.

which, extending into the UV region, strongly overlaps the ground state absorption spectrum. The behavior of DPP shown in Figure 1 is representative for all three compounds. Comparison of the intensity of this T-T absorption with that of anthracene in cyclohexane¹¹ ($\epsilon(23695)$ 6.1×10^4 M⁻¹ cm⁻¹) leads to the following extinction coefficients (M⁻¹ cm⁻¹) for a 3-MP solution at room temperature: DMP $\epsilon(22200)$ $6.2 \pm 2 \times 10^4$; MPP $\epsilon(22500)$ $9.4 \pm 3 \times 10^4$, and DPP (22500) $9.8 \pm 3 \times 10^4$.

At the excitation wavelength of the nitrogen laser, the T-T absorption is still considerable. Here the ϵ values are estimated to be $\sim 1.6 \times 10^4$, 1.2×10^4 , and 1×10^4 for DMP, MPP, and DPP, respectively. With the exception of a slight blue shift, the T-T absorption spectrum in the 3-MP matrix at 77 K is very similar to that at room temperature. The triplet lifetime τ_T , however, is strongly temperature dependent. Between 295 and 77 K, τ_T increases from $\sim 8 \times 10^{-6}$ to ~ 1.2 s (cf. Table I). The latter value coincides with the phosphorescence lifetime.

Continuous irradiation with energy >3.5 eV or pulsed irradiation with the nitrogen laser (repetition frequency 7 Hz) of an oxygen free sample of DPP in a 3-MP matrix at 77 K produces a new absorption which consists of a band with distinct vibrational structure centered at ~ 22000 cm⁻¹ (cf. Figure 1) and a broad structureless band in the near-infrared region peaking around $1.5 \mu\text{m}$. The former absorption is attributed to the cation radical DPP^{•+}, the latter is the well-known absorption spectrum of the matrix-trapped electron e_t⁻. From the published extinction¹² of e_t⁻ ($\epsilon(6000)$ 3.0×10^4 M⁻¹ cm⁻¹) and $\epsilon(21370)$ 1.2×10^4 M⁻¹ cm⁻¹ is derived for the cation radical at its absorption maximum. To verify the assignment of the DPP^{•+} absorption, the radical was also generated by chemical means. Tetranitromethane in 3-MP at room temperature oxidizes DPP to DPP^{•+} and is itself reduced to the trinitromethane

radical anion with a 1:1 stoichiometry.¹³ The spectrum and its extinction of the DPP^{•+} produced in this manner proved to be identical with that of the species formed upon irradiation. The properties and the behavior of DMP and MPP are very similar to those described for DPP.

Given the fact that in the three dihydrophenazine molecules the T-T absorption and the ground state absorption strongly overlap at the laser wavelength and the intersystem crossing process is over 40 times slower than the laser pulse duration, a simple method allows proof of the biphotonic nature of the photoionization. At low repetition frequency of the laser (0.1-Hz single pulse extraction frequency) the generated triplet molecules have relaxed ($\tau_p \sim 1$ s) prior to excitation by a consecutive pulse. At high repetition frequency (7 Hz), however, consecutive pulses hit a relatively high concentration of triplets. Consequently the generation of ionized products only at a high frequency demonstrates that the photoionization is biphotonic involving the lowest triplet state T₁ as an intermediate. The properties of these molecules thus enable one to control the amount of ionized products by simply varying the repetition frequency of the laser pulses. It should be mentioned that this mechanism is clearly observed only at low or moderate light intensity of the laser pulses ($<10^{23}$ photons cm⁻² s⁻¹). At high intensity ($1-2 \times 10^{25}$ photons cm⁻² s⁻¹) the frequency dependence is partly lost because already one single pulse induces ionization. In all these experiments the formation of cation radicals and e_t⁻ was ascertained by the thermally stimulated recombination luminescence (TSL) described below.

If a previously irradiated sample is slowly warmed, a sudden strong luminescence is observed when a particular temperature is reached. To illustrate this behavior the emission intensity vs. temperature curve of DPP in 3-MP

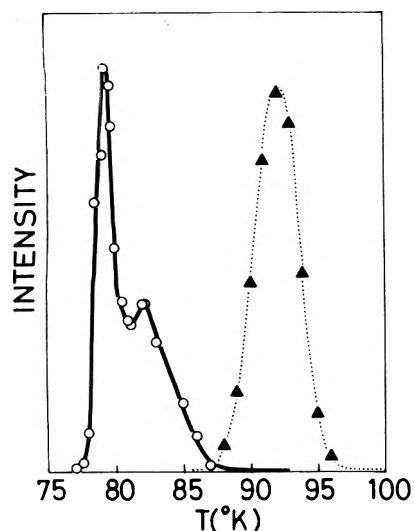


Figure 2. Intensity of the thermally stimulated recombination luminescence of DPP vs. temperature. The curve on the left ($T_{\max} = 79 \pm 2$ K) refers to 3-MP, the one on the right ($T_{\max} = 92 \pm 2$ K) to 2-MTHF.

is presented in Figure 2. The corresponding curve for a 2-methyltetrahydrofuran (MTHF) glass shows the matrix dependence. The luminescence intensity reaches a maximum at 79 ± 2 K for 3-MP and at 92 ± 2 K for 2-MTHF. These results agree well with recently published differential thermal analysis data.¹⁴ They demonstrate that TSL is due to the recombination of thermally mobilized electrons with radical cations.

On the other hand, when the temperature of an irradiated sample is kept constant at 77 K a weak emission can be detected which lingers for several hours. The spectral properties of this isothermal recombination luminescence (ITL) are depicted in Figure 3, along with the natural luminescence. (Each ITL spectrum is a sum of at least five smoothed single spectra recorded at times after irradiation (>2 h) where the intensity of the recombination luminescence changes less than 5% over one scan.) It is easily recognized that the ITL of DMP, MPP, and DPP consists of fluorescence and phosphorescence. The latter,

however, is greatly enhanced with respect to the former as compared with the natural luminescence. This observation, expressed in terms of the ratio of the phosphorescence to fluorescence quantum yields ϕ_p/ϕ_f and ϕ_{RP}/ϕ_{RF} for ITL, is given in Table I. The ITL spectra and the ϕ_{RP}/ϕ_{RF} ratio were found to be independent of the time recorded after irradiation in the range 15 min to about 5 h. A closer look at the ITL spectra reveals that they are slightly red shifted with respect to the natural emission. The 0-0 band of the fluorescence is shifted 200 (DMP), 180 (MPP), and ~ 40 cm^{-1} (DPP), that of the phosphorescence 420 (DMP), 260 (MPP), and ~ 80 cm^{-1} (DPP). Moreover, the bandwidths of the vibrations of the ITL are generally smaller by $\sim 30\%$ and the intensity pattern of the vibrations is changed which is particularly pronounced in MPP.

The decay of the ITL intensity of DMP in 3-MP at 77 K as shown in Figure 5 is similar to those of the DPP and MPP molecules. The kinetics of the decay appears to be complex but independent of the wavelength. Arbitrarily we have divided it into a fast and a slow component by extrapolating the slow decay to zero time and subtracting it from the total signal. The fast component fits first-order kinetics with $\tau = 100$ s, the rate of the slow component, expressed in terms of the half-life $t_{1/2}$, is ~ 100 min for DMP, MPP, and DPP.

The gas phase ionization potentials IP of DMP and MPP were recently measured by photoelectron spectroscopy.¹⁵ The adiabatic IP_g was found to be 6.2 eV for DMP and 6.1 eV for MPP. Owing to experimental difficulties the IP_g of DPP could not be determined by this method. However, a correlation of the above IP's with the known anodic half-peak potentials of the three amines¹⁶ leads to IP_g = 5.9 eV for DPP. As has been shown for a series of aromatic amines the IP_g values are lowered by 0.9 eV in a 3-MP matrix.¹⁷ Consequently, the threshold of photoionization for DMP, MPP, and DPP in a 3-MP glass is expected to be 5.3, 5.2, and 5.0 eV, respectively.

Discussion

The lowest triplet state T_1 of the three amines¹⁰ lies about 2.4 eV (19300 cm^{-1}) above S_0 . Using a N_2 laser

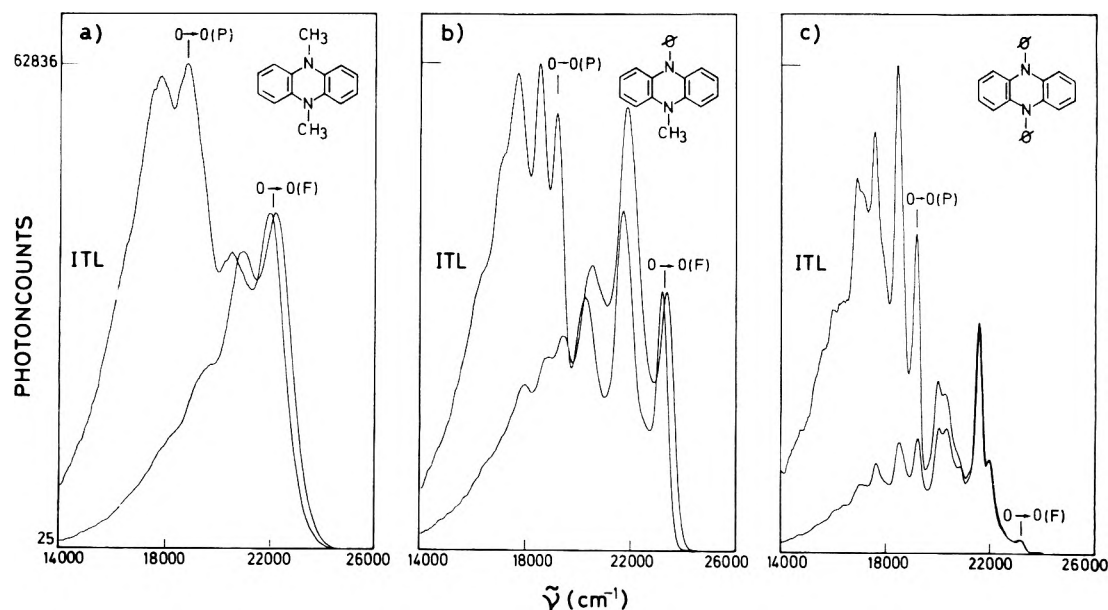


Figure 3. Isothermal recombination luminescence spectra (upper curve) of DMP, MPP, and DPP in 3-MP at 77 K. The lower curves correspond to the normal fluorescence (F) and phosphorescence (P). The 0-0 band of the normal fluorescence is arbitrarily normalized to that of the ITL. The ITL spectra, which were recorded >2 h after irradiation, are each a sum of at least five smoothed single spectra. All emission spectra are corrected for the spectral response of the detection system.

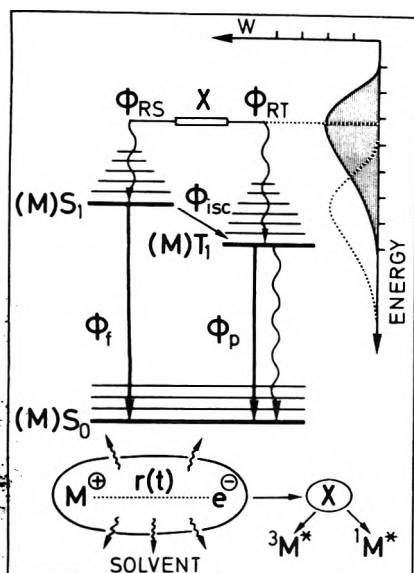
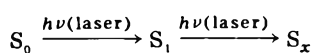


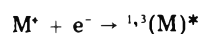
Figure 4. Molecular energy level diagram and hypothetical energy distribution function of the "transition state X" formed during recombination.

excitation source the biphotonic ionization mechanism with T_1 as the intermediate thus leads to a state with an energy of 6.1 eV. This is well above (0.8–1.1 eV) the ionization threshold of the three molecules in a 3-MP glass. Under high laser light intensity an additional mechanism is operative. The intense $S_1 \rightarrow S_x$ ($x > 1$) absorption around 33 000 and 15 000 cm^{-1} observed by laser flash technique and the fact that already one strong laser pulse produces ionization products suggest that this mechanism involves the steps



In addition, the strong overlap between the fluorescence and the T-T absorption spectrum (cf. Figure 1 and 3) favors reabsorption of an emitted photon by another triplet molecule. The contribution to photoionization by such a process seems to be significant considering both the lifetime of S_1 and T_1 (cf. Table I) and the relatively high concentration of S_1 and T_1 produced by intense laser pulses.

As has been shown earlier,¹⁸ the electronically excited singlet and triplet molecules formed upon recombination of the separated charges



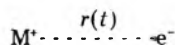
are produced by the same rate-determining step. Based on this mechanism the ratio α of singlet to triplet molecules generated can be expressed in a straightforward manner in terms of the normal emission and ISC quantum yields ϕ ($\phi > 0$) and the areas (photons cm^{-1}) of the recombination fluorescence A_{RF} and phosphorescence A_{RP} (cf. Figure 4)

$$\alpha = \frac{\phi_{RT}}{\phi_{RS}} = \frac{A_{RP}\phi_{isc}\phi_f}{A_{RF}\phi_p} - \phi_{isc} \quad (1)$$

Since the quantum yields pertinent to this equation have been determined for all three compounds (cf. Table I) the ratios are immediately accessible: $\alpha(\text{DMP}) = 2.8$, $\alpha(\text{MPP}) = 2.8$, and $\alpha(\text{DPP}) = 2.3$. If the recombination process is energetic enough that no energy restrictions exist as to the generation of a molecule in an excited singlet or triplet state, it appears that α should be equal to three in view of the threefold spin degeneracy of the triplet state.¹⁹ Taking into account the inherent experimental errors in

quantum yield determinations, particularly when fluorescence and phosphorescence overlap, the α values of DPP and MPP are in excellent agreement with this statistical value. Although the observed α of DPP is smaller, in this case it still lies within the error limits of $\alpha = 3$.

Assuming that all recombination events end with the formation of triplets ${}^3M^*$ and singlets ${}^1M^*$ in the statistical ratio we shall consider the recombination process in some detail. Bullot and Albrecht²⁰ have demonstrated that the photoejected electron remains correlated with its parent cation. Under the Coulomb field of the positive center the electron migrates from trap to trap approaching the cation until the reaction sphere is reached where a "transition state" (X) is formed whose products are ${}^1,3(M)^*$ molecules. During this recombination the dynamic system



interacts with its surroundings (solvent cage). For a given matrix the energy of the state X is therefore dependent on the initial separation distance $r(t_0)$ of the cation and its ejected electron. The narrower the initial distribution function with respect to r , the narrower the energy distribution of the X states (cf. Figure 4). As long as most of the transition states have energies equal to or greater than S_1 , an α value close to three is expected. If, however, the maximum of this energy distribution drops below the S_1 state the ratio α is shifted in favor of T_1 (and also $M(S_0^*)$) and greatly exceeds the statistical value. This situation may be realized when a weakly interacting solvent such as a nonpolar hydrocarbon is replaced by a highly polar solvent. Including the energy requirement, α is always equal to or greater than three or expressed in terms of a measureable quantity, the enhancement factor $(\phi_{RP}/\phi_{RF})/(\phi_p/\phi_f) \geq 4$. Evidently the latter relationship is only valid if all hot triplet molecules generated from X relax to the emitting level of T_1 , otherwise an apparent $\alpha < 3$ is possible.

Comparing this result with experimental findings other than those presented here is difficult. The lack of reliable quantum yield data at low temperature leave most of the few α values in the literature suspect to large errors. The photostimulated recombination luminescence of indole and tryptophan in an ether glass^{4a} gives rise to $\alpha = 4.4$. A change of the solvent to the highly polar solvent mixture ethylene glycol-water alters the α of indole to 20. For diphenylamine and carbazole in an ether matrix one derives an α value of 2.5 ± 0.5 and 4.9 ± 0.5 , respectively, using the data of Muller et al.^{4b} in conjunction with our own $\phi_{ISC(77)}$ of 0.89 for diphenylamine and 0.56 for carbazole.²¹ The consistency of the available data with the proposed mechanism is encouraging. It then seems worthwhile to establish some additional α values, preferably derived from ITL experiments.

The small but clearly discernable differences between the ITL and the normal emission spectra indicate that the geometries of the T_1 and S_1 molecules produced via X differs slightly from those they assume after having absorbed a photon. Generally for large and rigid molecules the change in nuclear configuration upon removal or addition of an electron is small. In the present amines, however, the heterocyclic ring is relatively flexible so that photoionization and charge recombination induces geometrical changes which are not completely annulled during the relaxation $T_x^* \rightarrow T_1$.

Possible transport mechanism of e_t^- in matrices have recently been reviewed by Willard.³ Under our experimental conditions diffusion, caused by local rearrangement

of matrix molecules and quantum mechanical tunneling, appear to be the most likely processes. Since, however, in our experiments the scavenger (cation) concentration is only of the order of 10^{-7} to 10^{-6} M, and thus a factor 10^3 smaller than the estimated trap concentration in 3-MP,²² tunneling is not considered to be the dominant process for cation- e_i^- distances $>10 \text{ \AA}$ ²³ (vide infra).

The interaction between the dynamic system ($M^+ \cdots e^-$) and a given matrix is proposed to depend on the initial separation $r(t_0)$ of the correlated cation and electron. Information about $r(t_0)$ is comprised in the ITL decay characteristics. More specific, the time behavior of the recombination luminescence depends on the spatial distribution of the trapped electrons around the cationic centers following photoionization, and the "diffusion" of e^- in the matrix under a (spherical) Coulomb field. In order to analyze the intensity $I(t)$ of ITL at 77 K and correlate it with the distribution of r , the Smoluchowski equation is applied in the form recently proposed by Ichikawa et al.²⁴ Following this method the Smoluchowski equation is written as

$$\frac{1}{D_0} \frac{W(r, \tau)}{\partial \tau} = \frac{\partial^2 W(r, \tau)}{\partial r^2} + \left\{ \frac{2}{r} + \frac{r_c}{r^2} \right\} \frac{\partial W(r, \tau)}{\partial r} \quad (2)$$

where $\tau = t/t_{1/2}$ is the corrected time (real time divided by half-life), $D_0 = Dt_{1/2}$ is the temperature independent diffusion coefficient, $r_c = e^2/\epsilon kT$ is the Onsager length, and $W(r, \tau)$ is the probability density of finding an electron at "time" τ a distance r away from the cation. The observed time profile of $I(t)$, directly proportional to the electron decay $P(t)$, is then expanded into a series

$$I(\tau) = \sum a_i \exp(-k_i \tau) \quad (3)$$

and the probability density is transformed as $W(r, \tau) = \sum_i R_i(r) \exp(-k_i \tau)$. With this procedure the Smoluchowski equation can be transformed into an ordinary differential equation

$$\frac{d^2 R_i(r)}{dr^2} + \left(\frac{2}{r} + \frac{r_c}{r^2} \right) \frac{dR_i(r)}{dr} + \frac{k_i}{D_0} R_i(r) = 0 \quad (4)$$

with the boundary conditions $[R_i(r)]_{r=r_0} = 0$ and $(dR_i(r)/dr)_{r=r_0} = k_i a_i / (4\pi r_0^2 D_0)$.

When normalized ($I(0) = 1$), the measured ITL time profile $I(\tau)$ (cf. insert Figure 5) corresponds to the electron decay $P(\tau)$. Within experimental error the decay curves for all three amines coincide showing $t_{1/2} = 140$ s. Moreover, the decay was found to be independent of the number of excitation pulses between $\sim 10^2$ – 10^3 and the annealing time between 25 min and 4 h. With regard to our relatively large sample size (inner tube diameter 1 cm, length 6 cm) the latter finding, which indicates an annealing time <25 min, is not unexpected in view of recent results.¹⁴

According to eq 3 the ITL decay is graphically analyzed as $I(\tau) = P(\tau) = 0.55 \exp(-1.45\tau) + 0.22 \exp(-0.37\tau) + 0.23 \exp(-0.07\tau)$. With this expression the initial distribution $W(r, 0)$ of the distance between e_i^- and the cation is numerically evaluated applying the Runge-Kutta-Nystrom method. Estimating $r_0 = 10 \text{ \AA}$ and $r_c(77 \text{ K}) = 1000 \text{ \AA}$ ($\epsilon \sim 2$) and setting $D_0 = 5, 10, 15 \text{ \AA}^2$ the results presented in Figure 5 are obtained. Since neither an experimental value, nor a rough estimate of $D(D_0)$ is available, D_0 was chosen such that the median value of $r_{1/2}(t=0)$ is about 25 \AA ($D_0 = 5 \text{ \AA}^2$, $r_{1/2} = 25 \text{ \AA}$; $D_0 = 10 \text{ \AA}^2$, $r_{1/2} = 30 \text{ \AA}$; $D_0 = 15 \text{ \AA}^2$, $r_{1/2} = 33 \text{ \AA}$). This estimate is based on an electrophotoluminescence study of the TMPD-3-MP system where Bullock and Albrecht²⁰ found

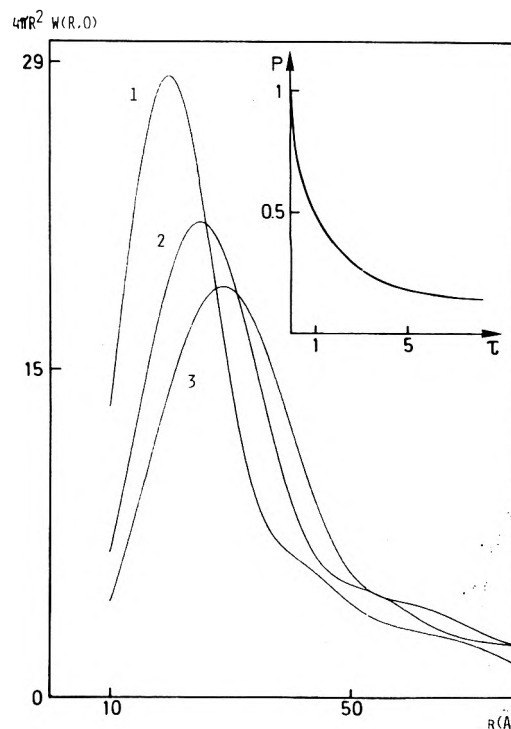


Figure 5. Distribution $W(r, t=0)$ of the distance between the trapped electrons and the cations immediately following photoionization. The corrected diffusion coefficients D_0 (\AA^2) assumed for the calculations were $5(r_{1/2} = 25 \text{ \AA})$; $10(r_{1/2} = 30 \text{ \AA})$, and $15(r_{1/2} = 33 \text{ \AA})$ for curve 1, 2, and 3, respectively. The insert shows the time profile of the ITL decay. The luminescence intensity is proportional to the decay of the electrons $P(\tau)$.

that the majority of electrons are initially separated between 15 and 40 \AA from the cations. Ignoring the unrealistic oscillatory behavior of the distribution curve²⁴ at large r , the shape of $W(r, 0)$ is close to a Gaussian. Probably most important is the narrowness of the distribution. The half-width is only about 10 – 14 \AA and most of the electrons are separated by less than 50 \AA from the cations. These results parallel those of Bullock and Albrecht²⁰ obtained with a similar system but with a different method. With caution the diffusion coefficient D is thus derived from $W(r, 0)$. With $t_{1/2} = 140$ s, the diffusion coefficient for electrons in a 3-MP matrix at 77 K is found to be $\sim 10^{-13} \text{ cm}^2 \text{ s}^{-1}$.

Acknowledgment. Support of this work by the Deutsche Forschungsgemeinschaft is greatly appreciated. Many thanks are due to Ms. E. Kayser for technical assistance, to Dr. W. Arndt and H.-H. Stassen for suggestions with the computer program, and to Ms. M. Mahaney for critically reading the manuscript.

References and Notes

- (1) A. C. Albrecht, *Acc. Chem. Res.*, **3**, 238 (1970).
- (2) R. Lesclaux and J. Jousset-Dubien, "Organic Molecular Photophysics", Vol. 1, J. B. Birks, Ed., Wiley-Interscience, New York, N.Y., 1973, pp 457–487.
- (3) J. E. Willard, *J. Phys. Chem.*, **79**, 2966 (1975).
- (4) (a) D. Muller, M. Ewald, and G. Durocher, *Can. J. Chem.*, **52**, 407 (1974); (b) *ibid.*, **52**, 3707 (1974).
- (5) (a) M. Aubally, M. Bazin, and R. Santus, *Chem. Phys. Lett.*, **31**, 340 (1975); (b) *Chem. Phys.*, **11**, 181 (1975).
- (6) J. Moan, K. K. Ho, and L. Kevan, *J. Chem. Phys.*, **63**, 1285 (1975).
- (7) H. Gilman and J. J. Dietrich, *J. Am. Chem. Soc.*, **79**, 6178 (1957).
- (8) O. Serafimov, H. J. Haik, and J. R. Huber, *Ber. Bunsenges. Phys. Chem.*, **80**, 536 (1976).
- (9) W. R. Ware, "Creation and Detection of the Excited State", Vol. I, Part A, A. A. Lamola, Ed., Marcel Dekker, New York, N.Y., 1971, pp 213–302.
- (10) J. V. Morris, U. Brühlmann, O. Serafimov, and J. R. Huber, *Ber. Bunsenges. Phys. Chem.*, **78**, 1348 (1974).
- (11) H. Labhart and W. Heinzelmann, in ref. 2, pp 298–356.

- (12) J. B. Gollivan and W. H. Hamill, *J. Chem. Phys.*, **44**, 1279 (1966).
 (13) B. H. J. Bielski and A. O. Allen, *J. Chem. Phys.*, **71**, 4544 (1967).
 (14) S. L. Hager and J. E. Willard, *J. Chem. Phys.*, **63**, 942 (1975).
 (15) H. J. Haink and J. R. Huber, *Chem. Ber.*, **108**, 1118 (1975).
 (16) R. F. Nelson, D. W. Leedy, E. T. Seo, and R. N. Adams, *Z. Anal. Chem.*, **224**, 184 (1967).
 (17) A. Bemas, M. Gauthier, and D. Grand, *J. Phys. Chem.*, **76**, 2236 (1972).
 (18) W. M. McClain and A. C. Albrecht, *J. Chem. Phys.*, **43**, 465 (1965).
 (19) B. Brocklehurst, *Nature (London)*, **221**, 921 (1969); B. Brocklehurst, G. Porter, and J. M. Yates, *J. Phys. Chem.*, **68**, 203 (1964).
 (20) J. Bullot and A. C. Albrecht, *J. Chem. Phys.*, **51**, 2220 (1969).
 (21) J. E. Adams, W. W. Mantulin, and J. R. Huber, *J. Am. Chem. Soc.*, **95**, 5477 (1973).
 (22) M. Shirom and J. E. Willard, *J. Am. Chem. Soc.*, **90**, 2184 (1968); A. Ekstrom, R. Suenram, and J. E. Willard, *J. Phys. Chem.*, **74**, 1888 (1970).
 (23) F. S. Dainton, M. J. Pilling, and S. A. Rice, *J. Chem. Soc., Faraday Trans. 2*, **71**, 1311 (1975).
 (24) T. Ichikawa, H. Yoshida, and K. Hayashi, *Bull. Chem. Soc. Jpn.*, **48**, 2685 (1975).

3. The System HBr + (Pr)₄NBr + H₂O at 25 °C. Application of Pitzer's Equations

Rabindra N. Roy,* James J. Gibbons, Ronald Snelling, James Moeller, and Terry White

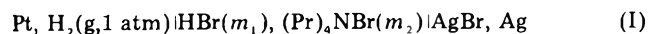
Department of Chemistry, Drury College, Springfield, Missouri 65802 (Received April 2, 1976; Revised Manuscript Received November 10, 1976)

The species tetrapropylammonium bromide has been used to study the effect of large-sized cations on the equilibrium properties of aqueous electrolyte solutions. Activity coefficients of HBr, in HBr + (Pr)₄NBr + H₂O at 25 °C, have been measured at total molality m (where $m = m_1 + m_2$) ranging from 0.05 to 2.0 mol kg⁻¹, using cells containing hydrogen and silver-silver bromide electrodes. It was found that Harned's rule is valid for $m = 0.05, 0.1$, and 0.25 mol kg⁻¹. The results were interpreted in terms of Pitzer's equations for cation-cation doublet (θ_{MN}), cation-anion-cation triplet (Φ_{MNX}), and other interaction parameters. At a dilute concentration (i.e., $m = 0.1$), the results have been discussed in light of the specific interaction coefficient, $\beta_{(\text{Pr})_4\text{N}^+\text{Br}^-}$, a Brønsted-Guggenheim parameter. Also, the results are discussed in terms of the water structural changes caused by the presence of the large-sized hydrophobic cation.

Introduction

The importance of understanding the effects of cation size on the thermodynamic behavior of aqueous electrolytes, as well as the nature of cation-cation and cation-anion-cation interactions, and the behavior of tetraalkylammonium salt-water mixtures, are well recognized.¹⁻⁵ In a continuation of several previous investigations resulting in the final calculation of the binary cation-cation interactions, θ_{MN} , for the three systems HBr + NH₄Br + H₂O,⁶ HCl + NH₄Cl + H₂O,⁷ and HBr + (Bu)₄NBr + H₂O,⁸ we have undertaken a course of electromotive force studies on the HBr + (Pr)₄NBr + H₂O system at 25 °C. Osmotic and activity coefficient data for pure (Pr)₄NBr solutions have been previously reported, from the results of gravimetric isopiestic vapor pressure techniques,^{9,10} but no thermodynamic data based on either isopiestic or emf techniques for aqueous mixtures of HBr + (Pr)₄NBr are available in the literature.

Emf measurements were made at 25 °C using a cell of the type



over the range of total molality m from 0.05 to 2.0 mol kg⁻¹.

Experimental Section

The tetrapropylammonium bromide was obtained from the Eastman Kodak Co., and was recrystallized twice from suitable solvents (such as benzene-ligroin mixtures).¹¹ The gravimetric analyses of the anion as the silver salt indicated that the molality of the solution was accurate to well within $\pm 0.02\%$. Quadruplicate gravimetric determinations of the stock solution of aqueous HBr (about 4 M) agreed to within $\pm 0.01\%$. The doubly distilled and deionized water used in this study had a specific conductivity of less than 1×10^{-6} mho cm⁻¹.

Emf measurements were made with a Leeds and Northrup K-3 potentiometer in conjunction with a Leeds and Northrup d.c. null detector (Model 9829). The cells were thermostated at 25.00 ± 0.01 °C by means of a constant temperature bath. Preparation of the electrodes (the thermal electrolytic type),¹² purification of the hydrogen gas, preparation of the solutions, and oxygen exclusion from the cells by means of hydrogen input have all been previously described.^{6,7} Preliminary emf measurements for 0.1 mol kg⁻¹ showed that the standard emf E° of the Ag|AgBr electrode was equal to 0.071 06 V, in identical agreement with the literature value¹³ of 0.071 06 V, assuming that the activity coefficient of HBr was 0.805¹⁴ at 0.1 mol kg⁻¹. In order to help avoid the significant solubility of AgBr at the highest constant total molality tested ($m = 2.0$ mol kg⁻¹), the cell with the hydrogen electrode was allowed to equilibrate for about 1 h before the Ag|AgBr electrode (kept in a separate standard-joint test tube containing a solution of the same composition) was transferred to the electrode compartment, thus avoiding a drift in the emf values. The equilibrium emf value was noted and recorded every 5 min until no deviation was observed.

Results and Discussion

The results of our various emf measurements, corrected to a partial hydrogen pressure of 1 atm, are summarized in Table I (supplementary material, see paragraph at end of text) as a function of the molality fraction y_2 (which is equal to m_2/m).

According to Harned's rule,¹⁴ the logarithm of the activity coefficient of each electrolyte in a mixture of a constant total ionic strength can be expressed by means of two Harned expressions:

$$\log \gamma_{\text{HBr}} = \log \gamma_{\text{HBr}}^\circ - \alpha_{12}m_2 - \beta_{12}m_2^2 \quad (\text{1})$$

and

$$\log \gamma_{(\text{Pr})_4\text{NBr}} = \log \gamma_{(\text{Pr})_4\text{NBr}}^\circ - \alpha_{21}m_1 - \beta_{21}m_1^2 \quad (2)$$

where γ_{HBr} is the activity coefficient of HBr in the mixture, $\gamma_{\text{HBr}}^\circ$ is the activity coefficient of pure HBr at the same ionic strength as the total ionic strength of the mixture, and α_{12} , β_{12} , etc., are the Harned interaction coefficients (which are independent of the composition but functions of the total ionic strength). From this, it is seen that the linear forms of eq 1 and 2 are known as Harned's equations.

The values of the parameter α_{12} , and the standard deviations $\sigma(\alpha_{12})$ and $\sigma(E)$ are given in Table I and were obtained from a combination of the Nernst equation

$$E = E^\circ - k \log m (m_1 + m_2)\gamma_1^2 \quad (3)$$

with the linear form of eq 1, which resulted in

$$E + k \log m_1 = E^\circ - k \log m - 2k \log \gamma_1^\circ + 2k \alpha_{12}m_2 \quad (4)$$

One can then express eq 4, after proper rearrangement, in a linear and a nonlinear form:

$$E + k \log m_1 = a + bm_2 \quad (5)$$

and

$$E + k \log m_1 = a + bm_2 + cm_2^2 \quad (6)$$

where $\alpha_{12} = b/2k$, $\beta_{12} = c/2k$, and $k = (RT \ln 10)/F$. The values of α_{12} presented in Tables I and II (supplementary material) are in excellent agreement among themselves, confirming thereby the constancy of $E^\circ = 0.07106$ V for the Ag|AgBr electrode. The values of α_{12} at 0.05, 0.1, and 0.25 were taken from the linear form (since Harned's rule is valid within this concentration range), while for those of the other four molalities (0.5, 1.0, 1.5, and 2.0 mol kg⁻¹), the values of the nonlinear form (given in Table I) were used.

Bronsted-Guggenheim Equation. If the Bronsted-Guggenheim equation is assumed to be valid at total molality $m = 0.1$ mol kg⁻¹ for mixtures of HBr (MX) and (Pr)₄NBr (NX), then we can write the expression for $\log \gamma_{\text{HBr}}$ at 25 °C as¹⁵

$$\log \gamma_{\text{HBr}} = -0.5108I^{1/2}/(1 + I^{1/2}) + \frac{1}{2}B_{\text{H,Br}}m_{\text{Br}} + \frac{1}{2}B_{\text{H,Br}}m_{\text{H}} + \frac{1}{2}B_{(\text{Pr})_4\text{N,Br}}m_{(\text{Pr})_4\text{N}} \quad (7)$$

where $I = m_1 + m_2 = m$, and $B_{(\text{Pr})_4\text{N,Br}} = 2\beta/2.3026$, which represents the specific interaction coefficient stemming from the interaction between the cation (Pr)₄N⁺ and the anion Br⁻. Similar explanations may be applied to the concept of $B_{\text{H,Br}}$. Comparison of eq 6 with the linear form of eq 1 leads to a description of the Harned coefficient, α_{12} , as

$$\alpha_{12} = \frac{1}{2}(B_{\text{H,Br}} - B_{(\text{Pr})_4\text{N,Br}}) \quad (8)$$

from which the value of $B_{(\text{Pr})_4\text{N,Br}}$ at $m = 0.1$ mol kg⁻¹ can easily be determined. The value of $B_{\text{H,Br}}$ (equal to 0.287 kg mol⁻¹) was supplied by Guggenheim and Turgeon¹⁶ and that for $\alpha_{12} = 0.3570$ is given in Table I. After computation, $B_{(\text{Pr})_4\text{N,Br}}$ at $m = 0.1$ mol kg⁻¹ is found to be -0.427, as compared with $B_{\text{NH}_4\text{,Br}} = +0.0122$,⁶ or $B_{(\text{Bu})_4\text{N,Br}} = -0.374$,⁸ and can be used to calculate the activity coefficient of (Pr)₄NBr.

Formalism According to Pitzer. The most common method for the evaluation of the interaction parameters such as α_{21} and β_{21} of eq 2 for the activity and osmotic coefficients of mixtures of strong electrolytes are due to

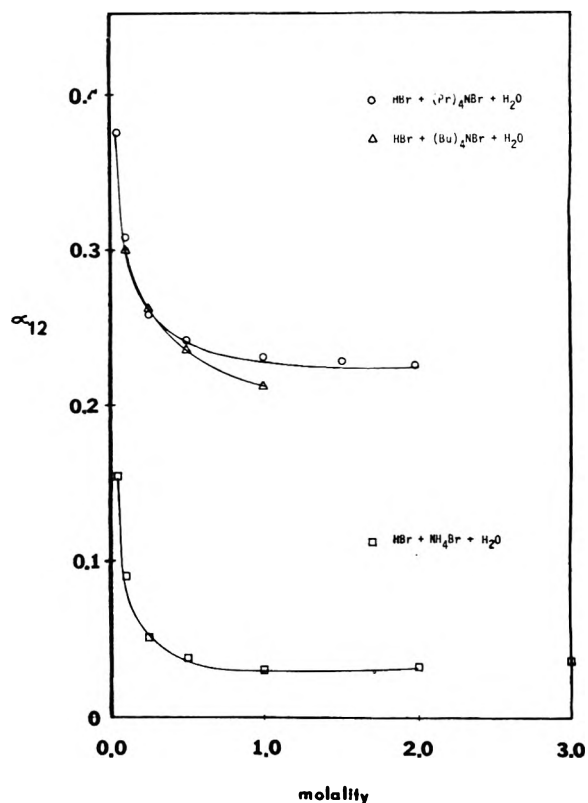


Figure 1. Harned interaction coefficient vs. total molality of Br⁻ for the HBr + (Pr)₄NBr + H₂O system at 25 °C. $\Delta \ln \gamma/m_2$ vs. the parameter $1/2(m_{\text{H}^+} + m_{\text{Br}^-})$.

Scatchard¹⁸ and McKay.¹⁹ In the present study, the more simplified expression of Pitzer¹⁻⁴ for α_{21} and the activity coefficient of HBr in mixtures of MX (HBr) and NX [(Pr)₄NBr] has been adopted, as has been previously done in prior work from this laboratory.^{6,8} This is due to the simplicity of the equations and the fact that each Pitzer parameter has some reasonable physical significance. The finalized version becomes

$$\ln \gamma_1 = f^\gamma + m[B_{\text{MX}}^\gamma + y_2(B_{\text{NX}}^\phi - B_{\text{MX}}^\phi + \theta_{\text{MN}}) + y_1y_2 m \theta'_{\text{MN}}] + m^2[C_{\text{MX}}^\gamma + y_2(C_{\text{NX}}^\phi - C_{\text{MX}}^\phi + \frac{1}{2}\psi_{\text{MNX}}) + \frac{1}{2}y_1y_2\psi_{\text{MNX}}] \quad (9)$$

where θ_{MN} indicates the interactions between H⁺ and (Pr)₄N⁺, and ψ_{MNX} is a measure of the degree of interaction between H⁺, (Pr)₄N⁺, and Br⁻. Equation 9 reduces to the more simplified version (eq 10) after imposing the conditions that $\theta'_{\text{MN}} = 0$, $\psi_{\text{MNX}} = 0$, and y_2 (at the limit) = 0:

$$\ln (\gamma_1/\gamma_1^\circ) = my_2(B_{\text{NX}}^\phi - B_{\text{MX}}^\phi + \theta) + m^2y_2(C_{\text{NX}}^\phi - C_{\text{MX}}^\phi) \quad (10)$$

Combination of the linear form of eq 1 with eq 10 and subsequent reduction leads to

$$\theta = -2.3026\alpha_{12} + f(\phi^0) \quad (11)$$

where

$$f(\phi^0) = (\beta_{\text{MX}}^\phi - \beta_{\text{NX}}^\phi) + (\beta_{\text{MX}}^1 - \beta_{\text{NX}}^1)[\exp(-2m^{1/2})] + m(C_{\text{MX}}^\phi - C_{\text{NX}}^\phi) \quad (12)$$

and

$$B_{\text{MX}}^\phi = \beta_{\text{MX}}^\phi + \beta_{\text{MX}}^1 \exp(-2m^{1/2}) \quad (13)$$

In eq 11, the Pitzer parameter θ (which, in Scatchard's notation is $b_{\text{A,B}}^{(0,1)}$, equal to 2θ ; $g_{\text{M,N}}$ according to Fried-

TABLE III: Values of the Parameter θ , $f(\phi^0)$, α_{12} , α_{21} , and ΔG^E for the HBr + (Pr)₄NBr + H₂O System at 25 °C

m , mol kg ⁻¹	$f(\phi^0)$	$2.3026\alpha_{12}$	$-\theta^a$	$-\alpha_{21}^b$	ΔG^E , cal kg ⁻¹
0.05	0.7683	0.9775	0.2092	0.2598	-0.13
0.1	0.6791	0.8220	0.1429	0.2211	-0.50
0.25	0.5414	0.7090	0.1677	0.1613	-3.1
0.50	0.4310	0.6703	0.2393	0.1134	-13
1.0	0.3247	0.6473	0.3226	0.0672	-50
1.5	0.2658	0.6397	0.3739	0.0416	-113
2.0	0.2244	0.6392	0.4118	0.0236	-201

^a From eq 11. ^b From eq 15.

man,²⁰ δ_{12} from the theory of Guggenheim;²¹ or g_{MN}^* in the Reilly, Wood, and Robinson²³ convention) is a constant that is characteristic of the mixtures but independent of the total molality (as opposed to α_{12} , which is a function of the total molality).

The values of the parameters of eq 12 have been furnished by Pitzer and Mayorga² for (MX), and those of (NX) by Pitzer,²³ who obtained a reasonable fit up to 1.8 m using the following constants:

$$\begin{aligned} \beta_{MX}^0 &= 0.1960 & \beta_{NX}^0 &= -0.0580 & C_{MX}^\phi &= 0.00827 \\ \beta_{MX}^1 &= 0.3564 & \beta_{NX}^1 &= -0.4510 & C_{NX}^\phi &= 0.0469 \end{aligned}$$

After substitution, the resulting equation employing these values becomes

$$f(\phi^0) = 0.2540 + 0.8074 \exp(-2m^{1/2}) - 0.03863m \quad (14)$$

The results of $f(\phi^0)$, θ , α_{12} (from Table I, with the first three values from the linear plots and the remaining four from the nonlinear plots), at each molality, are listed in Table III. It is known⁷ that the emf of cell I is a function of θm . Hence, the weighted average value of θ (apparent) = -0.3428 has more significance at higher molalities than the unweighted average. It is interesting to note from Table III, that the values of θ for the present study decrease with an increase in m , whereas those for the HBr-NH₄Br-H₂O system show that this trend is reversed. This decrease in θ at higher concentrations implies the existence of less hard-core contact between the pairs of (Pr)₄N⁺ and H⁺.

It is also of some significance to calculate α_{21} and compute the trace activity coefficients, γ_1^{tr} , from the following expressions (using the value of θ (actual) = -0.17 obtained from eq 18), where Ψ is taken in account:

$$-2.3026\alpha_{21} = (B_{MX}^\phi - B_{NX}^\phi) + m(C_{MX}^\phi - C_{NX}^\phi) + \theta \quad (15)$$

and

$$\log(\gamma_1^{tr}/\gamma_1^0) = -m\alpha_{12} \quad (16)$$

Equation 16 is obtained with the condition that $y_2 = 1$ and hence $\gamma_1 = \gamma_1^{tr}$ as in the linear form of eq 1. The values of α_{21} and ΔG^E (which are computed from eq 17) are also presented in Table III:

$$\Delta G^E = 2y_1y_2RTm^2\theta \quad (17)$$

where $y_1 = y_2 = 0.5$ and $\theta = -0.17$.

As expected, the excess Gibbs free energy of mixing is significantly higher for the HBr-(Pr)₄NBr-H₂O system than that for the HBr-NH₄Br-H₂O system. This difference is due to cation-cation, cation-anion-cation, and hydrophobic interactions.

All of the calculations discussed thus far were based on the premise that $\Psi_{H^+, (Pr)_4N^+, Br^-} = 0$. It seems appropriate

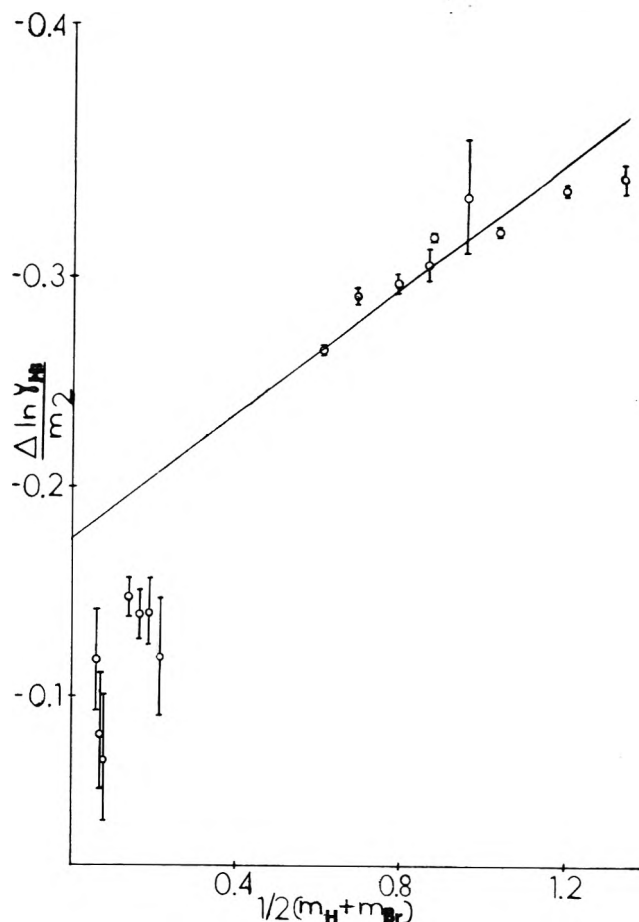


Figure 2. $\Delta \ln \gamma/m_2$ vs. the parameter $1/2(m_{H^+} + m_{Br^-})$.

to compute θ_{MN} and Ψ_{MNX} in the case where Ψ_{MNX} (a measure of the ternary interactions) is not equal to zero. Pitzer²⁴ has derived the following equations, which enable one to do this:

$$\Delta \ln \gamma_{HBr}/m_{(Pr)_4N^+} = \theta_{H^+, (Pr)_4N^+} + 1/2(m_{Br^-} + m_{H^+})\Psi_{H^+, (Pr)_4N^+, Br^-} \quad (18)$$

in which $\Delta \ln \gamma_{HBr} = \ln \gamma_{\text{expt}} - \ln \gamma_{\text{calcd}}$. The values for $\ln \gamma_{\text{expt}}$ were those obtained from eq 3, whereas those for $\ln \gamma_{\text{calcd}}$ were evaluated from

$$\ln \gamma_{HBr} = f\gamma + m[B_{MX}^\gamma + y_2(B_{NX}^\phi - B_{MX}^\phi)] + m^2[C_{MX}^\gamma + y_2(C_{NX}^\phi - C_{MX}^\phi)] \quad (19)$$

where

$$f\gamma = -A\phi[m^{1/2}/(1 + 1.2m^{1/2}) + (2/1.2) \ln(1 + 1.2m^{1/2})] \quad (20)$$

and

$$A\phi = 1/3A_\gamma = 0.392 \text{ (for H}_2\text{O at 25 °C)} \quad (21)$$

B_{MX}^ϕ and B_{NX}^ϕ are the same as those previously shown in eq 13

$$C_{MX}^\gamma = 3/2C_{MX}^\phi \quad (22)$$

and

$$B_{MX}^\gamma = 2\beta_{MX}^0 + (2\beta_{MX}^1/4m)[1 - \exp(-2m^{1/2})](1 + 2m^{1/2} - 2m) \quad (23)$$

Figure 2 represents the plot of the left side of eq 18 against the Ψ coefficient on the right. A straight line graph

with the intercept $\theta = -0.17$ and slope $\Psi = -0.15$ was obtained. This is a useful result and verifies Pitzer's equations, in that there should be a single value of θ and Ψ which become nearly constants at higher molality. As evident from Figure 2, the values of $\Delta \ln \gamma_{\text{HBr}}/m_2$ are neglected in the molality range $m = 0.05$ to 0.5 , since $\Delta \ln \gamma_{\text{HBr}}$ is small due to very little ternary interactions in this dilute region. As expected, the effects of the ternary interactions are greater with an increase in m , whereas the trend for θ is just the opposite (i.e., less prominent at higher molalities). The cosphere effects are considered by Ramanathan, Krishnan, and Friedman²⁵ to have a larger role for aqueous solutions of tetraalkylammonium halides. The relatively high values of θ at low m in the present study reflect the fact that interactions (which include interpenetration and entangling of the propyl chains) between H^+ and $(\text{Pr})_4\text{N}^+$ are of increasing intensity. The value of $\theta_{\text{H}^+(\text{Pr})_4\text{N}^+}$ decreases from a higher value at low molality to a relatively constant value at high molality, whereas that for $\theta_{\text{H}^+,\text{NH}_4^+}$ ⁶ indicates that the trend is reversed.

The triple interactions Ψ_{MMM} , Ψ_{NNN} , and Ψ_{XXX} are believed to be exceedingly small, but Ψ_{MNX} is of reasonable significance when $(\text{Pr})_4\text{N}^+$, H^+ , and Br^- ions come together at higher concentrations, since the propyl chains may be pushed aside to permit the closer approach of the Br^- and H^+ ions to the center of the substituted N^+ . Interpretations of this type of large-sized tetraalkyl hydrophobic cation-anion systems have been made by Rasaiah,²⁶ Frank and Evans,²⁷ and Wood and Anderson.²⁸ The tetraalkylammonium salts tighten the structure of water around them in a way similar to some aliphatic hydrocarbons. Thus, there will be a large structural effect of $(\text{Pr})_4\text{N}^+$ (as compared with NH_4^+) in aqueous solution, which is dependent upon the structure-making properties of the $(\text{Pr})_4\text{N}^+$ ion.^{29,30} Similar studies for $\text{HBr} + (\text{Et})_4\text{NBr} + \text{H}_2\text{O}$ are currently in progress to gain more insight on the complex behavior of mixed aqueous electrolytic solutions.

Acknowledgment. The authors gratefully acknowledge the personal guidance and assistance provided by Professor K. S. Pitzer at the University of California (Berkeley), who not only supplied most of the various parameters required for many of the calculations contained herein, but also furnished several private communications without which this paper could not have been written. Thanks are also

extended to Professor R. H. Wood for his kind comments and constructive criticisms.

Supplementary Material Available: Tables I and II containing additional details concerning the evaluation of the emf data for individual total molalities of $\text{HBr} + (\text{Pr})_4\text{NBr} + \text{H}_2\text{O}$ (3 pages). Ordering information is available on any current masthead page.

References and Notes

- (1) K. S. Pitzer, *J. Phys. Chem.*, **77**, 268 (1973).
- (2) K. S. Pitzer and G. Mayorga, *J. Phys. Chem.*, **77**, 2300 (1973).
- (3) K. S. Pitzer and G. Mayorga, *J. Solution Chem.*, **3**, 539 (1974).
- (4) K. S. Pitzer and J. J. Kim, *J. Am. Chem. Soc.*, **96**, 5701 (1974).
- (5) H. S. Harned and R. A. Robinson, "Multicomponent Electrolyte Solutions", Topic 15, Vol. 2, "International Encyclopedia of Physical Chemistry and Chemical Physics", Pergamon Press, Oxford, England, 1968.
- (6) R. N. Roy and E. Swenson, *J. Solution Chem.*, **4**, 431 (1975).
- (7) R. A. Robinson, R. N. Roy, and R. G. Bates, *J. Solution Chem.*, **3**, 837 (1974).
- (8) R. N. Roy, J. J. Gibbons, C. Krueger, and T. White, *J. Chem. Soc., Faraday Trans. 1*, **72**, 2197 (1976).
- (9) S. Lindenbaum and G. E. Boyd, *J. Phys. Chem.*, **64**, 911 (1964).
- (10) W. Wen, K. Miyajima, and A. Otsuka, *J. Phys. Chem.*, **75**, 2148 (1971).
- (11) A. K. R. Unni, L. Elias, and H. I. Schiff, *J. Phys. Chem.*, **67**, 1216 (1963).
- (12) R. G. Bates in "Determination of pH", 2nd ed, Wiley, New York, N.Y., 1973, pp 283, 331.
- (13) H. B. Hetzer, R. A. Robinson, and R. G. Bates, *J. Phys. Chem.*, **66**, 1423 (1962).
- (14) R. A. Robinson and R. H. Stokes in "Electrolyte Solutions", 2nd ed, Butterworths, London, 1959, pp 481, 438.
- (15) G. N. Lewis and M. Randall in "Thermodynamics", revised by K. S. Pitzer and L. Brewer, McGraw-Hill, New York, N.Y., 1961, Chapter 23.
- (16) E. A. Guggenheim and J. C. Turgeon, *Trans. Faraday Soc.*, **51**, 747 (1955).
- (17) W. Wen and C. L. Chen, *J. Chem. Eng. Data*, **20**, 384 (1975).
- (18) G. Scatchard, *J. Am. Chem. Soc.*, **83**, 2636 (1961).
- (19) H. A. C. McKay, *Trans. Faraday Soc.*, **51**, 903 (1955).
- (20) H. L. Friedman in "Ionic Solution Theory", Interscience-Wiley, New York, N.Y., 1962.
- (21) E. A. Guggenheim, *Trans. Faraday Soc.*, **62**, 3446 (1966).
- (22) P. J. Reilly, R. H. Wood, and R. A. Robinson, *J. Phys. Chem.*, **75**, 1305 (1971).
- (23) K. S. Pitzer, private communication.
- (24) K. S. Pitzer, *J. Solution Chem.*, **4**, 249 (1975).
- (25) P. S. Ramanathan, C. V. Krishnan, and H. L. Friedman, *J. Solution Chem.*, **1**, 237 (1972).
- (26) J. C. Rasaiah, *J. Chem. Phys.*, **52**, 704 (1970).
- (27) H. S. Frank and M. W. Evans, *J. Phys. Chem.*, **13**, 507 (1945).
- (28) R. H. Wood and H. L. Anderson, *J. Phys. Chem.*, **71**, 1871 (1967).
- (29) W. Y. Wen and S. L. Saito, *J. Phys. Chem.*, **68**, 2639 (1964).
- (30) R. L. Kay, T. Vituccio, C. Zarvoyski, and D. F. Evans, *J. Phys. Chem.*, **70**, 2336 (1966); R. L. Kay and D. F. Evans, *ibid.*, **70**, 2325 (1966).

Monomer Concentrations in Binary Mixtures of Nonmicellar and Micellar Drugs

D. Attwood

Pharmacy Department, University of Manchester, Manchester M13 9PL, England (Received September 15, 1976)

Aqueous mixtures of (a) two nonmicellar antiacetylcholine drugs (proprantheline bromide and methantheline bromide) and (b) a micellar antiacetylcholine drug (adiphenine hydrochloride) in combination with a nonmicellar drug (proprantheline bromide) have been examined by light scattering methods. Limiting monomer concentrations, m'_{mon} , were determined either from inflections in the light scattering plots or by integration of the light scattering data according to $\ln x = \int_0^x \{(M/M_{\text{app}}) - 1\} d \ln c$ (where M and M_{app} are the monomer and apparent aggregate weight, respectively, and x is the weight fraction of monomers). The variations of m'_{mon} with the composition of proprantheline-methantheline mixtures could be predicted using equations derived for ideal mixing of micellar surfactants. Appreciable nonideality of mixing was indicated for the adiphenine-proprantheline systems.

Studies of mixtures of ionic hydrocarbon chain surfactants in aqueous solution have led to the general conclusion that the mixed micelle may be regarded as an ideal solution of its components.¹⁻³ Critical micelle

concentrations (cmcs) of the mixtures fall between values of the pure components and the variation of cmc with solution composition may generally be predicted on the assumption of ideality of mixing.

Recent studies⁴ have shown that the self-association in aqueous solutions of the antiacetylcholine drugs, propantheline and methantheline bromide, was not consistent with the mass action model of micelle formation. The pattern of association could be adequately reproduced using a nonmicellar, stepwise association model in which the products of each stage of the association are present in solution in significant amounts, giving a highly poly-disperse system. Although such systems do not possess a critical concentration region at which aggregate formation commences, it may be shown from the light scattering data that the monomer concentration in equilibrium with the aggregates in the systems increases asymptotically toward a limiting concentration, m'_{mon} , as the solution concentration increases. Furthermore, surface tension vs. log concentration plots⁵ for these compounds exhibit inflection points at apparent cmcs which are in reasonable agreement with m'_{mon} values from light scattering. In this investigation the variation of the apparent cmc with solution composition in mixtures of the two nonmicellar drugs, propantheline and methantheline bromide, is reported. The applicability of equations derived for the variation of the cmc in mixtures of micellar surfactants is examined.

In contrast, antiacetylcholine drugs with hydrophobic groups based on diphenylmethane, for example, adiphenine hydrochloride, exhibit typically micellar behavior.⁶ Light scattering plots for such compounds show well-defined inflection points at cmc values similar to those indicated from other techniques. This paper reports on the degree of interaction between components in mixed micellar-nonmicellar systems of propantheline bromide and adiphenine hydrochloride, as determined from the variation of apparent cmc with solution composition. Adiphenine was chosen because of its high cmc compared with propantheline, thereby giving a wide range of cmc values for the mixed systems.

Experimental Section

Materials. Propantheline bromide [(2-hydroxyethyl) diisopropyl methylammonium bromide xanthene-9-carboxylate] and methantheline bromide [diethyl (2-hydroxyethyl) methylammonium bromide xanthene-9-carboxylate] were gifts from G. D. Searle and Co. Ltd. Adiphenine hydrochloride (2-diethylaminoethyl diphenylacetate hydrochloride) was obtained from Ciba Laboratories. Propantheline and methantheline bromide are subject to the purity requirements of the British Pharmacopoeia and the United States National Formulary, respectively, and, as such, contain not less than 98.0% of the specified compound. Adiphenine hydrochloride is of equivalent purity according to information from the suppliers.

Light scattering measurements were made at 303 K with a Fica 42000 photogonio diffusometer (A.R.L. Ltd.) using a wavelength of 546 nm. Aqueous solutions were clarified by ultrafiltration through 0.1 μm Millipore filters until the ratio of the light scattering at angles of 30 and 150° did not exceed 1.10. Refractive index increments were measured at 546 nm using a differential refractometer.

Results and Discussion

Propantheline-Methantheline Mixtures. Light scattering plots for varying molar ratios of these two nonmicellar compounds are presented in Figure 1. The curves all showed a continuous increase in the scattering at 90°, with increase in overall solution concentration, m (mol kg^{-1}). No discontinuities in the concentration dependence of S_{90} , attributable to a cmc, were observed. Monomer concentrations were calculated as a function of the total

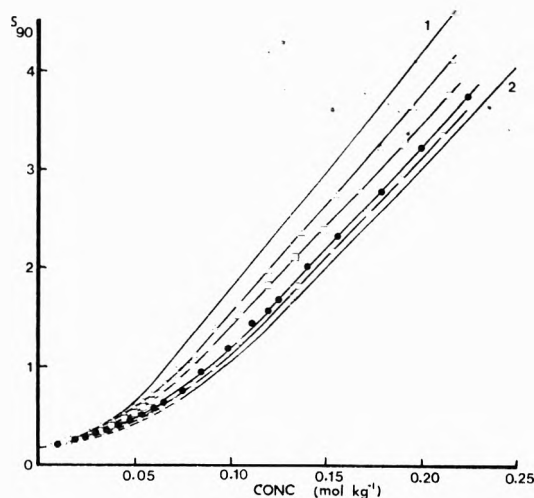


Figure 1. Concentration dependence of the scattering ratio, S_{90} , for aqueous mixtures of propantheline bromide and methantheline bromide. Mol fractions of propantheline: (O) 0.10, (●) 0.25, (□) 0.50, (Δ) 0.75. Data for propantheline (curve 1) and methantheline (curve 2) alone from ref 4.

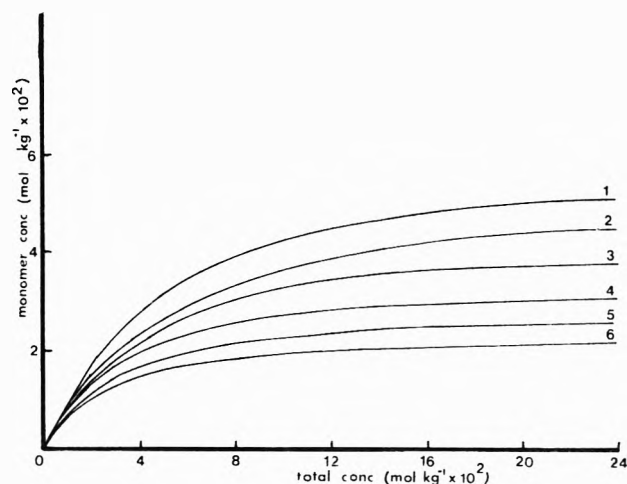


Figure 2. Variation of monomer concentration with total solution concentration as calculated from eq 1 for aqueous mixtures of propantheline and methantheline bromide. Mol fractions of propantheline: (1) 0.0, (2) 0.10, (3) 0.25, (4) 0.50, (5) 0.75, (6) 1.00. Data for propantheline and methantheline alone from ref 5.

solution concentration, c , (g dm^{-3}) from⁷

$$\ln x = \int_0^c \{ (M/M_{\text{app}}) - 1 \} d \ln c \quad (1)$$

where M and M_{app} are the monomer and apparent aggregate weights, respectively, and x is the weight fraction of monomers. This treatment does not take into account nonideality effects arising from interactions between the charged aggregates. For each system, the monomer concentration asymptotically approached a limiting value, m'_{mon} , as the concentration increased (Figure 2). Values of m'_{mon} for propantheline and methantheline alone are in agreement with apparent cmc values derived from surface tension data.⁵ Figure 3 shows the variation of m'_{mon} with the composition of the mixed systems.

The cmc, C_m , of ideal mixed systems of ionic micellar components 1 and 2 is related to the cmc, C_{i_a} , of each surfactant and the mole fraction, x_i , of each component in the system by³

$$C_m^\theta = (C_{2a}C_{1a})^\theta / (x_1C_{2a}^\theta + x_2C_{1a}^\theta) \quad (2)$$

The constant, θ , is defined by

$$\log C_{i_g} = \log A_i - (\theta_i - 1) \log g \quad (3)$$

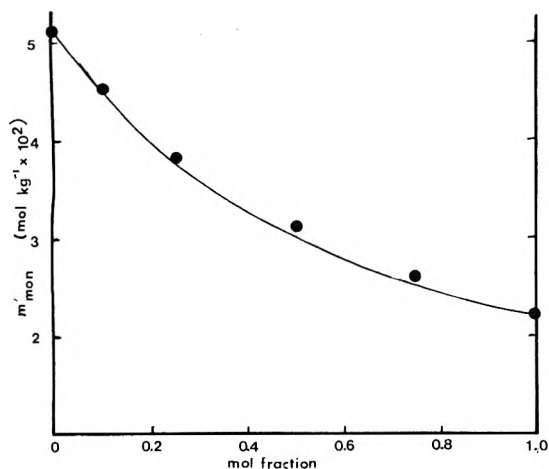


Figure 3. Limiting monomer concentration, m'_{mon} , as a function of mol fraction of propantheline in aqueous mixtures of propantheline and methantheline bromide. Continuous line represents expected variation for ideal mixing of ionic micellar components from eq 2.

TABLE I: Stepwise Equilibrium Constants for Propantheline-Methantheline Mixtures Calculated from Eq 4

Mol fraction propantheline	Equilibrium constants, $\text{dm}^3 \text{mol}^{-1}$		
	K_2	K_3	K_4
0.0 ^a	2.8	33	4
0.10	4.3	19	3
0.25	5.0	25	12
0.50	8.5	35	14
0.75	11.5	60	15
1.00 ^a	12.5	76	25

^a Values from ref 4.

where C_{1g} is the cmc of a single surfactant in the presence of a total counterion concentration, g . The constant A_i is the cmc in the absence of added electrolyte. Surface tension measurements⁵ on propantheline bromide solutions containing added electrolyte have established a linear relationship between log apparent cmc and log counterion concentration from which a value of $\theta = 1.3$ may be calculated. Assuming a similar θ value for methantheline bromide and applying eq 2 gives a predicted m'_{mon} variation as shown by the continuous line in Figure 3. Although there is no theoretical justification for the use of eq 2 for mixed nonmicellar systems, it is of interest to note that this equation gives an excellent correlation with the experimental data. Ideal mixing of the two components is not unexpected in view of the similarity of structure of the two components.

Stepwise equilibrium constants K_N for the mixed systems were evaluated as described previously^{4,8,9} using an analytical treatment proposed by Steiner.⁷

$$\{(M_w/xM) - 1\}/(xc/M) = 4K_2 + 9K_2K_3(xc/M) \dots + N \left(\prod_{N=2}^N K_N \right) (xc/M)^{N-2} \quad (4)$$

Table I shows the expected general increase in the magnitude of the K_N values for low aggregation numbers N , as the mole fraction of the more hydrophobic component, propantheline, is increased. Equilibrium constants for higher N values were not calculated because of the cumulative nature of errors in the determination of K_N . Errors in K_N arising from a neglect of interactions between the charged aggregates is also least significant for these lower values.

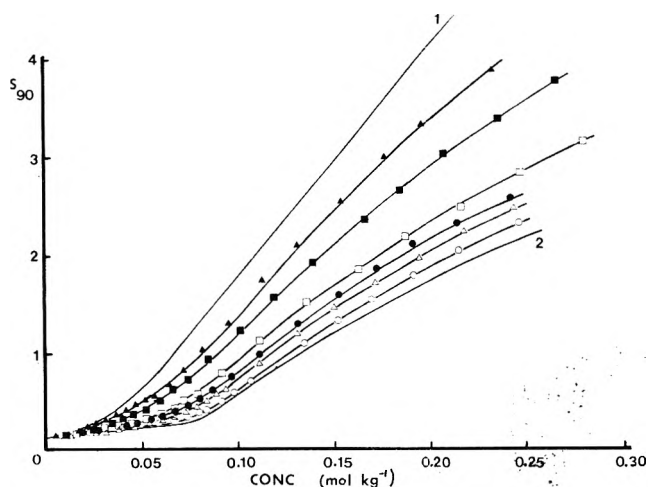


Figure 4. Concentration dependence of the scattering ratio, S_{90} , for aqueous mixtures of adiphenine hydrochloride and propantheline bromide. Mol fraction of propantheline: (O) 0.05, (Δ) 0.14, (\bullet) 0.20, (\square) 0.25, (\blacksquare) 0.50, (\blacktriangle) 0.75. Data for propantheline (curve 1) and adiphenine (curve 2) from ref 2 and 6, respectively.

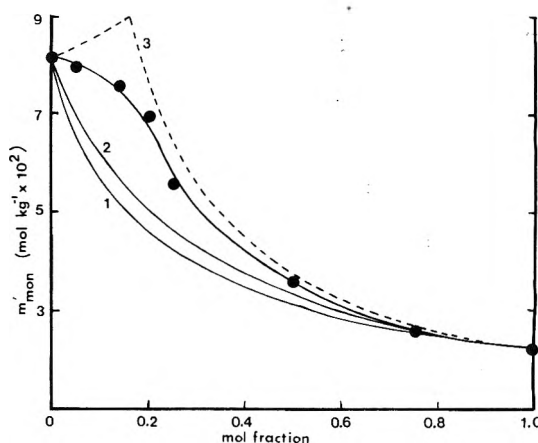


Figure 5. Limiting monomer concentration, m'_{mon} , as a function of mol fraction of propantheline in aqueous mixtures of propantheline bromide and adiphenine hydrochloride. Curves 1 and 2 show expected values for ideal mixing (eq 2) with θ values of 1.8 and 1.3, respectively. Curve 3 shows expected values for complete demixing of components (eq 5).

Propantheline-Adiphenine Mixtures. The cmcs of mixtures with adiphenine/propantheline molar ratios >0.8 were determined directly from the light scattering plots (Figure 4). The curves representing the scattering at high solution concentration were extrapolated to intersect lines representing monomeric scattering; the point of intersection was equated with the cmc in the usual way. The inflections in the light scattering plots became progressively less distinct as the propantheline content of the mixture increased and the limiting monomer concentrations for such systems were estimated using eq 1. Figure 5 shows the variation of m'_{mon} with the composition of the mixed system.

Equation 2, derived for the ideal mixing of micellar components, was applied to this system. Previous investigations of the effect of electrolyte on other diphenylmethane derivatives¹⁰ have established the applicability of eq 3 and have indicated a mean value of θ of approximately 1.8. Assuming this θ value for adiphenine hydrochloride and applying eq 2 gave a cmc variation significantly different from that determined experimentally (Figure 5). For the extreme case of mixtures of ionic surfactants in which the aggregates exist independently of each other, the counterion of one component depresses

the cmc of the other. An indication of the variation of cmc with total concentration in such systems is given by the approximate relationship¹¹

$$C_m = C_{ia} \text{ antilog } \{(\log x_i^{-1})/\theta_i\} \quad (5)$$

Applying eq 5 to each component separately gives the demixing curve represented by the dashed line of Figure 5. The experimental m'_{mon} values lie between the theoretical curves for ideal mixing and complete demixing of components, suggesting a significant degree of nonideality of the mixing process. The apparent lack of interaction between the two components is a consequence of the differences in their structure and mode of association. Propäntheline has a large, almost planar hydrophobic moiety and is thought to associate by face-to-face stacking. In contrast, the hydrophobic group on the adiphenine

molecule has sufficient flexibility to promote micellization of this compound. Clearly the incorporation of such a molecule into the propantheline aggregate would have a considerable disruptive influence on the stacking process.

References and Notes

- (1) K. Shinoda, T. Nakagawa, B. Tamanushi, and T. Isemura, "Colloidal Surfactants", Academic Press, London, 1963, p 64; K. Shinoda, *J. Phys. Chem.*, **58**, 541 (1954).
- (2) H. Lange, *Kolloid Z.*, **131**, 96 (1953).
- (3) K. J. Mysels and R. J. Otter, *J. Colloid Sci.*, **16**, 474 (1961).
- (4) D. Attwood, *J. Phys. Chem.*, **80**, 1984 (1976).
- (5) D. Attwood, *J. Pharm. Pharmacol.*, **28**, 762 (1976).
- (6) D. Attwood, *J. Pharm. Pharmacol.*, **28**, 407 (1976).
- (7) R. F. Steiner, *Arch. Biochem. Biophys.*, **39**, 333 (1952).
- (8) D. Attwood and O. K. Udeala, *J. Phys. Chem.*, **79**, 889 (1975).
- (9) D. Attwood and O. K. Udeala, *J. Pharm. Sci.*, **65**, 1053 (1976).
- (10) D. Attwood and O. K. Udeala, *J. Pharm. Pharmacol.*, **27**, 395 (1975).
- (11) P. Mukerjee and A. Y. S. Yang, *J. Phys. Chem.*, **80**, 1388 (1976).

Identification and Localization of Cluster and Hydroxylated Forms of Divalent Cation Oxide in Y Zeolite

Antoine Abou-Kals,[†] Claude Mirodatos, Jean Massardier, Denise Barthomeuf,[‡] and Jacques C. Vedrine*

Institut de Recherches sur la Catalyse, C.N.R.S., 79, boulevard du 11 novembre 1918, 69626 Villeurbanne Cedex, France (Received August 20, 1976)

Publication costs assisted by Centre National de la Recherche Scientifique

γ irradiation of Mg and Ca exchanged Y zeolites has been performed to characterize these materials, the paramagnetic species created being studied by means of ESR spectroscopy. It was observed in particular that F-type centers were formed with $g_{\text{av}} = 2.0008$ and $\Delta H_{\text{pp}} = 3.5$ Oe for MgY samples and $g_{\text{av}} = 2.0004$, $\Delta H_{\text{pp}} = 3.5$ Oe and $g_{\text{av}} = 1.9967$, $\Delta H_{\text{pp}} = 5.0$ Oe for CaY samples. These centers, in small concentration at least below 600 °C, are characteristic of pure metal oxide, MO. Detailed ESR experiments as a function of heat treatment conditions and exchange level and complementary experiments using IR spectroscopy and x-ray diffraction strongly suggested that small clusters of MO were formed in large cavities, excluding hexagonal prisms and sodalite cages, by dehydration of M(OH)⁺ ions, mainly at high temperatures (>600 °C). The number of MO entities in the clusters could not be determined precisely but was tentatively estimated to be within a range from 2 to 10. A M(H₂O)⁺ species was identified and localized in sodalite cages. Its formation is discussed in terms of reaction between M(OH)⁺ species localized inside the sodalite cages and H atoms from OH groups giving rise to the 3550-cm⁻¹ IR band and the 1.4-Oe wide ESR signal of trapped H atoms rather than in terms of ionization of occluded water molecules.

Introduction

γ irradiation has been shown to be a fruitful method giving rise to paramagnetic species which stem from entities characteristic of a lattice itself,¹⁻⁴ often active as adsorption sites^{5,6} and which could be studied using ESR spectroscopy.

Type Y zeolites, with Na⁺ ions being more or less extensively exchanged with divalent cations such as Mg²⁺ or Ca²⁺, have been shown to present a strong Brønsted acidity and subsequently a high catalytic activity for isomerization and cracking reactions.⁷ It had been postulated that OH groups giving rise to a new IR band at 3685 cm⁻¹ corresponded to Mg(OH)⁺ or at 3675 cm⁻¹ to Ca(OH)⁺⁷ ac-

cording to the following equilibrium due to the polarizing effect of the divalent cations on water molecules:⁸



The created H⁺ are acidic and contribute to the 3640- or 3550-cm⁻¹ IR bands as structural OH groups in HY zeolites.⁹

If such samples are heated at 400 °C under a CO₂ atmosphere, formation of magnesium or calcium unidentate carbonates and structural acidic OH groups has been shown to occur while catalytic activity was subsequently observed to increase.^{7,10}

Exchanged cations have been shown to occupy cationic sites in the zeolite framework and to move toward inner sites by dehydration.^{11,12}

The purpose of the present work was to study divalent cation exchanged zeolites by means of ESR spectroscopy after γ irradiation, to characterize paramagnetic species arising from structural entities of the material itself and

[†] Permanent address: Faculté des Sciences, Université Libanaise Hadath, (Liban) et C.N.R.S. libanais.

[‡] Present address: Laboratoire de Catalyse organique, L.A. C.N.R.S. 231, ESCIL, 43, boulevard du 11 novembre 1918, 69621 Villeurbanne, France.

TABLE I: Chemical Composition of the Zeolite Samples^a

Catalysts	NaHY	Magnesium series						Calcium series				
Na ⁺ ions per unit cell	7.5	7.1	8.2	8.0	7.1	8.1	7.5	3.5	3.5	3.5	3.5	3.5
M ²⁺ ions per unit cell	0	5.3	7.6	9.1	12.5	14.7	19.3	9.9	16.0	18.6	23.8	26.2
M = Mg or Ca												

^a The theoretical number of protons per unit cell after NH₄⁺ decomposition can be obtained by the difference between 56 and the total cation equivalent amount.

thus afford a further insight into the nature of the action of divalent cations and their localization.

Experimental Section

Materials. The starting material was a Linde NaY zeolite. CaY samples were prepared by direct exchange of Na⁺ ions with Ca²⁺ from chloride solutions while MgY samples were obtained by first exchanging Na⁺ ions with NH₄⁺ to an 85% level and then NH₄⁺ with Mg²⁺ ions from magnesium chloride solutions. The zeolites were heated at 380 °C in a dry air flow for 15 h in order to evolve NH₃ and then at 550 °C for the same duration. Chemical compositions of the catalysts are given in Table I.

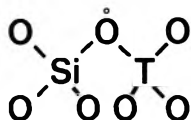
Spectroscopic Measurements. ESR spectra were recorded on a Varian E 9 spectrometer equipped with a dual cavity and referred to a standard sample (DPPH or strong pitch). IR spectra were scanned on a Perkin-Elmer Model 125 grating spectrophotometer. The powder was placed in standard 5-mm o.d. silica tubes for ESR experiments or pressed into 18-mm diameter wafers inserted in a quartz sample holder for IR study.

The samples were treated in oxygen at the desired temperature for 15 h and then outgassed at the same temperature for 10 h under about 10⁻⁵ Torr vacuum.

Irradiation was performed in a ⁶⁰Co γ cell at liquid nitrogen temperature (LNT) for doses of about 2 Mrads. 90% ¹³C enriched CO₂ was supplied by the French Atomic Commission (CEA) and used without further purification.

Results and Discussion

γ irradiation at LNT of dehydrated NaY and HY zeolites has been shown previously to give rise to trapped H atoms¹³ and V-type centers.¹ The latter centers corresponded to an ESR spectrum composed of a broad line, about 40 Oe wide, with $g_{av} = 2.017$ and a more or less well-resolved hyperfine structure assigned to the interaction with Al nuclei.¹ They were postulated to correspond to the following V-type center (hole of electron in a p_z oxygen orbital) arising from structural entities where T is an Al or Si nucleus



In the case of CaY zeolite, F-type centers with $g = 1.999$ and V-type centers with $g_{\perp} = 2.046$ and $g_{\parallel} = 2.0011$ have been reported and related to the presence of Ca²⁺ ions.¹⁴

Typical ESR spectra we have obtained for Mg- and CaY zeolites heated at 400 °C are composed of a doublet with an about 500-Oe splitting assigned to trapped H atoms¹³ and overlapping signals around $g = 2$. This central part of the spectrum is shown in Figures 1 and 2 for different microwave powers. It can be obviously decomposed into the classical broad signal of V-type center (Si-O-T) mentioned above which will not be considered further and three other signals (I, II, T) of which ESR parameters are reported in Table II. In the following the properties of

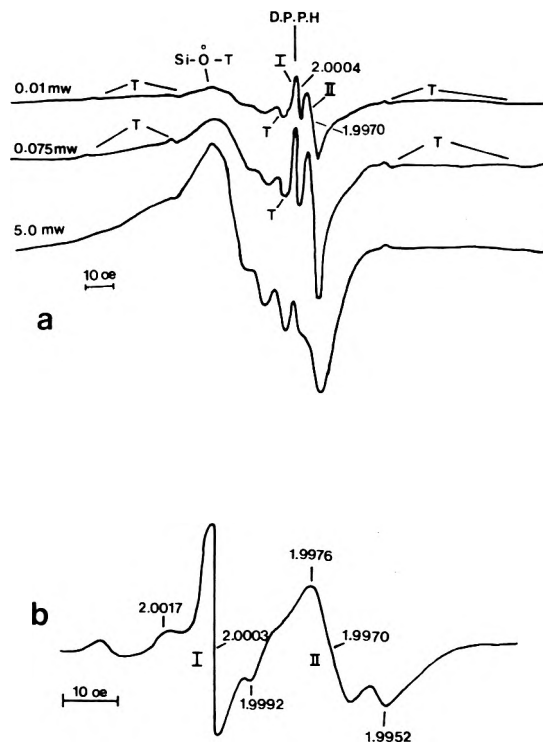


Figure 1. Central part of the ESR spectra of CaY sample (16 Ca²⁺ per unit cell) evacuated at 400 °C, irradiated and recorded at LNT. I, II, T, and Si-O-T refer to the signals described in the text and the microwave power is indicated on each spectrum. X and (a) and Q band (b).

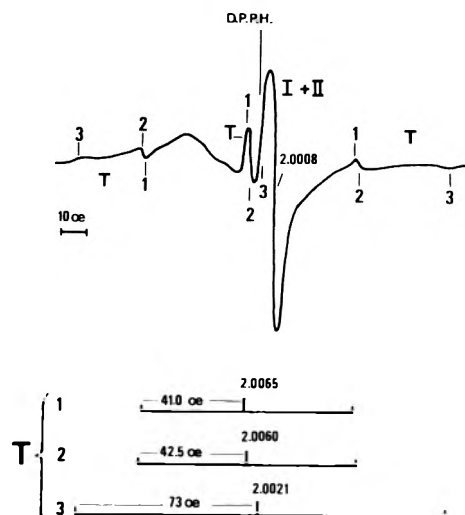


Figure 2. Central part of the ESR spectra of MgY sample (12.5 Mg²⁺ per unit cell) evacuated at 400 °C, irradiated and recorded at LNT. I, II, T, and Si-O-T refer to the signals described in the text and 1, 2, 3 to the three components of the triplet T. The microwave power in X band is 0.075 mW.

signals I and II will be considered first and secondly those of the triplet T.

1. *Cluster Species.* First of all it is important to note that V-type centers as detected previously for pure metal

TABLE II: ESR Parameters of Paramagnetic Species Related to Ca or Mg Ions in Different Matrices

Material	Centers	Mg ²⁺			Ca ²⁺		Ref
		<i>g</i> values	hyperfine splittings, Oe	ΔH_{pp} , Oe	<i>g</i> values	ΔH_{pp} , Oe, or hyperfine splittings (X band)	
Y zeolite	I	2.0008		3.5	2.0017	3.5	This work
					2.0003		
					1.9992		
Y zeolite	II				1.9976		
					1.9970		
		1.9952					
Y zeolite	Triplet		(H ¹)		(H ¹)		
		2.0065	41.0 ± 0.5		2.0063	40 ± 0.5	15
		2.0060	42.5 ± 0.5		2.0060	42 ± 0.5	
		2.0021 ± 0.0002	73.0 ± 0.5		2.0021 ± 0.0002	74 ± 0.5	
Pure oxide	V	(I)2.0385			(I)2.0710		16 (for MgO)
		(II)2.0023			(II)2.0015		17 (for CaO)
	F { S S _H	2.0007	²⁵ Mg	3.5	2.000		3
		1.9998	-25.5		¹ H	1.997	
Ne	MgOH·	(I)2.0007	-111.7	5.3			18
		(II)2.0017	-107.4	3.6			
Ar	MgOH·	(I)2.0013	-114.8	4.9			18
		(II)2.0020	-110.1	3.0			
Ar	MgH· or CaH·	(I)2.0020	-75.5	105.4	1.9966		19
		(II)2.0002	-80.7	106.4	2.0013		
Ar	Mg ⁺	2.0006	-212.5				18

oxide⁴ and CaY zeolite¹⁴ were not obtained in CaY and MgY samples of this experiment. The two signals I and II are quite similar but of weak intensity with respect to those recorded for pure metal oxides and which were assigned to surface F-type centers,³ namely, to electrons trapped in lattice oxygen vacancies. Their *g* values are less than *g_e* and they are very readily saturated by increasing microwave power (Figure 1). They can therefore be assigned also to F-type centers. It is worth noting that only one F-type center was reported on CaY zeolite (*g* = 1.999).¹⁴ We are of the opinion that in fact there were two overlapping signals, i.e., that the same types of F-centers were obtained.

Cautious study of steady saturation at temperatures ranging from LNT to room temperature was performed for types I and II centers as a function of microwave power. It turned out that their spin-lattice relaxation time *T*_{1e} followed a *T*⁻² law. The saturation was of homogeneous type for CaY samples, while mainly of heterogeneous type for MgY ones. The latter saturation type presumably arises from underlying and unresolved hyperfine structure due to ²⁵Mg isotope (*I* = 5/2) of 10% natural abundance. In the case of CaY samples the ⁴³Ca isotope (*I* = 7/2) was of negligible influence since the natural abundance is too low (0.13%). It follows that a small interaction between the unpaired electron and divalent cations does exist. This strongly supports our postulation that F-type centers are closely related to M²⁺ cations and not to lattice vacancies of zeolite which would behave quite differently²¹ mainly concerning microwave saturation, hyperfine structure, and *g* factor values.

It was observed that oxygen immediately reacted with the above two F-type centers on zeolite samples at LNT giving rise to new ESR spectra with the following parameters: *g_z* = 2.067, *g_y* = 2.009, and *g_x* = 2.002 for MgY zeolite; *g_z* = 2.059 and 2.047, *g_y* = 2.0095, and *g_x* = 2.003 for CaY zeolite. Such signals can be obviously attributed to O₂⁻ species, the *g_z* values for such O₂⁻ species being quite in accord with species adsorbed on divalent cations.²² These results also clearly show that F-type centers are

readily accessible to molecular oxygen and are very reactive toward oxygen. Therefore it turns out that they are located not in small cages such as hexagonal prisms or sodalite cages but rather in large cavities such as supercages or framework holes.

By comparison experiments on pure magnesium oxide were performed by activating magnesium hydroxide at temperatures ranging from 400 to 700 °C and then γ irradiating it at LNT. Usual F- and V-type centers in such oxides were obtained, F-type center intensity increasing with dehydration temperature. Molecular oxygen immediately reacted at LNT with F-type centers giving rise to the well-known O₂⁻ ions²³ (*g_z* = 2.077, *g_y* = 2.0073, and *g_x* = 2.0011) but did not react with V-type centers. These results clearly show that F-type centers are located at the surface of the oxide (they have been designated S or S_H)³ while V-type centers are located within the bulk in agreement with other findings.⁴ Excess of molecular oxygen did not broaden the V-type center signals, i.e., these centers might be located at a distance larger than 10 Å from the surface.²⁴ Since superficial F-type centers characteristic of MO were obtained in the case of heated Mg- and CaY zeolite samples, while bulk V-type centers were not, it follows that in these materials MO crystallites are formed whose size is small (Φ < 20 Å). One can then reasonably suggest that these crystallites are of the cluster type and are located in relatively small cavities such as supercages rather than at the surface of the zeolite grains. Steric hindrance should limit the cluster size to about 10 MO entities while formation of F-type centers characteristic of the oxide necessitates at least two MO entities.

The number of F-type centers in Mg- and CaY zeolites was found to increase as a function of dehydration temperature and divalent cation content as shown in Figures 3 and 4. Therefore one can conclude that such MO clusters are formed by dehydration and that their number is directly depending on the divalent cation content.

The intensity of the IR band at 3685 cm⁻¹ attributed to Mg(OH)⁺ ions parallels that of F-type center signal as a function of Mg²⁺ content (Figure 4). Moreover the F-type

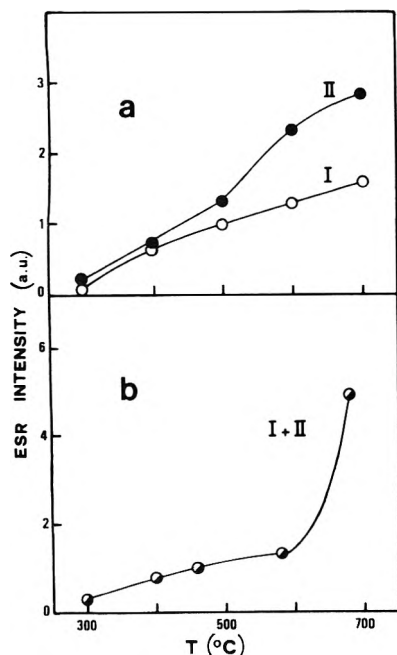


Figure 3. Variations of ESR intensity for signals I and II as a function of dehydration temperature: (a) CaY (16 Ca^{2+} per unit cell) and (b) MgY (12.5 Mg^{2+} per unit cell).

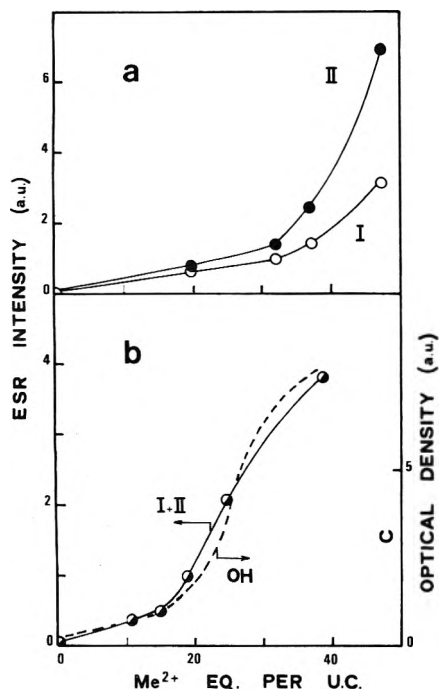


Figure 4. Variations of ESR intensity for signals I and II as a function of divalent cation exchange level for CaY (a) and MgY (b) zeolites. The variations of 3685-cm^{-1} IR band intensity (from ref 10) are given for comparison. Dehydration was performed at 400°C .

center intensity increases with dehydration mainly when heating the sample above 600°C , i.e., when the 3685-cm^{-1} IR band intensity decreased (Figure 5). Therefore it can be postulated that the MgO clusters arise from $\text{Mg}(\text{OH})^+$ by dehydration. It is worthwhile to note that the 3640-cm^{-1} and 3550-cm^{-1} IR bands due to structural OH groups (Figure 5) decrease in intensity for lower dehydration temperature than for the 3685-cm^{-1} IR band. It follows that dehydration of $\text{Mg}(\text{OH})^+$ ions presumably occurred between themselves rather than between such an ion and lattice structural OH groups.²⁵ This gives rise to Mg O Mg □ entities with oxygen vacancies which are ionized in F-type centers. One could also expect that Mg^{2+} ions

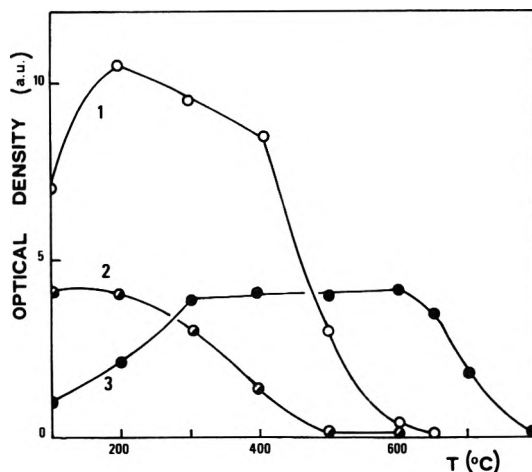


Figure 5. Variation of the intensity of OH group IR bands for MgY sample (12.5 Mg^{2+} per unit cell) as a function of dehydration temperature: (1) 3640-cm^{-1} ; (2) 3550-cm^{-1} ; and (3) 3685-cm^{-1} .

formed by dehydration were ionized by γ irradiation into Mg^+ ions. However careful analysis of the ESR spectrum showed that the expected hyperfine splitting (212.5 Oe)¹⁸ was not observed, which ruled out the possibility of confusing F-type center with such an ion in S state. X ray experiments were performed and showed that large crystallites of MO were not produced providing additional support to the above postulation that small clusters were formed, although X ray diffraction is not sensitive enough to be really unambiguous mainly for MgO.

It was previously shown⁷ that if divalent cation exchanged zeolites were heated at 400°C under vacuum and then under a CO_2 atmosphere at the same temperature, two unidentate carbonate species were formed. One was stable at 500°C under vacuum (IR bands at $1580, 1410\text{-cm}^{-1}$ for MgY and $1485, 1425\text{-cm}^{-1}$ for CaY) whereas the other disappeared when heating at this temperature ($1520, 1490\text{-cm}^{-1}$ IR bands for MgY and unresolved bands around 1450-cm^{-1} for CaY). It was postulated⁷ that the stable type involved certain lattice oxygen atoms whose reactivity was due to the presence of divalent cations, while the unstable form incorporated oxygen atoms from the $\text{M}(\text{OH})^+$ ions giving rise to new acidic and structural hydroxyl groups.

Highly dehydrated zeolite samples ($T \approx 700^\circ\text{C}$), corresponding to high F-type center concentration, were treated at 400°C under a CO_2 atmosphere. Compared to previous work on the same sample dehydrated and treated with CO_2 at 400°C ,⁷ one observed by IR that the stable unidentate carbonate species were of much smaller intensity. This indicates that much less lattice oxygen atoms are activated by divalent cations when the samples are dehydrated at higher temperatures. This conclusion is also quite in agreement with our above postulation that small clusters of MO are formed by dehydration, since divalent cations in such clusters lose their own individuality and then no longer induce the reactivity of certain framework oxygen atoms with CO_2 .

Carbonate ions are known to give under irradiation at LNT CO_2^- radicals²⁶ which can be studied by ESR. Using ^{13}C enriched CO_2 to improve the resolution of the spectrum two types of CO_2^- radicals were obtained as shown in Figure 6 with ESR parameters reported in Table III. These two CO_2^- species are not related to the two unidentate carbonate identified by IR since ESR intensities decreased similarly when 400°C carbonated samples are evacuated at 500°C before irradiation, i.e., when unstable carbonate species are evolved. Consequently, it turns out that CO_2^- radicals characteristics are depending on the

TABLE III: ESR Parameters of Stable CO₂^{-s} and Unstable CO₂^{-r} (Rotating) Radicals Stabilized on Different Samples γ or UV Irradiated^a

	NaY zeolite ^b	MgX zeolite ^c	CaY zeolite	MgY zeolite		MgO 450 °C	
	<i>g</i> tensor values	<i>g</i> tensor values hyperfine splittings, Oe	<i>g</i> tensor values	<i>g</i> tensor values	Hyperfine splittings, Oe	<i>g</i> tensor values	Hyperfine splittings, Oe
CO ₂ ^{-s}	1.9974 2.0016 2.0030 <i>a</i> _{iso} = 155 Oe	1.9989 2.0033 2.0033 <i>a</i> _{iso} = 169	1.9967 2.0015 2.0024	1.997 2.0012 2.0030	163 212 166 <i>a</i> _{iso} = 178 Oe	1.997 2.0015 2.0030	181 ^d 225 183 <i>a</i> _{iso} = 196 Oe
CO ₂ ^{-r}			2.0018 ΔH_{pp} = 2.5 Oe	2.0008 2.0012 2.0028 <i>g</i> _{av} = 2.0016	146 208 146 <i>a</i> _{iso} = 167 Oe	2.0015 ΔH_{pp} = 2.5	132 ^e 171 132 <i>a</i> _{iso} = 145 Oe

^a Note that the *g* values are identical for a given divalent cation. The hyperfine splittings only slightly differ which presumably arise from a matrix effect which changes the $\angle\text{OCO}$ angle and therefore the sp hybridization and unpaired electron spin density on the carbon atom. ^b Reference 27. ^c Reference 28. ^d Reference 29. ^e Reference 30.

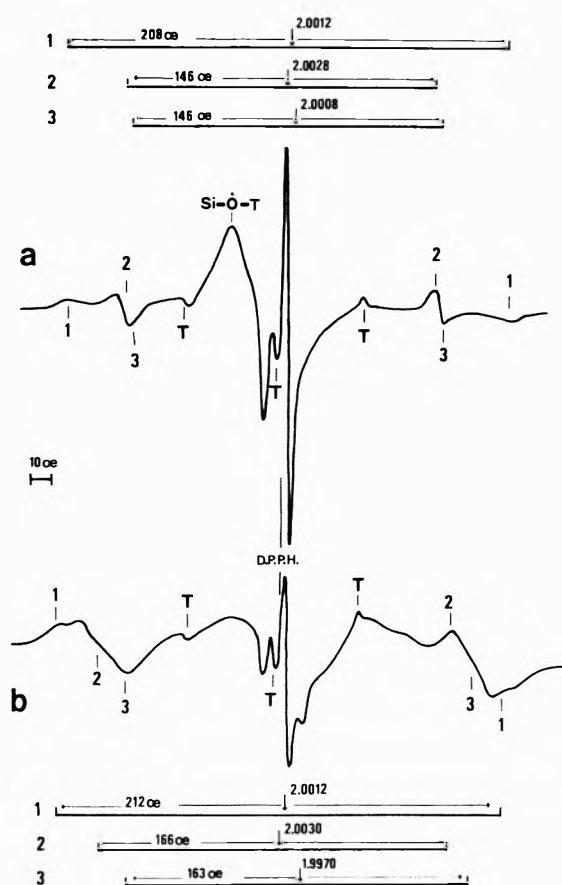


Figure 6. ESR spectra at LNT of MgY samples irradiated after treatment at 400 °C under ¹³C enriched CO₂: (a) recording directly after irradiation (CO₂^{-r}). (b) recording after warming to room temperature (CO₂^{-s}).

nature of their trapping site rather than on the carbonate species. Moreover it is important to note that the ESR parameters of CO₂⁻ radicals in carbonated Mg and Ca zeolites are quite similar to those observed for pure MO^{29,30} where trapping sites are known to be F-type centers of the oxide. These findings confirm that MO clusters are formed.

These results concerning the introduction of alkaline earth cations are difficult to compare with those obtained by Schoonheydt et al.³¹ which deal with transition metal ions (Ni, Cu), introduced in larger amount than the cationic exchange capacity (CEC) of the zeolite. Our results (namely, (i) limitation of the exchange to 75 and 100% of

the CEC for Mg and Ca, respectively, (ii) the increase of the 3640-cm⁻¹ IR band intensity toward the cation exchange level and not its decrease,³¹ and, lastly (iii) the dehydration temperature different from that of pure hydroxides)⁷ seem to rule out the possibility of the formation of metal hydroxide or polynuclear complexes during preparation. In our case the metal oxide clusters are formed during dehydration of M(OH)⁺ species.

The dehydration mechanism had already and widely been discussed, the formation of M(OH)⁺ species being often postulated.²⁵ Uytterhoeven et al.³² suggested that M(OH)⁺ reacts with M²⁺ to give M²⁺O M⁺ species located in the sodalite cages (M⁺ in site I') and protons which react with the lattice creating structural OH groups. Dehydration could occur between M(OH)⁺ and structural OH groups giving rise to MO and lattice oxygen vacancies as suggested by Ward.²⁵ Another possibility is dehydroxylation of the M(OH)⁺ entities between themselves giving (M O M □)_n clusters, with oxygen vacancies, in the supercage as proposed in this paper on the basis of ESR and IR experiments.

2. *Hydroxylated Species.* Another interesting defect in divalent cation exchanged zeolite after γ irradiation corresponds to the triplet T of which ESR parameters are given in Table II. It was recently assigned to a M(H₂O)⁺ ion.¹⁵ The variations of the ESR triplet intensity as a function of dehydration temperature and magnesium cation exchange level are given in Figure 7 and can be compared with the variations of intensity of 1.4-Oe wide ESR lines due to trapped H atoms and of 3550-cm⁻¹ IR band due to structural OH groups (Figures 5 and 7). Some data for CaY zeolite indicate a similar behavior for both divalent cations. It is important to notice that molecular oxygen does not react with the defect nor broaden the ESR signal. It follows that the M(H₂O)⁺ ions are located in the sodalite cage and that they might be formed by the reaction of H atoms with hydroxylated species. Since triplet signals were not observed for zeolites not exchanged with divalent cations where as H atoms were detected, one can reasonably suggest that these hydroxylated species are M(OH)⁺ ions, involved in the formation of M(H₂O)⁺ ions according to



The rather small intensity of the triplet (a tenth of F-type center one) indicates that only a small part of M(OH)⁺ ions located inside sodalite cages are involved in

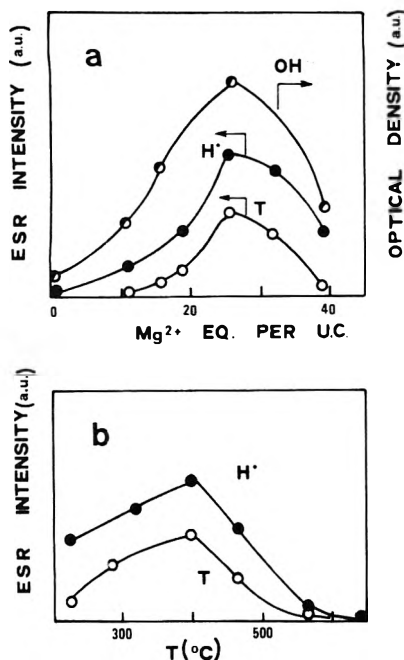


Figure 7. Variations of H atom yield and triplet intensity for MgY samples as a function of (a) cation exchange level (dehydration at 400 °C), (b) dehydration temperature (12.5 Mg²⁺ per unit cell). The variations of the 3550-cm⁻¹ IR band intensity (from ref 10) are given for comparison.

reaction 2. Previous correlation between trapped H atom yield corresponding to the 1.4-Oe wide ESR line and OH groups giving rise to the 3550-cm⁻¹ IR band^{10,33} allows the conclusion that H atoms involved in reaction 2 arise from 3550-cm⁻¹ IR band OH groups which are known to be pointing inside the sodalite cages (O₃H).³⁴ This result supports the conclusion that M(H₂O)⁺ ions and therefore some of M(OH)⁺ ions are located inside the sodalite cages. These results are also in agreement with those of Olson³⁵ who has observed nonframework oxygen atoms located in site II' of the sodalite cage after heating CaY samples at 400 °C.

It may be noted that M(H₂O)⁺ ions were not stabilized in the supercage, since the ESR signal is not broadened by oxygen filling the cage, although most of the M(OH)⁺ ions are present. This presumably arises from the peculiar stabilizing matrix effect of the sodalite cage. It also shows that trapping cavity size is very critical which may explain why such species were not identified before.

Conclusion

This study led us to show that, beside M²⁺ cations which occupy cationic sites in the zeolite framework, M(OH)⁺ entities in Ca and MgY zeolites may (i) give rise by dehydration mainly at temperatures larger than 500 or 600 °C to small (MO)_n clusters located inside the supercages,

and (ii) be transformed by γ -rays into M(H₂O)⁺ ions stabilized inside the sodalite cages for a small amount of them.

The presence of small amounts of M(OH)⁺ inside the sodalite cages up to temperatures of at least 600 °C and presumably 800 °C seems to be demonstrated by the formation of M(H₂O)⁺ ions in such cages upon γ irradiation, which is consistent with the occurrence of non-framework oxygen atoms in sites II' at high temperatures.³⁵

Acknowledgment. We thankfully acknowledge the gift of Ca Y zeolite samples by Dr. R. Beaumont.

References and Notes

- (1) A. Abou-Kais, J. C. Vedrine, and J. Massardier, *J. Chem. Soc., Faraday Trans. 1*, **71**, 1697 (1975).
- (2) A. Abou-Kais, J. C. Vedrine, J. Massardier, and G. Dalmaj-Imelik, *J. Catal.*, **29**, 120 (1973).
- (3) A. J. Tench and R. L. Nelson, *J. Colloid Interface Sci.*, **26**, 364 (1968).
- (4) J. H. Lunsford, *J. Phys. Chem.*, **68**, 2312 (1964).
- (5) R. R. Hentz and D. K. Wickenden, *J. Phys. Chem.*, **73**, 817 (1969).
- (6) G. M. Muha, *J. Phys. Chem.*, **70**, 1390 (1966).
- (7) C. Mirodatos, P. Pichat, and D. Barthomeuf, *J. Phys. Chem.*, **80**, 1335 (1976).
- (8) C. J. Planck, *Proc. Int. Congr. Catal.*, **3rd**, 1964, **1**, 727 (1965).
- (9) J. W. Ward, *Adv. Chem. Ser.*, **No. 101**, 380 (1971); J. B. Uytterhoeven, L. G. Christner, and W. K. Hall, *J. Phys. Chem.*, **69**, 2117 (1965).
- (10) C. Mirodatos, A. Abou-Kais, J. C. Vedrine, P. Pichat, and D. Barthomeuf, *J. Phys. Chem.*, **80**, 2366 (1976).
- (11) P. Gallezot, Y. Ben Taarit, and B. Imelik, *J. Catal.*, **26**, 48 (1972).
- (12) J. M. Bennett and J. V. Smith, *Mater. Res. Bull.*, **3**, 633, 933 (1968).
- (13) A. Abou-Kais, J. C. Vedrine, J. Massardier, G. Dalmaj-Imelik, and B. Imelik, *J. Chim. Phys.*, **69**, 561 (1972).
- (14) K. M. Wang and J. H. Lunsford, *J. Phys. Chem.*, **74**, 1512 (1970).
- (15) A. Abou-Kais and J. C. Vedrine, *Chem. Phys. Lett.*, **45**, 117 (1977).
- (16) J. E. Wertz, J. W. Orton, and P. Auzins, *Discuss Faraday Soc.*, **31**, 140 (1961); *J. Appl. Phys.*, **33**, 322 (1962).
- (17) A. J. Shuskus, *J. Chem. Phys.*, **39**, 849 (1963).
- (18) J. M. Brom and W. Weltner, *J. Chem. Phys.*, **58**, 5322 (1973).
- (19) L. B. Knight and W. Weltner, *J. Chem. Phys.*, **54**, 3875 (1971).
- (20) J. Vedrine, G. Dalmaj, and B. Imelik, *J. Chim. Phys.*, **65**, 1780 (1968).
- (21) D. N. Starnires and J. Turkevich, *J. Am. Chem. Soc.*, **86**, 757 (1964).
- (22) P. H. Kasai, *J. Chem. Phys.*, **43**, 3322 (1965).
- (23) J. H. Lunsford and J. P. Jayne, *J. Chem. Phys.*, **44**, 1487 (1966).
- (24) V. B. Kazansky, G. B. Pariisky, and A. I. Burshtein, *Opt. Spektrosk.*, **13**, 83 (1962).
- (25) J. W. Ward, *J. Phys. Chem.*, **72**, 4211 (1968); *J. Catal.*, **10**, 34 (1968).
- (26) D. W. Ovenall and D. H. Whiffen, *Proc. Chem. Soc.*, 420 (1960); *Mol. Phys.*, **4**, 315 (1961); J. A. Marshall, A. R. Reinberg, R. A. Serway, and J. A. Hodges, *Mol. Phys.*, **8**, 225 (1964).
- (27) J. C. Vedrine, J. Massardier, and A. Abou-Kais, *Can. J. Chem.*, **54**, 1678 (1976).
- (28) K. Sogabe, A. Hasegawa, Y. Yamada, and M. Miura, *Bull. Chem. Soc. Jpn.*, **45**, 3362 (1972).
- (29) P. Meriaudeau, J. C. Vedrine, Y. Ben Taarit, and C. Naccache, *J. Chem. Soc., Faraday Trans. 2*, **71**, 736 (1975).
- (30) P. Meriaudeau, Y. Ben Taarit, J. C. Vedrine, and C. Naccache, *J. Chem. Soc., Faraday Trans. 2*, **73**, 76 (1977).
- (31) R. A. Schoonheydt, L. J. Vandamme, P. A. Jacobs, and J. B. Uytterhoeven, *J. Catal.*, **43**, 292 (1976).
- (32) J. B. Uytterhoeven, R. Schoonheydt, B. V. Liengme, and W. K. Hall, *J. Catal.*, **13**, 425 (1969).
- (33) A. Abou-Kais, J. Massardier, G. Dalmaj-Imelik, and B. Imelik, *J. Chim. Phys.*, **69**, 570 (1972).
- (34) E. Dempsey and D. H. Olson, *J. Catal.*, **15**, 309 (1969).
- (35) D. H. Olson, *J. Phys. Chem.*, **72**, 1400 (1968).

⁴T₂ State Lifetimes and Intersystem Crossing Efficiencies in Chromium(III) Complexes

Francesco Castelll and Leslie S. Forster*

Department of Chemistry, University of Arizona, Tucson, Arizona 85721 (Received April 1, 1976)

The risetime of ²E → ⁴A₂ emission following pulsed excitation into ⁴T₂ has been recorded for several Cr³⁺ complexes with varying ⁴T₂ → ²E separations in fluid and rigid glass solutions and in crystals. Only a lower limit (~10⁹ s⁻¹) for the ⁴T₂ → ²E rate could be established. The products of the intersystem crossing efficiency (Φ_{2E}) and the ²E → ⁴A₂ radiative rate have also been measured as a function of temperature, by pulsed techniques, for Cr(CN)₆³⁻, Cr(en)₃³⁺, and Cr(acac)₃ in noncrystalline and crystalline media and the effect of temperature on Φ_{2E} inferred.

Introduction

Cr(III) complexes have been the subject of extensive photochemical and photophysical investigation.¹ Both fluorescence (⁴T₂ → ⁴A₂) and phosphorescence (²E → ⁴A₂) emissions have been observed, but phosphorescence is by far the more common. The identity of the photoreactive state, ⁴T₂ or ²E, has been a question of great interest. In at least four cases, Cr(CN)₆³⁻, Cr(en)₃³⁺, Cr(phen)₃³⁺, and Cr(NH₃)₆³⁺, much if not all of the photochemistry originates in ⁴T₂.²⁻⁵ Consequently, quantitative data on the photophysical properties of ⁴T₂, studied under photochemically relevant conditions, will be of value in the elucidation of the photochemical primary process mechanism. Two photophysical parameters of interest are the ⁴T₂ lifetime and the intersystem crossing efficiency (Φ_{2E}). The ⁴T₂ lifetime in ruby, as determined from the risetime of ²E → ⁴A₂ emission, is less than 0.5 × 10⁻⁹ s.^{6,7} The possibility that this quantity might be dependent upon the relative ⁴T₂ and ²E energies prompted us to examine Cr(III) complexes with varying ⁴T₂ → ²E separations. We now report on measurements of the ⁴T₂ lifetimes of Cr(CN)₆³⁻, Cr(en)₃³⁺, Cr(acac)₃, Cr(C₂O₄)₃³⁻, and Cr(urea)₆³⁺. In addition, the effect of temperature on Φ_{2E} has been studied.

Experimental Section

Pulsed excitation was obtained with an Avco C-950 N₂ laser either alone (λ 337 nm, pulse width ~10 ns) or as a pump for the following dye lasers: PBD (λ 366 nm); α-NPO (λ 398 nm); 7-diethylamine-4-methylcoumarin (λ 454 nm); and rhodamine 6G (λ 580 nm). Except in the case of rhodamine 6G where the lasing cavity was tuned with an echelle grating, the laser radiation was simply filtered through a CuSO₄ solution.

The detection system differed somewhat in the two different types of measurements:

(a) *Risetimes.* The ²E → ⁴A₂ emission profile was monitored with an RCA C-31034 photomultiplier operating at 1700 V. The output across 50 Ω was fed into a Tektronix 7904 oscilloscope with a 7A19 amplifier and the resultant display photographed. The oscilloscope was externally triggered by a signal from scattered laser light striking a fast photodiode. The emission was first passed through a solution filter (K₂Cr₂O₇ or Cr(acac)₃) and then through a 0.25-m Jarrell-Ash monochromator. Particular care was exercised to avoid scattered light and impurity luminescence. For Cr(CN)₆³⁻, the monochromator was replaced by a high-pass interference filter because the emission spectrum was broad. A 90° excitation-emission geometry was used. At room temperature, interference from scattered light was negligible, but at low temperatures in

glassy solutions of Cr(CN)₆³⁻ where the emission intensity is very low, scattering from the dewar could not be completely eliminated.

(b) *I(0).* In the determination of the total emission intensity at t = 0, I(0) the excitation was the same as that used for the risetime measurements. The monochromator was removed from the detection train and the photomultiplier load varied from 50 to 10 000 Ω as dictated by the sample lifetime. To keep the average anode current within prescribed limits, when long-lived emission was involved a neutral density filter was inserted in front of the photomultiplier tube. The sample was placed in a dewar and the temperature adjusted with a stream of cold N₂ gas. The excitation wavelength was close to the absorption maximum and for noncrystalline samples, the Cr³⁺ concentration was high enough to limit the light penetration depth to a small value. This eliminated any effect of temperature on the sample absorbance. No crystallite formation occurred when rigid glasses were produced.

The absolute luminescence quantum yields of [Cr(en)₃](ClO₄)₃ and [(n-C₄H₉)₄N]₃[Cr(CN)₆] powders were measured as previously described.⁸ In the comparison of I(0) for different powders, e.g., K₃(Co,Cr)(CN)₆ and [(n-C₄H₉)₄N]₃[Cr(CN)₆], the samples were mounted reproducibly, using the same geometry as in the steady state absolute quantum yield determinations.

Results and Discussion

Risetime Measurements. ⁴T₂ Lifetimes. When ⁴T₂ is above ²E, the time evolution of the ⁴T₂ and ²E populations, following δ function excitation of ⁴T₂, is described by the equations

$$[{}^4T_2] = \frac{[{}^4T_2]_0}{\lambda_2 - \lambda_1} [(\lambda_2 - k_T)e^{-\lambda_1 t} + (-\lambda_1 + k_T)e^{-\lambda_2 t}] \quad (1)$$

$$[{}^2E] = \frac{[{}^4T_2]_0 k_4}{\lambda_2 - \lambda_1} [e^{-\lambda_1 t} - e^{-\lambda_2 t}] \quad (2)$$

where the first-order rate constants are defined in Figure 1. [⁴T₂]₀ is the population of ⁴T₂ at the instant of excitation, k_T = k₂ + k₃ + k₄ + k_R^T, k_E = k₅ + k₆ + k₄ + k_R^E, and λ_{1,2} = 1/2[(k_E + k_T) ± ((k_T - k_E)² + 4k₄k₄)^{1/2}]. These equations assume thermally equilibrated populations within ⁴T₂ and ²E but not between the two states. Fluorescence can be categorized as prompt or delayed. The "lifetime" of ⁴T₂ (τ_F⁻¹ = k₂ + k₃ + k₄ + k_R^T) can, in principle, be determined by measuring the decay of the prompt fluorescence. However, when ⁴T₂ is above ²E, the prompt

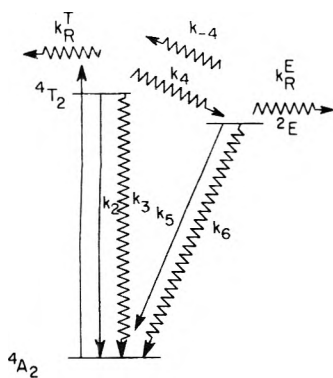


Figure 1. Radiative (\rightarrow) and nonradiative (\rightsquigarrow) transitions in Cr^{3+} complexes.

fluorescence is so weak that none has been detected from any Cr^{3+} complex.^{7,9-11} An alternative procedure for measuring ${}^4\text{T}_2$ relaxation rates involves monitoring the time dependence of phosphorescence as described in eq 2.

It should be noted that, in general, the prompt fluorescence decay constant, λ_2 , contains a contribution from k_{-4} and is not identical with k_T . Under the conditions encountered here, viz., the ${}^4\text{T}_2$ - ${}^2\text{E}$ energy difference is much larger than kT , $k_{-4} \ll k_4$, and $\lambda_2 \simeq k_T$. Equations 1 and 2 apply to δ function excitation and, when $1/\lambda_1$ and/or $1/\lambda_2$ are not large compared to the excitation pulse width and detection system response time, allowance must be made for the resultant distortion of the intensity-time profile.¹² The measured time evolution ($F(t)$) is given by the convolution integral

$$F(t) = \int_0^t G(t-t') I(t') dt' \quad (3)$$

where $I(t)$ is the true emission response function and $G(t)$ describes the time dependence of the excitation source, measured under the same conditions as $F(t)$. External triggering must be used to establish a common time base for $F(t)$ and $G(t)$. In the risetime measurements $I(t) = \text{constant}(e^{-\lambda_1 t} - e^{-\lambda_2 t})$; λ_1 and λ_2 are adjusted to give the best fit between the experimental and calculated $F(t)$ curves.

The measured risetime profile of $\text{Ru}(\text{bipy})_3^{2+}$ in deoxygenated EPA at 77 K is compared to synthetic curves in Figure 2. Since $\lambda_1 \simeq 0.2 \times 10^9 \text{ s}^{-1}$, on the time scale used here, $I(t) = \text{constant}(1 - e^{-\lambda_2 t})$. The experimental risetime corresponds closely to the synthetic curve calculated from eq 3 with $\lambda_2 = 10^9 \text{ s}^{-1}$. The slopes for $\lambda_2 = 10^9$ and 10^{10} s^{-1} are barely distinguishable but the $\lambda_2 = 0.5 \times 10^9 \text{ s}^{-1}$ slope is distinctly smaller. Although the experimental curve fits the $\lambda_2 = 10^9 \text{ s}^{-1}$ curve best, in view of triggering uncertainties and the very small differences in slope for $\lambda_2 \geq 10^9 \text{ s}^{-1}$, we can only assert that λ_2 is not smaller than 10^9 s^{-1} .

The phosphorescence risetime data for the other complexes were estimated by two different methods:

(i) Direct comparison of oscilloscope traces made under identical excitation and detection conditions. Within each of the following groups, identical risetime curves were recorded: $\text{Ru}(\text{bipy})_3^{2+}$ in EPA (77 K) and $\text{Cr}(\text{en})_3^{3+}$ in H_2O (298 K); $\text{Cr}(\text{urea})_6(\text{ClO}_4)_3$, $\text{Cr}(\text{urea})_6\text{I}_3$, $\text{NaMg}(\text{Al,Cr})(\text{C}_2\text{O}_4)_3 \cdot 9\text{H}_2\text{O}$ (all at 77 K), and ruby at 298 K.

(ii) Fitting the risetime curves by Pollack's procedure.⁶ If $1/\lambda_2$ is much shorter than the duration of the excitation pulse, $I(t) = \int_0^t P(t) dt$, where $P(t)$ describes the excitation pulse profile. The risetime curves for $\text{Cr}(\text{CN})_6^{3-}$ in a methanol:ethylene glycol:water (2:1:1 v/v) solution at 298 K and $\text{Cr}(\text{acac})_3$ in ethanol at 77 K were indistinguishable from $I(t)$ computed in this manner.

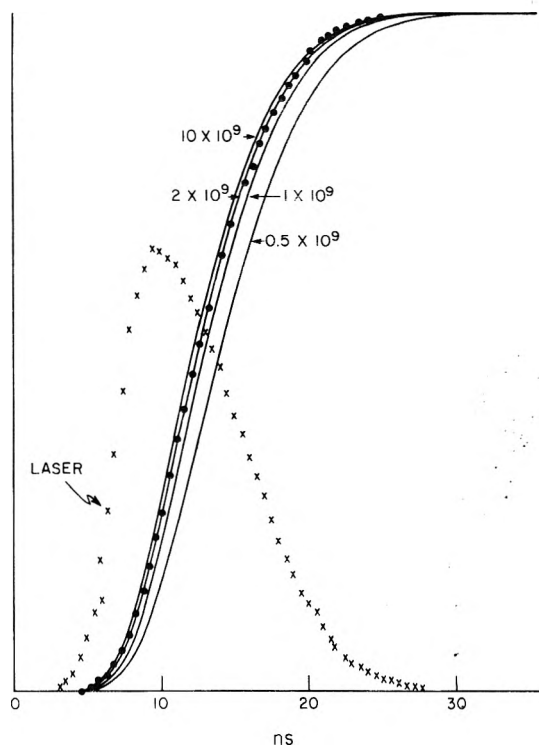


Figure 2. Convolved synthetic risetime profiles ($\lambda_1 = 0$) for various λ_2 : (●) experimental $\text{Ru}(\text{bipy})_3^{2+}$ and $\text{Cr}(\text{en})_3^{3+}$ risetimes.

Pollack⁶ used an apparatus with slightly better response time and was able to establish $\lambda_2 \geq 2 \times 10^9 \text{ s}^{-1}$ for ruby. The inclusion of ruby in the above lists strongly supports the assigned lower limit for λ_2 . We conclude that, in all reported examples, no measurable delay between ${}^4\text{T}_2$ excitation and ${}^2\text{E}$ population has been observed, i.e., $\lambda_2 \geq 10^9 \text{ s}^{-1}$. Indeed, theoretical estimates of k_4 ¹³ for ruby suggest a very fast ${}^4\text{T}_2 \rightsquigarrow {}^2\text{E}$ process (10^{13} s^{-1}) and in a recent report ${}^2\text{E}$ of $\text{Cr}(\text{acac})_3$, $[\text{Cr}(\text{NCS})_6]^{3-}$, and $\text{trans}[\text{Cr}(\text{NH}_3)_2(\text{NCS})_4]^-$ was populated within 10 ps.¹⁴ Although λ_2 depends upon k_3 as well as k_4 , in general, $k_4 \gg k_3$.¹⁵ Our data do not permit a determination of the effect of ${}^4\text{T}_2$ - ${}^2\text{E}$ separation on k_4 , but even in complexes with a small energy gap, e.g., $\text{Cr}(\text{urea})_6^{3+}$, $\lambda_2 \geq 10^9 \text{ s}^{-1}$. This indicates that $k_4 \geq 10^9 \text{ s}^{-1}$, irrespective of ${}^4\text{T}_2$ - ${}^2\text{E}$ separation. Scattered light interfered in the risetime measurement of $\text{Cr}(\text{CN})_6^{3-}$ in alcohol-water glass at 77 K and the lower limit of λ_2 is $5 \times 10^7 \text{ s}^{-1}$ in this instance. In view of the picosecond results,¹⁴ the intersystem crossing rates probably exceed 10^{11} s^{-1} in all cases.

$I(0)$ Intensities, Φ_{2E} . In general, both the phosphorescence yield and lifetime decrease with temperature. The relationship of Φ_p/τ_p to the intersystem crossing efficiency, Φ_{2E} , can depend upon the ${}^4\text{T}_2$ - ${}^2\text{E}$ energy gap (Δ) if k_{-4} is appreciable.¹⁶

In the steady state limit

$$\Phi_p/\tau_p = \Phi_{2E} k_5 \quad (4)$$

whereas in the equilibrium limit

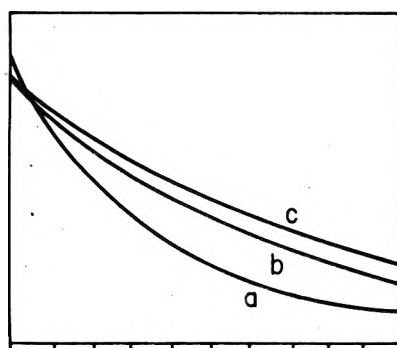
$$\frac{\Phi_p}{\tau_p} = \frac{\Phi_{2E} k_5}{1 + 3e^{-\Delta/hT}} \quad (5)$$

If Δ exceeds 1000 cm^{-1} , eq 4 and 5 are essentially indistinguishable below 300 K, but for a small Δ , there is an appreciable difference between the two expressions. Whenever the decrease in τ_p is large and primarily due to ${}^4\text{T}_2$ back-transfer, and delayed fluorescence is observed ($k_3 \simeq k_2$), then the equilibrium limit applies, $k_4 \gg k_5 + k_6$

TABLE I

	Φ_p^a		τ_p , ms		$\Phi_p/\tau_p = k_5$, s ⁻¹		$I(0)_{298}/I(0)_{LT}$
	LT ^b	298 K	LT	298 K	LT	298 K	
			Cr(CN) ₆ ³⁻				
Alcohol-water	0.042 ^c			3.33 ^c	12.6	(15.2) ^d	1.20
K ₃ Co(CN) ₆	0.99	0.99	120	61	8.3	16.2	1.94
[(C ₄ H ₉) ₄ N] ₃ [Cr(CN) ₆]	0.111	0.0042	8.7	0.28	12.8	15.0	1.32
						(16.9) ^d	
			Cr(en) ₃ ³⁺				
Alcohol-water	0.009 ^c			0.100 ^c	90	(90) ^d	1.0
[Cr(en) ₃](ClO ₄) ₃	0.0038	0.0019	0.055	0.017	69	112	1.7

^a Steady state measurement. ^b Low temperature limit. ^c Reference 23. ^d Calculated from $(k_5)_{LT}$ and $I(0)_{298}/I(0)_{LT}$. (See text.)



- a) 223°K: 20 μs/div
 b) 205°K: 50 μs/div
 c) 145°K: 500 μs/div

Figure 3. Phosphorescence decays of Cr(CN)₆³⁻ in alcohol-water solution.

and $k_4 \gg k_2 + k_3$. The latter condition prevails because the ⁴T₂ lifetime is much smaller than 1/k₂. For the complexes studied here, eq 4 is sufficiently accurate.

In eq 4 and 5, the absolute phosphorescence quantum yield is required. This quantity is notoriously difficult to obtain accurately,¹⁷ although several Φ_p determinations in Cr³⁺ complexes have been reported.^{8,18} However, variations in Φ_p/τ_p can be monitored by measuring τ_p and the relative Φ_p , separately. Alternatively, changes in Φ_p/τ_p can be directly evaluated by pulsed techniques. This is accomplished by extrapolating the phosphorescence decay curve to $t = 0$ (Figure 3). On the time scale of these measurements, the risetimes are negligible. If only ²E → ⁴A₂ emission is monitored

$$I(0)/I_{abs} = \text{constant } \Phi_{2E} k_5 \quad (6)$$

The advantage of determining Φ_p/τ_p in a single measurement is most evident in a temperature range where both Φ_p and τ_p are changing rapidly. In this case the ratio will be more reliable when obtained by an $I(0)$ measurement. Furthermore, the increased sensitivity permits extension to higher temperatures, where the steady state emission intensity is low. If the $I(0)$ temperature dependence is used as a measure of $\Phi_{2E} k_5$ changes, care must be taken to minimize any variation in I_{abs} with temperature. Since the excitation pulse intensity was quite constant and the concentrations were sufficiently high to produce nearly complete absorption, I_{abs} was very constant. One artifact that cannot be easily eliminated is the effect of refractive index variation in solutions.¹⁷ Depending upon the experimental geometry, the measured intensity should vary as $1/n - 1/n^2$. For alcoholic glasses at 77 K $n \approx 1.43$, whereas at room temperature $n \approx 1.35$. An 11%

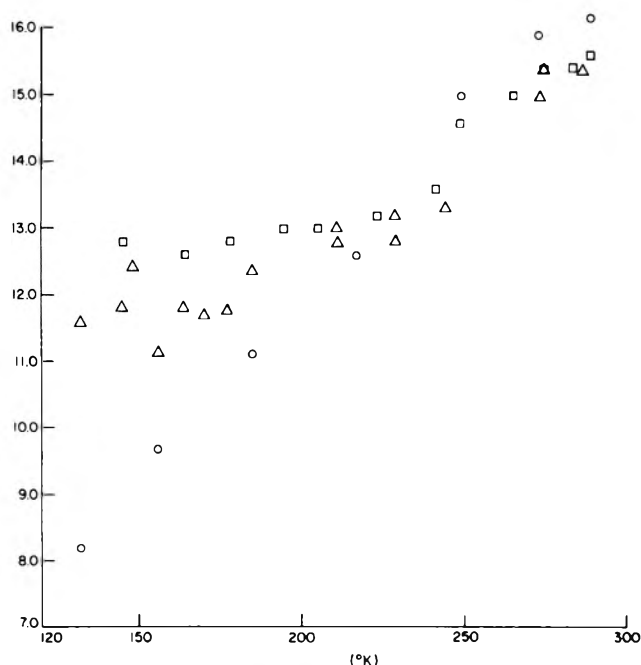


Figure 4. Change in Cr(CN)₆³⁻ $I(0)$ with temperature. The values are normalized with k_5 (298 K) in Table I: (□) alcohol-water; (○) K₃Co(CN)₆; (Δ) [(C₄H₉)₄N]₃[Cr(CN)₆].

increase in apparent intensity would be expected between 77 and 300 K if the $1/n^2$ dependence prevails. Actually, the results described below indicate that no correction need be applied.

Any delayed fluorescence due to back transfer should be minimal in the systems under study here. Since both fluorescence and phosphorescence are monitored, delayed fluorescence would lead to an apparent increase in $\Phi_{2E} k_5$ as the temperature is raised.

Cr(CN)₆³⁻. The decay curves of Cr(CN)₆³⁻ in alcohol-water solution are shown at several temperatures in Figure 3 and the variation in $I(0)$ with temperature is indicated in Figure 4 for this complex in three environments: (a) methanol, water, and ethylene glycol (2:1:1 v/v); (b) K₃Co(CN)₆ (5 and 10% Cr³⁺); and (c) [(C₄H₉)₄N]₃[Cr(CN)₆]. In Table I the variations in the values of Φ_p/τ_p , obtained from separate τ_p and steady state Φ_p measurements, are compared to the changes in $I(0)$ for room temperature and the low temperature limits (LT). The following points are noteworthy:

(i) In alcohol-water solution, $I(0)$ does not change as the glass melts (~170 K) even though the refractive index should decrease abruptly in this region.

(ii) The ratio $[I(0)]_{298}/[I(0)]_{LT}$ increases in the sequence: Cr(CN)₆³⁻ in alcohol-water < [(C₄H₉)₄N]₃[Cr(CN)₆] < K₃(Co,Cr)(CN)₆.

(iii) The absolute $I(0)$ values at constant I_{abs} are the same at room temperature for 5% $\text{K}_3(\text{Co,Cr})(\text{CN})_6$ and $[(\text{C}_4\text{H}_9)_4\text{N}]_3[\text{Cr}(\text{CN})_6]$. Appropriate corrections for the absorption by Co^{3+} at 366 nm and $\text{Co}^{3+} \rightsquigarrow \text{Cr}^{3+}$ energy transfer were made.¹⁸

(iv) As expected the ratios of $I(0)$ at room and low temperature are essentially the same as the corresponding Φ_p/τ_p ratios. This agreement confirms the reliability of the steady state Φ_p values.

The absolute phosphorescence yield of $\text{Cr}(\text{CN})_6^{3-}$ in $\text{K}_3\text{Co}(\text{CN})_6$ is nearly unity at room temperature.¹⁸ Consequently $\Phi_{2E} = 1$ for this system, i.e., $k_4 \gg k_2 + k_3$. The temperature dependence of $I(0)$ can be ascribed to the thermal enhancement of k_5 . In $\text{K}_3\text{Co}(\text{CN})_6$, Cr^{3+} ions are in centrosymmetric sites¹⁹ and most of the ${}^2E \rightarrow {}^4A_2$ transition probability is vibronically induced, a circumstance which leads to a marked temperature dependence for k_5 .²⁰ This is evidenced by the twofold decrease in τ_p in the interval 77 to 300 K while Φ_p is unchanged.²¹ The ${}^2E \leftarrow {}^4A_2$ absorption also increases two-threefold from 77 to 300 K. It appears that $k_5 \approx 1/\tau_p$ ($k_6 \approx 0$) and $\Phi_{2E} = 1$ at all temperatures in $\text{K}_3(\text{Co,Cr})(\text{CN})_6$ mixed crystals.

Since the room temperature absolute values of $I(0)$ are the same for $[(\text{C}_4\text{H}_9)_4\text{N}]_3[\text{Cr}(\text{CN})_6]$ and $\text{K}_3(\text{Co,Cr})(\text{CN})_6$, it is reasonable to infer that the $(k_5)_{298}$ values are equal in the two environments and that $\Phi_{2E} = 1$ for $[(\text{C}_4\text{H}_9)_4\text{N}]_3[\text{Cr}(\text{CN})_6]$ as well. However, as the temperature is reduced, the decrease in Φ_p/τ_p is not as marked in the latter case. This result means that the thermal enhancement of k_5 in $[(\text{C}_4\text{H}_9)_4\text{N}]_3[\text{Cr}(\text{CN})_6]$ is not as large as that in the $\text{K}_3\text{Co}(\text{CN})_6$ host, a conclusion that is reasonable if the Cr^{3+} sites are not centrosymmetric in the former environment. The emission spectra support this interpretation.^{19,22} The 0-0 band is much more intense relative to the vibronic structure in $[(\text{C}_4\text{H}_9)_4\text{N}]_3[\text{Cr}(\text{CN})_6]$ than in $\text{K}_3(\text{Co,Cr})(\text{CN})_6$.

The temperature dependence of $I(0)$ appears to be qualitatively similar for $\text{Cr}(\text{CN})_6^{3-}$ in alcohol-water solution and in $[(\text{C}_4\text{H}_9)_4\text{N}]_3[\text{Cr}(\text{CN})_6]$ (Figure 4). Of particular interest is the near constancy between 145 and 225 K. Above 225 K, the curves are nearly the same in all three environments. The plateau corresponds to $(k_5)_{\text{LT}}$, the allowed contribution to the ${}^2E \rightarrow {}^4A_2$ radiative rate. Apparently, solvent induced distortions of $\text{Cr}(\text{CN})_6^{3-}$ in alcohol-water solution destroy the center of symmetry for each individual ion, thus increasing the allowed component of the transition probability. This is true even though a given excited ion samples a wide range of environments during its lifetime in fluid media.⁹ The room temperature k_5 listed in Table I for $\text{Cr}(\text{CN})_6^{3-}$ in alcohol-water solution was calculated from eq 4 by assuming $\Phi_{2E} = 1$. Consequently, it is a lower limit. It is clear that $(k_5)_{\text{LT}}$ is larger in the alcohol-water and $[(\text{C}_4\text{H}_9)_4\text{N}]_3[\text{Cr}(\text{CN})_6]$ environments than in the centrosymmetric $\text{K}_3\text{Co}(\text{CN})_6$ crystal. It should be noted that a transcription error was made in reporting the low temperature Φ_p for $\text{Cr}(\text{CN})_6^{3-}$ in alcohol-water glass;²³ the correct value is 0.042.

In the foregoing discussion of the k_5 variation with temperature, the temperature invariance of Φ_{2E} has been assumed. This assumption is plausible for the crystalline systems where $\Phi_{2E} = 1$ at room temperature. The situation in the alcohol-water host is less certain. In the first place, photosolvation of $\text{Cr}(\text{CN})_6^{3-}$ occurs in fluid media. It has been shown that this reaction occurs in the 4T_2 state.^{2,24} Since back transfer is inefficient in $\text{Cr}(\text{CN})_6^{3-}$ the reaction must compete with intersystem crossing. The photolysis yield in DMF varies from 0.01 at -50°C to 0.08 at 25°C . In H_2O , the quantum yield is 0.10 at 25°C , but in 50%

ethanol-water mixture is only 0.04.²⁴ Consequently, any change in $I(0)$ due to photolysis in alcohol-water solutions would be within experimental error.

A more serious question concerning the magnitude of Φ_{2E} is raised by a study of direct and sensitized $\text{Cr}(\text{CN})_6^{3-}$ phosphorescence in DMF, where it was shown that $\Phi_{2E} \leq 0.5$.²⁵ Since approximately 10% of the molecules react with DMF and at most 50% cross over to 2E , 40% of the excited molecules return to the ground state nonradiatively by ${}^4T_2 \rightsquigarrow {}^4A_2$. This radiationless process might be a reversible photodissociation and would then be included in k_3 . It is possible in alcohol-water solution that Φ_{2E} is in fact unity at low temperatures and that a thermally induced decrease in Φ_{2E} is masked by a concomitant increase in k_5 to $\sim 30 \text{ s}^{-1}$. This interpretation requires an unreasonably large thermal enhancement in k_5 between 225 and 298 K. Alternatively, Φ_{2E} might be ~ 0.5 at all temperatures due to a large but temperature invariant k_3 , either intramolecular or due to photodissociation followed by viscosity dependent geminate recombination, but then k_3 would have to be larger in noncrystalline media. The difference in solvent systems, DMF vs. alcohol-water, should also be noted.

$\text{Cr}(\text{en})_3^{3+}$. For $\text{Cr}(\text{en})_3^{3+}$ dissolved in diethylene glycol monoethyl ether-water solution, Φ_p and τ_p did not change with temperature in a parallel manner,²⁶ an observation that prompted us to reexamine this problem with the more reliable pulse method. Within experimental error ($\sim 5\%$), $I(0)$ is constant for $\text{Cr}(\text{en})_3^{3+}$ in alcohol-water solution from 150 to 293 K. Again, no change occurs in the melting region of the glassy solution. Since $I(0)$ was monitored at many intermediate temperatures, and it is unlikely that both Φ_{2E} and k_5 would both change in such a manner as to maintain a constant $\Phi_{2E}k_5$ product, the temperature invariance of both k_5 and Φ_{2E} is presumed.

The marked trigonal distortion in $\text{Cr}(\text{en})_3^{3+}$ leads to dominant 0-0 bands in the ${}^2E \rightarrow {}^4A_2$ emission spectra and $(k_5)_{\text{LT}}$ is larger than in $\text{Cr}(\text{CN})_6^{3-}$ (Table I). The vibronically induced contribution to k_5 is small as indicated by the negligible thermal enhancement of k_5 .

In $[\text{Cr}(\text{en})_3][\text{Cr}(\text{CN})_6]$, $\Phi_{2E} = 1$ for both $\text{Cr}(\text{en})_3^{3+}$ and $\text{Cr}(\text{CN})_6^{3-}$.²⁷ However, when $[\text{Cr}(\text{en})_3](\text{ClO}_4)_3$ is warmed from 140 to 300 K, $I(0)$ increases nearly twofold. We do not believe that this change reflects an increase in either Φ_{2E} or k_5 , but rather is an artifact due to emission reabsorption. The bulk of the emission is concentrated in the 0-0 ${}^2E \rightarrow {}^4A_2$ lines. As the temperature is decreased, these lines narrow and the reabsorption increases. No reabsorption correction⁸ has been used in computing the $[\text{Cr}(\text{en})_3](\text{ClO}_4)_3$ Φ_p since the 0-0 line width was smaller than the monochromator bandwidth. Analogous radiation trapping is encountered in ruby at low temperatures.²⁸

Measurements of photolysis quenching by metal ions and sensitized phosphorescence has led to $\Phi_{2E} \approx 0.6-0.7$ for $\text{Cr}(\text{en})_3^{3+}$ in H_2O .^{5,29} The total photolysis yield is 0.40, but the yield in 4T_2 prior to intersystem crossing is only 0.15. In this scheme $\sim 20\%$ of the molecules return to the ground state directly via ${}^4T_2 \rightsquigarrow {}^4A_2$.

We conclude that the $\text{Cr}(\text{en})_3^{3+}$ Φ_{2E} is not temperature dependent in any environment and suggest that only photolysis and/or dissociation followed by geminate recombination compete with intersystem crossing in this complex.

$\text{Cr}(\text{acac})_3$. This complex was chosen for study because evidence has been obtained for a large thermal enhancement of k_3 in some environments.¹⁵ For example, in a plastic host, k_3 competes effectively with k_4 above $\sim 115 \text{ K}$ as evidenced by a decrease in Φ_p/τ_p . Yet in mixed

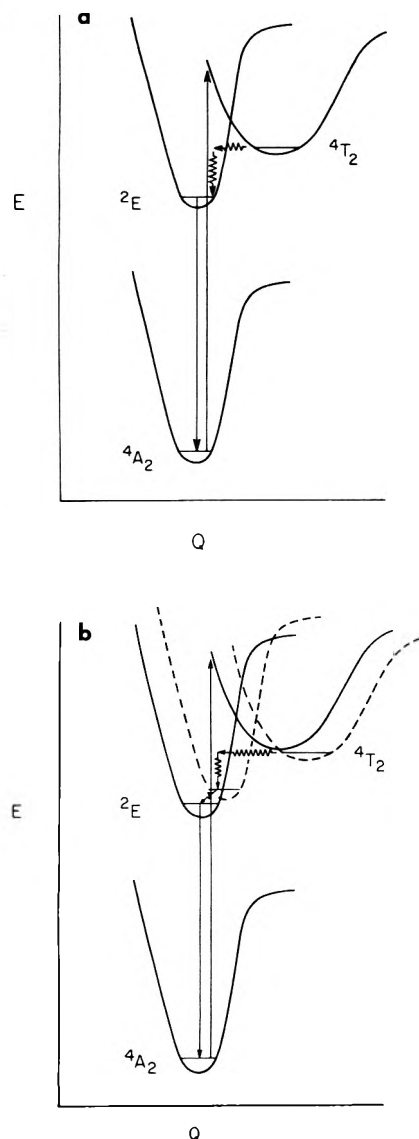


Figure 5. Potential energy curves: (a) no solvent relaxation; (b) solvent relaxation included.

crystals of 10% Cr³⁺:Al(acac)₃, no corresponding change in Φ_p/τ_p was observed.³⁰ In accord with this latter observation, $I(0)$ is unaffected by temperature in 10% Cr³⁺:Al(acac)₃. The higher sensitivity of the pulsed measurements made it possible to extend the temperature range to 277 K. In contrast, when Cr(acac)₃ is dissolved in absolute ethanol, $I(0)$ decreases with temperature above 150 K, but more slowly than in the plastic. Apparently, in a noncrystalline host, k_3 increases so rapidly with temperature that ${}^4T_2 \xrightarrow{k_3} {}^4A_2$ becomes an important process at higher temperatures, but the k_3 variation is different in the plastic and alcohol environments. Macroscopic viscosity is not the controlling factor. It must be emphasized that the $I(0)$ change is not due to any refractive index artifact.

Photophysics vs. Photochemistry. "Thexi" States. In Figure 1 it is assumed that the photophysical (k_2, \dots, k_6) and photochemical (k_R) rate constants are associated with processes arising in thermally equilibrated, i.e., Boltzmann, distributions. However, it is quite possible that some processes precede thermalization. For example, if intersystem crossing to 2E were faster than vibrational relaxation in 4T_2 , k_4 and Φ_{2E} would represent a before-relaxation process and the ${}^2E \rightarrow {}^4A_2$ risetime would not correspond to the lifetime of the photochemically active, equilibrated 4T_2 thexi state.¹ In crystalline or rigid

noncrystalline systems, the Figure 5a potential curves are adequate. In this case the vibrational relaxation involves modes of both the complex and its environment and the dissipation rates are $\sim 10^{13} \text{ s}^{-1}$. If the complex and/or solvent molecules are mobile, additional, possibly slower, relaxation processes are possible, and Figure 5b is the more appropriate. If solvent orientation is the slowest process, the difference between the solid and broken curves in Figure 5b is most marked when a polar molecule is excited in a polar medium and the dipole moment direction differs in the ground and excited states. Most solvent molecules must then rotate to maximize the solute-solvent interaction energy. We are dealing here with nonpolar complexes, and though localized bond dipoles may interact with the solvent, no solvent reorientation is likely in the excited state. 4A_2 and 2E are both derived from the t_2^3 configuration and should have similar equilibrium geometries, but 4T_2 arises from t_2^2e . An expansion of some 0.1 Å would accompany the $t_2 \rightarrow e$ orbital jump,³¹ and the translational diffusion time of the solvent will dictate whether Figure 5a can still be used.

The $I(0)$ constancy in Cr(en)₃³⁺, although the solvent changes from a rigid glass to a fluid, is clear evidence that solvent relaxation does not affect the 4T_2 photophysical processes in this species. Kane-Maguire et al.³² have found an excitation wavelength dependence for both Φ_p and the quenchable part of the photoracemization yield. These results were interpreted as indicating before relaxation intersystem crossing, a conclusion consistent with the $I(0)$ constancy.

For Cr(CN)₆³⁻, the solvent melting point, as monitored by the relaxation of 2E , is 170 K.⁹ However, the 4T_2 lifetime is much shorter than the 2E lifetime and it is possible that the abrupt $I(0)$ change of Cr(CN)₆³⁻ in alcohol-water at 230 K is due to solvent relaxation, but the thermal enhancement of k_5 makes it difficult to be certain in this respect. If solvent relaxation is the origin of the $I(0)$ change, it is noteworthy that intersystem crossing would then be larger in the thexi state.

In the absence of fluorescence direct photophysical monitoring of thexi states will continue to pose a problem.

Acknowledgment. This work was supported by the National Science Foundation (MPS 74-18553).

References and Notes

- (1) P. D. Fleischauer, A. W. Adamson, and G. Sartori, *Prog. Inorg. Chem.*, **17**, 1 (1972).
- (2) H. F. Wasgestian, *J. Phys. Chem.*, **76**, 1947 (1972).
- (3) N. A. P. Kane-Maguire and C. H. Langford, *J. Am. Chem. Soc.*, **94**, 2125 (1972).
- (4) C. H. Langford and L. Tipping, *Can. J. Chem.*, **50**, 887 (1972).
- (5) R. Ballardini, G. Varani, H. F. Wasgestian, L. Moggi, and V. Balzani, *J. Phys. Chem.*, **77**, 2947 (1973).
- (6) S. A. Pollack, *IEEE J. Quantum Electron.*, **QE4**, 703 (1968).
- (7) P. N. Everett, *J. Appl. Phys.*, **41**, 3193 (1970).
- (8) F. Castelli and L. S. Forster, *J. Lumin.*, **8**, 252 (1974).
- (9) F. Castelli and L. S. Forster, *J. Am. Chem. Soc.*, **95**, 7223 (1973).
- (10) F. Castelli and L. S. Forster, *Phys. Rev. B*, **11**, 920 (1975).
- (11) F. Castelli and L. S. Forster, *J. Am. Chem. Soc.*, **97**, 6306 (1975).
- (12) W. Ware in "Creation and Detection of the Excited State", A. A. Lamola, Ed., Vol. 9, Marcel Dekker, New York, N.Y., 1972, pp 213-302.
- (13) W. H. Fonger and C. W. Struck, *Phys. Rev. B*, **11**, 3251 (1975).
- (14) A. D. Kirk, P. E. Hoggard, G. B. Porter, M. C. Rockley, and M. W. Windsor, *Chem. Phys. Lett.*, **37**, 199 (1976).
- (15) L. S. Forster, *Adv. Chem. Ser.*, No. **150**, 172 (1976).
- (16) G. B. Porter in "Concepts in Inorganic Photochemistry", A. Adamson and P. Fleischauer, Ed., Wiley, New York, N.Y., 1975, Chapter 2.
- (17) J. N. Demas and G. A. Crosby, *J. Phys. Chem.*, **75**, 991 (1971).
- (18) F. Castelli and L. S. Forster, *J. Phys. Chem.*, **78**, 2122 (1974).
- (19) R. A. Condrate and L. S. Forster, *J. Chem. Phys.*, **48**, 1514 (1968).
- (20) T. M. Dunn in "Modern Coordination Chemistry", J. Lewis and R. G. Wilkins, Ed., Interscience, New York, N.Y., 1960, Chapter 4.
- (21) F. D. Camassei and L. S. Forster, *J. Chem. Phys.*, **50**, 2603 (1969).
- (22) H. L. Schlafer, H. Wagener, H. F. Wasgestian, and G. Herzog, *Ber. Bunsenges. Phys. Chem.*, **75**, 878 (1971).

- (23) K. K. Chatterjee and L. S. Forster, *Spectrochim. Acta*, **20**, 1603 (1964).
 (24) N. Sabbatini, M. A. Scandola, and V. Carassiti, *J. Phys. Chem.*, **77**, 1307 (1973).
 (25) N. Sabbatini, M. A. Scandola, and V. Balzani, *J. Phys. Chem.*, **78**, 541 (1974).
 (26) W. Geis, H. F. Wasgestan, and H. Kelm, *Ber. Bunsenges. Phys. Chem.*, **76**, 1093 (1972).
 (27) F. Castelli and L. S. Forster, *Chem. Phys. Lett.*, **30**, 465 (1975).
 (28) F. Varsanyi, D. L. Wood, and A. L. Schawlow, *Phys. Rev. Lett.*, **3**, 544 (1959).
 (29) F. Bolletta, M. Maestri, and V. Balzani, *J. Phys. Chem.*, **80**, 2499 (1976).
 (30) W. Targos and L. S. Forster, *J. Chem. Phys.*, **44**, 4342 (1966).
 (31) K. W. Hipps and G. A. Crosby, *Inorg. Chem.*, **13**, 1543 (1974).
 (32) N. A. P. Kane-Maguire, J. E. Phifer, and C. G. Toney, *Inorg. Chem.*, **15**, 593 (1976).

The Contribution of Higher Order Cluster Terms to the Activity Coefficients of the Small Ions in Polyelectrolyte Solutions

Kunihiko Iwasa*¹ and Jan C. T. Kwak

Department of Chemistry, Dalhousie University, Halifax, Nova Scotia, Canada B3H 4J3 (Received November 30, 1976)

Publication costs assisted by the National Research Council of Canada

The contribution of higher order terms appearing in the cluster expansion theory for polyelectrolyte solutions to the free energy and to the activity coefficients of the small ions is evaluated by examining two types of approximations. It is shown that the contributions of these higher terms to the nonideality of the ionic activities is quite appreciable even for polyions with charge densities lower than the so-called critical values, and result in an appreciable difference between the predicted activity coefficients of counterions and coions, in agreement with experimental results for polyelectrolytes with low charge densities. The comparison with experimental data also shows that the first term approximation suggested by Manning and Zimm is in fact better than Manning's later summed up version. Our calculations show a reasonable agreement of the first term approximation with experimental data for polyion charge densities ξ not exceeding 1.5 for the case of monovalent counter- and coions. For higher ξ values we are unable to get such an agreement, because the calculated coion activity coefficients are too high. The valence dependence of the activity coefficients of counterions and coions is also discussed.

I. Introduction

For about 25 years a number of theoretical evaluations of the thermodynamic properties of polyelectrolyte solutions have been reported.²⁻⁴ Among these theories, the limiting law set forth by Manning^{5,6} has a special importance because of its simplicity and statistical mechanical basis as well the reported agreement with experiments especially for polymers with high charge densities.^{5,7-9} Although the rigid rod model for the polymer used in the limiting law and many other treatments seems rather crude considering the actual molecular configuration, this model does give the best agreement with the results of activity measurements when compared to other models examined so far.^{2-4,10,11} This would suggest that the local polymer structure is very important in the evaluation of activity coefficients.

Such treatments have however tended to emphasize analytical solutions based on first-order approximations, and more complete numerical evaluations especially of the higher order terms which appear in the cluster theory have been relatively ignored. In this paper we will try a systematic examination of the contribution of these higher order terms formulated by statistical mechanical methods.^{6,10-13} Although an attempt to verify the limiting law based on the Poisson-Boltzmann equation has been reported,¹⁴ the use of the nonlinearized PB equation in polyelectrolyte solutions as well as in all electrolyte solutions is not well justified. Only the linearized approximation, i.e., the Debye-Hückel term, gives consistent results with other formalisms.

The calculations based on statistical mechanical methods which we are going to examine in this paper can be

classified into two types. The first type is based on the assumption of a uniform but discrete distribution of charged groups along the polymer and also evaluates the first higher cluster term.^{10,13} The second type assumes a continuous distribution of the polymer charge along the backbone and gives a summed up expression of higher terms with a similar character.⁶ This combination of charge distribution models and higher terms approximations is accidental, since there is no implied correlation between model employed and principle of evaluation of higher terms. We will show that at least for the systems studied in this paper no significant difference between the discrete and continuous charge models exists, and therefore our comparisons will be between the results for the first higher term and the summed higher terms calculations only, even though the model used in these two evaluations is different. For convenience, we will introduce the following terminology: *discrete model*, *continuous model*, *first term approximation*, and *summed up approximation*.

Finally, we should remember here that polymer-polymer interactions are neglected compared with other interactions in the present as well as in all other treatments reported so far. Neglecting these interactions may be justified at low polymer concentrations and in solutions with appreciable added salt content.¹¹ In order for our calculations to be valid we will therefore limit ourselves to such systems.

II. The Debye-Hückel Term

In this section we will briefly summarize the Debye-Hückel (DH) contribution (equivalent to the ring term contribution^{6,13} or to the random phase approximation^{10,11}) to the free energy and the activity coefficients as given by

two different models, i.e., the discrete and continuous models.

We will consider a system of volume V , which consists of ν mobile ion species and polyions. We denote the concentration of the i th mobile ion species with valence z_i by n_i , and the equivalent concentration of polymers by n_e . Thus we have a relation

$$\sum_i n_i z_i = n_e \quad (1)$$

For the sake of simplicity we will confine ourselves hereafter to polymers with monovalent negative charged groups. Extension to polymer systems with the opposite charge or different valence is straightforward.

We will call the radius of the polymer rod a , and the average spacing of the charged groups b . The reduced polymer charge density ξ , which is one of the characteristic quantities of our system, is defined as

$$\xi = e^2 / (\epsilon b k T) \quad (2)$$

where e is the elementary charge, ϵ the dielectric constant of the solvent, k Boltzmann's constant, and T the temperature.

The discrete model gives the DH term contribution to the excess free energy, F_{DH} , of the system as

$$F_{DH} / (V k T) = -\kappa^3 / 12\pi - \xi n_e [\ln(1 - e^{-\kappa b}) - \kappa b] \quad (3a)$$

The first term arises from the mobile ion–mobile ion interaction and the second from the polyion–small ion interaction. For the continuous model the second term on the right-hand side of (3a) is replaced by

$$\xi n_e [K_0(\kappa a) + \log a] \quad (3b)$$

where we denote by κ the Debye–Hückel parameter of the system

$$\kappa^2 = \lambda \mu_2 \quad (4)$$

with $\lambda = 4\pi e^2 / (\epsilon k T)$ and

$$\mu_m = \sum_i n_i z_i^m \quad (5)$$

where the summation is over all mobile (small) ions.

The quantity μ_m is the m th moment of the charge concentration.

The activity coefficient γ_i of the i th mobile ion species is given by

$$\ln \gamma_i = \frac{\partial}{\partial n_i} (F^{\text{ex}} / V k T) \quad (6)$$

where we denote F^{ex} the total excess free energy of our system. Since we are expanding the excess free energy F^{ex} , the logarithm of the activity coefficient is additive corresponding to each expansion term. If we can assume that our system is dilute so that the Debye–Hückel parameter κ is small enough to satisfy both $\kappa a \ll 1$ and $\kappa b \ll 1$, we find for both models:

$$\ln \gamma_i^{\text{DH}} = -(8\pi)^{-1} \kappa \lambda z_i^2 - 1/2 \xi z_i^2 n_e \mu_2^{-1} \quad (7)$$

where γ_i^{DH} is the Debye–Hückel contribution to the activity coefficient. We should notice here that the first term on the right-hand side of eq 7 is important when comparing theory with experiment.¹⁶ When κa and κb are not small, eq 3a for the discrete model gives

$$\ln \gamma_i^{\text{DH}} = -(8\pi)^{-1} \kappa \lambda z_i^2 - 1/2 \xi z_i^2 n_e \mu_2^{-1} f_d(\kappa b) \quad (8a)$$

where

$$f_d(x) = x [e^{-x} / (1 - e^{-x}) - 1] \quad (8b)$$

In the continuous model $f_d(\kappa b)$ in eq 8a is replaced by $f_c(\kappa a)$, with

$$f_c(x) = x K_1(x) \quad (8c)$$

If the activity coefficient is measured at constant polymer concentration, a difference between the two models is expected only in solutions with excess salt (large κ) but compared to experimental uncertainties this difference is unimportant even in this region. A difference may also be expected at lower charge densities, but again the absolute value of the difference is not big enough to exceed the experimental uncertainties, and moreover any nonuniformity in the polymer charge distribution would be expected to have a comparable importance.

For the case when $\xi = 1$ at 25 °C, we have $b = 7.1$ Å. In this region, b is comparable to the radius a , as given by the geometry of the polymer. We conclude that, at the relatively low experimental polymer concentrations employed, there is no significant difference between the two charge distribution models considered.

III. Higher Order Terms

In this section we will examine the contribution to the free energy of higher order terms arising in the cluster expansion theory for polyelectrolyte solutions. We will examine two approximations to evaluate these terms. In the following we will mention only those higher order terms which arise from polyion–mobile ion interactions. Higher terms expressing mobile ion–mobile ion interactions are not considered here and consequently we will compare our calculations with experimental data which have been corrected for such interactions in the absence of polymer.^{10,16} One approximation is to just pick up the first higher order term; we will call this the first term approximation. The other approximation is to sum up all similar terms in the expansion, which we call the summed up approximation. At the moment, the convergence of the expansion is not clear.

In the first term approximation, the contribution F_f of the higher terms to the excess free energy is^{10,13}

$$F_f / V k T = 1/2 n_e (\xi \mu_2)^{-1} \sum_j n_j (2\xi z_j)^3 Y_3(\kappa a) / 3! \quad (9)$$

where we define

$$Y_m(x) = -\int_x^\infty y K_0^m(y) dy \quad (10)$$

In the summed up approximation the contribution F_s is expressed as⁶

$$F_s / (V k T) = 1/2 n_e (\mu_2 \xi)^{-1} (H + I + J) \quad (11)$$

where

$$H = 1/2 (\kappa a)^2 \mu_0 \quad (11a)$$

$$I = 2\xi \mu_1 + \xi \mu_2 \quad (11b)$$

$$J = -\sum_i n_i \sum_{m=1}^{\infty} (2\xi z_i)^m Y_m(\kappa a) / m! \quad (11c)$$

where we have used equalities of modified Bessel functions in (11b).¹⁵ The quantity μ_m is already defined by (5). The term given by the right-hand side of (9) is included in J . The essential difference between these two approaches centers on the question of whether or not this kind of contribution should indeed be summed up.

Next, we will examine the contribution of these higher terms to activity coefficients. The first term approximation gives, from eq 5 and 9

$$\ln \gamma_i^f = 2\xi^2 n_e z_i^2 (3\mu_2)^{-1} \{z_i Y_3(\kappa a) + {}^{1/2}\mu_3 \mu_2^{-1} [(\kappa a)^2 K_0^3(\kappa a) - 2Y_3(\kappa a)]\} \quad (12)$$

If we assume that the condition $\kappa a \ll 1$ is satisfied, we have

$$\ln \gamma_i^f \simeq 2\xi^2 n_e z_i^2 (3\mu_2)^{-1} (z_i - \mu_3 \mu_2^{-1}) Y_3(0) \quad (13)$$

where $Y_3(0) = -0.5859$. We should notice here that the contribution expressed by (13) is of comparable magnitude as the DH contribution given by eq 7 even if ξ is equal to unity. This means that the higher terms' contribution is important even in the range of $\xi \leq 1$. If we consider a mono-monovalent added salt, we have $\mu_3 = n_e$, and when salt is in excess we find from (13)

$$\ln \gamma_i^f \simeq 2n_e (3\mu_2)^{-1} Y_3(\kappa a) z_i \quad (14)$$

This means that there is *no* contribution of the first higher term to $\ln \gamma_{\pm}$, because $\ln \gamma_+^f$ and $\ln \gamma_-^f$ will cancel each other out in the calculation of $\ln \gamma_{\pm}$. This corresponds to Manning and Zimm's numerical calculation,¹³ although these authors overestimated $Y_3(\kappa a)$ by using an asymptotic form of $K_0(z)$.

We are able to evaluate the next higher terms which correspond to the terms with $m = 4, 5, \dots$ in (11c). In evaluating these terms, we are essentially approaching the summed up approximation. A similar treatment as given above shows that the term with $m = 4$ does not give an important contribution if $\kappa a \ll 1$ while the next term with $m = 5$ is similar to the first higher term discussed above, including its sign. It is only multiplied by a smaller factor. This difference between terms with m even or odd is generalized. Therefore we can expect the summed up approximation to give higher values for the activity coefficients. Since the importance of the first higher term is clear at $\xi = 1$, the summed up approximation gives an appreciable contribution of the higher order terms. Although such a numerical calculation has been mentioned earlier,¹⁷ the reported result is inconsistent with our present calculation in this respect.

Equations 5 and 11 give the contribution of the summed up approximation to the logarithm coefficients

$$\ln \gamma_i^s = n_e (2\xi \mu_2)^{-1} \{ {}^{1/2}(\kappa a)^2 + 2\xi(z_i - z_i^2 \mu_1 \mu_2^{-1}) + z_i^2 \mu_2^{-1} \sum_j n_j F_j - F_i + {}^{1/2}(\kappa a)^2 z_i^2 \mu_2^{-1} \sum_j n_j (\exp[2\xi z_j K_0(\kappa a)] - 1) \} \quad (15)$$

where we have defined a function

$$F_j \equiv F(\kappa a, z_j \xi) = \int_{\kappa a}^{\infty} y (\exp[2\xi z_j K_0(y)] - 1) dy \quad (15a)$$

Considering practical values of κa smaller than unity, and high ξ values, an important contribution arises from the last three terms on the right-hand side of (15), which correspond to J in (11). If $y \ll 1$, we can replace $K_0(y)$ by $\ln y$, and we have

$$\exp[2\xi z_j K_0(y)] \simeq y^{-2\xi z_j} \quad (15b)$$

This function for counterions is sharply dependent on ξ . For $\xi \gg 1$ and $z_j > 0$, the integrand of (15a) can be replaced by $\gamma^{1-2\xi z_j}$ and F_j shows a κa dependence as $(\kappa a)^{2(1-\xi z_j)}$. This implies that F_j 's of the counterion species are important under this condition. On the other hand if $\xi \leq 1$, the evaluation of (15a) is not so simple, because such a singular behavior is not expected. In Figure 1, the de-

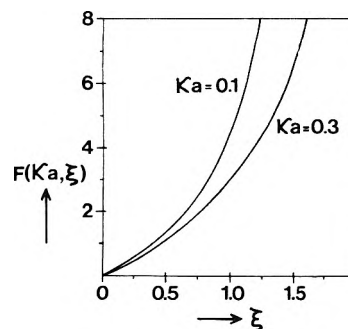


Figure 1. Function $F(\kappa a, \xi)$ defined by eq 15a vs. charge density ξ .

pendence of the function $F(\kappa a, \xi)$ on κa and ξ is shown. The value of the function $F(\kappa a, \xi)$ increases sharply with decreasing κa , especially when ξ is greater than unity.

In conclusion, according to eq 6, the first term approximation yields the activity coefficient of the i th mobile ion species as

$$\ln \gamma_i = \ln \gamma_i^{\text{DH}} + \ln \gamma_i^f + C \quad (16)$$

where we denote the contribution of the higher terms arising from the mobile ion–mobile ion interactions, not considered in this paper, by C . $\ln \gamma_i^f$ is given by eq 12–14 depending on the simplifications used. In the case of the summed up approximation for the higher terms, $\ln \gamma_i^f$ is replaced by $\ln \gamma_i^s$ given by eq 15. Complete neglect of the higher terms leads to $\ln \gamma_i = \ln \gamma_i^{\text{DH}}$, the Debye–Hückel approximation with $\ln \gamma_i^{\text{DH}}$ given by eq 7–8.

IV. Numerical Examinations

In this section we discuss the numerical comparison of the two approximations for the higher order cluster terms as well as comparisons with experimental data.

To begin our calculation, we will assume the polymer concentration n_e to be constant. The polymer concentration enters our expressions through $\kappa_0 a$ where κ_0 is the Debye–Hückel parameter under salt free conditions, given by $\kappa_0^2 = \lambda n_e$. It should be mentioned that the polymer radius a (or, to be exact, the minimal approach distance between mobile ions and the axis of the polyion) is not a well-defined quantity. It has been noticed that differences in the activity coefficients of similar counterion species appear when the polymer concentration increases.¹⁸ This may indeed indicate that the difference between ionic species can be described in terms of ionic radii, with or without the hydration shell, which difference in radius would in turn modify the approach distance a , since a change in a is expressed via a term κa containing the polymer concentration n_e .

If we omit the contributions of mobile ion–mobile ion interactions, i.e., the first term on the right-hand side of eq 7 and higher order terms not mentioned in this paper, we can conveniently describe our results as a function of the ratio $X = n_e/n_3$. Therefore, as we discussed before, we will compare experimental data for our calculations after we have corrected the data for these mobile ion–mobile ion interactions.¹⁶ Although experiments are not always carried out at constant polymer concentration, we can compare our calculations to those experiments by varying $\kappa_0 a$ over a reasonable range.

IV-1. *Monovalent Counterions and Coions.* In Figure 2, we plot the logarithm of the activity coefficient γ_i at $\xi = 1$ against the ratio X . There is an appreciable difference between the first term approximation (curve f) and the summed up approximation (curve s), both in γ_+ and γ_- , and of course also in γ_{\pm} . The most important result is however that both of these approximations yield an ap-

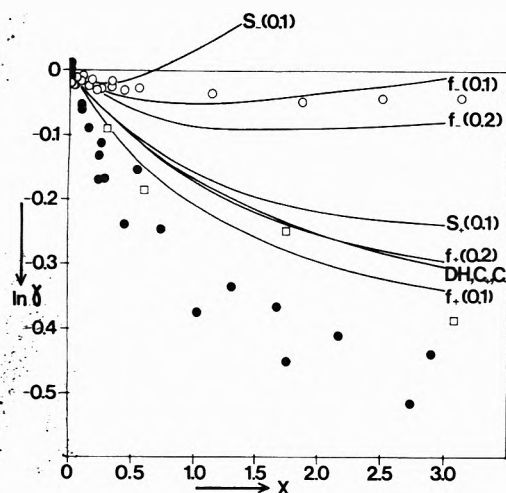


Figure 2. Activity coefficients at $\xi = 1$ as a function of $X = n_e/n_s$: DH, Debye-Hückel approximation; C, DH approximation plus condensation;⁵ f, first term approximation; s, summed up approximation; +, counterion, -, coion. Numbers in brackets are $\kappa_0 a$ values. Experimental points for κ -carrageenan ($\xi = 1.05$):¹⁹ (●) Na^+ , (□) K^+ , (○) Cl^- .

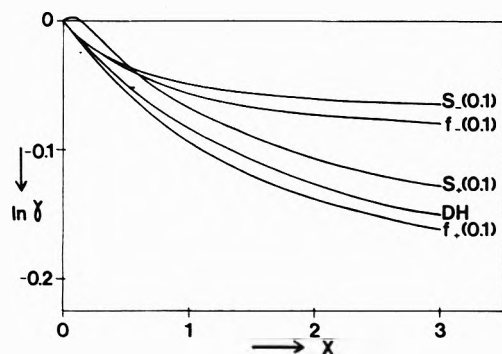


Figure 3. Calculated activity coefficients at $\xi = 0.5$. Notations are the same as in Figure 2.

preciable difference between the activity coefficients of the counterion and of the coion *even* at $\xi = 1$. This difference is not seen in the Debye-Hückel term and indicates the importance of the higher order terms. Formalisms based on counterion condensation at $\xi = 1$ of course give the same result as the DH approximation, i.e., they do not predict a difference between γ_+ and γ_- . At higher ξ values, counterion condensation theory assumes the difference between γ_+ and γ_- to be caused by the counterion condensation term only, the DH term being symmetrical for γ_+ and γ_- with $\xi_{\text{net}} = 1$. Our calculation shows that the higher terms cause a considerable asymmetry between γ_+ and γ_- at $\xi = 1$.

A series of experimental data on κ -carrageenan,¹⁹ a polysaccharide with a ξ value stated to be 1.05, are also shown in Figure 2. The first-order approximation shows a reasonable agreement with these data for both counter- and coions. The value of ξ for κ -carrageenan may not be so precise considering the nature of this polymer, but we can still regard our calculations to be at least in qualitative agreement with the experiments. At $\xi = 0.5$ we find little difference between the two approximations as shown in Figure 3. However even at this low ξ value γ_+ and γ_- are different, although the difference is smaller than at $\xi = 1$. So far as the first term approximation is concerned, we are able to get rather reasonable agreement with experiments on polymers with ξ values a little higher than unity, i.e., at $\xi = 1.38$ ²⁰ and 1.5.¹⁹ These are shown in Figures 4 and 5; the theoretical curves are calculated using eq 13. As is seen, eq 13 predicts that the coion activity

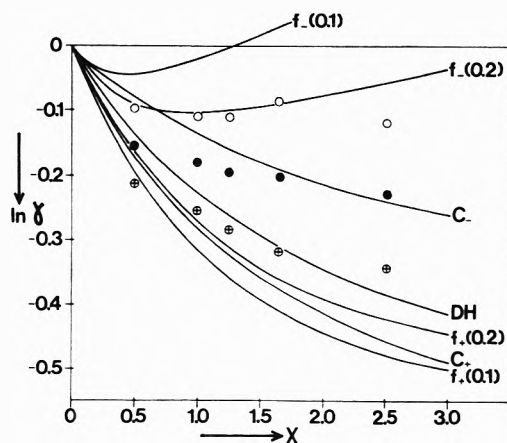


Figure 4. Activity coefficients at $\xi = 1.38$. Notations for the theoretical curves are the same as in Figure 2. Experimental points for sodium carboxymethylcellulose:²⁰ (●) Na^+ , (○) Cl^- , (●) $\gamma_{\pm}(\text{NaCl})$.

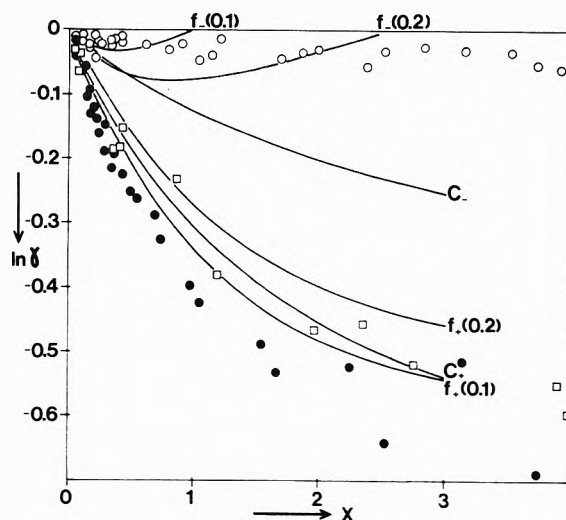


Figure 5. Activity coefficients at $\xi = 1.5$. Notations for the theoretical curves are the same as in Figure 2. Experimental data for λ -carrageenan:¹⁹ (●) Na^+ , (□) K^+ , (○) Cl^- .

coefficient γ_- increases with increasing X at larger X values, while there is no such tendency in the experimental data. Because of this situation we also get higher γ_{\pm} values, even though there is good agreement for γ_+ .

The first term approximation also gives higher values than the limiting law based on counterion condensation, especially for coions. The summed up approximation gives far larger values under these conditions and is not shown in the figures.

For polymers with higher charge densities, e.g., $\xi = 2$ or higher, we cannot get agreement by either of the approximations, mainly because the difficulty in γ_- becomes serious compared with the case $\xi \approx 1$. For these high ξ values the condensation formalism gives reasonable agreement with experiment, although its values for γ_{\pm} are often somewhat lower than the experimental data in the region where $X > 1$.⁹ We notice that evaluation of the higher terms reverses this trend, resulting in values for γ_+ higher than experimental data.

Our inability to get agreement with experiment in systems with large ξ and large X can be attributed to a number of reasons even if we do not consider the possible importance of polyion-polyion interactions. One reason could be that the increasing inhomogeneity of the system with increasing charge density introduces other terms not evaluated by us. Another reason is that the radii of the ions should be introduced explicitly.

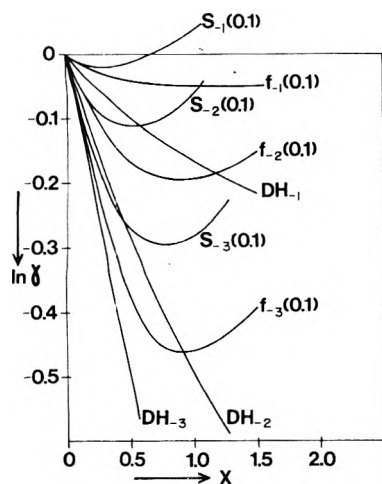


Figure 6. Calculated activity coefficients of coions of different charge at $\xi = 1.0$. Notations are the same as in Figure 2. Index denotes charge of coion, i.e., $f_{-3}(0.1)$ is first term approximation for coion of charge -3 with $\kappa a = 0.1$.

Our calculations have shown that the change in the counterion activity coefficients in the $\xi = 1$ region predicted by the higher terms as approximated in this work is not as sharp as predicted by condensation theory. If we do assume that counterion condensation does indeed take place when ξ exceeds unity, we could modify condensation theory to include a first higher term contribution at $\xi_{\text{net}} = 1$, obtaining a better agreement with experiment at high X values. However it is not clear whether such a treatment is justified.

IV-2. *Divalent Counterions.* The behavior observed in the divalent counterion system is quite similar to the mono-monovalent added salt system, so far as the comparison between the different approximations is concerned. Although activity measurements carried out on this system with large ξ values, e.g., $\xi = 2.8$, show better agreement with the limiting law values based on condensation theory than in the mono-monovalent salt case,^{9,20} our calculation of the higher terms does not suggest such a behavior.

IV-3. *Coions with Higher Valencies.* The Debye-Hückel term is symmetric with respect to the valencies of coions and counterions. On the other hand, the higher terms are asymmetric and make the valence dependence of the coion activity coefficient less sharp than that of the counterion. In Figure 6 the dependence of the coion activity coefficient on X is shown for coion valencies of -1 , -2 , and -3 , for polymers with $\xi = 1$. Although the valence dependence of γ_{\pm} is clear, it is not by far as strong as just the Debye-Hückel approximation predicts. No experimental data for the valence of the coion activity coefficient

are available, but there are experimental data for the coion tracer diffusion coefficients which essentially indicate that the lowering of the coion diffusion coefficient as X increases is virtually independent of the coion valency.²¹ Considering the close parallel between activity coefficients and tracer diffusion coefficients,²² our results for the activity coefficients suggest that the higher order terms also play an important role in the diffusion coefficient.

Finally, we should emphasize that the higher terms contribution to the activity coefficients is important even if the charge density ξ of the polymer is equal to or smaller than the so called critical values. Therefore an appreciable difference in the activity coefficients of counterions and of coions for polyions with ξ about equal to or lower than the critical value is inevitable. Since other theories are essentially based on the Debye-Hückel approximation at this ξ further experimental studies of polyelectrolytes with near critical charge densities should prove valuable. Agreement in this range of ξ values is necessary in order to proceed to systems with higher charge densities, which are of greater practical interest.

Acknowledgment. It is our pleasure to thank Dr. H. Maeda and Dr. Gerald S. Manning for their suggestions which inspired us to begin this work. The financial support of Killam Trust to the first author (K.I.) is acknowledged. The research of the second author is supported by the National Research Council of Canada.

References and Notes

- (1) Present address, Department of Chemistry, Indiana University, Bloomington, Ind. 47401.
- (2) S. A. Rice and M. Nagasawa, "Polyelectrolyte Solutions", Academic Press, New York, N.Y., 1961.
- (3) (a) N. Imai and T. Onishi, *J. Chem. Phys.*, **30**, 1115 (1959); (b) F. Oosawa, "Polyelectrolytes", Marcel Dekker, New York, N.Y., 1971.
- (4) G. S. Manning, *Annu. Rev. Phys. Chem.*, **23**, 117 (1972).
- (5) G. S. Manning, *J. Chem. Phys.*, **51**, 924 (1969).
- (6) G. S. Manning, *J. Chem. Phys.*, **51**, 3249 (1969).
- (7) D. Dolar, "Polyelectrolytes", E. Selegny, Ed., D. Reidel, Dordrecht, 1974.
- (8) G. E. Boyd, D. P. Wilson, and G. S. Manning, *J. Phys. Chem.*, **80**, 808 (1976).
- (9) J. C. T. Kwak, M. C. O'Brien, and D. A. MacLean, *J. Phys. Chem.*, **79**, 2381 (1975).
- (10) K. Iwasa, *J. Chem. Phys.*, **62**, 2976 (1975).
- (11) K. Iwasa, *J. Chem. Phys.*, **64**, 3679 (1976).
- (12) K. Iwasa, *J. Chem. Phys.*, **64**, 2174 (1976).
- (13) G. S. Manning and B. H. Zimm, *J. Chem. Phys.*, **43**, 4250 (1963).
- (14) A. D. MacGillivray, *J. Chem. Phys.*, **56**, 80 (1972).
- (15) See, e.g., G. N. Watson, "Theory of Bessel Functions", 4th ed, Cambridge University Press, London, 1958.
- (16) K. Iwasa and J. C. T. Kwak, *J. Phys. Chem.*, **80**, 215 (1976).
- (17) J. Bailey, *Biopolymers*, **12**, 1705 (1973).
- (18) Y. M. Joshi and J. C. T. Kwak, to be submitted for publication.
- (19) T. J. Podlas and P. Ander, *Macromolecules*, **2**, 432 (1969).
- (20) M. Rinaudo and M. Milas, *Chem. Phys. Lett.*, **41**, 456 (1976).
- (21) M. Kowblansky and P. Ander, *J. Phys. Chem.*, **80**, 297 (1976).
- (22) G. S. Manning, *J. Chem. Phys.*, **51**, 934 (1969).

Excited State Chemistry of Indigoid Dyes. 5. The Intermediacy of the Triplet State in the Direct Photoisomerization and the Effect of Substituents¹

Andree D. Kirsch and George M. Wyman*

Department of Chemistry, University of North Carolina—Chapel Hill, Chapel Hill, North Carolina 27514 (Received July 15, 1976; Revised Manuscript Received December 2, 1976)

Publication costs assisted by the U.S. Army Research Office

Quenching of the direct photochemical trans \rightarrow cis isomerization of thioindigo dyes by oxygen is attributable to the intermediacy of the triplet state. From a study of the dependence of the quantum yields and photostationary state concentrations on the oxygen concentration for nine such dyes the approximate triplet lifetimes could be estimated. The quantum yields for the cis \rightarrow trans isomerization were found to be unaffected by oxygen, unless the compounds contained chlorine substituents; this indicates the quenching of a common triplet intermediate in the isomerization of the latter. All of the compounds studied also undergo photosensitized isomerization to a common photostationary state the position of which is a function of the oxygen concentration. In addition, the fluorescence quantum yields were determined for the trans isomers. The mechanism of the photoisomerization process and the effect of substituents on the quantum yields and rates of the various excited state processes are discussed. The similarities found between these results and the data from recent reports on the effect of substituents on the photoisomerization of some thionaphthoindigos and on the photoisomerization and fluorescence of stilbenes suggest that the resonance stabilization of the trans S_1 state plays an important part in determining the excited state behavior of molecules of this type.

Introduction

Although the photochemical cis-trans isomerization of olefins is a well-known phenomenon, the mechanism of such reactions has not been fully elucidated to date. Thus the controversy between proponents of the singlet route vs. the triplet mechanism for the direct photoisomerization of stilbene has not been resolved as yet.² Interestingly enough, evidence has been presented recently to the effect that the photoisomerization of several 4-nitrostilbenes takes place via the triplet state in the trans \rightarrow cis direction, but by way of a singlet mechanism in the opposite direction,³ attesting to the importance of substituent effects in such reactions.

In a recent communication⁴ we reported preliminary evidence for the intermediacy of the triplet state in the direct photoisomerization of two thioindigo dyes by an oxygen-quenching technique. We now wish to report the results of our investigation of the direct and sensitized photoisomerization of thioindigo and eight of its ring-substituted derivatives and our conclusions regarding the mechanism of the isomerization of such compounds. In addition, the effect of substituents on the rates and/or quantum yields of the various excited state processes will be discussed and compared to what has been reported in the literature for some related molecules.

Experimental Section

Materials. Dyes I, II, and IV–VIII were provided through the generosity of Professor W. Luetke, Organic Chemistry Institute, University of Goettingen. Their purification was accomplished by recrystallization and/or vacuum sublimation, as required. Dyes 0 and III have been described previously.⁵ Merck Uvasol and Fischer ACS Grade benzene was used as the solvent. The tin(IV) tetraphenyltetrahydroporphyrin used as sensitizer was prepared according to the method of Whitten, Yau, and Carroll.⁶ 1,2;5,6-Dibenzanthracene was purchased from

the Eastman Kodak Co. and recrystallized from benzene before use.

Spectroscopic Measurements. Absorption spectra were determined on a Cary Model 17 spectrophotometer, using fused quartz absorption cells. Fluorescence emission was measured using a Hitachi-Perkin-Elmer MPF-3 spectrofluorimeter. The fluorescence spectra were corrected as described in ref 5.

Photostationary States. The photostationary states induced by monochromatic radiation that are required for the calculation of the absorption spectra of the pure isomers⁷ were obtained by irradiation of the solutions with light from a tunable Spectra-Physics argon-ion laser (458.0–514.5-nm region) or a mercury arc equipped with an interference filter to isolate the 546-nm line. Photostationary states not requiring monochromatic irradiation were obtained using the light source described in an earlier paper.⁸

Quantum Yield Measurements. The quantum yields for the trans \rightarrow cis isomerization ($\phi_{t \rightarrow c}$) were determined on solutions contained in rectangular 1-cm absorption cells mounted along with a mercury-lamp light source in an optical bench. Interference filters were used to isolate the 546 or 577–579-nm lines, as required. An air-saturated benzene solution of dye 0 was used as the secondary reference⁵ and the concentrations of the sample and reference solutions were adjusted to result in equal optical densities at the wavelength used for irradiation. Irradiation was carried out to 6–10% conversion and the result corrected for the reverse reaction according to the method of Lamola and Hammond.⁹ With one exception, quantum yields for the cis \rightarrow trans isomerization ($\phi_{c \rightarrow t}$) were calculated by multiplying the measured $\phi_{t \rightarrow c}$ values with the quantum yield ratios ($\phi_{c \rightarrow t}/\phi_{t \rightarrow c}$) obtained from photostationary state measurements according to eq 2 in ref 5. Only for dye III was $\phi_{c \rightarrow t}$ determined directly against the secondary reference (dye 0).

Determination of the fluorescence quantum efficiencies (ϕ_f) was carried out as described previously⁵ except that the value of $\phi_f = 0.70$ was used for rhodamine B in ethanol which was used as the reference in this work.¹⁰ The greater

* Address correspondence to the author at the Chemical and Biological Science Division, Department of the Army, U.S. Army Research Office, Research Triangle Park, N.C. 27709.

TABLE I: Absorption and Fluorescence Spectra of Thioindigo Dyes in Benzene

Dye	Substituents	λ_{\max}^t	ϵ_t	ϵ_c	λ_{\max}^c	ϵ_t	ϵ_c	λ_{iso}	ϵ_{iso}	λ_{\max}^f
0	None	543	16 700	1000	484	3915	13 400	502	8190	593
I	4,4',7,7'-Tetramethyl-	553	17 560	900	493	5120	14 850	511	9790	599
II	5,5'- <i>tert</i> -Butyl-	554	15 940	910	492	4420	13 410	512	8830	601
III	6,6'-Diethoxy-	516	14 800	795	458	5005	12 000	476	8535	553
IV	6,6'-Dichloro-4,4'-dimethyl-	537	20 630	1150	481	5095	16 140	497	9925	584
V	6,6'-Dichloro-7,7'-dimethyl-	543	17 535	945	484	4690	14 300	502	8950	593
VI	4,4'-Dichloro-	548	14 560	740	486	3075	12 040	505	6565	591
VII	5,5'-Dichloro-7,7'-dimethyl-	563	14 285	680	499	3980	11 695	518	7805	604
VIII	7,7'-Dichloro-	544	17 365	960	488	5085	14 265	504	9105	594

sensitivity of the MPF-3 instrument resulted in higher values for dyes 0 and III than reported earlier.⁵

Excited State Lifetimes. Excited state lifetimes for dyes I, II, and IV–VIII in benzene solution were determined by the single-photon counting technique through the courtesy of Drs. H. Staerk and M. Schulz.

Oxygen-Quenching Experiments. Degassing of the solutions was accomplished by repeated freeze–thaw cycles at liquid N₂ temperatures, using a vacuum-line equipped with a mercury diffusion pump. Degassing was continued until the pressure (at 77 K) was stabilized at 4–8 × 10⁻⁶ Torr. The desired concentrations of oxygen were introduced into the solutions by allowing them to reach thermal equilibrium at room temperature on a vacuum line to which controlled amounts of oxygen or air had been admitted. The resulting oxygen concentrations were calculated according to Henry's law. (An air-saturated benzene solution at 25 °C was assumed to be 0.0016 M in O₂.³)

Sensitized Isomerizations. Whenever possible, tin(IV) tetraphenyltetrahydroporphyrin ($E_T = 36.5$ kcal) was used as the sensitizer (under conditions similar to those described previously¹¹), since its strong absorption at 611 nm permitted the selective excitation of the sensitizer. 1,2;5,6-Dibenzanthracene ($E_T = 52.2$ kcal) was used as the sensitizer for dyes III, IV, and VIII. For III and IV this was to ensure that the energy difference between sensitizer and dye would be sufficient to allow energy transfer at or near the diffusion-controlled rate, while for VIII this was necessary, because that dye was found to undergo a photochemical reaction with the porphyrin. Excitation of these solutions was carried out in the 365–400-nm region using a mercury arc equipped with a Bausch & Lomb monochromator and a Corning filter that cut off all light of $\lambda > 400$ nm. The concentrations of sensitizer and substrate were so adjusted that >95% of the exciting light was absorbed by the sensitizer.

While the photostationary states reached by the air-saturated solutions of these dyes are sufficiently stable for spectroscopic measurements, it was found that prolonged irradiation of the degassed solutions generated a catalyst (presumably free radicals) that produced thermal cis–trans isomerization. In order to minimize this undesirable side reaction, the photostationary states were first approached by producing (by direct irradiation) mixtures of isomers similar in composition to the expected photostationary state, followed by addition of the sensitizer and degassing. Thus it was possible to reduce the length of the irradiation required for reaching the photostationary state and minimize catalyst formation.

Results

(a) **Absorption and Fluorescence Spectra.** In general, the visible absorption spectra calculated for the pure cis and trans isomers of these dyes by the method described in ref 7 are very similar to those reported previously for thioindigo⁵ using another method of computation based

on a combination of fluorescence and absorption measurements;¹² moreover, the curve of each cis isomer shows the characteristic “tail” at long wavelengths. Since absorption curves for *cis*- and *trans*-6,6'-dichloro-4,4'-dimethylthioindigo have also been published recently,⁷ the appropriate absorption spectra data for all of the dyes studied in this work are only tabulated in Table I. (The data for thioindigo and its 6,6'-diethoxy derivative have been recalculated resulting in minor changes from those reported in ref 5.) The corrected fluorescence spectra show the expected mirror-image relationship to the absorption spectra of the trans isomers with clearly distinguishable shoulders on the long-wavelength side of the emission maxima, but they fail to exhibit the sharp spike at ~620 nm that had been reported previously for trans thioindigo.¹² The wavelengths for the corrected emission maxima are also listed in Table I.

It is important to note that the fluorescence and absorption spectra are independent of the concentration of dissolved oxygen with respect to both curve shape and intensity.

(b) **Cis–Trans Isomerization.** Every one of the nine dyes exhibited both direct and sensitized photoisomerization similar to that shown by thioindigo.^{5,11}

(c) **Quantum Yields.** The fluorescence quantum yields (ϕ_f), the initial trans–cis isomerization quantum yields ($\phi_{t \rightarrow c}^0$), and the derived quantum yields for the reverse reaction ($\phi_{c \rightarrow t}^0$) and intersystem crossing (ϕ_{ISC}) for degassed solutions are summarized in Table II. The quantum yields for intersystem crossing (ϕ_{ISC}) were not determined directly, but were estimated by combining the appropriate quantum yields with the decay ratios observed in the sensitized isomerizations according to the equations

$$\phi_{\text{ISC}}^t = \phi_{t \rightarrow c} \left(1 + \left(\frac{[t]}{[c]} \right)_{\text{PSS}} \right)$$

$$\phi_{\text{ISC}}^c = \phi_{c \rightarrow t} \left(1 + \left(\frac{[c]}{[t]} \right)_{\text{PSS}} \right)$$

(These equations are based on the assumption that all of the S₀ → T₁ decay occurs from the “phantom” triplet.) The quantum yields for nonradiative decay of the excited singlet states (ϕ_d^t and ϕ_d^c) were calculated by difference.

Since the effect of dissolved oxygen on $\phi_{t \rightarrow c}$ was amenable to Stern–Volmer treatment,¹³ “Stern–Volmer constants” (K_{SV}) were determined graphically (cf. ref 4) and included in Table III. For dyes 0–V these SV plots were based on a minimum of four oxygen concentrations; for dyes VI–VIII, due to solubility difficulties, K_{SV} was determined from two measurements: air-saturated and degassed.

(d) **Photostationary State Concentrations.** The photostationary state (PSS) concentrations (under comparable conditions) were determined spectroscopically and the ratio of isomer concentrations was plotted as a function of the oxygen concentration for both the direct and the

TABLE II: Lifetimes, Quantum Yields, and Rate Constants for the Direct Photoisomerization of Thioindigo Dyes^a

Dye	τ_S^t , ns	τ_T^t , ns	ϕ_f	$10^7 k_f$	$10^7 k_f^{\text{calcd}}$ $k_f^{\text{(trans)}}$	$\phi^0_{t \rightarrow c}$	ϕ^t_{ISC}	$10^7 k^t_{ISC}$	ϕ_d^t	$10^7 k_d^t$	$\phi^0_{c \rightarrow t}$	$\phi^{\text{air}}_{c \rightarrow t}$	ϕ^c_{ISC}	ϕ_d^c	$10^7 k_f^{\text{calcd}}$ $k_f^{\text{(cis)}}$
0	13.4	300	0.71	5.3	3.4	0.11	0.23	1.7	0.06	0.45	0.45	0.45	(0.85) ^c	(0.15) ^c	3.6
I	13.5	300	0.67	5.0	3.7	0.10	0.22	1.6	0.11	0.81	0.45	0.45	(0.90) ^c	(0.10) ^c	4.4
II	10.1	300	0.45	4.5	3.4	0.10	0.25	2.5	0.30	3.0	0.45	0.45	(0.76) ^c	(0.24) ^c	4.2
III	0.9	140	0.04	4.4	4.0	0.45	1.02	113	0	0	0.45 ^b	0.45	(0.80) ^c	(0.20) ^c	4.4
IV	10.5	200	0.62	5.9	4.1	0.14	0.46	4.3	0	0	0.32	0.43	0.46	0.54	4.5
V	9.3	200	0.62	6.7	3.7	0.13	0.40	4.3	0	0	0.29	0.40	0.43	0.57	4.1
VI	12.9	580	0.68	5.3	2.6	0.07	0.22	1.7	0.10	0.78	0.34	0.46	0.50	0.50	2.9
VII	13.2	365	0.38	2.9	2.9	0.05	0.17	1.3	0.43	3.3	0.30	0.42	0.43	0.57	3.4
VIII	13.0	140	0.64	4.9	3.1	0.07	0.23	1.8	0.13	1.0	0.34	0.45	0.49	0.51	3.5

^a Solvent, benzene; temperature, 25 °C. ^b Determined directly on a solution containing > 90% cis isomer. ^c Calculated on the basis of the triplet mechanism that is considered unlikely.

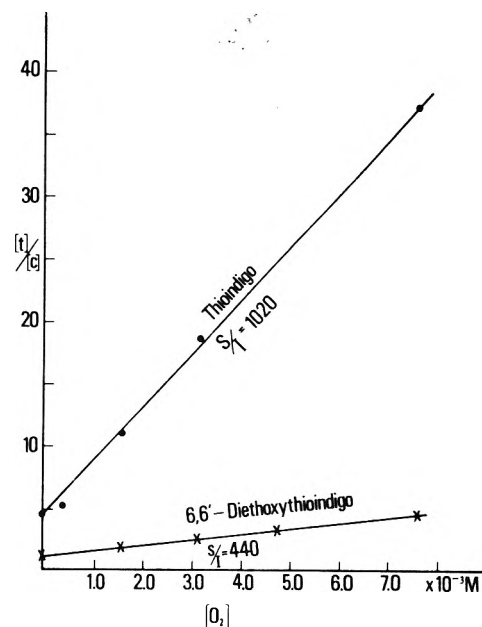


Figure 1. Plots of the ratio of isomer concentrations ($[trans]/[cis]$) at the photostationary state vs. oxygen concentration for thioindigo (●) and 6,6'-diethoxythioindigo (X). Direct irradiation of benzene solutions at room temperature. Data normalized to correspond to irradiation at the isosbestic point ($\epsilon_c = \epsilon_t$; hence $[t]/[c] = \phi_{c \rightarrow t}/\phi_{t \rightarrow c}$) for each dye.

sensitized isomerizations. For the direct isomerization the same number of data points were obtained as for the quantum yield measurements described above; such plots for dyes 0 and III are shown in Figure 1. The PSS concentrations obtained during the sensitized isomerization of all dyes were determined only on the degassed and air-saturated solutions. The slope/intercept ratios (S/I) derived from these measurements and the isomer concentrations observed at the PSS in the sensitized reactions have been tabulated in Table III.

(e) *Lifetimes and Rate Constants.* The experimentally obtained (oxygen-independent) singlet lifetimes (τ_S) and the triplet lifetimes (τ_T) calculated from the K_{SV} values, using $k_q = 3.1 \times 10^{14}$ have also been included in Table II. The specific rate constants for several of the excited state processes of the trans isomers could also be calculated from their quantum yields and τ_S and are shown in Table II.

(f) *Triplet Energies.* The triplet energy for dye III ($E_T = 32.1$ kcal) was determined from its $T_1 \leftarrow S_0$ absorption at 890 nm in a saturated benzene-ethylene bromide solution. It is believed that, based on their behavior toward the sensitizers and quenchers used in this work, the remaining compounds have E_T values in the 27–32-kcal range.

Discussion

The observation that dissolved oxygen quenches the direct photoisomerization of trans-0 without in any way diminishing the intensity of its fluorescence immediately suggests that trans \rightarrow cis isomerization has to involve the triplet state as the intermediate. (This is in sharp contrast with the previously reported quenching of the isomerization of such compounds by phenols which is accompanied by a corresponding quenching of the fluorescence and must therefore involve the singlet state.¹⁵) Triplet state intermediates of several thioindigo derivatives have recently been observed by conventional flash photolysis at 77 K¹⁶ and by laser-flash techniques at room temperature.^{14,16}

TABLE III: Stern-Volmer Treatment of Quantum Yields and Photostationary State Data^a

Dye	Direct				Sensitized				
	K_{SV}	S/I	α	Kinetic scheme	$(t)^0/(c)^0$	$(t)^{air}/(c)^{air}$	S/I	α	Kinetic scheme
0	950	1020	0.93	A or B'	53/47	75/25	1038	0.92	B'
I	930	910	1.02	A	50/50	78/22	1590	0.57	B
II	930	1000	0.93	A or B'	59/41	79/21	1010	0.92	B'
III	420	440	0.95	A or B'	56/44 ^b	68/32 ^b	419	1.0	B'
IV	620	1010	0.61	B	69/31 ^b	86/14 ^b	1100	0.56	B
V	620	975	0.64	B	67/33	84/16	991	0.63	B
VI	1810	2545	0.71	B	68/32	91/9	2425	0.74	B
VII	1195	1630	0.73	B	70/30	90/10	1785	0.67	B
VIII	440	875	0.51	B	70/30 ^b	85/15 ^b	893	0.50	B

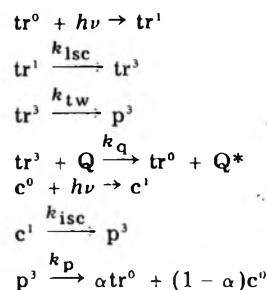
^a The sensitizer was tin(IV) tetraphenyltetrahydroporphyrin, except where indicated. ^b 1,2,5,6-Dibenzanthracene sensitizer.

It was not without trepidation that we settled on the use of oxygen as the quencher for our Stern-Volmer studies, since (1) its concentration cannot be varied as conveniently as that of a liquid or a solid quencher, and (2) it is a versatile reagent that has recently been observed to enhance the rates of the trans \rightarrow cis photoisomerization of some diaryethylenes,¹⁷ while for stilbene¹⁸ and some nitrostilbenes³ it has been reported to quench the photoisomerization without affecting the isomer concentrations. However, the low (~ 30 kcal) triplet energies of our substrates¹¹ severely restricted our choice of usable quenchers and we are pleased to report that, with respect to the thioindigos, oxygen behaves solely as a quencher that functions by energy transfer from the appropriate triplet state of the substrate; this mode of quenching was also confirmed by the evidence that singlet oxygen was produced under these conditions.⁴

Mechanism of the Direct Photoisomerization. It is clear from these results that the first step in the trans \rightarrow cis isomerization process involves intersystem crossing (ISC) from the S_1 state to the triplet manifold followed by rapid relaxation to the T_1 state, presumably with retention of the trans geometry. However, from the standpoint of the entire photoisomerization process (both directions), there are several alternative pathways involving the subsequent (or complementary) steps that need to be considered.

In their recent paper on the nitrostilbenes,³ Bent and Schulte-Frohlinde outlined two of these mechanisms: In their Scheme A the trans triplet is rapidly converted to the twisted ("phantom") triplet which can relax to either cis or trans ground states and which can be quenched exclusively to the trans isomer (by azulene or ferrocene). The cis \rightarrow trans reaction in this "scheme" does not involve the triplet at all; twisting occurs in the S_1 state with subsequent relaxation of the twisted S_1 state to cis and trans ground state molecules. Their Scheme B is identical with Scheme A in the trans \rightarrow cis direction, but they propose that here the cis \rightarrow trans isomerization proceeds via ISC to the common "phantom" triplet state whose behavior has already been described. The two mechanisms are readily distinguishable: Since Scheme A involves two separate and distinct (T_1 and S_1) twisted intermediates, $\phi_{c \rightarrow t}$ is independent of the quenchers that affect $\phi_{t \rightarrow c}$. In contrast, if Scheme B is followed and the "phantom" triplet is the common intermediate in both directions, the reduction of $\phi_{t \rightarrow c}$ at a given quencher concentration is accompanied by a corresponding increase in $\phi_{c \rightarrow t}$. These differences are easily seen when the ratio of isomer concentrations ($[trans]/[cis]$) at the PSS is plotted vs. $[Q]$; when quenching involves the common intermediate (Scheme B), $S/I = K_{SV}/\alpha = k_{qt}/\alpha$, where α represents the fraction of "phantom" triplets that decay to trans in the absence of quencher.

Scheme B'



We find that in order to arrive at a satisfactory interpretation of our results we need to modify their Scheme B by further distinguishing between the quenching of the transoid triplet before it has had a chance to relax to the phantom "triplet" (this is similar to Fischer's mechanism for the photoisomerization of the stilbenes¹⁹), and their Scheme B that involves the quenching of a triplet state intermediate (perhaps a transoid triplet that is in equilibrium with the "phantom" triplet) which can readily be reached from both cis and trans configurations and which is quenched solely to the trans isomer.¹⁸ Since in their paper they described their two schemes, we only need to add Scheme B' using the same symbols that were used in ref 3.

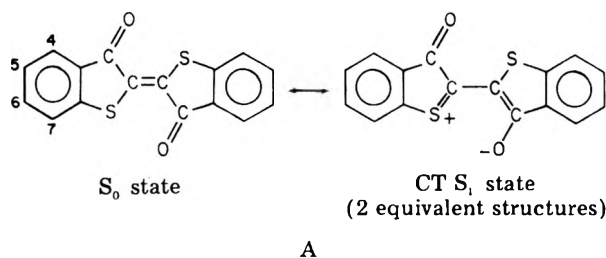
The need for a third alternative pathway became apparent when we found that for dyes 0, II, and III the S/I values for both the direct and sensitized reactions corresponded closely to the respective K_{SV} values (i.e., $\alpha = 1.0 \pm 0.1$; cf. Table III). This indicates that the intermediate that is quenched by oxygen is not a common intermediate, but accessible only from the trans side. In the direct reaction this could be explained on the basis of Scheme A, but since the sensitized reaction proceeds via the triplet manifold, it was necessary to develop a triplet state mechanism (e.g., scheme B') that is consistent with these observations. Unfortunately, our results are unable to distinguish between Schemes A and B' for the direct isomerization of these compounds, since neither involves a common intermediate.

Perusal of the K_{SV} and S/I columns (direct and sensitized) in Table III discloses that the five chlorine-substituted dyes follow Scheme B. In each instance both S/I values are considerably larger than K_{SV} and the two sets of S/I ratios are in good agreement with each other, confirming that for these compounds both the direct and the sensitized isomerizations take place by the same triplet state mechanism. With one exception (VIII) the values calculated for α (by dividing K_{SV} by S/I) are in reasonable agreement with the values obtained from sensitized PSS measurements in the absence of air.

Compound I presents a special case. In the direct reaction $S/I \sim K_{SV}$, but for the sensitized reaction $S/I = K_{SV}/0.57$. Thus it seems that only in the sensitized isomerization of this dye is the "phantom" triplet the common intermediate; in contrast, the direct reaction appears to follow Scheme A, viz. cis to trans isomerization takes place by a singlet mechanism. The mechanism that is applicable to the photoisomerization of each dye is also indicated in Table III.²⁰

Effect of Substituents. In an earlier paper in this series the effects of variations in chemical structure on the excited processes of some thioindigo dyes were discussed.⁵ Since at that time the involvement of the triplet state in the photoisomerization had not been discovered as yet and the interpretation of the results was consequently based on the assumption of a singlet state mechanism in both directions, an in depth reexamination of the excited state behavior of molecules of this type is in order.

Both spectroscopic and quantum-mechanical evidence indicates that the first excited singlet (S_1) state of thioindigo dyes is the charge transfer (CT) state resulting from the partial transfer of electrons from the heteroatom to the carbonyl oxygen, as shown in A.²¹ (For convenience,

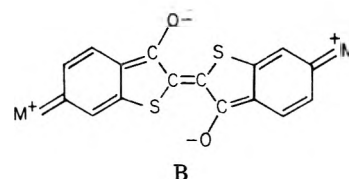


the numbering system used for molecules of this type is also indicated.) The remarkably low potential energy of the first excited states of the trans isomers not only of the thioindigos, but also of indigo and selenindigo and their derivatives (these compounds are among the smallest conjugated organic compounds that absorb in the orange to red regions of the visible spectrum!) has prompted a number of theoretical and experimental spectroscopic investigations in recent years.^{21b,23-25} One may conclude from their results that there is extensive resonance stabilization of the S_1 state in the thioindigos which is further enhanced by strong $S \cdots O$ no-bond interaction for the trans isomers,²⁵ similar to that first proposed by Rogers, Margerum, and Wyman.²² Since in the cis isomers this $S \cdots O$ interaction is destroyed and probably even replaced by $O \cdots O$ and $S \cdots S$ repulsions, λ_{max} for the cis isomers is always at shorter wavelengths than for the corresponding trans forms (cf. Table I). While, in general, the cis isomers of other conjugated olefins absorb more intensely at shorter wavelengths than do their counterparts (cf. stilbenes²⁶ or azobenzenes²⁷), the wide separation in absorption peaks shown in Table I appears to be unique for the indigoid dyes and is most probably attributable to dipolar attraction/repulsion between heteroatom and carbonyl oxygen.²⁵

Excited State Processes of the Trans Isomers. It is known from both experimental and theoretical studies that the S_1 state of *trans*-stilbene lies in a shallow energy well and that rotation and/or intersystem crossing require a slight activation energy (~ 2 kcal/mol).² Since we find that, for thioindigo, fluorescence and ISC are the only pathways for deactivating the S_1^t state, we conclude that it follows the same mechanism, except that due to the enhanced dipolar $S \cdots O$ attraction the energy well in the S_1^t state is deeper than it is for stilbene, and that all the molecules that surmount this energy barrier intersystem cross to an appropriate triplet state T_n^t . At the present

time, we have only preliminary evidence to the effect that the *trans* \rightarrow *cis* isomerization of dye II in MCH involves an activated process with an energy of activation of ca. 3 kcal/mol.²⁸ On the other hand, it is known that for *trans*-stilbene $\phi_f \sim 0.05^2$ and $k_f \sim 4 \times 10^8$ ²⁹ at room temperature, hence the rates of the competing nonradiative processes (twisting and/or ISC) for deactivating the S_1^t state must be of the order of 8×10^9 , i.e., greater by more than two orders of magnitude than the $k_{ISC} = 1.7 \times 10^7$ that we find for thioindigo (cf. Table II). This provides strong indirect evidence for the existence of a relatively high energy barrier in the S_1^t state of the latter. Since the direct isomerization of the *trans* thioindigo dyes takes place exclusively via ISC, we conclude that the S_1^t energy surface must exhibit an uphill slope as the molecule is twisted.

From this perspective it is then possible to interpret the observed effect of substituents on the excited state processes of the *trans* isomers. It is immediately apparent from Table II that, as expected (since their absorption curves are quite similar), substituents have little effect on k_f ; the observed k_f values are also in good agreement with the values calculated from the absorption spectra.⁵ In sharp contrast, substituents in the 6,6' positions enhance k_{ISC} by factors of 2 (for Cl) and ~ 50 (for C_2H_5O), while substituents in the other positions have virtually no effect. It is interesting to note that these same substituents also uniquely affect the absorption spectra: 6,6'-dichloro-thioindigos exhibit a weak absorption band and the 6,6'-diethoxy compounds have a very intense band in the near-uv region.³⁰ Such bands are completely absent in the spectra of all the other simple thioindigo dyes studied in this work or described in the literature and are most probably attributable to increasing contributions from the *p*-chloro- and *p*-ethoxyphenylketo- conjugation that is in



competition with the indigo chromophore, as shown in structure B. The resulting destabilization of the S_1^t state can also be seen in the hypsochromic shifts of λ_{max} in Table I (although for dye V the expected hypsochromic shift is apparently compensated for by the effect of methyl groups³¹). Thus the spectroscopic evidence supports the view that the enhancement in the ISC rates result from a reduction in the depth of the energy well and a concomitant lowering of the energy barrier due to resonance destabilization of the S_1^t state. The effect of the strongly electron-donating ethoxy group is so marked that with respect to τ_S and ϕ_f dye III resembles *trans*-stilbene far more than it does the other thioindigos (cf. Table IV)! (An alternative and reasonable, though in view of the above reasoning less likely explanation for the enhancement of k_{ISC} in the two chlorine-containing dyes would involve a position-dependent internal heavy atom effect, similar to what has recently been observed in the photoisomerization of some bromostilbenes³² and the behavior of chlorophenylthalenes³³ and some norbornene derivatives.³⁴)

The $S_0 \leftarrow S_1$ nonradiative decay processes ("internal conversion") of molecules of this complexity are not well understood at the present time, although it has been possible to arrive at a number of useful correlations from the wealth of accumulated experimental data.³⁵ In general, only for two of the nine dyes studied in this work (II and VII) is there an indication of appreciable ($\phi_d > 0.13$) ra-

diationless decay from the S_1^t state (cf. Table II). A comparison of dyes I and II is particularly instructive in this respect, since their absorption and fluorescence spectra are very similar (cf. Table I) and the values for $\phi_{t \rightarrow c}$ are also identical (Table II). The stronger fluorescence of I is noticeable even to the naked eye and the differences in ϕ_d^t and k_d^t are no doubt attributable to the additional degrees of freedom for dissipating electronic energy by vibrational relaxation through the *tert*-butyl groups. The reasons for the relatively high values for ϕ_d^t and k_d^t for dye VII are less clear; perhaps there is a reason for more efficient radiationless decay for 5-methyl substituted thioindigos than for those substituted in the 4 and 7 positions (dye I); or alternatively, the abnormally high value for ϕ_d^t may have resulted from a combination of experimental artifacts in this instance (low $\phi_{t \rightarrow c}$, poor solubility, low accuracy of the fluorescence spectrum at $\lambda > 640$ nm).

Excited State Processes of the Cis Isomers. In contrast with the trans isomers, the cis isomers do not fluoresce, hence a study of their behavior in the excited state must, of necessity, be qualitative. It is, of course, possible to calculate approximate values for k_f^c from their absorption spectra (cf. Table II) that turn out to be quite similar to those obtained for k_f^t ; thus the absence of measurable luminescence must be attributable to competition from very fast ($k_c^c > 10^{10}$) radiationless decay processes: e.g., twisting, ISC, and/or internal conversion to the ground state.

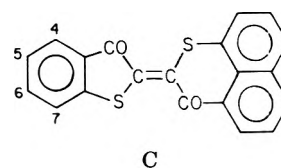
It has been shown above that for dye I the direct cis \rightarrow trans isomerization takes place by a singlet mechanism and we are inclined to believe that dyes 0, II, and III follow the same pathway.²⁰ This suggests that the twisting of the S_1^c state occurs at a rate that is so fast at room temperature as to preclude any appreciable fluorescence or ISC. In contrast, we find that the cis \rightarrow trans isomerization of dyes IV–VIII proceeds via the triplet manifold, suggesting that the “internal heavy atom effect” of the chlorine atoms results in sufficient enhancement of k_{ISC}^c to make it predominate over the twisting of the singlet.

Although an enhancement of k_{ISC} by ca. 2 orders of magnitude due to α chlorination of naphthalene has been reported,³⁶ in the thioindigos the effect due to the introduction of two chlorine is either considerably larger or it must be accompanied by a change in the shape of the potential energy curve of the S_1^c state that results in a reduction of the rate constant for twisting coupled with an enhancement of the rate of internal conversion to S_0^c .

The Nature of the Triplet States. In contrast with stilbene¹⁸ and some of the nitrostilbenes,³ quenching of the triplet state of each of the thioindigos studied in this work results in every instance in its deactivation to the trans isomer. This strongly suggests that, unlike the mechanism most recently invoked for the stilbenes,¹⁸ the trans (tr^3) and twisted (p^3) triplet states postulated in the mechanism above are two distinct species. In compounds 0, II, and III there appears to be no access from p^3 to tr^3 at room temperature, presumably due to the existence of an appreciable energy barrier. On the other hand, for dye I and for all the chlorine-substituted thioindigos (IV–VIII) the p^3 and tr^3 states appear to be quasi-isoenergetic and in rapid equilibrium with each other. The reasons underlying this perturbation of the triplet state energy levels by the methyl groups or the chlorine substituents are not at all clear at the present time.

Comparison with Other Systems. Thionaphthioindigos. Mostoslavskii et al. have recently published a study of the effect of substituents on the quantum yields of the cis-

trans isomerization of a series of thionaphthioindigos (C).³⁷



In general, they have found that $\phi_{c \rightarrow t} / \phi_{t \rightarrow c} \sim 10$ (with the exception of the 4,5-benzo-substituted compound), $\phi_{c \rightarrow t} \sim 0.3$, and that the substitution of electron-donating groups in the 6 positions increases $\phi_{t \rightarrow c}$. They also report fluorescence for the trans isomers in each instance, but they have not measured its quantum yield nor the excited state lifetimes. They found a surprising wavelength dependence of the isomerization quantum yields, with different values for wavelengths on either side of the isosbestic point (with ϕ at the isosbestic wavelength in some instances coinciding with ϕ in the trans band, at others in the cis region). It appears that this last finding was probably due to the error introduced by the graphical method they used for calculating the absorption curves of the two isomers³⁸ which erroneously assumes that at the wavelength of the absorption maximum of each isomer there is only negligible absorption due to the other. Although it is unclear from their paper whether oxygen was excluded from their solutions and the quantitative aspects of their results are in doubt, their data are in qualitative agreement with our results on the effect of substituents on the thioindigos.

Comparison with Other Systems. Stilbenes. The excited state processes of the stilbenes and a variety of their derivatives have been extensively studied, but the exact mechanism of their photoisomerization is still the subject of controversy.^{2,39} The stilbenes undergo all of the same photochemical processes (direct and sensitized isomerization, fluorescence from the trans isomer, and radiationless decay) as have been reported for the thioindigos; their photochemistry is complicated by a photocyclization reaction of the cis isomer to 9,10-dihydrophenanthrene.

Since the S_1 state of stilbene is a π, π^* state,^{26,29} the effect of substituents is not as pronounced on the excited state processes, as it is with the thioindigos. Although the agreement in the quantum yield data reported for the various excited state processes of the stilbenes and their derivatives by different investigators leaves something to be desired,^{40,41} it is evident from Table IV that there is sufficient qualitative agreement to permit a comparison with the thioindigos. In the first place, just as with the thioindigos and the thionaphthioindigos, the quantum yield of the cis \rightarrow trans isomerization is relatively little affected by substituents. On the other hand, with respect to the excited state processes of the trans isomers, even cursory inspection of the quantum yield data in Tables II and IV discloses sharp contrasts: For the stilbenes in nonpolar solvents (with one exception) $\phi_{t \rightarrow c} > \phi_{c \rightarrow t}$ and ϕ_f is much smaller than either, while for the thioindigos (with one exception) $\phi_{c \rightarrow t} > \phi_{t \rightarrow c}$ and ϕ_f is comparable to $\phi_{c \rightarrow t}$, hence greater than $\phi_{t \rightarrow c}$. The exception among the stilbenes is the 4-dimethylamino-4'-nitro derivative where, due to the interaction of the conjugated donor and acceptor substituents (as shown by the bathochromic shift of λ_{max} to ca. 425 nm), the S_1 state probably has a great deal of CT character,⁴² hence would be expected to resemble the thioindigos.⁴³ Conversely, among the thioindigos only the 6,6'-diethoxy derivative, in which the chromophore resonance is weakened (cf. hypsochromic shift to 516 nm) due to the effect of the substituents (see above), shows quantum yields comparable to stilbene: For this com-

TABLE IV: Quantum Yields for the Excited State Processes of Some Stilbenes (25 °C)

Substituents	Solvent	λ_{exc} , nm	$\phi_{t \rightarrow c}$	$\phi_{c \rightarrow t}$	ϕ_f	Ref
None	Alkane	313	0.50	0.35	0.06	40
	Alkane	313	0.40	0.22	nr ^a	41b
	Alkane	313	0.59	0.32	nr	41c
4-Methoxy-	Alkane	313	0.46	0.25	0.03	40
	Alkane	313	0.40	0.29	nr	41b
4-Chloro-	Alkane	313	0.60	0.42	0.08	40
	Alkane	313	0.41	0.21	nr	41b
4-Methoxy-4'-nitro-	Alkane	313	0.60	0.38	~0	40
	Alkane	366	0.67	0.24	nr	41a
	MeOH/EtOH	405	0.10	0.39	nr	40
	MeOH	366	0.07	0.48	nr	41a
	EtOH	366	0.13	0.40	nr	41a
4-Dimethylamino-4'-nitro-	Alkane	436	0.22	0.45	0.20	40
	Alkane	436	0.16	0.37	nr	41a
	Toluene	436	0.04	0.55	nr	40
	Benzene	436	0.013	0.40	nr	41a

^a Not reported.

pound $\phi_{c \rightarrow t}^0 = \phi_{t \rightarrow c}^0$ and ϕ_f is much smaller than either.⁴⁴

Gegiou, Muszkat, and Fischer attributed the anomalous behavior of 4-dimethylamino-4'-nitrostilbene to preferential stabilization of the dipolar T_1 state by solvation with polar and/or polarizable solvents. In their opinion, due to its planarity and since the separation of charges is greatest in the trans form, this configuration would be expected to gain most in stability by solvation, sufficient in this instance to lower its energy below that of the twisted intermediate.⁴⁰ Regrettably this explanation fails to account for the concomitant considerable increase of the fluorescence quantum yield (cf. Table IV), nor is it applicable to the indigoid dyes, since in these the greatest distance that separates opposite charges, hence the largest dipole moment can be found in the cis isomers.

On the other hand, the same considerations of resonance stabilization of the trans S_1 state that have been advanced to explain the effect of substituents for the thioindigos appear to provide a satisfactory explanation for the behavior of the stilbenes. Thus it appears that in most stilbenes the energy well in the trans S_1 state is so shallow at room temperature as to allow most molecules to overcome the energy barrier to twisting or ISC ($\phi \sim 0.79$, based on the quantum yield data for stilbene in ref 40). Appreciable resonance stabilization and a concomitant deepening of the energy well in the trans S_1 state does not occur in the stilbenes until a para donor substituent is introduced in conjugation with a para' acceptor, as shown by the reduced value of $\phi_{t \rightarrow c}$ for the 4-dimethylamino-4'-nitro derivative (cf. Table IV). The observed enhancement of the fluorescence quantum yield, of course, results from the slower rate of the competing twisting or ISC processes in the S_1 state. It is interesting that, in contrast with the former, the 4-methoxy-4'-nitro compound requires further stabilization by solvation with polar (hydroxylic) solvents before any such reduction of $\phi_{t \rightarrow c}$ (cf. Table IV), presumably due to a greater depth of the potential well in the S_1 state, becomes noticeable.⁴⁵ (Unfortunately the value for ϕ_f for the *p*-methoxy-*p'*-nitro compound in alcohol at room temperature has not been reported.)

In summary there appears to be a close analogy between the excited state behavior of the trans isomers of the stilbenes and the thioindigos, based on considerations of resonance stabilization of the S_1 state. Compounds of both series with relatively large $S_1 \leftarrow S_0$ splittings (ordinary stilbenes and thioindigos involving relatively destabilized chromophores, e.g., compound III) show relatively high rates for twisting and/or ISC and low fluorescence quantum yields. The trans isomers of ordinary thioindigos

($\lambda_{max} > 530$ nm) and of stilbenes containing conjugated electron donor and electron acceptor substituents in the para,para' positions ($\lambda_{max} > 350$ nm) show relatively high fluorescence quantum yields and appear to have to overcome a considerable energy barrier in the excited state en route to isomerization, hence they exhibit relatively low trans \rightarrow cis quantum yields. The relatively high activation energy of isomerization observed for 4-dimethylamino-4'-nitrostilbene (5.5 kcal/mol in aliphatic hydrocarbons, 11 kcal/mol in toluene) is consistent with these generalizations, while the low value (1 kcal/mol in MeOH/EtOH) reported for this barrier for the corresponding 4-methoxy compound⁴⁰ appears to contradict them. In the only temperature-dependent study reported for a thioindigo to date, Ross found no activation energy in the photoisomerization of a compound similar to III in toluene solution between 25 and 90 °C,⁴⁶ where a small (1–2 kcal/mol) activation energy might have been expected. Our preliminary data indicate a fourfold increase in the $\phi_{c \rightarrow t}/\phi_{t \rightarrow c}$ ratio for dye II in lowering the temperature from room temperature to –42 °C.²⁸ Although this confirms the existence of an appreciable barrier to twisting for the trans isomer (roughly estimated to be ca. 3 kcal/mol), as expected on the basis of these considerations, the individual quantum yields and the excited state lifetime will first have to be determined at –42 °C before the exact value of this activation energy can be calculated. It is hoped that further temperature-dependence studies will result in a complete elucidation of these questions.

Acknowledgment. The authors wish to express their appreciation to Professor D. G. Whitten and to Drs. K.-H. Grellmann and F. H. Quina for their helpful interest and advice and to the Chemistry Department, Duke University for the use of their spectrofluorimeter. Special thanks are due to Professor W. Lüttke for providing most of the dyes used in this study. Financial support of this research by the Max Planck Society and the U.S. Army Research Office is gratefully acknowledged.

References and Notes

- (1) (a) The work on air-saturated solutions, including the calculation of the spectra of the pure isomers was carried out in the Spectroscopy Department of the Max Planck Institute for Biophysical Chemistry, Goettingen, German Federal Republic, during the tenure of a guest professorship by one of us (G.M.W.). (b) Presented in part at the VIIIth International Conference on Photochemistry, Edmonton, Alberta, Canada, Aug 1975.
- (2) J. Saltiel et al. in "Organic Photochemistry", Vol. 3, O. L. Chapman, Ed., Marcel Dekker, New York, N.Y., 1973, pp 1–113.
- (3) D. V. Bent and D. Schulte-Frohlinde, *J. Phys. Chem.*, **78**, 451 (1974).
- (4) A. D. Kirsch and G. M. Wyman, *J. Phys. Chem.*, **79**, 543 (1975).
- (5) G. M. Wyman and B. M. Zarnegar, *J. Phys. Chem.*, **77**, 831 (1973).

- (6) D. G. Whitten, J. C. Yau, and F. A. Carroll, *J. Am. Chem. Soc.*, **93**, 2291 (1971).
- (7) G. M. Wyman, *Mol. Photochem.*, **6**, 81 (1974).
- (8) G. M. Wyman and A. F. Zenhausern, *J. Org. Chem.*, **30**, 2348 (1965).
- (9) A. A. Lamola and G. S. Hammond, *J. Chem. Phys.*, **43**, 2129 (1965).
- (10) Cf. J. N. Demas and G. A. Crosby, *J. Phys. Chem.*, **75**, 1007-1011 (1973).
- (11) G. M. Wyman, B. M. Zarnegar, and D. G. Whitten, *J. Phys. Chem.*, **77**, 2584 (1973).
- (12) J. Blanc and D. L. Ross, *J. Phys. Chem.*, **72**, 2817 (1968).
- (13) O. Stern and M. Volmer, *Z. Phys.*, **20**, 183 (1919).
- (14) From laser-flash measurements on dye III; K.-H. Grellmann and P. Hentschel, private communication.
- (15) G. M. Wyman and B. M. Zarnegar, *J. Phys. Chem.*, **77**, 1204 (1973).
- (16) D. Schulte-Frohlinde, H. Herrmann, and G. M. Wyman, *Z. Phys. Chem. (Frankfurt am Main)*, **101**, 115 (1976).
- (17) (a) G. Fischer and E. Fischer, *Mol. Photochem.*, **6**, 463 (1974); (b) P. Bortolus and G. Galiazzo, *J. Photochem.*, **2**, 361 (1974).
- (18) J. Saltiel and B. Thomas, *J. Am. Chem. Soc.*, **96**, 5660 (1974).
- (19) D. Gegiou, K. A. Muszkat, and E. Fischer, *J. Am. Chem. Soc.*, **90**, 12 (1968).
- (20) Although a triplet mechanism has only been rigorously ruled out for dye I, in view of the similarity of the S-V data for dyes 0-III, it is unlikely for 0, II, and III.
- (21) (a) G. M. Wyman and W. R. Brode, *J. Am. Chem. Soc.*, **73**, 1487 (1951); (b) M. Klessinger, *Tetrahedron*, **22**, 3355 (1966).
- (22) D. A. Rogers, J. D. Margerum, and G. M. Wyman, *J. Am. Chem. Soc.*, **79**, 2464 (1957).
- (23) (a) E. Wille and W. Luetke, *Chem. Ber.*, **106**, 3240 (1973); (b) L. Fitjer and W. Luetke, *ibid.*, **105**, 919 (1972).
- (24) (a) S. Daehne and D. Leupold, *Angew. Chem.*, **78**, 1029 (1966); (b) S. Daehne and D. Leupold, *Ber. Bunsenges. Phys. Chem.*, **70**, 618 (1966).
- (25) J. Suehnel, K. Gustav, R. Paetzold, and J. Fabian, *Z. Phys. Chem.*, **257**, in press.
- (26) D. L. Beveridge and H. H. Jaffe, *J. Am. Chem. Soc.*, **87**, 5340 (1965).
- (27) A. H. Cook, D. G. Jones, and J. B. Palya, *J. Chem. Soc.*, 1315 (1939).
- (28) K. H. Grellmann and G. M. Wyman, unpublished data.
- (29) R. H. Dyck and D. S. McClure, *J. Chem. Phys.*, **36**, 2326 (1962).
- (30) G. M. Wyman and W. R. Brode, *J. Am. Chem. Soc.*, **73**, 1487 (1951).
- (31) Cf. for 6,6'-dichloroindigo in benzene: λ_{max} , 535 nm.
- (32) J. Saltiel, D. W.-L. Chang, and E. D. Megarity, *J. Am. Chem. Soc.*, **96**, 6521 (1974).
- (33) J. B. Gallivan, *J. Phys. Chem.*, **73**, 3070 (1969).
- (34) N. J. Turro, G. Karvamos, J. Fung, and A. L. Lyons, Jr., *J. Am. Chem. Soc.*, **94**, 1392 (1972).
- (35) For a recent review, cf. B. R. Henry and W. Siebrand in "Organic Molecular Photophysics", Vol. 1, J. B. Birks, Ed., Wiley, New York, N.Y., 1973, pp 153-239.
- (36) V. L. Ermolaev and K. K. Svitashv, *Opt. Spectrosc.*, **7**, 399 (1959).
- (37) M. A. Mostoslavskii, V. V. Yadrinskii, and O. K. Yadrinskaya, *Russ. J. Phys. Chem.*, **44**, 1700 (1970).
- (38) I. Y. Bershtein and Y. L. Kaminskii, *Opt. Spektrosk.*, **15**, 381 (1963).
- (39) (a) E. Fischer, *Mol. Photochem.*, **5**, 227 (1973); (b) J. Saltiel, *ibid.*, **5**, 231 (1973).
- (40) D. Gegiou, K. A. Muszkat, and E. Fischer, *J. Am. Chem. Soc.*, **90**, 3907 (1968).
- (41) (a) D. Schulte-Frohlinde, H. Blume, and H. H. Gusten, *J. Phys. Chem.*, **66**, 2486 (1962); (b) H. Gusten and L. Klasinc, *Tetrahedron Lett.*, **26**, 3097 (1968); (c) H. Stegemeyer, *J. Phys. Chem.*, **66**, 2555 (1962).
- (42) In hydroxylic solvents (where solvent stabilization of such dipolar CT states is expected) 4-methoxy-4'-nitrostilbene exhibits a $\phi_{\text{CT}}/\phi_{\text{CT}}^{\text{CT}}$ ratio ~ 4 .⁴⁰
- (43) The author is indebted to Professor D. Schulte-Frohlinde for first calling his attention to this similarity.
- (44) The similarity of the excited state behavior of other indigo dyes with still weaker chromophores to that of the stilbenes has already been discussed in ref 5.
- (45) It should be noted that this mechanism is compatible with both (singlet and triplet) pathways that have been proposed for the direct photoisomerization of stilbenes.
- (46) D. L. Ross, *Appl. Opt.*, **10**, 571 (1971).

Solvent-Induced Polarization Phenomena in the Excited State of Composite Systems with Identical Halves. 1. Effects of Solvent Medium on the Fluorescence Spectra of 1,2-Dianthrylethanes

Toyo Haru Hayashi, Tatsuo Suzuki, Noboru Mataga,*

Department of Chemistry, Faculty of Engineering Science, Osaka University, Toyonaka, Osaka 560, Japan

Yoshiteru Sakata, and Soichi Misumi

Institute of Scientific and Industrial Research, Osaka University, Suita, Osaka 565, Japan (Received August 20, 1976)

Both 1,2-di(1-anthryl)ethane (I) and 1,2-di(9-anthryl)ethane (II) show intramolecular excimer fluorescence spectra with a peak at 460 nm, in addition to the fluorescence from the locally excited (LE) state of anthracene. The ratio Φ_{D} (excimer fluorescence yield)/ Φ_{M} (LE fluorescence yield) increases with increasing solvent polarity. In addition, intramolecular photodimerization was also found to depend upon the solvent polarity. Experimental results were analyzed assuming an intramolecular CT (charge transfer) transient state in polar solvents, and compared with 9,9'-bianthryl, about which it has been clarified that "solvent-induced polarization" occurs.

Introduction

It has been demonstrated that the electronic structure of some molecular composite systems of the type, A-(CH₂)_n-D, are liable to change remarkably by the interaction with polar solvent molecules in the excited electronic state, where A is an electron acceptor group such as pyrenyl or anthryl, and D is the *N,N*-dimethylanilino group.¹⁻⁵ The CT state (A⁻(CH₂)_n-D⁺)* is stabilized by the interaction with polar solvent molecules and these systems show a quite large red shift of the exciplex fluorescence in strongly polar solvents. However when A and D are identical aromatic molecules, such phenomenon has not been found until now except for the special case of 9,9'-bianthryl found

by Schneider and Lippert.⁶ 9,9'-Bianthryl shows exciplex fluorescence whose maximum wavelength depends upon solvent polarity, along with LE fluorescence. In relation to this phenomenon, it has recently been proven, by means of S_n ← S₁ spectral measurements with a ps laser photolysis method,⁷ that the excited state of 9,9'-bianthryl in a polar solvent such as acetone has an ion pair structure composed of the anthracene anion and cation. No other example of a solvent-induced polarization in the excited state has been found for a molecule or molecular complex containing two identical aromatic groups.

In view of this, it may be interesting to examine other composite systems with identical halves in regard to the

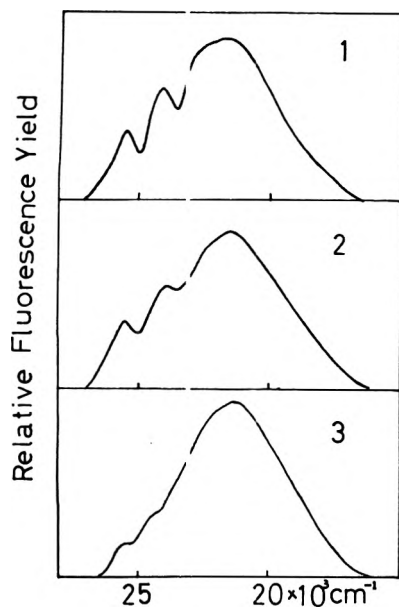


Figure 1. Fluorescence spectra of I in cyclohexane (1), acetone (2), and acetonitrile (3).

solvent-induced polarization phenomena. We have found that the fluorescence of 1,2-dianthrylethanes and [2.2]-(1,3)pyrenophane show some dependence upon the solvent polarity, which indicates the occurrence of the solvent-induced intramolecular charge transfer in the excited state. In this report, the results for 1,2-dianthrylethanes will be given.

Experimental Section

Details of the synthesis of dianthrylethanes are described elsewhere.⁸ Spectrograde solvents were used without further purification. Fluorescence spectra were measured on an Aminco-Bowman spectrophotofluorometer calibrated to give correct quantum spectra using a standard tungsten lamp. Fluorescence lifetimes were determined by using a pulsed nitrogen gas laser of about 1 kW peak power as the exciting light source combined with a monochromator, 1P28 photomultiplier, a sampling oscilloscope, and an X-Y recorder. The time resolution of this system was about 2.5 ns. Absorption spectra were measured with a Cary 15 spectrometer. All sample solutions were deaerated by means of freeze-pump-thaw cycles. Fluorescence quantum yields were determined using 9,10-diphenylanthracene as a standard. The photochemical reaction yields, i.e., the intramolecular photodimerization reactions, were determined by means of potassium ferrioxalate actinometry.

Results

Fluorescence spectra of I in some solvents of different polarity are shown in Figure 1. Excitation spectra monitored at 400 and 500 nm were not different in various solvents, and agree with the absorption spectra. The absorption spectra are also similar to that of 1,4-dimethylantracene, which suggests that there is no appreciable interaction between two anthracene moieties in the ground state of I. Similar results were also obtained for II, except that the intensity ratio (Φ_D/Φ_M) of II is considerably smaller than that of I, as indicated in Figure 2.

Although the broad structureless emission band with peak at 460 nm becomes quite remarkable in strongly polar solvent, it does not show a red shift depending upon the solvent polarity. Moreover, the broad emission cannot be observed in a highly viscous solution at low temperature.

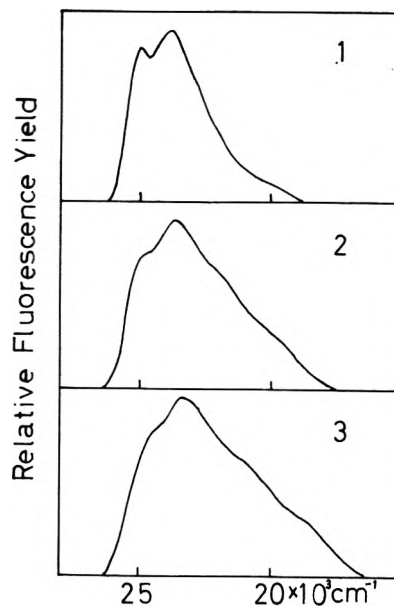


Figure 2. Fluorescence spectra of II in cyclohexane (1), acetone (2), and acetonitrile (3).

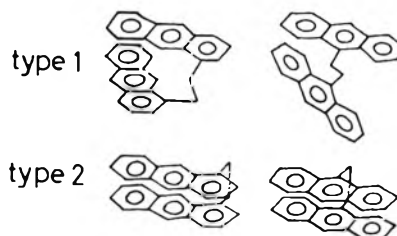


Figure 3. Conformation of type 1 and type 2 excimers of I and II.

Therefore, the broad structureless emission may be ascribed to the excimer state formed through intramolecular rearrangement in the excited state. The lifetime of the excimer fluorescence was ca. 60 ns at about 25 °C. This excimer state seems to have a type 1 conformation as indicated in Figure 3 in view of the following results. (a) The steric hindrance of methyl groups substituted at 4,4' positions of I is indifferent to excimer formation. (b) Excitation of the photocleavage product of the intramolecular dimer of I and/or II in rigid matrices at 77 K gave another type of excimer which fluoresces with a peak at 530 nm. The lifetimes of those excimers of I and II were respectively 70 and 90 ns, in comparison with 60 ns for the excimer fluorescence observed at room temperature. The excimer observed at 77 K may have a type 2 conformation and may be the precursor of the intramolecular photodimer, which seems consistent with the fact that the observed lifetimes are rather short even at 77 K. Thus, the excimer observed at room temperature may have type 1 conformation which is disadvantageous for dimerization. (c) The rather small Stokes shift of the excimer fluorescence at room temperature compared with that at 77 K indicates that the interaction energy between the two moieties is not large because of the deviation from the complete overlap of the two moieties.

Measurements on the temperature dependence of (Φ_D/Φ_M) of I were performed in acetonitrile, ethanol, and methylcyclohexane solutions. (Φ_D/Φ_M) decreases as the temperature is lowered, and only the monomer fluorescence can be observed in rigid solvents at 77 K. The values of activation energy for the formation of type 1 excimer were obtained from an Arrhenius plot of (Φ_D/Φ_M) vs. $1/T$. The value of 1.8 kcal/mol was obtained for acetonitrile solution in the vicinity of room temperature. The values

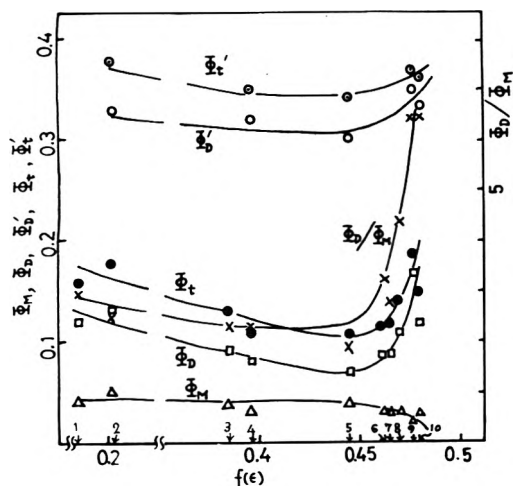


Figure 4. Effect of solvent polarity upon the fluorescence yield of I in: (1) cyclohexane, (2) hexane, (3) ethyl acetate, (4) methyl acetate, (5) methyl isobutyl ketone, (6) 2-propanol, (7) acetone, (8) ethanol, (9) acetonitrile, (10) methanol.

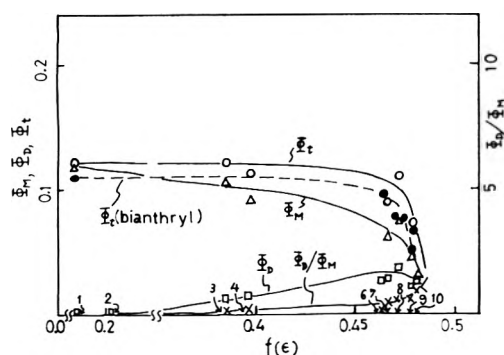


Figure 5. Effect of solvent polarity upon the fluorescence yields of II and 9,9'-bianthryl. The numbering of the solvents is the same as in Figure 4.

for ethanol as well as methylcyclohexane solutions were about 4 kcal/mol, though it was not possible to obtain accurate data.

The dependence of Φ_M , Φ_D , (Φ_D/Φ_M) , and $\Phi_t = \Phi_D + \Phi_M$ upon the solvent polarity parameter,

$$f(\epsilon) = \frac{\epsilon - 1}{2\epsilon + 1}$$

where ϵ is the dielectric constant of the solvent, is indicated in Figures 4 and 5. In the case of II, Φ_M decreases to some extent and Φ_D increases a little with increase of $f(\epsilon)$ in the region $f(\epsilon) < 0.46 \sim 0.47$. In the region $f(\epsilon) > 0.46 \sim 0.47$, however, Φ_t decreases considerably with increase of $f(\epsilon)$, indicating the presence of some quenching process induced by the interaction with polar solvent molecules. Contrary to the case of II, Φ_t does not decrease even in the high polarity region, in the case of I. In solvents of medium polarity, Φ_t as well as Φ_D decreases with increase of solvent polarity. Thus, the behavior of I is rather complicated.

In order to examine the possibility of involvement of the solvent dependent photodimerization we have measured the photodimerization yields of I in various solvents. It was confirmed that the quantum yield of photodimerization of I is independent of its concentration. Therefore, the dimerization is considered an intramolecular process.

A somewhat distinct relation was found between the dimerization yield and solvent polarity as indicated in Figure 6. When the photodimerization yields are added to Φ_t , the corrected values (Φ_D') become almost independent of the solvent polarity. Nevertheless, there is still a slight

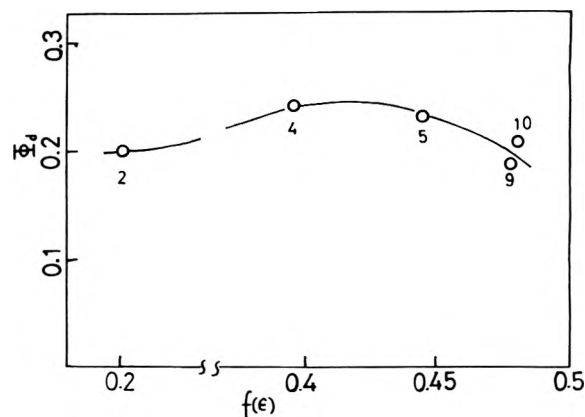


Figure 6. Effect of solvent polarity upon the photodimerization yield, Φ_D , of I. The numbering of the solvents is the same as in Figure 4.

depression in the region of $f(\epsilon) \sim 0.4 \sim 0.45$. The behavior of the corrected values Φ_D' in this polarity region is analogous to that of Φ_t' , but the extent of its increase in the region of $f(\epsilon) > 0.45$ is larger than in the case of Φ_t' . That is, there seems to be a net increase of Φ_D' in strongly polar solvent.

Discussion

1. *Effect of Temperature upon Intramolecular Excimer Formation.* Both the dielectric constant ϵ and the viscosity η of a solvent increase with decreasing temperature. The increase of ϵ would bring out the increase of (Φ_D/Φ_M) , whereas the increase of η would lead to a decrease of (Φ_D/Φ_M) . Experimental results suggest that the temperature dependence of (Φ_D/Φ_M) is not governed by the variation of ϵ , but by that of η . However, the excimer formation process necessarily involves hindered rotations about the methylene chain. It is possible that both the hindered rotation itself and the solvent viscosity are affected by the temperature change. Therefore, the activation energies for the excimer formation may be due to the activation required to overcome the rotational barriers of the methylene chain and the activation energy connected with the solvent viscosity. It is difficult to estimate the contributions from these two effects separately.

2. *Effects of Solvent Polarity upon the Fluorescence Yields.* When a dipole moment μ is located in a medium with dielectric constant ϵ , a reaction field \vec{F} which acts upon the dipole moment is produced,¹⁰ so that the stabilization energy of the dipole is given by

$$E_S = \vec{\mu} \cdot \vec{F} = \frac{\mu^2}{a^3} \frac{\epsilon - 1}{2\epsilon + 1} = \frac{\mu^2}{a^3} f(\epsilon) \quad (1)$$

where a is the radius of a spherical cavity in which the dipole moment μ is situated. The results of the measurements of various quantum yields can be correlated with this $f(\epsilon)$ as shown in Figures 4–6.

In the case of II, in the region of $f(\epsilon) < 0.46 \sim 0.47$, the increase of Φ_D with increase of $f(\epsilon)$ seems to be correlated with the decrease of Φ_M . The remarkable decrease of Φ_t in the region of $f(\epsilon) > 0.46 \sim 0.47$ is quite similar to the behavior of 9,9'-bianthryl⁷ as indicated in Figure 5. In the case of 9,9'-bianthryl, the ion pair structure is realized in the excited state in strongly polar solvents. In the case of an exciplex, the increase of fluorescence quenching with increase of the solvent polarity is a rather familiar phenomenon.^{1,2,4,5} Although the fluorescent state of the present system is not a polar state but an excimer state, the quenching analogous to the case of 9,9'-bianthryl seems to arise in the CT intermediate state in strongly polar solvents.

The behavior of I can be understood by taking into account the photodimerization which depends upon the solvent polarity, as described already. The peculiar dependence of the intramolecular photodimerization upon the solvent polarity as indicated in Figure 5 seems to suggest that two inactivation processes are competing with each other. One process is photodimerization and the other excimer formation. The photodimerization seems to overcome the excimer formation in solvents of medium polarity, but in more polar solvents the latter overcomes the former.

Since the precursor of the photodimerization is considered to be the type 2 excimer,^{8,9} the above results means that there is a competition between type 1 and type 2 excimer formation depending upon the solvent polarity, although the microscopic mechanism of the competition of this solvent dependence is not very clear at the present stage of the investigation. Furthermore, the small depression of Φ_t' as well as Φ_D' in the region of $f(\epsilon) \sim 4.5$ suggests that the photodimerization process is accompanied by a quenching leading to the ground state or the triplet state.

It is known that II undergoes intramolecular photodimerization with a yield of 0.19.¹¹ However, contrary to the case of I, the photodimerization of II does not seem to show such a peculiar dependence upon the solvent polarity, since Φ_t as well as Φ_D do not show the depression in the medium polarity region.

It should be noted here that the remarkable increase of (Φ_D/Φ_M) of I in strongly polar solvents seems to correspond to the remarkable decrease of Φ_t of II as well as 9,9'-bianthryl in strongly polar solvents and also to the increase of $\Delta\nu$ of 9,9'-bianthryl in these solvents, where $\Delta\nu$ is the difference between the wavenumber of absorption 0-0 transition and that of the fluorescence maximum. This result suggests that these behaviors of I, II, and 9,9'-bianthryl all originate from a state of common nature, i.e., the CT state.

Summarizing the above discussions, the behaviors of I with regard to type 1 excimer formation may be explained as follows.

Excimer could be formed through two paths: (1) intramolecular association of the excited and ground state counterpart and (2) creation of solvent induced CT state which undergoes excimer formation before the quenching common to the fluorescence of 9,9'-bianthryl and II in strongly polar solvents.

Just as in the case of 9,9'-bianthryl, the postulated CT state for the present system, stabilized owing to the interaction with polar solvents, is not improbable on the basis

of energy level consideration. The energy of the CT state above the ground state in acetonitrile can be estimated according to the following expression for the free energy change:

$$\Delta G = E_{1/2}(A|A^+) - E_{1/2}(A^-|A) - \frac{e^2}{\epsilon a} \quad (2)$$

where $E_{1/2}(A|A^+)$ and $E_{1/2}(A^-|A)$ are the oxidation and reduction potentials of anthracene, respectively, and a is the separation between the two anthracene rings.

We use the value of 0.96 V vs. SCE for $E_{1/2}(A|A^+)$ and -1.99 V vs. SCE for $E_{1/2}(A^-|A)$. Thus, $\{E_{1/2}(A|A^+) - E_{1/2}(A^-|A)\} = 2.95$ eV, which is lower than the excitation energy to the lowest excited singlet state of anthracene (3.18 eV). The energy of the CT state should be lower than this owing to the Coulombic interaction between the cation and anion. For example, ΔG can be estimated to be 2.85 eV taking $\epsilon = 37$ and $a = 4$ Å. Actually, ϵ should be less than 37 in the region between ions at a separation of 4 Å, resulting in a smaller value of ΔG than 2.85 eV. Thus, in strongly polar solvent, the CT state is actually situated below the lowest LE singlet state.

We also investigated whether solvent-induced polarization occurs or not in such cases as 1,3-biscarbazolylpropane, 1,2-diphenylethane, and 1,2-dinaphthylethane in polar solvents. However, solvent-induced polarization was not observed in those cases. In the case of 1,3-biscarbazolylpropane, direct excimer formation might be more easy than CT state formation, while the intramolecular CT state might not be stabilized sufficiently even in strongly polar solvents in the case of 1,2-diphenylethane as well as 1,2-dinaphthylethane.

References and Notes

- (1) N. Mataga in "The Exciplex", M. Gordon and W. R. Ware, Ed., Academic Press, New York, N.Y., 1975, p 113, and papers cited there.
- (2) N. Mataga, T. Okada, H. Masuhara, N. Nakashima, Y. Sakata, and S. Misumi, *J. Lumin.*, **12/13**, 159 (1976).
- (3) S. Masaki, T. Okada, N. Mataga, Y. Sakata, and S. Misumi, *Bull. Chem. Soc. Jpn.*, **49**, 1277 (1976).
- (4) T. Okada, T. Fujita, and N. Mataga, *Z. Phys. Chem. (Frankfurt am Main)*, **101**, 57 (1976).
- (5) T. Okada, T. Saito, and N. Mataga, *Bull. Chem. Soc. Jpn.*, in press.
- (6) F. Schneider and E. Lippert, *Ber. Bunsenges. Phys. Chem.*, **72**, 1155 (1968).
- (7) N. Nakashima, M. Murakawa, and N. Mataga, *Bull. Chem. Soc. Jpn.*, **49**, 854 (1976).
- (8) T. Hayashi, N. Mataga, Y. Sakata, S. Misumi, M. Morita, and J. Tanaka, *J. Am. Chem. Soc.*, **98**, 5910 (1976).
- (9) T. Hayashi, T. Suzuki, N. Mataga, Y. Sakata, and S. Misumi, *Chem. Phys. Lett.*, **38**, 599 (1976).
- (10) L. Onsager, *J. Am. Chem. Soc.*, **58**, 1486 (1936).
- (11) R. Livingston and K. S. Wei, *J. Am. Chem. Soc.*, **89**, 3098 (1967).

Solvent-Induced Polarization Phenomena in the Excited State of Composite Systems with Identical Halves. 2. Effects of Solvent Polarity upon the Fluorescence of [2.2](1,3)Pyrenophane

Toyoharu Hayashi, Noboru Mataga,*

Department of Chemistry, Faculty of Engineering Science, Osaka University, Toyonaka, Osaka 560, Japan

Teruo Umemoto, Yoshiteru Sakata, and Solchi Misumi

Institute of Scientific and Industrial Research, Osaka University, Suita, Osaka 565, Japan (Received August 20, 1976)

The fluorescence spectrum as well as the absorption spectrum of [2.2](1,3)pyrenophane (metapyrenophane) in nonpolar solvents such as methylcyclohexane are rather similar to those of pyrene. In polar solvents, metapyrenophane showed a broad structureless fluorescence band with maximum at 475 nm along with pyrene monomer-like emission at shorter wavelengths. The experimental results reported here suggest that the shorter wavelength fluorescence is from the locally excited (LE) state of metapyrenophane and the longer wavelength fluorescence is from the intramolecular excimer state. Furthermore, it was found that this excimer state may be formed through the intramolecular charge transfer intermediate state, namely, the "solvent-induced polarization" state.

Introduction

Investigations on the solvent effects upon the fluorescence and $S_n \leftarrow S_1$ absorption spectra of 9,9'-bianthryl have revealed that a CT (charge transfer) state is produced in polar solvents between separated intramolecular aromatic rings.^{1,2} In case of 9,9'-bianthryl, the CT state is a fluorescent state, and its fluorescence band is red shifted with increasing solvent polarity. 1,2-Dianthrylethanes, as described in the preceding papers,³⁻⁵ show intramolecular excimer fluorescence along with the fluorescence from the LE state. The study of the solvent dependence of the fluorescence yields of 1,2-dianthrylethanes suggested the existence of an intermediate CT state in the excimer formation process.^{3,5} In view of its molecular structure, 1,2-dianthrylethanes can pass into a partially overlapped sandwich structure which emits excimer fluorescence, whereas 9,9'-bianthryl cannot form such a structure. No other example of such a solvent-induced polarization in the excited state has been found for a molecule or molecular complex containing the same two aromatic groups, except for metapyrenophane (mePy), the results of which will be reported in the following.

Intramolecular excimer formation of mePy also depends upon solvent polarity. In contrast to the case of 1,2-dianthrylethanes, intramolecular excimer formation in nonpolar solvents as well as any effective photochemical reaction did not occur in case of mePy, which makes the analysis of experimental results much more explicit.

Experimental Section

mePy,^{6a} [2.2](2,7)pyrenophane (parapyrenophane, paPy),^{6b} and metacyclo[2.2](1,3)pyrenophane^{6c} were synthesized according to the methods reported elsewhere.⁶ Experimental procedures for the measurements were almost the same as those described elsewhere.³⁻⁵

The experimental results obtained with a sample of mePy in acetonitrile solution deaerated by means of freeze-pump-thaw cycles were not different from those with a sample under a nitrogen gas atmosphere. Therefore, measurements were conducted in nitrogen saturated sample solutions. A sample solution was flushed with

nitrogen gas for 15 min and then the cuvet was sealed off.

Results

1. *Solvent Effects upon Absorption and Fluorescence Spectra.* The absorption spectrum of mePy was practically the same in several solvents. The spectrum is composed of bands corresponding to those of the absorption spectrum of pyrene itself, but they are somewhat broadened and shifted to the red as indicated in Figure 1. The absorption intensity of the band corresponding to the 1L_b band of pyrene may not be so different from that of pyrene, whereas the band corresponding to the 1L_a band of pyrene showed a bathochromic shift concealing the 1L_b band to some extent. At any rate, there does not seem to be a strong interaction between the π -electronic systems of mePy in its ground state, since the absorption bands of pyrene show a considerable red shift even when one pyrene group is replaced by benzene or by alkyl substitution at the 1,3 positions.⁷

The absorption spectrum of paPy is shown in Figure 2 for comparison. The absorption bands of paPy can be briefly interpreted as follows. The band around 320 nm might be assigned to 1L_a blue shifted owing to an exciton type of interaction. This blue shift is opposite to the case of mePy and might be understood on the basis of the conformations of these cyclophanes as well as the fact that the transition moment of the 1L_a band is along the long molecular axis. Furthermore, a distinct transannular band at longer wavelength was observed in the absorption spectrum of paPy.

From the above results, it could be said that there is not as strong an interaction between the π -electronic systems in mePy compared with paPy. The relatively small magnitude of interaction between the π -electronic systems in mePy might lead to marked dependence of the fluorescent state upon solvent polarity, in contrast to the case of paPy.

As indicated in Figure 3, the fluorescence spectrum of mePy in methylcyclohexane was substantially similar to that of pyrene. This fluorescence originates from the LE state, and is called LE fluorescence here. The fluorescence spectrum remained unchanged at temperatures from just

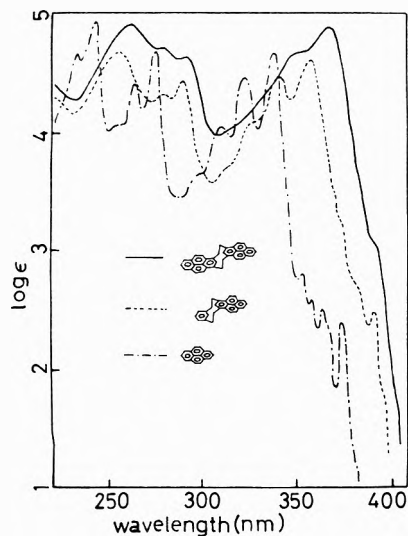


Figure 1. Absorption spectra of [2.2](1,3)pyrenophane and related compounds in tetrahydrofuran solution.

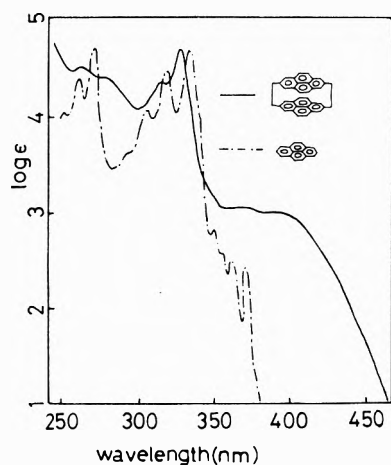


Figure 2. Absorption spectra of [2.2](2,7)pyrenophane and pyrene in tetrahydrofuran solution.

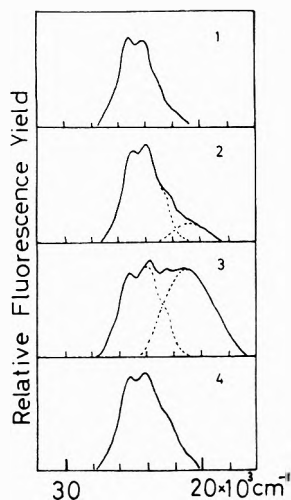


Figure 3. Fluorescence spectra of [2.2](1,3)pyrenophane in several solvents of different polarity: (1) in methylcyclohexane at room temperature; (2) in methyl isobutyl ketone at room temperature; (3) in acetonitrile at room temperature; (4) in acetonitrile at 77 K.

above the melting point of methylcyclohexane to room temperature. These facts suggest that any particular change of electronic state due to the transannular interaction does not occur also in the excited state, in nonpolar solvents. On the other hand, in polar solvents such as

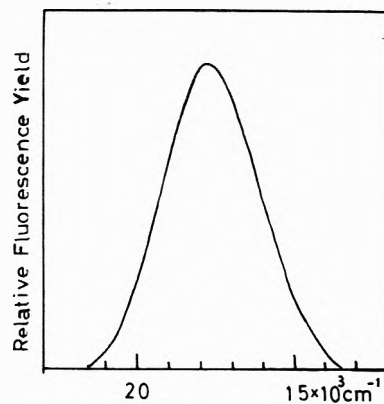


Figure 4. Fluorescence spectrum of [2.2](2,7)pyrenophane in methylcyclohexane solution.

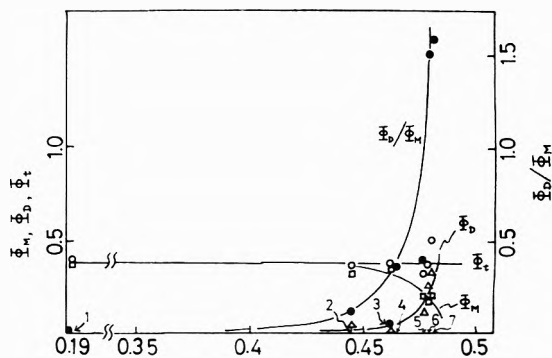


Figure 5. Dependence of the fluorescence quantum yields of [2.2](1,3)pyrenophane on the solvent polarity: Φ_M (\square); Φ_D (Δ); Φ_D/Φ_M (\bullet); $\Phi_T = \Phi_M + \Phi_D$ (\circ). The solvents used were: (1) methylcyclohexane, (2) methyl isobutyl ketone, (3) 2-propanol, (4) acetone, (5) methanol, (6) dimethylformamide, (7) acetonitrile.

acetonitrile, another broad structureless emission with a maximum wavelength of 475 nm was observed along with the LE fluorescence band. The excitation spectrum of the broad emission band was the same as that of the LE band, and is in accordance with the absorption spectrum of mePy. One can recognize the existence of this broad band also in methyl isobutyl ketone solution at approximately the same wavelength, although its intensity is much weaker than in acetonitrile solution.

The broad fluorescence band observed in many other polar solvents always showed a maximum at 475 nm. Therefore, it seems to be intramolecular excimer fluorescence, and the excimer state may be formed from the LE state of mePy via an intramolecular CT state. This excimer fluorescence was not observed in the temperature region where the solvent became sufficiently rigid as is indicated in acetonitrile solution in Figure 3. This result suggests that the transformation LE state \rightarrow excimer state necessitates the orientation of polar solvent molecules.

In contrast to mePy, paPy showed always only a broad fluorescence band corresponding to the transannular absorption band in nonpolar as well as polar solvents. For the purpose of comparison, the fluorescence spectrum of paPy is shown in Figure 4. One can see that the fluorescence band of paPy lies at much longer wavelength (560 nm) than the excimer band of mePy.

2. *The Effects of Solvent Polarity upon the Fluorescence Yields.* The yields of LE fluorescence Φ_M , the excimer fluorescence Φ_D , their ratio (Φ_D/Φ_M), and their sum $\Phi_T = \Phi_M + \Phi_D$ are plotted against the parameter $f(\epsilon) = (\epsilon - 1)/(2\epsilon + 1)$ in Figure 5, where ϵ is the solvent dielectric constant. The stabilization energy of a dipole moment μ in the polar solvent with dielectric constant ϵ is given by $(\mu^2 f(\epsilon)/a^3)$, where a is the radius of a spherical

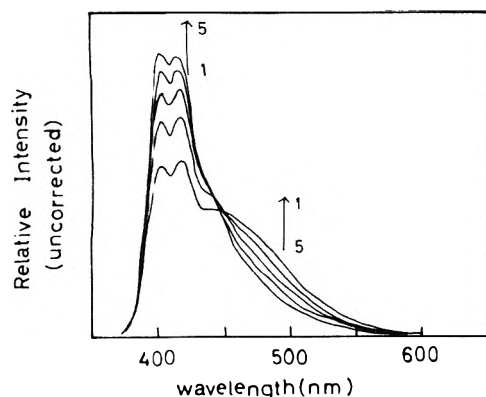


Figure 6. Temperature dependence of the fluorescence spectrum of [2.2](1,3)pyrenophane in acetone solution: (1) -58°C , (2) -41°C , (3) -24°C , (4) -8°C , (5) $+8^{\circ}\text{C}$.

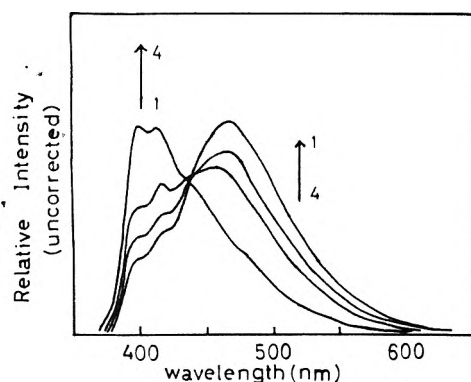


Figure 7. Temperature dependence of the fluorescence spectrum of [2.2](1,3)pyrenophane in dimethylformamide solution: (1) -53°C , (2) -36°C , (3) -16°C , (4) $+51^{\circ}\text{C}$.

cavity containing the dipole moment $\bar{\mu}$.

(Φ_D/Φ_M) increases remarkably with increase of the solvent polarity parameter $f(\epsilon)$ but Φ is approximately constant throughout the range of $f(\epsilon)$ values examined here. The values in alcoholic solutions deviate from the correlation curve suggesting the specificity of alcoholic solvents.

3. Temperature Dependence of Fluorescence Spectra in Polar Solvents. As shown in Figure 6, the isoemissive point was observed in acetone solution over a considerable temperature range from above the melting point of acetone to room temperature. A similar behavior was also found for other polar solvent such as dimethylformamide as shown in Figure 7. The isoemissive point in these spectra is indicative of a two-component system. As the temperature was lowered, (Φ_D/Φ_M) increased, while the excimer fluorescence band did not show any shift. Since the dielectric constant of these solvents increases with temperature lowering, the above result means that (Φ_D/Φ_M) increases with increase of $f(\epsilon)$.

The above temperature effect upon (Φ_D/Φ_M) is in marked contrast to the case of 1,2-di(1-anthryl)ethane, where (Φ_D/Φ_M) decreased as the temperature was lowered.⁵ The temperature change will affect the excimer formation through the temperature effects upon ϵ , the solvent viscosity η , and the hindered rotations about the methylene chains. In contrast to the case of 1,2-di(1-anthryl)ethane, the present result indicates that the temperature dependence of (Φ_D/Φ_M) of mePy is not governed by η and the hindered rotations of methylene chains but is regulated by the variations of ϵ .

4. Fluorescence Decay Times. Under our experimental conditions, a rise curve for the excimer fluorescence or two-component decay of the LE fluorescence of mePy was

TABLE I: Fluorescence Lifetimes of [2.2](1,3)Pyrenophane in Various Solvents

Solvent ^a	λ , ^b nm	Temp, ^c $^{\circ}\text{C}$	τ , ns	$1/\tau$, 10^6 s^{-1}	k_{DM} , 10^6 s^{-1}
MCH	390	RT	150	6.7	
MIBK	400	RT	90	11	4
Acetone	400	RT	78	13	6
ACN	390	RT	50	20	13
ACN	500	RT	50	20	13
DMF	400	RT	43	23	16
DMF	500	RT	43	23	16
DMF	500	-60	30	33	26
MeOH	400	RT	85	12	5
MeOH	400	-70	110	9.1	2.8

^a MCH = methylcyclohexane, MIBK = methyl isobutyl ketone, ACN = acetonitrile, DMF = *N,N*-dimethylformamide, MeOH = methanol. ^b The wavelength at which the fluorescence decay was observed. ^c The temperature at which the observation was made. RT indicates room temperature.

not observed. Both LE and excimer fluorescence gave the same decay time. Moreover, this decay time becomes shorter with increase of (Φ_D/Φ_M) . Experimental results are summarized in Table I.

Discussion

1. Consideration of the Molecular Structure of the Excimer State of mePy. It has been recently reported⁸ that metacyclophane shows an intramolecular excimer emission along with a LE emission in the nonpolar solvent, cyclohexane. There are, however, some distinct differences between the fluorescence states of mePy and metacyclophane. Namely, the total fluorescence quantum yield for the latter, $\Phi = \text{ca. } 3 \times 10^{-5}$, is much smaller compared with that for the former, $\Phi = 0.4 \sim 0.5$; an excimer emission was observed in nonpolar solvents in case of metacyclophane, but in case of mePy, excimer fluorescence was observed only in polar solvents and not in nonpolar solvents.

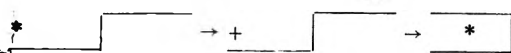
It is known that the anti \rightarrow syn isomerization of metacyclophane is very difficult in the ground state because of a large activation energy, 27 kcal/mol.⁹ However, in the case of mePy in polar solvents, it might be possible to overcome this barrier for isomerization by sufficient transannular interaction in the intramolecular CT state probably including a Coulombic attraction force in the excited state. The energy of the CT state estimated later on seems to support this argument. The remarkable effect of the stabilization of the CT state upon mePy excimer formation, caused by the interaction with polar solvents, is demonstrated also by the temperature effect on the (Φ_D/Φ_M) value in polar solvents as described in section 3 of the Results.

We can obtain some information about the structure of the intramolecular excimer state of mePy by examining the relationship among the excimer fluorescence spectra of mePy, intermolecular pyrene excimer, and paPy. As shown in Figure 4, the broad structureless excimer type fluorescence band with a maximum at 560 nm was observed in the case of paPy, while the maximum wavelengths for the fluorescence of intermolecular pyrene excimer and intramolecular mePy excimer are 480 and 475 nm, respectively. The longer wavelength excimer emission of paPy compared with mePy and intermolecular pyrene excimer seems to be a consequence of stronger interaction between pyrene rings in the case of paPy than in the case of mePy excimer and intermolecular excimer. Thus, two pyrene rings of intermolecular pyrene excimer and/or mePy intramolecular excimer seems to be paired loosely,

compared with the nearly complete parallel sandwich pair of paPy.

The differences between the molecular structures of mePy and paPy excimer states would be reflected in such a parameter as radiative rate constant.

2. *Dependence of the Excimer Formation on Solvent Polarity.* The experimental results suggest that there exists a CT intermediate state in the transformation from the LE state to the excimer state of mePy:



where the LE, CT, and intramolecular excimer states are abbreviated as,



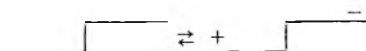
respectively.

Just as in the case of 1,2-di(1-anthryl)ethane,⁵ the dependence of (Φ_D/Φ_M) of mePy on $f(\epsilon)$ resembles that of $\Delta\nu^{1,2}$ of 9,9'-bianthryl on $\Delta f = (\epsilon - 1)/(2\epsilon + 1) - 1/2(n^2 - 1)/(2n^2 + 1)$, where n is the solvent refractive index, and $\Delta\nu$ is the amount of the Stokes shift of the fluorescence. This resemblance suggests that the magnitude of stabilization of CT state in polar solvents might determine the rate of conversion



The remarkable increase of (Φ_D/Φ_M) due to the anti \rightarrow syn isomerization via the CT state occurs effectively in the range of $f(\epsilon) \geq 0.46 \sim 0.47$, in accordance with the case of 1,2-dianthrylethanes.⁵ This result seems to suggest that the relation among the relevant energy levels connected with the isomerization of mePy are rather similar to those of 1,2-dianthrylethanes.

3. *Energy Level of CT State in Polar Solvents.* We use a similar expression to that described in previous reports^{3,5} for the energy level of CT state. The free energy change for the reaction



can be given by

$$\Delta G = E_{1/2}(P|P^+) - E_{1/2}(P^-|P) - \frac{e^2}{\epsilon a} \quad (1)$$

where $E_{1/2}(P|P^+)$ and $E_{1/2}(P^-|P)$ are oxidation potential and reduction potential of pyrene, respectively, and a is the distance between cation and anion. We use the values of -2.07 V vs. SCE of pyrene in dimethylformamide for $E_{1/2}(P^-|P)$, 1.16 V vs. SCE of pyrene in acetonitrile for $E_{1/2}(P|P^+)$, since the dielectric constant of acetonitrile resembles that of dimethylformamide. Therefore, $\{E_{1/2}(P|P^+) - E_{1/2}(P^-|P)\} = 3.23$ eV. Considering the stabilization due to Coulombic interaction between cation and anion, the CT state would be situated sufficiently below the LE state (3.18 eV).

An accurate estimation of the Coulombic interaction energy is rather difficult because the microscopic ϵ in eq 1 cannot be estimated definitely. For the CT state most unfavorable energetically, ΔG can be estimated to be 3.17 eV, where $\epsilon = 37$ and $a = 7$ Å. Even in this case, the CT state is situated nearly at the same energy as the LE state. In the actual system, the dielectric constant ϵ in the expression $(e^2/\epsilon a)$ may be reduced appreciably and the distance a is smaller than 7 Å, to give a more stable CT state energetically.

4. *Kinetics of Intramolecular Excimer Formation.* The mechanism of intramolecular excimer formation may be represented by the following scheme:



where M^* is the LE state, D^* the intramolecular excimer state, M the ground state of the anti form of mePy, and D the ground state of the syn form of mePy. In eq 2, k_f represents the radiative rate constant of LE fluorescence and k_i the radiationless rate constant, k_f' and k_i' represent those of excimer, respectively.

On the basis of eq 2, the following relations are given under stationary state condition:

$$\frac{[D^*]}{[M^*]} = \frac{k_{DM}}{k_D + k_{MD}} = K_e \quad (3)$$

$$\frac{\Phi_D}{\Phi_M} = \frac{k_f'}{k_f} K_e = \frac{k_f' k_{DM}}{k_f k_D + k_{MD}} \quad (4)$$

where $k_D = k_f' + k_i'$. The plot of (Φ_D/Φ_M) vs. k_{DM} would give a linear relationship with an intercept of $(\Phi_D/\Phi_M) = 0$, by considering that only k_{DM} would depend on solvent polarity. It will be shown later on that this relation is approximately valid.

The time dependence of $[M^*]$ and $[D^*]$ after δ -pulse excitation is given by the following formula under condition that $[D^*]$ at $t = 0$ is zero:

$$[M^*] = \frac{[M^*]_0}{\lambda_2 - \lambda_1} \{(\lambda_2 - X) \exp(-\lambda_1 t) + (X - \lambda_1) \exp(-\lambda_2 t)\} \quad (5)$$

$$[D^*] = \frac{k_{DM}[M^*]_0}{\lambda_2 - \lambda_1} \{\exp(-\lambda_1 t) - \exp(-\lambda_2 t)\} \quad (6)$$

where

$$2\lambda_{1,2} = X + Y \mp \{(Y - X)^2 + 4k_{DM}k_{MD}\}^{1/2} \quad (7)$$

$$X + Y = k_M + k_D + k_{DM} + k_{MD}$$

$$Y - X = k_D - k_M + k_{MD} - k_{DM}$$

$$k_M = k_f + k_i$$

In our present system, $k_D \geq 5 \times 10^8$ s⁻¹ as we shall see later. The value of k_{MD} is usually smaller than that of k_{DM} , and the former is much smaller than the latter for intramolecular systems. For example, in the case of 1,3-dinaphthylpropane, $k_{DM} = 1.2 \times 10^8$ s⁻¹ and $k_{MD} = 1.6 \times 10^4$ s⁻¹ in a mixed solvent of glycerol + ethanol.¹¹ So then, the value of $4k_{DM}k_{MD}$ in eq 7 might be neglected in comparison with $(Y - X)^2$. Therefore, $\lambda_1 \approx X$ and $\lambda_2 \approx Y$, leading to the single exponential decay of the LE fluorescence as it was actually observed. The excimer fluorescence did not reveal a delayed rise curve, experimentally, which suggests that $Y \gg X$. Thus, the observed decay time of LE fluorescence and/or excimer fluorescence would give a value of $X (= k_M + k_{DM})$, and $Y = k_D + k_{MD} \sim k_D$ should be larger than 5×10^8 s⁻¹. The value of k_M can be estimated from the experimental data in methylcyclohexane solution, where excimer formation does not occur to any extent. With the values of fluorescence

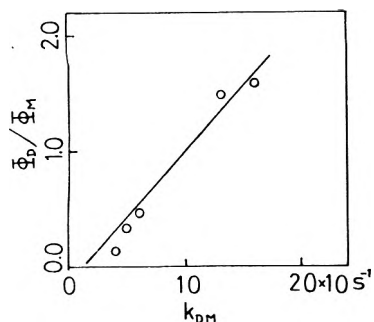


Figure 8. Plots of (Φ_D/Φ_M) vs. k_{DM} for various solutions of [2.2](1,3)pyrenophane at room temperature.

quantum yield (0.4) and decay time (150 ns) in methylcyclohexane solution, k_f and k_M have been evaluated as 2.8×10^6 and 6.7×10^6 s $^{-1}$, respectively. Subtracting the value of k_M from that of X , k_{DM} would be obtained. The results are shown in Table I.

As indicated in Figure 8, the plot of (Φ_D/Φ_M) vs. k_{DM} gave an approximately linear relationship. Thus, the relation between (Φ_D/Φ_M) and k_{DM} in eq 4 was confirmed to be valid approximately. The slope can be calculated from eq 4 as follows:

$$\frac{k_f'}{k_f} \frac{1}{k_D + k_{DM}} \sim \frac{k_f'}{k_f} \frac{1}{k_D} = \frac{q_D}{k_f} \quad (8)$$

The intrinsic fluorescence quantum yield of the excimer, (k_f'/k_D) , is estimated to be 0.4~0.5. Substituting this q_D value and $k_f = 2.8 \times 10^6$ s $^{-1}$ into eq 8, the slope has been evaluated to be $1.4 \sim 1.8 \times 10^{-7}$ s. On the other hand, the slope obtained from Figure 8 is ca. 1.1×10^{-7} s which is in relatively good agreement with those calculated above.

As it is described in section 1 of the Discussion, the maximum wavelength of excimer fluorescence of mePy is shorter than that of intermolecular pyrene excimer, and is much shorter than that of paPy. This result seems to indicate the smallest interaction between pyrene rings in the excimer state is due to the most loose structure of the mePy excimer among these three. The difference between the molecular structures of mePy and paPy excimers appears to be reflected in the lifetimes of these excimers. Namely, compared with the lifetime of 80 ns for paPy at room temperature, the intrinsic lifetime for mePy excimer is much shorter. If the k_D value for mePy excimer is assumed to be 10^9 s $^{-1}$, the radiative lifetime $\tau_f' = 1/k_f'$ can be evaluated to be 2 ns by using the value of $q_D \sim 0.5$. On the other hand, τ_f' for paPy evaluated from the integrated absorbance of the longest wavelength transannular band was 220 ns. At any rate, the difference between the radiative lifetimes of the mePy excimer and paPy is considerable, which seems to originate from the difference between their molecular structures.

5. *Conditions Necessary for Solvent-Induced Polarization in the System with Identical Halves.* It may be rather difficult to predict complete conditions necessary for this phenomenon, in view of the fact that few examples have been found until now. Nevertheless, it seems useful to deduce requirements for the solvent-induced polarization to take place from the results obtained here and in the previous reports.^{3,5} They are summarized as follows.

(a) Excimer configuration is completely prohibited, or that configuration is not easily formed.

An example of the former is 9,9'-bianthryl in a polar solvent, where emission resulted from the intramolecular CT state with band maximum depending upon solvent polarity. Examples of the latter are 1,2-dianthrylethanes

and mePy, where the intramolecular CT state would take part in the formation of the excimer state.

(b) It is necessary that the CT state is situated lower than or very close to the LE state energetically.

This condition might be realized for a molecule which consists of aromatic rings with low oxidation potential and high reduction potential in solvents with sufficient polarity. For example, comparing naphthalene and anthracene or pyrene, the CT state might be situated above the LE state for the former, whereas lower for the latter in acetonitrile solution.

6. *Remarks on the Nature of the Interactions between Halves in Excimers and Exciplexes.* It should be noted here that the results of the present report as well as the previous ones^{3,5} might be useful for the elucidation of the nature of the interactions between the components of excimers and exciplexes.

From the studies upon the typical intramolecular exciplex systems of the type A-(CH₂)_n-D, where A is an electron acceptor such as pyrenyl or anthryl and D is the *N,N*-dimethylanilino group, it has been established that the exciplex does not seem to have strong geometrical preferences.¹²⁻¹⁵ The electronic structure of these typical hydrocarbon-amine exciplexes (not only the intramolecular ones but also intermolecular ones) seems to be very polar, i.e., they have the structure of an almost pure ion pair.¹⁴⁻¹⁶ Therefore, their binding energy may be ascribed to the classical Coulombic attraction between ions with very small overlap of electron clouds, leading to small geometrical preferences.

In the CT states of 1,2-dianthrylethanes and mePy in polar solvents, the overlap of the electron clouds between the halves seems very small just as in the case of the above exciplex systems. However, in the case of 1,2-dianthrylethanes and mePy with identical halves, the excimer state has lower energy than the ion-pair state. For the excimer state to be realized, the overlap between the electron clouds of the halves seems to be of crucial importance, leading to the change of the geometrical structure to the overlapping sandwich type. Thus, the excimer interaction is essentially quantum mechanical just as in the case of homopolar bonding, whereas the bonding in typical exciplexes is classical electrostatic in nature. There might be exciplexes or excimers with an intermediate nature of bonding as it was first proposed by one of the present authors (N.M.).¹⁷ The excited state of *p*-(9'-anthryl)-*N,N*-dimethylaniline seems to be an example for such a case and, moreover, its intramolecular exciplex state shows gradual change of electronic structure depending upon the solvent polarity.^{12,18} However, a definite example of such a system has not yet been demonstrated unambiguously in the case of intermolecular exciplexes.

References and Notes

- (1) F. Schneider and E. Lippert, *Eur. J. Biochem. Phys. Chem.*, **72**, 1155 (1968); **74**, 624 (1970).
- (2) N. Nakashima, M. Murakawa, and N. Mataga, *Bull. Chem. Soc. Jpn.*, **49**, 854 (1976).
- (3) T. Hayashi, T. Suzuki, N. Mataga, Y. Sakata, and S. Misumi, *Chem. Phys. Lett.*, **38**, 599 (1976).
- (4) T. Hayashi, N. Mataga, Y. Sakata, S. Misumi, M. Morita, and J. Tanaka, *J. Am. Chem. Soc.*, **98**, 5910 (1976).
- (5) T. Hayashi, T. Suzuki, N. Mataga, Y. Sakata, and S. Misumi, *J. Phys. Chem.*, preceding article in this issue.
- (6) (a) T. Umamoto, T. Kawashima, Y. Sakata, and S. Misumi, *Chem. Lett.*, 837 (1975); (b) T. Umamoto, S. Satani, Y. Sakata, and S. Misumi, *Tetrahedron Lett.*, 3159 (1975); (c) T. Umamoto, T. Kawashima, Y. Sakata, and S. Misumi, *ibid.*, 463 (1975).
- (7) K. Okamoto, A. Itaya, and S. Kusabayashi, *Chem. Lett.*, 1167 (1974).
- (8) H. Shizuka, T. Ogiwara, and T. Morita, *Bull. Chem. Soc. Jpn.*, **48**, 3385 (1975).
- (9) R. W. Griffin, Jr., and R. A. Coburn, *Tetrahedron Lett.*, 2751 (1964); *J. Am. Chem. Soc.*, **89**, 4638 (1967).

- (10) J. B. Birks, "Photophysics of Aromatic Molecules", Wiley, London, 1970, pp 301-371.
- (11) P. Avouris, J. Kordas, and M. A. El-Bayoumi, *Chem. Phys. Lett.*, **26**, 373 (1974).
- (12) T. Okada, T. Fujita, M. Kubota, S. Masaki, N. Mataga, R. Ide, Y. Sakata, and S. Misumi, *Chem. Phys. Lett.*, **14**, 563 (1972); R. Ide, Y. Sakata, S. Misumi, T. Okada, and N. Mataga, *Chem. Commun.*, 1009 (1972).
- (13) N. Mataga in "The Exciplex", M. Gordon and W. R. Ware, Ed., Academic Press, New York, N.Y., 1975, p 113.
- (14) N. Mataga, T. Okada, H. Masuhara, N. Nakashima, Y. Sakata, and S. Misumi, *J. Lumin.*, **12/13**, 159 (1976).
- (15) S. Masaki, T. Okada, N. Mataga, Y. Sakata, and S. Misumi, *Bull. Chem. Soc. Jpn.*, **49**, 1277 (1976).
- (16) H. Fujiwara, N. Nakashima, and N. Mataga, to be submitted for publication.
- (17) N. Mataga, T. Okada, and K. Ezumi, *Mol. Phys.*, **10**, 203 (1966); N. Mataga, T. Okada, and N. Yamamoto, *Chem. Phys. Lett.*, **1**, 119 (1967).
- (18) T. Okada, T. Fujita, and N. Mataga, *Z. Phys. Chem. (Frankfurt am Main)*, **101**, 57 (1976).

Charge Transfer Triplet State of *p*-Nitroaniline

J. Wolleben and A. C. Testa*

Department of Chemistry, St. John's University, Jamaica, New York 11439 (Received September 29, 1976)

Flash photolytic, phosphorescence, and photochemical results are used to demonstrate that the lowest triplet state of *p*-nitroaniline is an intramolecular charge-transfer state. An absorption maximum appearing at 595 nm and observed at temperatures below -160°C is assigned to triplet-triplet absorption. A variable temperature flash photolysis study of *p*-nitroaniline in EPA indicates that a photochemical process generating a radical at room temperature is inhibited as the temperature is lowered. This transient peak appearing at 410-510 nm is attributed to the anilino radical, $\text{NO}_2\text{-Ar-NH}$. Transient spectra and decay kinetics are presented.

Introduction

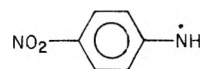
A polar molecule such as *p*-nitroaniline is of interest to photochemists due to the possibility of intramolecular charge transfer effects; i.e., the molecule is bifunctional possessing an electron donor and acceptor group. The molecule is known to phosphoresce and presumably the observation of the triplet and its characterization via flash photolysis appears worthy of investigation. Although benzene has been shown to give rise to a triplet-triplet absorption with a wavelength maximum at 240 nm^1 and a much weaker band at 430 nm^2 most derivatives of benzene when flashed usually result in a dissociative process producing radicals. Of the two related molecules, nitrobenzene and aniline, the triplet-triplet absorption of the former has not been observed while the latter exhibits a triplet-triplet absorption at 420 nm^3 . In the case of nitrobenzene, which does not phosphoresce, we have previously shown that a rapid radiationless decay ($\sim 10^{-9}$ s at room temperature) from the lowest triplet makes it difficult to observe its triplet-triplet absorption.⁴ In view of the continuing interest in inter- and intramolecular charge-transfer effects a variable temperature flash photolysis study of *p*-nitroaniline was undertaken.

Experimental Section

Reagent grade *p*-nitroaniline was purified by sublimation. Spectrograde EPA (5:5:2 ether-pentane-ethyl alcohol) obtained from Matheson Coleman and Bell was used as received. Room temperature flash photolysis studies (100 J) were performed in 12-cm cells while a 10-cm cell in conjunction with an optical Dewar was employed for the variable temperature studies. Experiments were generally carried out at 2×10^{-4} M *p*-nitroaniline. Samples were vacuum degassed at 10^{-4} Torr, before flame sealing. Photoreduction experiments were performed as described elsewhere,⁵ and phosphorescence lifetimes were determined with the conventional xenon flash lamp technique.

Results

Flash photolysis of 2×10^{-4} M *p*-nitroaniline at room temperature in degassed EPA results in a transient absorption in the wavelength region 410-510 nm (peaks at ~ 450 and ~ 480 nm), exhibiting a first-order decay constant of $265 \pm 45\text{ s}^{-1}$. The spectrum of this transient, which is most likely due to a radical, is shown in Figure 1. By performing a variable temperature study we were able to observe a diminution of the dissociative mode as the temperature is lowered and the complete disappearance of this transient for the temperatures lower than -100°C . This radical is observed down to -95°C , and at -85°C its first-order decay constant is $40 \pm 6\text{ s}^{-1}$. The origin of this radical is most probably fission of the N-H bond leading to an anilino type radical, i.e.

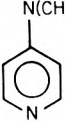


Porter et al.⁶ have shown that the flash photolysis of anilines gives rise to the anilino radical, which exhibits an absorption at ~ 400 nm. A comparison of the ultraviolet spectrum of aniline, $\lambda_{\text{max}} 280$ nm, with that of *p*-nitroaniline, $\lambda_{\text{max}} 360$ nm, i.e., an 80-nm shift, suggests that the anilino radical of *p*-nitroaniline might be expected at ~ 480 nm. It thus appears reasonable that the transient radical observed is the anilino radical.

The vibrational spacing of $\sim 1350\text{ cm}^{-1}$ between the two peaks, which is in reasonable agreement with the known value for the symmetric stretching frequency of the nitro group, may indicate that it is left intact in the formation of this radical. The cation of anilines, which absorb at ~ 425 nm, have also been observed in flash experiments,⁶ however, we do not consider this a likely process in *p*-nitroaniline since electron ejection to the solvent should be hindered by the presence of the nitro group.

Upon further cooling of *p*-nitroaniline to -160°C a new short-lived absorption is observed, whose decay is first-

TABLE I: Triplet-Triplet Absorption Maxima

Structure	240 nm ^a (430 nm) ^b	420 nm ^c	460 nm ^c 480 nm ^d	500 nm ^e	560 nm ^c	595 nm
						
						
						
						
						
						

^a Reference 1. ^b Reference 2. ^c Reference 7. ^d Reference 3. ^e Reference 8.

TABLE II: Phosphorescence Lifetime Data at 77 K

Compound	$\tau_0(\text{EPA}), \text{s}$	$\lambda_{\text{phos}}, \text{nm}$
Nitrobenzene		No phosphorescence
Aniline	4.5 ^a	416 ^b
<i>p</i> -Nitroaniline	0.37 ± 0.01, ^c 0.40, ^d 0.24 ± 0.02 ^e	518, 542, ~580 ^d
<i>p</i> -Nitro- <i>N</i> -methylaniline	0.44 ± 0.03, ^c 0.23 ± 0.05 ^e	
<i>p</i> -Nitro- <i>N,N</i> -dimethylaniline	0.42, ^d 0.22 ± 0.02 ^e	530, 552, ~590 ^d
<i>N,N</i> -Dimethylaniline	2.6 ^a	

^a Reference 10. ^b Reference 11. ^c This study. ^d Reference 12, EtOH glass. ^e Reference 9.

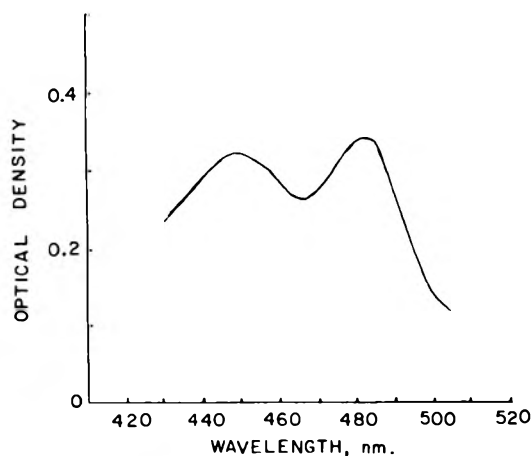


Figure 1. Room temperature absorption transient observed during the flash photolysis of 2×10^{-4} M *p*-nitroaniline (degassed) in EPA. Lifetime is 3.8 ms.

order and which exhibits a peak absorption at 595 nm. At this temperature the lifetime of the transient is ~ 0.2 ms and when the temperature is cooled to -170°C the optical density has reached an upper limit. Further cooling thereafter only lengthens the lifetime of this decaying species. The decay constant of this species is $5.6 \pm 1.0 \times 10^3 \text{ s}^{-1}$ at -170°C and $8.7 \pm 1.1 \text{ s}^{-1}$ at -190°C . The absorption spectrum of this low temperature transient is given in Figure 2. In order to definitively assign this absorbing species the measurement of phosphorescence was performed at -190°C in the flash photolysis cell with the monochromator set at 520 nm, since *p*-nitroaniline is known to phosphoresce at this wavelength. The measured decay constant, $6.8 \pm 0.1 \text{ s}^{-1}$, which is in satisfactory agreement with that for the 595-nm absorbing transient, allowing for uncertainties due to temperature fluctuation, firmly establishes that it is due to triplet-triplet absorption of *p*-nitroaniline.

Discussion

Although two transients are observed in the variable temperature studies of *p*-nitroaniline in EPA, the triplet-triplet absorption observed at 595 nm is certainly more interesting from the standpoint of implicating charge

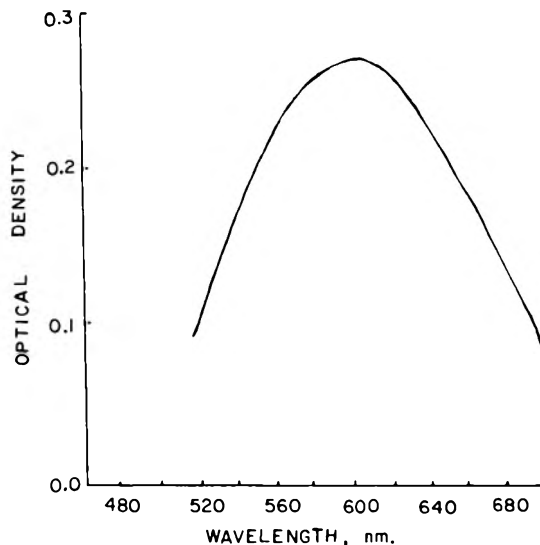


Figure 2. Triplet-triplet absorption spectrum of 2×10^{-4} M *p*-nitroaniline (degassed) in EPA measured at -170°C . Lifetime of triplet is 0.25 ms.

transfer effects. While being a benzene derivative containing a donor and an acceptor substituent, the absorption maximum of the triplet-triplet in *p*-nitroaniline appears at much higher wavelengths than it does in the related molecules given in Table I, which are arranged in the order of increasing wavelength. This large shift toward the visible in the case of *p*-nitroaniline relative to benzene and aniline indicates that the triplet-triplet absorption involves an intramolecular charge transfer. In a recent phosphorescence study of nitroanilines McGlynn et al.⁹ have concluded that the intervention of n,π^* states in this molecule is unimportant, which is supported by the flash photolysis and photochemical results reported here. Evidence for the strong intramolecular charge transfer character of the lowest triplet state of *p*-nitroaniline is obtained from a comparison of the photoreduction quantum yields for aromatic nitro compounds in isopropyl alcohol. While the photoreduction yield of nitrobenzene in isopropyl alcohol is 1.14×10^{-2} ,⁵ we have determined that this value is reduced to 3.9×10^{-3} for *p*-methyl-nitrobenzene and is only 7.2×10^{-4} for *p*-nitroaniline.

The charge transfer character of the lowest triplet state can also manifest itself in phosphorescence data. We have measured the phosphorescence lifetime of *p*-nitroaniline and *p*-nitro-*N*-methylaniline at 77 K in EPA in order to compare it with the related molecules given in Table II. It is readily seen that while nitrobenzene does not phosphoresce, aniline has a lifetime of 4.5 s; however, incorporation of the nitro group as an electron acceptor reduces the phosphorescence lifetime of aniline by approximately one order of magnitude.

In summary, we note that the lowest triplet of *p*-nitroaniline is characterized as an intramolecular charge transfer state in which charge transfer from the amine to the ring has been accentuated by the presence of the nitro group as an electron acceptor. Experimentally this effect is manifested in three ways: (a) a long wavelength triplet-triplet absorption characterized as an intramolecular charge transfer band, (b) negligible photoreduction

compared to nitrobenzene, and (3) an order of magnitude decrease in the phosphorescence lifetime relative to aniline. It would appear that the flash photolysis approach may be a convenient way to investigate intramolecular charge transfer triplet states.

References and Notes

- (1) T. S. Godfrey and G. Porter, *Trans. Faraday Soc.*, **62**, 7 (1966).
- (2) R. Astier and Y. Meyer, *Chem. Phys. Lett.*, **3**, 399 (1969).
- (3) K. Kimura, S. Arimitsu, N. Yamamoto, and H. Tsubomura, *Bull. Chem. Soc. Jpn.*, **41**, 1274 (1968).
- (4) R. Hurley and A. C. Testa, *J. Am. Chem. Soc.*, **90**, 1949 (1968).
- (5) R. Hurley and A. C. Testa, *J. Am. Chem. Soc.*, **88**, 4330 (1966).
- (6) E. J. Land and G. Porter, *Trans. Faraday Soc.*, **59**, 2027 (1963).
- (7) K. Cadogan and A. Albrecht, *J. Phys. Chem.*, **73**, 1868 (1968).
- (8) A. C. Testa, *J. Chem. Phys.*, **57**, 3019 (1972).
- (9) O. S. Khalil, C. J. Seliskar, and S. P. McGlynn, *J. Chem. Phys.*, **58**, 1607 (1973).
- (10) E. C. Lim and Chakrabarti, *J. Chem. Phys.*, **47**, 4726 (1967).
- (11) K. Kimura and H. Tsubomura, *Mol. Phys.*, **11**, 349 (1966).
- (12) J. S. Brinen and B. Singh, *J. Am. Chem. Soc.*, **93**, 6623 (1971).

Thermodynamics of Nonpolar Mixtures Exhibiting Liquid-Liquid Phase Equilibria. Aliphatic and Aromatic Esters with Alkanes

G. Manzini and V. Crescenzi*

Istituto di Chimica, Università di Trieste, Trieste, Italy (Received September 20, 1976)

Publication costs assisted by Consiglio Nazionale delle Ricerche, Rome

The critical solution behavior of 10 aliphatic (or aromatic) ester-*n*-heptane systems has been studied. Enthalpy and volume of mixing data (25 °C) are also provided in a few cases. Thermodynamic parameters characterizing each mixture studied by us as well as a number of different ester-alkane systems described in the literature are discussed and correlated in terms of the chemical constitution of component species.

Introduction

In previous papers from this laboratory the thermodynamic properties of a number of pure liquid esters and of their solutions in common organic solvents (toluene and 1,4-dioxane) have been discussed.¹⁻⁴ We wish to illustrate here additional results obtained in a thermodynamic characterization of mixtures of eight different aliphatic diesters and of two aromatic monoesters with *n*-heptane which exhibit liquid-liquid phase equilibria in an experimentally convenient range of temperatures. Compounds considered are: the diformates of 1,4-butanediol (BDF), 1,6-hexanediol (HDF), and 1,8-octanediol (ODF); the diacetates of 1,2-ethanediol (EDA) and 1,4-butanediol (BDA); the dimethyl esters of succinic (DMSuc), adipic (DMAd), and suberic acid (DMSub); benzyl acetate (BzA) and methyl phenyl acetate (MPha). Critical temperatures and a few enthalpy and volume of mixing data for the systems mentioned above as well as analogous literature data are discussed in terms of characteristic molecular properties of the components on the basis of a statistical thermodynamic theory of solutions due to Flory.⁵ This theory is found to provide a simple and rather successful mean to correlate the equilibrium properties also of such strongly nonideal mixtures.

Experimental Section

n-Heptane was a C.Erba-RS (chromatographic grade) sample, and was used without further purification.

The preparation and purification of the esters, and the experimental procedures followed in the calorimetric and density measurements have already been described.²⁻⁴

The binodials have been obtained using weighted mixtures of each ester and *n*-heptane in air-tight tubes which were placed in a thermostatic bath (or in a non-silvered dewar flask for temperature measurements below 20 °C). The equilibrium temperatures were determined both on mixing and on demixing, i.e., heating or cooling the thermostatic bath at a rate of about 0.1 deg/min. Both the mixtures and the bath were stirred by means of teflon-covered magnetic stirrers. The difference between the equilibrium temperatures determined on heating and on cooling was generally less than 0.2 °C.

Results and Discussion

The experimental binodial curves are given in Figure 1 as functions of the ester "hard-core" volume fraction, ϕ_2 .⁵ The corresponding critical temperatures, T_c , are listed in Table I.

For BDA, DMAd, ODF, DMSub, BzA, and MPha, a few results of the measurements of the heats of mixing with *n*-heptane at 25 °C are given in Table II (obviously, in the case of BDA and DMAd, volume fractions within the miscibility gaps were avoided). Data on the excess volumes on mixing *n*-heptane with DMAd and DMSub, respectively, are reported in Figure 2. An analysis of the whole set of experimental data is profitably made on the basis

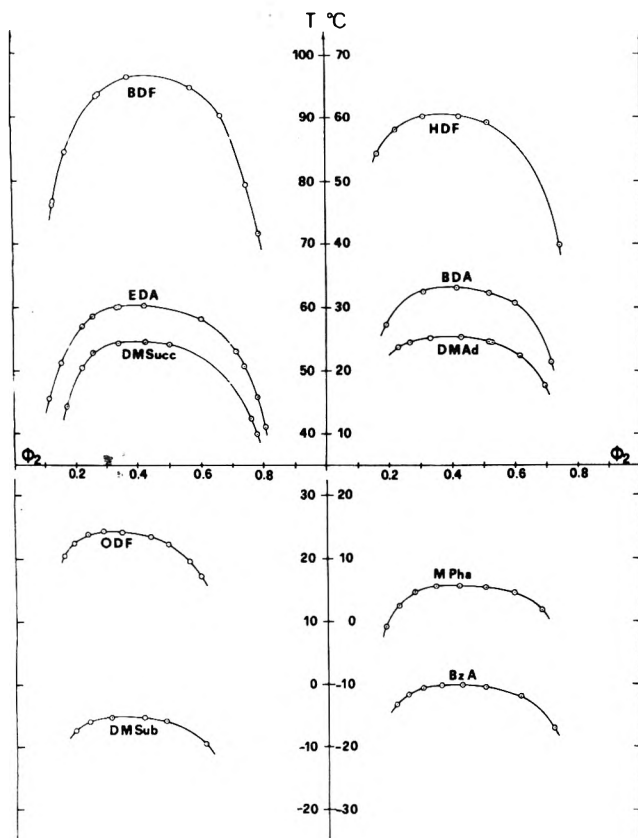


Figure 1. Experimental binodal curves for the *n*-heptane-ester mixtures. ϕ_2 is the ester hard-core volume fraction.⁵

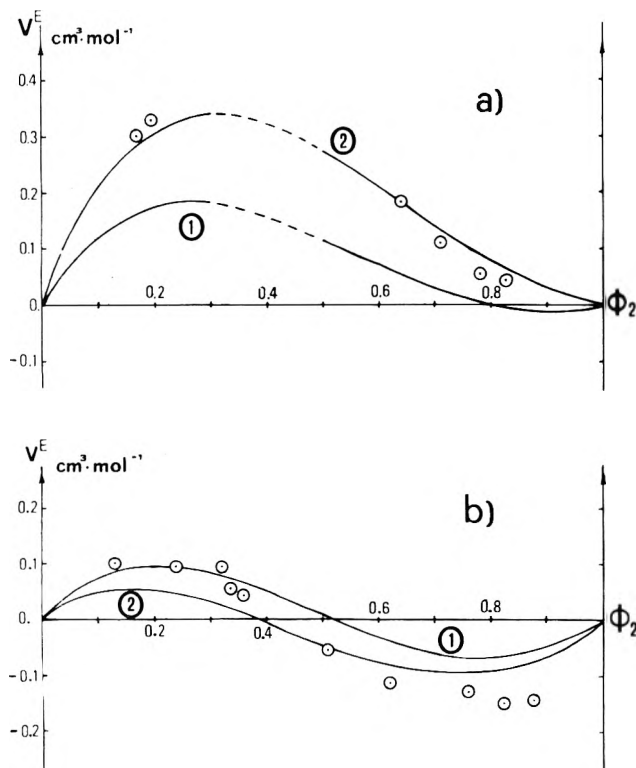


Figure 2. Excess volumes of mixing for (a) *n*-heptane-DMAAd: (O) experimental data, (1) calculated using $X_{12} = 50 \text{ J/cm}^3$ from calorimetric data, (2) calculated using $X_{12} = 56 \text{ J/cm}^3$ (best fit); (b) *n*-heptane-DMSub: (O) experimental data, (1) calculated using $X_{12} = 43 \text{ J/cm}^3$ from calorimetric data; (2) calculated using $X_{12} = 41 \text{ J/cm}^3$ (best fit). ϕ_2 is the ester hard-core volume fraction.

of the theory of Flory. In particular, we shall follow closely the theoretical approach clearly outlined by Flory⁵ (as already applied with success by us in previous instances^{3,4})

TABLE I

	V^* , cm^3/mol	T^* , K	P^* , J/cm^3	X_{12}^* , (UCST)	X_{12}^* , (CAL)	X_{12}^* , (VOL)	T_c , K	$\phi_{2,c}^a$	$10^3 \alpha$, K^{-1}	V_M , cm^3/mol	S_1/S_2
1,4-Butanediol diformate	106.9	5550	714	69			370	0.44(0.49)	0.90	131.2	0.91
1,2-Ethanediol diacetate	105.6	5080	733	64			334	0.44(0.49)	1.055	132.9	0.90
Dimethyl succinate	105.6	5300	732	61			328	0.44(0.49)	0.975	131.2	0.90
1,6-Hexanediol diformate	135.9	5670	652	52			334	0.40(0.46)	0.865	165.8	0.93
1,4-Butanediol diacetate	135.7	5450	657	47	55		306	0.42(0.46)	0.93	167.3	0.93
Dimethyl adipate	133.8	5460	674	46	50	56	298	0.42(0.46)	0.925	164.8	0.92
1,8-Octanediol diformate	165.0	5750	617	40	45		297	0.37(0.43)	0.85	200.6	0.95
Dimethyl sebacate	161.9	5530	640	37	43	41	268	0.38(0.44)	0.905	198.8	0.94
Methyl phenyl acetate	116.3	5750	670	46	55		278	0.45	0.85	141.4	1.02
Benzyl acetate	116.6	5580	667	45	51		263	0.45	0.89	142.9	1.02
<i>n</i> -Heptane	113.8	4674	427						1.24	147.4	

^a Numbers in parentheses are $\phi_{2,c}$ values derived from eq 12 and 13 of ref 6 imposing the experimental T_c data and the S_1/S_2 ratios given in the last column.

TABLE II

	ϕ_2	ΔH_M , J/mol 10^{-3}
BDA	0.16	0.92
	0.725	1.46
	0.80	1.22
DMA _d	0.205	1.02
	0.285	1.32
	0.58	1.62
	0.675	1.58
	0.765	1.24
ODF	0.48	1.58
	0.55	1.58
	0.65	1.50
DMS _{ub}	0.355	1.43
	0.46	1.47
	0.62	1.54
MPha	0.47	1.57
	0.535	1.65
BzA	0.525	1.48

and the extension of such approach made by Abe and Flory⁶ to the treatment of liquid-liquid phase equilibria.

We shall limit ourselves here to briefly recall that, according to this theory, parameters required for interpretation of results for binary nonpolar liquid mixtures consist of the characteristic pressure, volume, and temperature (P^* , V^* , T^*) for each pure component (to be determined from experimental molar volume V_M , thermal expansion coefficient α_T , and thermal pressure coefficient γ , data via the equation of state⁵), and of a single parameter, X_{12} , taking account of differences in energy (density) between contact interactions of like and unlike neighbors.

The changes of thermodynamic state functions on mixing depend in fact on the characteristic parameters and the X_{12} parameter only, besides, naturally, of temperature and composition. For the latter variable, besides to the segment fraction ϕ , also the site fraction θ is needed:

$$\theta_2 = (1 - \theta_1) = \frac{\phi_2}{(S_1/S_2)\phi_1 + \phi_2}$$

where S_1/S_2 is the ratio of contact sites per segment for the components 1 and 2.¹⁶ Studying the excess properties of homogeneous mixtures at near ambient temperature agreement between experiments and theory has been satisfactorily achieved in many cases;⁷⁻¹¹ moreover the resulting X_{12} values would be simply correlated with the chemical structure of the components via characteristic exchange enthalpy parameters (X_{ij}) between different chemical groupings (i, j, \dots) each contributing a given fraction ($\alpha_i, \alpha_j, \dots$) to the total molecular surfaces.^{3,4}

In the case of mixtures exhibiting liquid-liquid phase separation the same theory has been extended in order to describe the characteristic binodal curves;⁶ these, as a consequence, afford an interesting, independent means to derive the important X_{12} parameter for such strongly nonideal systems at temperatures generally different from 25 °C, of course.

These X_{12} values are identified here as $X_{12}(\text{UCST})$, i.e., from upper critical solution temperatures measurements. Strict validity of the underlying theory would require X_{12} to be independent of temperature; experience shows, however, that X_{12} often decreases moderately with increasing temperature. This would, at least in part, reflect the slight variation of the characteristic parameters, V^* and P^* , with temperature, besides other possible inaccuracies of the theory. It seems therefore worthwhile to test the validity of such a theory in cases for which X_{12} becomes accessible from both UCST measurements and

TABLE III

1-2	T_c , °C, K	X_{12} (UCST), J/cm ³	10^3 α_{T_1} , K ⁻¹	10^3 α_{T_2} , K ⁻¹
c-Pentane-methyl formate	254	85	1.32	1.5
c-Hexane-methyl formate	271	88	1.22	
c-Heptane-methyl formate	278	85	1.0	
c-Octane-methyl formate	288	86	0.99	
c-Pentane-methyl acetate	216	59		1.38
c-Hexane-methyl acetate	231 ^a	61		
c-Heptane-methyl acetate	240	59		
c-Octane-methyl acetate	248	59		

^a Calculated value, as described in ref 12.

from excess properties (ΔH_M) at 25 °C.

Treatment of our T_c and $\phi_{2,c}$ data (Table I) with the aid of the aforementioned theory (in particular, of expressions (12) and (13) of ref 6) using the necessary equation-of-state parameters for each species considered, leads to the $X_{12}(\text{UCST})$ values also reported in Table I.¹⁷

It appears that both differences in equation-of-state parameters (in particular P^* and T^*) between components and the X_{12} parameter concur in determining the T_c value in each case. Indeed one can see that, as a general trend, the higher T_c is the higher the X_{12} value results but also that for diesters having nearly the same critical temperature (in *n*-heptane) different X_{12} values are required owing to differences in their P^* and T^* parameters. For instance, the markedly higher T_c exhibited by the diformate/*n*-heptane mixture with respect to the mixtures of the other diesters of equal molecular weight (e.g., BDF with respect to EDA and DMS_{uc}, etc.) are mainly ascribable to the relatively low thermal expansion coefficients, α_r , of the diformates and only in part to higher X_{12} values.

Just the same holds true if one compares the T_c data for the MPha/*n*-heptane mixture with that of the BzA/*n*-heptane mixture. In our opinion, these results show once more, qualitatively if not quantitatively, the correctness of the treatment of Flory.

In order to reinforce the validity of these considerations we have examined also a few T_c data recently reported in the literature for cycloalkane-aliphatic esters mixtures.¹² Compounds involved, the associated T_c values, the characteristic parameters of pure components, and the $X_{12}(\text{UCST})$ derived therefrom as outlined above are given in Table III. It appears evident that, for each of the two esters considered, varying the partner in the mixture from cyclopentane to cyclooctane (i.e., varying the characteristic parameters and *not* the chemical nature of the partner) affects rather seriously the T_c values but changes $X_{12}(\text{UCST})$ only slightly (within the uncertainty in X_{12} due only to experimental errors).

To proceed further in our analysis, let us consider the few X_{12} values ($X_{12}(\text{CAL})$) derived from the calorimetric enthalpy of mixing data of Table II and from the volume of mixing data of Figure 2 ($X_{12}(\text{VOL})$). Analysis of these X_{12} values reveals an acceptable agreement or, better, that differences between $X_{12}(\text{CAL})$ and $X_{12}(\text{VOL})$ are not worse than normally encountered for different systems.¹⁸ Moreover $X_{12}(\text{CAL})$ results are systematically higher than $X_{12}(\text{UCST})$ by about 10–20%. It is also interesting to

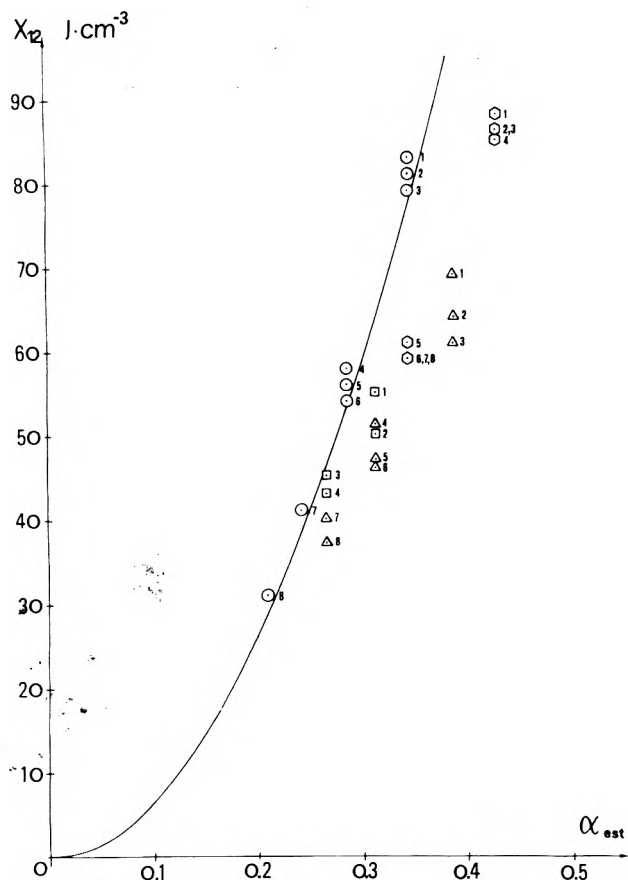


Figure 3. The X_{12} parameter for the alkane-ester mixtures as a function of the "ester type" site fraction of the ester considered. From UCST data. \odot : (1) *c*-hexane-methyl formate, (2) *c*-octane-methyl formate, (3) *c*-pentane-methyl formate, (4) *c*-heptane-methyl formate, (5) *c*-hexane-methyl acetate, (6) *c*-octane-methyl acetate, (7) *c*-pentane-methyl acetate, (8) *c*-heptane-methyl acetate. Δ : (1) *n*-heptane-BDF, (2) *n*-heptane-EDA, (3) *n*-heptane-DMSucc, (4) *n*-heptane-HDF, (5) *n*-heptane-BDA, (6) *n*-heptane-DMA, (7) *n*-heptane-ODF, (8) *n*-heptane-DMSub. From calorimetric data. \circ : (1) *n*-dodecane-methyl acetate, (2) *n*-octane-methyl acetate, (3) *n*-hexane-methyl acetate, (4) *n*-octane-ethyl acetate, (5) *n*-dodecane-ethyl acetate, (6) *n*-hexane-ethyl acetate, (7) *n*-hexane-*n*-propyl acetate, (8) *n*-hexane-*n*-butyl acetate. \square : (1) *n*-heptane-BDA, (2) *n*-heptane-DMA, (3) *n*-heptane-ODF, (4) *n*-heptane-DMSub. The full line was calculated according to eq 2. (See text.)

point out that the theory succeeds in accounting for the marked dissymmetry of the V^E against ϕ_2 plots (Figure 2) in one of which (DMSub/*n*-heptane) a change of sign of V^E is even exhibited. Another relevant observation is that, different from ΔH_M , which is largely due to X_{12} contributions, V^E is heavily dependent on the equation-of-state terms. For example, would X_{12} be zero, V^E had to result strongly negative in our cases; the quite high actual X_{12} values have therefore the effect of nearly neutralizing the equation-of-state contribution to V^E . In other words the theory succeeds in accounting for large positive ΔH_M values and for small or nearly zero V^E values at the same time.

Finally we wish to comment briefly on the correlation between X_{12} and the "chemical" composition of the esters. As mentioned above, using the approximate form of eq 10 of ref 3, we have expressed the X_{12} values as a function of the contact site fractions, α_i , of the various (chemical) types (aliphatic, aromatic, ester, etc.) of each component, and of the corresponding exchange-energy density parameters X_{ij} :

$$X_{12} \approx - \sum_{i>j} (\alpha_{i,1} - \alpha_{i,2})(\alpha_{j,1} - \alpha_{j,2})X_{ij} \quad (1)$$

On the basis of ΔH_M data from our laboratory and from the literature, and evaluating the α values according to the method of Bondi¹⁴ we have derived the following best fit values:³ $X_{al,arom} = 40$; $X_{al,est} = 700$; and $X_{arom,est} = 350$ J/cm³.

In the case of alkane-aliphatic esters, mixtures of our concern, eq 1 simply reduces to

$$X_{12} \approx X_{al,est} \alpha_{est}^2 \quad (2)$$

α_{est} being the "ester type" site fraction of a given aliphatic ester.

Considering our present X_{12} values (Tables I and II) as well as additional X_{12} values derivable from different ΔH_M literature data for the acetates of methyl, ethyl, propyl, and butyl alcohols in *n*-alkanes,¹⁵ and adopting for the estimation of α_{est} our usual procedure,³ we obtain the X_{12} vs. α_{est} plot of Figure 3.

The parabolic curve has been drawn according to eq 2, with $X_{al,est} = 650$ J/cm³.

This value which optimizes agreement with X_{12} (CAL) data is less than 10% lower than that previously estimated,³ such difference may be considered to fall within the experimental errors of the set of ΔH_M data taken from different sources. Figure 3 therefore reinforces our conclusion that X_{12} (CAL) can indeed be correlated with ester-like site fractions, α_{est} , using a common value of the $X_{al,est}$ parameter, but also clearly shows that the X_{12} (UCST) values are then systematically lower than the corresponding (experimental and/or theoretical) X_{12} (CAL) ones, as already mentioned above. This discrepancy cannot be simply attributed to a dependence of X_{12} on temperature (our X_{12} (UCST) in fact pertain to mixtures with T_c values both below and above 25 °C; see Tables I and II) but might be, for instance, considered as a symptom of the necessity of introducing in the expression for the chemical potentials a term such as Q_{12} .¹³

Acknowledgment. This work has been sponsored by the Italian Consiglio Nazionale delle Ricerche, Rome.

References and Notes

- (1) G. Manzini and V. Crescenzi, *Polymer*, **14**, 343 (1973).
- (2) G. Manzini and V. Crescenzi, *Macromolecules*, **8**, 195 (1975).
- (3) G. Manzini, V. Crescenzi, and R. Furlanetto, *Macromolecules*, **8**, 198 (1975).
- (4) V. Crescenzi and G. Manzini, *J. Polym. Sci., Part C*, in press.
- (5) P. J. Flory, *J. Am. Chem. Soc.*, **87**, 1833 (1965).
- (6) A. Abe and P. J. Flory, *J. Am. Chem. Soc.*, **88**, 2887 (1966).
- (7) R. Battino, *J. Phys. Chem.*, **70**, 3408 (1966).
- (8) G. C. Benson and J. Singh, *J. Phys. Chem.*, **72**, 1345 (1968).
- (9) J. Singh, H. D. Peug, and G. C. Benson, *J. Phys. Chem.*, **72**, 1939 (1968).
- (10) E. L. Washington and R. Battino, *J. Phys. Chem.*, **72**, 4496 (1968).
- (11) R. Battino, *J. Phys. Chem.*, **72**, 4503 (1968).
- (12) G. Spinolo, P. Ferloni, and P. Franzosini, *Gazz. Chim. Ital.*, **103**, 747 (1973).
- (13) B. E. Eichinger and P. J. Flory, *Trans. Faraday Soc.*, **64**, 2035 (1968).
- (14) A. Bondi, *J. Phys. Chem.*, **68**, 441 (1964).
- (15) "International Data Series", A, no. 2, 1973, p. 133; no. 1, 1974, pp. 15, 16, 17; no. 2, 1974, pp. 121, 122, 124, 125.
- (16) The quantity S_1/S_2 may be obtained with sufficient reliability from estimates of the surface to volume ratios for the two species of the mixture and is not considered an adjustable parameter; we evaluated the S_1/S_2 ratios as previously specified,³ assuming direct proportionality between the number of contact sites and the van der Waals surfaces of the molecules as determined by Bondi¹⁴ (see Table I). This method, often inadequate for polymeric solutions, as pointed out by Flory, gives, in the case of small molecules, results substantially agreeing with those obtainable using the method proposed by Flory.
- (17) Calculations were performed with a Fortran program using a CDC-6200 computer at the Computing Center of the University of Trieste.
- (18) More serious discrepancies have been found between X_{12} values derived from free energy and enthalpy data in the case of polymer solutions. This fact has led to the introduction in the theory of an additional parameter, Q_{12} , which formally takes account of the change in entropy connected with the exchange of neighboring species.¹³

Electron Paramagnetic Resonance of Rare Earth Ions in Zeolites[†]

Lennox E. Iton*

Solid State Science Division, Argonne National Laboratory, Argonne, Illinois 60439

and J. Turkevich

Department of Chemistry, Princeton University, Princeton, New Jersey 08540 (Received October 4, 1976)

Publication costs assisted by Argonne National Laboratory and the U.S. Energy Research and Development Administration

The EPR spectra of Gd^{3+} and Eu^{2+} in Y zeolite and zeolon (mordenite) have been extensively studied at X- and Q-band frequencies. An essential realization in understanding the spectra in these materials is the importance of randomness in the spin Hamiltonian parameters, hence the similarity to spectra of Gd^{3+} in several different glasses. A detailed explanation of the spectra in terms of cation locations and ligand coordination is given; the point symmetries are always orthorhombic or lower, even for the fully hydrated ions, which display the familiar phase transition behavior at low temperature. The largest zero-field splittings occur when the dehydrated ions are bound in a one-sided coordination to the zeolite framework, and the resulting signal is readily interpreted in the random vector model approach; it is never observed for Gd^{3+} in Y zeolite in the calcining conditions used, indicating the retention of extraframework OH in the coordination sphere of Gd^{3+} ions in type I' sites. Eu^{3+} ions can be reduced by γ irradiation of the hydrated zeolites at 77 K, or by vacuum calcining; the resulting Eu^{2+} ion spectra reflect the different site distributions and ligand environments achieved in the two cases. Successive reduction-oxidation cycles can be effected with the europium. By devising an empirical correlation with Allred-Rochow electronegativities, the intrinsic splitting parameters, $|b_{21}|$, for the S-state ions with silicate and aluminate oxygen ligands were estimated. The extreme inhomogeneous broadening caused by the randomness prohibits detailed interpretation of the spectra of the non-S-state ions.

I. Introduction

Because of their profound catalytic importance and their provision of large, well-defined surface areas, molecular sieve zeolites have become the focus of a range of disparate research activities. They continue to attract the interest of mineralogists, crystallographers, and physical and catalysis chemists. An assortment of spectroscopic techniques have been brought to bear in these investigations, ranging from Mossbauer spectroscopy, through UV, IR, and Raman spectroscopies, to a variety of magnetic resonance techniques. Despite their industrial importance, few spectroscopic investigations have been made of zeolites exchanged with rare earth (RE) cations, the efforts having been concentrated on zeolites containing nontransition ions or first transition period ions. Many of these RE ions, however, have paramagnetic ground states in their usual valence states, and their electron paramagnetic resonance (EPR) spectra have been extensively studied in simple ionic crystal hosts.

The EPR technique was first applied to the detailed study of ions in an exchanged zeolite by Turkevich and co-workers.¹ Since then, several further studies have been made on ions such as Cu^{2+} , Mn^{2+} , Fe^{3+} , Co^{2+} , Ni^{2+} , and Ti^{3+} , the resonance behavior often being used as a monitor of the state of the zeolite rather than for providing phenomenological information on the spin Hamiltonian of the ion itself. EPR has also been much used for the study of radical ions and paramagnetic molecules adsorbed on zeolites,² thus providing information on reactive intermediates. For both theoretical and practical reasons, the EPR spectra of the S-state ions, Eu^{2+} and Gd^{3+} , are the most conveniently studied of the rare earth series, and they will be the ones emphasized in this paper, although results obtained on other ions will be briefly presented.

The synthetic faujasite, Linde type Y zeolite, is the most important zeolite in industrial use. RE ion-exchanged forms have superior catalytic properties in alkylation, isomerization, and cracking reactions. The principal focus in this paper is on RE exchanged Y zeolite, but experiments on exchanged synthetic mordenite (zeolon) are also reported and discussed. The crystal structures of both of these zeolites are known, and Meier and Olson³ have published stereoprojections of the framework structures, respectively, cubic ($Fd3m$) and orthorhombic ($Cmcm$) for the faujasite and mordenite. The exchangeable cation sites have also been well described for the Y-zeolite structure, but the data compiled by Smith⁴ suggest that site distribution of cations is a function both of detailed material treatment and cation identity, and should preferably be determined on an individual basis, although some general trends are evident. The amount of data available on exchange cation sites in mordenite is much less abundant, and only recently have Smith and co-workers^{5,6} published the first results for a divalent exchange ion. The nomenclature of Smith⁴⁻⁶ will be used in this paper to label cation sites.

We will present here⁷ extensive results of X- and Q-band EPR measurements on Gd^{3+} and Eu^{2+} in Y zeolite and mordenite over a wide temperature range, and for calcined and hydrated samples. Additional results on the EPR of Gd^{3+} in aqueous solution, Eu^{2+} in Eu_2O_3 , and the chemical behavior of europium in zeolites, are combined with recent theoretical models of S-state ion EPR, and of magnetic resonance spectra of ions in glasses, and with published results on optical and EPR spectra of RE ions in glasses, to emerge with a comprehensive picture of the behavior of the ions in the zeolite lattices, the factors dominating the observed forms of the EPR spectra, and estimates of the magnitudes of the intrinsic ground state splitting parameters for the S-state ions in the aluminosilicate lattice. We give also, in section V(1), a brief, critical discussion of some previously published work on the EPR of Gd^{3+} and Eu^{2+} in synthetic faujasites.

[†] Based on work performed under the auspices of the U.S. Energy Research and Development Administration. Contribution C3029-17.

* Address correspondence to this author at the Solid State Science Division, Argonne National Laboratory, Argonne, Ill. 60439.

II. Theory.

II(1). *Form of the Spin Hamiltonian.* A full general treatment of the EPR of rare earth (RE) ions is given in the treatise by Abragam and Bleaney.⁸ There, the operator equivalents formalism for representation of the spin Hamiltonian is described in detail. The phenomenological Hamiltonian to be dealt with here consists only of terms corresponding to electronic Zeeman and effective crystal field (CF) interactions:

$$\mathcal{H} = \mathcal{H}_{\text{Zeeman}} + \mathcal{H}'_{\text{CF}} \quad (1)$$

There is experimental justification for the omission of a hyperfine interaction term (\mathcal{H}_{hf}), as will be seen later. Other smaller terms can also be neglected.

For the $4f^7$ (half-filled shell) ions, Gd^{3+} and Eu^{2+} , the Russell-Saunders ground term is $^8\text{S}_{7/2}$, so the general Zeeman interaction term:

$$\mathcal{H}_{\text{Zeeman}} = \beta \mathbf{H} \cdot \mathbf{g} \cdot \mathbf{J} \quad (2a)$$

where \mathbf{H} is the applied magnetic field; \mathbf{g} is the electronic g -factor tensor; \mathbf{J} is the total angular momentum = $\mathbf{L} + \mathbf{S}$; \mathbf{L} is the orbital angular momentum; \mathbf{S} is the spin angular momentum; β is the Bohr magneton; can be simplified (for $\mathbf{L} = 0$) to

$$\mathcal{H}_{\text{Zeeman}} = g_0 \beta \mathbf{H} \cdot \mathbf{S} \quad (2b)$$

where g_0 is the isotropic, free electron value. Expression 2b is adequate (for our purposes) even though the true ionic ground states are not pure $^8\text{S}_{7/2}$, but rather, contain small admixtures of higher $^6\text{P}_{7/2}$ and $^6\text{D}_{7/2}$ states;⁹ these produce only a small shift in the g value.

The small spin-orbit admixtures are, however, very important in that they mediate the interaction of the ion with the crystal field, which does not couple directly to the spins. They are thus responsible for the ground state splittings, and hence for the ligand effects in the EPR spectra. The explanation of the magnitudes of these splittings has evaded theorists for a long time,¹⁰ and they are still not well understood (see following section); however, the operator equivalents parametrization of the effective crystal field interaction does not depend on the exact nature of the interaction mechanism, but does reflect the symmetry of the crystal field. For a cubic CF, this fine structure term has the form:

$$\mathcal{H}'_{\text{CF}} = (1/60)b_4(O_4^0 + 5O_4^4) + (1/1260)b_6(O_6^0 - 21O_6^4) \quad (3)$$

where the O_k^q are the spin operators of k th degree, and the b_k are the corresponding coefficients. For noncubic symmetries, second degree terms enter the Hamiltonian and, invariably, they are dominant. Hence, for our polycrystalline system, where the spectral line widths are large and orientational dependences cannot be measured, it is sufficient to restrict the Hamiltonian to terms of second degree in the spin operators:

$$\mathcal{H}'_{\text{CF}} = (1/3)(b_2^0 O_2^0 + b_2^2 O_2^2) \quad (4)$$

All physically distinct situations for this expression are included in the range $0 \leq |b_2^2/b_2^0| \leq 1$, so that the appropriate full-spin Hamiltonian for all but cubic crystal fields is

$$\mathcal{H} = g_0 \beta \mathbf{H} \cdot \mathbf{S} + (1/3)(b_2^0 O_2^0 + b_2^2 O_2^2) \quad (5)$$

Nicklin¹¹ has computed the energy levels for this Hamiltonian for a spin $S = 7/2$ system for a full range of $|b_2^2/b_2^0|$, at selected values of $|b_2^2/b_2^0|$ over the range 0 to 1. The published calculations are restricted only in that

H is constrained to the three principal axis directions of (5).

There are two important extremes when perturbation theory approaches are appropriate, viz.: (a) the strong-field Zeeman effect limit, for $\mathcal{H}_{\text{Zeeman}} \gg \mathcal{H}_{\text{CF}}$; and (b) the weak-field Zeeman effect limit or strong crystal field case, for $\mathcal{H}_{\text{CF}} \gg \mathcal{H}_{\text{Zeeman}}$. An important feature of the latter is that the effective g values of the allowed EPR transitions are independent of the actual magnitudes of b_2^0 and b_2^2 , being completely determined by the ratio $|b_2^2/b_2^0|$. The former case is typical for Gd^{3+} and Eu^{2+} in cubic crystals at X-band microwave frequencies.

II.(2) *Theory of the Spin Hamiltonian Parameters.* The long-standing inability to account for the magnitudes of the S-state ions' ground state splittings has persisted despite the detailed analysis of splitting mechanisms such as was made by Wybourne.¹² It is now recognized that the dominant contribution is not electrostatic, stemming instead from covalency effects due to overlap between the ion and the ligands. The most successful empirical model has been the recently formulated superposition model due to Newman and Urban.¹³ This model assumes that the total CF can be constructed from a sum of axially symmetric contributions from the ligands, and it can be applied to experimental spin Hamiltonian parameters if these result from processes linear in the crystal field. The model is parametrized in terms of intrinsic parameters, $\bar{b}_k(R)$, which represent the axially symmetric contribution of a single ligand at a distance R from the ion. Thus, for the spin Hamiltonian parameters of second degree:

$$b_2^q = \sum_i K_2^q(\theta_i, \phi_i) \bar{b}_2(R_i) \quad (6)$$

where the $K_2^q(\theta_i, \phi_i)$ are the coordination factors for the i th ligand located at position (R_i, θ_i, ϕ_i) . The parameters in the true CF potential are similarly decomposed:

$$A_2^q\langle r^2 \rangle = \sum_i K_2^q(\theta_i, \phi_i) \bar{A}_2(R_i) \quad (7)$$

where the $\bar{A}_2(R)$ are the corresponding intrinsic parameters. For the second degree terms, q takes values 0 and 2.

The superposition model yields the result that the largest contributions to the intrinsic splitting parameter, \bar{b}_2 , come from the relativistic crystal field and the correlation crystal field; but, because these are cancelling contributions, the dominant resultant mechanism is the ordinary crystal field.⁹ However, this implies that the \bar{b}_2 do not directly reflect the CF interaction that would be obtained, say, from optical data; even more emphatically, the experimental b_k^q do not directly reflect this interaction mechanism.

II.(3) *EPR Spectra of Ions in Glasses.* It is relevant to introduce the subject of the spectra of glasses because, as will be seen, some of the spectra observed in this study closely resemble spectra of Gd^{3+} found in several glasses. The essential notion that will be repeatedly emphasized is that of the random character of the glass structure, which has the consequence of engendering a continuous range of small distortions of the local symmetry at the ion sites. Therefore, there will be a random distribution in the crystal field (and spin Hamiltonian) parameters associated with each basic ion site. This is a complication, not typical of polycrystalline powders, that can have profound influence on the experimental magnetic resonance spectrum; it has been found to be important even for a single crystal of nonstoichiometric materials, where line shape can be dominated by randomness in a spin Hamiltonian parameter.¹⁴

The traditional method of treating this complication has been either (a) to ignore it and simply analyze the spectrum as for a polycrystalline powder, or (b) to introduce it artificially, post facto, by applying convolution methods to treatment (a). Such treatments have been criticized by Peterson and co-workers^{15,16} who have recently presented a new statistical approach in which randomness is naturally introduced as a starting condition. We relate this approach only in enough detail to make the discussion in section V.4 readily understandable.

The central idea is to represent the experimental EPR spectrum as a reduced probability density function (reduced pdf). Randomness is introduced by writing the pertinent spin Hamiltonian parameters as random variables in a joint density function (jdf), with arbitrarily variable means and central moments,¹⁷ from which the reduced pdf is generated. Thus, the spectrum can be described by a reduced pdf in either the field, H , or the effective g value,¹⁸ g , given by $p_H(\alpha')$ or $p_g(\alpha)$, respectively. For an axial system, such as was treated by Peterson et al.,¹⁵ the reduced pdf is generated from a joint density function in the random variables $g_{\parallel}, g_{\perp}, \theta$, using the rules of random vector theory¹⁷ for making the appropriate transformations:

EPR spectrum (or some features thereof)
 $\leftarrow p_H(\alpha') \cdot |J_g(H)| = p_g(\alpha) \quad (8)$

$$p_g(\alpha) = \iint p_{g_{\parallel}, g_{\perp}}(\alpha, \beta, \gamma) d\beta d\gamma$$

$$= \iint p_{\theta, g_{\parallel}, g_{\perp}}(\delta, \beta, \gamma) \cdot |J_{\theta, g_{\parallel}, g_{\perp}}(g, g_{\parallel}, g_{\perp})| d\beta d\gamma$$

$$= \iint p_{\theta}(\delta) p_{g_{\parallel}, g_{\perp}}(\beta, \gamma) \cdot |J_{\theta, g_{\parallel}, g_{\perp}}(g, g_{\parallel}, g_{\perp})| d\beta d\gamma \quad (9)$$

where $J_x(\vec{r})$ is the Jacobian for the transformation of the random vector (variable) x to the random vector (variable) \vec{r} ; $\alpha, \alpha', \beta, \gamma$, and δ are dummy variables; and the fact that θ , the angle between the field and the symmetry axis, is an uncorrelated random variable has been used to decompose the three-dimensional jdf.

The variational problem is thus limited to the two-dimensional joint density function, $p_{g_{\parallel}, g_{\perp}}(\beta, \gamma)$, for which a convenient shape can be assumed, and its mean values, variances and covariances¹⁷ (the two-dimensional versions of the central moments), arbitrarily varied so as to generate the experimental spectrum.

III. Experimental Section

III(1). *Material Preparations and Analyses.* Rare earth ion-exchanged Y-zeolite materials were prepared from ultrapure Na-Y zeolite starting material by contact of the powder with the appropriate solution at room temperature. For the preparation of samples in which the paramagnetic rare earth is magnetically diluted by coexchange with La^{3+} , 0.3 N (0.1 M) solutions containing LaCl_3 and MCl_3 in an $n:1$ mole ratio (where M is a trivalent rare earth ion) were used, with $n = 50$ or 9. (In the case of Ce^{3+} , the nitrate salt was used instead.)

Selected materials were analyzed commercially¹⁹ for rare earth ion content, and the H_2O content was checked by thermogravimetric analysis. The latter established a H_2O content of 240 molecules/unit cell in the original hydrated Na-Y zeolite material prior to exchange. Representative data on the rare earth ion concentrations and unit cell occupancies are tabulated in Table I, but, as is made clear in section V, essential results discussed were insensitive to dilution in the concentration ranges investigated.

Na/Gd mordenite was prepared by partial exchange of Na zeolon (large-pore synthetic mordenite) in the manner described above. The zeolon starting material, and a sample partially exchanged with Eu^{3+} , were obtained from

TABLE I: Data on Analysis of Representative Samples of Rare Earth Ion-Exchanged Y Zeolite

RE ions present	[RE ion] concn, wt %		Mean occupancies of RE ions per unit cell ^a	
			x	y
La	9.60		12	
La;Gd	9.92	0.15	12.3	0.17
La;Gd	6.50	0.70	7.9	0.8
La;Eu	5.61	0.12	7.2	0.14
La;Eu	3.30	0.34	4	0.37
Gd		2.75		3
Dy		7.66		8
Yb		5.68		6

^a x and y are defined by the general unit cell formula $\text{Na}_{56-3(x+y)} \text{La}_x \text{M}_y \text{Al}_{56} \text{Si}_{136} \text{O}_{384} \cdot 240\text{H}_2\text{O}$.

Professor W. Delgass. Unfortunately, the zeolon contained a sizeable impurity of Fe^{3+} which showed prominently in EPR spectra if other paramagnetic ions were present only in very low concentration, unless the material was reduced (with hydrogen) in the pretreatment.

III(2). *Sample Treatments.* Some spectra were recorded using samples that had not been pretreated, having simply been put in a closed tube with atmospheric ambient. Generally, though, the exchanged Y-zeolite samples were sealed in quartz tubes after degassing for 1 h at room temperature at 10^{-3} Torr pressure; such treatment yields samples that are yet substantially hydrated. Dehydrated samples were sealed in vacuo after calcining at 825 K for 15–20 h. Because it is always necessary to confine the material to the sample tube during pretreatment with a glass wool plug, slight paramagnetic contamination occurred in a few instances when the plug was slightly charred. Q-band samples of Gd- and Eu-containing Y-zeolite samples were always pretreated in tandem with X-band samples by using a special dual tube arrangement; this guaranteed identity in sample pretreatments.

Special reduction and reoxidation experiments were performed on Eu-containing samples, including Y zeolite, mordenite, and Eu_2O_3 (Alfa inorganics; purity 99.99% on rare earth oxide base). Samples, in quartz EPR tubes fitted with high vacuum stopcocks, were first evacuated and calcined in vacuo at 825 K as previously described; they were then heated in 600 Torr of H_2 for a period of 18 h and sealed off as H_2 -reduced material. Samples in the reduced state were stored under the H_2 gas ambient. Samples retaining the stopcock closure were later reoxidized after EPR examination. After pumping off the H_2 , O_2 gas was introduced at pressures of 600 Torr and the sample heated to the desired temperature and maintained there for 12 h; after cooling the sample to room temperature, the O_2 was pumped off and the evacuated sample examined by EPR. This oxidation procedure could be subsequently repeated at progressively higher temperatures, with EPR examination after each stage. To confirm the cyclic capacity of the reduction-oxidation sequences, fully oxidized samples were reduced again with H_2 at 725 K, examined by EPR, then reoxidized a second time and reexamined. The H_2 gas (Liquid Carbonic, 99.99% purity) used in these experiments was further purified by passage through a Deoxo catalytic purifier and molecular sieve-containing cold trap. O_2 gas (Liquid Carbonic 99.6% purity) was purified by vacuum distillation from a liquid nitrogen-cooled trap.

Degassed or untreated samples of europium containing zeolite were γ irradiated at 77 K by exposure to 4.3 Mrads of ^{60}Co radiation. Before spectroscopic examination, the sealed sample tubes were carefully flame annealed to

remove paramagnetic defects; the sample was maintained at 77 K throughout this operation.

III(3). *Spectroscopic Measurements.* EPR spectra were obtained using commercial Varian spectrometers: the E-12 at X-band (9.3 GHz) with either a rectangular TE₁₀₂ mode cavity or a TE₁₀₄ mode dual cavity, and the V4561 at Q-band (34 GHz) with a cylindrical TE₀₁₁ mode cavity. All spectra were recorded with 100-kHz modulation. Temperatures from 77 K to room temperature (295 K) were accessible with conventional insert dewar and variable temperature (E257) accessories; measurements at 4.2 K were obtained using a special liquid helium insert dewar having a narrow tail that fits into the X-band microwave cavity.

Effective g values were measured by comparison with standard pitch ($g = 2.0028$) or DPPH ($g = 2.0037$) signals. The use of the dual cavity in X-band experiments enhanced the accuracy of these measurements. In addition, nonlinearity of the magnetic field sweep was corrected for by making absolute field measurements with a Nuclear Magnets Corp. precision gaussmeter with ancillary power amplifier (Boonton Radio Co., Type 230 A) and frequency counter (Hewlett-Packard, 5245 L).

Microwave power saturation studies were routinely performed. For the S-state ion X-band spectra, these studies were exhaustive at both 295 and 77 K, with the applied power in the range 0.01–200 mW. The low power extremes of this range were facilitated by a low power bridge accessory. Difficulties were encountered in the very high power range for hydrated zeolites, the high H₂O content causing substantial microwave loss at room temperature.

Zero-field paramagnetic resonance experiments were attempted on Y-zeolite samples containing Eu²⁺ and Gd³⁺. The spectrometer was the broad-band frequency sweeping instrument described by Bernstein and Dobbs.²⁰ Both resonant cavity and helix modes of operation were tried, so as to cover the frequency range 1–8 GHz. No signals were seen; this might have been due to instrument insensitivity. However, an intrinsic problem lies in the EPR signal line widths; the square wave modulated (100 G maximum excursion) difference method of detecting the resonance puts a modest upper limit on the line width of signals that can be readily observed.

Aqueous solution spectra at 295 K were obtained with the use of a special flat cell designed for that purpose.

IV. Results

IV(1). *S-State Ions at X Band.* In Table II are collated the data on the principal features of the X-band spectra of Gd³⁺ and Eu²⁺ in Y zeolite, and it is immediately striking that many lines appear that have effective g values which are much greater than 2.00, so that the situation being dealt with is quite unlike that typical for the more common ionic hosts. It is also at once apparent that the spectra are significantly affected by the state of the zeolite and, further, that there are important dissimilarities in the spectra of these isoelectronic and otherwise very similar ions. We consider these results in more detail.

(A) *Gd³⁺ in Hydrated Zeolites.* Figure 1 shows the appearance of the spectrum of Gd³⁺ in a sample of hydrated Na/Gd-Y zeolite. At room temperature (nominally 298 K), virtually all of the resonance intensity is in a broad ($\Delta H_{pp} = 350$ G), fairly symmetric line at $g = 1.99$; other lines are visible at low field (i.e., high g_{eff}), but are very minor features of the spectrum as is evident from Figure 1a. There is a drastic change in the form of the spectrum when the sample is cooled to 77 K (Figure 1b); much intensity is in a line at $g = 1.98$, but now its symmetry is

TABLE II: Principal Features of X-Band Spectra of S-State Rare Earth Ions in Y Zeolite

(i) Gd ³⁺					
Hydrated				Calcined	
298 K		77 K		77 K	
g value	ΔH_{pp} , G	g value	ΔH_{pp} , G	g value	ΔH_{pp} , G
1.99	350	1.98	245	1.95	380
		2.4			
		2.79		2.78	
				3.5	
5.90	150	5.90	140	5.84	110
13.0		13.5		14.3	
				~50	

(ii) Eu ²⁺ at 77 K			
Hydrated (γ irradiation)		Calcined/H ₂ reduced	
g value	ΔH_{pp} , G	g value	ΔH_{pp} , G
~2.0	(obscured)	1.9	
		2.26	
2.83		2.86	
		4.89	250–300
5.95	155	6.00	>150
~15			

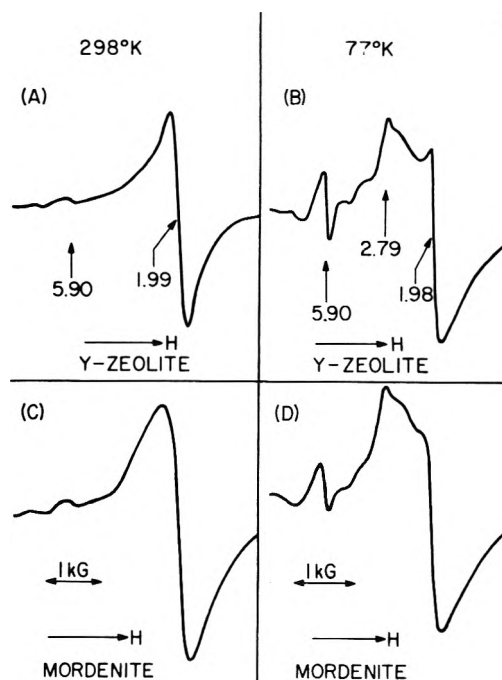


Figure 1. EPR spectra of Gd³⁺ ions in hydrated Na/Gd-Y zeolite and Na/Gd mordenite: (a) the Y zeolite at 298 K; (b) the Y zeolite at 77 K; (c) the mordenite at 298 K; (d) the mordenite at 77 K.

considerably distorted by new signals appearing on its low-field side, and the relative intensities of low field lines have become markedly enhanced. In particular, two additional lines which are very prominent in this spectrum are identified by g values of 5.90 and 2.79, the latter being part of the asymmetric complex signal in the region of the low-field lobe of the principal line.

Figures 1c and 1d illustrate that the behavior just described for the Y zeolite is quite faithfully duplicated by the Gd³⁺ ion spectra for a hydrated sample of Na/Gd-mordenite. The line width of the 298 K signal is substantially larger in this sample ($\Delta H_{pp} = 600$ G), and the

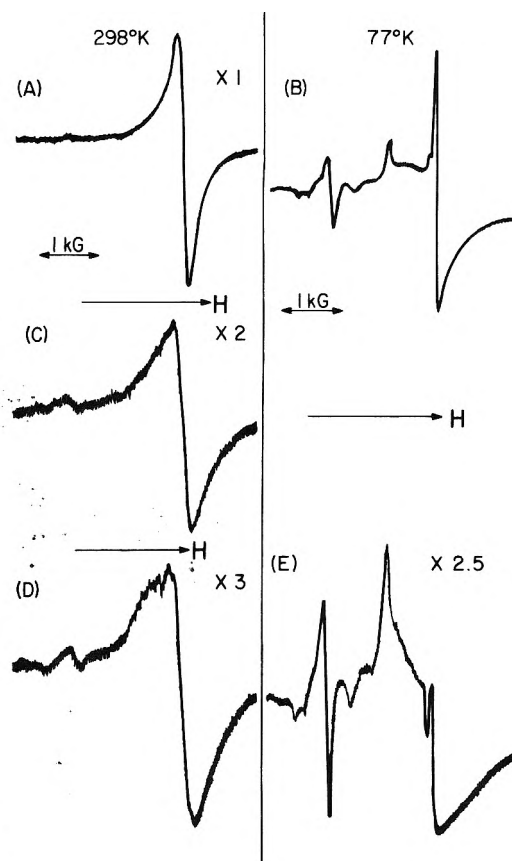


Figure 2. Effect of room temperature evacuation on the spectrum of Gd^{3+} ions in Na/La/Gd-Y zeolite (La:Gd \sim 50:1): (a) untreated hydrated sample at 298 K, and (b) at 77 K; (c) 298 K spectrum after 5-min evacuation; (d) sample evacuated for 60 min observed at 298 K, and (e) at 77 K.

features at 77 K are less sharply resolved, both probably attributable to a higher Gd^{3+} concentration in the mordenite.

The spectrum of the Gd^{3+} ions in the Y zeolite remains essentially unchanged in form upon extensive magnetic dilution by coexchange with La^{3+} ions, demonstrating that no important features of the spectra are caused by pairs or higher aggregates of Gd^{3+} ions. The sensitivity of the spectral form detail to even the mildest dehydration treatment is best demonstrated by a sample of "hydrated" Na/La/Gd-Y zeolite with a 50:1 La:Gd ratio. Figure 2 shows spectra of this material as a function of the duration of room temperature degassing pretreatment. The spectrum of the untreated material (Figure 2a) at 298 K shows only the symmetric line at $g = 1.99$, here with the sharpest of the room temperature line widths observed; the data in Table III(ii) indicate how this line width varies in concert with the Gd^{3+} concentration. At 77 K the $g = 1.99$ line is very sharp ($\Delta H_{pp} = 40$ G), retaining its first derivative shape although the low-field lobe has a much smaller second moment than the high field lobe; the g values of the other main features of the 77 K spectrum are shifted slightly from those listed in Table II(i), occurring at $g = 2.83$ and 5.84 compared to 2.79 and 5.90 , respectively. The facile broadening of the $g = 1.99$ line with evacuation is apparent from Figure 2c where the sample had been pumped for only 5 min. After 60 min pumping, the low field ($g = 5.84$) line has become readily visible and the $g = 1.99$ line has broadened further; at 77 K, the $g = 5.84$ and 2.83 lines have become very prominent, and the low-field lobe of the $g = 1.99$ line is no longer visible. (There is a small sharp line at a g value of ~ 2.1 which is due to a small impurity of Cu^{2+} and is not in fact a part

TABLE III: Line Width Variations of $g \sim 2$ Line for Gd^{3+} in Y Zeolite and in Aqueous Solution

(i) $Gd(NO_3)_3$ solution					
Gd^{3+} conc, %	ΔH_{pp} , G				
	298 K	77 K			
1	350	1080			
0.1	450				
0.01	520				
(ii) (Untreated) Hydrated Y Zeolite					
Sample	[Gd^{3+}], wt %	La : Gd ratio	ΔH_{pp} , G		
			298 K	77 K	
Na/Gd-Y	2.75	0	350	245	
Na/La/Gd-Y	0.70	9:1	300		
Na/La/Gd-Y	0.15	50:1	265	40	
(iii) Effect of Partial Dehydration by Room Temperature Evacuation on Na/La/Gd-Y Zeolite (50 : 1)					
Duration of degassing treatment, min	ΔH_{pp} , G				
	298 K	77 K			
0	265	50			
5	400				
60	530		Undefined		
(iv) Calcined Y Zeolite at 77 K					
Sample	La : Gd ratio	ΔH_{pp} , G			
Na/Gd-Y	0	380			
Na/La/Gd-Y	50 : 1	Undefined			

of the Gd^{3+} spectrum.) There are summarized in Table III(iii) the line width variation data illustrated in Figure 2.

(B) Gd^{3+} in Aqueous Solution. In order to compare the behavior in the hydrated zeolite with that of Gd^{3+} in aqueous solution, spectra were obtained for $Gd(NO_3)_3$ solution at various concentrations. The spectrum in each case, at 298 K, consisted of a broad, symmetric line with a g value at 1.995. The line width increased with dilution; the data on this are listed in Table III(i). A 1% solution gave a line width equal to that of the Na/Gd-Y zeolite sample at 298 K ($\Delta H_{pp} = 350$ G); freezing the solution to 77 K produced no new spectral features; instead the signal remained symmetric but broadened considerably (by a factor of ~ 3).

(C) Gd^{3+} in Calcined Zeolites. Calcining of the Na/Gd-Y zeolite at 825 K resulted in the spectrum shown in Figure 3a; this will subsequently be identified as the U spectrum. Compared with the low temperature spectrum of the hydrated sample (Figure 1b), much similarity is apparent, except that the low field lines at $g = 5.84$ and 2.78 have become very prominent; the latter is no longer flanked by the unresolved components at $g = 2.4$, and the former is shifted slightly so that its g value coincides with that found in the degassed Na/La/Gd-Y zeolite of Figures 2b and 2e. In addition, there is a small but unmistakable new feature at very low field ($g \sim 50$), and the prominent line now appearing at $g = 1.95$ shows a better defined low-field lobe than in any other sample observed at 77 K. Despite disparities in line shape detail, Figure 2e is materially the same as Figure 3a, and is thus also the U spectrum. For comparison, Figure 3b shows the spectrum of calcined Na/Gd mordenite; unlike the situation with the hydrated samples, marked differences are apparent between the spectra of the calcined samples. In particular, the sharpest prominent feature in the case of the mordenite occurs at a g value of 4.93 ($\Delta H_{pp} = 190$ G), and has

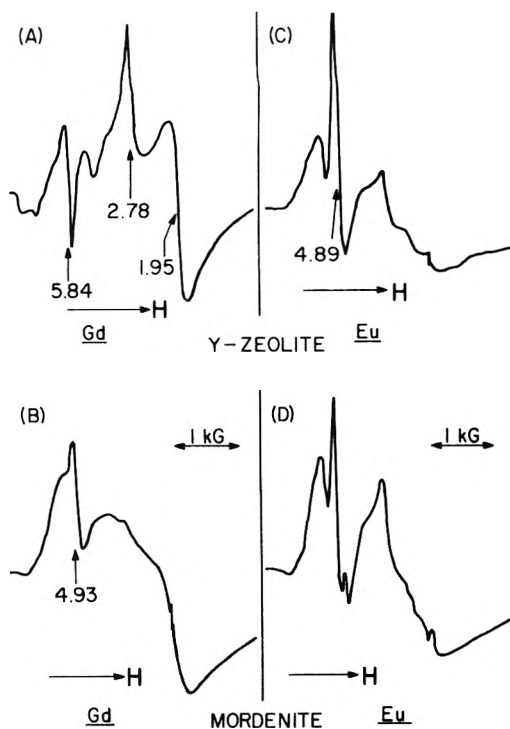


Figure 3. Comparison of the EPR spectra of Gd^{3+} and Eu^{2+} in calcined zeolites: (a) Na/Gd-Y zeolite; (b) Na/Gd mordenite; (c) Na/Eu-Y zeolite; (d) Na/Eu mordenite.

no counterpart in the Y-zeolite material. Only very weak evidence of the prominent $g = 5.84$ and 2.78 lines occurs in the mordenite, the former as a low-field shoulder to the $g = 4.93$ line, the latter as a small bump in a very broad, featureless but strong absorption that extends through and beyond the $g = 2$ region. (There is a very small, sharp line superimposed on the broad line in the $g = 2$ region; this is attributed to an impurity.)

The spectrum of Figure 3a is temperature invariant over the range 77–295 K. At 4.2 K, there is a marked diminution in the relative amplitude of the $g = 1.95$ signal, but the form of the spectrum is otherwise unchanged. This contrasts with the demonstrated temperature dependence of the U spectrum in the degassed material (Figures 2e and 2d).

(D) Eu^{2+} in Calcined Zeolites. The spectrum of Eu^{2+} is obtained when the Eu^{3+} exchanged zeolite is calcined in vacuo, or reduced at high temperature in the presence of H_2 gas. The essential data appropriate to the resulting spectra are tabulated in Table II(ii). In Figure 3c is shown a typical spectrum obtained by calcining a sample of Na/Eu-Y zeolite at 825 K. Juxtaposed to the spectrum of the calcined Na/Gd-Y zeolite shown in Figure 3a the marked difference is immediately obvious. The most prominent line in the Eu^{2+} spectrum is a fairly narrow line ($\Delta H_{pp} \sim 250$ – 300 G) with $g = 4.89$, which has no parallel in the Gd^{3+} spectrum in the Y zeolite, but rather corresponds closely to the $g = 4.93$ line for Gd^{3+} in the calcined mordenite. In one Y-zeolite sample, this signal appeared at a slightly shifted field position ($g = 4.55$), but the higher g value was otherwise general. The prominent features of the Gd-Y zeolite spectrum do indeed appear in the Eu-Y zeolite spectrum as secondary features: a line with $g = 6.00$ is partially resolved on the low-field side of the principal line, and the peak at $g = 2.86$ is evident, although not as dramatically outstanding. The other very important difference lies in the low absorption intensity in the $g = 2$ region for the Eu^{2+} spectrum. Also, there is no resonance at extremely low fields (in the $g \sim 50$ region).

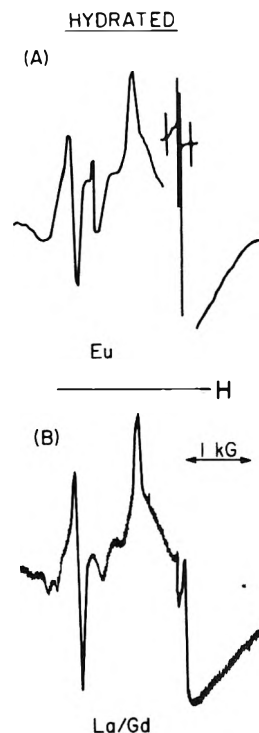


Figure 4. Comparison of the EPR spectra of Gd^{3+} and Eu^{2+} in hydrated Y zeolite: (a) γ -irradiated hydrated Na/Eu-Y at 77 K; (b) hydrated Na/La/Gd (50:1) Y at 77 K.

Figure 3d shows a spectrum of a calcined sample of Na/Eu mordenite. It is seen that the main features of Figure 3c are reproduced in form, if not in detail. (The small, sharp feature on the high-field side of the $g = 4.89$ line is due to an incompletely reduced impurity of Fe^{3+}). The contrast must be drawn between the similarity of the Eu^{2+} spectra in calcined Y zeolite and mordenite, and the disparity of the Gd^{3+} spectra in the same materials.

Magnetic dilution of the europium by coexchange with La^{3+} did not affect the spectrum shown in Figure 3c, indicating, as in the case of Gd^{3+} , that none of the features are caused by pairs or larger clusters of Eu^{2+} ions. It is noted that, unless reduction is complete, Eu^{3+} itself acts as a diamagnetic diluent of Eu^{2+} (although special problems might arise if there were rapid electron exchange in Eu^{2+} - Eu^{3+} pairs). The spectrum is also temperature invariant between 77 and 295 K, and at 4.2 K, only minor changes in the relative intensities of the components appear.

(E) Eu^{2+} in Hydrated Zeolites. The spectrum of Eu^{2+} in a (partially) hydrated Y zeolite was obtained from a Na/Eu-Y zeolite sample γ irradiated at 77 K. The spectrum shown in Figure 4a is that from a sample that had been pretreated by pumping at room temperature for 90 min; for comparison, there is juxtaposed in Figure 4b a reproduction of Figure 2e showing the spectrum of Na/La/Gd-Y zeolite (50:1 La:Gd ratio) that had been prepumped at 298 K for 60 min. The similarities in the prominent features at $g = 2.83$ and $g \sim 5.9$ are obvious. (The very sharp signal at $g = 4.34$ of the Eu sample is due to an impurity of Fe^{3+} ; this spectrum was obtained from an earlier, less pure batch of Y zeolite.) There is clear evidence in the Eu^{2+} spectrum of an ion-related signal in the $g \sim 2$ region, analogous to that in the Gd^{3+} spectrum; however, this feature is partially obscured by sharp, strong signals due to radiation-induced defects in the zeolite (trapped H \cdot atoms, and hole and electron centers). Table II(ii) contains the data on the Eu^{2+} ion in the hydrated host as well. The contrast with the calcined material is ap-

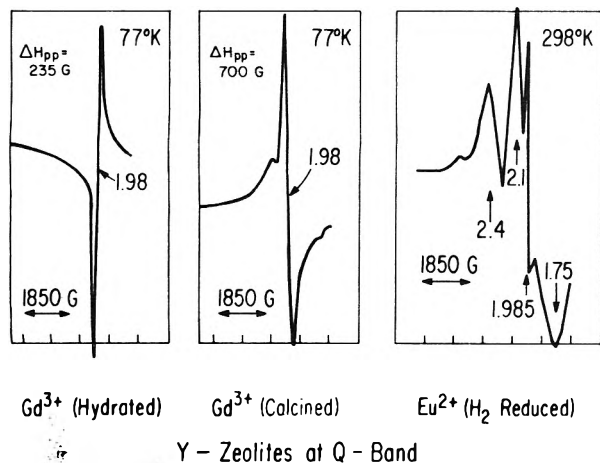


Figure 5. Q-band EPR spectra of Gd^{3+} and Eu^{2+} in Y zeolite: (a) hydrated Na/Gd-Y at 77 K; (b) calcined Na/Gd-Y at 77 K; (c) H_2 reduced Na/Eu-Y at 298 K.

parent from the comparison of Figures 4a and 3c.

(F) *Microwave Power Saturation Behavior in Zeolites.* The detailed examination of the microwave saturation behavior of these S-state ion spectra failed to reveal any additional information. Differential saturation of the various signals was observed at the highest H_1 fields in the cases of multicomponent spectra. For example, in the case of Gd^{3+} in calcined Y zeolite, the low field signals saturated less readily than the $g = 2.0$ signal. This established, with a high degree of confidence, that the main components in the spectrum are not simply the components of the same anisotropic (orthorhombic) transition; beyond that, its implications are not unequivocal.

(G) *Eu^{2+} in Eu_2O_3 .* The spectra of Eu^{2+} so far reported are very unusual indeed; not only do signals appear at very high effective g values, but there is also the complete absence of any hyperfine structure typical of the two magnetic isotopes $^{151}Eu(I = 5/2)$ and $^{153}Eu(I = 5/2)$. In an attempt to observe the spectrum of Eu^{2+} in a more conventional ionic host solid that might yet provide an unusual crystal field environment, a study was made of a sample of Eu_2O_3 that had been calcined in a reducing atmosphere of H_2 gas. A weak ESR signal consisting of a single line with $g = 4.89$ ($\Delta H_{pp} = 180$ G), having a low-field shoulder in the $g \sim 6$ region, was obtained. A second weak, very sharp signal, with $g = 2.0028$ and $\Delta H_{pp} = 6$ G, was also obtained. Both signals were readily established as being due to reduction products that could be reoxidized; reheating the reduced sample in an O_2 atmosphere at 525 K was sufficient to destroy both signals, although both signals partially survived oxygen treatment at 375 K.

IV.(2) *S-State Ions at Q Band.* (A) *Gd^{3+} in Y Zeolite.* The spectra of the Gd^{3+} and Eu^{2+} in Y zeolite proved to be strongly microwave frequency dependent in the 9–35-GHz range. In Figure 5 are retraced the principal features of the spectra recorded at Q band (34 GHz); for both Gd^{3+} and Eu^{2+} , the signal intensity is concentrated entirely in the region close to $g = 2$, in dramatic contrast to the corresponding X-band spectra. It must be noted that in each case, very weak signals (not shown) were observed at low field (high g value), but these were in all cases of negligible consequence, being more than two orders of magnitude (~ 160 times) lower in intensity than the principal absorption. In Figure 5a, the 77 K spectrum of Gd^{3+} in hydrated Y zeolite is shown; that is to be compared with Figure 1b which showed the X-band spectrum of the same material. The single $g = 1.98$ line ($\Delta H_{pp} = 235$ G) is sharper than the comparable line at X band, strongly

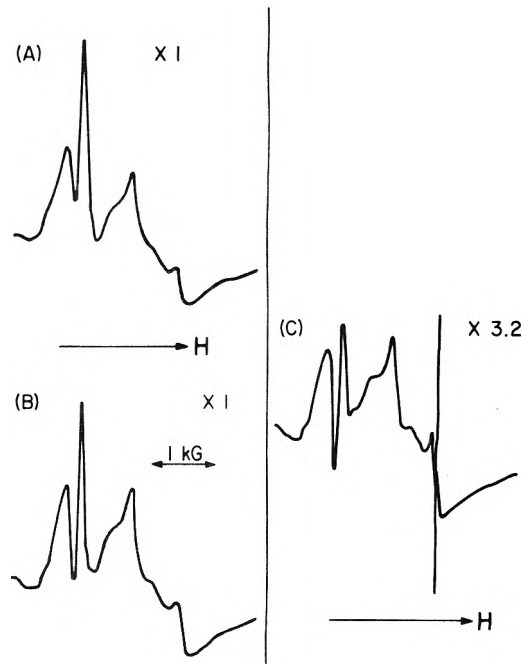


Figure 6. Effect of progressive reoxidation on the spectrum of Eu^{2+} in Y zeolite: (a) sample after H_2 reduction at 725 K; (b) sample after prolonged exposure to several Torr pressure of air at 298 K; (c) sample after heating to 373 K with 100 Torr of O_2 .

manifesting the tendency of the spectrum to collapse around the free-ion g value at high microwave frequency. The marked temperature dependence of the spectrum of the hydrated material at X band is also lost at Q band, the 298 K spectrum being essentially unchanged from the 77 K spectrum illustrated (the line width is identical, although there is a small shift in the measured g value to 1.99).

Calcining the Na/Gd-Y zeolite material results in the spectrum shown in Figure 5b, which is to be compared with the corresponding X-band spectrum shown in Figure 3a. The line width is seen to be considerably broader in the calcined material ($\Delta H_{pp} = 700$ G) than in the hydrated analogue at Q band; in addition, there are weak flanking shoulders on both the low and high field sides of the main ($g = 1.98$) line. It should also be noted that for both hydrated and calcined samples, as can be seen from Figures 5a and 5b, the second moments of the derivative signals are larger on the high field side than on the low field side.

(B) *Eu^{2+} in Y Zeolite.* In Figure 5c is shown the spectrum due to Eu^{2+} formed by high temperature reduction; the corresponding X-band spectrum is the one shown in Figure 3c. Although the spectrum has begun to collapse toward the free-ion g value, it remains more complicated than the Gd^{3+} ion spectra in Q band; four major components can be distinguished, with effective g values of 2.4, 2.1, 1.985, and 1.75. In the X-band spectrum of this material, there are no dominant sharp features with $g < 2.5$, although there is broad absorption intensity throughout the region.

IV.(3) *Redox Behavior of Europium.* It was readily established, through a series of reduction and reoxidation experiments, that the europium ions in the Y zeolite could be cycled between the divalent and trivalent states. The reoxidation experiments were also very informative in another regard, since they reveal some essential differential behavior in the ions responsible for different features in the spectrum. Figure 6 shows the result of progressive reoxidation of a Na/Eu-Y zeolite that had been reduced with H_2 at 725 K. In Figure 6a, the spectrum of the sample following the initial reduction is presented. The sample

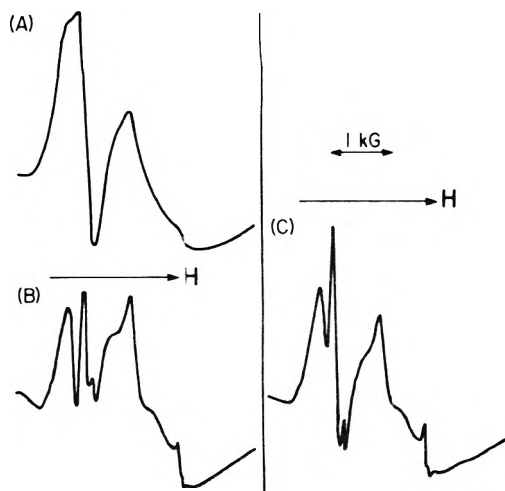


Figure 7. Effect of air on the spectrum of Eu^{2+} in mordenite: (a) sample after H_2 reduction at 725 K; (b) sample, containing several Torr pressure of air, after prolonged exposure to this pressure at 298 K; (c) sample as in (b) after pumping the air off at 298 K.

was stored at room temperature in a tube equipped with a high-vacuum stopcock which leaked a moderate amount of air over a 2-month period; the spectrum at that stage was as presented in Figure 6b. The transformation is modest, but significant; the relative signal intensity of the dominant $g = 4.89$ line is diminished, with the concomitant relative enhancement of the lines at $g = 6.00$ and 2.86 . This behavior is paralleled by the Eu^{2+} in mordenite and, as Figure 7 illustrates, the effect is ever more dramatic. Because the Eu^{3+} concentration was fairly high in the mordenite material, the spectrum of the extensively reduced sample, shown in Figure 7a, has its detail obscured through spin-spin interaction line broadening; after 2 months, the spectral resolution has dramatically improved, with the $g = 4.89$ line suppressed more completely than the $g = 6.00$ and 2.86 lines. In the mordenite material, unlike the case of the Y zeolite, the presence of gaseous O_2 in the sample tube had a very marked effect on the appearance of the spectrum, for when the air was pumped off at room temperature, the intensity of the $g = 4.89$ line shows a pronounced relative enhancement (Figure 7c). The suppression of signal intensity by gaseous O_2 is clearly selective for the $g = 4.89$ line in the mordenite.

One sees reinforced further in Figure 6c that the Eu^{2+} ions responsible for the signal at $g = 4.89$ are chemically distinct from the others in that they are more readily susceptible to oxidation. The sample at this stage had been exposed to O_2 at 373 K; a substantial concentration of Eu^{2+} remains, but the $g = 4.89$ signal has clearly been more effectively eliminated. The signals at $g = 6.00$ and 2.89 appear to behave in concert throughout, maintaining the same relative intensities. Treatment with O_2 at 515 K was sufficient to eliminate completely the $g = 4.89$ signal, but there were weak residual signals at $g = 6.00$ and 2.86 after 12 h of such treatment. No trace of the Eu^{2+} spectrum remained after treatment with O_2 at 725 K.

In Figure 6c there appears a very sharp feature of large signal amplitude in the $g = 2$ region. The signal is asymmetric with $g = 2.0029$ and line width $\Delta H_{pp} = 6.5$ G. While it is not definitively identified, this signal is ascribed to an oxo species that is formed at moderate temperatures (it is not formed at room temperature), but is unstable at high temperatures; O_2 treatment at 515 K causes the signal intensity to decrease, and following O_2 treatment at 725 K, the signal is completely absent.

IV.(4) *Non-S-State Ions.* We are not aware of any previous publications on the EPR spectra of non-S-state

TABLE IV: Parameters of Dominant Features of Non-S-State Rare Earth Ion Spectra at X Band in Y Zeolite^a

Ion	Hydrated		Calcined	
	g value	ΔH_{pp} , G	g value	ΔH_{pp} , G
Ce^{3+}	1.98	2500	1.64	1900
Nd^{3+}	2.73	1250		
Tb^{3+}	8.3 (22)	700		
Dy^{3+}	5.45	1270	7.80	960
Ho^{3+}	17.5	350		
Er^{3+}	6.55	1240	7.12	760
Tm^{3+}	9.2 (17.7)	≥ 600		
Yb^{3+}	3.45	2550	{ 4.77 2.98 }	{ ≥ 220 ≥ 640 }

^a No resonances were observed for samples containing Sm^{3+} and Pr^{3+} , and the radioactive ion Pm^{3+} was not studied.

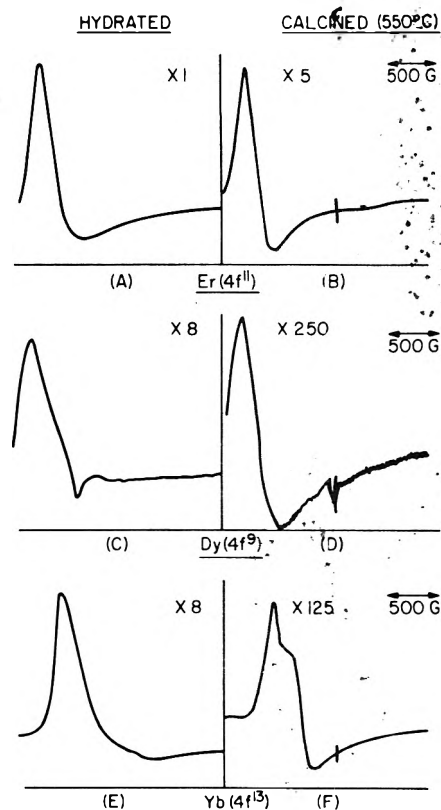


Figure 8. EPR spectra of Kramer ions in Y zeolite— Er^{3+} , Dy^{3+} , and Yb^{3+} : (a) Er^{3+} in hydrated sample; (b) Er^{3+} in calcined (825 K) sample; (c) Dy^{3+} in hydrated sample; (d) Dy^{3+} in calcined (825 K) sample; (e) Yb^{3+} in hydrated sample; (f) Yb^{3+} in calcined (825 K) sample.

RE ions in glasses or disordered solids; for this reason some results obtained from measurements on partially exchanged Y zeolites at 4.2 K are included here. Data on degassed and calcined samples for each ion are compiled in Table IV and some representative spectra are shown in Figures 8 and 9. The line widths are extremely large; in general, ranging from 650 to 2550 G for the Kramer ions, viz. Ce^{3+} , Nd^{3+} , Dy^{3+} , Er^{3+} , and Yb^{3+} . Calcining caused changes, typically, in the widths, shapes, and positions of the signals, as illustrated in Figure 8 for some Kramer ions; in the case of Nd^{3+} , no signal was observed in the calcined material. This disappearance of the signal upon calcining occurred in all cases for the non-Kramer ions, Tb^{3+} , Ho^{3+} , and Tm^{3+} , which were also distinguished by the very unusual signal line shapes in the hydrated materials, as illustrated in Figure 9. In the case of Ho^{3+} , the signal was unusually weak even in the hydrated material.

The extremely broad aspects of these signals, devoid of

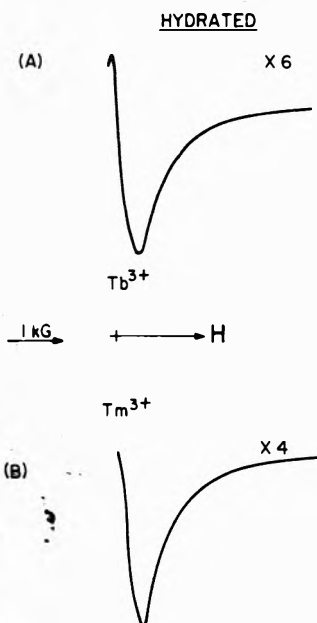


Figure 9. EPR spectra of non-Kramers ions in Y zeolite: (a) Tb^{3+} in hydrated sample; (b) Tm^{3+} in hydrated sample.

sharp features, prohibit meaningful analyses of these spectra; they will not be discussed further. A possible qualitative rationale for the line shapes in the case of non-Kramers ions has been advanced by Iton.²¹

V. Discussion

The discussion is structured around the X-band spectrum of Gd^{3+} in calcined Y zeolite—the U spectrum. Similar spectra have been observed in a variety of glasses doped with Gd^{3+} , e.g., methanol glass,²² borate glasses,^{22,23} phosphate ($ZnO \cdot P_2O_5$) glasses,^{23,24} a chalcogenide ($Tl_2 \cdot SeAs_2Se_3$) glass,²⁵ silicate glasses;^{11,23} the same spectrum was also found for Eu^{2+} in a $ZnO \cdot P_2O_5$ glass.²⁴ We regard this ubiquitousness as an integral feature which must be explained in any interpretation of these results, and accordingly present a detailed qualitative argument to the effect that the form of the U spectrum is actually a consequence of the randomness characteristic of glasses, and should not be approached from the viewpoint of a few, specific, well-defined site symmetries, even when the matrix is a crystalline zeolite.

With this realization, temperature-, valence-, material state-, and host-dependent variations in the spectra are considered, yielding plausible conclusions regarding cation site locations and atomic environs of the S-state ions in the zeolites. In the course of this, some more generalized inferences will be made regarding RE ion–ligand interactions in glasses and crystals. Much corroborative use is made of results from optical studies of non-S-state ions, particularly Eu^{3+} fluorescence, since the S-state ions have no f–f absorptions in the visible. Parallel reasoning of this nature has also been employed by Newman and Urban¹³ in deriving intrinsic parameter values in the superposition model. It is first necessary, however, to remark on previous interpretations of these spectra in zeolites and in glasses.

V.(1) *Previous Interpretation in Zeolite Systems.* The only other published work on the EPR of Gd^{3+} and Eu^{2+} in zeolites is that of Nicula;^{25,26} we contradict many of those results and interpretations. That work reported X-band spectra of hydrated and calcined Y-zeolite containing Gd^{3+} and Eu^{2+} , and also the X zeolite analogues containing Gd^{3+} . First, many of the reported g values are incorrect, particularly those for the important low field signals corresponding to g values > 2.5 (this is due to nonlinearity

in the magnetic field sweep; similar errors seem to have been made in some reports on glasses²³). Hence, calculated specific point symmetries are subject to these errors, and the assignments of axial, rhombic, hexagonal, and trigonal symmetry sites in the weak-field Zeeman effect limit to features of the U spectrum are undermined. Moreover, as will be elaborated upon, we consider the approach of assuming a distinct site symmetry for each spectral feature to be inappropriate, and our Q band results suggest that the zero field splittings may not be sufficiently large for the perturbation treatment in the strong CF limit to be valid at X band. (An even stronger argument for this assertion is given in the next section.) It might be added that at the level of our approximation, i.e., eq 5, axial, hexagonal, and trigonal point symmetries are indistinguishable, all being characterized by having $b_2^2 = 0$; however, the fluorescence spectra for Eu^{3+} in both Y zeolite and the glasses indicate that the point symmetries at the cation sites are orthorhombic or lower, so that these assignments are questionable on this basis as well. [See section V(3).]

Most dubious of Nicula's interpretations, we feel, is that of attributing signals to the Eu^{2+} ion in material in which, chemically, only Eu^{3+} could be expected. We claim to be able to show unequivocally that such assignments are incorrect, recognizing that the Eu^{3+} ion ($4f^6$) has a diamagnetic ground state (7F_0). In untreated hydrated zeolite exchanged with Eu^{3+} ions, no Eu^{2+} is expected to be present; the appearance of a very broad signal ($\Delta H_{pp} > 1100$ G, $g \sim 2.2$ – 2.6) at 77 and 295 K in such samples seems to require the presence of Fe^{3+} , identifiable by a sharp signal at $g = 4.3$. Both of these signals were misassigned as being due to Eu^{2+} . We find that they are eliminated by H_2 reduction at 725 K, but are regenerated under strenuous reoxidation conditions (O_2 at 725 K), so the chemical situation is incompatible with the Eu^{2+} assignment. The same behavior is exhibited by impure mordenite samples, but is absent in purer Y zeolite material. Analysis of a sample of the material used by Nicula established an iron content of 450 ppm. We suggest that the broad signal is due to a ferrimagnetic Fe_3O_4 impurity, an assignment chemically compatible with the observations; such signals have previously been identified in zeolites containing iron impurities.^{27,28} The temperature-dependent g value and markedly non-Curie behavior of the signal intensity suggest that it is a ferromagnetic resonance signal; a possibility such as Eu_3O_4 is discounted because it is an antiferromagnet with $T_N = 5$ K.²⁹ (EuO is chemically unsupportable and has $T_C = 69$ K; Eu_2O_3 did not give an EPR signal prior to treatment.)

V.(2) *Previous Interpretation in Glasses.* The X-band U spectrum is readily recognized, by the high g values of some of the lines, as corresponding to systems outside the common strong-field Zeeman effect limit. The frequency dependence between 9.2 and 34 GHz in Y zeolite is the same as that found by Nicklin for the silicate glass system,¹¹ so that the problem of interpretation is identical for that, and we assert, for other glasses as well.^{22–25} The acute frequency dependence of the spectra makes it clear that the zero-field splittings are comparable to the X-band microwave quanta in energy. Earlier attempts at interpreting the U spectrum have been manifestly inadequate, but the more recent analysis of Nicklin et al.³⁰ has been extremely thorough and is worthy of special attention.

That interpretation is based on the assumption of three distinct types of Gd^{3+} sites being responsible for the three main features of the spectrum. The component with $g \sim 2.0$ is attributed to ions in cubic or rhombic sites where

the crystal field splittings are small (strong-field Zeeman effect limit). The signal at $g = 5.9$ is assigned to ions in strong crystal fields of cubic symmetry, having the Γ_7 doublet as the zero-field ground doublet. (Such a doublet would, in theory, give rise to an isotropic transition with $g = 6.00$.) The signal at $g = 2.8$ – 2.9 is attributed to ions in sites having orthorhombic or lower symmetry, with $b_2^0 = 2.06$ GHz and $b_2^2 = 1.86$ GHz, in the Hamiltonian of eq 5. The calculated zero-field splittings of the doublets in such a crystal field are¹¹ 11.3, 7.6, and 10.2 GHz; our attempt to observe a 7.6-GHz zero-field transition was unsuccessful; the higher energy transitions are outside the operating range of our zero-field spectrometer.²⁰

The Nicklin et al. interpretation is perhaps the best possible in that framework, recognizing that for orthorhombic or lower symmetries important spectral features may arise for magnetic field directions away from any of the principal axes of the Hamiltonian (5). Our reservations about this interpretation stem from: (a) the need to use two markedly different sets of spin Hamiltonian parameters to account for the lines at $g = 5.84$ and 2.86 , which, experimentally, always occur together, and, in reoxidation of Eu^{2+} , also are annihilated in concert; (b) optical data which indicate that the site symmetries are much lower than cubic (See following section.); (c) the absence in all of the literature of large zero-field splittings for these S-state ions in cubic symmetry sites, i.e., large enough to allow a weak-field Zeeman effect limit treatment; indeed, the other extreme is usually the case. (There is a singular exception to this, the case of Tb^{4+} in ThO_2 ,⁸ where the degree of covalency is believed to be very high.); (d) the form of the spectrum at very low frequencies.

This last point has generally been overlooked in previous attempts to analyze the X-band U spectrum. Garifyanov et al.^{22,31} have found that for methanol and borate glasses between 0.1 and 0.6 GHz, the U spectrum collapsed to a single line having $g = 4.7$. Now, any signal assigned with the assumption of the weak-field Zeeman effect limit at X band must perforce show no field dependence at lower frequencies; the significance of the low frequency result is to cast doubt on any such assignments except for lines with $g \sim 4.7$. Actually, because the signal at 260 MHz is so broad²² (70 G; which would correspond at this frequency to a range in g values from 41 to 2.5, about the peak value of 4.7) such X-band assignments cannot be rigorously excluded; however, the absence of distinctive features at positions corresponding to prominent X-band features is suggestive. This result will be used later to justify the use of the weak-field Zeeman effect limit in interpreting the X-band $g = 4.9$ line in calcined Eu^{2+} -containing materials.

Nicklin et al.³⁰ do acknowledge the possibility that a single type of site with b_2^0 values distributed over a wide range could give rise to all the spectral features. This is essentially the viewpoint being promulgated here, and some evidence obtained from optical studies reported in the literature is now reviewed to buttress this argument.

V.(3) *Evidence from Optical Studies of Glasses.* The results from optical spectroscopy of RE ion-containing glasses point unequivocally to the existence of a wide distribution of low symmetry sites. It is argued on this basis that the interpretation of the EPR spectra of the S-state ions in zeolites must be approached in the same way since randomness is the common property of the glasses that is usually distinctive to these noncrystalline matrices, but which can be expected in Y zeolite, unlike usual polycrystalline powders. The low symmetry of the RE ion environment in glasses is confirmed by fluorescence spectra of Eu^{3+} . Complete lifting of the degeneracies of

the ${}^5\text{D}_0$ – ${}^7\text{F}_2$ (fivefold) transitions demonstrates that the local site symmetries are orthorhombic or lower.³² A similar result obtained for Eu^{3+} in hydrated Y zeolite in the Raman spectral studies of Beuchler and Turkevich³³ establishes the same conclusion for the zeolite hosts.

Several interpretations of the optical spectra have been suggested. Rice and DeShazer³⁴ concluded that the absorption spectra of Eu^{3+} in phosphate or borosilicate glasses could be explained by assuming three different basic types of C_s site symmetry, each ion being seven coordinate, analogous to the sites present in the sesquioxide (Eu_2O_3); however, inhomogeneous broadening indicated a range of distortions with respect to each basic site geometry. Reisfeld^{35,36} estimated from this inhomogeneous broadening in phosphate, silicate, and germanate glasses that ~ 50 – 70 slightly different sites of C_s symmetry contributed to each spectrum, proposing a model in which the small variations in the CF parameters were caused by the progressive distortions of a near-cubic array of eight ligands. Very recently, Brecher and Riseberg,³⁷ on the basis of a laser-induced fluorescence line narrowing spectral study of Eu^{3+} in silicate glass, have offered a model in which C_{2v} symmetry is preserved at each ion site, but the progressive incursion of a ninth ligand into the basic eightfold coordination shell generates a distribution of local site environments. Irrespective of detailed differences, the conclusion is universal that the ions are in CF's of orthorhombic (C_{2v}) or lower (C_s) symmetry with a wide distribution of distortions of the basic site geometry. It is claimed here that this notion of the random distribution in the crystal field parameters is intrinsically more important in these glasses and zeolite systems than a simple variety of site symmetries such as can also occur in certain ionic single crystals, e.g., ultraphosphates and mixed ultraphosphates of Gd^{3+} and Eu^{3+} : $\text{GdP}_5\text{O}_{14}$ and $\text{Gd}_x\text{Eu}_{1-x}\text{P}_5\text{O}_{14}$.³⁸ One notes that C_{2v} and C_s symmetries cannot be distinguished from the EPR spectra of powders or glasses, both being characterized simply by $b_2^2 \neq 0$.

The other important point to arise from the optical spectroscopy results is that whereas the Gd^{3+} EPR spectra are very insensitive to the nature of the host in a number of glasses, the optical spectra reveal distinct trends in the glass-RE ion interactions. Indeed, the concept of glass electronegativities has been established from the trend in covalent interaction strengths, determined experimentally from the magnitudes of the nephelauxetic effect parameter and the relative intensities of hypersensitive f-f transitions ($\Delta J = 2$). The resulting electronegative series of glasses is aquo ion \geq phosphate glass \geq borate glass \geq silicate glass \geq tungstate glass \geq germanate glass. This supports the approach we are advocating, since EPR spectra that are the resultants of broad distributions of CF parameters would conceal trends in ion-ligand interaction strength.

In fact, the importance of random distributions in spin Hamiltonian parameters has been established even for the case of a single crystal of a nonstoichiometric material. Peterson and Carnevale¹⁴ have shown that the angular dependence of the NMR line width in such a case is quantitatively explained by a statistical spread in the quadrupole coupling constant. Baumhoer et al.³⁹ have recently shown that in doped distorted single crystals, a Monte Carlo technique generating a distribution function for the field gradients due to a random distribution of defects satisfactorily explains the shape of NMR spin echo signals.

V.(4) *Approach to a Quantitative Interpretation.* With the operating premise of randomness as the dominant consideration for these spectra, the random vector model

of Peterson et al.^{15,16} should be the preferred method of analysis. The experimental results indicate that the $g = 4.9$ line, for Eu^{2+} in all calcined materials and for Gd^{3+} in calcined mordenite, behaves independently and may be treated separately. Assume that (i) the weak-field Zeeman effect limit is appropriate, and (ii) the average site symmetry is axial. Two important consequences follow: viz. (a) the actual magnitude of b_2^0 is numerically inconsequential; and (b) the four pairs of zero-field levels may be treated as being independent of each other, and the $m_J = \pm 1/2$ is the only pair that is relevant. It yields $g_{\parallel} = 2.0$, $g_{\perp} = 8.0$. The problem becomes formally analogous to that treated by Peterson et al.¹⁵ for Fe^{3+} , ground state ${}^6S_{5/2}$. Equation 9 reduces to

$$p_g(\alpha) = \iint \alpha p_{g_{\parallel}, g_{\perp}}(\beta, \gamma) \times [(\beta^2 - \gamma^2)(\alpha^2 - \gamma^2)]^{-1/2} d\beta d\gamma \quad (10)$$

A prominent peak appears when $p_{g_{\parallel}, g_{\perp}}(\beta, \gamma)$ overlaps the line $\beta = \gamma$; in the ${}^8S_{7/2}$ system, this occurs in the vicinity of $g = 5.0$ for $p_{g_{\parallel}, g_{\perp}}(\beta, \gamma)$ having large variances and a large negative covariance. There is an alternative interpretation of this signal (based on the strong CF limit calculations of Nicklin¹¹). For $b_2^2/b_2^0 = 0.30$, there is a near-isotropic transition having $g_x = 4.65$, $g_y = 4.56$, and $g_z = 5.19$; a distribution of spin Hamiltonian parameters with this average symmetry would also give rise to a line with $g = 4.9$. The form of the Q-band spectrum allows an estimate of limits on b_2^0 as $3 \text{ GHz} < |b_2^0| < 10 \text{ GHz}$.⁴⁰ A choice between the two interpretations is not automatically made; the former has the virtue that the randomness is introduced in a formal mathematical manner, while the latter seems more compatible with the essential low symmetry nature of these sites. One notes, however, that the mathematical assumption of an average axial symmetry does not conflict with the optical data in the way that an assignment of a physically exact axial point symmetry does.

Interpreting the U spectrum in the random vector model approach is a more complex problem because the simplifying assumption of the weak-field Zeeman effect limit cannot be made. The actual magnitude of the b_2^0 is thus numerically all-important and, furthermore, one has a complete multilevel problem involving all eight mixed m_J states and a wide range of transition probabilities. There should thus be a manifold of joint probability density functions, each of which is, in full, five-dimensional: $p_{g_x, g_y, g_z, \theta, \psi}$. Moreover, because of the breakdown of consequence (a), the starting jpdf's should have the b_2^0 as random variables. In the absence of analytic transformations to the g , as random variables, the forms of the $p_{g_x, g_y, g_z, \theta, \psi}$ are not transparent, and they cannot be simple and symmetric. A full treatment of the problem is beyond the scope of this paper; we hope to treat it in a future publication.

Lacking this, we are for the moment limited to making a crude estimate of the magnitude of $|b_2^0|$ from the relative intensity of the weak, low-field signals in the Q-band spectrum of Gd^{3+} in calcined Y zeolite. These are interpreted as forbidden ($\Delta m_J = 2$) transitions, and their intensities relative to the allowed transitions should be of order $\sim (b_2^0/h\nu)^2$. [This is strictly appropriate to an axially symmetric CF Hamiltonian having $b_2^2 = 0$, but is acceptable for this crude estimate.] The experimental intensity reduction factor of $\sim 1/160$ corresponds to a value of $|b_2^0| \sim 2.7 \text{ GHz}$. This is a plausible value, and is, we suggest, near the upper limit of the range of b_2^0 values in the distribution.

(It should be noted that even the failure of a random vector model calculation to analyze correctly the U

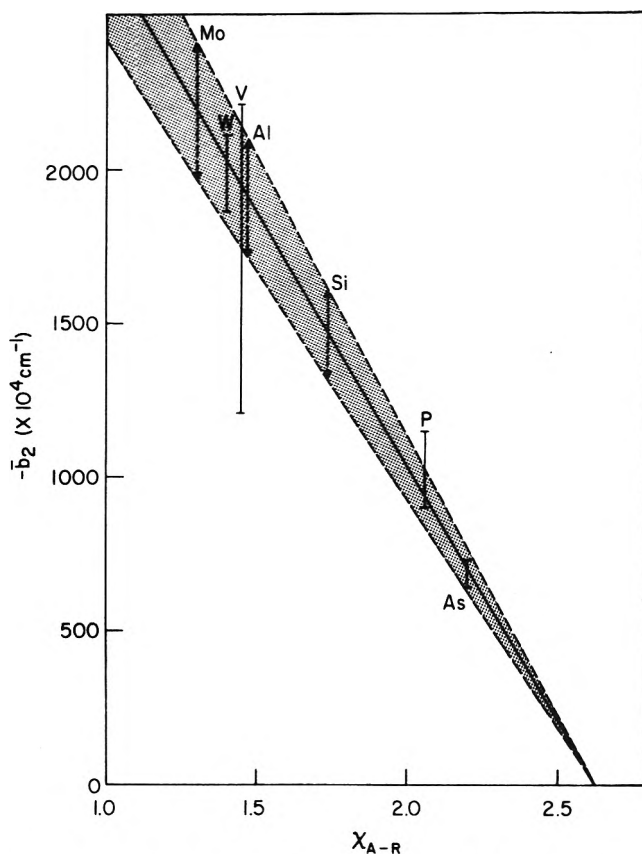


Figure 10. Empirical correlation between calculated $|\bar{b}_2|$ intrinsic splitting parameters for Gd^{3+} ions with MO_4 ligands, and the Allred-Rochow electronegativities of the element M; shown for $M = \text{As}, \text{P}, \text{V}$, and V . Predicted ranges of $|\bar{b}_2|$ are shown for $M = \text{Mo}, \text{Si}$, and Al .

spectrum detail should not mitigate the contention that a distribution of the spin Hamiltonian parameters is an essential premise here; such failure would be regarded as an inadequacy of the calculation rather than a misapprehension of the underlying physics. The detailed model interpretations which follow in section V(6) are not predicated on the ultimate success of the random vector model, per se.)

V.(5) *The Intrinsic Splitting Parameters.* Glass electronegativity is not a discriminatory parameter for the S-state ion EPR spectra. The most fundamental parameters are the intrinsic splitting parameters, \bar{b}_2 , in the Newman and Urban superposition model. These parameters cannot be determined in general without accurate knowledge of the surroundings of the ion in the matrix; for glasses, in particular, the existence of a random distribution of the site distortions makes it impossible to extract the \bar{b}_2 from the experimental EPR spectra. In order to estimate values for the \bar{b}_2 , we show that there exists an empirical correlation between the \bar{b}_2 for tetrahedral MO_4 oxy anions and the electronegativities of the atoms M.

In Figure 10 are plotted the available data¹³ on calculated \bar{b}_2 parameters for Gd^{3+} in various crystals having such anions vs. the Allred-Rochow electronegativities (χ_{A-R}) of the central atom M.⁴¹ The solid vertical bars indicate the range of the calculated \bar{b}_2 values for each anion. Two different types of crystal structure are represented in the data, viz. zircons and scheelites. It is found that a "best fit" straight line can be made to intersect all of the range bars, with most of the data points lying within the shaded area in a $\pm 10\%$ range of this line. (The values for VO_4 show an unusually large scatter, and fall on both sides of the shaded area.)

This correlation awaits the accumulation of more calculated \bar{b}_2 values for a stringent test of its validity. The experimental spin Hamiltonian parameters for several silicates and molybdates have already been tabulated;¹⁰ the predicted ranges of \bar{b}_2 for these systems are shown by broken vertical bars. It can be projected that the MoO_4 data will fall within or just below the predicted range. (This projection is made by inspection on the basis of the similarity of b_2^0 values for molybdates and tungstates; however, one cannot generally project \bar{b}_2 values from b_2^0 values. We do not use the b_2 data of Vishwamittar and Puri⁴² because their calculations for the tungstates do not agree with those of Newman and Urban¹³.) Thus, it seems that a reliable estimate of the $|\bar{b}_2|$ for SiO_4 group ligands is $\sim 1300\text{--}1600 \times 10^{-4} \text{ cm}^{-1}$ (4.3–5.3 GHz). This range of values should be appropriate to silicate glasses as well as single crystals, and also to the zeolites. The exchanged cations in the zeolites will have some of their ligand O atoms bonded directly to Al rather than Si, especially since the type I' sites are more likely to be occupied by the RE ion when the Al content of the nearby 6 ring is high;⁴³ applying the empirical correlation scheme to tetrahedral AlO_4 groups, the predicted estimate for $|\bar{b}_2|$ is the range $\sim 1700\text{--}2100 \times 10^{-4} \text{ cm}^{-1}$ (5.7–7.0 GHz).

V.(6) *Site Assignments and Model Environments.* (a) *Y Zeolite.* In their work on Cu^{2+} in Y zeolite, Turkevich and co-workers¹ had observed the effect of a "phase transition" on the EPR spectrum of the solvated cations in the hydrated zeolite as the sample was cooled from 295 to 77 K. The behavior was ascribed to the transition from a state of freely tumbling solvated ions in the supercage at room temperature to a state of immobilized ions on the cavity walls at low temperature. The same kind of transition is apparent in the Gd^{3+} spectra. Nicula et al.²⁵ have reasoned that the ions responsible for the low field (high g value) features of the spectrum of the hydrated material are not hydrated; this conclusion is correct, in that those ions are not *fully* hydrated; however, we think that it should be modified according to the following model.

Consider Figure 2. The low field features are due to *partially* dehydrated ions, which still contain some H_2O molecules in the coordination sphere, immobilized near to the supercage cavity walls in type II sites. (A few such ions exist even in samples that have not been vacuum treated because the material has been aspirated in preparation.) The dominant $g \sim 2.0$ feature is due to fully hydrated ions tumbling in the supercage with a mean location equivalent to a type V site (the location of hydrated Ce^{3+} in faujasite as determined by X-ray diffraction⁴⁴). Room temperature evacuation gradually removes free molecular H_2O from the supercages, leaving some H_2O in the sodalite cages.⁴⁵ Some ions enter the sodalite cage, where they occupy type I' sites, having one or more H_2O as extraframework ligands; these ions account for the increased prominence at 298 K of the low field features as seen in Figures 2c and 2d. Most of the ions remain in the supercage,⁴⁶ partially dehydrated; they still have H_2O ligands and are mobile at room temperature, tumbling or exchanging rapidly between type II sites (of which there are 4 per supercage). Virtually all of the ions in the supercage are now sufficiently denuded that on freezing they are localized near the walls and experience the stronger crystal field provided by direct interaction with the framework ligands; hence, the low temperature spectrum of Figure 2e resembles the U spectrum of the calcined material although the site distribution and local environments of ions are not identical in the two cases. The temperature dependence of this spectrum is different from that of the calcined material

because here, at low temperature, the relaxation of the ions is by spin-lattice mechanisms, but converts at room temperature to relaxation via the motion of the ligated complex ions, which produces a modulation of the zero-field splitting—the solution-type mechanism.^{47,48}

The broadening of the room temperature $g = 2.0$ signal with increasing dehydration is consistent with increasing CF anisotropy (increasing $|b_2^0|$) for the tumbling complexed ions. This is due to the growing deviation from cubic symmetry as H_2O molecules are removed from the coordination sphere; however, it should not be assumed that the fully hydrated mobile ion in the supercage has cubic or other high degree of symmetry. In aqueous solution, the microsymmetry around Eu^{3+} ions is D_{2h} , and in alcoholic solution it is C_{2v} , both orthorhombic system point groups;⁴⁹ the same is claimed here for the hydrated Gd^{3+} ions, i.e., a distorted cubic or distorted octahedral ligand array. Thus, one should modify the assertion, sometimes made,²³ that the increasing contribution of the low field lines in the spectrum is synonymous with the growth of the *number* of low symmetry centers having orthorhombic distortions; an additional requirement is that the contributing low symmetry centers now possess zero-field splittings comparable to the Zeeman energy.

Important distinctions do exist between the room temperature resonance behavior of the hydrated ions in aqueous solution and in the untreated zeolite. Table III(i) and (ii) indicate how the solution spectrum is exchange narrowed at higher concentrations, while the zeolite spectrum is dipole broadened; the latter observation implies that the intracavity tumbling of the hydrated Gd^{3+} ion is not completely isotropic so that the dipole-dipole interactions are not averaged to zero. Freezing causes the solution spectrum to be considerably broadened by unaveraged dipole-dipole interactions, this being exaggerated by the tendency toward solute segregation in frozen aqueous solutions (as has previously been noted for Gd^{3+} solutions by Ross⁵⁰). However, fluorescence spectroscopy has shown that the CF symmetry for hydrated Eu^{3+} is virtually unchanged between fluid and frozen solutions, and that the distribution of local symmetries is not broad; together with the weaker intrinsic interaction with H_2O ligands, these factors rationalize the absence of prominent low field features in the spectrum of the frozen solution.

Upon calcining, all the Gd^{3+} ions enter the sodalite cages and are localized predominantly in type I' sites (as determined, for example, by X-ray diffraction for La^{3+} in Y zeolite⁴³). There are no longer any H_2O molecules in the coordination sphere, but we claim that there remains an OH ligand, approximately in the U-site position, in addition to the framework O_3 and O_2 ligands at the I' site. Ignoring more distant neighbors and framework distortions, the ideal point symmetry at this ion site would be C_{3v} . The ions do not become mobile at room temperature, so the form of the spectrum is invariant between 77 and 298 K.

The assertion of the presence of the OH ligand is supported by the IR spectral results⁵¹ which indicate that OH groups, bonded to the cations, remain in Ce-Y zeolite after vacuum calcination at 900 K. These are generated by the hydrolysis reaction: $\text{M}^{3+}\text{-OH}_2 \rightarrow \text{M}^{3+}\text{-OH} + \text{H}^+$, with the cleaved proton moving to a framework oxygen atom. This apparently does not occur with divalent cations,⁵¹ e.g., Ca^{2+} . Hence reduced Eu^{2+} ions can be completely dehydrated under the conditions used, and would be distributed among types I, I', and II sites, along with the residual Na^+ ions. Unreduced Eu^{3+} ions are expected to occupy type I' sites, retaining an extra-

framework OH ligand, as do the Gd^{3+} ions.

The reoxidation experiments prove that the ions responsible for the $g = 4.9$ line are more easily oxidized than the others; hence this signal is assigned to Eu^{2+} ions in type II and type I' sites, neither having any extraframework ligands. These ions have a one-sided coordination, and the type II site ions, especially, are readily accessible to O_2 , being in the supercages. Conversely, the site I ions are resistant to oxidation due to their sheltered location in the hexagonal prisms. The loss of the seventh ligand from the ions in types I' and II sites, from the superposition model viewpoint, would produce a larger resultant $|b_2^0|$ value, consistent with the assumption, made in section V.(4), of the weak-field Zeeman effect limit at X band. (An example of this kind of manifestation has been found in the case of Gd^{3+} in CdS .⁵²) Ideally, the six-coordinate Eu^{2+} ion (three O_3 and three O_2 ligands at I', or three O_2 and three O_4 ligands at II) is also in a site of trigonal symmetry (C_{3v}), so that the use of a mean axial symmetry in the random vector model interpretation of the signal (section V.(4)) is very plausible. Of course, even in the absence of framework distortions, these symmetries break down when next nearest neighbors are considered. The arguments of Newman and Urban¹³ bolster the notion that the intrinsic parameters for Eu^{2+} and Gd^{3+} are essentially the same, so that significant differences in $|b_2^0|$ for the ions in analogous sites must be due to local coordination differences; the models for the Y zeolite that we present are compatible with this view.

The bare Eu^{2+} ions which move into type I sites have a more symmetric coordination; it is not cubic (octahedral), however, because it has been found⁵³ that La^{3+} ions in type I sites are displaced significantly from the center of the hexagonal prism along the triad axis, presumably due to the covalent character of the bonding. These ions would contribute to components in the spectrum analogous to the Gd^{3+} U spectrum. There is apparently no significant population of bare Gd^{3+} ions in sites having one-sided coordination in the calcined Y zeolite; any Gd^{3+} ions which are completely denuded of extraframework ligands would move into the hexagonal prisms, occupying type I sites, and contributing to the U spectrum.

The Eu^{2+} ion spectrum produced by γ irradiation of hydrated zeolites is explained in the same manner as that for Gd^{3+} ions in uncalcined zeolites at low temperature, and confirms the inference made from the spectra of the calcined materials; i.e., that the very large zero-field splitting occurs only when the absence of extraframework ligands results in highly asymmetric one-sided coordination of the ion at a wall site. The seven-coordinate Gd^{3+} ions in type I' sites have smaller zero-field splittings and give rise to U-spectrum features as in the room temperature degassed material.

(b) *Mordenite*. The model derived to explain the Y-zeolite spectra can be extended, without inconsistencies, to the mordenite, despite the markedly different crystal structure. We use Smith's notation,^{5,6} consistent with the Gramlich convention. Gd^{3+} ions in hydrated mordenite are mainly in type VII sites, fully coordinated with H_2O , diffusing and tumbling at room temperature; these are analogous to the Y zeolite site V ions. Some Gd^{3+} ions are also hydrated with two H_2O ligands in type I sites in the distorted 8-rings; however, we think that this depends on the extent of Na^+ ion replacement; the large occupancy found by Mortier et al.⁶ for hydrated Ca^{2+} in this type of site corresponds to the complete replacement of Na^+ . Freezing the material dampens the motion and causes some partially hydrated ions in the large channels to be

localized in type VI wall sites, giving rise to the low field, U-spectrum components as in the Y-zeolite case (where the analogous sites are type II, hydrated). Those hydrated ions in type I sites are not expected to contribute significantly to this phase transition manifestation since their bonding to the framework precludes tumbling at room temperature. Mortier et al.⁶ have implied that these ions may be able to diffuse at room temperature, but they also find that there is no change in the occupancy of the type I sites when Ca mordenite is dehydrated at elevated temperature, so we will assume that there is no diffusion of these ions.

With the loss of H_2O upon vacuum calcination, ions from type VII sites move to framework-bound sites, primarily types VI and IV. These are highly asymmetric sites with one-sided coordination, the former being a wall site in the large channel, the latter displaced from a near circular 8-ring; these ions are, therefore, the analogues of the bare Eu^{2+} ion in types II and I' sites in Y zeolite. They are responsible for the prominent $g = 4.9$ signal now appearing for both Eu^{2+} and Gd^{3+} ions. The exposed locations account for the greater susceptibility of Eu^{2+} ions in these sites to magnetic and chemical interactions with O_2 . Dehydrated ions remain in type I sites, in distorted 8-rings; this is a less highly asymmetric site since the coordination is not one-sided; the U-spectrum features are assigned to ions in these sites.

V.(7) *Disorder and Randomness in the Zeolites*. Both Y zeolite and mordenite have considerable Al-Si framework disorder because the Si:Al ratio exceeds unity.^{4,5} Only the extreme X zeolite, having Si:Al = 1, is mathematically constrained to have Si-Al long range order although, in general, X zeolite would have less of this disorder than the Y. In addition, there do exist random positional displacements of both framework and extraframework atoms, and particularly of exchangeable cations, giving rise to a small range in the various ion-ligand distances and bond angles associated with each site. Randomness of either kind results in a variation in the crystal fields at a given type of cation site, so these factors are responsible for the glasslike randomness that we claim is an essential feature to be recognized in formulating an interpretation of the EPR spectra. This is true even for X zeolite; the composition of the X zeolite used by Nicula²⁵ was not given, but it is quite unlikely to have been 1:1 in Si:Al; so both randomness factors would contribute as in the other zeolites.

In Eu_2O_3 , we propose that the reduced Eu^{2+} ions have O^{2-} ions missing from the coordination sphere (initially of low, C_s symmetry in the ideal crystal), either because the ion is on the surface or because of charge-compensating defect formation. The resulting asymmetry results in large zero-field splittings and the appearance of a $g = 4.9$ line as found for one-sided coordinated ions in the zeolites. A distribution in the spin Hamiltonian parameters in this system would arise from randomness in the defect structure, a situation paralleling reported instances previously mentioned.^{14,39} As in all cases with the zeolites, hyperfine structure due to ^{151}Eu and ^{153}Eu nuclei is not resolved because the structural inhomogeneities make the EPR line widths too broad.

V.(8) *Redox Behavior of Europium*. Europium, like iron⁵⁴ and copper,⁵⁵ has been shown to undergo reversible oxidation-reduction sequences by adsorption of the appropriate gas in Y zeolite. As pointed out by Boudart for the iron system, this property might be exploited in regenerative oxidation catalyst applications. The interaction of O_2 with Eu^{2+} may occur either as weak adsorption

without electron transfer, or as actual chemical oxidation. The former gives rise primarily to magnetic effects and accounts for the reversible room temperature behavior observed in the zeolite spectra; it is manifested exclusively with the exposed ions at wall sites which are responsible for the $g = 4.9$ signal. The oxidative reaction at intermediate temperatures is believed to follow: $\text{Eu}^{2+} + \text{O}_2 \rightarrow \text{Eu}^{3+}-\text{O}-\text{O}^-$. The C_2^- EPR signal so resulting has been characterized in the case of Ti^{3+} oxidation,⁵⁶ and was reported without characterization for Ni^+ oxidation⁵¹ in Y zeolite; on chemical grounds, therefore, it is contended that the paramagnetic oxidation product observed for both zeolites, as well as for Eu_2O_3 , is O_2^- . However, the assignment could not be made unequivocally on strictly spectroscopic grounds by comparison with the many O_2^- EPR characterizations made with zeolites^{56,57} and oxide surfaces,⁵⁸ mainly from ionizing radiation experiments. As was found for Ni^+ , the reoxidation of the Eu^{2+} ions "hidden" in type I sites is highly activated and requires high temperatures to be completely effected. The O_2^- bond to Eu^{3+} does not survive these highest temperatures.

VI. Summary

It has been shown (inferentially) that the form of the EPR spectra of S-state ions in synthetic faujasite and mordenite is dictated in part by randomness in the local structure, and hence in the spin Hamiltonian parameters, at a given site. Previous interpretations assigning a different specific point symmetry to each principal feature in the spectrum are shown to be questionable.

The spectra of the ions in the calcined zeolites depend basically on whether or not there are extraframework ligands for ions in wall sites. When the coordination is one-sided, as it is for Eu^{2+} in types I' and II sites in Y zeolite, and for Gd^{3+} and Eu^{2+} in types VI and IV sites in mordenite, the zero-field splittings are very large and the X-band spectra are dominated by a signal at $g \sim 4.9$. This signal can be interpreted in the random vector model with a distribution of crystal fields having mean axial symmetry, with a large variance, and a large negative covariance of the g factor components. The estimated range of the axial effective CF spin Hamiltonian parameters is $3 \text{ GHz} < |b_2^0| < 10 \text{ GHz}$. Gd^{3+} and Eu^{2+} ions in type I sites in mordenite, Eu^{2+} ions in type I sites in Y zeolite, and Gd^{3+} in type I' sites in Y zeolite (these retain an extraframework OH ligand) all yield complex X-band spectra of the form designated as the U spectrum—the spectrum found for Gd^{3+} in several glasses. The zero-field splittings in these situations are smaller, and the spectra revert to the strong-field Zeeman effect limit form at Q band; it is estimated that $|b_2^0| \lesssim 2.7 \text{ GHz}$ for the U spectrum.

Actual point symmetries for the ions in all of these sites is orthorhombic or lower, probably C_s . The same is true even for fully hydrated ions in type V sites in Y zeolite and type VII sites in mordenite. The hydrated ions tumble and have some solution-like EPR properties at room temperature, the zero-field splittings being small. With freezing or partial dehydration, ions are localized on the supercage or large channel walls, experiencing stronger, more asymmetric crystal fields, with a resulting change of the X-band spectrum from purely strong-field Zeeman effect limit-type, having $g \sim 2.0$, to U type. While the ions retain H_2O in the coordination sphere, i.e., in the absence of calcining, the large CF splittings consistent with the weak-field Zeeman effect limit at X band do not manifest themselves in the spectra.

An empirical correlation method, using Allred-Rochow electronegativities, has been devised to facilitate estimation of the second degree intrinsic splitting parameters for the

S-state ions with silicate and aluminate oxygen ligands. For Si, $|b_2^0| \sim 4.3\text{--}5.3 \text{ GHz}$; for Al, $|b_2^0| \sim 5.7\text{--}7.0 \text{ GHz}$.

Reduction of Eu^{3+} ions in these zeolites can be effected at very low temperatures by γ irradiation of the hydrated zeolites, or chemically at elevated temperatures with H_2 ; partial reduction occurs spontaneously upon calcining in vacuo. The two extremes yield Eu^{2+} in different sites and with different coordinations; they are hydrated and trapped in the supercages in the former instance, but are denuded and enter the sodalite cages and hexagonal prisms in the latter (for Y-zeolite matrix). This difference is apparent from the EPR spectra. The europium can be carried through successive reduction-oxidation cycles, with the relative ease of oxidation of Eu^{2+} in "hidden" and exposed sites being readily discriminated from the spectra. $\text{Eu}^{3+}-\text{O}-\text{O}^-$ is a stable oxidation product at intermediate temperatures, but does not survive at high temperatures.

EPR spectra of non-S-state rare earth ions in a random polycrystalline host are reported for the first time, but the extreme inhomogeneous broadening precludes definitive interpretations. Spectra of the non-Kramers ions were observable only in uncalcined materials where they yielded very unusual line shapes.

Acknowledgment. The support of the U.S. ERDA is gratefully acknowledged. We thank Dr. J. Rabo (Union Carbide Corporation), who provided the ultrapure Na-Y zeolite, and Professor W. N. Delgass (Purdue University) who provided the sodium zeolon and a europium exchanged sample. We thank Dr. G. M. Dobbs who helped us with the zero-field EPR experiment, Dr. A. M. Ozer who obtained the measurements on Gd^{3+} in solution, and Dr. G. E. Peterson (Bell Telephone Laboratories) who provided manuscripts prior to publication.

References and Notes

- (1) (a) A. Nicula, D. Stamires, and J. Turkevich, *J. Chem. Phys.*, **42**, 3684 (1965); (b) J. Turkevich, Y. Ono, and J. Soria, *J. Catal.*, **25**, 44 (1972).
- (2) D. N. Stamires and J. Turkevich, *J. Am. Chem. Soc.*, **86**, 749 (1964).
- (3) W. M. Meier and D. H. Olson, *Adv. Chem. Ser.*, No. 101, 386 (1971).
- (4) J. V. Smith, *Adv. Chem. Ser.*, No. 101, 401 (1971).
- (5) W. J. Mortier, J. J. Pluth, and J. V. Smith, *Mater. Res. Bull.*, **10**, 1037 (1975).
- (6) W. J. Mortier, J. J. Pluth, and J. V. Smith, *Mater. Res. Bull.*, **11**, 15 (1976).
- (7) A preliminary report has been presented: L. Iton, A. Nicula, and J. Turkevich in "Proceedings of the 3rd International Congress on Molecular Sieve Zeolites, Zurich (1973)". J. B. Uytterhoeven, Ed., Leuven University Press, Louvain, Belgium, 1973, p. 332.
- (8) A. Abragam and B. Bleaney, "Electron Paramagnetic Resonance of Transition Ions", Oxford University Press, London, 1970.
- (9) D. J. Newman, *Solid State Commun.*, **18**, 667 (1976).
- (10) H. A. Buckmaster and Y. H. Shing, *Phys. Status Solidi, A*, **12**, 325 (1972).
- (11) R. C. Nicklin, Ph.D. Thesis, Iowa State University; published as Technical Report US AEC, 1967, IS-T-203.
- (12) B. G. Wybourne, *Phys. Rev.*, **148**, 317 (1966).
- (13) D. J. Newman and W. Urban, *Adv. Phys.*, **24**, 793 (1975).
- (14) G. E. Peterson and A. Carnevale, *J. Chem. Phys.*, **56**, 4848 (1972).
- (15) G. E. Peterson, C. R. Kurkjian, and A. Carnevale, *Phys. Chem. Glasses*, **15**, 52 (1974).
- (16) G. E. Peterson, C. R. Kurkjian, and A. Carnevale, *Phys. Chem. Glasses*, **15**, 59 (1974); **16**, 63 (1975).
- (17) J. M. Wozencraft and I. M. Jacobs, "Principles of Communication Engineering", Wiley, New York, N.Y., 1955, Chapters 2 and 3.
- (18) Defined by $g = h\nu/\beta H$ where $h\nu$ is the microwave quantum. Experimental signals will usually be identified by their effective g values, with the omitted subscript "eff" being understood.
- (19) Baron Consulting Co., Connecticut.
- (20) G. M. Dobbs and E. R. Bernstein, *Rev. Sci. Instrum.*, **44**, 1314 (1973).
- (21) L. E. Iton, Ph.D. Thesis, Princeton University, unpublished.
- (22) N. S. Garif'yanov, R. Kh. Timerov, and N. F. Usacheva, *Sov. Phys. Solid State*, **4**, 2448 (1962).
- (23) G. G. Mshvelidze and Kh. I. Gaprindashvili, *Sov. Phys. Solid State*, **13**, 2860 (1972).
- (24) G. O. Karapetyan, D. M. Yudin, and D. G. Gallimov, *Bull. Acad. Sci. USSR, Phys. Ser.*, **31**, 814 (1967).
- (25) A. Nicula and E. Trif, *Proc. Congr. AMPERE, 17th*, 1973, 543 (1974).
- (26) A. Nicula and J. Turkevich, *Rev. Roum. Phys.*, **19**, 191 (1974).

- (27) L. S. Singer and D. N. Stamires, *J. Chem. Phys.*, **42**, 3299 (1965).
 (28) E. G. Derouane, M. Mestdagh, and L. Vielvoye, *J. Catal.*, **33**, 169 (1974).
 (29) L. Holmes and M. Schieber, *J. Appl. Phys.*, **37**, 968 (1966).
 (30) R. C. Nicklin, J. K. Johnstone, R. G. Barnes, and D. R. Wilder, *J. Chem. Phys.*, **59**, 1652 (1973).
 (31) N. S. Garif'yanov and M. M. Zaripov, *Sov. Phys. Solid State*, **6**, 1209 (1964).
 (32) (a) C. R. Kurkjian, P. K. Gallagher, W. R. Sinclair, and E. A. Sigety, *Phys. Chem. Glasses*, **4**, 239 (1963); (b) P. K. Gallagher, C. R. Kurkjian, and P. M. Bridenbaugh, *Phys. Chem. Glasses*, **6**, 95 (1965).
 (33) E. Beauchler and J. Turkevich, *J. Phys. Chem.*, **76**, 2325 (1972).
 (34) D. K. Rice and L. G. DeShazer, *Phys. Rev.*, **186**, 387 (1969).
 (35) R. Reisfeld, *Structure Bonding*, **13**, 53 (1973).
 (36) R. Reisfeld and N. Lieblich, *J. Phys. Chem. Solids*, **34**, 1467 (1973).
 (37) C. Brecher and L. A. Riseberg, *Phys. Rev. B*, **13**, 81 (1976).
 (38) R. Parrot, C. Barthou, B. Canny, B. Blanzot, and G. Collin, *Phys. Rev. B*, **11**, 1001 (1975).
 (39) W. Baumhoer, J. Thiemann, and O. Kanert, *Phys. Status Solidi B*, **73**, 155 (1976).
 (40) The estimated limits are revised from our preliminary communication⁷ on the basis of the magnitudes of the intrinsic splitting parameters estimated in section V(5).
 (41) F. A. Cotton and G. Wilkinson, "Advanced Inorganic Chemistry", Wiley-Interscience, New York, N.Y., 1962, p 92.
 (42) Vishwamittar and S. P. Puri, *J. Chem. Phys.*, **61**, 3720 (1974).
 (43) J. V. Smith, J. M. Bennett, and E. M. Flanigen, *Nature (London)*, **215**, 241 (1967).
 (44) D. H. Olson, G. T. Kokotailo, and J. F. Charnell, *J. Colloid Interface Sci.*, **28**, 305 (1968).
 (45) N. N. Tikhomirova and I. V. Nikolaeva, *J. Catal.*, **40**, 135 (1975).
 (46) J. Scherzer, J. L. Bass, and F. D. Hunter, *J. Phys. Chem.*, **79**, 1194 (1975).
 (47) (a) B. R. McGarvey, *J. Phys. Chem.*, **61**, 1232 (1957); (b) H. Levanon, G. Stein, and Z. Luz, *J. Chem. Phys.*, **53**, 876 (1970).
 (48) N. N. Tikhomirova, I. V. Nikolaeva, V. V. Demkin, E. N. Rosolovskaya, and K. V. Topchieva, *J. Catal.*, **29**, 105 (1973).
 (49) E. V. Sayre, D. G. Miller, and S. Freed, *J. Chem. Phys.*, **26**, 109 (1957).
 (50) R. T. Ross, *J. Chem. Phys.*, **42**, 3919 (1965).
 (51) J. A. Rabo, C. L. Angell, P. H. Kasai, and V. Schomaker, *Discuss. Faraday Soc.*, **41**, 328 (1966).
 (52) W. Urban, E. Siegel, and W. Hillmer, *Phys. Status Solidi B*, **62**, 73 (1974).
 (53) J. M. Bennett and J. V. Smith, *Mater. Res. Bull.*, **3**, 865 (1968).
 (54) R. L. Garten, W. N. Delgass, and M. Boudart, *J. Catal.*, **18**, 90 (1970).
 (55) C. Naccache, M. Che, and Y. Ben Taarit, *Chem. Phys. Lett.*, **13**, 109 (1972).
 (56) Y. Ono, K. Suzuki, and T. Keii, *J. Phys. Chem.*, **78**, 218 (1974).
 (57) K. M. Wang and J. H. Lunsford, *J. Phys. Chem.*, **75**, 1165 (1971).
 (58) J. H. Lunsford, *Catal. Rev.*, **8**, 135 (1974).

Electron Spin Resonance Studies of Anisotropic Ordering, Spin Relaxation, and Slow Tumbling in Liquid Crystalline Solvents. 2^{1a}

K. V. S. Rao, Carl F. Polnaszek,^{1b} and Jack H. Freed*

Department of Chemistry, Cornell University, Ithaca, New York 14853 (Received October 12, 1976)

A study is reported of the ESR line shapes in the slow-tumbling region for a cholestane (CSL) spin probe in nematic phase V solution. The line shapes are analyzed in terms of the Polnaszek, Bruno, Freed theory for spectra from slowly tumbling probes in ordered fluids. Rather good agreement with experiment is obtained from the slower motional spectra ($\tau_R > 5 \times 10^{-9}$ s where τ_R is the rotational correlation time) utilizing a single term ordering potential. For these slow-motional spectra, effects of proton inhomogeneous broadening are relatively small. It is shown in this study on CSL that for $\tau_R > 10^{-9}$ s a motional-narrowing theory will lead to erroneous predictions for τ_R and ordering that become more serious as τ_R increases. The previous application of motional-narrowing theory by other workers to this probe is discussed in this light. The effects of various other factors upon the spectral simulations are discussed. In particular, it is shown that the spectra for this highly ordered probe should not be very sensitive to various aspects of model dependence of the reorientational motion as discussed in part I nor to effects from director fluctuations. Also the slower tumbling spectra are rather insensitive to anisotropy in τ_R (but the anisotropy may be determined from the faster motional spectra). Nevertheless, contributions from these effects could modify somewhat the values of τ_R and ordering that are obtained. The slow tumbling spectra are also insensitive to the angle of tilt of the nitroxide magnetic-tensor principal axis system in the x - y plane with respect to the molecular orientational axes. Our results show that the tilt angle of the magnetic z axis should not be very different from 0° .

I. Introduction

In part I we presented a detailed study of anisotropic ordering, line shapes, and relaxation for the weakly ordered perdeuterated 2,2,6,6-tetramethyl-4-piperidone *N*-oxide (PD-Tempone) nitroxide radical.² This radical offered the advantages that one could achieve a high degree of spectral resolution for accurate spin-relaxation studies, because inhomogeneous broadening due to unresolved intramolecular proton or deuteron interactions is minimized. A major objective of that work was to apply the Polnaszek, Bruno, Freed (PBF) theory³ (appropriately generalized²) for slow tumbling in ordered fluids to a system exhibiting good resolution and definition. That study indicated the existence of anomalies in the line shape, particularly in the

incipient slow-tumbling region, which was later borne out by studies as a function of pressure,⁴ and were tentatively ascribed to slowly relaxing components of torque acting on the probe molecule.

The importance of slow-tumbling analyses increases when one employs larger and more highly ordered probes. One such probe that is commonly used is 3-spiro-[2'-*N*-oxyl-3',3'-dimethyloxazolidine] (5 α -cholestane) or CSL. It is highly ordered to a degree more typical of the liquid crystal molecules than is Tempone. While only preliminary accounts of the analysis of its ESR spectrum, when dissolved in liquid-crystalline systems, in terms of slow tumbling theory has previously been given,⁵⁻⁷ we note that many workers have unhesitatingly applied motional-

TABLE I: Magnetic Parameters for CSL in Phase V^a

$A_z = 33.44$	$g_z = 2.0021$
$A_x = 5.27$	$g_x = 2.0089$
$A_y = 5.27$	$g_y = 2.0058$
$a_N = 14.66 \pm 0.01$	$g_0 = 2.0056 \pm 0.0001$

^a See text.

narrowing theory, in various degrees of sophistication, to the spectra obtained in nematic and smectic phases. We wish, in this work, to give a more detailed account of our efforts to simulate observed spectra from nematic solutions of the cholestane spin label in terms of the PBF theory. One important question we deal with is the extent to which motional-narrowing theories are adequate vs. the need for complete simulations. The other questions relate to our ability to interpret these spectra in terms of molecular ordering and motional dynamics. The fact that the cholestane ESR spectrum is significantly broadened by proton inhomogeneous structure reduces the resolution, hence the sensitivity of the spectrum to subtle effects of ordering and motional dynamics. Thus, we have not felt that an analysis as thorough and detailed as the one we have given for PD-Tempone is entirely appropriate. In particular, we focus much of our attention on the lower-temperature, slower-tumbling spectra ($5 \times 10^{-9} \text{ s} < \tau_R \lesssim 10^{-7} \text{ s}$), in part because this is a region wherein the inhomogeneous proton broadening is of less significance in the spectral simulations. It is in that region that we are able to achieve good fits to the experimental data by means of the PBF theory, and it is quite clear that motional narrowing theory is inadequate even though it has been extensively employed by other workers.

II. Experimental Section

The spin probe (3-spiro-[2'-N-oxyl-3',3'-dimethyl-oxazolidine]) 5 α -cholestane was obtained from Synvar Associates and the liquid-crystalline solvent phase V from EM Laboratories.

Most of the ESR measurements were performed on a Varian E-12 spectrometer. The temperature in the active region of the cavity was controlled by a Varian E-257 variable temperature control unit. The other aspects of the experimental methods are as described earlier.^{2,4,6,8,9}

III. Analysis and Discussion

(A) *Magnetic Parameters.* The rigid, but isotropic, spectrum of CSL was recorded at -152°C in order to obtain magnetic parameters. However, because of proton inhomogeneous broadening it was impossible to resolve the central part of the spectrum. Therefore only a_z and g_z could unambiguously be determined for CSL in phase V. The magnetic parameters have been reported¹⁰ for CSL in single crystals of cholesteryl chloride. The value of a_z (31.9 G) is different from the value obtained (33.44 G) for CSL in phase V, but the g_z values obtained for the two systems are the same. So we used the g values observed for CSL in cholesteryl chloride.^{10a} We also measured the isotropic values of a_N and g . The value of a_\perp was obtained by assuming $a_\perp = a_x = a_y$, so the equation $a_\perp = \frac{1}{2}(3a_N - a_z)$ applies, where a_N is the measured value of isotropic splitting constant. The magnetic parameters for CSL in phase V used in the present work are given in Table I. Various results for a_N and a_z are presented in Table II for CSL in different solvents. The a_N and a_z values observed for CSL in phase V are similar to those observed in non-hydrogen bonding solvents, as one would expect.

(B) *Slow Tumbling Simulations.* The spectra of CSL in the nematic phase V were recorded from -26 to $+65^\circ\text{C}$. We have simulated the ESR spectra of CSL in phase V

TABLE II: a_N and a_z Values for CSL in Different Solvents

Solvent	a_N	a_z	Ref
Phase V	14.66	33.44	Present work
CF ₃ CH ₂ OH	15.75	35.4	<i>a</i>
EtOH	15.0		<i>a</i>
Pentane/heptane	14.2	32.3	<i>a</i>
Perdeuterated benzene	14.4	33.5	<i>a</i>
Me ₂ SO	14.8		<i>a</i>
Egg lecithin	15.1	34.2	<i>b</i>
Brain lipid	14.67	33.3	7a
Brain lipid + cholesterol (30%)	15.56	35.0	<i>a</i>
Lecithin + cholesterol (50%)	15.01	32.7	17
Cholesteryl chloride	14.7	31.9	10

^a C. F. Polnaszek, unpublished. ^b J. Israelachvili et al., *Biochim. Biophys. Acta*, 382, 125 (1975).

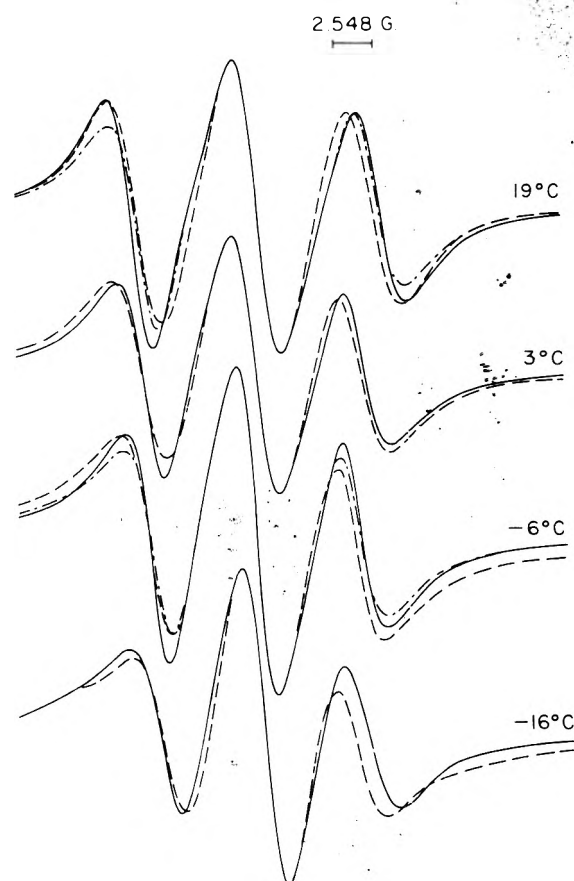


Figure 1. Comparison of experimental and simulated spectra at several temperatures for CSL in phase V: (---) experimental results; (—) theoretical result based upon isotropic Brownian diffusion with the τ_R , λ , and A' values given in Table III; (— · —) theoretical result based upon anisotropic Brownian diffusion model. The values used for the simulations with the anisotropic diffusion mode at 19°C are $\tau_{R\perp} = 1.7 \times 10^{-8} \text{ s}$, $N_y = 5$, $\lambda = 4.3$, and $A' = 0.9 \text{ G}$, and at -6°C , $\tau_{R\perp} = 7.8 \times 10^{-8} \text{ s}$, $N_y = 5$, $\lambda = 6.0$, and $A' = 1.3 \text{ G}$.

by using the PBF approach.²⁻⁴ Typical spectra simulated at temperatures -16 , -6 , $+3$, and $+19^\circ\text{C}$ along with the experimental spectra at these temperatures are shown in Figure 1. The appropriate values of τ_R , the isotropic rotational correlation time, and ordering potential parameter λ were obtained by trial-and-error for each slow-motional spectrum in order to achieve the best agreement.^{11a} We used a simple one term potential $U(\beta)$ given by $U(\beta)/kT = -\lambda \cos^2 \beta$, where β is the angle between the molecular symmetry axis and the director aligned along the dc-magnetic field (cf. section C for further discussion). It is seen from Figure 1 that the agreements are quite good,

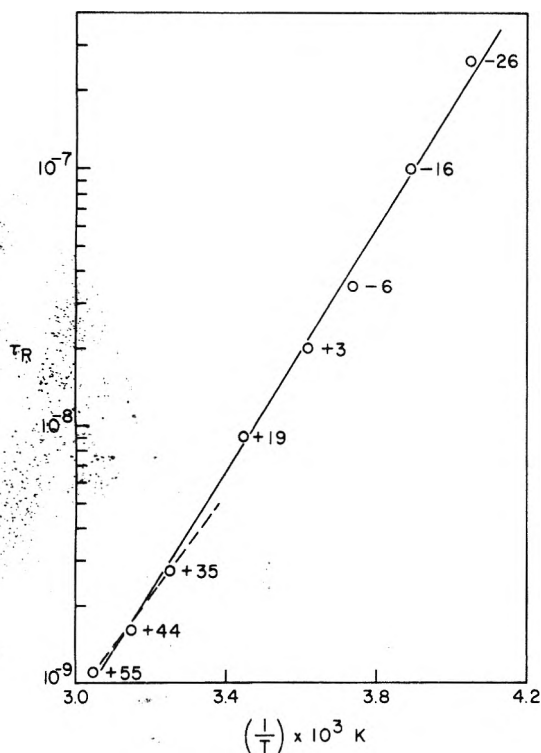


Figure 2. Graph of τ_R vs. $(1/T) \times 10^3$ K for CSL in phase V. The values of τ_R at the different temperatures are given in Table III.

TABLE III: Correlation Times, λ , and A' Values for CSL in Nematic Phase V at Different Temperatures

Temp, °C	$10^9 \tau_R$ s	λ	$\langle D_{00}^2 \rangle$	A' , G ^a
65	0.9	2.65	0.40	1.75
55	1.1	3.3	0.48	1.75
44	1.6	4.0	0.56	1.7
35	2.7	4.1	0.57	1.5
19	9	4.5	0.61	1.45
3	20	5.3	0.67	1.5
-6	35	6.0	0.71	1.8
-16	100	6.9	0.76	2.2
-26	260	7.6	0.78	2.5

^a These are based on assuming an overall Lorentzian broadening. When the spectra were simulated by a Gaussian convolution to better represent the effects of inhomogeneous broadening, then the residual line width A' attributable to a Lorentzian component is significantly reduced for the higher temperature spectra (e.g., for 55 °C, $A' = 0.3$ G with Gaussian width 2.15 G), but only slightly reduced for the lower temperature spectra (e.g., for -16 °C, $A' = 1.5$ G with the Gaussian width 2.0 G).

although not perfect. Also, the values of τ_R so obtained yield a good Arrhenius-type plot vs. $1/T$ with an activation energy of 10.9 kcal/mol from the lower temperature spectra (cf. Figure 2). This is only a little greater than the value 9.6 kcal/mol obtained for PD-Tempone in phase V.² Hence the τ_R values used here are probably close to the correct values (see also section C). The τ_R values obtained in this manner (in which an isotropic rotational diffusion model was used for CSL in phase V) and the corresponding λ , $\langle D_{00}^2 \rangle$ (the usual order parameter S), and A' (the residual line width which is the difference between experimental and theoretical values^{2,4}) at the different temperatures are given in Table III. A plot of λ and the corresponding $\langle D_{00}^2 \rangle$ values vs. temperature is shown in Figure 3. The temperature dependence of λ and $\langle D_{00}^2 \rangle$ is similar to that observed for PD-Tempone in different liquid crystal solvents^{2,6} although the values for λ and $\langle D_{00}^2 \rangle$ are, as expected, greater in the present case. A plot

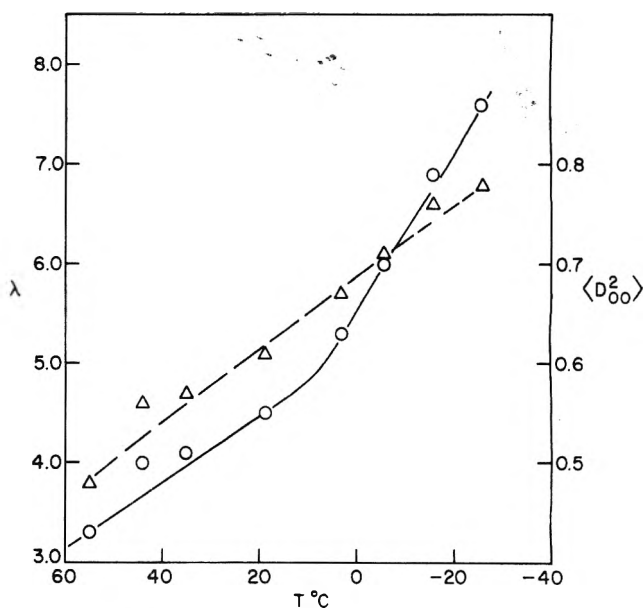


Figure 3. Graph of λ (O) and $\langle D_{00}^2 \rangle$ (Δ) vs. temperature: (—) λ vs. T ; (---) $\langle D_{00}^2 \rangle$ vs. T . The λ and $\langle D_{00}^2 \rangle$ values at different temperatures are given in Table III.

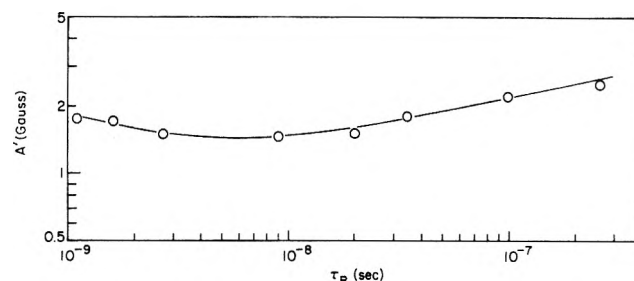


Figure 4. Graph of the residual line width A' in G vs. τ_R . The values of A' and τ_R are given in Table III.

of A' vs. temperature is shown in Figure 4. The values of τ_R and λ required to simulate the spectra at the highest temperature does not appear to fit the extrapolated curves from the lower temperature results (cf. Figures 2 and 3). The probable reasons are (1) the onset of model-dependent effects in the slow motional region at lower temperatures which are not apparent in the higher temperature spectra;^{8,9} (2) the appearance of anomalies observed for PD-Tempone in isotropic⁹ and in anisotropic solvents^{2,4} for τ_R of the order of 10^{-9} s; (3) hydrodynamic and critical effects on the magnitude and direction of the director; and (4) the pronounced effects of inhomogeneous broadening upon the higher temperature spectral line shapes. We discuss these factors below.

For small nitroxides such as PD-Tempone, it has been shown earlier that in the slow motional region a moderate jump diffusion model gives a better fit with the experimental spectrum than the Brownian model. The τ_R values needed⁹ to fit a slow motional spectrum with the moderate jump model are somewhat smaller than the τ_R values obtained by using a Brownian model. This is in agreement with the observation that a linear extrapolation of τ_R values at high temperatures (55, 44, and 35 °C) will give lower values at the lower temperatures (19, 3, -6, and 16 °C) than the τ_R values obtained by using Brownian model at the corresponding temperatures. Thus, if the moderate jump diffusion model were used, the values of activation energy would be reduced somewhat, and then would be in better agreement with the value obtained for PD-Tempone in phase V. (We note that the use of these different models has very little effect on the overall best-fit line shapes for

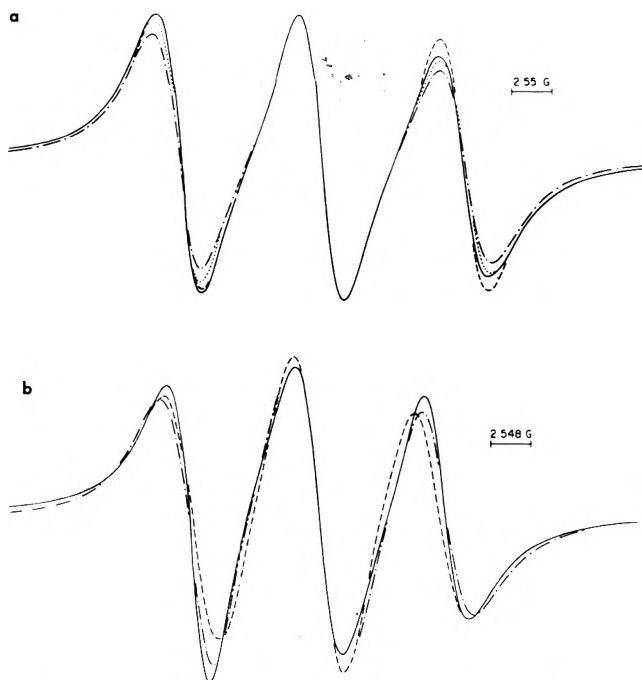


Figure 5. (a) Comparison of the simulated spectra at $\tau_R = 1.8 \times 10^{-9}$, $\lambda = 4.5$ with different values of ϵ' : (— — —) $\epsilon'_{ps} = 20$, $\epsilon'_{s} = 1.0$, $A' = 2.5$ G; (·····) $\epsilon'_{ps} = 5$, $\epsilon'_{s} = 1$, $A' = 2.4$ G; (—) $\epsilon'_{ps} = \epsilon'_{s} = 1.0$, $A' = 2.15$ G; and (— — —) $\epsilon'_{ps} = \epsilon'_{s} = 5.0$, $A' = 2.4$ G. (b) Comparison of the simulated spectra with and without including the contributions due to director fluctuations. (---) Experimental spectrum at 19 °C; (—) simulated spectrum with $\tau_R = 7.5 \times 10^{-9}$; $\lambda = 4.3$, A' for $M = 0$ line = 1.0 G and A' for $M = \pm 1$ lines = 0.75 G; (— · —) simulated spectrum with $\tau_R = 7 \times 10^{-9}$, $\lambda = 4.3$, A' for all the three lines = 1.0 G.

these highly ordered and broad line shapes.) In particular, a least-squares fit of all the τ_R values vs. $(1/T)$ gives an activation energy of 10.5 kcal/mol. However, except for the possibility of some model dependence, the lower temperature results are the more reliable ones, as we have noted.

Incipient slow tumbling spectra (i.e., $\tau_R \sim 10^{-9}$ s) of PD-Tempone in different solvents have been successfully explained only after taking into account the effects of fluctuating torques and slowly relaxing local structure, with the most prominent effects showing up in liquid-crystalline^{2,4,9} solvents. Some spectra of CSL in phase V were simulated including the fluctuating torques in terms of ϵ' (i.e., the spectral densities, $j(\omega) = \tau_R/[1 + \epsilon'\omega^2\tau_R^2]$) as was done for PD-Tempone.^{2,4,9} A major difficulty in any attempt to fit these spectra with values of $\epsilon' \neq 1$ is the absence of accurate motional-narrowing results for τ_R and λ which could then be extrapolated into the slow-tumbling region as initial guides to the fitting. Another is the problem that the spectra are not well resolved, so the effect on the simulated spectra of varying ϵ' is small. This can be seen from Figure 5a, which shows simulated spectra for CSL in phase V, at $\tau_R = 1.8 \times 10^{-9}$, $\lambda = 4.5$, and with ϵ' values of 20, 5, and 1. These spectra are not as sensitive to the value of ϵ' as the spectra of PD-Tempone.^{2,4,9} Hence even if the anomalies observed for PD-Tempone^{2,4,9} are present in CSL in phase V, the nature of the spectra observed does not really allow an identification of such anomalies. Some attempts at varying ϵ' (which required changes in τ_R and λ in order to obtain reasonable fits) were made, but they tended to emphasize the uncertainty of such fits. [Note that in ref 9, it was pointed out that apparent jump-model effects on slow tumbling spectra may on more fundamental grounds also be ascribed to a fluctuating torque model which gives rise to a predicted

ϵ' effect in the incipient slow-motional region.]

We now note that at temperatures close to the nematic-isotropic transition temperature, there may be effects of the critical orientational fluctuations that have been observed^{11b} for PD-Tempone in MBBA. The critical fluctuations may extend over a larger temperature range than was observed for PD-Tempone in MBBA,^{11b} because of the greater ordering of the CSL probe. Furthermore, we have not included any effects from possible director fluctuations in the nematic region. At present, it is difficult to assess to what extent these will contribute static (or inhomogeneous) broadening effects vs. dynamic (or homogeneous) broadening. This is because the range of correlation times for the independent hydrodynamic modes extends from very slow to rather fast,² so it is not clear at which point motional averaging with respect to such fluctuations is important. If we were to blithely assume the applicability of the motional-narrowing formula given in ref 2 (and y -axis ordering, cf. section C), then we would estimate a contribution to A' of 0.24 G and to C (i.e., width contributions only to the $M_I = \pm 1$ ESR transitions) of -0.12 G (noting that the equations in ref 2 require an additional factor of 2 which was omitted), and the contributions should be rather temperature insensitive. We show a simulation in Figure 5b in which this effect is exaggerated (to allow for slow motional and static contributions) by using an A' for the $M_I = \pm 1$ transitions which is $1/4$ G smaller than that for the $M_I = 0$ transition. This leads to greater disagreement with experiment. However, the spectral effect is seen to be roughly opposite to that from the ϵ' correction in Figure 5a. Thus the possibility of nearly canceling contributions cannot really be ruled out for these fairly small effects. [One can, of course, attempt to fit an experimental spectrum by simultaneously adjusting τ_R , λ , the ϵ' corrections, hydrodynamic corrections, as well as the rotational anisotropy and tilt of the molecular magnetic axes discussed in section C while using different rotational diffusion models, but there is no justification for this in view of the very limited spectral resolution, so we content ourselves with considering these effects individually.]

Another complicating factor for the spectra at the higher temperatures is the effect of inhomogeneous broadening. In the isotropic phase V these splittings were partially resolved. Marriott et al.¹² have resolved these splittings in nonviscous solvents and assigned them by partial deuteration of CSL. They showed that there are three different proton splittings greater than 0.6 G. In the nematic phase V, the proton splittings were not resolved, even though the experimental line width at the highest temperature was less than in the isotropic phase. A proper analysis of their inhomogeneous broadening would involve a consideration of the effects of the only partially averaged anisotropic proton hyperfine components.² Since no such information was conveniently obtainable, and since the ensuing analysis of the line shapes (including slow-motional effects) is still complex, we have not attempted the corrections for inhomogeneous broadening as were done in our previous studies.^{2,4,9} A convolution of the spectrum with a Gaussian envelope^{6,13} is a reasonable way to include the effects of many (unknown) proton splittings in the nematic phase, but introduces one further adjustable parameter. We have in most of our analyses included inhomogeneous broadening effects into the residual broadening contribution A' added to each transition. Since the inhomogeneous broadening effects are relatively minor for the broad lines obtained for $\tau_R > 5 \times 10^{-9}$ s, there is no problem in getting good agreement in line shapes

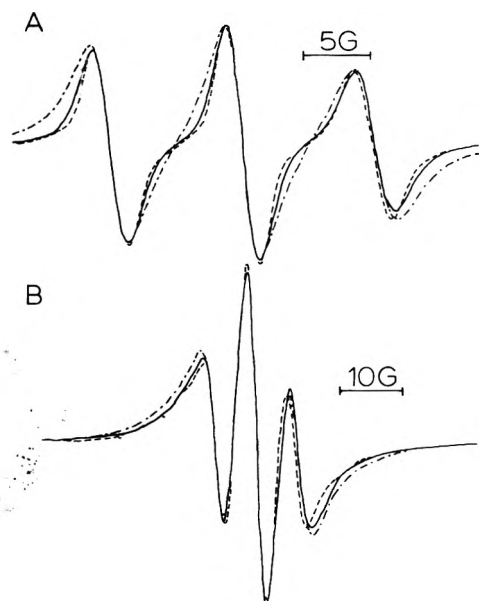


Figure 6. Effect of Gaussian convolution on calculated line shapes at (A) 55 °C and (B) -16 °C. All values as in Figure 1 and Table III: (---) experimental result; (—) Gaussian convolution; (- · - ·) Lorentzian shape.

between simulation and experiment (cf. for Figure 1). However, as τ_R becomes shorter, the discrepancies between simulated and experimental line shapes become greater, and we have found that a Gaussian convolution does improve the overall agreement of the line shapes without significantly changing the relevant relaxation parameters except for A' (cf. Table III). This is illustrated in Figure 6.

(C) *Ordering and (Anisotropic) Rotational Diffusion.* Since the overall shape of CSL may be approximated as a cylinder of length 24 Å and diameter of 6 Å,¹² it is expected to align so that the cylinder axis is parallel to the director of the liquid crystal. In the coordinate system used in our earlier studies^{2,4,9} the magnetic y axis of the nitroxide group is nearly parallel to the cylinder axis. Thus the ordering tensor can reasonably be assumed to be axially symmetric along the magnetic y axis (or slightly tilted). Our previously quoted spectral simulations and the values of λ given are based upon this assignment.

CSL is also expected to exhibit axially symmetric rotational diffusion about its long axis. A theoretical anisotropy ratio N_y can be estimated using the dimensions of the molecule¹² and the appropriate expression.^{9,14} For CSL we predict $N_y = 4.7$. Also our estimated value of N_y is 5 for CSL in the isotropic phase of phase V at 85 °C and $\tau_R = 2.5 \times 10^{-10}$. We have simulated the ESR spectra with a value of $N_y = 5$ at +19 °C and at -6 °C. The correlation time $\tau_{R\perp}$ for rotation about an axis perpendicular to the symmetry axis that is required for the best fit at +19 °C with $N_y = 5$ is 1.7×10^{-8} , so the value of the correlation time, $\tau_{R\parallel}$, for rotation about the symmetry axis is 3.3×10^{-9} . (Note that $N \equiv \tau_{R\perp}/\tau_{R\parallel}$). The mean correlation time $\bar{\tau}_R$, which is defined as $(\tau_{R\perp}\tau_{R\parallel})^{1/2}$, is 7.5×10^{-9} compared to 7.0×10^{-9} , the value obtained for an isotropic diffusion model. At -6 °C the value of $\bar{\tau}_R$ is the same as τ_R in the isotropic diffusion model. The value of λ that has to be used for simulation of the best fit with $N_y = 5$ is nearly the same as the value used in isotropic diffusion at both 19 and -6 °C. There is very little difference for such long τ_R 's between the theoretical spectra for an isotropic diffusion model and anisotropic diffusion for $N_y \approx 5$ as has previously been shown (cf. Figures 13 and 14 of ref 8). However, one can obtain the B and C line width coeffi-

icients in the usual manner.^{2,4,8,9} For the spectra at 55, 44, and 35 °C, the ratio C/B is nearly independent of the procedure for obtaining B and C ; i.e., we have used (1) the uncorrected values, (2) the values corrected for inhomogeneous broadening using the isotropic proton splittings,²² or (3) the values obtained by convolution with a Gaussian.¹³ For these spectra in the incipient slow tumbling region we obtain $N_y \approx 3-4$, assuming no tilt in the nitroxide, $x-y$ plane. [Note that the "apparent" value of N_y increases close to the transition point on both sides of the phase transition.²³]

Thus, even if there is some anisotropy in the rotation of CSL in phase V, its effect on the τ_R and λ values seems to be small. Also, the effects of anisotropic diffusion on the spectral line shapes decreases as τ_R gets larger. This is in part due to the decreasing sensitivity of ESR spectra to motional effects as correlation times become larger than 10^{-7} s. [Also as the N_y value gets larger, the relative change in the simulated spectrum becomes smaller.]

We now wish to estimate the values of τ_R expected from the geometry of CSL and a modified Stokes-Einstein theory to see whether our results in Table III are reasonable for CSL. More precisely, we let $\tau_R = 4\pi r_e^3 \eta / 3kT$, which defines r_e , the effective rotational radius. We then follow the procedure in I used for PD-Tempone to estimate $r_e \approx 3.6$ Å for CSL from our experimental values of τ_R over the range of temperature from +15 to -6 °C (compared to 1.13 Å for PD-Tempone). The estimated geometric hydrodynamic radius r_0 (cf. part I and ref 9) is for CSL, about 6.2 Å, so that $\kappa \equiv (r_e/r_0)^3 \approx 0.2$. We have found, in our previous work on PD-Tempone in a variety of solvents that the Wirtz theory¹⁵ [which gives $\kappa = [6(r_s/r_0) + (1 + r_s/r_0)^{-3}]^{-1}$, with r_s the equivalent of r_0 but for the solvent] predicts very well the value of κ obtained from experiment as above. Since CSL and the phase V molecules are of similar size and shape, let us take $r_s/r_0 \sim 1$, which yields $\kappa \sim 1/6$ or very good agreement considering our rough approximations. It appears, therefore, that our experimental τ_R values are of the correct order.

We now consider the possibility that the magnetic axis of the nitroxide radical in DSL is tilted from the symmetry axis of alignment of the molecule by rotation in the $x-y$ plane of the nitroxide magnetic tensor principal axes.^{12,16,18} Luckhurst et al.¹⁶ estimate the tilt (or rotation) angle to be 20°, whereas Hemminga and Berendsen^{17b} estimate the angle to be smaller than 15°. We attempted to fit the slow motional spectrum of CSL in phase V at 3 °C by simulations with a tilt angle of 20°. The main effects of the tilt upon the simulated ESR spectrum for CSL in phase V are found to be an increase in the apparent g value of the calculated spectrum and an increase in the ratio a_{10}/a_{0-1} (cf. section IV) of the two hyperfine splittings when compared to spectra simulated with no tilt. Best agreement is obtained with a tilt of about 15°. However the simulated spectra were otherwise identical and the calculated C/B ratio was unaffected. Note that increased values of a_{10}/a_{0-1} may also result from fluctuating torques and presumably also slowly relaxing local structure,² thus we do not believe our result to be conclusive. The effect of tilt was not investigated in the higher temperature nematic spectra, but in the isotropic phase, the effect of a 20° tilt is merely to increase the estimated value of N_y from 5 to 8.

We have also investigated the effect of rotating the nitroxide magnetic z axis from its presumed orientation perpendicular to the long molecular axis. This has much more dramatic effect on the spectrum, by increasing the apparent splittings and widths, roughly equivalent to a

TABLE IV: Correlation Times from Slow Motional Simulations and from Subsequent Motional Narrowing Analysis and λ Values from Slow Motional Simulations and from Observed Splittings

Temp, °C	τ_R , ns, from slow motional theory	τ_R , ns, from motional narrowing analysis ^b	λ from slow motional theory	λ from obsd splittings
	0.3 ^a	0.296	0.29	
	0.52 ^a	0.50	1.09	
	0.72 ^a	0.69	1.52	
65	0.9		2.65	2.75
55	1.1	1.4	3.3	3.5
44	1.6	1.56	4.0	4.3
35	2.7	1.08	4.1	4.8
19	9	1	4.5	6.4
3	20	1.2	5.3	7.8
-6	35	1.3	6.0	9.9
-16	100	2.04	6.9	14.0
-26	260		7.6	20.0

^a These fast τ_R values are just to show the agreement between the slow motional and fast motional analyses. They do not correspond to any experimental temperatures for CSL in nematic phase V. ^b The calculated τ_R values are from B coefficients. The N_y values, calculated from motional narrowing analysis, for some temperatures are given in the caption of Figure 7.

reduction in λ . However, increasing λ does not significantly improve the simulations (since the probe is already so highly ordered that λ can only have a marginal effect on the splittings). Thus we can conclude that this rotation angle is close to zero.

IV. Validity of Motional Narrowing Approach and Relation to Other Work

Several studies of the relaxation behavior of CSL in ordered systems have recently been published.^{7,16-22} These studies have typically used simple motional narrowing theory for the line width analysis. We have found that the ESR spectrum of phase V at the elevated temperature of 55 °C²³ has asymmetric lines. Also the low-field splitting constant $a_{1,0}$ (the separation between the low field and the central line) is greater than the high field splitting constant $a_{0,-1}$ (the separation between the high field line and the central line). These features are usually indicative of the onset of the slow motional region in ESR.⁵ Since the value of τ_R at +55 °C (1.1×10^{-9} s) is still quite fast, the observed asymmetries might be largely due to the overlap of the three broadened lines. Such overlap effects (including modified relaxation behavior) are automatically included in the slow motional analysis developed by PBF.³ In the previous studies on CSL (with the exception of ref 7a, b) no such analysis was attempted. Also, those "simple" motional narrowing studies neglected the frequency dependence of secular and pseudo-secular terms. This is not justified for $\tau_R > 10^{-6}$ s.

In an effort to determine the range of validity of a motional-narrowing analysis for CSL in ordered fluids, we have performed the following test. We have taken typical simulated slow tumbling spectra using the PBF theory in which τ_R ranged from 3×10^{-10} to 10^{-7} s and we measured the line widths of the three lines. Then the fast motional theory (as given by PBF) and the already determined values of λ were utilized to obtain τ_R . These values are given in Table IV. One clearly sees that the correlation times obtained from the motional-narrowing theory do not agree with those obtained from the complete slow-motional theory for values of $\tau_R \geq 2 \times 10^{-9}$ s.²⁴ To further emphasize the inadequacy of motional-narrowing theory for these

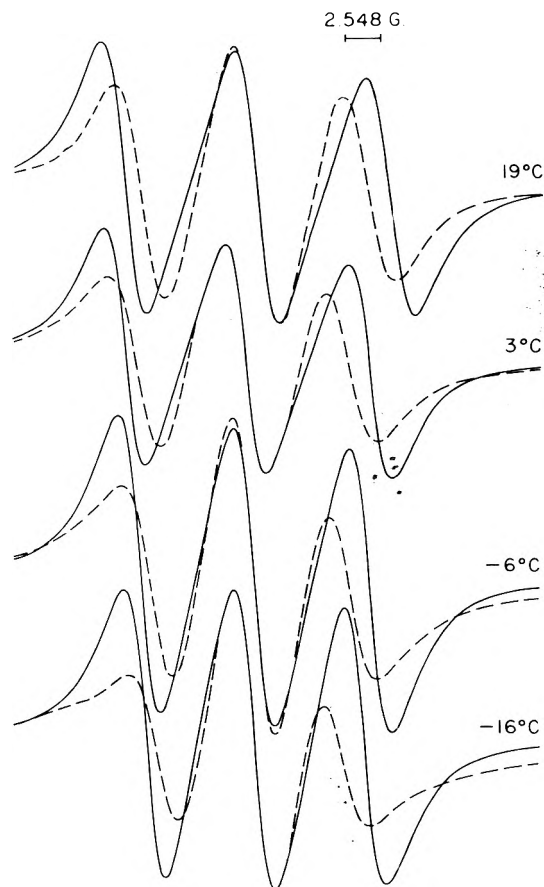


Figure 7. Comparison of experimental and simulated spectra at 19, 3, -6, and at -16 °C for CSL in phase V: (---) experimental result; (—) theoretical result based on anisotropic Brownian diffusion with the values, at +19 °C, $\tau_R = 1 \times 10^{-9}$, $N = 1.5$, $\lambda = 4.3$, and $A' = 2.7$ G; at +3 °C, $\tau_R = 1.2 \times 10^{-9}$, $N = 1.5$, $\lambda = 5.3$, and $A' = 2.7$; at -6 °C, $\tau_R = 1.3 \times 10^{-9}$, $N = 17$, $\lambda = 6.0$, and $A' = 2.4$; and at -16 °C, $\tau_R = 2.04 \times 10^{-9}$, $N = 44$, $\lambda = 6.8$, and $A' = 2.0$ G.

spectra, we have used the PBF theory to simulate the spectra for 19, 3, -6, and -16 °C, but with the τ_R and N_y values obtained from the motional narrowing analysis. They are compared with the experimental spectra in Figure 7. It is obvious from this figure that the spectra simulated in this way are not at all in agreement with the experimental spectra.

In the usual analysis, appropriate for motional-narrowing spectra, the ordering parameters, hence λ , are obtained from the spectral line position shifts. We have also checked this approach for the CSL spectra by comparing the values of λ obtained in this simple manner with the values found from the complete simulations employing the PBF theory. They are also given in Table IV, and one can see that the two λ values do not agree except for $T \geq 65$ °C. Hence it is not justified to use the values of the order parameter calculated from the splittings for CSL in phase V. From the analysis of the τ_R and λ values given above, it appears that the simple motional narrowing theory should not be used for the analysis of CSL in phase V over most of the accessible temperature range.

Luckhurst et al.^{16b} have studied CSL in a smectic A liquid crystal. They calculated $\langle P_4 \rangle$ (the average of the fourth rank Legendre polynomial) using the strong jump model. In the strong jump diffusion model, the spectral densities may be shown to depend^{6,25} explicitly on $\langle P_4 \rangle$ in the motional narrowing region. However, one must be careful that the molecular dynamics, which can be complex,^{24,11b} is treated correctly. No temperature dependence of the system has been reported. This study also neglects

the effect of the inhomogeneous broadening on the B and C coefficients. The calculated values of $\tau_{R\perp}$ are 1.4×10^{-8} from B and 3.0×10^{-8} from C . These τ_R values are, as we have seen, too large for motional narrowing theory to be valid.

Luckhurst and Poupko¹⁹ have studied the CSL in phase IV. They have again used the motional narrowing theory to estimate the ordering term $\langle P_4 \rangle$. The observed line shape asymmetry was attributed by these authors to a spread in director orientations due to thermal fluctuations. Also the calculated value of anisotropy in rotation depended on temperature ranging from $N = 16.7$ to 7.6 as the temperature decreased. These features are most likely indications of slow motional effects. Their calculated values of $\tau_{R\perp}$ are 1.6×10^{-9} at 70°C , 2×10^{-9} at 49°C , and 7×10^{-9} at 23°C . Hence, at the lower temperatures one is not justified in using motional narrowing theory. This study also neglects the effect of ordering on the unresolved proton splittings.

Luckhurst and Yeates²² have recently reported ESR studies of CSL in phase V along with other mesogens. They studied the angular dependence of the line width coefficients, by aligning the nematic phase using a strong electric field, to get the value of $\langle P_4 \rangle$. The λ value calculated from the value of $\langle P_2 \rangle \equiv \langle D_{00}^2 \rangle$ given at 34°C is 4.7 which very nearly agrees with our value of 4.8 at 35°C given in Table V based on the motional-narrowing analysis. However, the spectrum at 35°C can be correctly simulated by a complete analysis only with a value of 4.1 . Hence, it is not justified to use the $\langle P_2 \rangle$ value calculated from the splittings. This study also neglected the effect of ordering on the proton splitting constant (hence on the inhomogeneous broadening) and its dependence on the angle between the director and the magnetic axis. Here also, the calculated rotational anisotropy, N , appeared to vary with temperature. The reported $\tau_{R\perp}$ values are at 34°C , 4.4×10^{-9} from B , 6.8×10^{-9} from C and at 21°C , 6.3×10^{-9} from B , and 1.26×10^{-8} from C . These $\tau_{R\perp}$ values are again too long for the motional narrowing theory to be applicable (cf. Table IV), and for meaningful values of N to be obtained.

Hemminga^{17a} has included the angular dependence of the proton splitting constant in his corrections for inhomogeneous broadening. He obtained a value of $N = \tau_{R\perp}/\tau_{R\parallel} = 40$ with $\tau_{R\perp} = 4.6 \times 10^{-8}$ for CSL in lecithin:cholesterol model membrane system using a motional narrowing analysis. Again this motion is too slow for motional narrowing theory to be valid. Also at these long τ_R values, the simulated spectra using slow motional analysis are rather insensitive to changes in the value of N especially when N is large. Hence it is not possible to obtain accurate values of N .

Pusnik et al.²⁰ and Pusnik and Schara²¹ have also studied CSL in the nematic and in smectic A and B phases of a mesogen. They also used motional narrowing theory to estimate the value of $\langle P_4 \rangle$, but they estimate $\tau_{\perp} \geq 10^{-8}$ s which is clearly too slow for motional narrowing theory to be valid. Also, they have not included the effects of unresolved proton splittings.

Schindler and Seelig^{18b} studied CSL in a liquid-crystalline bilayer at 24°C . They report $N_y = 5.5$ and $\tau_{R\perp} = 1.2 \times 10^{-9}$. The motional narrowing approximation should be valid for this system.

V. Conclusions

It has been possible to simulate slow tumbling spectra using the PBF theory that are in good agreement with experimental spectra obtained with CSL in phase V solvent. Rather good and consistent results are obtained

particularly for the reduced temperatures, where $\tau_R > 5 \times 10^{-9}$ s, since the effects of inhomogeneous broadening due to proton superhyperfine structure as well as fluctuations in director magnitude and/or direction should be relatively less important. Our best fits were obtained with a single parameter ordering potential, no tilt of the magnetic z axis, and a somewhat anisotropic τ_R with an activation energy of 10.9 kcal/mol, almost in agreement with the activation energy obtained from the accurate study of PD-Tempone probe in the same solvent. These spectral fits were fairly insensitive to various model-dependent features such as anisotropy in rotation (except for the higher temperatures upon which our assignment of $N_y \approx 3-4$ is based), deviations from Brownian motion, and tilt of the magnetic axes in the $x-y$ plane relative to the molecular ordering axes. However, it appears that if such features are existent, then they are probably not very prominent in most of our cases. It was shown that for CSL in phase V a motional narrowing analysis is inadequate for obtaining accurate values of ordering parameter λ and τ_R over most of the nematic range, so the complete PBF theory is needed. Recent results using CSL probes in other studies on ordered fluids have typically not faced up to this necessity.

Acknowledgment. We thank Ms. J. Brown for obtaining the experimental spectra and Dr. D. Thomas for a copy of his Gaussian convolution subroutine.

References and Notes

- (1) (a) Supported in part by Grant No. CHE75-00938 from the National Science Foundation. (b) Present address: Division of Biological Sciences, National Research Council of Canada, Ottawa, Canada K1A 0R6.
- (2) C. F. Polnaszek and J. H. Freed, *J. Phys. Chem.*, **79**, 2283 (1975).
- (3) C. F. Polnaszek, G. V. Bruno, and J. H. Freed, *J. Chem. Phys.*, **58**, 3185 (1973).
- (4) J. S. Hwang, K. V. S. Rao, and J. H. Freed, *J. Phys. Chem.*, **80**, 1490 (1976).
- (5) J. H. Freed in "Spin Labeling Theory and Applications", L. J. Berliner Ed., Academic Press, New York, N.Y., 1975, Chapter 3.
- (6) C. F. Polnaszek, Ph.D. Thesis, Cornell University, Ithaca, N.Y., 1976.
- (7) (a) M. J. Neal, K. Butler, C. F. Polnaszek, and I. C. P. Smith, *Mol. Pharmacol.*, **12**, 144 (1976); (b) B. Cannon, C. F. Polnaszek, K. W. Butler, L. G. Eriksson, and I. C. P. Smith, *Arch. Biochem. Biophys.*, **165**, 613 (1975).
- (8) S. A. Goldman, G. V. Bruno, C. F. Polnaszek, and J. H. Freed, *J. Chem. Phys.*, **56**, 716 (1972).
- (9) J. S. Hwang, R. P. Mason, L. P. Hwang, and J. H. Freed, *J. Phys. Chem.*, **79**, 489 (1975).
- (10) (a) W. L. Hubbell and H. M. McConnell, *J. Am. Chem. Soc.*, **93**, 314 (1971); (b) B. J. Gaffney and H. M. McConnell, *J. Magn. Reson.*, **16**, 1 (1974).
- (11) (a) Some trends on the effects of varying τ_R and λ are illustrated in PBF. They are useful in obtaining best fits of τ_R and λ . We summarize them here. As τ_R gets larger, not only do the widths increase, but the ratios of the amplitudes of the two outer lines with respect to the central line decrease. As the ordering increases, the lines sharpen, the apparent splitting decreases, and the ratios of the amplitudes of the outer lines to the central line increases. (b) K. V. S. Rao, J. S. Hwang, and J. H. Freed, *Phys. Rev. Lett.*, **37**, 515 (1976).
- (12) T. B. Marriott, G. B. Birrell, and O. H. Griffith, *J. Am. Chem. Soc.*, **97**, 627 (1975); T. B. Marriott, Ph.D. Thesis, University of Oregon, Eugene, Oreg., 1974.
- (13) (a) M. K. Bowman, H. Hase, and L. Kevan, *J. Magn. Reson.*, **22**, 23 (1976); (b) D. D. Thomas, unpublished.
- (14) J. H. Freed, *J. Chem. Phys.*, **41**, 2077 (1964).
- (15) J. Jonas, *Adv. Magn. Reson.*, **6**, 73 (1973).
- (16) (a) G. R. Luckhurst and M. Setaka, *Mol. Cryst. Liq. Cryst.*, **19**, 295 (1973); (b) G. R. Luckhurst, M. Setaka, and C. Zannoni, *Mol. Phys.*, **28**, 49 (1974).
- (17) (a) M. A. Hemminga, *Chem. Phys.*, **6**, 87 (1974); (b) M. A. Hemminga and H. J. C. Berendsen, *J. Magn. Reson.*, **8**, 133 (1972).
- (18) (a) H. Schindler and J. Seelig, *J. Chem. Phys.*, **59**, 1841 (1973); (b) *ibid.*, **61**, 2946 (1974).
- (19) G. R. Luckhurst and R. Poupko, *Chem. Phys. Lett.*, **29**, 191 (1974).
- (20) F. Pusnik, M. Schara, and M. Sentjurs, *J. Phys. (Paris)*, **36**, 665 (1975).
- (21) F. Pusnik and M. Schara, *Chem. Phys. Lett.*, **37**, 106 (1976).
- (22) G. R. Luckhurst and R. N. Yeates, *J. Chem. Soc., Faraday Trans. 2*, **72**, 996 (1976).

- (23) These effects are consistent with the observations of critical orientational fluctuations observed^{11b} for PD-Tempone in MBBA.
- (24) We have attempted to calculate values of τ_R and N following the prescription of Luckhurst and Yeates.²² We obtained from our spectra

values of $\tau_R \lesssim 10^{-9}$ s for all temperatures and the mean value of N , was 0.4 for Brownian diffusion. For strong jump diffusion, we could not get any meaningful solutions for $\tau_{R,1}$ or N .

- (25) G. R. Luckhurst and A. Sanson, *Mol. Phys.*, **24**, 1297 (1972).

An Electron Spin-Lattice Relaxation Mechanism Involving Tunneling Modes for Trapped Radicals in Glassy Matrices. Theoretical Development and Application to Trapped Electrons in γ -Irradiated Ethanol Glasses

Michael K. Bowman* and Larry Kevan

Department of Chemistry, Wayne State University, Detroit, Michigan 48202 (Received October 15, 1976)

A new electron spin-lattice relaxation mechanism for molecular radicals in glassy matrices is developed theoretically and tested experimentally. The mechanism depends on modulation of the electron nuclear dipolar interaction between a trapped radical and nearby magnetic nuclei by the motion of tunneling nuclei or groups of nuclei in the disordered glass. In glassy systems it appears that modulation by tunneling modes is much more effective than modulation by lattice phonons for electron spin-lattice relaxation in low and intermediate temperature ranges, typically to ~ 100 K. The quantitative mechanism predicts: (a) that the spin-lattice relaxation rate T_1^{-1} is linearly proportional to temperature, (b) that T_1^{-1} is dependent on glass preparation to the extent that this affects the number and distribution of tunneling groups, (c) that T_1^{-1} is sensitive to the isotopic composition of the glass, (d) that T_1^{-1} for a given radical is larger by several orders of magnitude in a glassy environment than in a crystalline one, and (e) that $T_1^{-1} \propto \omega^{-2}$ where ω is the EPR frequency. Predictions (a) to (d) have been tested and supported by T_1 measurements vs. temperature on trapped electrons in C_2H_5OH , C_2D_5OH , and C_2H_5OD glasses. The measurements were made with a pulsed EPR spectrometer by the saturation recovery technique.

I. Introduction

The electron spin-lattice relaxation of transition metal ions and rare earth metal ions in ionic crystals has been extensively studied in the past 45 years since Waller's original paper on spin-lattice relaxation in 1932.¹ As a result, nearly all the spin-lattice relaxation mechanisms that have been investigated both experimentally and theoretically are constrained by the conditions found in these systems. That is, strong crystalline fields and spin-orbit coupling are assumed for the ion in the crystal and the dynamics of the lattice is described in terms of the Debye model with only few modifications for the effects of phonon lifetime and crystal defects.²

The study of the spin-lattice relaxation of molecular radicals in molecular crystals and glasses is still in its infancy. The first report of the temperature dependence of the spin-lattice relaxation of an organic radical was made in 1957.³ The spin-lattice relaxation time (T_1) was measured at four temperatures between 1.2 and 300 K and no attempt was made to explain either the magnitude of T_1 , which was many orders of magnitude longer than that of transition metal ions, or the spin-lattice relaxation mechanisms involved. Nine years later, three surveys of different classes of radicals (organic, organosulfur, and peroxy) were reported.⁴⁻⁶ Over the limited range of temperature in these studies, T_1 was proportional to T^{-n} where n varied from 1 to 3. More importantly, for determining the relaxation mechanism, the spin-lattice relaxation rates in each study were found to be highly correlated with the square of the g factor deviation from

the free electron value of 2.0023 and hence with spin-orbit coupling. This suggested that the Kronig-VanVleck spin-lattice relaxation mechanism was important. Other studies have supported this.^{7,8} The internal motions and hindered rotations of a molecular radical have also been suggested as an important relaxation mechanism.⁹⁻¹²

At this same time, careful studies of the spin-lattice relaxation mechanisms of F centers (trapped electrons) in alkali halide crystals have shown that the electron nuclear dipolar (END) and isotropic hyperfine interactions between the unpaired electron and its surrounding magnetic nuclei can make important contributions to the electron relaxation.^{13,14}

An extensive study of the spin-lattice relaxation of a number of hydro-, deuterio-, and fluorocarbon radicals produced by ionizing radiation in single crystals of the parent compound has been made by Dalton, Kwiram, and Cowen.^{15,16} They report that the Kronig-VanVleck relaxation mechanism is responsible for the spin-lattice relaxation of all but the fluorinated radicals. The spin-lattice relaxation of the fluorinated radicals is dominated by modulation of the END interaction. In addition, they report observing an Orbach-like process in some of the samples in which the intermediate state is suggested to be an excited vibrational state of the radical instead of an excited electronic state as in the usual Orbach process.

Although these studies have demonstrated several important relaxation mechanisms for molecular radicals in single crystals, they by no means include all the dominant mechanisms in molecular glasses. DPPH in polystyrene has been the subject of two spin-lattice relaxation studies.^{17,18} Between 1 and 300 K, the relaxation rate is proportional to the temperature. This is a surprising

* Present Address: Argonne National Laboratory, Chemistry Division, Argonne, Ill. 60439

result. Whatever the relaxation mechanism, if the low temperature relaxation represents a direct process (absorption or emission of lattice phonons resonant with the EPR transition), then a much stronger temperature dependence is expected above at least 50 K due to a Raman, Orbach, or other higher order process involving multiple phonon scattering. What is almost more surprising is that the T_1 of the triphenylmethyl radical³ in a single crystal host is about four orders of magnitude longer at 1.2 K than the T_1 of DPPH¹⁷ in glassy polystyrene at the same temperature. Although it has been noticed that nuclear spin-lattice relaxation is usually faster in glassy samples than in crystalline samples of the same compound,¹⁹⁻²² the paucity of careful relaxation studies of the same radical in both glassy and crystalline states has prevented such comparisons in EPR. Reinecke and Ngai²¹ have proposed a model for nuclear relaxation in which nuclear spin energy is removed by a "Raman" type process involving two tunneling modes and Rubinstein and Reising²² have considered the effect of tunneling modes on the scattering of low energy phonons in connection with nuclear spin-lattice relaxation.

We have recently investigated the electron spin-lattice relaxation of trapped electrons and trapped hydrogen atoms in a number of molecular glasses.²³ It is found that the relaxation rate at low temperature is proportional to the temperature and is several orders of magnitude faster than reported for those radicals in single crystals.^{13,14,24} Here, we wish to present a new relaxation mechanism, unique in some respect to the glassy state, which may be responsible for the low temperature spin-lattice relaxation of many molecular radicals in molecular glasses.

II. Theory

Electron spin-lattice relaxation occurs due to a time-dependent perturbation of the electron spin by its environment. In a calculation of the spin-lattice relaxation rate as a function of temperature in solids, it is necessary to have some model for the dynamics of the solid lattice. The lattice dynamics is almost always described using the Debye model²⁵ of a monoatomic crystal²⁶ although some consideration has been given to the effects of lattice anharmonicity,²⁷ crystalline defects,²⁸⁻³⁷ and optical phonons.^{38,39}

Lattice Dynamics. The assumptions of the Debye model seem quite reasonable for most crystals and this model has been quite successful in predicting not only the temperature dependence of the spin-lattice relaxation rate of a number of paramagnetic metal ions in ionic crystals, but also many of the physical properties of crystals at low temperatures. The record of the Debye model has not been as good in low temperature glasses, however. For example, although it predicts that the heat capacity at low temperatures should be proportional to the cube of the temperature for both glasses and crystals, the heat capacity of glasses is linearly proportional to the temperature and is many times greater than that of a crystal of the same substance.⁴⁰ Several other physical properties of glasses at low temperature are equally anomalous, suggesting the presence of additional low energy modes in glasses that are lacking in crystals.⁴⁰⁻⁴²

Tunneling Modes. A recent model for the low temperature lattice dynamics of a glass is that of Phillips⁴³ and of Anderson, Halperin, and Varma.⁴⁴ This model envisions that, in a glass, there are a number of atoms or molecules for which the local potential has more than one minimum. If the potential for these atoms or molecules increases rapidly enough away from the minima, the only thermally populated states below room temperature will be the

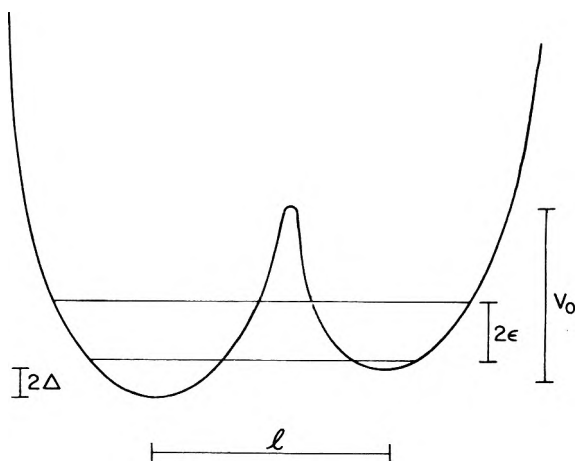


Figure 1. Symbolic diagram of the double potential well of the tunneling particle. The distance l separates the two minima which differ in energy by 2Δ . The barrier between minima is V_0 and the energy difference between the two tunneling states is 2ϵ .

coupled tunneling states of the multiple potential well.

For our purposes, we will describe these tunneling modes in the same manner as Phillips⁴³ did. The tunneling particle is in a potential field which can be represented by the one-dimensional potential function in Figure 1. It is formed from two harmonic oscillator potentials with minima displaced by distance l and energy 2Δ . Between the two minima is an energy barrier of height V_0 . The two lowest energy levels (the only ones populated at the temperatures considered here) have energies of $\pm\epsilon = (\Delta_0^2 + \Delta^2)^{1/2}$ where $\Delta_0 = \hbar\Omega(\sigma/\pi)^{1/2}e^{-\sigma}$ and Ω is the frequency of oscillation in one of the isolated harmonic potentials comprising the total potential, $\sigma = (mV_0\hbar^{-2})^{1/2}l$, and m is the mass of the tunneling particle.

Phillips^{43,45} has both calculated the temperature dependence of the relaxation time of tunneling modes and measured this same quantity in low temperature dielectric relaxation experiments on polyethylene. The relaxation time of tunneling modes τ is given by $1/\tau = w_{12} + w_{21}$ where w_{12} and w_{21} are transition rates between the two energy levels in each direction. This is closely related to the characteristic correlation time τ_c for the tunneling particle given by $1/\tau_c = n_1w_{12} + n_2w_{21}$ where n_1 and n_2 are the populations of the two levels. If the tunneling modes are assumed to be in thermal equilibrium at a temperature T then

$$\frac{1}{\tau_c} = \frac{1}{2\tau \cosh^2(\epsilon/kT)} \propto \frac{b^2 \Delta_0^2 \epsilon}{v^5 \rho} \operatorname{csch}\left(\frac{2\epsilon}{kT}\right) = D\epsilon \operatorname{csch}\left(\frac{2\epsilon}{kT}\right) \quad (1)$$

where b is the strength of coupling between the tunneling mode and the lattice phonons, v is the velocity of sound in the solid, and ρ is the density of the solid.

Tunneling Mode-Electron Spin Interaction. The motion of the tunneling particle can affect the electron spin of a radical in several ways. Since we are concerned here with radicals having little spin-orbit coupling, the main interaction between the electron spin and the motion of the tunneling particle is the END interaction.

By expanding the dipolar interaction around the coordinate j along which tunneling occurs we have

$$\mathcal{H}_{\text{END}}(t) = \langle \mathcal{H}_{\text{END}} \rangle + \frac{\partial \mathcal{H}_{\text{END}}}{\partial j} (j(t) - \langle j \rangle) + \dots$$

where $\langle \rangle$ denote the time average. Since j takes on only

one of two values, the spin-lattice relaxation rate between spin states $|\sigma_1\rangle$ and $|\sigma_2\rangle$ is given by

$$\frac{1}{T_1} = \frac{1}{\hbar^2} |\langle \sigma_1 | \frac{\partial \mathcal{H}_{\text{END}}}{\partial j} | \sigma_2 \rangle|^2 \frac{2\tau_c}{1 + \omega^2 \tau_c^2} = \omega^2 C \frac{\tau_c}{1 + \omega^2 \tau_c^2} \quad (2)$$

where ω is the EPR frequency. Measurements by Phillips⁴⁵ on tunneling modes in polyethylene indicates that the characteristic correlation time τ_c is much greater than the inverse of the EPR frequency ω at x-band so that eq 2 can be written as

$$\frac{1}{T_1} = \frac{2}{\hbar^2} |\langle \sigma_1 | \frac{\partial \mathcal{H}_{\text{END}}}{\partial j} | \sigma_2 \rangle|^2 \frac{1}{\omega^2 \tau_c} = \frac{C}{\omega^2 \hbar^2} |\langle \sigma_1 | \frac{\partial \mathcal{H}_{\text{END}}}{\partial j} | \sigma_2 \rangle|^2 \frac{b^2 \Delta_0^2 \epsilon}{v^5 \rho} \text{csch} \left(\frac{2\epsilon}{kT} \right) \quad (3)$$

This has the same temperature dependence as does spin-lattice relaxation via a symmetric double potential tunneling mode³¹ and via the tunneling rotation of a methyl group.¹⁰

Spin-Lattice Relaxation Rate. The calculation of the spin-lattice relaxation rate for molecular radicals in a glass can now be attempted. Since, for most molecular radicals in glasses, $T_2 \ll T_1$ and the spectral diffusion time within an EPR line is short compared with T_1 , the T_1 for radicals in the glass, each of which may interact differently with neighboring tunneling modes, is determined by the average spin-lattice relaxation rate for the assemblage of radicals. Thus

$$\langle T_1^{-1} \rangle = N^{-1} \sum_{i=1}^N T_1^{-1}(i)$$

and the calculation of the spin-lattice relaxation rate is then the integration of eq 3 over the appropriate distributions of l , $\partial \mathcal{H}_{\text{END}}/\partial j$, b , Δ_0 , and ϵ . Assuming that l , $\partial \mathcal{H}_{\text{END}}/\partial j$, b , and Δ_0 are not correlated with ϵ , we may write

$$\frac{1}{T_1} = \frac{2}{\omega^2 \hbar^2} \left\langle |\langle \sigma_1 | \frac{\partial \mathcal{H}_{\text{END}}}{\partial j} | \sigma_2 \rangle|^2 \frac{b^2 \Delta_0^2}{v^5 \rho} \right\rangle \times \int_0^\infty \epsilon \text{csch} \left(\frac{2\epsilon}{kT} \right) n(\epsilon) d\epsilon = \langle \text{CD} \rangle \int_0^\infty \epsilon \text{csch} \left(\frac{2\epsilon}{kT} \right) n(\epsilon) d\epsilon \quad (4)$$

where $n(\epsilon)$ is the density of tunneling modes with an energy splitting between tunneling levels of 2ϵ .

The distribution of tunneling mode splittings, $n(\epsilon)$, is not known in glasses. Our model for the tunneling mode dynamics requires that $\epsilon \ll \hbar\Omega$, so that $n(\epsilon)$ must be large for small ϵ and must effectively vanish for ϵ/k of the order of 50 K. This is reasonable on physical grounds. Large ϵ requires Δ and $V_0^{1/2}l$ to be large, but l is limited to about twice the diameter of the tunneling group and V_0 and Δ are likely to be negatively correlated. We shall therefore use four different distributions of tunneling mode splittings to examine the effect of the form of the distribution on the temperature dependence of the spin-lattice relaxation rate.

Delta Function Distribution. For $n(\epsilon) = \delta(\epsilon - \epsilon')$, which corresponds to identical tunneling modes, eq 4 gives

$$\frac{1}{T_1} = \langle \text{CD} \rangle \epsilon' \text{csch} \left(\frac{2\epsilon'}{kT} \right) \quad (5)$$

in agreement with Murphy³¹ and Gamble et al.¹⁰ The

interesting feature to note about eq 5 is that for $kT > 2\epsilon'$

$$\frac{1}{T_1} = \langle \text{CD} \rangle \frac{kT}{2\epsilon} \quad (6)$$

which is a different high temperature limit from the usual $T_1^{-1} \propto T^2$ limit for most relaxation mechanisms.

Inverse ϵ Distribution. For a distribution given by

$$n(\epsilon) \propto \begin{cases} 0 & \text{for } \epsilon < \Delta_0 \\ \epsilon^{-1} & \text{for } \epsilon \geq \Delta_0 \end{cases}$$

(we realize that there must also be a limit at large ϵ since $\int_0^\infty n(\epsilon) d\epsilon$ must converge) eq 4 becomes

$$\frac{1}{T_1} \propto \langle \text{CD} \rangle \int_{\Delta_0}^\infty \epsilon \text{csch} \left(\frac{2\epsilon}{kT} \right) \frac{1}{\epsilon} d\epsilon = \langle \text{CD} \rangle \int_{\Delta_0}^\infty \text{csch} \left(\frac{2\epsilon}{kT} \right) d\epsilon = \langle \text{CD} \rangle \frac{kT}{2} \ln \coth \left(\frac{\Delta_0}{kT} \right) \quad (7)$$

For $kT \gg \Delta_0$, eq 7 becomes

$$\frac{1}{T_1} \propto \langle \text{CD} \rangle \frac{kT}{2} \ln \left(\frac{kT}{\Delta_0} \right) \quad (8)$$

In any reasonable temperature range above 4.2 K, eq 8 is very close to being linearly proportional to temperature.

Step Function Distribution. A step function distribution for $n(\epsilon)$ may be chosen by the conditions

$$n(\epsilon) \propto \begin{cases} 0 & \text{for } \epsilon < \Delta_0 \\ \text{constant} & \text{for } \Delta_0 \leq \epsilon \leq \epsilon_m \\ 0 & \text{for } \epsilon > \epsilon_m \end{cases}$$

for which there are a constant number of tunneling modes with splitting between ϵ and $\epsilon + d\epsilon$ within a certain range of ϵ and no modes outside that range. The average spin-lattice relaxation time is then given as

$$\frac{1}{T_1} \propto \langle \text{CD} \rangle \int_{\Delta_0}^{\epsilon_m} \epsilon \sum_{n=0}^\infty e^{-(2n+1)2\epsilon/kT} d\epsilon \quad (9)$$

where the csch function has been expanded as an infinite series. Integration of eq 9 yields

$$\frac{1}{T_1} \propto \langle \text{CD} \rangle kT \sum_{n=0}^\infty \frac{\exp[-(2n+1)2\Delta_0/kT]}{(2n+1)^2} \left\{ (1 - \exp[-(2n+1)2p/kT]) (kT + 2\Delta_0(2n+1)) - 2p(2n+1) \exp[-(2n+1)2p/kT] \right\} \quad (10)$$

where $p = \epsilon_m - \Delta_0$. When $p \ll kT$, the infinite sum in eq 10, is proportional to $T^{-1} \text{csch} 2\Delta_0/kT$ so that $T_1^{-1} \propto \text{csch} (2\Delta_0/kT)$. When p is no longer much smaller than kT , which occurs as the temperature is lowered, and the range of splittings of tunneling modes becomes comparable to the thermal energy, the spin-lattice relaxation rate becomes a much stronger function of temperature.

Low Energy Distribution. If all the tunneling mode energies are well below thermal energy (i.e., $n(\epsilon) \neq 0$ only when $\epsilon \ll kT$) then $\text{csch} (2\epsilon/kT)$ can be expanded keeping only the first term, $kT/2\epsilon$, and so

$$\frac{1}{T_1} \propto \langle \text{CD} \rangle \int_0^\infty \epsilon \frac{kT}{2\epsilon} n(\epsilon) d\epsilon = \langle \text{CD} \rangle \frac{kT}{2} \int_0^\infty n(\epsilon) d\epsilon \quad (11)$$

The integral in eq 11 is just the number of tunneling modes

and is not a function of temperature so $T_1^{-1} \propto T$.

General Form of the Temperature Dependence. We have calculated the functional form of the temperature dependence of spin-lattice relaxation due to tunneling modes at temperatures well in excess of the tunneling mode splitting in eq 5, 7, 10, and 11. All of these functions have in common that, above a certain temperature, the spin-lattice relaxation rate is proportional to the temperature of the sample. In addition eq 5, 7, and 10, which are valid for lower temperatures also, have a much stronger temperature dependence at very low temperatures.

This is in strong contrast to the more normal relaxation mechanisms due to lattice phonons which have been well studied in single crystals doped with paramagnetic transition metal ions. There, the relaxation rate at very low temperatures is constant, then becomes linear with temperature above about 2 K, and finally increases at a rate between T^2 and T^0 at higher temperatures before falling back to T^2 far above the Debye temperature of the crystal. Because of the different forms of temperature dependence of spin-lattice relaxation due to tunneling modes and lattice phonons, it is not unexpected to find that different mechanisms are dominant in different temperature regions. Also, we expect that the characteristic correlation time is underestimated by eq 1 at temperatures above 100 or 200 K as discussed by Phillips.^{43,45}

In studies of simple molecular radicals in glasses we have found that the spin-lattice relaxation rate is often affected by cross relaxation with paramagnetic impurities below about 4 K, is dominated by tunneling modes between 4 and 100 K, and is a complex function of several mechanisms above 100 K.

Effect of Isotopic Doping. Preparation of glasses having different nuclear isotopic compositions affects the spin-lattice relaxation rate in two ways. The first is by modifying the END interaction between the isotopically substituted nucleus and the radical, and the second is by altering the dynamics of the tunneling mode itself.

The portion of the END Hamiltonian connecting different electron spin states is

$$\mathcal{H}_{\text{END}} = \frac{\gamma_e \gamma_n \hbar^2}{r^3} \left[-(1/4)(S^+I^- + S^-I^+)(1 - 3 \cos^2 \theta) - (3/2)(S^+I_z + S^-I_z) \sin \theta \cos \theta - (3/4)(S^+I^+ + S^-I^-) \sin^2 \theta \right] \quad (12)$$

where r is the length of the vector \hat{r} between the radical and the nucleus under consideration and θ is the angle between \hat{r} and \hat{H}_0 , the static magnetic field. Since fast spectral diffusion is assumed, all the terms in eq 12 are important. Assuming that all relative orientations between the radical and the tunneling direction are equally probable, the average of $|\langle \sigma_1 | (\partial \mathcal{H}_{\text{END}} / \partial j) | \sigma_2 \rangle|^2$ over all angles θ , this average being denoted by a single overhead bar, is

$$\begin{aligned} \overline{|\langle \sigma_1 | \frac{\partial \mathcal{H}_{\text{END}}}{\partial j} | \sigma_2 \rangle|^2} &= \frac{l^2}{3} \frac{1}{2} \int_0^{\pi/2} \sin \theta \\ &\times \sum_{m_1} \sum_{m'_1} \left(\langle +m_1 | \frac{\partial \mathcal{H}_{\text{END}}}{\partial r} | -m'_1 \rangle^2 \right. \\ &\left. + \langle +m_1 | \frac{1}{r} \frac{\partial \mathcal{H}_{\text{END}}}{\partial \theta} | -m'_1 \rangle^2 \right) d\theta \quad (13) \end{aligned}$$

where $\langle + |$ and $\langle - |$ represent the two electron spin functions of the radical and $\langle m_1 |$ and $\langle m'_1 |$ represent the nuclear spin functions of the tunneling nucleus. The evaluation of eq 13 for a tunneling proton yields $33l^2\gamma_e^2\gamma_H^2\hbar^4/30r^8$ while

evaluation for a deuteron yields $702l^2\gamma_e^2\gamma_D^2\hbar^4/360r^8$. The ratio of these transition moments is

$$\begin{aligned} \frac{|\langle \sigma_1 | l \frac{\partial \mathcal{H}_{\text{END}}}{\partial j} | \sigma_2 \rangle_D|^2}{|\langle \sigma_1 | l \frac{\partial \mathcal{H}_{\text{END}}}{\partial j} | \sigma_2 \rangle_H|^2} \\ = \frac{\gamma_D^2}{\gamma_H^2} \frac{39}{11} \approx 0.084 \quad (14) \end{aligned}$$

Assuming that ϵ is determined more by Δ than Δ_0 , the term in eq 3 most sensitive to isotopic substitution is $\Delta_0^2 \nu^{-5} \rho^{-1}$. This term is basically a function of density since both Δ_0 and ν depend on density. The velocity of sound ν is proportional to the reciprocal square root of matrix density, and $\Delta_0 \propto m^{-1/4} \exp(-m^{1/2})$ where m is the mass of the tunneling particle. For many organic and aqueous glasses, deuteration increases the glass density by about 10%.

This magnitude of the deuteration effect on relaxation rates is determined by the identity of the tunneling particle. If the tunneling particle contains no hydrogen nuclei and the END interaction responsible for inducing spin-lattice relaxation does not involve hydrogen nuclei, deuteration does not change the END transition moment. Then we find

$$T_1(\text{H})/T_1(\text{D}) = 0.9^{-3/2} = 1.17 \quad (15)$$

If the END interaction with hydrogen nuclei is dominant and deuteration produces little change in the mass of the tunneling particle, then

$$T_1(\text{H})/T_1(\text{D}) = 0.084 \times 0.9^{3/2} = 0.10 \quad (16)$$

Finally, if the tunneling particle mass is determined directly by the mass of the hydrogen nucleus (e.g., rotational tunneling of a methyl group or tunneling of a hydrogen nucleus), then

$$\begin{aligned} \frac{T_1(\text{H})}{T_1(\text{D})} &= 0.84 \times 0.9^{-3/2} \left(\frac{m_D}{m_H} \right)^{-1/2} \frac{\exp(-2m_D^{1/2})}{\exp(-2m_H^{1/2})} \\ &= 0.030 \quad (17) \end{aligned}$$

Thus deuteration of an organic or aqueous glass will produce a change in the spin-lattice relaxation rate ranging from a 20% increase to a 97% decrease.

III. Experimental Section

The electron spin-lattice relaxation times of trapped electrons in $\text{C}_2\text{H}_5\text{OH}$, $\text{C}_2\text{D}_5\text{OH}$, and $\text{C}_2\text{H}_5\text{OD}$ were measured between 5 and 150 K on a time domain X-band EPR spectrometer built in this laboratory.²³ It is a single klystron superheterodyne spectrometer with 60-MHz IF and 14-MHz bandwidth with synchronous demodulation of the IF. It is operated using the saturation recovery technique for measuring T_1 . A pulse of 40-mW microwaves or less is applied to the EPR signal of the radical whose T_1 is to be measured for a length of time longer than any relaxation time of the sample in order to saturate or partially saturate the EPR signal. After the saturating pulse, the recovery of the EPR signal from saturation is monitored with microwaves coherent with the saturating pulse but at a level low enough not to disturb directly the electron spin populations. No magnetic field modulation is used while measuring the recovery of the EPR signal from saturation or while saturating the EPR signal. This spectrometer has measured spin-lattice relaxation times ranging from 200 ns to 1 s and can monitor the recovery of the EPR signal with microwave powers ranging from 400 μW to 40 pW.

The recovery of the EPR signal from saturation is recorded using either a PAR TDH-9 waveform eductor or

a PAR 162 boxcar averager. The conditioned output from either of these data acquisition devices is processed by a logarithmic amplifier and recorded on an X-Y recorder. The spin-lattice relaxation rate is then recovered from the slope of the straight lines on the X-Y recorder.

The temperature dependence of T_1 is determined by fitting the equation

$$T_1^{-1} = D^2 T + O^2 \exp(-t^2/T) \quad (18)$$

to the experimental data. The parameters D , O , and t are varied with a weighted, non-linear, iterative, least-squares computer program supplied by the Wayne State University Computer and Data Processing Center⁴⁶ which uses the Marquardt method.⁴⁷ In each iteration, the data were weighted by the current predictions of T_1 using eq 18. The linear function of temperature in eq 18 represents the tunneling relaxation mechanism discussed in section II. The exponential function of the temperature represents the relaxation mechanisms dominant at high temperatures and is used in preference to a different function more for its utility than for any theoretical reason.

The EPR cavity is a Varian V-4531 rectangular single cavity. An Air Products LTD 30110 Helitran unit inserted into the cavity cools the sample. The sample cavity serves as the dispersive element in the AFC loop so the klystron frequency is locked at all times to the sample cavity. The sample temperature is stabilized using an Artronix 5301 temperature controller to drive the heater in the Helitran unit. The Artronix 5301 senses the temperature near the sample with a 50- Ω , 0.25-W carbon resistor. The temperature of the helium gas stream immediately above the sample is measured by the GaAs diode sensor of a PAR 156 cryothermometer or by a Digitek digital thermometer using a copper-constantan thermocouple.

The magnetic field is provided by a Varian 9-in. magnet with a Mark I Fieldial control.

The C_2H_5OH used was anhydrous Rossville Gold Shield alcohol, anhydrous C_2H_5OD was obtained from Stohler Isotope Chemicals, and anhydrous C_2D_5OH was from Merck Sharpe and Dohme of Canada, Ltd. These chemicals were used as received without further purification and without the addition of water. Samples were made by sealing these chemicals in short sections (4-5 cm) of evacuated spectroil quartz tubing. The samples were carefully frozen by slowly lowering each tube into liquid nitrogen at the fastest rate which gave very little bubbling of the liquid nitrogen. The freezing was performed as reproducibly as possible since the freezing rate appears to affect the structure of the glass.^{23,48}

The samples were irradiated in a US Nuclear Corporation GR-9 Co-60 γ -irradiator at a dose rate of approximately 0.16 Mrad/h to a dose of 1 Mrad. During and after irradiation, the samples were kept in liquid nitrogen in the dark.

IV. Results and Discussion

The spin-lattice relaxation rates of trapped electrons in the three ethanol samples are plotted as a function of temperature in Figure 2. Care was taken during the measurements that the saturating pulse was much larger than any relaxation time of the sample (pulse lengths varied from 15 ms at high temperatures to 1 s at low temperatures) and that the microwave power used to monitor the recovery did not perturb the spin system (microwave powers varied from 100 to 0.1 nW). The relaxation rates under these conditions were found to be independent of pulse length or monitoring power. The solid lines in Figure 2 are the least-squares fits of eq 18

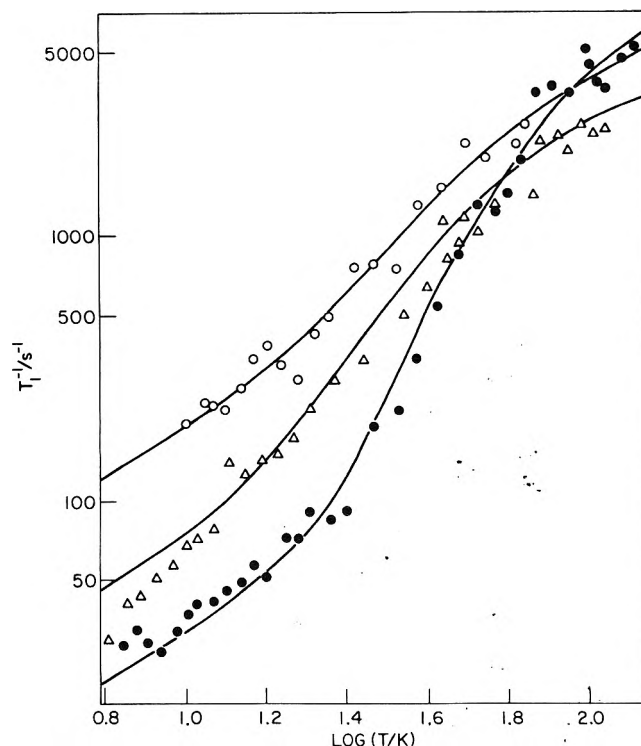


Figure 2. The spin-lattice relaxation rate as a function of temperature of trapped electrons in C_2H_5OH (open circles), C_2H_5OD (open triangles), and C_2D_5OH (solid dots). The lines are the least-squares fits described in the text.

TABLE I: Optimized Parameters of $1/T_1 = D^2 T + O^2 \exp(-t^2/T)$ for Relaxation Rates of Trapped Electrons in Ethanol Glasses

Matrix	$D^2, s^{-1} K^{-1}$	O^2, s^{-1}	t^2, K
C_2H_5OH	18.9	4.74×10^3	84
C_2H_5OD	7.30	4.71×10^3	92
C_2D_5OH	3.22	1.69×10^4 ^a	148 ^a

^a The magnitude of the correlation between these parameters is greater than 0.90.

to the data points. The coefficients of these fits are listed in Table I. It is seen that the data are well represented by eq 18 without invoking a temperature independent term expected for a cross relaxation mechanism. Apparently cross relaxation from trapped electrons in ethanol glasses to any other radical at the dose and temperatures used in this study is unimportant.

A striking feature of the results in Table I is that the coefficient of the relaxation process whose rate is proportional to temperature, i.e., D^2 , shows a strong deuteration dependence. This is entirely as predicted on the basis of the theory presented in section II. In fact it is not unreasonable to extrapolate a value for the C_2D_5OD glass prepared in the same fashion of less than $1.9 s^{-1} K^{-1}$ as predicted by eq 16 and 17.

It is generally accepted that the trapped electron in ethanol consists of an electron trapped in the combined potential fields of four or six ethanol molecules oriented with either the OH bond dipoles or molecular electric dipoles oriented toward the trapped electron.^{49,50} In either case, the hydroxyl groups are nearest the electron and are the strongest contributors to the trapped electron's total hyperfine interaction. The ethyl group is farther away and interacts less strongly. As a result, the EPR line width of the trapped electron is much larger in C_2D_5OH than C_2H_5OD . Since the hydroxyl group has a large bond dipole and is closest to the trapped electron, the hydroxyl is presumably held rather rigidly by the electric field of the

trapped electron. In contrast, the ethyl group should be much less restricted in its motion as should the hydroxyl groups of molecules which do not participate in the electron trap. As a consequence, the spin-lattice relaxation model presented here predicts that the tunneling of the ethyl groups is more important than hydroxyl group tunneling for the electron spin-lattice relaxation. This is exactly what is observed.

Anything that affects the structure of the glass and the number and distribution of tunneling modes, e.g., the freezing rate of the matrix, should have a large effect on the coefficient of the relaxation process which varies linearly with temperature. We have observed this in several systems and this makes exact quantitative comparison between different samples somewhat risky.

A further test that the relaxation process with a linear temperature dependence seen here is to be identified with the tunneling mechanism is that the coefficient of the observed rate (D^2) must be much larger than the coefficient of the similar term in the relaxation of a trapped electron in a crystalline environment. This criterion can be assessed from the relaxation data on trapped electrons (F centers) in alkali halide single crystals.^{13,14} The coefficient of the relaxation process whose rate is linearly proportional to temperature is about $10 \text{ s}^{-1} \text{ K}^{-1}$ for electrons in ethanol glass compared to $5 \times 10^{-5} \text{ s}^{-1} \text{ K}^{-1}$ for electrons in KCl crystals! The F centers and trapped electrons in alcohol glasses are quite comparable in both their optical and magnetic properties^{49,51} except for their spin-lattice relaxation mechanism. Spin-lattice relaxation of F centers at low temperature is due to modulation of the END interaction by lattice phonons, while modulation of the crystalline field by lattice phonons is ineffective in crystals containing no heavy atoms. We conclude that relaxation of trapped electrons in ethanol glass is due to modulation of the END interaction by tunneling modes associated with the glass structure and that this is much more effective than modulation by lattice phonons. Experiments on trapped electrons and trapped hydrogen atoms in other crystalline and glassy matrices show the same striking difference. These studies will be reported elsewhere.

V. Conclusion

We have described an electron spin-lattice relaxation mechanism expected to be important for molecular radicals in glasses. The mechanism depends on modulation of the END interaction between the radical and nuclei in its glassy environment by the motion of tunneling nuclei or groups of nuclei in the glass. This mechanism predicts: (a) that $T_1^{-1} \propto T$ above a few degrees Kelvin, (b) that T_1^{-1} is dependent on the preparation of the glass to the extent that the preparation affects the number and distribution of tunneling groups, (c) that T_1^{-1} is sensitive to the isotopic composition of the glass, (d) that T_1^{-1} for a given molecular radical is much larger in a glass than in a single crystal, and (e) $T_1^{-1} \propto \omega^{-2}$ where ω is the EPR frequency.

The results of T_1 measurements on trapped electrons in $\text{C}_2\text{H}_5\text{OH}$, $\text{C}_2\text{D}_5\text{OH}$, and $\text{C}_2\text{H}_5\text{OD}$ glasses in comparison with the literature results on T_1 measurements of F centers (trapped electrons) in KCl crystals support the tunneling mechanism for glasses. We find (a) $T_1^{-1} \propto T$ for trapped electrons in ethanol glass between 7 and about 100 K, (b) that the relaxation rate in a glass depends on the details of glass preparation, (c) that T_1 is sensitive to deuteration of the glass, and (d) that the relaxation rate of trapped electrons is about 10^5 times larger for the $T_1^{-1} \propto T$ process

in ethanol glass than in KCl crystals. We have been unable to test prediction (e) because we are experimentally limited to T_1 measurements at a single EPR frequency.

Acknowledgment. This research was supported by the U.S. Energy Research and Development Administration under Contract E(11-1)-2086. Michael Bowman is grateful to the National Science Foundation and to Wayne State University for Graduate Fellowships.

References and Notes

- (1) I. Waller, *Z. Phys.*, **79**, 370 (1932).
- (2) A. A. Manenkov and R. Orbach, Ed., "Spin-Lattice Relaxation in Ionic Solids", Harper and Row, New York, N.Y., 1966.
- (3) S. I. Weissman, G. Feher, and E. A. Gere, *J. Am. Chem. Soc.*, **79**, 5584 (1957).
- (4) T. S. Zhuravleva, *Zh. Strukt. Khim.*, **7**, 800 (1966).
- (5) K. Akasaka, *J. Chem. Phys.*, **45**, 90 (1966).
- (6) I. V. Aleksandrov, L. Ya. Dzhavakhishvili, and G. D. Kettladze, *Teor. Eksp. Khim.*, **2**, 97 (1966).
- (7) I. M. Brown, *J. Chem. Phys.*, **55**, 2377 (1971).
- (8) I. M. Brown and D. J. Sloop, *J. Chem. Phys.*, **47**, 2659 (1967).
- (9) M. Fujimoto and J. Janicka, *J. Chem. Phys.*, **55**, 5 (1971).
- (10) W. I. Gamble, I. Miyagawa, and R. L. Hartman, *Phys. Rev. Lett.*, **20**, 415 (1968).
- (11) H. Yoshida, K. Hayashi, and S. O. Kamura, *Ark. Khim.*, **23**, 177 (1964).
- (12) S. K. Rengan, M. P. Khakhar, B. S. Prabhananda, and B. Venkatarams, *J. Pure Appl. Chem.*, **32**, 287 (1972).
- (13) D. W. Feldman, R. W. Warren, and J. G. Castle, Jr., *Phys. Rev. A*, **135**, 470 (1964).
- (14) H. Panepucci and L. F. Mollenauer, *Phys. Rev.*, **178**, 589 (1969).
- (15) L. R. Dalton, A. L. Kwiram, and J. A. Cowen, *Chem. Phys. Lett.*, **14**, 77 (1972).
- (16) L. R. Dalton, A. L. Kwiram, and J. A. Cowen, *Chem. Phys. Lett.*, **17**, 495 (1972).
- (17) T. J. B. Swanenburg, N. J. Poulis, and G. W. J. Drewes, *Physica*, **24**, 713 (1963).
- (18) J. Turkevich, J. Soria, and M. Che, *J. Chem. Phys.*, **56**, 1463 (1972).
- (19) J. Haupt, *Proc. Colloq. AMPERE*, **16th**, 630 (1970).
- (20) (a) M. Rubinstein and P. C. Taylor, *Phys. Rev. B*, **9**, 4258 (1974); (b) J. Szeftel and H. Alloul, *Phys. Rev. Lett.*, **34**, 657 (1975); (c) M. Rubinstein, H. A. Resing, T. L. Reinecke, and K. L. Ngai, *ibid.*, **34**, 1444 (1975).
- (21) T. L. Reinecke and K. L. Ngai, *Phys. Rev. B*, **12**, 3476 (1975).
- (22) M. Rubinstein and H. A. Resing, *Phys. Rev. B*, **13**, 959 (1976).
- (23) M. K. Bowman, Ph.D. Dissertation, Wayne State University, 1975.
- (24) D. W. Feldman, J. G. Castle, Jr., and J. Murphy, *Phys. Rev. A*, **138**, 1208 (1965).
- (25) C. Kittel, "Introduction to Solid State Physics", 4th ed. Wiley, New York, N.Y., 1971, Chapter 6.
- (26) I. V. Aleksandrov, *Zh. Eksp. Teor. Fiz.*, **48**, 864 (1965); *Teor. Eksp. Khim.*, **1**, 211 (1965).
- (27) I. V. Aleksandrov, *Teor. Eksp. Khim.*, **2**, 67 (1966).
- (28) P. G. Klemens, *Phys. Rev.*, **125**, 1795 (1962).
- (29) D. W. Feldman, J. G. Castle, Jr., and J. Murphy, *Phys. Rev. A*, **138**, 1208 (1965).
- (30) P. G. Klemens, *Phys. Rev. A*, **138**, 1217 (1965).
- (31) J. Murphy, *Phys. Rev.*, **145**, 241 (1966).
- (32) I. V. Aleksandrov and V. P. Sakun, *Zh. Eksp. Teor. Fiz.*, **52**, 136 (1967).
- (33) V. P. Sakun, *Fiz. Tverd. Tela*, **9**, 2404 (1968).
- (34) R. Hernandez and M. B. Walker, *Phys. Rev. B*, **4**, 3821 (1971).
- (35) V. Ya. Zevin and V. I. Konovalou, *Fiz. Tverd. Tela*, **14**, 866 (1972).
- (36) G. G. Sergeeva, *Fiz. Tverd. Tela*, **14**, 1511 (1972).
- (37) D. S. Tsitskishvili, *Fiz. Tverd. Tela*, **15**, 3422 (1973).
- (38) C.-Y. Huang, *Phys. Rev.*, **154**, 215 (1967).
- (39) V. L. Vinetskii and V. Ya. Kravchenko, *Fiz. Tverd. Tela*, **7**, 319 (1965).
- (40) R. C. Zeller and R. O. Pohl, *Phys. Rev. B*, **4**, 2029 (1971).
- (41) C. L. Choy, R. G. Hunt, and G. L. Salinger, *J. Chem. Phys.*, **52**, 3629 (1970).
- (42) A. A. Antonlou and J. A. Morrison, *J. Appl. Phys.*, **36**, 1873 (1965).
- (43) W. A. Phillips, *J. Low Temp. Phys.*, **7**, 351 (1972).
- (44) P. W. Anderson, B. I. Halperin, and C. M. Varma, *Phil. Mag.*, **25**, 1 (1972).
- (45) W. A. Phillips, *Proc. R. Soc. (London)*, Ser. A, **319**, 565 (1970).
- (46) "Least-Squares Estimation of Non-Linear Parameters", WSU 21450, Wayne State University Computer and Data Processing Center, 1970.
- (47) D. W. Marquardt, IBM Publication SHARE SDA 3094.01 (NLIN).
- (48) B. Bales, J. Helbert, and L. Kevan, *J. Phys. Chem.*, **78**, 221 (1974).
- (49) L. Kevan, *Adv. Radiat. Chem.*, **4**, 181 (1974).
- (50) L. Kevan, *J. Phys. Chem.*, **79**, 2846 (1975).
- (51) J. J. Markham, "F-Centers in Alkali Halides", Academic Press, New York, N.Y., 1966.

Nuclear Magnetic Resonance Relaxation Studies of Carbonic Anhydrase Derivatives in Frozen Solutions

E. Hsi and R. G. Bryant*

Department of Chemistry, University of Minnesota, Minneapolis, Minnesota 55455 (Received March 17, 1976; Revised Manuscript Received December 15, 1976)

Publication costs assisted by the National Institutes of Health

Proton longitudinal and transverse NMR relaxation time measurements at 30 MHz are reported for frozen solutions of carbonic anhydrase with and without manganous ion at the active site. Although longitudinal relaxation of the manganous free samples requires two time constants, only one is required when manganous ion occupies the active site. It is concluded that the water in the immediate vicinity of the protein molecule samples the active site manganous ion on a time scale short compared with a microsecond and that relaxation of water protons caused by protein protons is significant.

Water interactions are central to an understanding of macromolecule structure and function, yet many questions remain concerning structural and dynamic details of water and its interactions with macromolecules.¹ Some physiological effects have been ascribed to various degrees of long range order imparted to water by its interaction with macromolecules.² X-Ray reports on crystalline proteins have provided some support for at least short range ordering of water molecules in protein crystals.³ On the other hand, some experiments suggest that the lifetimes of what structures exist must be very short.⁴ NMR relaxation measurements provide a direct method for investigation of water-macromolecule interactions in a variety of environments including solutions and semisolid systems such as tissue.^{5,6}

The major difficulty with magnetic resonance studies of protein hydration has been that the effects observed on the water NMR spectrum are small for protein solutions due to the very large concentration of the bulk solvent molecules and what is thought to be a rapid mixing of solvent between all environments in the sample. This difficulty may be overcome in part by freezing the solution. Most of the water forms ice which has relaxation parameters very different from that of noncrystalline water remaining unfrozen. Study of the unfrozen water signal then focuses on water which interacts with the protein surface so intimately that it does not form part of the ice lattice. It is encouraging that measurements of absolute water proton intensities from NMR CW and pulsed experiments agree with other estimates of the number of water molecules thought to interact strongly with the protein surface even though in general complex phase behavior may arise in frozen solutions of salts or more complicated molecules.⁷⁻⁹ It has been previously shown that the NMR relaxation of frozen lysozyme solutions is very similar to that in lysozyme crystals.⁴ Therefore study of the more easily handled solutions permits an efficient approach to additional details of hydration.

Previous measurements of water-protein systems have suggested that diffusion of water in the region immediately adjacent to the protein is very fast even at temperatures well below the freezing point of water.⁴ Although there have been two populations of water protons reported below the freezing event,^{4,8} interpretation of relaxation for the dominant component has involved the suggestion that the

diffusion of the average water molecule at the protein surface is characterized by correlation times on the order of nanoseconds at 240 K. The present work was undertaken to probe the rate at which water molecules sample the active site crevice in a metalloenzyme at subfreezing temperatures.

Experimental Section

Proton relaxation times were measured at 30 MHz on a pulsed NMR spectrometer built in this laboratory.¹⁰ The 90° pulse width was 3 μ s and the spectrometer recovery time was about 5 μ s. T_1 was measured using a 180°-90° pulse sequence and T_2 by the Gill-Meiboom modification of the Carr-Purcell pulse sequence.¹¹ The temperature of the probe was regulated to within 1° with the Varian variable temperature controller using liquid nitrogen as the cryogenic fluid and nitrogen as the carrier gas. The variable temperature controller was calibrated with a diode thermometer.

Bovine carbonic anhydrase (BCA) was obtained from Worthington Biochemical Corp. No attempt was made to separate the isozymes. Apo-BCA was prepared by two methods. Early work was done by dialyzing the native BCA against 0.01 M phosphate buffer at pH 5 containing 0.01 M o-phenanthroline for 7 days with one change of buffer.¹² The apoenzyme was then concentrated on a Diaflow ultrafiltration cell for the NMR experiment. A more efficient chelating agent, pyridine-2,6-dicarboxylic acid was used in later work.¹³ Zinc content was determined on a Jarrel-Ash atomic absorption spectrometer.

Mn-BCA was made by dialyzing the apoenzyme against 0.01 M phosphate buffer at pH 8 containing 10^{-4} M Mn^{2+} for 2 days with one change of buffer. The Mn-BCA was then dialyzed against 0.01 M phosphate buffer containing 10^{-5} M Mn^{2+} at pH 8. The Mn-BCA was then concentrated on a Diaflow ultrafiltration cell for the NMR experiment.

In the control experiment a 8.6% native BCA solution was dialyzed against a 10^{-3} M phosphate buffer at pH 8 containing 2×10^{-5} M $MnCl_2$ for 24 h. Free Mn^{2+} concentration was measured on a Varian E-3 ESR spectrometer by comparison of the signal intensity against a standard Mn^{2+} solution using identical conditions of modulation amplitude and microwave power. Total Mn content was assayed by digesting the protein with ammonium peroxydisulfate followed by oxidation of the manganous ion to permanganate with potassium periodate

* Camille and Her.ry Dreyfus Teacher Scholar 1974-1979.

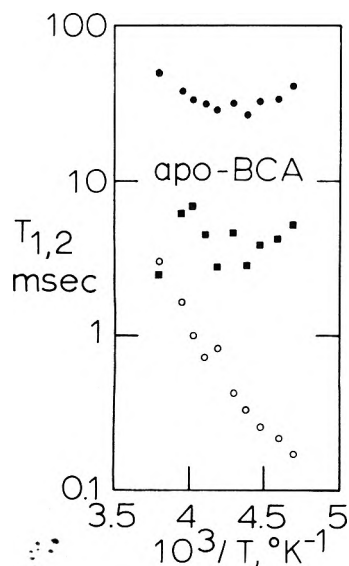


Figure 1. Proton transverse and longitudinal NMR relaxation times at 30 MHz for a frozen 10% solution of apobovine carbonic anhydrase as a function of reciprocal temperature: (●) slow longitudinal relaxation component; (■) fast longitudinal relaxation component; (○) transverse relaxation times.

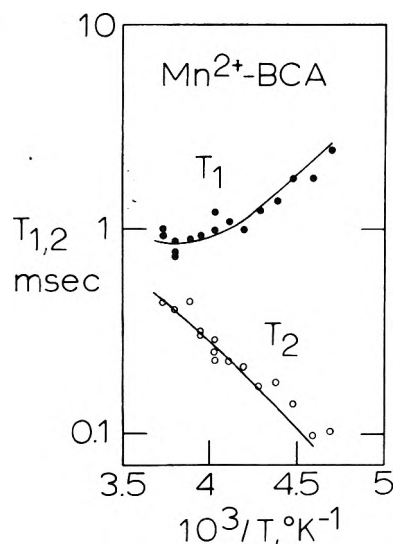


Figure 2. Proton transverse and longitudinal NMR relaxation times at 30 MHz for a frozen 10% solution of the manganous derivative of bovine carbonic anhydrase as a function of reciprocal temperature: (●) longitudinal relaxation times; (○) transverse relaxation times.

and measuring the permanganate optically at 525 nm. BCA concentration was measured optically at 280 nm using the absorbance $E_{280}^{1\%} = 18$.¹⁴

Results

Proton relaxation data are shown in Figure 1 for a frozen 10% solution of apocarbonic anhydrase. Longitudinal relaxation was characterized by two exponentials: the slowest relaxation component plotted passes through a broad minimum as a function of temperature and corresponds to approximately 65% of the signal intensity. The faster longitudinal relaxation component accounts for approximately 35% of the signal intensity. Transverse relaxation was characterized by a single exponential to within experimental error. The slope of T_2 against the reciprocal of temperature corresponds to an activation energy of 6.6 kcal/mol for the apoenzyme sample; however, the meaning of this number is unclear.

Proton relaxation data are shown in Figure 2 for frozen 10% apocarbonic anhydrase solution which had been

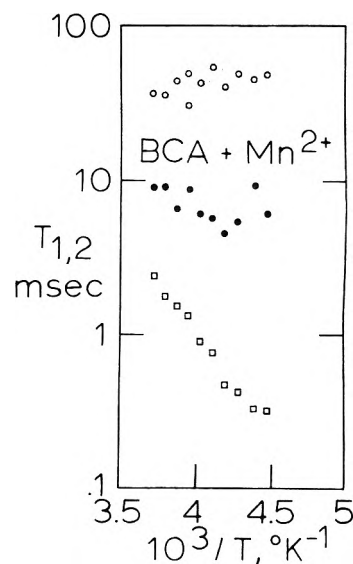


Figure 3. Proton transverse and longitudinal NMR relaxation times at 30 MHz for a frozen 10% solution of native carbonic anhydrase containing 2×10^{-5} M Mn^{2+} ion as a function of reciprocal temperature: (○) the major longitudinal component; (●) the minor longitudinal component; (□) the transverse relaxation times.

TABLE I

Sample	Temp, °C	T_1 , ms	T_2 , ms
Mn^{2+} BCA	20	60, 64	35, 36
Mn^{2+} BCA	-10	2.4	0.90, 0.79
Mn^{2+} BCA + 5x diamox	20	79, 79	115, 108
Mn^{2+} BCA + 5x diamox	-10	3.2	1.0, 0.89
Mn^{2+} BCA + 30x diamox	20	144	112, 106
Mn^{2+} BCA + 30x diamox	-10	5.8, 5.0	102
apo-BCA	20	512	369

dialyzed against successive changes of solution containing 2×10^{-5} M manganous ion. The dominant form of the enzyme contains a manganous ion at the active site region. Metal analysis data are consistent with there being a metal bound to free ratio in excess of 20 at pH 8 where the NMR measurements were made. Transverse relaxation in the manganous derivative is characterized by a single relaxation time to within experimental error. Longitudinal relaxation is characterized by two components: one component in the range of 60 ms comprises only about 5% of the signal and the remaining short component which is plotted. An Arrhenius plot of the transverse relaxation data gives a slope of 3.1 kcal/mol. The dominant longitudinal relaxation time appears to approach a minimum value at high temperatures close to the freezing event.

Two types of experiments were done to determine the sources of relaxation. The magnitudes of the relaxation effects due to manganese ions not coordinated directly to the active site region of the enzyme were determined by studying a 8.6% native enzyme solution which contained 2×10^{-5} M manganous ion. Relaxation results for this system with zinc at the active site are summarized in Figure 3. To within experimental error the transverse relaxation is characterized by a single relaxation time and an apparent activation energy of 6.2 kcal/mol. The longitudinal relaxation is described by two exponentials; the faster component which is plotted comprising 60% of the signal. The effects of chemical exchange of water in and out of the active site region were determined by measuring the relaxation rates in frozen and unfrozen solutions in the presence of excess inhibitor, diamox. These results are summarized in Table I. It is important

to note that addition of a large excess of inhibitor does not restore the water relaxation to the values appropriate to the diamagnetic apoenzyme or native enzyme.

Discussion

The data shown in Figure 1 for the metal free carbonic anhydrase are similar to that previously reported for other diamagnetic protein solutions.⁸ Two longitudinal relaxation times are required to fit the data and the ratio of either longitudinal relaxation time to the transverse relaxation time is much greater than predicted by the equations describing liquid relaxation.¹⁵ The data shown in Figure 3, which are for a sample containing more manganous ion than is expected to be in equilibrium with manganous ion bound at the active site in the manganous derivative, are different in some detail from that of the metal free sample. However, two longitudinal relaxation times are required and the ratio of either of them to the transverse relaxation time is large. We therefore conclude that the dramatic effects shown in Figure 2 when manganous ion is placed at the enzyme active site are not due to extraneous manganous ion, which may be in equilibrium with binding sites at the protein surface.

When the manganous derivative of carbonic anhydrase is prepared, a very small residual of slowly relaxing longitudinal relaxation component is observed which may arise from two sources: (1) The equilibrium constant for binding of manganous to the enzyme is small enough that with present conditions some enzyme molecules may not have a manganese ion bound to the active site. (2) The preparation of a completely zinc free apoenzyme is difficult. Frequently a residual zinc concentration on the order of 5% is retained. In either case two relaxation components would result: a minor one due to the diamagnetic molecules and a major one for those containing manganese. Since both of these problems are likely in the present case, we conclude that for the manganese enzyme derivative longitudinal relaxation is characterized by a single exponential. In what follows we will therefore consider only the short relaxation time representing 95% of the signal.

The transverse relaxation time in the manganese derivative is shifted by approximately a factor of 8 at the highest temperature compared with the values of the apoenzyme. This result implies that although the paramagnetism makes very significant contributions to the transverse relaxation time, nonnegligible contributions arising from diamagnetic sources may remain. On the other hand, paramagnetic effects are clearly dominant for longitudinal relaxation in the manganese derivative.

In general the relaxation equation will contain contributions from each physical or chemical environment experienced by the water protons:¹⁶

$$\frac{1}{T_{i=1,2}} = \frac{P_D}{T_{iD}} + \frac{P_M}{T_{iM} + \tau_M} \quad (1)$$

where P_D is the large fraction of water protons not at the paramagnetic site; P_M the fraction of water protons coordinated to the manganous ion; T_{iD} the relaxation time, either T_1 or T_2 , at diamagnetic sites which we may characterize using the apoenzyme data; τ_M the mean residence time for the water at the manganous ion site; and T_{iM} the relaxation time for the water protons at the manganous ion site. By subtraction of the diamagnetic term obtained from the apoenzyme data, we may isolate the paramagnetic contribution. Since paramagnetic effects clearly dominate longitudinal relaxation

$$1/T_1 = P_M/T_{1P} \quad (2)$$

T_{1P} is estimated to be on the order of 2 μ s by making absolute intensity measurements to establish the total water concentration and assuming that the manganous ion has only one coordinated water molecule. In general

$$1/T_{1P} = 1/(T_{1M} + \tau_M) \quad (3)$$

where T_{1M} is the longitudinal relaxation time at the manganous ion. Estimates for the mean residence time for water coordinated to manganese are generally close to 2×10^{-8} s or shorter.¹⁷ Therefore a very dramatic change in the metal ligand exchange rate would be required in the present case to place the longitudinal relaxation in the intermediate exchange region over the temperature range studied. The observed longitudinal relaxation equation is then apparently dominated by T_{1M} which simplifies at this field strength to

$$1/T_{1M} = \frac{2}{15} \frac{\gamma^2 g^2 \beta^2 S(S+1)}{r^6} \left\{ \frac{3\tau_c}{1 + \omega_i^2 \tau_c^2} \right\} + \frac{2}{3} \left(\frac{A}{\hbar} \right)^2 S(S+1) \left\{ \frac{\tau_e}{1 + \omega_s^2 \tau_e^2} \right\} \quad (4)$$

where τ_c is the correlation time for the nuclear-electron dipole-dipole interaction, γ the proton magnetogyric ratio, S the electron spin quantum number, g and β the usual magnetic parameters for the electron, ω_i the Larmor frequency for the proton, A the hyperfine coupling constant, ω_s the Larmor frequency for the electron, and τ_e the correlation time for the contact interaction represented in the second term. A similar equation may be written for T_2 .¹⁸

$$1/T_{2M} = \frac{1}{15} \frac{\gamma^2 g^2 \beta^2 S(S+1)}{r^6} \left\{ 4\tau_c + \frac{3\tau_c}{1 + \omega_i^2 \tau_c^2} \right\} + \frac{1}{3} \left(\frac{A}{\hbar} \right)^2 S(S+1) \left\{ \tau_e + \frac{\tau_e}{1 + \omega_s^2 \tau_e^2} \right\} \quad (5)$$

If the scalar term is neglected, the ratio of $T_{1M}:T_{2M}$ at the T_1 minimum becomes 1.83 which is very close to that observed in the present experiments shown in Figure 2. A significant scalar contribution would greatly increase this ratio; therefore, neglecting it appears to be justified.

The major problem to further interpretation is lack of precise knowledge of the correlation times appearing in eq 4 and 5. In each case two contributions may be important

$$1/\tau_c = 1/\tau_M + 1/\tau_{ie} \quad (6)$$

where τ_{ie} is a correlation time for electron-nuclear interactions which may be T_{1e} or T_{2e} . We may neglect any rotation of the whole protein molecule in this case because the complete lack of any protein proton signal in the frozen sample requires that the protein move very slowly if at all. Although we may put limits on values of τ_M , it is difficult to estimate the values to τ_{ie} . The magnitudes of the mean residence time for water molecules at the active sites of manganese enzymes at approximately room temperature may range from values slightly longer than that for the manganous ion (2×10^{-8} s)¹⁹ to 5×10^{-9} s.²⁰ The activation energy for water exchange with the metal is expected to be in the vicinity of 8 kcal/mol which indicates that, at the temperatures of the present experiments, the mean residence time will be long compared with 5×10^{-9} s which is the value of the correlation time dominating relaxation at the T_1 minimum at 30 MHz, the frequency of these experiments. On this basis therefore it is unlikely that the mean residence time of the water molecule at the man-

TABLE II

Equations	Parameters
$1/T_1 = (2K/5)x/(1 + x^2)$	$K = 6.0 \times 10^3 \text{ s}^{-1}$
$1/T_2 = y/T_2^0 + (K/15)\{4x + 3x/(1 + x^2)\}$	$E_a = 4.0 \text{ kcal/mol}$
$x = \exp\{(1/T - 1/T_0)E_a/R\}$	$E_d = 5.7 \text{ kcal/mol}$
$y = \exp\{(1/T - 1/T_0)E_d/R\}$	$T_0 = 263.2 \text{ K}$

ganeous ion determines the correlation time for the nuclear relaxation. The electronic contribution remains.

The assumption that electronic relaxation time, τ_{ie} , makes a dominant contribution to determining the relaxation in this system is supported by the low value of the activation energy observed for both longitudinal and transverse relaxation. It seems unlikely that the activation energy for water exchange from the metal could be as low as observed in Figure 2. It is also unlikely that the water molecule lifetime could be as short as implied by the value of the correlation time at the T_1 minimum. The extrapolation of this result to temperatures where the protein begins to rotate when the solution melts must be made with great care because such a rotation will contribute to both the effective correlation time, τ_c , and the electronic correlation time represented in eq 8 as τ_{ie} .

In spite of the uncertainties in these deductions a single activation parameter may be assumed for the correlation time, τ_c , and the consequences of this assumption tested by comparison with the data. In the present case the T_1 data may be fit well assuming a single activation energy for the relaxation as shown by the solid line in Figure 2. The magnitude of the paramagnetic contribution to the transverse relaxation time, T_{2p} , which may be directly estimated from the data in a similar way, requires that T_{2p} not be dominated by the exchange lifetime appearing explicitly in eq 3. Considerations concerning the calculation of the experimental parameters similar to those just presented for T_1 yields the solid line shown in Figure 2. The parameters used to fit both T_1 and T_2 are listed in Table II.

The quality of the calculated relaxation times demonstrates that to within the experimental errors of our measurements the approximations in eq 4 and 5 and the assumption of a single activation energy for the correlation time dominating relaxation lead to calculated relaxation times which are consistent with the data. Additional concerns remain. Outer sphere relaxation contributions to the observations may be important in general. Two features of the present case would appear to minimize this contribution: (1) The diamagnetic part of the relaxation is already very efficient and may in some instances compete effectively with the first coordination sphere paramagnetic relaxation processes. (2) The geometrical

limitations on the access of the water to the active site manganous ion coupled with the lack of macromolecule rotation implies that the dipolar contribution to second sphere relaxation would decrease more rapidly than r^{-3} .²¹ On the other hand, the protein itself represents an abnormal ligand because of its size. The protein protons may be strongly coupled magnetically. Since the motion of the protein is minimal, T_2 for the protein protons is short so that proton spin diffusion within the protein molecule itself may be rapid on the time scale of the relaxation times measured. Since large concentrations of the inhibitor molecule changed the water molecule relaxation rate by only a factor of 2 in the frozen solutions of the manganous derivative, we may conclude either that the inhibitor does not effectively displace water at the manganous ion site or that there is efficient relaxation of the water protons brought about through the protein proton spin system. That the inhibitor changes the water proton relaxation rate significantly permits the conclusion that exchange of water with the manganous ion position in the crevice of the protein is rapid; however, failure of the inhibitor to restore the basic features of the results for the diamagnetic proteins suggest that significant coupling and relaxation between the water and protein protons occurs in these samples.

Acknowledgment. The financial support of this work by the National Institutes of Health (GM 18719) and the National Science Foundation (BMS 74-23137) is gratefully acknowledged.

References and Notes

- (1) I. D. Kuntz and W. Kauzman, *Adv. Protein Chem.*, **28**, 239 (1974).
- (2) H. H. C. Jellinek, Ed., "Water Structure at the Water-Polymer Interface", Plenum Press, New York, N.Y., 1972.
- (3) J. J. Birkhoff and D. M. Blow, *J. Mol. Biol.*, **68**, 187 (1972).
- (4) E. Hsi, J. E. Jentoft, and R. G. Bryant, *J. Phys. Chem.*, **80**, 412 (1976).
- (5) R. Cooke and I. D. Kuntz, *Ann. Rev. Biophys. Bioeng.*, **3**, 95 (1974).
- (6) H. J. C. Berendson in "Water, A Comprehensive Treatise", Vol. 5, F. Franks, Ed., Plenum Press, New York, N.Y., 1975.
- (7) I. D. Kuntz, *J. Am. Chem. Soc.*, **93**, 516 (1971).
- (8) E. Hsi and R. G. Bryant, *J. Am. Chem. Soc.*, **97**, 3220 (1975).
- (9) J. E. Ramirez, J. R. Cavonagh, and J. M. Purcell, *J. Phys. Chem.*, **78**, 807 (1974).
- (10) E. Hsi, Ph.D. Thesis, University of Minnesota, Minneapolis, Minn., 1975.
- (11) S. Meiboom and D. Gill, *Rev. Sci. Instrum.*, **29**, 688 (1958).
- (12) S. Lindskog and B. G. Malmstrom, *J. Biol. Chem.*, **237**, 1129 (1962).
- (13) C. Storm, personal communication.
- (14) R. P. Davis, "The Enzymes", Vol. 5, 2nd ed, P. D. Boyer, H. Lardy, and K. Myrback, Ed., Academic Press, New York, N.Y., 1961, p 545.
- (15) N. Bloembergen, E. M. Purcell, and R. V. Pound, *Phys. Rev.*, **73**, 679 (1948).
- (16) T. J. Swift and R. E. Connick, *J. Chem. Phys.*, **37**, 307 (1962).
- (17) R. A. Dweck, "Nuclear Magnetic Resonance in Biochemistry", The Clarendon Press, Oxford, 1973, Chapter 10.
- (18) Reference 17, Chapter 9.
- (19) N. Bloembergen and L. O. Morgan, *J. Chem. Phys.*, **34**, 842 (1961).
- (20) J. Reuben and M. Cohn, *J. Biol. Chem.*, **245**, 662 (1970).
- (21) Z. Luz and S. Meiboom, *J. Chem. Phys.*, **40**, 2686 (1964).

Structural Investigations of Unsubstituted Polymethylenediphosphonic Acids. 1. The Crystal and Molecular Structure of Methylenediphosphonic and Ethane-1,2-diphosphonic Acids¹

S. W. Peterson,* E. Gebert, A. H. Reiss, Jr.,* M. E. Druyan,² G. W. Mason, and D. F. Peppard

Chemistry Division, Argonne National Laboratory, Argonne, Illinois 60439 (Received May 24, 1976; Revised Manuscript Received December 20, 1976)

Publication costs assisted by Argonne National Laboratory

A previously discussed correlation between an increase in hydrogen-bond strength with a decrease in P–O(H) distance in methylene-substituted diphosphonic acids is not upheld for hydrogen bonding in unsubstituted polymethylenediphosphonic acids. Strong asymmetric hydrogen bonds link $-(OH)P(=O)QH$ moieties into infinite chains spiralling about 2_1 axes and cross linking the molecules to form three-dimensional molecular chains in both methylenediphosphonic acid (PCP), $CH_2(PO_3H_2)_2$, and ethane-1,2-diphosphonic acid (PC_2P), $(CH_2)_2(PO_3H_2)_2$. PCP and PC_2P show short P–C bond distances (1.793(2) and 1.786(2) Å, respectively) as compared with substituted diphosphonic acids (~ 1.83 Å). PCP crystallizes in the monoclinic space group, P_1/c , with unit cell dimensions $a = 7.836(4)$, $b = 5.497(3)$, $c = 13.766(7)$ Å, $\beta = 103.60(2)^\circ$, and $Z = 4$. PC_2P crystallizes in the monoclinic space group $P2_1/c$ with unit cell dimensions, $a = 5.856(2)$, $b = 5.272(2)$, $c = 11.665(4)$ Å, $\beta = 100.69(2)^\circ$, and $Z = 2$. Three-dimensional x-ray data were collected for both compounds using a GE XRD-490 automated diffractometer. Full-matrix least-squares refinement of PCP gave a final $R_F = 0.036$ for a total of 1017 unique reflections, while a similar refinement of PC_2P gave a final $R_F = 0.046$ for 1019 unique reflections. Implications for cation coordination and liquid-liquid extraction chelation sites are discussed for ionized PCP and PC_2P .

Introduction

Considerable interest has been focused on methylene-substituted and unsubstituted diphosphonic acids, because of their favorable binding characteristics toward metal cations.³ Recently, structural investigations of both types of diphosphonic acids have appeared within this Journal.^{4,5} Ethane-1-hydroxy-1,1-diphosphonic acid monohydrate, $(CH_3)C(OH)(PO_3H_2)_2 \cdot H_2O$,⁴ gave evidence for what the authors believed to be a correlation in diphosphonic acids between hydrogen bond strength and phosphorus–oxygen bond length. The authors noted that a decrease in the P–O(H) bond length correlated with a decrease in hydrogen bond distance and a lengthening of the related P=O distance. They explained these effects in terms of a delocalization and buildup of negative charge density on the phosphoryl oxygens due to attraction of the phosphonic protons to their hydrogen-bond acceptor. However, we believe what the authors were observing was the P–O(H) bond shortening and P=O bond lengthening which occurs in very strong hydrogen bonds due to the formation of a more symmetrical hydrogen bond, not a general correlation. A recent structural study of $CH_2(PO_3H_2)_2$, PCP,⁵ showed that the above correlation does not hold for a molecule where longer hydrogen bonds are involved, however, an earlier determination of PCP showed somewhat different bond distances.⁶ Therefore, we wish to report the very precisely determined molecular and crystal structures of $CH_2(PO_3H_2)_2$, PCP, and $(CH_2)_2(P-O_3H_2)_2$, PC_2P . The recently completed structural determination of $(CH_2)_3(PO_3H_2)_2$, PC_3P , will be published shortly. Highly accurate structural data on a number of diphosphonic acids will be necessary in order to further evaluate the small (0.01 Å) differences in bond lengths involved in the above correlation.

Experimental Section

Collection and Reduction of X-Ray Data. Samples of PCP and PC_2P were prepared by the method of Moedritzer and Irani.⁷ Recrystallization from methanol re-

TABLE I: Experimental Details for PCP

Cell constants:	$T = 27^\circ C$, $a = 7.836(4)$ Å, $b = 5.497(3)$ Å, $c = 13.766(7)$ Å, $\beta = 103.60(2)^\circ$
Cell volume:	576.33 Å ³
Molecular weight of asymmetric unit:	176.001 g/mol
Calculated density:	2.026 g cm ⁻³
Measured density:	2.026(2) g cm ⁻³ by flotation in $CH_2Cl + CH_3Br$
Z:	4
Space group:	$P2_1/c$ (C_{2h}^5 ; no. 14)
Radiation:	Mo $K\alpha$, $\lambda = 0.71069$ (Ross 1 filter)
Attenuator:	Cu foil at 10 000 Hz
Take-off angle:	2.0°
Maximum 2θ :	50.0° ($\pm hkl$)
Scan type:	coupled θ - 2θ
Scan width:	1.6°
Scan speed:	0.1° steps
Counting time:	4 s/step (background 16 s each side of peak)
Crystal:	
	b axis mounted
	Volume = 0.859×10^{-3} cm ³ ($\sim 0.01 \times 0.01 \times 0.0176$ cm)
	Absorption coefficient = 7.165 cm ⁻¹
	Maximum transmission factor = 0.89
	Minimum transmission factor = 0.86
	Number of reflections collected = 1017
	R_F for all reflections = 3.60% (1017)
	R_F for reflections where $F_o > 1\sigma F_o = 3.39\%$ (965)
	$wR_F^2 = 8.96\%$

sulted in the formation of clear triangular-prism crystals.

(a) *PCP*. A crystal with approximate dimensions $0.010 \times 0.010 \times 0.013$ cm was mounted along the b axis for study. Preliminary oscillation, Weissenberg, and precession photographs revealed $2/m$ Laue symmetry and the systematic absences $h0l$ for $l = 2n + 1$ and $0k0$ for $k = 2n + 1$. This is consistent with the centrosymmetric monoclinic space group $P2_1/c$ [C_{2h}^5 ; no. 14].

A GE XRD-490 automated x-ray diffractometer was used for data collection. Accurate unit-cell parameters were obtained by least-squares from the angular coordinates of 14 reflections measured in a 2θ range of 27 – 33° .

TABLE II: Experimental Details for PC₂P

Cell constants: $T = 25^\circ\text{C}$, $a = 5.856(2)\text{ \AA}$,
 $b = 5.272(2)\text{ \AA}$, $c = 11.665(4)\text{ \AA}$, $\beta = 100.69(2)^\circ$
Cell volume: 353.88 \AA^3
Molecular weight of asymmetric unit: 190.28 g/mol
Calculated density: 1.783 g cm^{-3}
Measured density: 1.757 g cm^{-3} by flotation
in $\text{CH}_2\text{Cl}_2 + \text{CH}_2\text{I}_2$
 $Z = 4$
Space group = $P2_1/c$ (C_{2h}^2 ; no. 14)
Radiation: Mo $K\alpha$, $\lambda = 0.71069$ (Ross 1 filter)
Attenuator: Cu foil at 10 000 Hz
Take-off angle: 2°
Maximum 2θ : 60.0° ($\pm hkl$)
Scan type: θ -coupled θ - 2θ
Scan width: 1.6°
Scan speed: 0.1° steps
Counting time: 4 s/step (background 16 s each
side of peak)
Crystal:
b axis mounted
Volume = $0.144 \times 10^{-4}\text{ cm}^3$
($0.036 \times 0.032 \times 0.013\text{ cm}$)
Absorption coefficient = 11.874 cm^{-1}
Maximum transmission factor = 0.86
Minimum transmission factor = 0.67
Number of reflections collected = 1064
 R_F for all reflections = 4.58% (1017)
 R_F for reflections where $F_o > 1\sigma F_o = 4.36\%$ (980)
 $wR_F^2 = 12.6\%$

Details specific to data collection and analysis are given in Table I. A description of the instrumentation used in this data collection has been given previously.⁸

(b) PC₂P. A clear parallelepiped crystal with dimensions $0.035 \times 0.032 \times 0.012\text{ cm}$ was mounted along the *b* axis. Preliminary x-ray photographs established the space group $P2_1/c$ also for PC₂P. The techniques for obtaining space group information, unit cell constants, and data collection and reduction were similar to those described above. Details specific for PC₂P data collection are given in Table II.

Solution and Refinement of the Structures. (a) PCP. The structure was independently solved; the positions of the phosphorus atoms were determined from a three-dimensional Patterson map. A Fourier map based on the phosphorus positions ($R_F = 0.68$) revealed the positions of the six oxygen and the one carbon atom ($R_F = 0.37$). The positions and isotropic thermal parameters were refined by full-matrix least-squares techniques converging at an $R_F = 0.139$. Four cycles of anisotropic least-squares refinement converged at $R_F = 0.060$. A difference Fourier map clearly revealed the positions of all six hydrogen atoms. Anisotropic least-squares refinement of all heavy atoms and isotropic least-squares refinement of all hydrogen atoms converged after three cycles to $R_F = 0.036$ for 1017 unique reflections, $R_{wF^2} = 0.089$, and $\Sigma_2 = 1.38$, where

$$R_F = \frac{\sum ||F_o| - |F_c||}{\sum F_o}$$

$$R_{wF^2} = \left[\frac{\sum w(F_o^2 - F_c^2)^2}{\sum wF_o^2} \right]^{1/2}$$

$$\Sigma_2 = \left[\frac{\sum w(F_o^2 - F_c^2)^2}{(N_o - N_R)} \right]^{1/2}$$

N_o is the number of independent observations and N_R is the number of parameters varied. A final difference Fourier map revealed no peaks above 0.55 e/\AA^3 . No parameter varied more than $\Delta/\sigma = 0.03$ in the last cycle of the refinement. Table III is a listing of the final positional parameters of all atoms and isotropic thermal parameters for hydrogen atoms in PCP. Table IV gives the anisotropic thermal parameters for non-hydrogen atoms in PCP.

TABLE III: Final Positional Parameters and Isotropic Thermal Parameters for PCP^a

Atom	x	y	z	B
P(1)	0.23569(7)	0.34786(10)	0.27013(4)	
P(2)	0.28647(8)	0.36825(11)	0.05649(4)	
C	0.2105(4)	0.5128(5)	0.15509(17)	
O(1)	0.4299(2)	0.3581(3)	0.32868(14)	
O(2)	0.1120(2)	0.4498(3)	0.32815(12)	
O(3)	0.2099(3)	0.0742(3)	0.24482(13)	
O(4)	0.4706(2)	0.2766(3)	0.08854(12)	
O(5)	0.1488(2)	0.1647(4)	0.02100(15)	
O(6)	0.2604(3)	0.5575(4)	-0.02907(13)	
H(1)	0.267(3)	0.650(5)	0.167(2)	2.2(7)
H(2)	0.097(4)	0.546(5)	0.134(2)	2.4(6)
H(3)	0.346(4)	0.595(6)	-0.042(2)	3.1(8)
H(4)	0.460(4)	0.493(6)	0.349(2)	3.6(8)
H(5)	0.120(5)	0.051(7)	0.223(2)	4.0(9)
H(6)	0.148(4)	0.124(5)	-0.029(2)	2.6(7)

^a Estimated standard deviations are given in parentheses.

TABLE IV: Anisotropic Thermal Parameters^a ($\times 10^4$) for PCP^b

Atom	B_{11}	B_{22}	B_{33}	B_{12}	B_{13}	B_{23}
P(1)	44(1)	114(2)	15(1)	3(1)	5(1)	-3(1)
P(2)	54(1)	137(2)	15(1)	-5(1)	9(1)	3(1)
C	71(4)	123(8)	22(1)	4(5)	14(2)	5(3)
O(1)	57(3)	149(7)	31(1)	-1(3)	-1(1)	-15(2)
O(2)	68(3)	194(6)	18(1)	31(3)	12(1)	7(2)
O(3)	69(3)	137(6)	26(1)	-16(4)	6(2)	-6(2)
O(4)	73(3)	156(6)	30(1)	14(3)	18(1)	15(2)
O(5)	111(4)	266(8)	20(1)	-82(4)	16(2)	-24(2)
O(6)	68(3)	267(8)	27(1)	20(4)	16(2)	36(2)

^a The anisotropic thermal parameter is in the form: $\exp\{-(B_{11}h^2 + B_{22}k^2 + B_{33}l^2 + 2B_{12}hk + 2B_{13}hl + 2B_{23}kl)\}$. ^b Standard deviations are given in parentheses.

TABLE V: Final Positional Parameters and Isotropic Thermal Parameters for PC₂P^a

Atom	x	y	z	B
P	0.24003(8)	0.19065(9)	0.14087(4)	
C	0.1312(3)	0.0284(4)	0.00754(17)	
O(1)	0.2103(3)	0.0394(3)	0.24619(14)	
O(2)	0.4968(3)	0.2354(4)	0.13254(17)	
O(3)	0.1215(3)	0.4546(3)	0.13885(15)	
H(1)	0.233(4)	-0.113(5)	0.002(2)	2.2(5)
H(2)	0.173(4)	0.117(4)	-0.056(2)	1.4(4)
H(3)	-0.032(5)	-0.013(6)	0.327(2)	2.8(6)
H(4)	0.448(7)	-0.150(7)	0.320(3)	4.9(9)

^a Estimated standard deviations are given in parentheses.

(b) PC₂P. The phosphorus, carbon, and oxygen atoms were located from a Patterson map ($R_F = 0.48$). Three cycles of isotropic full-matrix least-squares refinement converged at an $R_F = 0.13$. Four additional cycles of anisotropic least-squares refinement converged at an $R_F = 0.053$. The hydrogen atoms were located quite easily at this stage from a difference Fourier map. Anisotropic (non-hydrogen atom) and isotropic (hydrogen atom) least-squares refinement converged after four cycles to a final $R_F = 0.046$ for 1019 reflections, $R_{wF^2} = 0.126$, and $\Sigma_2 = 2.04$. A final difference Fourier revealed no electron density above 0.68 e/\AA^3 . No parameter varied by more than $\Delta/\sigma = 0.10$ in the last cycle of refinement. Table V is a listing of the final positional parameters of all atoms and isotropic thermal parameters for hydrogen atoms on PC₂P, while Table VI lists the anisotropic thermal parameters of all non-hydrogen atoms of PC₂P.

A comparison of the observed and calculated structure-factor amplitudes is available as supplementary material (see paragraph at end of text regarding supple-

TABLE VI: Anisotropic Thermal Parameters^a ($\times 10^3$) for PC₂P^b

Atom	B_{11}	B_{22}	B_{33}	B_{12}	B_{13}	B_{23}
P	111(2)	148(2)	32(1)	-11(1)	13(1)	-10(1)
C	121(5)	188(6)	34(1)	-10(5)	13(2)	-14(2)
O(1)	162(4)	215(5)	39(1)	32(4)	13(2)	17(2)
O(2)	132(4)	359(7)	66(2)	-84(5)	34(2)	-76(3)
O(3)	260(6)	150(5)	51(1)	33(4)	50(2)	7(2)

^a The form of the anisotropic thermal parameter is $\exp\{-(B_{11}h^2 + B_{22}k^2 + B_{33}l^2 + 2B_{12}hk + 2B_{13}hl + 2B_{23}kl)\}$. ^b Estimated standard deviations are given in parentheses.

TABLE VII: Interatomic Distances for PCP^a

Bond	Distance, Å	Bond	Distance, Å
(a) Intramolecular Distances			
P(1)-O(1)	1.547(2)	P(2)-O(4)	1.493(2)
P(1)-O(2)	1.502(2)	P(2)-O(5)	1.551(2)
P(1)-O(3)	1.546(2)	P(2)-O(6)	1.549(2)
P(1)-C	1.795(3)	P(2)-C	1.791(2)
C-H(1)	0.87(3)	C-H(2)	0.88(3)
(b) Non-Hydrogen Bonding Interactions to 3.3 Å			
O(1)---O(2)	2.540(3)	O(5)---O(6)	2.487(3)
O(1)---O(3)	2.409(3)	O(5)---O(5')	2.902(4)
O(2)---O(3)	2.578(3)	O(5)---O(3)	3.046(3)
O(4)---O(5)	2.549(3)	O(3)---O(6)	3.129(3)
O(4)---O(6)	2.599(3)	P(1)---P(2)	3.061(2)

^a Estimated standard deviations are given in parentheses.

TABLE VIII: Interatomic and Torsion Angles for PCP^a

Angle	Deg	Angle	Deg
(a) Interatomic Angles			
O(1)-P(1)-O(2)	112.9(1)	O(4)-P(2)-O(5)	113.7(1)
O(2)-P(1)-O(3)	114.6(1)	O(4)-P(2)-O(6)	113.4(1)
O(1)-P(1)-O(3)	102.3(1)	O(5)-P(2)-O(6)	106.7(1)
C-P(1)-O(1)	109.4(1)	C-P(2)-O(4)	113.3(1)
C-P(1)-O(2)	109.3(1)	C-P(2)-O(5)	103.2(1)
C-P(1)-O(3)	108.1(1)	C-P(2)-O(6)	105.7(1)
P(1)-C-P(2)	117.2(1)	H(1)-C-H(2)	108(21)
(b) Torsion Angles			
O(4)-P(2)-P(1)-O(3)	22.3(1)		
O(6)-P(2)-P(1)-O(2)	34.5(2)		
O(5)-P(2)-P(1)-O(1)	34.9(1)		

^a Estimated standard deviations are given in parentheses.

mentary material) for both PCP and PC₂P.

Scattering factors for neutral atoms were taken from the compilation of Cromer and Waber.⁹ The values for phosphorus, oxygen, and carbon atoms were corrected for anomalous dispersion using the values of Cromer.¹⁰ Computational programs used for these structural determinations were RTMON,¹¹ data collection and reduction; DATLIB,¹² absorption, Lorentz, and polarization corrections; S5XFLS,¹³ least-squares refinement; S5FOUR,¹³ Fourier synthesis; ORFFE,¹³ distances and angles calculation; and ORTEP,¹⁴ molecular drawing. All calculations were carried out on the Xerox Sigma V Computer of the Chemistry Division, ANL, and the IBM 370/195 of the Applied Mathematics Division, ANL.

The Molecular and Crystal Structures. (a) PCP. Intramolecular bond distances are given in Table VII; the corresponding interatomic angles and torsion angles are given in Table VIII. The hydrogen bond distances are given in Table IX. Figure 1 is a drawing of the PCP molecule indicating atom labeling. Molecular packing and hydrogen bonding are shown in Figure 2. The non-hydrogen positions and the bond distances and angles derived here for PCP are in good agreement with those of Calvo,⁵

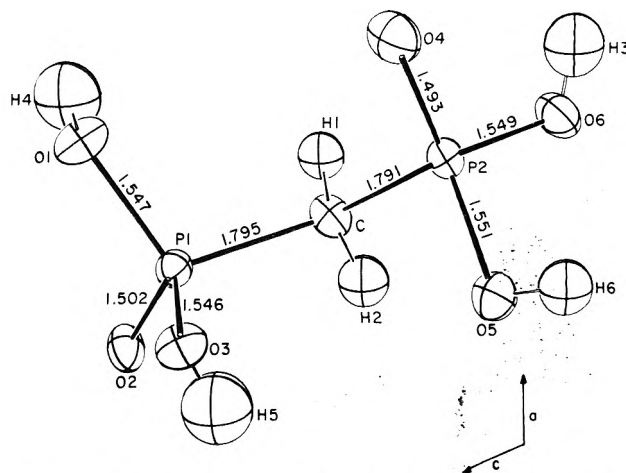


Figure 1. The PCP molecule showing atom labels and bond distances.

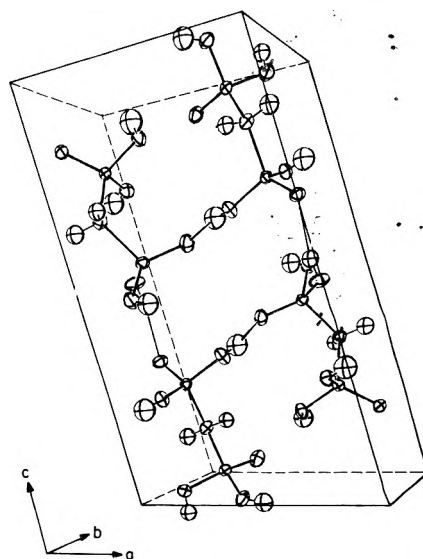


Figure 2. The unit cell of the PCP crystal showing molecular packing and hydrogen bonding.

TABLE IX: Hydrogen-Bonded Distances and Bond Angles in PCP^a

Bond	Distance, Å	Angle, deg
O(6)-H(3)-O(4)	2.542(3)	170(4)
O(6)-H(3)	0.75(4)	
O(4)-H(3)	1.85(4)	
O(1)-H(4)-O(4)	2.604(3)	172(4)
O(1)-H(4)	0.81(4)	
O(4)-H(4)	1.80(4)	
O(3)-H(5)-O(2)	2.565(3)	173(4)
O(3)-H(5)	0.71(4)	
O(2)-H(5)	1.87(4)	
O(5)-H(6)-O(2)	2.677(3)	170(3)
O(5)-H(6)	0.73(3)	
O(2)-H(6)	1.95(4)	

^a Estimated standard deviations are given in parentheses.

but differ substantially from the earlier report.⁶ Therefore, our present discussion will focus only on hydrogen bonding involving the PCP molecule.

Every phosphonyl hydrogen of PCP is asymmetrically bonded to two oxygen atoms to form an extensive three-dimensional network of hydrogen bonds involving all molecules of the unit cell. Each P=O oxygen is an acceptor for two intermolecular hydrogen bonds while each P-O(H) oxygen is bonded to a single hydrogen. Three distinctive hydrogen bonded configurations are found: (a) 16-membered rings sitting at an inversion center containing

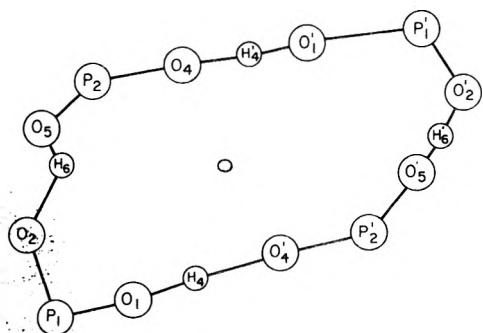


Figure 3. A 16-membered hydrogen bonded-ring formed by several PCP molecules.

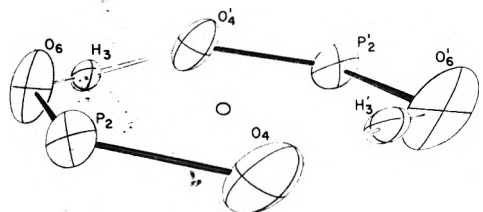


Figure 4. An eight-membered hydrogen-bonded ring formed by two PCP molecules.

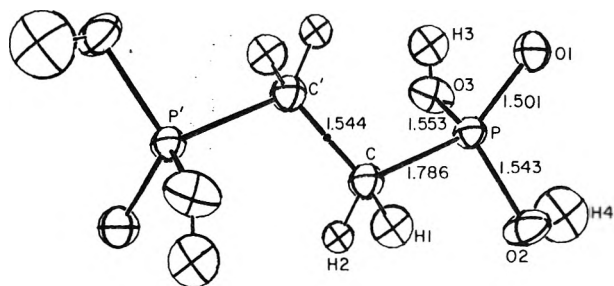


Figure 5. The PC_2P molecule showing atom labels and bond distances.

four hydrogen bonds involving H(4) and H(6) where $O(1)-H(4)-O(4) = 2.604(3)$ Å, and $O(5)-H(6)-O(2) = 2.677(3)$ Å (see Figure 3); (b) eight-membered rings sitting at an inversion center containing two hydrogen bonds involving H(3) where $O(6)-H(3)-O(4) = 2.542(3)$ Å (see Figure 4); (c) hydrogen-bonded chains which spiral around the b axis (the 2_1 screw axis) and contain hydrogen bonds involving H(5) where $O(2)-H(5)-O(3) = 2.565(3)$ Å. The lengths of the various hydrogen bonds probably reflect the constraints of the system of which they are a part, i.e., the hydrogen bonds of the 16-membered ring are longer than

TABLE X: Interatomic Distances and Hydrogen-Bonded Distances and Angles in PC_2P^a

Bond	Distance, Å	Angle, deg
(a) Interatomic Distances		
P-O(1)	1.501(2)	
P-O(2)	1.543(2)	
P-O(3)	1.553(2)	
P-C	1.786(2)	
C-H(1)	0.97(3)	
C-H(2)	0.94(2)	
C-C'	1.544(4)	
P...P	4.395(3)	
(b) Hydrogen Bonds		
O(3)-H(3)-O(1)	2.527(2)	174(4)
O(3)-H(3)	0.74(4)	
O(1)-H(3)	1.86(4)	
O(2)-H(4)-O(1)	2.543(3)	152(4)
O(2)-H(4)	0.85(4)	
O(1)-H(4)	1.79(4)	

^a Estimated standard deviations are given in parentheses.

TABLE XI: Interatomic Angles in PC_2P^a

Angle	Deg
O(1)-P-O(2)	113.3(1)
O(1)-P-O(3)	111.6(1)
O(2)-P-O(3)	107.5(1)
C-P-O(1)	112.4(1)
C-P-O(2)	102.3(1)
C-P-O(3)	109.2(1)
C'-C-P	112.3(2)

^a Estimated standard deviations are given in parentheses.

those of the more constrained eight-membered ring and spiral configurations. We have recently shown^{8,15} that di-*tert*-butylphosphonic acid exists in the solid state as a distinct phosphonic acid dimer composed of an eight-membered asymmetrically hydrogen-bonded ring with an O-H-O distance of 2.486(9) Å. In PCP, no intramolecular hydrogen bonding exists even though many intramolecular O...O' interactions are within 2.4-3.0 Å. (See Table VII.)

(b) PC_2P . Table X contains intramolecular bond distances and hydrogen bond distances and angles; bond angles and torsion angles are given in Table XI. Figure 5 is a drawing of the PC_2P molecule with the atoms identified. Molecule packing and hydrogen bonding within the unit cell are shown in Figure 6.

Molecules of PC_2P pack within the unit cell such that the center of the C-C' bond is located at a center of in-

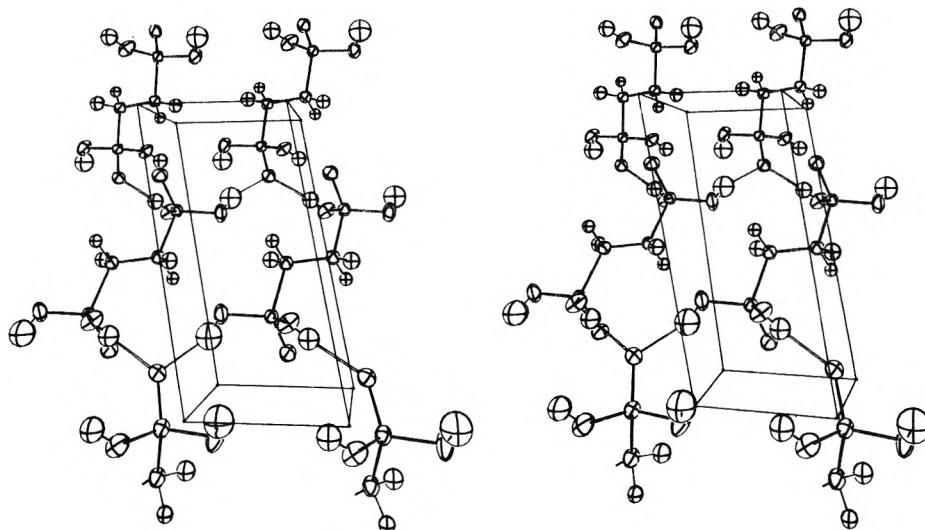


Figure 6. The unit cell of the PC_2P crystal showing molecular packing and hydrogen bonding.

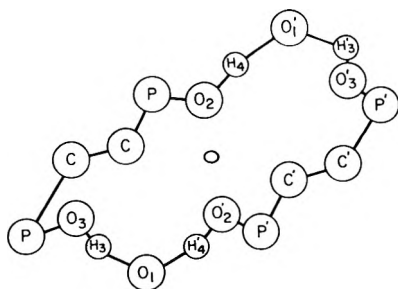
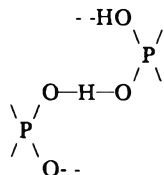


Figure 7. An 18-membered hydrogen-bonded ring formed by several PC_2P molecules.

version (i), thus the asymmetric unit is half of the PC_2P molecule. For n odd, molecules within the series $(C-H_2)_n(PO_3H_2)_2$ cannot have an inversion center; however, when n is even, as in the present case, an inversion center is possible. The presence of the center largely determines the conformation of PC_2P . Thus the CH_2 groups are staggered when viewed down the C-C bond as are the $O=P(OH)OH$ moieties when viewed down the P-P vector. In addition, the C-C(H)H is staggered with respect to $O=P(OH)OH$ when viewed down the C-P bond although this is not required by symmetry. This latter configuration must be determined by packing and hydrogen bonding in which each phosphonyl oxygen is an acceptor for two hydrogen bonds involving OH groups from two separate PC_2P molecules. Infinite hydrogen bond spirals centered on each 2_1 axis (parallel to b) extend throughout the lattice similar to those previously observed for a number of substituted phosphoric and phosphinic acids¹⁶



In addition, there are large 18-membered hydrogen-bonded rings (see Figure 7) formed in which two PC_2P molecules are linked through hydrogen bonding to two phosphonyl-oxygen acceptors from another pair of molecules. In effect, the infinite spirals cross link PC_2P molecules in forming the large rings (see Figure 7).

There is no intramolecular hydrogen bonding even though it is a steric possibility. Each hydrogen is asymmetrically bonded to two oxygens with $P=O$ oxygens bonding to two hydrogens as in the PCP case. The hydrogen bond lengths are: $O(3)-H(3)-O(1) = 2.527(2)$ Å where $O(3)-H(3) = 0.74(4)$ Å while $O(1)-H(3) = 1.86(4)$ Å, and $O(2)-H(4)-O(1) = 2.543(3)$ Å where $O(2)-H(4) = 0.85(4)$ Å while $O(1)-H(4) = 1.79(4)$ Å. These hydrogen bonds are somewhat shorter than those found for the PCP molecule. The shortening probably results from the better packing which the molecules can achieve because of the inherent center of symmetry of the PC_2P molecule.

The phosphorus atom is tetrahedrally coordinated to three oxygen atoms and one carbon atom with bond distances of $P-O(1) = 1.501(2)$ Å, $P-O(2) = 1.543(2)$ Å, $P-O(3) = 1.553(2)$ Å, $P-C = 1.786(2)$ Å, and bond angles of $O(1)-P-O(2) = 113.3(1)^\circ$, $O(1)-P-O(3) = 111.6(1)^\circ$, $O(2)-P-O(3) = 107.5(1)^\circ$, $C-P-O(3) = 109.2(1)^\circ$. The bond length of $P-O(1)$, the phosphonyl group, shows considerable double bond character while $P-O(2)$ and $P-O(3)$ have normal lengths for P-OH bonds. The π character of $O(1)$ is also reflected in the bond angles involving $O(1)$ which are seen to be large. The P-C-C-P chain is planar due to the inversion center on the C-C' bond. The P-C-C'

bond angle of $112.3(2)^\circ$ in PC_2P may be compared to the $P(1)-C-P(2)$ bond angle of $117.2(1)^\circ$ in PCP indicating reduced repulsion due to substitution of the less polar CH_2 group. From previous NMR and IR results,⁷ a significant amount of P-P coupling is shown for $n \leq 3$ in this diphosphonic acid series.

Discussion

The possible correlation between hydrogen bond strength, decreased P-O(H) distance, and increased $P=O$ distance is not upheld for the PCP and PC_2P materials. Our structural findings support Calvo et al.⁵ on the PCP structure and we extend the information about the phosphonic acids with the PC_2P study. In PCP, P-O(-H) distances are shown to be equal within errors of the estimated standard deviations; however, hydrogen-bonding distances varied from $2.542(3)$ to $2.677(3)$ Å. Also, each $P=O$ is involved in two hydrogen bonds of different length. In PC_2P , P-O(H) distances differ by 0.01 Å with the longer hydrogen bond associated with the shorter P-O(H) distance in direct conflict with the above correlation. As in PCP, the $P=O$ group also bonds to two different hydrogen atoms. A correlation between P-O(H) distances and hydrogen-bonded distances for all diphosphonic acids is thus inappropriate. In the ethane-1-hydroxy-1,1-diphosphonic acid material⁴ very short hydrogen bonds ($2.450(4)$ and $2.479(4)$ Å) exist compared to $2.527(2)$ Å in PC_2P and $2.542(2)$ Å in PCP. It seems likely that the correlation observed in the case of ethane-1-hydroxy-1,1-diphosphonic acid is appropriate for very strong hydrogen bonds and merely reflects the formation of more symmetrical hydrogen bonds at these short spacings causing the P-O(H) and $P=O$ -groups to become more nearly equivalent.

In the PC_2P molecule, a slight decrease in the average P-C distance is observed compared to the PCP molecule, $1.786(2)$ and $1.793(2)$ Å, respectively. This small difference resulting from the introduction of an additional CH_2 group probably stems from weaker repulsive forces between the methylene hydrogens and the phosphonic acid groups. These P-C distances are substantially shorter than those in the substituted methylenediphosphonic acids; for example, in the ethane-1-hydroxy case, P-C bond distances of 1.832 and 1.840 Å are found.⁴ The longer distances in the latter example are probably due to the presence of electron-withdrawing substituents on the methylene carbon.

Ionized forms of PCP and PC_2P will have up to six chelation sites where actinide and lanthanide cations may be bound. Assuming a chelation involving intra diphosphonic coordination, varying the size of the carbon chain will cause the bite of the ligand to change, therefore varying the size of the metal-ligand chelation rings which can be formed, their conformation, and stability. Cation extraction characteristics of these materials will be discussed in a subsequent report.

Supplementary Material Available: A listing of calculated and observed structure factor amplitudes (16 pages). Ordering information is given on any current masthead page.

References and Notes

- (1) Work performed under the auspices of the U.S. Energy Research and Development Administration.
- (2) Department of Biochemistry, Loyola University School of Dentistry, Maywood, Ill. 60153.
- (3) (a) D. F. Peppard, *Annu. Rev. Nucl. Sci.*, **21**, 365-396 (1971); (b) E. K. Hulet and D. D. Bode, *MTP Int. Rev. Sci., Inorg. Chem., Ser. One*, **7**, 1-45 (1972); (c) C. F. Callis, A. F. Kerst, and J. W. Lyons,

- "Coordination Chemistry", S. Kirschner, Ed., Plenum Press, New York, N.Y., 1969, pp 223-247; (d) V. A. Uchtman, *J. Phys. Chem.*, **76**, 1304 (1972).
- (4) V. A. Uchtman and R. A. Gloss, *J. Phys. Chem.*, **76**, 1298 (1972).
- (5) D. De La Matter, J. J. McCullough, and C. Calvo, *J. Phys. Chem.*, **77**, 1146 (1973).
- (6) F. M. Lovell, Abstracts of the American Crystallographic Association, July 26-31, 1964, J-11, Bozeman, Mont.
- (7) K. Moedritzer and R. R. Irani, *J. Inorg. Nucl. Chem.*, **22**, 297 (1961).
- (8) M. E. Druyan, A. H. Reis, Jr., E. Gebert, S. W. Peterson, G. Mason, and D. F. Peppard, *J. Am. Chem. Soc.*, **98**, 4801 (1976).
- (9) "International Tables for X-ray Crystallography", Vol. IV, Kynoch Press, Birmingham, England, 1974, p 71.
- (10) "International Tables for X-ray Crystallography", Vol. IV, Kynoch Press, Birmingham, England, 1974, p 148.
- (11) An IBM 1130 program written by J. Scherer at ANL.
- (12) An IBM 370/195 program written by H. A. Levy.
- (13) SSFOUR, SSXFLS, and SSFFE are Sigma 5 versions of the programs: FOURIER by R. J. Dellaca and W. T. Robinson, ORXFLS3 written by W. R. Busing and H. A. Levy, and ORFFE3 written by W. R. Busing and H. A. Levy.
- (14) ORTEP written by C. Johnson.
- (15) A. H. Reis, Jr., S. W. Peterson, M. E. Druyan, E. Gebert, G. W. Mason, and D. F. Peppard, *Inorg. Chem.*, **15**, 2748 (1976).
- (16) D. Fenske, R. Mattes, J. Lons, and K. F. Tebbe, *Chem. Ber.*, **106**, 1139 (1973), and references therein.

Structural Investigations of Methylene-diphosphonic Acids. 2. The Molecular and Crystal Structure of Propane-1,3-diphosphonic Acid¹

E. Gebert, A. H. Reis, Jr.,* M. E. Druyan,² S. W. Peterson,* G. W. Mason, and D. F. Peppard

Chemistry Division, Argonne National Laboratory, Argonne, Illinois 60439 (Received May 24, 1976; Revised Manuscript Received December 20, 1976)

Publication costs assisted by Argonne National Laboratory

Propane-1,3-diphosphonic acid, $(\text{CH}_2)_3(\text{PO}_3\text{H}_2)_2$, PC_3P , crystallizes in the noncentrosymmetric, monoclinic, space group Pc [C_2^2 , no. 7] with unit cell constants $a = 9.540(2)$, $b = 9.964(2)$, $c = 9.705(2)$ Å, $\beta = 118.90(1)^\circ$, and $Z = 4$. The asymmetric unit of PC_3P consists of two crystallographically unique molecules. The structure was solved by a combination of direct methods, Fourier, and least-squares refinement techniques; the final $R_F = 0.024$ for 1412 independent unique reflections. The two PC_3P molecules within the asymmetric unit have quite different conformations. Hydrogen-bonded rings of differing size shape the P-C-C-P backbone of one PC_3P molecule into an almost planar conformation, while the backbone of the other molecule is distorted into a distinctive nonplanar conformation. Eight intermolecular hydrogen bonds of lengths varying from 2.579(8) to 2.711(5) Å are involved in four rings of 10, 12, 14, and 16 members. The hydrogen bond length appears to be correlated with the size of the hydrogen bonded ring in which it participates.

Introduction

Chemical and physical properties have been measured for the series of methylenediphosphonic acids, $(\text{C}-\text{H}_2)_n(\text{PO}_3\text{H}_2)_2$, where $n = 1-6$.³ The observed melting points, IR spectra, and NMR spectra show interesting changes as n increases. In a previous paper,⁴ we have discussed the molecular and crystal structures of $(\text{C}-\text{H}_2)(\text{PO}_3\text{H}_2)_2$, PCP, and $(\text{CH}_2)_2(\text{PO}_3\text{H}_2)_2$, PC_2P . Each of these materials contains an interwoven network of strong intermolecular hydrogen bonds formed between phosphonic acid groups. The two halves of P-C-C-P are related by a center of symmetry hence the backbone is precisely planar. The planar conformations affect both the physical and chemical properties of each material. Planarity of the backbone is not required for $(\text{CH}_2)_3(\text{P}-\text{O}_3\text{H}_2)_2$, PC_3P , hence this molecule is likely to be structurally quite different than PCP or PC_2P . An x-ray structural investigation of PC_3P was undertaken in order to investigate the correlation of structure with chemical and physical properties and to better define the potential binding sites for metal ions.

Experimental Section

Collection and Reduction of X-Ray Data. Propane-1,3-diphosphonic acid, PC_3P , was prepared by the method of Moedritzer and Irani.³ Crystals of sufficient size and quality were grown from a benzene solution by slow evaporation. A diamond shaped plate ($0.038 \times 0.038 \times 0.025$ cm) was selected for data collection. Preliminary oscillation, Weissenberg, and precession photographs showed 2/m Laue symmetry and gave the systematic

TABLE I: Experimental Details for PC_3P

Formula:	$(\text{CH}_2)_3(\text{PO}_3\text{H}_2)_2$
Formula weight:	204.06 g equiv
Space group:	Pc [C_2^2 , no. 7]
Extinctions:	$h0l, l = 2n + 1$
Cell constants:	$a = 9.540(2)$, $b = 9.964(2)$, $c = 9.705(2)$ $\beta = 118.90(1)^\circ$
Cell volume:	807.67 Å ³
Calculated density:	1.68 g cm ⁻³
Measured density:	1.66 g cm ⁻³ [by flotation in $\text{CCl}_4 + \text{HCBBr}_3$]
Number of molecules in the asymmetric unit:	2 ($Z = 4$)
Radiation:	(data collection) Mo $K\alpha$, $\lambda = 0.71073$, 2° take-off angle
Absorption coefficient:	5.214 cm ⁻¹
Maximum 2θ :	50°
Scan width:	1.6°
Scan speed:	0.1° steps
Counting time:	4 s/step (background 16 s each side of peak)
Crystal:	b axis mounted
Volume:	0.296×10^{-4} cm ³ ($0.038 \times 0.038 \times 0.025$ cm)
Maximum transmission factor:	0.90
Minimum transmission factor:	0.86
Number of reflections above $\sigma = 1$:	1391
Number of independent reflections:	1412
R_F factor for all reflections:	0.024
R_F factor for all reflections above 1σ :	0.024
wR_F :	0.057

absences as $h0l$ for $l = 2n + 1$, which is consistent with the two monoclinic space groups, Pc [C_2^2 , no. 7] and $P2_1/c$ [C_2^2 , no. 13]. Accurate unit-cell lattice constants were determined by least-squares analysis of x-ray powder diffraction

TABLE II: Final Positional and Isotropic Thermal Parameters for PC₃P^a

Atom	x	y	z	B ₀
P(1)	0.6384 ^b	0.2892 (1)	0.7396 ^b	
P(2)	1.2070 (2)	0.4817 (1)	1.2176 (2)	
P(3)	0.0624 (2)	-0.0124 (1)	0.2769 (2)	
P(4)	0.6341 (1)	-0.1850 (1)	0.7818 (1)	
O(1)	0.4642 (4)	0.2596 (4)	0.6992 (4)	
O(2)	0.6447 (4)	0.3809 (3)	0.6143 (4)	
O(3)	0.7199 (3)	0.1575 (3)	0.7551 (3)	
O(4)	1.2620 (4)	0.5450 (3)	1.1124 (4)	
O(5)	1.2572 (4)	0.3326 (3)	1.2550 (4)	
O(6)	1.2783 (4)	0.5631 (3)	1.3736 (4)	
O(7)	-0.0139 (4)	-0.1543 (3)	0.2421 (4)	
O(8)	0.0206 (3)	0.0673 (3)	0.3830 (4)	
O(9)	0.0052 (4)	0.0646 (4)	0.1196 (4)	
O(10)	0.6625 (4)	-0.0528 (3)	0.8748 (3)	
O(11)	0.5528 (3)	-0.2834 (3)	0.8369 (3)	
O(12)	0.7976 (4)	-0.2439 (3)	0.8119 (4)	
C(1)	0.7349 (5)	0.3860 (4)	0.9154 (5)	
C(2)	0.9137 (6)	0.4023 (5)	0.9769 (5)	
C(3)	0.9956 (6)	0.4765 (4)	1.1340 (5)	
C(4)	0.2725 (5)	-0.0433 (5)	0.3604 (5)	
C(5)	0.3503 (5)	-0.0967 (5)	0.5277 (5)	
C(6)	0.5179 (5)	-0.1507 (4)	0.5769 (5)	
H(1)	0.686 (6)	0.461 (5)	0.885 (6)	3.3 (11)
H(2)	0.716 (5)	0.349 (5)	0.984 (6)	2.9 (10)
H(3)	0.928 (6)	0.438 (5)	0.909 (7)	3.6 (11)
H(4)	0.964 (6)	0.305 (5)	0.992 (6)	3.6 (11)
H(5)	0.954 (7)	0.584 (6)	1.122 (7)	5.4 (14)
H(6)	0.983 (6)	0.428 (5)	1.214 (6)	3.4 (11)
H(7)	0.308 (5)	0.035 (5)	0.352 (5)	2.3 (9)
H(8)	0.293 (5)	-0.111 (4)	0.294 (5)	2.7 (9)
H(9)	0.358 (5)	-0.028 (4)	0.594 (5)	2.6 (9)
H(10)	0.281 (5)	-0.164 (4)	0.536 (5)	2.4 (9)
H(11)	0.516 (5)	-0.223 (5)	0.530 (5)	2.7 (9)
H(12)	0.584 (5)	-0.084 (4)	0.555 (5)	1.8 (8)
H(13)	0.429 (9)	0.308 (7)	0.684 (9)	5.6 (23)
H(14)	0.614 (6)	0.333 (5)	0.537 (6)	3.2 (11)
H(15)	1.340 (8)	0.326 (6)	1.270 (8)	4.9 (15)
H(16)	1.283 (8)	0.530 (6)	1.441 (7)	4.2 (15)
H(17)	0.008 (7)	0.022 (6)	0.075 (7)	3.0 (16)
H(18)	-0.099 (7)	-0.161 (6)	0.235 (7)	4.3 (14)
H(19)	0.681 (6)	0.003 (5)	0.847 (6)	2.5 (11)
H(20)	0.870 (6)	-0.188 (4)	0.836 (5)	2.2 (9)

^a Estimated standard deviations are given in parentheses. ^b The x and y coordinates were fixed in the least-squares refinement because of the polar axes along x and z.

data. The crystal mounted along the crystallographic b axis was placed on a GE XRD-490 automated diffractometer for data collection. Details specific to data collection and analysis are given in Table I. Specific details on the instrumentation used in this data collection have been described previously.⁵

Solution and Refinement of the Structure. The structure was solved by the application of direct methods using the program MULTAN-74.⁶ Phillips, Howells, and Rogers statistics,⁷ and $|E^2 - 1|$ and $|E|$ values supplied by MULTAN indicated that the noncentrosymmetric space group *Pc* is preferred, and thus two unique PC₃P molecules per asymmetric unit are indicated. MULTAN supplied the coordinates of 26 peaks for a solution whose combined figure of merit was 2.513. Analysis of the interpeak distances and angles permitted assignment of all 22 non-hydrogen atoms. Subsequent Fourier and isotropic full-matrix least-squares refinements converged at $R_F = 0.12$. The positions of all hydrogen atoms were located from difference Fourier maps. Several cycles of anisotropic full-matrix least-squares refinement of all non-hydrogen atoms and positional refinement of the hydrogen atoms with fixed isotropic thermal parameters ($B = 5.0 \text{ \AA}^2$) converged at $R_F = 0.028$. Further refinement varying the

TABLE III: Final Anisotropic Thermal Parameters^a ($\times 10^4$) for PC₃P^b

Atom	β_{11}	β_{22}	β_{33}	β_{12}	β_{13}	β_{23}
P(1)	56 (1)	41 (1)	62 (1)	0 (1)	28 (1)	-1 (1)
P(2)	61 (2)	53 (1)	57 (1)	-7 (1)	30 (1)	-7 (1)
P(3)	57 (2)	61 (1)	58 (1)	4 (1)	30 (1)	6 (1)
P(4)	55 (1)	47 (1)	59 (1)	3 (1)	24 (1)	-5 (1)
O(1)	63 (4)	65 (4)	112 (5)	-1 (4)	38 (4)	3 (3)
O(2)	122 (5)	59 (3)	72 (4)	-19 (3)	47 (4)	-5 (3)
O(3)	76 (4)	52 (3)	114 (4)	4 (3)	52 (3)	-1 (3)
O(4)	88 (4)	92 (3)	66 (4)	-19 (3)	43 (3)	-8 (3)
O(5)	75 (5)	59 (3)	146 (6)	4 (3)	45 (4)	-4 (3)
O(6)	105 (5)	78 (3)	58 (4)	-22 (3)	36 (4)	-12 (3)
O(7)	94 (5)	69 (3)	133 (5)	-2 (3)	71 (4)	-2 (3)
O(8)	77 (4)	73 (3)	89 (4)	10 (3)	44 (4)	-4 (3)
O(9)	104 (6)	78 (4)	71 (5)	7 (3)	34 (4)	8 (4)
O(10)	111 (5)	55 (3)	83 (4)	12 (3)	52 (4)	2 (3)
O(11)	73 (4)	71 (3)	78 (4)	15 (3)	28 (3)	-16 (3)
O(12)	64 (4)	62 (3)	129 (5)	7 (3)	32 (4)	8 (3)
C(1)	67 (6)	72 (5)	72 (5)	-4 (4)	42 (5)	-7 (4)
C(2)	79 (7)	84 (5)	58 (6)	-11 (4)	36 (5)	-16 (4)
C(3)	70 (7)	73 (5)	75 (6)	-1 (4)	43 (5)	-11 (4)
C(4)	71 (7)	75 (5)	70 (6)	11 (4)	35 (5)	14 (4)
C(5)	64 (6)	92 (5)	66 (5)	13 (4)	40 (5)	15 (4)
C(6)	72 (6)	73 (5)	60 (5)	-8 (4)	32 (5)	2 (4)

^a The form of the anisotropic thermal parameter is $\exp[-(\beta_{11}h^2 + \beta_{22}k^2 + \beta_{33}l^2 + 2\beta_{12}hk + 2\beta_{13}hl + 2\beta_{23}kl)]$. ^b Estimated standard deviations are given in parentheses.

isotropic thermal parameters of the hydrogen atoms gave a final $R_F = 0.024$, $R_F^2 = 0.043$, $R_{wF^2} = 0.057$, and $\Sigma_2 = 2.20$ for 1412 unique reflections, where

$$R_F = \frac{\sum |F_o| - |F_c|}{\sum |F_o|}$$

$$R_{wF^2} = \left[\frac{\sum w(F_o^2 - F_c^2)^2}{\sum wF_o^2} \right]^{1/2}$$

$$\Sigma_2 = \left[\frac{\sum w(F_o^2 - F_c^2)^2}{(N_o - N_R)} \right]^{1/2}$$

N_o is the number of independent observations and N_R is the number of parameters varied. A final difference Fourier map revealed no peaks above 0.33 e/\AA^3 . No parameter varied by more than $\Delta/\sigma = 0.28$ in the last cycle of the refinement. The very satisfactory measures of agreement which were achieved are attributed to the extensive hydrogen bonding which knits the molecules tightly and restricts thermal disorder.

A comparison of the observed and calculated structure factor amplitudes is available as supplementary material (see paragraph at end of text regarding supplementary material).

Scattering factors for neutral atoms were taken from the compilation of Cromer and Waber.⁸ The phosphorus, oxygen, and carbon atoms were corrected for anomalous dispersion using the values of Cromer.⁹ Computational programs used for these structural determinations were RTMON,¹⁰ data collection and reduction; DATALIB,¹¹ absorption, Lorentz, and polarization corrections; DATASORT,¹² data sorting; S5XFLS,¹³ least-squares refinement; S5FOUR,¹³ Fourier synthesis; ORFFE3,¹³ distance and angles calculation; and OR-TEPII,¹⁴ molecular drawing. All calculations were carried out on the Xerox Sigma V computer of the Chemistry Division, ANL, and the IBM 370/195 of the Applied Mathematics Division, ANL.

Table II is a listing of the final positional parameters of all atoms and the isotropic thermal parameters for hydrogen atoms in PC₃P. Final anisotropic thermal parameters for all non-hydrogen atoms are given in Table III.

The Molecular and Crystal Structure. Interatomic distances for PC₃P are given in Table IV, while interatomic angles are given in Table V. Torsion angles are shown

TABLE IV: Interatomic Distances for PC_3P^a

Bond	Distance, Å	Bond	Distance, Å
(a) Intramolecular Distances			
P(1)-O(3)	1.495 (3)	P(3)-O(8)	1.499 (4)
P(1)-O(1)	1.540 (5)	P(3)-O(7)	1.551 (4)
P(1)-O(2)	1.545 (3)	P(3)-O(9)	1.553 (6)
P(2)-O(4)	1.495 (5)	P(4)-O(11)	1.500 (4)
P(2)-O(5)	1.549 (4)	P(4)-O(10)	1.545 (3)
P(2)-O(6)	1.554 (7)	P(4)-O(12)	1.556 (4)
P(1)-C(1)	1.780 (10)	P(3)-C(4)	1.789 (10)
P(2)-C(3)	1.774 (10)	P(4)-C(6)	1.781 (13)
C(2)-C(1)	1.519 (9)	C(5)-C(4)	1.518 (10)
C(2)-C(3)	1.526 (10)	C(5)-C(6)	1.528 (8)
C(1)-H(1)	0.85 (5)	C(4)-H(7)	0.88 (5)
C(1)-H(2)	0.86 (5)	C(4)-H(8)	1.02 (5)
C(2)-H(3)	0.82 (6)	C(5)-H(9)	0.92 (5)
C(2)-H(4)	1.06 (5)	C(5)-H(10)	0.97 (5)
C(3)-H(5)	1.13 (6)	C(6)-H(11)	0.85 (5)
C(3)-H(6)	0.97 (5)	C(6)-H(12)	1.01 (4)
(b) Non-Hydrogen Bonding Interactions			
O(1)-O(3)	2.449 (7)	O(7)-O(9)	2.533 (5)
O(1)-O(2)	2.544 (7)	O(7)-O(8)	2.534 (5)
O(2)-O(3)	2.527 (5)	O(8)-O(9)	2.488 (5)
O(4)-O(6)	2.470 (5)	O(10)-O(11)	2.478 (4)
O(4)-O(5)	2.541 (4)	O(10)-O(12)	2.534 (5)
O(5)-O(6)	2.533 (5)	O(11)-O(12)	2.493 (5)
P(1)-P(2)	5.505 (2)	P(3)-P(4)	5.558 (2)
P(1)-P(2)'	4.620 (2)	P(2)-P(4)'	4.824 (6)
P(1)-P(3)'	4.763 (3)	P(2)-P(2)'	4.866 (1)
P(1)-P(4)'	4.543 (2)	P(3)-P(4)'	4.556 (2)
P(1)-P(4)'	4.745 (2)	P(3)-P(3)'	4.859 (1)
		P(3)-P(4)'	4.874 (4)

^a Estimated standard deviations are given in parentheses.

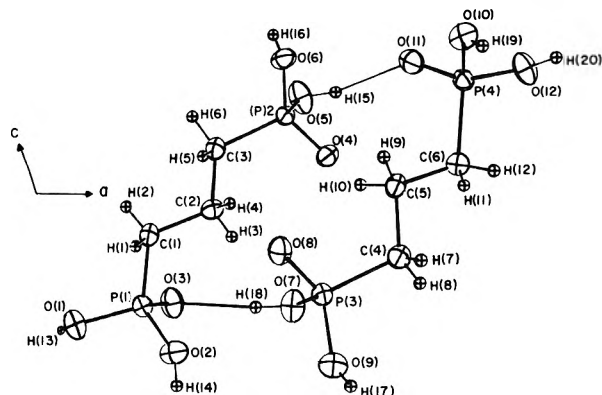


Figure 1. Sixteen-membered ring formed by PC_3P asymmetric unit.

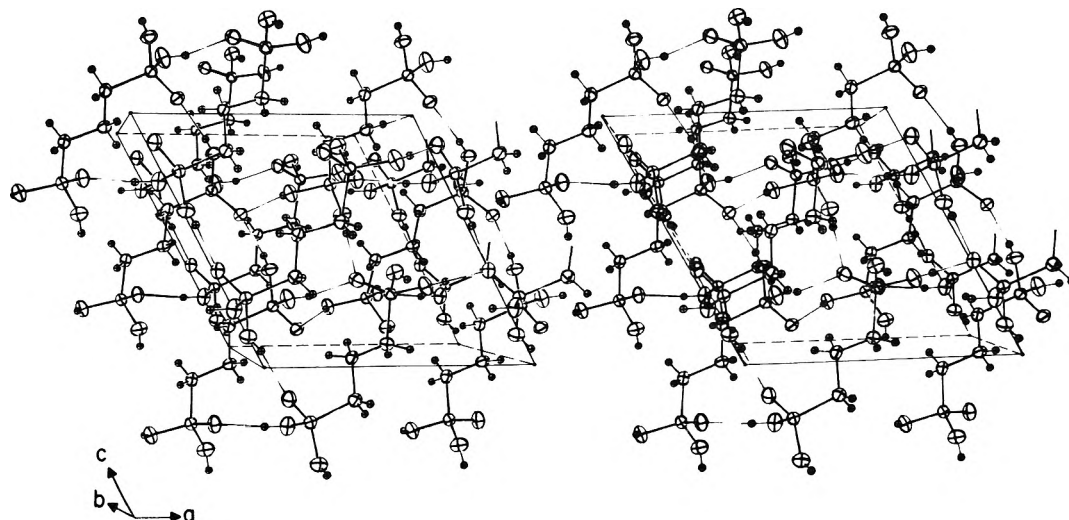


Figure 2. Stereoview of the packing of PC_3P molecules within the unit cell. The hydrogen bonding is clearly shown.

TABLE V: Interatomic Angles for PC_3P^a

Angle	Deg	Angle	Deg
(a) Interatomic Angles			
O(1)-P(1)-O(2)	111.1 (6)	O(7)-P(3)-O(9)	109.4 (5)
O(1)-P(1)-O(3)	107.6 (2)	O(7)-P(3)-O(8)	112.4 (3)
O(2)-P(1)-O(3)	112.4 (3)	O(8)-P(3)-O(9)	109.3 (2)
O(4)-P(2)-O(5)	113.2 (2)	O(10)-P(4)-O(12)	109.6 (5)
O(4)-P(2)-O(6)	108.2 (2)	O(10)-P(4)-O(11)	108.9 (2)
O(5)-P(2)-O(6)	109.4 (4)	O(11)-P(4)-O(12)	109.3 (2)
C(1)-P(1)-O(1)	110.0 (6)	C(4)-P(3)-O(7)	104.3 (3)
C(1)-P(1)-O(2)	103.6 (2)	C(4)-P(3)-O(8)	113.1 (5)
C(1)-P(1)-O(3)	112.1 (5)	C(4)-P(3)-O(9)	108.3 (6)
C(3)-P(2)-O(4)	113.4 (5)	C(6)-P(4)-O(10)	109.1 (3)
C(3)-P(2)-O(5)	103.5 (3)	C(6)-P(4)-O(11)	111.9 (4)
C(3)-P(2)-O(6)	109.0 (6)	C(6)-P(4)-O(12)	108.0 (6)
P(1)-C(1)-C(2)	113.4 (6)	P(3)-C(4)-C(5)	114.0 (7)
P(2)-C(3)-C(2)	113.0 (7)	P(4)-C(6)-C(5)	114.2 (7)
C(1)-C(2)-C(3)	112.3 (7)	C(4)-C(5)-C(6)	110.7 (7)
H(1)-C(1)-H(2)	111 (5)	H(7)-C(4)-H(8)	109 (4)
H(3)-C(2)-H(4)	106 (5)	H(9)-C(5)-H(10)	107 (4)
H(5)-C(3)-H(6)	112 (4)	H(11)-C(6)-H(12)	107 (4)

^a Estimated standard deviations are given in parentheses.

TABLE VI: Torsion Angles for PC_3P^a

Angle	Deg
P(1)-C(1)-C(3)-P(2)	-2.7 (8)
P(3)-C(4)-C(6)-P(4)	-42.6 (8)
P(1)-C(1)-C(2)-C(3)	-175.7 (3)
P(2)-C(3)-C(2)-C(1)	174.0 (3)
P(3)-C(4)-C(5)-C(6)	166.9 (3)
P(4)-C(6)-C(5)-C(4)	168.3 (3)

^a Estimated standard deviations are given in parentheses.

in Table VI. Table VII lists the hydrogen bonded distances and angles. Atom labels and bond distances are shown in Figure 1 while molecular packing and hydrogen bonding are shown in Figure 2.

The crystal structure of PC_3P consists of two crystallographically unrelated and unique molecules of $(C_2H_5)_3(PO_3H_2)_2$. The atoms in each molecule are oriented to form P-C-C-C-P chains which are linked by hydrogen bonded bridges, O(3)-H(18)-O(7) = 2.603(4) Å and O(11)-H(15)-O(5) = 2.580(10) Å, forming the asymmetric unit of the unit cell (see Figure 1). Analysis of the torsion angles (Table VI) of the two independent PC_3P molecules clearly shows that they adopt differing conformations. The torsion angles P(1)-C(1)-C(3)-P(2) = -2.7°, P(1)-

TABLE VII: Intermolecular Hydrogen-Bonded Distances and Angles^a

Bond	Distance, Å	Angle, deg	Ring system (no. of members)
O(1)-H(13)-O(4)	2.579 (8)	168 (10)	12
O(1)-H(13)	0.57 (7)		
O(4)-H(13)	2.02 (7)		
O(2)-H(14)-O(11)	2.584 (10)	159 (5)	12, 14
O(2)-H(14)	0.81 (5)		
O(11)-H(14)	1.81 (5)		
O(5)-H(15)-O(11)	2.580 (10)	169 (7)	12, 16
O(5)-H(15)	0.73 (7)		
O(11)-H(15)	1.86 (7)		
O(6)-H(16)-O(4)	2.628 (5)	171 (7)	12
O(6)-H(16)	0.72 (6)		
O(4)-H(16)	1.92 (6)		
O(9)-H(17)-O(8)	2.711 (5)	161 (8)	14
O(9)-H(17)	0.62 (5)		
O(8)-H(17)	2.12 (5)		
O(7)-H(18)-O(3)	2.603 (4)	168 (6)	10, 14, 16
O(7)-H(18)	0.78 (6)		
O(3)-H(18)	1.83 (6)		
O(10)-H(19)-O(3)	2.580 (5)	176 (5)	10
O(10)-H(19)	0.68 (5)		
O(3)-H(19)	1.90 (5)		
O(12)-H(20)-O(8)	2.585 (7)	178 (5)	10, 14
O(12)-H(20)	0.83 (5)		
O(8)-H(20)	1.75 (5)		

^a Estimated standard deviations are given in parentheses.

C(1)-C(2)-C(3) = -175.7(3)°, and P(2)-C(3)-C(2)-C(1) = 174.0(3)° for unit 1 [P(1)-C(1)-C(2)-C(3)-P(2)] indicate a nearly planar molecular backbone. However, the torsion angles P(3)-C(4)-C(6)-P(4) = -42.6°, P(3)-C(4)-C(5)-C(6) = 166.9(3)°, and P(4)-C(6)-C(5)-C(4) = 168.3(3)° for unit 2 [P(3)-C(4)-C(5)-C(6)-P(4)] show a distinct nonplanar conformation attributed to rotations about the C(4)-C(5) and C(5)-C(6) bonds. This result may be contrasted with the related (CH₂)₂(PO₃H₂)₂, PC₂P, molecule⁴ where the P-C-C-P chain unit is planar.

The coordination around the P atoms is essentially tetrahedral as indicated by the interatomic angles given in Table V. Each P is bound to three oxygen atoms and one carbon atom. Two P-O bond distances represent P-O single bonds while the third shows considerable double bond character (see Table IV). Average P=O, P-O(H), and P-C distances are 1.497(3), 1.549(9), and 1.781(8) Å, respectively. The C-P-O angles show small deviations from a tetrahedral value depending upon the environment of the oxygen atom. The C-P=O angles have an average value of 112.6(8)° whereas C-P-O angles, where the oxygen is hydrogen bonded to phosphonyl oxygens O(11) or O(3), average to 105.1(10)° and those C-P-O angles where the oxygen is hydrogen bonded to O(4) or O(8) average to 108.9(13). The latter differences seem to indicate a greater amount of strain present for hydrogen bonding involving O(11) and O(3). The O(3) and O(11) atoms are involved in eight hydrogen bonded ring networks while the O(4) and O(8) atoms are involved in only five ring networks.

The average C-C distance, 1.523(5) Å, in PC₃P is appreciably shorter than the C-C distance, 1.544(4) Å, observed for PC₂P. This difference may be attributed to a shielding of the carbon atoms from the electron-withdrawing phosphonic acid groups. In PC₂P, both carbon atoms are adjacent to phosphonic acid groups, while in PC₃P the central carbon is shielded by the additional methylene groups. Average P-C-C and C-C-C angles in PC₃P are 113.7(7) and 111.5(8)°, respectively.

Table IV shows the P...P interactions within the unit cell. The average P...P interaction distance within a

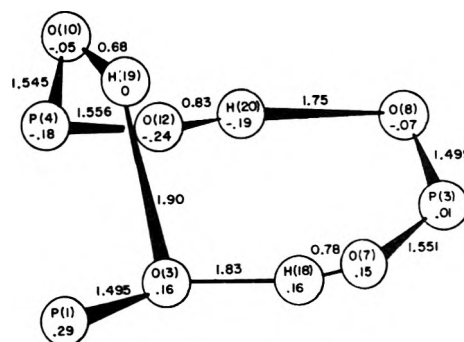


Figure 3. Fourteen-membered ring formed by hydrogen bonding involving three of the four phosphorus atoms. The y coordinate for each atom is given in the circle.

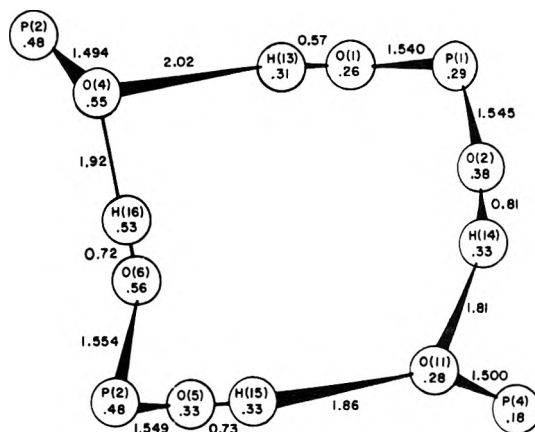


Figure 4. Twelve-membered ring formed by hydrogen bonding. The y coordinate for each atom is given in the circle.

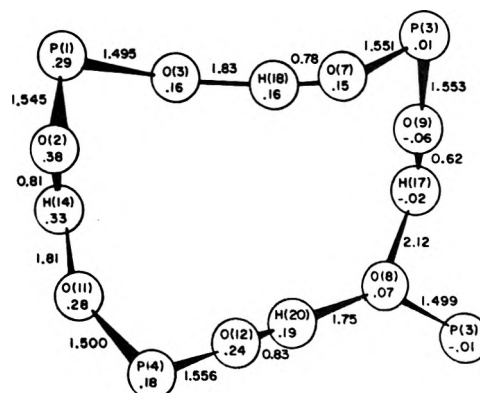


Figure 5. Ten-membered ring formed by hydrogen bonding involving only two of the four phosphorus atoms. The y coordinate for each atom is given in the circle.

molecule of PC₃P, 5.53(3) Å, is larger than the close intermolecular P...P interactions of average distance, 4.72(3) Å. This compound represents a crossover point within the series (CH₂)_n(PO₃H₂)₂ where members with n ≥ 3 will show closer intermolecular P...P contacts than intramolecular contacts.

The hydrogen bonding observed in the crystal structure of PC₃P is quite similar to that previously observed for PCP and PC₂P. Each P=O oxygen participates in two hydrogen bonds, while each P-O(H) group is active in a single hydrogen bond (Table VII). Of the eight hydrogen bonds which are formed, two participate in linking two PC₃P molecules into a 16-membered ring (Figure 1). However, these hydrogen bonds also participate in smaller H-bonded rings (see Figure 3-5). Figures 3-5 show hydrogen-bonded rings of 14-, 12-, and 10-members, respectively, which are formed by the eight hydrogen bonds.

TABLE VIII: Physical and Chemical Data of Methylene-diphosphonic Acids $(\text{CH}_2)_n(\text{PO}_3\text{H}_2)_2^c$

n	$M_p, ^\circ\text{C}$	^{31}P NMR ^a	P=O stretching, ^b cm^{-1}	P-OH stretching, ^b cm^{-1}
1	200	-16.7	1215	2695, 2273
2	220-223	-27.4	1220	2690, 2272
3	178	-28.2	1208	2660, 2336
4	217-220	-31.6	1205	2690, 2326
5	155	-31.9	1212	2625, 2326
6	206-208	-30.6	1170	2675, 2309

^a ^{31}P NMR chemical shifts in ppm relative to 85% H_3PO_4 . ^b KBr pellets. ^c Reference 3.

Several hydrogen bonds are unique to only one of the ring systems. Seven of the eight hydrogen bonds are quite short and lie within the range of 2.579(8) to 2.628(5) Å; the eighth bond shows a distance of 2.711(5) Å. This latter distance, which is significantly longer and therefore weaker than the other hydrogen bonds, is found only in the 14-membered ring, the largest of the rings which contain unique hydrogen bonds.

Discussion

Two different conformations of the same molecule existing together in the same crystal is structurally unusual. The conformational differences result from group rotations about C-C single bonds in the nonplanar conformer which are undoubtedly in response to hydrogen bond and packing forces. The phosphonic acid moieties of the nonplanar PC_3P backbone contain atoms P(3) and P(4), which are part of the 10- and 14-membered ring (Figures 5 and 3). The 10-membered ring is highly nonplanar and shows considerable strain in the puckering of the P(4)-O(10)-H(19)-O(3) part of the ring. The phosphonic ring group involving P(4) rotates about the C(5)-C(6) bond to form the strong 2.580(5)-Å, O(10)-H(19)-O(3), hydrogen bond. The phosphonic acid group containing P(3) must be rotated also in order to form the strong remaining 2.585-Å, O(12)-H(20)-O(8), and 2.603-Å, O(7)-H(18)-O(3), hydrogen bonds of the 10-membered ring. Thus, the rotations of the phosphonic acid groups to achieve strong hydrogen bonds lead to the -42.6° dihedral angle between P(3) and P(4) as viewed down the C(4)-C(6) vector.

In this study of PC_3P and in the previous study of PCP and PC_2P , the longest hydrogen bonds are part of the largest hydrogen-bonded rings. As the ring size decreases so does the length of the longest hydrogen bonds observed in the ring until very short (~ 2.50 Å) hydrogen bonds are observed for the eight-membered rings and spiral hydrogen-bonded units.¹⁵ In PCP, the 16-membered rings contain 2.604(3)- and 2.677(3)-Å hydrogen bonds, while the eight-membered ring and spirals show 2.542(3)- and 2.565(3)-Å hydrogen bonds, respectively. In PC_2P , spiral bonds of 2.527(2) and 2.543(2) Å were observed. In PC_3P , as was discussed above, similar trends hold. Therefore, the trend that the smaller the ring size the stronger the hydrogen bonding seems to hold in these unsubstituted polymethylene-diphosphonic acids.

Moedritzer and Irani³ have measured the melting points, the ^{31}P NMR chemical shifts, and the IR spectra for $(\text{CH}_2)_n(\text{PO}_3\text{H}_2)_2$ molecules of $n = 1, 6$ (see Table VIII). The structural parameters which we have deduced by x-ray

diffraction for $n = 1-3$ show correlations with this chemical and physical data. The strongest hydrogen bonding occurs in PC_2P corresponding to the highest melting point, 223 $^\circ\text{C}$, the weakest in PC_3P corresponding to a low melting point of 178 $^\circ\text{C}$, while PCP shows an intermediate hydrogen bond strength and a melting point of 200 $^\circ\text{C}$. It is quite clear that for $n = 4, 6$, since the melting point has again increased, the molecules may have a center of symmetry and strong spiral hydrogen bonds may be formed. For $n = 5$, the melting point drops to 155 $^\circ\text{C}$ indicating a very loose hydrogen-bonded system.

The ^{31}P NMR data indicate that for $n > 3$ the influence of one phosphonic acid group on the other is completely shielded by the methylene carbons. For $n = 3$, the phosphorus atoms are 5.5 Å apart and are not completely shielded by the methylene carbons. It might be speculated that, if a similar hydrogen bonded network is established in solution, the intermolecular phosphorus atoms which have an average distance of 4.72 Å are actually influencing the chemical shifts.

The IR P=O stretching frequency shows a constant value for $n = 1-3$ confirming what has been observed structurally that all P=O bond distances in each of the three materials fall within a very small range of 1.493(2)-1.502(2) Å. The P-O-H frequency remains constant at $n = 1, 2$ but increases 60 cm^{-1} for one vibration and decreases 30 cm^{-1} for the other vibration for $n = 3$. Structurally, all P-O(H) distances are similar for all three molecules where a range of 1.540(5)-1.556(4) Å is observed; however, the minimum and maximum distances listed are observed in PC_3P and the P-O(H) frequency changes may be indicative of this deviation.

Acknowledgment. We wish to acknowledge the assistance of Dr. Paul Johnson in the use of the MULTAN program.

Supplementary Material Available: A listing of calculated and observed structure factor amplitudes (8 pages). Ordering information is given on any current masthead page.

References and Notes

- (1) Work performed under the auspices of the U.S. Energy Research and Development Administration.
- (2) Department of Biochemistry, Loyola University School of Dentistry, Maywood, Ill. 60153.
- (3) K. Moedritzer and R. R. Irani, *J. Inorg. Nucl. Chem.*, **22**, 297 (1961).
- (4) S. W. Peterson, E. Gebert, A. H. Reis, Jr., M. E. Druyan, G. W. Mason, and D. F. Peppard, *J. Phys. Chem.*, preceding paper in this issue.
- (5) M. E. Druyan, A. H. Reis, Jr., E. Gebert, S. W. Peterson, G. Mason, and D. F. Peppard, *J. Am. Chem. Soc.*, **98**, 4801 (1976).
- (6) MULTAN-74 written by P. Main, M. M. Woolfson, and G. Germain.
- (7) E. R. Howells, D. C. Phillips, and D. Rogers, *Acta Crystallogr.*, **3**, 210 (1950).
- (8) "International Tables for X-ray Crystallography", Vol. IV, Kynoch Press, Birmingham, England, 1974, p 71.
- (9) "International Tables for X-ray Crystallography", Vol. IV, Kynoch Press Birmingham, England, 1974, p 148.
- (10) An IBM 1130 program written by J. Scherer at ANL.
- (11) An IBM 370/195 program written by H. A. Levy.
- (12) An IBM 370/195 program written by H. A. Levy.
- (13) SSXFLS and SSFOUR are Sigma 5 versions of the programs: ORXFLS3 written by W. R. Busing and H. A. Levy and FOURIER by R. J. Dellaca and W. T. Robinson. OFFEE3 written by W. R. Busing and H. A. Levy.
- (14) OR-TEPII written by C. Johnson.
- (15) A spiral hydrogen bonded unit has a similar eight-membered repeat as if an eight-membered ring were broken and then linked to another opened ring.

A Urey-Bradley Force Field for Bromochlorofluoromethane

M. Diem[†] and D. F. Burow*

Bowman-Oddy Laboratories, Department of Chemistry, University of Toledo, Toledo, Ohio 43606 (Received August 16, 1976)

Publication costs assisted by the University of Toledo

A Urey-Bradley type force field was calculated for bromochlorofluoromethane from previously reported vibrational data. Many of the ambiguities inherent in the previously reported general valence force field (GVFF) are thereby avoided. Harmonic frequencies were used to improve the fitting of ν_1 . Calculated frequencies and potential energy distributions obtained from the two force fields are compared. Differences in the descriptions of ν_2 and ν_3 between the two force fields are discussed.

I. Introduction

We recently reported vibrational assignments and normal coordinate analyses of bromochlorofluoromethane¹ and 1-bromo-1-chloro-1-fluoroethane² as part of an effort to study the normal vibrations of simple chiral molecules. A problem which arises in the determination of the force fields of these molecules is the lack of symmetry; thus the number of force constants required for complete description of the molecule far exceeds the number of observed frequencies. In the case of bromochlorofluoromethane, 55 distinct force constants are required to define the potential energy in a generalized valence force field (GVFF) yet there are only nine fundamental modes. A GVFF for bromochlorofluoromethane, constructed by transferring the 55 force constants from similar molecules and fitting nine fundamental frequencies, had been reported earlier by El-Sabban and Zwolinski,³ however, we found this force field to be inadequate for the description of the observed frequencies of the deuterated species. Thus, a GVFF was calculated using 24 frequencies of four isotopic species and 21 force constants.¹ The resulting field was somewhat ambiguous, because selected interaction constants had to be neglected. The choices of interaction constants utilized, however, can influence the resulting diagonal constants to a certain extent.

Here, we report an alternative approach to the force field of bromochlorofluoromethane. The Urey-Bradley force field (UBFF) provides a useful formalism for dealing with the ambiguities inherent in the GVFF treatment of this molecule, since 45 off-diagonal elements f_{ij} in the force constant matrix

$$f_{ij} = \partial^2 V / \partial S_i \partial S_j \quad i \neq j \quad (1)$$

are replaced by six quadratic terms of the form^{4,5}

$$F_{ij} = \partial^2 V / \partial r_{ij}^2 \quad (2)$$

where S_i and S_j are internal coordinates, F_{ij} is a nonbonded quadratic interaction constant, and r_{ij} is the corresponding nonbonded distance. The redundancy introduced by adding r_{ij} as a coordinate leads to the necessity of including six linear, nonbonded interaction constants, F'_{ij} , in addition to a linear bend-bend interaction constant, ρ , the "intramolecular tension".^{4,6} With the widely used assumption^{4,7}

$$F'_{ij} = -0.1F_{ij} \quad (3)$$

a pentatomic molecule of tetrahedral or similar structure can be described by 17 force constants. Thus, the Urey-Bradley formalism seems especially suitable for the treatment of a molecule of C_1 symmetry since the rather arbitrary omission of certain interaction constants is avoided.

II. Experimental Section

Synthesis of HCBrcIF and DCBrcIF, structural data, instrumentation utilized, as well as Raman and mid-infrared data were previously reported.¹ Near-infrared spectra (4000-6300 cm^{-1}) were obtained on a Cary 14 spectrophotometer. Samples were contained in a 10-cm gas cell equipped with Infracil windows. Sample pressure was ca. 300 Torr for the near-infrared measurements.

The Urey-Bradley Z matrix was calculated using a slightly modified version of the Schachtschneider program UBZM.⁸ The kinetic energy matrix elements computed previously¹ were utilized. The force field was perturbed to reproduce the observed frequencies using standard procedures.⁸ All computations were carried out on a Univac 1110 computer.

III. Results and Discussion

The observed fundamental frequencies for HCBrcIF and DCBrcIF are listed in Table I, along with calculated frequencies and differences between observed and calculated values using both GVFF and UBFF.

Although the overall frequency fit is better with the Urey-Bradley field (0.50 vs. 0.60%), the accuracy of the calculated C-H and C-D stretching frequencies remains unsatisfactory. In an attempt to improve this situation the restrictions of eq 3 were removed for $F'_{\text{H-F}}$, $F'_{\text{H-Cl}}$, and $F'_{\text{H-Br}}$ and these constants were varied independently. Although the overall frequency fit improved slightly, the discrepancies between observed and calculated frequencies persisted in the C-H stretching modes.

Scherer and Overend⁹ reported a similar problem with the UBFF description of the C-H and C-D modes of methyl halides. For these molecules, the error, Δ , could be reduced drastically by the use of harmonic frequencies, ω_i , instead of the observed frequencies, ν_i . For HCBrcIF, sufficient data to calculate all harmonic frequencies are not readily available due to Fermi resonance between several overtones and fundamentals.¹ Thus, the C-H stretching mode was treated as the only significantly anharmonic vibration.

Values for ω_1 were obtained from the overtone $2\nu_1$, observed at 5930.3 (d_c) and 4475.0 cm^{-1} (d_1), by a diatomic approximation of the mode. The harmonic frequencies are found to be 3146.8 and 2317.0 cm^{-1} for d_0 and d_1 com-

[†] Present address: Department of Chemistry, Syracuse University, Syracuse, N.Y. 13210.

TABLE I: Observed and Calculated Frequencies (cm^{-1}) for $\text{HCBBr}^{35}\text{ClF}$ and $\text{DCBr}^{35}\text{ClF}^e$

Observed frequencies	Calculated frequencies					
	GVFF	Δ^a	UBFF ^b	Δ	UBFF ^c	Δ
$\text{HCBBr}^{35}\text{ClF}$						
ν_1 3025.7 ω_1 3146.8 ^d	3039.4	-13.7	3058.4	-32.7	3162.7	-15.9
ν_2 1310.9	1301.7	9.2	1312.8	-1.9	1311.9	-1.0
ν_3 1205.0	1203.3	1.7	1206.4	-1.4	1206.3	-1.3
ν_4 1078.3	1073.8	4.5	1081.4	-3.1	1082.0	-3.7
ν_5 787.8	795.2	-7.4	791.7	-3.9	791.4	-3.6
(ν_5 784.4)	(791.2)	(-6.8)	(789.2)	(-4.8)	(788.8)	(-4.4)
ν_6 663.8	669.7	-5.9	653.1	10.7	652.5	11.3
ν_7 426.7	425.9	0.8	427.2	-0.5	427.3	-0.6
(ν_7 422.8)	(422.0)	(0.8)	(423.5)	(-0.7)	(423.5)	(-0.7)
ν_8 314.5	309.8	4.7	314.2	0.3	314.2	0.3
ν_9 225.7	225.1	0.6	225.7	0.0	225.7	0.0
(ν_9 222.6)	(221.7)	(0.6)	(222.2)	(0.4)	(222.2)	(0.4)
$\text{DCBr}^{35}\text{ClF}$						
ν_1 2264.0 ω_1 2317.0 ^d	2251.1	12.9	2218.0	46.0	2295.3	21.7
ν_2 974.6	977.3	-2.7	972.5	2.1	972.2	2.4
ν_3 919.2	922.5	-3.3	917.1	2.1	917.4	1.8
ν_4 1083.0	1088.4	-5.4	1081.8	1.2	1082.3	0.7
ν_5 749.7	743.8	5.9	745.9	3.8	746.5	3.2
(ν_5 746.3)	(740.1)	(6.2)	(743.0)	(3.3)	(743.5)	(2.8)
ν_6 620.7	614.0	6.7	629.3	-8.6	627.4	-6.7
ν_7 424.9	422.9	2.0	424.6	0.3	424.8	0.1
(ν_7 421.4)	(419.2)	(2.2)	(421.0)	(0.4)	(421.2)	(0.2)
ν_8 313.0	309.2	4.1	314.1	-0.8	313.6	0.3
ν_9 224.2	224.7	-0.5	224.7	-0.5	224.7	0.5
(ν_9 221.1)	(221.3)	(-0.2)	(221.2)	(-0.1)	(221.2)	(-0.1)

^a $\Delta = \nu_{\text{obsd}} - \nu_{\text{calcd}}$. ^b Standard UBFF. ^c UBFF, using ω_1 instead of ν_1 . ^d Harmonic frequencies. ^e Frequencies for ³⁷Cl species in parentheses.

TABLE II: Potential Energy Distribution in Terms of Diagonal Force Constants^a

Mode	Frequency, cm^{-1}	Description: GVFF	Description: UBFF
HCBBrClF			
ν_1	3025.7	0.99 C-H	1.01 C-H
ν_2	1310.9	0.68 HCl; 0.26 HCF	0.83 HCF; 0.27 HCB
ν_3	1205.0	0.50 HCF; 0.45 HCB	0.64 HCl; 0.49 HCB
ν_4	1078.3	0.95 C-F	1.11 C-F
ν_5	787.8	0.83 C-Cl; 0.22 FCCl	0.77 C-Cl; 0.35 C-Br
ν_6	663.8	0.56 C-Br; 0.21 FCBr; 0.17 ClCB	0.45 C-Br; 0.20 C-Cl; 0.17 ClCB
ν_7	426.7	0.50 FCCl	0.56 FCCl
ν_8	314.5	0.50 FCBr; 0.42 C-Br	0.58 FCBr; 0.24 C-Br
ν_9	225.7	0.65 ClCB; 0.21 FCCl	0.73 ClCB
DCBrClF			
ν_1	2264.0	0.97 C-H	1.04 C-H
ν_2	974.6	0.39 HCl; 0.21 C-F; 0.20 HCB	0.85 HCF; 0.27 HCB
ν_3	919.2	0.68 HCF; 0.27 HCB	0.59 HCl; 0.27 HCB; 0.24 C-Cl
ν_4	1083.0	0.78 C-F; 0.20 HCl	1.11 C-F
ν_5	749.7	0.68 C-Cl; 0.14 FCCl; 0.14 HCl	0.58 C-Cl; 0.21 C-Br
ν_6	620.7	0.46 C-Br; 0.22 HCB; 0.20 FCBr	0.45 C-Br; 0.15 ClCB
ν_7	424.9	0.50 FCCl	0.57 FCCl
ν_8	313.3	0.50 FCBr; 0.43 C-Br	0.58 FCBr; 0.24 C-Br
ν_9	224.2	0.65 ClCB; 0.20 FCCl	0.73 ClCB

^a Only major contributors are listed.

pounds, respectively (Table I). It is apparent that the use of the C-H harmonic frequencies shifts the calculated C-H frequencies in the right direction and improves the overall frequency fit (0.38 vs. 0.50%), although discrepancies between observed and calculated values still persist.

Otherwise, the agreement between observed and calculated frequencies in the UBFF is good for the heavy atom bending, the hydrogen-carbon-halogen bending as well as the C-F and C-Cl stretching modes. The only other mode exhibiting a sizable difference between observed and calculated frequencies is ν_6 , the C-Br stretching fundamental. We attribute this difference to extensive Fermi resonance of ν_6 with $2\nu_8$ and $\nu_7 + \nu_9$ in the d_0 and with $2\nu_8$ in the d_1 species,¹ which prevents an accurate determination of the unperturbed frequencies.

The potential energy distributions (PED) of the two UB fields are not significantly different although K_{CH} differs by ca. 8%. The main contributions of internal coordinates to the normal modes (cf. Table II) are similar for UBFF and GVFF for ν_1 and ν_4 through ν_9 , although the mixing between internal coordinates differs to some extent for the two force fields. As expected, the agreement is good particularly for the three low frequency bending motions. There are, however, some differences in the PED of ν_2 and ν_3 as described by GVFF and UBFF. It is these modes where difficulties in the calculations are expected, because these two modes are combinations of three internal coordinates; the other seven fundamental modes can be described by one internal coordinate as the major contributor.

TABLE III: Relative Raman Intensities ($\nu_2 = 100$) and Depolarization Ratios of ν_2 and ν_3 of Bromochlorofluoromethane- d_0 and - d_1

	HCBrcIF		DCBrClF	
	<i>I</i>	ρ	<i>I</i>	ρ
ν_2	6	0.40	19	0.15
ν_3	4	0.30	7	0.24

In the d_0 species, ν_2 is calculated to be a mixture of the HCCl and HCF internal coordinates (0.68 and 0.26, respectively) in the GVFF, whereas in the UBFF approach, this same mode is described as a mixture of the HCF and HCBrc coordinates (0.83 and 0.27, respectively). For the deuterated species, the UBFF description of ν_2 is the same as it is in the d_0 compound, whereas the GVFF description of this mode changes appreciably between d_0 and d_1 due to the introduction of the C-F mixing. Similar behavior is exhibited by ν_3 . Here, however, the GVFF predicts a similar composition of ν_3 for both d_0 and d_1 compounds (0.50 HCF and 0.45 HCBrc; 0.68 HCF and 0.27 HCBrc, respectively), whereas the UBFF predicts different compositions (0.64 HCCl and 0.49 HCBrc for d_0 and 0.59 HCCl, 0.27 HCBrc, and 0.24 C-Cl for d_1).

The above-mentioned changes in the description of ν_2 and ν_3 pose some interesting questions about the validity of the calculated force fields. It should be pointed out that in the Urey-Bradley calculations, there is little computational ambiguity since no force constants were omitted. Before comparing the UBFF results with the ones obtained using the GVFF, one has to ascertain that the GVFF PED obtained in ref 1 is not dependent on the choice of the interaction constants. Both available GVFF calculations,^{1,3} however, agree in the overall description of ν_2 and ν_3 : ν_2 is a mixture of HCF and HCCl coordinates and ν_3 is a mixture of HCBrc and HCF coordinates, although the composition varies between the descriptions in ref 1 and 3. Inspection of Table II reveals that the differences in the descriptions of ν_2 and ν_3 , for both the d_0 and d_1 species, can be explained as an interchange of composition by ν_2 and ν_3 between GVFF and UBFF approaches. Similar effects are not uncommon in force field calculations when new interaction constants are introduced or interaction constants are varied strongly. Since the hydrogen-carbon-halogen interaction constants in the UBFF are well within the range of previously published values (cf. Table IV), and no constants were omitted, the UBFF PED might prove to be more reliable.

Unfortunately, it is virtually impossible to distinguish experimentally between the different descriptions of ν_2 and ν_3 . However, an attempt was made to clarify the nature of the change in the character of ν_2 and ν_3 upon deuteration as suggested by the GVFF results. If indeed a sizable change occurs upon deuteration, gas-phase IR band envelopes as well as Raman depolarization ratios should be indicative of this change. The relative Raman intensities as well as the depolarization ratios are indeed different for ν_2 and ν_3 of the d_0 and d_1 compounds (cf. Table III). Depolarization ratios are only very qualitative indicators. The gas-phase infrared band envelopes should be much more sensitive, since different contributions to a normal mode should alter the direction of the dipole change within the inertial axis framework, thus giving rise to different rotational-vibrational envelopes. The analysis of the band shapes, however, is complicated by the fact that in this molecule, none of the inertial axes coincides with any bond; thus all bands are hybrids of A, B, and C type envelopes. Preliminary results indicate that the observed band shapes are rather similar for d_0 and d_1 compounds. The situation

TABLE IV: Refined Urey-Bradley Force Constants^a for Bromochlorofluoromethane

	UBFF ^b	UBFF ^c	Lit. values
K_{CCl}	2.0398	2.0315	2.09 ^d
K_{CF}	4.0867	4.0867	4.10 ^c
K_{CH}	3.9207	4.2783	3.90 ^{b,g} -4.37 ^{c,d}
K_{CBr}	1.8813	1.8813	1.72 ^d
H_{ClCF}	0.4814	0.4814	0.24 ^e
H_{ClCH}	0.1132	0.1132	0.02 ^f -0.29 ^d
H_{ClCBr}	0.2886	0.2886	0.08 ^e
H_{FCH}	0.0272	0.0248	0.11 ^f -0.27 ^d
H_{FCBr}	0.5988	0.5936	0.21 ^e
H_{HCBrc}	0.1988	0.1995	0.25 ^d
$F_{Cl \cdot F}$	0.8430	0.8430	0.72 ^e
$F_{Cl \cdot H}$	0.6418	0.6626	0.57 ^d -0.93 ^f
$F_{Cl \cdot Br}$	0.5246	0.5246	0.55 ^{e,g}
$F_{F \cdot H}$	1.3763	1.3836	1.12 ^d -1.21 ^f
$F_{F \cdot Br}$	0.4445	0.4445	0.55 ^e
$F_{H \cdot Br}$	0.6302	0.6009	0.48 ^d -0.95 ^f
ρ	-0.2307	-0.2307	(-0.2)-(-0.3) ^e

^a For nomenclature of the force constants, see ref 12. All values are reported in mdyne/A. The bending constants are not normalized. ^b UBFF, observed frequencies. ^c UBFF, harmonic frequencies for ν_1 . ^d Reference 9. ^e Reference 10. ^f Reference 11. ^g Reference 12.

is further complicated by the presence of Fermi resonance between ν_3 and $\nu_5 + \nu_7$ in the d_0 species. Thus, the question of whether the changes in ν_2 and ν_3 are real cannot yet be answered unambiguously. This ambiguity is another consequence of the asymmetry of the molecule; i.e., without substantially more data, some aspects of the field will remain indeterminant.

Table IV shows the refined Urey-Bradley force constants along with a range of values of published force constants for halomethanes.⁹⁻¹² The standard errors⁸ calculated for the force constants are ca. 7% on the average for stretching and nonbonded constants and ca. 25% on the average for the generally very small bending force constants and for ρ . Most of the stretching and nonbonded force constants seem to transfer well between bromochlorofluoromethane and previously reported molecules; even methyl halide force constants agree reasonably well with the refined constants obtained for HCBrcIF. For the halogen-carbon-halogen bending constants, however, a similar trend is observed in both GVFF and UBFF calculations: these constants must be increased considerably to fit the observed frequencies. Table IV also shows the value of K_{C-H} , the carbon-hydrogen force constant, obtained from the harmonic frequencies. Three other force constants, namely, the nonbonded interactions F_{F-H} , F_{Cl-H} , and F_{Br-H} were varied after the harmonic values for ν_1 were introduced; however, the overall frequency fit could not be improved significantly since ν_2 and ν_3 depend very critically on the values of these three constants. Use of harmonic frequencies for ν_2 and ν_3 certainly would improve the overall frequency fit; unfortunately, $2\nu_2$ and $2\nu_3$ were observed in the d_0 compound, but not in the d_1 molecule.

In summary, the UBFF has been shown to yield a better overall frequency fit than the GVFF (0.38 vs. 0.60%) for a molecule as complex as bromochlorofluoromethane. The definition of the potential energy by only 17 force constants eliminates most of the ambiguities inherent in other force fields. Significant additional improvement of the force field would require further harmonic and band contour analyses.

Acknowledgment. The authors gratefully acknowledge the financial support for this work by the Research

Corporation, by National Science Foundation Grant MPS73-04656A01, and by the University of Toledo Research Award program.

References and Notes

- (1) M. Diem and D. F. Burow, *J. Chem. Phys.*, **64**, 5179 (1976).
- (2) B. A. Hudgens and D. F. Burow, Thirty-First Symposium on Molecular Spectroscopy and Structure, Columbus, Ohio, 1976, Paper WD-9, to be published.
- (3) M. Z. El-Sabban and B. Zvolinski, *J. Mol. Spectrosc.*, **19**, 231 (1966).
- (4) H. C. Urey and C. A. Bradley, *Phys. Rev.*, **38**, 1969 (1931).
- (5) T. Simanouti, *J. Chem. Phys.*, **17**, 245 (1949).
- (6) See, for example, E. B. Wilson, J. C. Decius, and P. C. Cross, "Molecular Vibrations", McGraw-Hill, New York, N.Y., 1955, pp 169-171.
- (7) For theoretical justification of this assumption, see, for example, L. S. Bartell and K. Kuchitsu, *J. Chem. Phys.*, **37**, 69 (1962).
- (8) J. H. Schachtschneider, "Vibrational Analysis of Polyatomic Molecules V and VI", Report No. 231-64, Shell Development Co., Emeryville, Calif. 94608, 1964.
- (9) J. Overend and J. R. Scherer, *J. Chem. Phys.*, **33**, 446 (1960).
- (10) L. H. Ngai and R. H. Mann, *J. Mol. Spectrosc.*, **38**, 322 (1971).
- (11) J. Aldous and I. M. Mills, *Spectrochim. Acta*, **19**, 1567 (1963).
- (12) T. Simanouti, *J. Chem. Phys.*, **17**, 848 (1949).

Monte Carlo Quasi-Classical Trajectory Study of Cl + HBr. Effect of Reactant Vibration on Reaction Rate and Product Energy

James Corgan Brown,[†] H. E. Bass,

Department of Physics and Astronomy, The University of Mississippi, University, Mississippi 38677

and Donald L. Thompson*

Departments of Physics and Chemistry, The University of Mississippi, University, Mississippi 38677 and University of California, Los Alamos Scientific Laboratory, Los Alamos, New Mexico 87545 (Received October 4, 1976)

Publication costs assisted by the University of California

Monte Carlo quasi-classical trajectories have been used to study the reactions $\text{Cl} + \text{HBr} \rightleftharpoons \text{HCl} + \text{Br}$ at 300 and 1000 K. A semiempirical valence-bond (London equation) formalism was used to represent the potential-energy surface. The surface was not adjusted for this reaction system, but was computed using parameters adjusted with kinetic information for related systems. The distributions of product molecules among vibrational and rotational states were computed and compared with experimental results (at 300 K); the agreement is good. The computed thermal rate coefficient is in good accord with the reported measured value. The effect of reactant vibrational energy on product distributions and reaction rate was investigated. The principle of detailed balancing in quasi-classical trajectories was also examined for a limited set of conditions for this system.

I. Introduction

We present here the results of a quasi-classical trajectory study of the forward and reverse reactions $\text{Cl} + \text{HBr} \rightleftharpoons \text{HCl} + \text{Br}$. The main purposes of this study are to examine the influence of reactant, vibration, and translational energy on the reaction rate and product energy partitioning, and to test the principle of detailed balancing applied to quasi-classical trajectories. The potential-energy surface (described in detail in section II) is of the semiempirical valence-bond formalism of Raff, Stivers, Porter, Thompson, and Sims.¹ Since the surface is obtained from atomic parameters adjusted to give agreement of the energy barriers with the activation energies of other reactions² ($\text{H}_2 + \text{Br} \rightarrow \text{HBr} + \text{H}$ and $\text{H}_2 + \text{Cl} \rightarrow \text{HCl} + \text{H}$), the first step in this work was to compute results that can be compared with experimental data to check the validity of the surface.

Atom-diatom molecule reactions involving hydrogen and halogen atoms have been studied extensively. Polanyi and co-workers,³ using infrared chemiluminescence techniques, have obtained extensive detailed information about the distribution of energy among internal states of products in exothermic reactions and about the effects of reactant vibration and rotation on endothermic reactions

by application of the principle of microscopic reversibility.

There have been several experimental studies of the reaction considered in this work. Maylotte, Polanyi, and Woodall^{3d} have reported results of infrared chemiluminescence measurements of reaction product energy distributions and reaction rates for this and similar reactions. Airey⁴ has studied this system in relation to the Cl + HBr pulsed chemical laser. Wodarczyk and Moore⁵ have measured the reaction rate for this system when the reaction is initiated by the laser photolysis of Cl_2 in a flowing Cl_2/HX gas mixture. Bergmann and Moore⁶ have studied the isotope effect on this reaction rate for the substitution of deuterium; they found that DBr reacts more slowly than HBr. There has also been a great deal of experimental data reported for related reactions. Cowley, Horne, and Polanyi^{3c} studied $\text{Cl} + \text{HI} \rightarrow \text{HCl} + \text{I}$ at enhanced collision energies using infrared chemiluminescence, and Polanyi and co-workers^{3e,f} have measured the effect of reactant vibration on the rate and product energy partitioning in $\text{F} + \text{HCl} \rightarrow \text{HF} + \text{Cl}$.

Polanyi and co-workers^{3b,7} have made use of the principle of microscopic reversibility to extract information about endothermic reactions from experimental chemiluminescence data of the reverse, exothermic reactions. It is reasonable to question whether the results of quasi-classical trajectories obey the principle of detailed balancing since the forward and reverse processes are not the same in the calculations. This was the subject of a detailed

[†] Current address: Department of Chemistry, University of Toronto, Toronto, Ontario M5S1A1, Canada.

* On leave from the Los Alamos Scientific Laboratory, 1975-1976.

three-dimensional trajectory study for the case of $F + H_2 \rightarrow HF + H$; the results indicated that microscopic reversibility would yield dependable information concerning the endothermic reaction, if the exothermic data referred to room temperature reagents.⁷ Kuppermann and co-workers^{8,9} found discrepancies between the forward and reverse reaction probabilities computed from collinear quasiclassical trajectories for $F + H_2(v=0) \rightleftharpoons HF(v=2,3) + H$ and $H + H_2(v=0) \rightleftharpoons H_2(v=1) + H$. Because of the limitations of available computer time we were not able to carry out extensive calculations to check detailed balance; we have, however, included in this work some examples to illustrate the degree to which the principle is obeyed for this reaction system.

II. Potential-Energy Surface

The potential-energy surface was obtained from the semiempirical formulation of Raff et al.¹ This nonionic, valence-bond formalism, which treats the systems as consisting of three electrons moving in the potential of a proton and the nonpolarizable Br^+ and Cl^+ cores, contains atomic parameters for each of the halogens. We make the assumption that these atomic parameters are the same for the atoms regardless of the chemical environment in which they are considered.

The analytical form of the potential is the London equation:

$$V = Q_{AB} + Q_{BC} + Q_{AC} - \{1/2[(J_{AB} - J_{BC})^2 + (J_{BC} - J_{AC})^2 + (J_{AC} - J_{AB})^2]\}^{1/2} \quad (1)$$

where Q_{ij} and J_{ij} are the Coulomb and exchange integrals, respectively. They are defined in terms of the singlet- ($^1E_{ij}$) and triplet-state ($^3E_{ij}$) energies using the Heitler-London equations:

$$Q_{ij} = 1/2[{}^1E_{ij} + {}^3E_{ij}] \quad (2)$$

and

$$J_{ij} = 1/2[{}^1E_{ij} - {}^3E_{ij}] \quad (3)$$

Overlap terms are neglected in eq 1-3. The singlet-state energies are given by the Morse function

$${}^1E_{ij} = {}^1D_{ij} \{1 - \exp[-\alpha_{ij}(R_{ij} - R_{eij})]\}^2 - {}^1D_{ij} \quad (4)$$

and the triplet-state energies are given by the Pederesen-Porter¹⁰ functions:

$${}^3E_{ij} = {}^3D_{ij} \{1 + \exp[-\beta_{ij}(R_{ij} - R_{eij})]\}^2 - {}^3D_{ij} \quad (5)$$

for $R_{ij} \leq R_{cij}$ and

$${}^3E_{ij} = C_{ij}(R_{ij} + A_{ij}) \exp(-\sigma_{ij}R_{ij}) \quad (6)$$

for $R_{ij} > R_{cij}$.

The values of the atom-pair potential parameters are listed in Table I. The parameters for HCl and HBr were taken from ref 2. The singlet-state parameters for BrCl were obtained as follows: 1D was taken from the compilation given by Herzberg.¹¹ The Morse exponential constant α was computed from

$$\alpha = \omega_e(2\pi^2 c \mu_{BrCl}/D_e h)^{1/2} \quad (7)$$

where μ_{BrCl} is the reduced mass of BrCl, c is the speed of light, D_e is the dissociation energy (from ref 15), h is Planck's constant, and ω_e ($= 440 \text{ cm}^{-1}$) is the fundamental vibrational frequency reported by Clyne and Coxon.¹² The

TABLE I: Potential-Energy Surface Parameters

Parameter	Atom pair		
	HBr ^a	HCl ^a	BrCl
1D , eV	3.91825	4.61534	2.275 ^b
α , au ⁻¹	0.95878	0.95848	1.0373 ^c
3D , eV	1.3668678	1.34956	1.51172
β , au ⁻¹	0.8360	0.79	0.32402
R_e , au	2.673	2.41	3.11720 ^d
C , eV au	12312.0	17634.0	12434.72
A , au	-2.9774	-2.88770	-2.83518
σ , au ⁻¹	2.366	2.561	2.196
R_c , au	3.7	3.5	3.4

^a From ref 2. ^b From ref 11. ^c Computed from data reported by Clyne and Coxon, ref 12. ^d From ref 13.

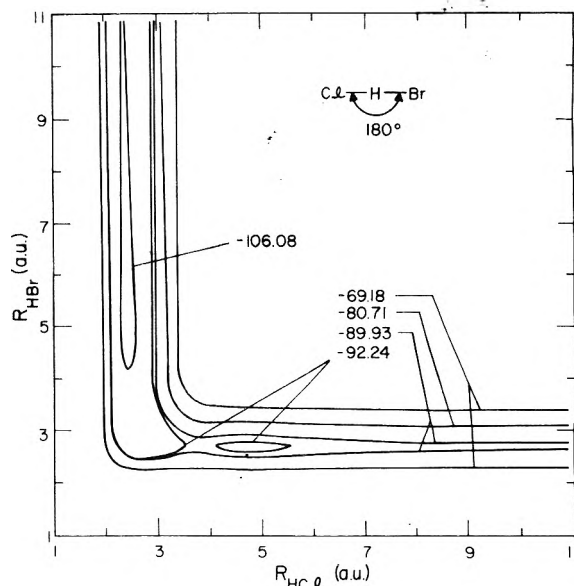


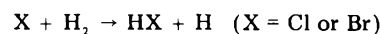
Figure 1. Contour map of the potential-energy surface for collinear collision paths of CHBr. Contour energies are in units of kcal/mol.

equilibrium internuclear separation R_e was taken from the semiempirical calculations of Pohl and Raff.¹³

The remaining BrCl parameters were computed by the method described by Raff et al.¹ In this formulation the potential-energy surface is parameterized through the electron core integral

$$\zeta_x = \langle \phi_x(i) | -Z_x/R_x | \phi_x(i) \rangle \quad (8)$$

where ϕ_x is the appropriate atomic orbital. The value of the integral ζ_x , the adjustable parameter in this formulation, was obtained by adjusting the barrier in the minimum potential-energy reaction pathway of



to be in slight excess of the experimental activation energy.² These atomic parameters are assumed to be transferable for descriptions of the forces in other reactions. The atomic parameter (ζ_x) values used are those computed by Porter et al.²

Figure 1 is a contour map of the potential-energy surface for collinear configurations of CHBr. There is a slight well in the Cl---HBr reactant valley. This well increases in depth slightly as the CHBr angle goes to 90° as can be seen by examining the contour map for this configuration in Figure 2.

III. Computational Methods

The basic methodology and equations for the classical mechanical problem have been described in detail by

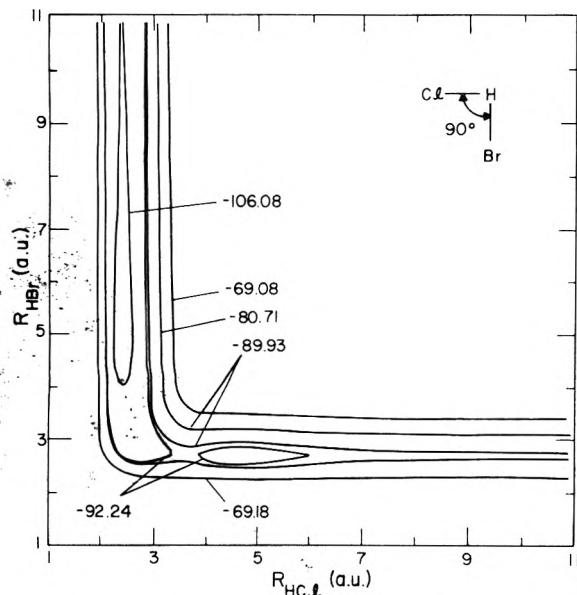


Figure 2. Contour map of the potential-energy surface for collision paths with the Br-H-Cl angle equal to 90° . Contour energies are in units of kcal/mol.

Porter, Karplus, and Sharma.¹⁴ A fourth-order Runge-Kutta-Gill¹⁵ integrator was used to integrate the 12 coupled, first-order differential equations; a constant step size of 4 or 8×10^{-16} s was used, depending on the initial conditions. The integration accuracy was checked by varying the step size, back integrating, and constancy of total energy. The statistical error in samples of trajectories was computed as previously described.¹⁶

To define the initial states of the collision trajectories values must be specified for the following variables: the impact parameter b , the relative translational velocity V_r , the internal energy quantum numbers v (vibration) and J (rotation), the diatomic vibrational-phase ρ , the reaction-shell radius R_s (a constant), and the orientation angles θ , ϕ , and γ (the angles θ and ϕ describe the orientation of the diatomic bond and γ the orientation of the plane of the diatomic angular momentum). Most of the variables were assigned values by Monte Carlo selection from the appropriate probability density functions.¹⁷ However, since we wished to study the effect of nonequilibrium values for certain of these variables most of the calculations reported here were done by arbitrarily assigning values to either or both v and V_r and averaging over the other variables by the Monte Carlo procedure.

The Monte Carlo selection procedures have been described elsewhere.¹⁷ Briefly, the procedure we used is as follows. The values of the relative velocity are selected from the appropriate distribution:

$$f(V_r) = A V_r^3 \exp(-\mu V_r^2 / 2\kappa T) \quad (9)$$

between the limits $V_{r,\min}$ ($= 9.8 \times 10^4$ cm/s) and $V_{r,\max}$ ($= 1.47 \times 10^6$ cm/s) in eq 9, A is the normalization constant, μ is the atom-diatomic molecule reduced mass, κ is the Boltzmann constant, and T is the temperature. Impact parameter values were selected by choosing random values of the orbital angular momentum quantum number l from a flat distribution on the range 0 to l_{\max} , where l_{\max} is given by

$$b_{\max} = [l_{\max}(l_{\max} + 1)]^{1/2} (h/2\pi\mu V_r) \quad (10)$$

(We found that $b_{\max} = 7$ au includes all reactive collisions for the conditions considered here.) The impact parameter values are given by

$$b = [l(l + 1)]^{1/2} (h/2\pi\mu V_r) \quad (11)$$

The vibrational phase was selected using the method of Porter, Raff, and Miller.¹⁸ The orientation angles θ , ϕ , and γ , and the internal states (when averaged over) were selected in the usual way.¹⁷ The value of the reaction-shell radius R_s was fixed at 10 au; at this separation the interaction of the atom with the diatomic molecule is negligible. The vibrational state v was held constant in most of the calculations and the rotational state J was selected by playing the Monte Carlo game.¹⁷

The rotational energy of the product molecule is computed using

$$E_r' = L'^2 / 2\mu r_e^2 \quad (12)$$

L' , the angular momentum of the diatom, can be computed exactly. In eq 12 μ and r_e are the reduced mass and equilibrium separation, respectively, of the diatom. The final state rotational quantum number J' is given by the closest integer solution of

$$E_r = B[J'(J' + 1)] - D[J'(J' + 1)]^2 \quad (13)$$

where B and D are constants.¹¹ The product vibrational energy E_v' is given approximately by

$$E_v' = E_{v_r}' - E_r' \quad (14)$$

where E_{v_r}' is the total internal energy of diatom; E_{v_r}' can be computed exactly. In using eq 14 it is assumed that the vibrational-rotational coupling energy is small relative to the vibrational energy. The product vibrational quantum state v' is then the closest integer solution of

$$E_v' = (v' + 1/2)\omega_e - (v' + 1/2)^2\omega_e x_e \quad (15)$$

where ω_e and $\omega_e x_e$ are constants.¹⁵

IV. Results and Discussion

We have carried out a series of quasi-classical trajectory calculations for the reactions $\text{Cl} + \text{HBr} \rightleftharpoons \text{Br} + \text{HCl}$. One of the objectives of this study was to compare the relative effectiveness of reactant energy in different vibrational states for promoting reaction. Also of interest is the testing of detailed balancing in quasi-classical trajectory calculations; these comparisons are made at 300 and 1000 K with the HCl or HBr molecule initially in the $v = 1, 2, 3$, or 4 vibrational state. The distribution of energy among the various product molecule modes was also examined. The reaction rates and product energy distributions are compared with experiment.

The thermal rate coefficient k for $\text{Cl} + \text{HBr} \rightarrow \text{HCl} + \text{Br}$ has been measured by Wodarczyk and Moore⁵ at 295 K by the laser photolysis of Cl_2 in a flowing Cl_2/HBr gas mixture; they obtained $k = 4.5 \times 10^{12}$ cm³/molecule s. The value obtained in these trajectory calculation is 30.2×10^{12} cm³/molecule s. This comparison indicates that the potential-energy surface used in this work is a reasonable one. It should be noted that this surface was not calibrated using kinetic data for this reaction.

Arnoldi, Kaufmann, and Wolfrum¹⁹ have measured the effect of reactant vibration on $\text{Br} + \text{HCl} \rightarrow \text{HBr} + \text{Cl}$. They report that at room temperature that exciting $\text{HCl}(v = 0)$ to $v = 2$ gives a rate enhancement of 10^{11} . We did not compute the $v = 0$ rate because of the very low reaction probability (based on the Arnoldi et al.¹⁹ results a rate coefficient of about 10 cm³/molecule s is estimated). We can, however, compare our computed rate coefficient of $(5.6 \pm 3.2) \times 10^{12}$ cm³/molecule s at 300 K for $\text{HCl}(v = 2)$ with the experimental value¹⁹ for $v = 2$ of $(8.8 \pm 3.1) \times 10^{11}$

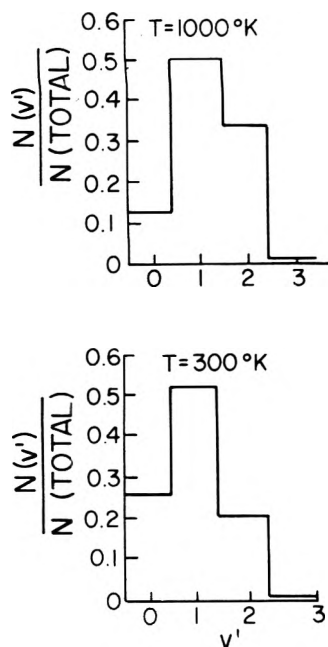


Figure 3. Computed distribution of final vibrational states for $\text{Cl} + \text{HBr} \rightarrow \text{HCl}(v') + \text{Br}$ at 300 and 1000 K; initial vibrational and rotational states thermally distributed.

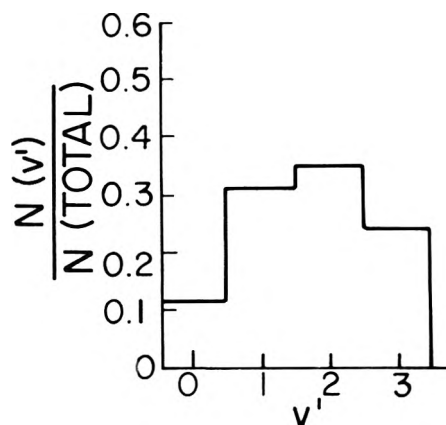


Figure 4. Computed distribution of final vibrational states for $\text{Cl} + \text{HBr}(v = 1) \rightarrow \text{HCl}(v') + \text{Br}$ at 300 K; initial rotational states thermally distributed.

$\text{cm}^3/\text{molecule s}$. The agreement is good.

The distribution of product vibrational states has been measured for the reaction $\text{Cl} + \text{HBr} \rightarrow \text{HCl} + \text{Br}$ by Maylotte, Polanyi, and Woodall^{3d} using an "arrested relaxation" variant of the infrared chemiluminescence technique. They found $N(v' = 2)/N(v' = 1) = 0.4$ with a reactant gas temperature of approximately 300 K. [Here, $N(v' = i)$ is the number of product molecules in the i th vibrational state.] Our calculations gave $N(v' = 2)/N(v' = 1) = 0.38$ at 300 K. This close agreement again supports our choice of the potential-energy surface. The overall distributions of HCl molecules among the final vibrational states are shown in Figure 3 at 300 and 1000 K, with initial v and J selected from thermal distributions; $N(v')$ is the number of molecules formed in the v' vibrational state. There is a definite temperature effect on the product vibrational distributions. Particularly noticeable is the shift in the relative populations of the $v' = 0$ and $v' = 2$ states; at both temperatures approximately half of the product molecules are in the $v' = 1$ state.

The effect of initial vibration on the product vibrational distribution is shown in Figure 4 for the case of $\text{Cl} + \text{HBr}(v = 1) \rightarrow \text{HCl}(v') + \text{Br}$ at 300 K. For these conditions the

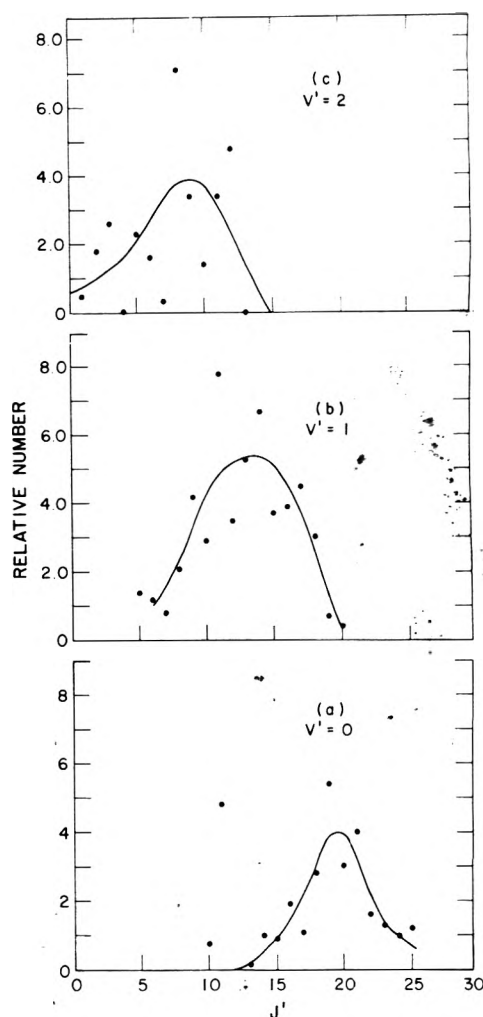


Figure 5. Computed distribution of final rotational states for $\text{Cl} + \text{HBr} \rightarrow \text{HCl}(v', J') + \text{Br}$ at 300 K; initial vibrational and rotational states thermally distributed. The points are the computed results; the solid line is a smooth curve fitted to the points.

final vibrational states 1, 2, and 3 are about equally populated, in contrast to the peaking that occurs under thermal conditions as shown in Figure 3.

The rotational states of the product molecules were computed by solving eq 13 for J . The distribution of products among rotational states at 300 K is shown in Figure 5 for final vibrational states (v') equal to 0, 1, and 2. Due to the large number of product rotational states available, the statistical fluctuations of the data points in Figure 5 are large. A solid line was drawn through the points by taking the average between the value for two successive J states and then visually drawing a line through the points so obtained. The curves should be considered only qualitatively correct. Maylotte, Polanyi, and Woodall^{3d} measured the most probable rotational quantum number (J') for $v' = 1$ to be 13 ± 1 compared to 12–13 found here and for $v' = 2$ to be 3 ± 1 compared to 9 found here. Figure 6 shows the effect of increasing reactant temperature on the rotational state distribution. The increased temperature shifts the rotational distribution to higher J' values but the most dramatic effect is the decreased breadth of the J' distribution.

In Figure 7 comparisons of the partitioning of the energy available to products E_T among rotation E_R , vibration E_V , and translation E_T , are illustrated for various conditions. The reaction probability is also given in Figure 7 for each set of conditions. There is not a significant change in the partitioning of the available energy for the processes Cl

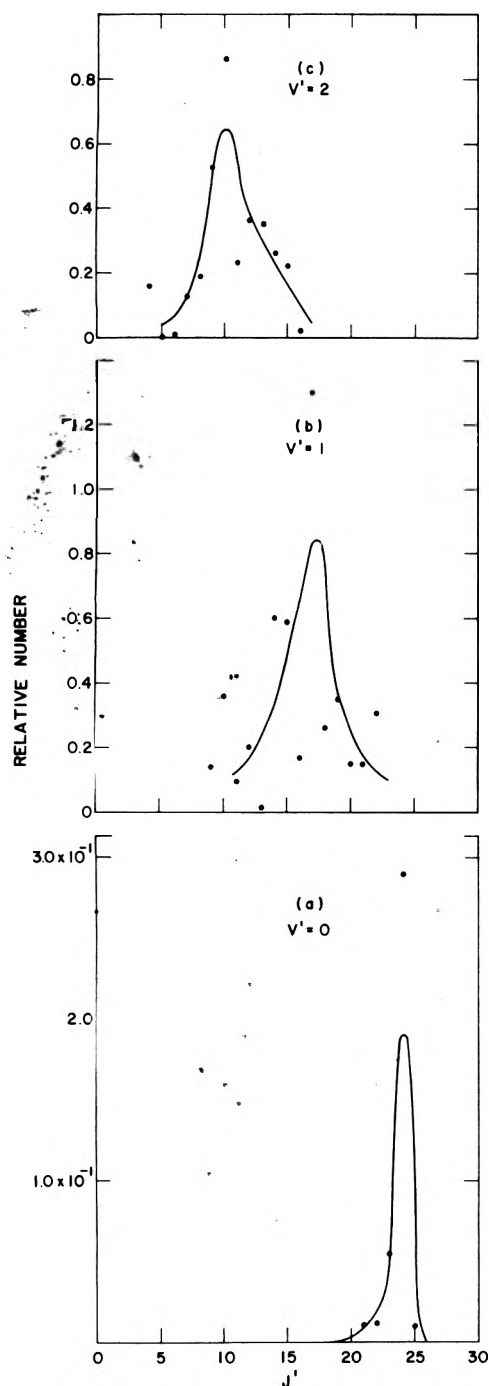


Figure 6. Computed distribution of final rotational states for $\text{Cl} + \text{HBr} \rightarrow \text{HCl}(v', J') + \text{Br}$ at 1000 K; initial vibrational and rotational states thermally distributed. The points are the computed results; the solid line is a smooth curve fitted to the points.

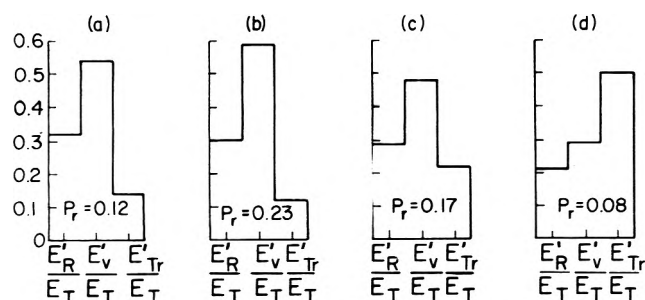


Figure 7. Computed partitioning of the energy available to the products in $\text{Cl} + \text{HBr} \rightarrow \text{HCl} + \text{Br}$ for various conditions. The reaction probability P_r is given for each case: (a) 300 K, v and J thermally distributed; (b) 300 K, $v = 1$, and J thermally distributed; (c) 1000 K, v and J thermally distributed; and (d) $E_{\text{rel}} = 0.65$ eV, v and J thermally distributed.

TABLE II: Computed Rate Coefficients for the Reaction $\text{Br} + \text{HCl}(v) \rightarrow \text{HBr} + \text{Cl}$ for 300 and 1000 K

T, K	v	$k(10^{13} \text{ cm}^3/\text{molecule s})$
300	1	^a
	2	0.56 ± 0.32
	3	2.12 ± 0.94
	4	2.96 ± 0.92
1000	0	^b
	1	0.56 ± 0.56
	2	4.34 ± 1.52
	3	3.88 ± 1.88
	4	7.06 ± 1.74

^a Only 150 trajectories were computed for $v = 1$, $T = 300$ K; no reactions occurred. ^b No reactions were observed out of the 250 trajectories computed for $v = 0$, $T = 1000$ K.

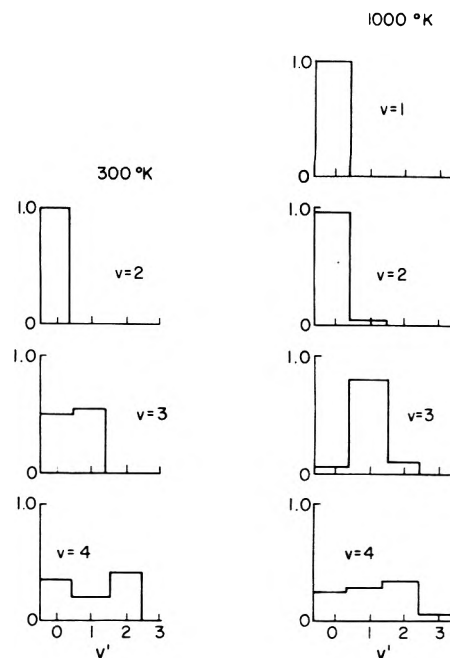


Figure 8. Computed product vibrational state distributions as a function of initial vibrational state at 300 and 1000 K for the reaction $\text{Br} + \text{HCl}(v) \rightarrow \text{Cl} + \text{HBr}(v')$.

+ HBr (v and J thermal) and $\text{Cl} + \text{HBr}$ ($v = 1$ and J thermal) as can be seen by comparing Figures 7a and 7b, however, the reaction probability is doubled. Changing the temperature from 300 to 1000 K produces a change in the partitioning, see Figures 7a and 7c, and about a 30% increase in the reaction probability. A dramatic change in energy partitioning is brought about by fixing the relative translational energy at 0.65 eV (which corresponds to approximately the energy difference in the $v = 0$ and $v = 1$ states of HBr) as illustrated in Figure 7d in which the internal states are thermally distributed for 300 K. It is interesting to note that the increased translational energy causes a decrease in the reaction probability.

The rate coefficient and the distribution of energy among various product modes with HCl in the vibrational states $v = 0, 1, 2, 3$, and 4 at 300 and 1000 K were computed for the reaction $\text{Br} + \text{HCl}$. The calculated rate coefficients are given in Table II. The distributions of product vibrational states for different initial reactant vibrational states are shown in Figure 8 for $T = 300$ and 1000 K. In these calculations, increasing the initial vibrational energy shifts the distribution of product molecules to higher vibrational states. The fraction of the total available energy in the vibrational modes of the products also increases with v at 1000 K but does not at 300 K.

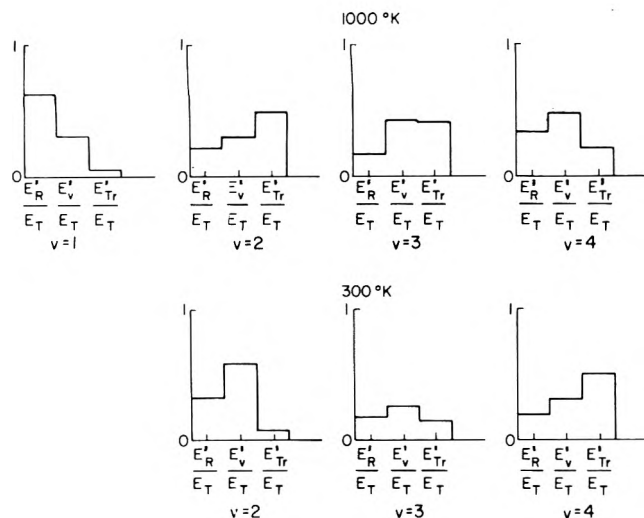
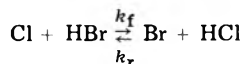


Figure 9. Computed partitioning of available energy among product modes as a function of initial vibrational state at 300 and 1000 K for the reaction $\text{Br} + \text{HCl}(v) \rightarrow \text{Cl} + \text{HBr}(v')$.

The partitioning of the available energy from the $\text{Br} + \text{HCl}(v)$ reactions for $v = 1, 2, 3$, and 4 is shown in Figure 9 for the temperatures 300 and 1000 K. At both temperatures, changes in v cause significant changes in energy partitioning. At 300 K, vibration is the dominant mode for deposition of the available energy for $v = 2$ and 3 with translation becoming more important for $v = 4$. However, at 1000 K vibration is more important than rotation and translation for only $v = 4$, being essentially comparable to translation for $v = 3$. Perhaps, the most interesting facet of these results is the dramatic shift in the relative importance of rotation and translation as v goes from 2 to 4.

Because of the combination of quantum mechanical rules (for assigning initial states) and classical mechanics (for computing the motion and thus assigning the final states) it is reasonable to question the validity of detailed balancing in quasi-classical trajectory calculations. Since we have computed rate coefficients for the forward and reverse reactions



we have the information to check detailed balancing in this case. A completely unequivocal statement on detailed balancing in quasi-classical trajectories would, however, require results of greater statistical accuracy than the computer time available for the present work permits. We should be able to detect a gross violation of the principle with the present results.

The equilibrium constant is

$$K = k_f/k_r = e^{-\Delta G/RT}$$

where $\Delta G = \Delta H - T\Delta S$ is Gibb's free energy. If we make the assumption that the entropy change ΔS is negligible then we can write

$$k_f = k_r \exp(-\Delta H/RT)$$

Let us consider the process $\text{Cl} + \text{HBr}(v=0) \rightarrow \text{Br} + \text{HCl}(v=1)$. The heat of reaction is -16.5 kcal/mol for $\text{Cl} + \text{HBr}(v=0) \rightarrow \text{Br} + \text{HCl}(v=0)$, and thus for the process we are considering the equilibrium constant computed from $K = \exp(-\Delta H/RT)$ gives 54.8 at 1000 K. The trajectory computed forward rate coefficient is 5.12×10^{13} $\text{cm}^3/\text{molecule s}$ and the reverse 5.6×10^{12} $\text{cm}^3/\text{molecule}$

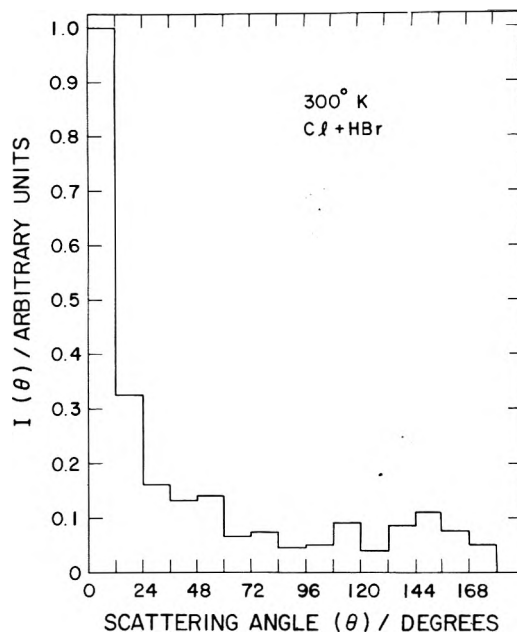


Figure 10. Computed differential scattering cross section for $\text{Cl} + \text{HBr} \rightarrow \text{HCl} + \text{Br}$ at 300 K. The angle θ is the angle between the final molecule velocity and the initial atom velocity.

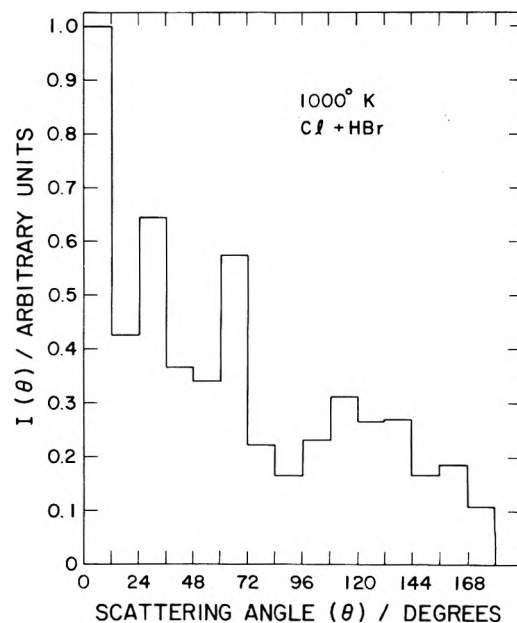


Figure 11. Computed differential scattering cross section for $\text{Cl} + \text{HBr} \rightarrow \text{HCl} + \text{Br}$ at 1000 K. The angle θ is the angle between the final molecule velocity and the initial atom velocity.

s. We obtain from these results $K_{\text{traj}} = 9.2$.

Product angular scattering distributions were also computed for thermal distributions at 300 (see Figure 10) and 1000 K (Figure 11) for $\text{Cl} + \text{HBr} \rightarrow \text{HCl} + \text{Br}$. Plotted in Figures 10 and 11 are the differential scattering cross sections ($I(\theta)/\sin \theta$), where θ is the angle made by the product molecule velocity and the initial reactant atom velocity. Therefore small θ values correspond to scattering into the forward hemisphere. There are, to our knowledge, no published results for the scattering distributions for this reaction. There are results (unpublished) by McDonald and Hershbach²⁰ for scattering in $\text{Cl} + \text{HI} \rightarrow \text{HCl} + \text{I}$, which strongly peaked in the forward direction for the two sets of conditions studied: relative translational energies of about 5 kcal/mol and thermal collision energies for 400 K. As can be seen in Figures 10 and 11 the trajectory results predict definite forward scattering for $\text{Cl} + \text{HBr}$

→ HCl + Br at 300 and 1000 K. We are not certain how close an analogy there is between the Cl + HBr and Cl + HI systems, though it does seem reasonable to expect qualitative similarities in the scattering. Trajectory calculations on Cl + HI → HCl + I using a surface of the same formulation as used here gave forward scattering at temperatures of 1000 and 2000 K, but isotropic to backward scattering at 300 K.²¹

Acknowledgment. D.L.T. wishes to express his gratitude to the Departments of Physics and Chemistry at Ole Miss for their hospitality during the course of this work. This work was supported in part by the U.S. Energy Research and Development Administration.

References and Notes

- (1) L. M. Raff, L. Stivers, R. N. Porter, D. L. Thompson, and L. B. Sims, *J. Chem. Phys.*, **52**, 3449 (1970).
- (2) R. N. Porter, L. B. Sims, D. L. Thompson, and L. M. Raff, *J. Chem. Phys.*, **58**, 2855 (1973).
- (3) See, for example, (a) K. G. Anlauf, J. C. Polanyi, W. H. Wong, and K. B. Woodall, *J. Chem. Phys.*, **49**, 5189 (1968); (b) K. G. Anlauf, D. H. Maylotte, J. C. Polanyi, and R. B. Bernstein, *ibid.*, **51**, 5716 (1969); (c) L. T. Cowley, D. S. Horne, and J. C. Polanyi, *Chem. Phys. Lett.*, **12**, 144 (1971); (d) D. H. Maylotte, J. C. Polanyi, and K. B. Woodall, *J. Chem. Phys.*, **57**, 1547 (1972); (e) L. J. Kirsch and J. C. Polanyi, *ibid.*, **57**, 4498 (1972); (f) A. M. G. Ding, L. J. Kirsch, D. S. Perry, J. C. Polanyi, and J. L. Schreiber, *Faraday Discuss., Chem. Soc.*, **55**, 252 (1973).
- (4) J. R. Airey, *J. Chem. Phys.*, **52**, 156 (1970).
- (5) F. J. Wodarczyk and C. B. Moore, *Chem. Phys. Lett.*, **26**, 484 (1974).
- (6) K. Bergmann and C. B. Moore, *J. Chem. Phys.*, **63**, 643 (1975).
- (7) D. S. Perry, J. C. Polanyi, and C. W. Wilson, Jr., *Chem. Phys. Lett.*, **24**, 484 (1974).
- (8) J. M. Bowman and A. Kuppermann, *Chem. Phys. Lett.*, **19**, 166 (1973).
- (9) J. M. Bowman, G. C. Schatz, and A. Kuppermann, *Chem. Phys. Lett.*, **24**, 378 (1974).
- (10) L. Pedersen and R. N. Porter, *J. Chem. Phys.*, **47**, 4751 (1967).
- (11) G. Herzberg, "Molecular Spectra and Molecular Structure. I. Spectra of Diatomic Molecules", 2nd ed, D. Van Nostrand, New York, N.Y., 1950.
- (12) M. A. A. Clyne and J. A. Coxon, *Proc. R. Soc. (London), Ser. A*, **298**, 424 (1967).
- (13) H. A. Pohl and L. M. Raff, *Int. J. Quantum Chem.*, **1**, 577 (1967).
- (14) M. Karplus, R. N. Porter, and R. D. Sharma, *J. Chem. Phys.*, **43**, 3259 (1965).
- (15) S. Gill, *Proc. Cambridge Phil. Soc.*, **47**, 96 (1951).
- (16) H. H. Suzukawa, Jr., D. L. Thompson, V. B. Chang, and M. Wolfsberg, *J. Chem. Phys.*, **59**, 4000 (1973).
- (17) L. M. Raff, D. L. Thompson, L. B. Sims, and R. N. Porter, *J. Chem. Phys.*, **58**, 5998 (1972). For a comprehensive description of Monte Carlo methods for quasi-classical trajectories, see R. N. Porter and L. M. Raff, "Classical Trajectory Methods in Molecular Collisions", in "Modern Theoretical Chemistry, Volume III. Dynamics of Molecular Collisions", W. H. Miller, Ed., Plenum Press, New York, N.Y., 1976.
- (18) R. N. Porter, L. M. Raff, and W. H. Miller, *J. Chem. Phys.*, **63**, 2214 (1975).
- (19) D. Arnoldi, K. Kaufmann, and J. Wolfrum, *Phys. Rev. Lett.*, **34**, 1597 (1975).
- (20) J. D. McDonald and D. R. Hershbach, "Molecular Beam Kinetics: Reaction of Chlorine Atoms with Hydrogen Iodide", unpublished; J. D. McDonald, Ph.D. Thesis, Harvard University, 1971.
- (21) H. E. Bass, L. S. Kenton, and D. L. Thompson, *Chem. Phys. Lett.*, **44**, 452 (1976).

Coupling between Tracer and Mutual Diffusion in Electrolyte Solutions

Pierre Turq,* Marius Chemla, Habib Latrous, and Jalel M'halla†

Laboratoire d'Electrochimie, ERA 310, Université Pierre et Marie Curie, 4, Place Jussieu-75230 Paris Cedex 05, France

(Received December 1, 1975; Revised Manuscript Received November 2, 1976)

Publication costs assisted by Université Pierre et Marie Curie

The coupling between tracer and mutual diffusion in electrolyte solutions is experimentally realized and theoretically analyzed. The essential coupling terms are the electrical diffusion potential gradient, and the activity coefficient gradient, arising from the individual excess chemical potential of each ion.

I. Introduction

Self-diffusion processes are among the most simple transport phenomena occurring in a given medium and are generally measured by special techniques using isotopically or spin-labeled compounds. On the other hand, the phenomenon of mutual or chemical diffusion, which can be easily observed experimentally, has been studied by many classical techniques. However its complete analysis involves a detailed consideration of several complicated effects.

The relationship between the chemical diffusion coefficient of an electrolyte and the separate ionic self-diffusion coefficients is simple at infinite dilution (Nernst-Hartley relation) but becomes more complex for finite values of the concentration. The equation describing these two phenomena requires different polynomials, and the terms beyond the limiting laws in $C^{1/2}$ were calculated only a few years ago.¹⁻³

The problem considered in the present study is the interdependence of tracer diffusion and of mutual diffusion in electrolyte solutions when these processes occur simultaneously.

Self- and mutual-diffusion processes are closely related in the following ways: (a) They are both consequences of the thermal motion of the particles and are expressed by the square-average displacement by unit time. (b) In an electrolyte solution, the value of the self-diffusion coefficient depends essentially on the ion-solvent interaction; other interactions give only a small contribution when the solution concentration is below 1 M.

Therefore, the tracer diffusion coefficient in the presence of a concentration gradient of electrolyte will depend not only on the local and instantaneous values of the concentration in the solution, but also on the fields of forces involved in the electrolyte diffusion.

In this case, we shall have together a tracer and an electrolyte flow which can occur in different directions.

We shall assume that a steady state will be locally established after a very short time; this means that the potentials and the corresponding fields take well-defined values at any place and any time. Also, in each elementary volume of the solution, an electrolyte flow and a tracer flow (of same or opposite direction) occur simultaneously. The tracer diffusion process, which has only a small dependence on the electrolyte concentration, occurs even in the presence of a countercurrent flow of electrolyte. In fact,

† With the technical coworkship of Yvette Roumegous.

it can even be accelerated by this countercurrent movement.

All these processes are generally nonstationary on the time scale of a diffusion experiment; consequently, a complicated set of differential equations is obtained, the solution of which is nonanalytical and only available through the use of numerical methods.

The coupling of tracer and mutual diffusion has several features and the most important of them are listed as follows:

The flow of the solvent which corresponds to the mutual diffusion of electrolyte and solvent in the chemical gradient of concentration. This solvent flow is negligible in dilute solutions, and its contribution to the tracer flow, in $C^{1/2}$, is only a small electrophoretic effect.¹

The electrical field which is established in the chemical gradient of concentration, if the ions of the diffusing electrolyte have different mobilities. This phenomenon leads to the largest coupling effects, even in dilute solutions; it was analyzed and observed by Plonka⁴ in membranes and independently by Turq and Chemla⁵ in solutions.

The gradient of the activity coefficient of the tracer which exists for both ions independently of their respective mobilities. This leads to a new effect not observed previously.

The aim of the present study is to distinguish between these different effects in a few experimental cases. For this purpose, we shall give briefly the mathematical expressions of flows and forces involved in these processes.

II. Flows and Forces

The equation giving the flow J_i of the particle i is

$$\vec{J}_i = C_i \vec{V}_i = C_i B_i \sum_k \vec{F}_i^k$$

where C_i is the concentration of the particle i , V_i is its velocity, B_i is the mobility of the particle i , and $\sum_k F_i^k$ is the sum of all the forces applied to the particle i .

The forces acting on the particle i are the following.

(1) *The Gradient of the Chemical Potential:*

$$\mu_i = \mu_i^\circ + kT \ln(C_i \gamma_i)$$

μ_i° is the standard chemical potential of the species i , γ_i is its activity coefficient, and kT is the Boltzmann factor. The corresponding force is

$$\vec{F}_i^\mu = -\vec{\nabla} \mu_i^\circ - kT \frac{\vec{\nabla} C_i}{C_i} - kT \vec{\nabla} \ln \gamma_i$$

In a given medium, the standard chemical potential μ_i° is a constant and the first term $\vec{\nabla} \mu_i^\circ$ vanishes. The term $kT(\vec{\nabla} C_i / C_i)$ represents the ordinary diffusion process and $kT \vec{\nabla} \ln \gamma_i$ the effect of the gradient of activity coefficient.

In the Debye-Hückel approximation

$$\ln \gamma_i = -\frac{e_i^2 K}{2DkT(1 + Ka)}$$

where K is the Debye K and D the dielectric constant of the solvent, and

$$\ln \gamma^\pm = -\frac{|e_i e_j| K}{2DkT(1 + Ka)}$$

(2) *Coulomb Forces.* (a) An electrical field exists in a solution if the ions of the diffusing electrolyte have different mobilities:

$$\vec{F}_i^e = e_i \vec{E}$$

e_i being the charge of the particle i .

The system we consider is composed of a solvent, an electrolyte dissociated into ν_2 ions 2 and ν_3 ions 3, at the concentration C and a tracer 1 at the concentration $C_1 \ll C$.

In the expression of the electrical field \vec{E} , we shall neglect the perturbation coming from the diffusion of 1.

The chemical potential of the solute 2-3 is

$$\mu = \nu_2 \mu_2 + \nu_3 \mu_3$$

The flow of the particle 2 is

$$\vec{J}_2 = C_2 \vec{v}_2 = -B_2 C_2 \vec{\nabla} \mu_2 + B_2 C_2 e_2 \vec{E} + C_2 \Delta \vec{v}_2$$

where $\Delta \vec{v}_2$ is the electrophoretic effect on the particle 2. (This effect will be developed further.)

The analogous expression for \vec{J}_3 is obtained by replacing 2 by 3. The electroneutrality of the solution prevents any charge separation, then

$$\vec{J}_2 = \vec{J}_3$$

$$\vec{E} = \frac{\nu_3 B_3 \vec{\nabla} \mu_3 - \nu_2 B_2 \vec{\nabla} \mu_2}{\nu_2 B_2 e_2 - \nu_3 B_3 e_3} + \frac{\nu_3 \Delta \vec{v}_3 - \nu_2 \Delta \vec{v}_2}{\nu_2 B_2 e_2 - \nu_3 B_3 e_3}$$

For a symmetrical electrolyte $\nu_2 = \nu_3$ and $\vec{v}_2 = \vec{v}_3$.

For dilute solutions (Debye-Hückel domain), it will be possible to make the following extrathermodynamic hypothesis

$$\vec{\nabla} \mu_2 = \vec{\nabla} \mu_3$$

which is equivalent to assume the equality of the activity coefficients of both ions of the electrolyte. We shall have in this case

$$\vec{E} = \frac{(B_3 - B_2) \vec{\nabla} \mu}{(\nu_2 + \nu_3)(B_2 e_2 - B_3 e_3)} + \frac{\Delta \vec{v}_3 - \Delta \vec{v}_2}{B_2 e_2 - B_3 e_3}$$

(b) The tracer species 1 is allowed to move separately from the other ions and must drag its ionic atmosphere, in the so-called relaxation field $\Delta \vec{X}_i$ with

$$\vec{F}_i^{\text{rel}} = e_i \Delta \vec{X}_i$$

The evaluation of the relaxation field requires the use of a convenient system of continuity equations.

By examining these continuity equations it can be seen that the only effect of the coupling between self- and mutual-diffusion for the relaxation effect in the diffusion of the tracer species is to replace the tracer diffusion term $\vec{k}_i B_i$ by

$$\vec{k}_i B_i - \vec{k}_j B_j$$

(where \vec{k}_i is the external force acting on the particle i). $\vec{k}_j B_j = \vec{v}$ for both 2 and 3 species. In the linear response region

$$\vec{v} = \frac{-B_2 B_3 \vec{\nabla} \mu}{B_2 + B_3} + \frac{B_3 \Delta \vec{v}_2 + B_2 \Delta \vec{v}_3}{B_2 + B_3}$$

and for the limiting law contribution

$$\vec{J}_1^{\text{rel}} = C_1 B_1 \left[-\left(-\vec{\nabla} \mu_1 + e_1 \vec{E} - \frac{\vec{v}}{B_1} \right) \frac{e_1^2}{3DkT} K(1 - q) \right]$$

with

$$q^2 = d(\mu_j)$$

and

$$K^2 = \frac{4\pi}{DkT} \sum_i C_i e_i^2$$

D is the dielectric constant of the medium.

(3) *Forces Resulting from an Electrophoretic Term.* The calculation of Δv_2 and Δv_3 is classical as far as the limiting law is concerned.⁶ We obtain the following values

$$\frac{B_3 \Delta \vec{v}_2 + B_2 \Delta \vec{v}_3}{B_3 + B_2} = \frac{\vec{\nabla} \mu K (B_3 - B_2)^2}{12\pi\eta(1 + Ka)(B_3 + B_2)^2}$$

and

$$\frac{\Delta \vec{v}_3 - \Delta \vec{v}_2}{B_2 e_2 - B_3 e_3} = \frac{\vec{\nabla} \mu}{e_2 (B_2 + B_3)} \left[\frac{K(B_3 - B_2)}{6\pi\eta(1 + Ka)(B_3 + B_2)} \right]$$

The above expression deals with the limiting law and involves the finite size correction $1 + Ka$.

Expression of the Total Tracer Flow. We are now able to write

$$\vec{J}_1 = -C_1 B_1 \vec{\nabla} \mu_1 + C_1^* B_1 e_1 \vec{E} + \vec{J}_1^{rel} + C_1 \Delta \vec{v}_1$$

In the next section we shall consider how it is possible to realize at a practical level an experiment of coupled self- and mutual-diffusion in electrolyte solutions.

III. Experimental Section

We have used the open-end capillary method of Anderson and Saddington⁷ which we have used previously in the determination of self-diffusion coefficients.^{8,9}

A capillary tube of small cross section and open at one end is filled with a solution containing the isotopic tracer. This capillary tube is immersed in a vessel, the volume of which is very large in comparison with the inner volume of the capillary tube. In a self-diffusion experiment the electrolyte concentration in the capillary tube and in the external vessel are identical.

In the coupled self- and mutual-diffusion processes, the electrolyte concentration in the capillaries and in the vessel differs. The concentration can be either higher in the capillary tube or in the vessel.

The tracer flow from the capillary tube will be coupled to an electrolyte flow of the same or opposite direction. What is measured in the experiment is the perturbation of this tracer flow from the coupling with the electrolyte flow.

The main difficulty in the interpretation of the results arises from the fact that this process is nonstationary, with a diffusion coefficient varying in time and space, because the different diffusion coefficients depend on the concentrations, and the flows on their gradients.

In order to simplify the treatment of the results, all the experiments were performed in capillaries of constant length and for diffusion times always very close to one another for a given tracer ion. Under these conditions, it is possible to measure the bulk tracer flow (or more precisely the ratio of the radioactivity in the capillary after diffusion over the initial radioactivity).

From this ratio γ we can define an "apparent diffusion coefficient" for the tracer. This coefficient is not really a diffusion coefficient, because the tracer flow is not simply proportional to the concentration gradient of the tracer.

This "apparent diffusion coefficient" is simply a convenient way of describing the influence of the coupling on the tracer flow.

For long diffusion times, we have

$$D_{ap} = \frac{4l^2}{\pi^2 t} \ln \left(\frac{8}{\pi^2 \gamma} \right)$$

where l is the capillary length, t the diffusion time, and γ the ratio mentioned above. For small diffusion time, the apparent diffusion coefficient is given by

$$D_{ap} = \frac{l^2 \pi}{4t} (1 - \gamma)^2$$

It is recognized in studies on self-diffusion that both these expressions give the same numerical result over a large range for γ .

IV. Numerical Solution of the Problem Using the Finite Difference Method

In order to obtain a quantitative treatment of the phenomenon, we have integrated with a finite difference method the partial derivative equations corresponding to the coupled diffusion process:

$$\frac{\partial C_1}{\partial t} + \vec{\nabla} \cdot \vec{J}_1 = 0 \quad \text{for the tracer}$$

$$\frac{\partial C}{\partial t} + \vec{\nabla} \cdot \vec{J} = 0 \quad \text{for the supporting electrolyte}$$

The calculations were made for a capillary 3 cm in length; the diffusion time corresponded to the operating conditions of each experiment.

The corresponding Fortran programs were executed on the 10070 CII computer of the University of Paris VI.

Two kinds of computation were made: (a) calculations with only zeroth order terms (without Debye-Hückel's correction of activity or transport coefficients) (FINZER); (b) calculations including all electrostatic corrections for the $C^{1/2}$ terms (limiting laws) (FINFRST).

The principle of the finite difference method is very simple: we cut time and space in sufficiently small intervals in order to replace the partial derivative equation by a finite difference equation. For practical reasons, in order to limit the price of such a calculation, the elementary space intervals are equal to 1/100 of the total length of the capillary. We have verified that this fraction was sufficiently small to allow the diffusion process to be correctly simulated.

Having chosen the space interval, the time interval cannot be selected in an arbitrary way; an upper limit is fixed by the self-diffusion coefficient of the considered species. This time step must be shorter than the characteristic diffusion time in the previously chosen space interval. This characteristic diffusion time is given by

$$t = \Delta l^2 / D$$

for $\Delta l = 3 \times 10^{-2}$ cm, $D = 10^{-5}$ cm²/s: $t \simeq 10^2$ s.

Practically, a Δt of 100 s is sufficient to obtain the right convergence of the process. The choice of a smaller Δt does not noticeably improve the results. The physical meaning of this condition is very simple: to apply the finite difference method, we need a time step smaller than the diffusion time of the particles through the space steps. This time step varies as the second power of the distance step.

In our coupled diffusion problem, we must remark that we cannot treat the electrolyte flow and the tracer flow symmetrically. In fact, the electrolyte flow is not modified by the tracer, present only at very low concentration, and it is only the tracer which undergoes the coupling effects.

We shall calculate successively these two flows; this means that the tracer flow will be adjusted at each time and at each point to the conditions arising from the electrolyte flow. We shall now give the algorithm of the finite difference method: we need the first and second

derivatives of the concentrations

$$\frac{\partial C}{\partial x}(x_i, t_j) = [C(x_{i+1}, t_j) - C(x_{i-1}, t_j)] / 2\Delta l$$

$$\frac{\partial^2 C}{\partial x^2}(x_i, t_j) = [C(x_{i+1}, t_j) + C(x_{i-1}, t_j) - 2C(x_i, t_j)] / \Delta l^2$$

We also need the divergence of some supplementary flows.

$$\frac{\partial}{\partial x} [J^S(x_i, t_j)] = [J^S(x_{i+1}, t_j) - J^S(x_{i-1}, t_j)] / 2\Delta l$$

In addition the fundamental algorithm is written as

$$C(x_i, t_{j+1}) - C(x_i, t_j) = \Delta t \left[D \frac{\partial^2 C(x_i, t_j)}{\partial x^2} - \frac{\partial J^S(x_i, t_j)}{\partial x} \right]$$

The calculation of the concentration increments is made at each time step for the supporting electrolyte and for the tracer. After the calculation has been made, the obtained concentrations permit the evaluation of the total flow of the tracer through the capillary and the calculation of its apparent diffusion coefficient.

V. Electrical Diffusion Potential (EPG)

By taking a supporting electrolyte the ions of which present a great difference in electrical mobilities, it is possible to realize an electrical diffusion field sufficiently intense so that the corresponding effects predominate and exceed all other contributions (namely, the relaxation and electrophoresis effects, gradient of activity coefficient). Under these conditions, the essential coupling term between tracer and mutual diffusion is the term of the electrical potential gradient.

For very high dilution, we can neglect the concentration-dependent effects and we obtain

$$\vec{J}_1^{\circ E} = -C_1 B_1 \vec{\nabla} \mu_1 - \frac{C_1 B_1 e_1 (B_3 - B_2)}{2e_2 (B_3 + B_2)} \vec{\nabla} \mu$$

and, by replacing the chemical potentials at the same approximation

$$\vec{J}_1^{\circ E} = -D_1 \vec{\nabla} C_1 - D_1 \frac{e_1 C_1 (B_3 - B_2)}{e_2 C_2 (B_3 + B_2)} \vec{\nabla} C_2$$

the coupling term is precisely

$$D_1 \frac{e_1 C_1 (B_3 - B_2)}{e_2 C_2 (B_3 + B_2)} \vec{\nabla} C_2$$

Sum Rules. Some simple sum rules can be derived for this limiting value. If we consider the flows $\vec{J}_1^{\circ D}$ and $\vec{J}_1^{\circ R}$ of a given tracer in the presence of two opposite gradients of supporting electrolyte $\vec{\nabla} C_2$ and $-\vec{\nabla} C_2$, we have

$$\vec{J}_1^{\circ D} = -D_1 \vec{\nabla} C_1 - D_1 \frac{(B_3 - B_2) e_1 C_1}{(B_3 + B_2) e_2 C_2} \vec{\nabla} C_2$$

$$\vec{J}_1^{\circ R} = -D_1 \vec{\nabla} C_1 + D_1 \frac{(B_3 - B_2) e_1 C_1}{(B_3 + B_2) e_2 C_2} \vec{\nabla} C_2$$

and

$$\vec{J}_1^{\circ D} + \vec{J}_1^{\circ R} = 2\vec{J}_1^{\circ S}$$

This means that the sum of the direct and reversed perturbed flows of the tracer is constant and equals twice the flow of tracer in self-diffusion. We can see that in a

TABLE I: Verification of the Product Rule in the EPG Effect

	C_2	C'_2	$\frac{(1 - \gamma_+^D)}{(1 - \gamma_+^R)}$	$\frac{(1 - \gamma_-^D)}{(1 - \gamma_-^R)}$
	10^{-1}	10^{-2}	0.29869	0.22219
	5×10^{-2}	10^{-2}	0.30030	0.22168
	2×10^{-2}	10^{-2}	0.2909	0.21919
	10^{-2}	10^{-2}	0.2874	0.21940

steady state experiment, for the same gradient of concentration of tracer, the sum of the apparent diffusion coefficients equals twice the value of the self-diffusion coefficient.

$$D_1^D + D_1^R = 2D_1^S$$

In the semi-infinite case of the open-end capillary method, the integrated flow out of the capillary is proportional to $1 - \gamma$. γ is related to the apparent diffusion coefficient

$$D = \frac{\pi l^2}{4t} (1 - \gamma)^2$$

In this case we shall have

$$1 - \gamma^D + 1 - \gamma^R = 2(1 - \gamma^S)$$

$$\gamma_1^D + \gamma_1^R = 2\gamma_1^S$$

and

$$(D_1^D)^{1/2} + (D_1^R)^{1/2} = 2(D_1^S)^{1/2} \quad (1)$$

for capillaries operating in the same conditions.

Product Rules. We can write in the case of low coupling:

$$\vec{J}_1^{\circ D} = \vec{J}_1^{\circ S} + \epsilon_1^c$$

$$\vec{J}_1^{\circ R} = \vec{J}_1^{\circ S} - \epsilon_1^c$$

$$|\vec{J}_1^{\circ D}| |\vec{J}_1^{\circ R}| = |\vec{J}_1^{\circ S}|^2 - O(\epsilon_1^c)^2$$

then, for the open-end capillary method

$$D_1^D D_1^R = (D_1^S)^2 \quad (2)$$

which is consistent with (1) at the second order in the coupling term. The product rules can also be written⁴ as

$$(1 - \gamma^D)(1 - \gamma^R) = (1 - \gamma^S)^2$$

From open-end capillary experiments performed by Turq and Chemla,⁵ it is possible to test this product rule. The results are given in Table I from which we observe that products are in good agreement.

Amplification of the Effect. To refine the interpretation of these phenomena, we can introduce the concentration dependent terms, involving all corrections in $C^{1/2}$ as in ref 5.

To give a new amplified example of the electrical diffusion potential gradient, we have carried out a set of experiments in which the ions of the supporting electrolyte have very different mobilities as

$$\Lambda_{H^+}^{\circ} = 349.81 \text{ and } \Lambda_{NO_3^-}^{\circ} = 71.46$$

We have studied the perturbation of the tracer diffusion of Ag^+ resulting from the simultaneous diffusion of HNO_3 with a concentration range between 2×10^{-2} and 1.1×10^{-1} M. First of all, we have measured the self-diffusion coefficient of silver in these media without any concentration gradient.

The self-diffusion coefficient of the silver ion decreases slowly with increasing concentration. The coupling shows an important effect: a countercurrent of HNO_3 accelerates the diffusion of Ag^+ tracer (Table II) quite considerably.

TABLE II: Tracer Ag⁺ in HNO₃ (D, 10⁻⁵ cm²/s)

	Coupled		Self	
Inactive solution C, M	AgNO ₃ , 10 ⁻²			
	HNO ₃ , 10 ⁻¹	HNO ₃ , 10 ⁻²	HNO ₃ , 10 ⁻¹	HNO ₃ , 10 ⁻²
Active solution C, M (Ag tracer)	AgNO ₃ , 10 ⁻²			
	HNO ₃ , 10 ⁻²	HNO ₃ , 10 ⁻¹	HNO ₃ , 10 ⁻¹	HNO ₃ , 10 ⁻²
D _{exp}	2.21 ± 0.03	0.99 ± 0.01	1.55 ± 0.02	1.56 ± 0.02
D _{FINFRST} (calcd)	2.204	0.922	1.597	1.610
D _{FINZER} (calcd)	2.244	1.011	1.667	1.667
Av capillary length, cm	2.933	2.928	2.923	2.922
γ _{av}	0.528	0.508	0.378	0.375
t, 10 ⁴ s	6.948	15.781	17.220	17.190

The product rule is verified in a satisfactory manner:
 HNO₃ self-diffusion of Ag⁺: D_{Ag⁺} = 1.55 × 10⁻⁵ cm²/s
 HNO₃ coupled diffusion of Ag⁺ (2 × 10⁻² M–HNO₃ 1.1 × 10⁻¹ M): D^D_{Ag⁺}D^R_{Ag⁺} = 1.523 × 10⁻⁵ cm²/s

The preceding description can become quantitative by using the finite difference method as mentioned above. As it is shown in Table II we observe a qualitative and quantitative agreement even without ionic strength corrections as in the case of the first approximation.

VI. Gradient of Activity Coefficient (ACG)

It is possible, by choosing a supporting electrolyte the ionic mobilities of which are identical, to perform an experiment where the electrical diffusion field is zero. Under these conditions, the essential coupling term between tracer and mutual diffusion is the activity coefficient gradient.

The tracer flow is now written as

$$\vec{J}_1 = -D_1 \left[\vec{\nabla} C_1 + C_1 \frac{d}{d \ln C} (\ln \gamma_1) \right] \vec{\nabla} C$$

$$\frac{d \ln \gamma_1}{dC} = - \frac{e_1}{4\pi DkT(1 + Ka)^2} \left(\frac{8Ne^2}{1000DkT} \right)^{1/2} \frac{1}{C^{1/2}}$$

$$= -A/C^{1/2}$$

The coupling term is

$$\vec{J}_{1\mu} = D_1 C_1 A \frac{\vec{\nabla} C}{C^{1/2}}$$

This coupling term exhibits an increment of the tracer flow in the direction of the electrolyte concentration gradient. Important is that this effect is proportional to C^{1/2} and therefore dependent upon ionic strength. We can, as for the electrical potential gradient effect, define some sum and product rules:

$$\vec{J}_1^D + \vec{J}_1^R = 2\vec{J}_1^S$$

in a steady state experiment and for two tracer species 1 and 1' in the same gradients of the tracer and of the supporting electrolyte

$$\frac{|J_{1\mu}|}{D_1} = \frac{|J'_{1\mu}|}{D'_1} \quad (3)$$

and therefore the coupling term is proportional to the self-diffusion coefficient of the tracer.

Experimental Determination. As for the electrical diffusion potential (EPG) effect, we must distinguish two kinds of experiment: "out" diffusion. The supporting electrolyte concentration in the capillary is larger than in the external vessel; "in" diffusion. The electrolyte concentration in the capillary is lower than that in the container.

D_{in}^{ap} and D_{out}^{ap} are calculated from the experimental ratio γ.

TABLE III: Influence of the Tracer in the Activity Coefficient Gradient Effect^a

	D ^S 10 ⁻² M	D ^S 10 ⁻¹ M	D _{out}	D _{in}	(D _{in} - D _{out}) expt	(D _{in} - D _{out}) calcd ^b
Na ⁺	1.29	1.32	1.25	1.38	0.13 ± 3	0.13
Ag ⁺	1.57	1.526	1.49	1.68	0.19 ± 3	0.16
I ⁻	1.99	2.02	1.97	2.17	0.20 ± 3	0.20

^a Na⁺, Ag⁺, I⁻ in a gradient of KNO₃. D, 10⁻⁵ cm²/s.

^b The calculated values are obtained by the finite difference method.

TABLE IV: Verification of the Proportionality Rule for the ACG Effect^a

	Na ⁺	Ag ⁺	I ⁻
D _{out} /D _{self}	0.958	0.963	0.983
D _{in} /D _{self}	1.057	1.085	1.082

^a The ratios D_{out}/D_{self} and D_{in}/D_{self} are independent from the nature and the charge of the tracer ion.

TABLE V: Influence of the Supporting Electrolyte in the ACG Effect^a

Salt	D(10 ⁻² M)	D(10 ⁻¹ M)	D _{out}	D _{in}	(D _{in} - D _{out}) × 100 expt	(D _{in} - D _{out}) × 100 calcd
KNO ₃	1.29	1.32	1.25	1.38	13 ± 3	13
CsBr	1.30	1.26	1.28	1.35	07 ± 2	10
CsI	1.32	1.33	1.26	1.39	13 ± 3	11

^a Na⁺ in KNO₃, CsBr, CsI. D, 10⁻⁵ cm²/s.

In order to verify that the activity coefficient gradient (ACG) effect is the essential term, we have taken an electrolyte with only a small residual EPG effect as KNO₃. First, we have determined that the ACG effect is mainly independent of the nature and of the charge of the tracer ion, but proportional to its self-diffusion coefficient as verified for Na⁺, Ag⁺, and I⁻ (Tables III and IV).

The concentration in the supporting electrolyte varies from 10⁻² to 10⁻¹ M and that of the salt containing the element of the tracer is equal to 10⁻² M in order to prevent any adsorption.

We have also verified, as shown in Table V, for a given tracer, that the ACG effect is, for dilute solutions, only slightly dependent on the nature of the supporting electrolyte, if its ionic mobilities are close to one another. This has been done for Na⁺ in KNO₃, CsBr, and CsI (for CsI, the ionic mobilities are identical to the precision of the experimental determinations). Detailed values are given in Table VI with the results of the finite differences method.

In order to separate the contribution of the residual EPG effect and the ACG effect we will now examine in the next section the exact balance between these two effects in the experimental cases studied above.

TABLE VI: Tracer Na⁺ in CsBr and CsI ($D, 10^{-5} \text{ cm}^2/\text{s}$)

	Coupled		Self	
		Na ⁺ in CsBr		
Inactive solution	NaCl 10 ⁻²	NaCl 10 ⁻²	NaCl 10 ⁻²	NaCl 10 ⁻²
C, M	CsBr 10 ⁻²	CsBr 10 ⁻¹	CsBr 10 ⁻²	CsBr 10 ⁻¹
Active solution	Na ⁺ Cl 10 ⁻²			
C, M (Na tracer)	CsBr 10 ⁻¹	CsBr 10 ⁻²	CsBr 10 ⁻²	CsBr 10 ⁻¹
$D(\text{expt})$	1.28 ± 0.01	1.36 ± 0.02	1.30 ± 0.02	1.26 ± 0.01
D_{FINZER}	1.336	1.334	1.335	1.335
D_{FINFRST}	1.230	1.3299	1.280	1.279
Capillary length, cm	2.930	2.930	2.930	2.930
$t, 10^4 \text{ s}$	15.670	9.231	15.710	15.280
		Na ⁺ in CsI		
Inactive solution	NaCl 10 ⁻²	NaCl 10 ⁻²	NaCl 10 ⁻²	NaCl 10 ⁻²
C, M	CsI 10 ⁻²	CsI 10 ⁻¹	CsI 10 ⁻²	CsI 10 ⁻¹
Active solution	Na ⁺ Cl 10 ⁻²			
C, M (Na tracer)	CsI 10 ⁻¹	CsI 10 ⁻¹	CsI 10 ⁻²	CsI 10 ⁻¹
$D(\text{expt})$	1.38 ± 0.02	1.26 ± 0.01	1.31 ± 0.02	1.31 ± 0.02
D_{FINZER}	1.332	1.338	1.335	1.335
D_{FINFRST}	1.225	1.335	1.280	1.279
Capillary length, cm	2.930	2.930	2.930	2.930
$t, 10^4 \text{ s}$	15.750	9.836	15.192	15.020

Comparison between the EPG and the ACG Effect.
The electrical field takes the simple form

$$\vec{E} = \frac{1}{e_2} (2t_2^\circ - 1) \left[\frac{1}{2} + \delta C^{1/2} \right] \vec{\nabla} \mu$$

$$= \frac{1}{e_2} (2t_2^\circ - 1) \left[\frac{1}{2} + \frac{kT}{6\pi\eta} \frac{K}{1 + \text{Ka} D_2^\circ + D_3^\circ} \right] \vec{\nabla} \mu$$

In aqueous solutions at 298 K for 1-1 electrolyte

$$\frac{kT}{6\pi\eta} K = 8.07 \times 10^{-6} C^{1/2}$$

Taking

$$\beta = (2t_2^\circ - 1) \left[\frac{1}{2} + \frac{kT}{6\pi\eta} \frac{K}{1 + \text{Ka} D_2^\circ + D_3^\circ} \right]$$

$$\vec{E} = \frac{\beta}{e_2} \vec{\Delta} \mu = 2\beta \frac{kT}{e_2 C} \left[1 + \frac{d \ln \gamma_\pm}{d \ln C} \right] \vec{\nabla} C$$

The EPG contribution to the tracer flow is therefore

$$\vec{J}_1^E = 2C_1 B_1 \frac{e_1 \beta kT}{e_2 C} \left[1 + \frac{d \ln \gamma_\pm}{d \ln C} \right] \vec{\nabla} C$$

The ACG contribution to the tracer flow is therefore

$$\vec{J}_1^A = -C_1 B_1 \vec{\nabla} (kT \ln \gamma_1) = -kT \frac{C_1}{C} \frac{d \ln \gamma_1}{d \ln C} B_1 \vec{\nabla} C$$

$$= -kT \frac{C_1}{C} \frac{d \ln \gamma_\pm}{d \ln C} B_1 \vec{\nabla} C$$

The last equation is written assuming that the Debye-Hückel approximation where $\gamma^\pm = \gamma_1$ is valid.

In the experiments, to prevent adsorption phenomena we need a certain amount of an electrolyte having one ion in common with the tracer. The concentration of this electrolyte will be m mole/l, the total electrolyte concentration will be $c = m + x$ mole/l, where x is the concentration of the diffusing electrolyte.

We have the following relationship for $\vec{\nabla} \mu$ and $d \ln X/d \ln \gamma^\pm$

$$\vec{\nabla} \mu = 2kT \vec{\nabla} \ln (x\gamma_\pm) = 2kT \frac{\vec{\nabla} x}{x} + 2kT \vec{\nabla} \ln \gamma_\pm$$

$$-\frac{\vec{\nabla} \mu}{kT \vec{\Delta} \ln \gamma_\pm} = -2 \left[1 + \frac{d \ln x}{d \ln \gamma_\pm} \right]$$

$$\ln \gamma_\pm = -AC^{1/2} = -A(x+m)^{1/2}$$

TABLE VII: Influence of the Residual EPG on the ACG Effect

Electrolyte	t_2°	$(\vec{J}_1^E/\vec{J}_1^A)$
KNO ₃	0.5070	0.279
CsBr	0.4970	-0.119
CsI	0.5012	0.051

and

$$\frac{d \ln x}{d \ln \gamma_\pm} = \frac{-2C^{1/2}}{Ax}$$

We obtain for the relative values of the EPG and ACG flows:

$$\vec{J}_1^E = -2 \frac{e_1}{e_2} \beta \left(1 + \frac{d \ln x}{d \ln \gamma_\pm} \right)$$

$$\vec{J}_1^A = -2 \frac{e_1}{e_2} (2t_2^\circ - 1) \left(\frac{1}{2} + \delta C^{1/2} \right) \left(1 - \frac{2C^{1/2}}{xA} \right)$$

with

$$\delta C^{1/2} = \frac{kT}{6\pi\eta} \frac{K}{D_2^\circ + D_3^\circ}$$

$$\left\langle \frac{\vec{J}_1^E}{\vec{J}_1^A} \right\rangle = \left\langle \frac{+e_1 \vec{E}}{-\vec{\nabla} kT \ln \gamma_1} \right\rangle = \frac{1}{C_2' - C_2} \int_{C_2}^{C_2'} \frac{J_1^E}{J_1^A} dC$$

$$= \frac{-2e_1}{e_2} (2t_2^\circ - 1) \left[\frac{1}{2} - \frac{2}{A(C_2'^{1/2} + C_2^{1/2})} \right.$$

$$- \frac{m^{1/2}}{A(C_2' - C_2)} \ln \left[\frac{C_2'^{1/2} - m^{1/2}}{C_2^{1/2} - m^{1/2}} \right]$$

$$\left. \times \frac{C_2^{1/2} + m^{1/2}}{C_2'^{1/2} + m^{1/2}} \right] + 2\delta \left[\frac{1}{3} \frac{C_2'^{3/2} - C_2^{3/2}}{C_2' - C_2} \right.$$

$$\left. - \frac{1}{A} - \frac{m \ln ((C_2' - m)/(C_2 - m))}{A(C_2' - C_2)} \right]$$

We have the following values for $(\vec{J}_1^E/\vec{J}_1^A)$ (Table VII).

It is always difficult to eliminate the electrical field effect completely and we must in any case separate the contribution of this effect to the total coupling.

VII. Conclusion

In this study we have considered a self-diffusion process coupled with a chemical diffusion phenomenon occurring in the same or in the opposite direction.

The first conclusion drawn from this work is that the transport of a given ion is only slightly influenced by a simultaneous chemical flow, which gives support to the description of the phenomenon by a random walk model.

The mathematical analysis and the experimental results show that the perturbation occurring through the chemical gradient comes essentially from the electrical diffusion potential gradient (EPG). The other important corrective terms result from the electrophoresis and the activity coefficient gradient (ACG).

We have derived the equations for the flow of the tracer ion in its most general form involving both chemical and tracer concentration gradients and have shown that the same macroscopic flow can accelerate a given type of ion and decelerate ions of an opposite charge.

We have also shown the importance of the influence of

a ionic activity coefficient gradient, experimentally as well as theoretically.

This opens the way to measurement of the individual ionic chemical potential, or at least of its gradient in the presence of several types of interactions.

References and Notes

- (1) L. Onsager, *Ann. N.Y. Acad. Sci.*, **46**, 421 (1945).
- (2) M. J. Pikal, *J. Phys. Chem.*, **75**, 660 (1971).
- (3) P. Turq, *Chem. Phys. Lett.*, **15**, 579 (1972).
- (4) (a) A. Plonka, *Nukleonika*, **9**, 487 (1964); (b) *ibid.*, **11**, 407 (1966); (c) *ibid.*, **11**, 643 (1966).
- (5) P. Turq and M. Chemla, *J. Chim. Phys.*, **69**, 681 (1972).
- (6) H. Falkenhagen, "Theorie der Elektrolyte", Hirzel, Leipzig, 1971.
- (7) J. S. Anderson and K. Saddington, *J. Chem. Soc.*, **5**, 381 (1949).
- (8) P. Turq, F. Lantelme, and M. Chemla, *Electrochim. Acta*, **14**, 1081 (1969).
- (9) H. Magdelenat, P. Turq, and M. Chemla, *Biopolymers*, **13**, 1535 (1974).

Oxygen Penetration into the Bulk of Palladium

C. T. Campbell, D. C. Foyt, and J. M. White*

Department of Chemistry, University of Texas, Austin, Texas 78712 (Received October 14, 1976)

Publication costs assisted by the National Science Foundation

The interaction of O₂ with polycrystalline Pd was investigated; above 250 °C a significant amount of oxygen is incorporated into the bulk at pressures far below the dissociation pressure of PdO. The rate of uptake into previously unexposed Pd foil was pressure independent, suggesting (1) that penetration into the bulk occurred from an oxygen-saturated surface and (2) that the rate was limited by the process in which chemisorbed oxygen moved out of the surface layer toward the interior of the Pd. The temperature dependence of the uptake rate in this pressure-independent region was characterized by an Arrhenius A factor of 5.2×10^{20} atoms cm⁻² min⁻¹ and an activation energy of 17 kcal mol⁻¹ (71 kJ mol⁻¹). After about 100 monolayers of oxygen were incorporated, the uptake rate began to decline and became unobservable after about 350 monolayers were incorporated. Equilibrium oxygen pressures above such extensively oxygen-treated samples were much lower than the reported dissociation pressures of PdO indicating that the palladium-oxygen system under these conditions should be characterized as a solid solution of oxygen in palladium. The role which this incorporation of oxygen may play in catalytic processes is discussed.

1. Introduction

Pd has received considerable attention as a catalyst, especially in studies of the oxidation of carbon monoxide. The interaction of oxygen with Pd is a key feature in such reactions, but one that has not been fully understood. Investigators¹⁻⁶ have cited evidence for some incorporation of oxygen into the bulk of Pd (above 250 °C) upon exposure to O₂ at pressures well below the dissociation pressures of PdO at these temperatures.^{4,6-13} Attempts to characterize and understand this phenomenon have been few and far from conclusive.^{3,5,6} Raub and Plate³ discuss their results in terms of a solid solution of oxygen while Chaston⁵ disagrees, suggesting that the oxygen uptake results from the oxidation of base metal impurities. Schmah and Minzl⁶ showed that Pd is not soluble in PdO but reported some data which support limited solubility of O in Pd. The possibility that the catalytic activity of Pd depends on oxygen uptake has been aptly demonstrated,^{1,2,14-16} and experimenters have resorted to prolonged pretreatment of the heated substrate with O₂ to achieve a stable catalyst.^{1,14-15,17-20}

The importance of oxygen incorporation into transition metals under conditions far removed from those where bulk oxide is stable has recently received renewed attention

in the catalysis and surface science literature. Excellent work on Pt^{21,22} and Ir^{23,24} has underscored the importance of studying the role which this oxygen incorporation plays.

The purpose of the work reported here was to extend and clarify our previous work¹ by examining the rate, extent, and reversibility of oxygen uptake and the dependence of these quantities on the substrate temperature, gas phase pressure, and substrate history. We have developed a qualitative model of the uptake which is consistent with our data and that of others. The results appear to follow the trend already established for Pt^{21,22} and Ir^{23,24} and point to the importance of investigating thoroughly the role of incorporated oxygen in influencing catalytic properties.

2. Experimental Section

Experiments were performed in a bakeable, stainless steel, ion-pumped vacuum chamber equipped with a calibrated capacitance manometer, the reference side of which was pumped with a small oil diffusion pump. Background pressures in the 730-cm³ experimental chamber were determined with a Bayard-Alpert type ionization gauge. Gases were introduced through a variable leak valve to selected pressures (measured with the ca-

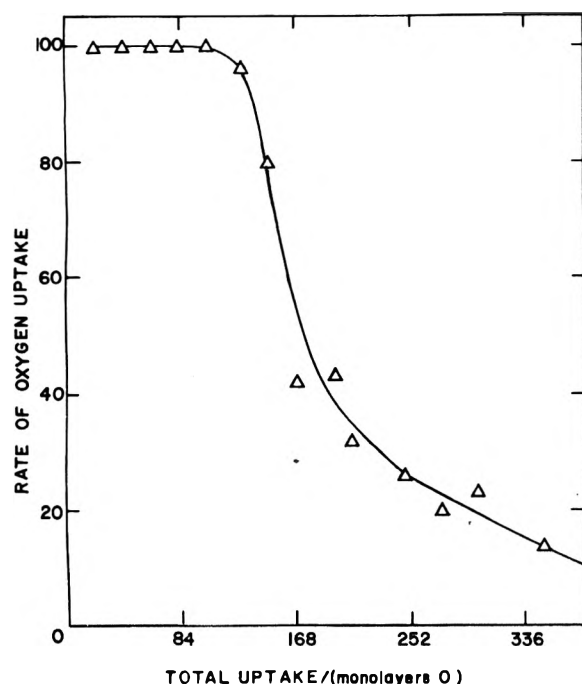


Figure 1. Uptake rate at 750 °C of oxygen on polycrystalline palladium as a function of the total oxygen uptake. The ordinate is arbitrarily scaled to 100 and this value corresponds to the rate shown in Figure 2 for 750 °C (1.06×10^{17} atoms $\text{cm}^{-2} \text{min}^{-1}$). One monolayer is taken as equivalent of 2×10^{15} oxygen atoms/ cm^2 of surface (macroscopically determined).

pacitance manometer) after the experimental chamber was isolated from the ion pump with a gold-seal high vacuum valve. Reagent grade gases were used throughout.

The substrates were polycrystalline Pd foils, usually $100 \times 10 \times 0.127$ mm, mounted between insulated stainless steel feedthru leads which provided for resistive heating. Substrate temperatures were calibrated as a function of the applied voltage using an iron-constantan thermocouple spot-welded to the palladium. The thermocouple was attached and this calibration procedure was carried out after the oxygen uptake experiments were completed. Effects due to the oxidation of walls or feedthrus were proven negligible, as the rate of oxygen uptake at a given temperature was found to be proportional to the geometric Pd surface area over the range 6–20 cm^2 . Spurious pressure variations due to gas temperature changes were proven negligible in background experiments with N_2 .

3. Results

Prior to measuring the rate of oxygen uptake, the sample was gradually heated to 750 °C while pumping to keep the total pressure below 2×10^{-7} Torr (1 Torr = 133.3 Pa). Upon reaching 750 °C the temperature was fixed until the pressure dropped below 3×10^{-8} Torr; then the sample was cooled to room temperature. The experimental chamber was then isolated, the ion gauge was turned off, and O_2 was introduced to a pressure of 3.5×10^{-2} Torr. After exposure for a period long enough for weakly bound CO to be displaced by oxygen,¹⁸ the experimental chamber was evacuated to a pressure of 10^{-6} Torr, isolated again, and refilled with a known pressure of O_2 , usually 3.5×10^{-2} Torr. The substrate was then heated while monitoring pressure as a function of time with the capacitance manometer.

In preliminary experiments reproducibility was a serious problem because the oxygen uptake rate (dP/dt) was a strong function of substrate history. However, when the above preliminary recipe was followed with samples from

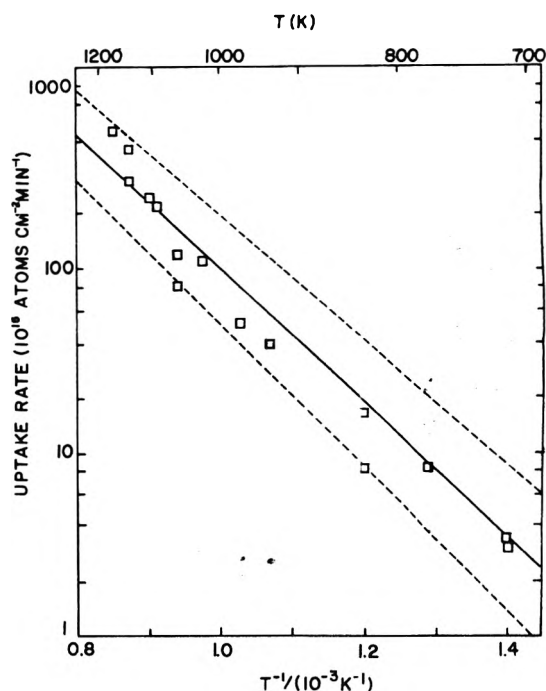


Figure 2. Arrhenius plot of the temperature dependence of the rate of oxygen incorporation into new palladium. The gas phase oxygen pressure at the start of each experiment was about 3.5×10^{-2} Torr.

the same stock, reproducibility was satisfactory, although still not excellent. Auger analysis of the starting material revealed small amounts of carbon and sulfur on the surface; however, the first heating in oxygen, at pressures as high as those used here, removes nearly all of this contamination.²⁵

Figure 1 shows the variation of the rate with the total amount of O_2 taken up at 750 °C. Here we have used the convenient units of monolayers, assuming 2×10^{15} atoms cm^{-2} and a surface area based on a smooth surface of 20 cm^2 . At this temperature the rate was constant for about 100 monolayers and then began to fall off quite sharply. Note particularly that continued uptake of oxygen is observed to the extent of about 345 monolayer units from gas phase O_2 at a pressure of about 3.5×10^{-2} Torr, well below the reported dissociation pressure of 45 Torr.⁷⁻¹³ After 345 monolayers, the rate of uptake became too slow to measure reliably with our apparatus.

We attempted to measure the equilibrium pressure of O_2 over the 150 and 345 monolayer substrates by heating at 900 °C for up to 4 h. The pressure attained over the 150 monolayer substrate was around 2×10^{-3} Torr. For the 345 monolayer substrate, equilibrium pressures were inconsistent but on the order of 10^{-2} Torr. This is to be compared with the dissociation pressure of PdO which is greater than 1 atm at 900 °C.⁷⁻¹¹ In addition, heating (900 °C) of the 345 monolayer substrate for up to 2 days under high vacuum effected no return to the starting conditions of Figure 1. Instead, after the quick uptake of a few monolayers, the Pd behaved much like a 230-monolayer-old substrate in its capacity to incorporate oxygen.

With relatively new substrates (left side of Figure 1) below 750 °C, we observed a linear decrease in pressure with time from the starting oxygen pressure ($\sim 3.5 \times 10^{-2}$ Torr) down to below 2×10^{-3} Torr, at which point the pressure levelled off. By varying the pressure we noted that the rate below 740 °C was independent of O_2 pressure between 3.8×10^{-1} and 2×10^{-3} Torr. Pressure effects above 750 °C were not determined. Figure 2 shows, in Arrhenius form, rates observed on new substrates at various temperatures. Below 350 °C the rate dropped off

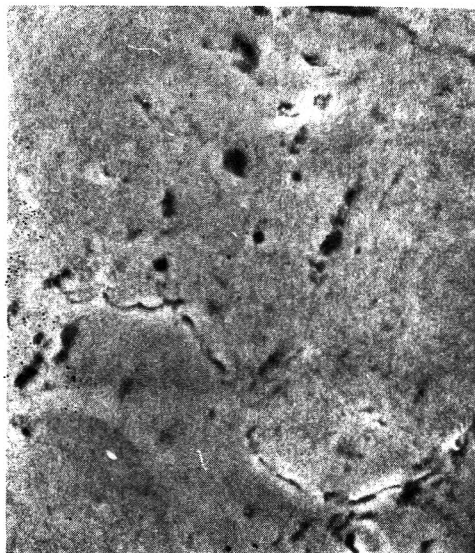


Figure 3. Electron micrograph of a new Pd surface ($\times 5200$).

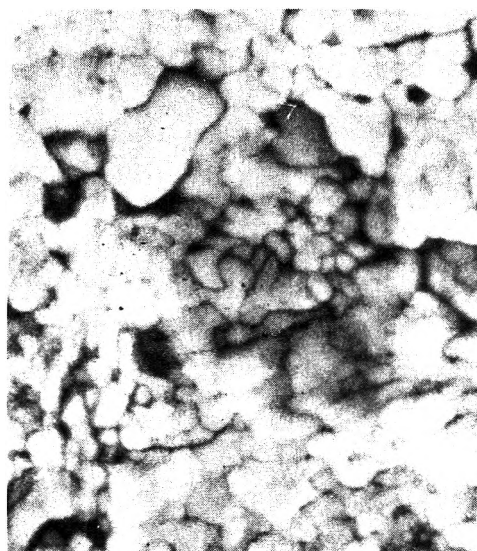


Figure 4. Electron micrograph of Pd which has taken up 345 monolayers of oxygen ($\times 5200$).

to some unobservably small value (cf. ref 26). For the temperatures and pressures discussed here, the rate, R , is well represented by

$$R = (5.2 \pm 2.4) \times 10^{20} \text{ atoms cm}^{-2} \text{ min}^{-1} \times \exp(-17 \pm 1 \text{ kcal mol}^{-1}/RT) \quad (1)$$

Electron micrographs of the new and the extensively oxygen-exposed Pd are shown in Figures 3 and 4, respectively. A considerable increase in surface roughness appears to accompany the oxygen penetration. This seems reasonable when we consider that penetration of oxygen must really involve some exchange of positions for the oxygen adatom and a Pd atom in the underlayer. The crevices might result from this exchange occurring preferentially at grain boundaries, as discussed by Ullman and Madix.²⁷ One thing seems clear, the uptake of oxygen is not simply chemisorption followed by diffusion into the bulk.

4. Discussion

The fact that below 750 °C the rate of oxygen penetration into a new substrate is independent of pressure in the range 3.8×10^{-1} to 2×10^{-3} Torr indicates that ad-

sorption is a fast step under these conditions and that the surface is saturated with almost a complete monolayer of adsorbed oxygen. The disappearance of oxygen LEED spots as well as a decrease in the work function of the Pd (111) surface unaccompanied by any O_2 desorption caused Ertl and Koch² to conclude that chemisorbed oxygen moves into the bulk of Pd above 250 °C. It must be this movement away from the surface which is the rate-limiting step for the work reported here. They also report an activation energy for this process of 20 kcal mol^{-1} ,² which is in reasonable agreement with our value of 17 kcal mol^{-1} . It can be expected that pressure will begin to affect this rate at very high temperatures, when oxygen surface coverage decreases. In passing it is worth noting that penetration into the bulk has been reported on the Pd (111) surface but has not been carefully studied on other single crystal surfaces.^{5,28,29}

The change in rate with the amount taken up (Figure 1) is not exactly what would be predicted by ordinary homogeneous diffusion kinetics, although the latter portion shows the expected "reciprocal" shape.³⁰ The departure from simple diffusion kinetics on new substrates is expected considering the energy barrier and the step-by-step character of the process.

The fact that the equilibrium pressure of oxygen above the Pd with 345-monolayers of oxygen is drastically smaller than the equilibrium (dissociation) pressure of PdO, coupled with the fact that Pd is insoluble in PdO,⁶ leads us to conclude that we are dealing with a solid solution of low concentration of oxygen in Pd, rather than stoichiometric PdO mixed with Pd. The 345 monolayers of oxygen thus corresponds to a maximum solubility of about 8×10^{-5} atoms of O/atom of Pd based on the total number of Pd atoms in the sample. It is believed that this is not a true saturation solubility, as kinetic factors probably precluded further oxygen uptake. For example, consider a situation in which the Pd is truly oxygen-saturated near the surface but the oxygen concentration gradually drops off into the bulk: the diffusion-limited rate of uptake would be extremely small in this case. As expected for solution thermodynamics, the equilibrium pressure of O_2 was lower after 150 monolayers of uptake than after 345 monolayers.

We expect that this solid solution is a precursor to the formation of the bulk stoichiometric oxide. Consider Pd at 400 °C with a pressure of 5×10^{-5} Torr of O_2 in the gas phase above it. Ertl² showed that the Pd surface is essentially saturated with adsorbed oxygen under these conditions. Since the bulk senses almost unit activity of oxygen at the surface, we must ask why the bulk oxide is not formed. Although the small departure of the surface coverage from unity might be responsible, it seems more logical that the saturation concentration of the solid solution of oxygen increases rapidly but smoothly with surface coverage and when the dispersed oxygen atoms become dense enough to strongly sense one another, stoichiometric PdO microcrystallites result. This corresponds to the dissociation pressure and any further increase in oxygen content will not change the chemical nature of this oxide, only the crystallite size. This explains the constant dissociation pressure found by Schmahl⁶ over a wide range of oxygen/Pd atom ratios. The formation of such uniformly dispersed microcrystallites has been directly observed in the initial oxidation of Ta by Nakamura et al.³¹ We should note that the formation of an essentially saturated surface layer of oxygen under conditions where the bulk oxide is unstable is by no means limited to Pd. Chesters and Somorjai,³² for example, have

recently observed a structured surface oxide on gold well below the dissociation pressure of gold oxide.

Finally we should remark that our observations are consistent with the break-in period associated with the use of Pd in the catalytic oxidation of CO.^{1,2,14-16} Baddour et al.¹⁴ observed an increasing rate of CO₂ formation with time during the break-in period, after which the rate stabilized. This break-in was also achieved using only oxygen pretreatment.¹⁴ Considering the tendency of adsorbed oxygen to migrate into the bulk of new Pd, and the variation of the rate with total uptake and, therefore, with time (Figure 1), it is easy to see how this phenomenon could arise. The rate of CO₂ production on these catalysts is proportional to the surface coverage of oxygen and, under steady-state conditions for a new catalyst, the oxygen coverage can be depleted by both the reaction to form CO₂ and by penetration into the bulk. After long exposure to oxygen, the latter becomes insignificant. We should clarify that, under the conditions used,¹⁴ the oxygen coverage was very small, while under our conditions here it is very large. The change in the rate of CO₂ production could also be attributed to a change in surface properties as the oxygen concentration increases. We thus conclude that many reports of oxidative catalysis over Pd could probably best be referred to as being over Pd containing a significant amount of oxygen in solid solution near the surface.

Acknowledgment. We are especially grateful to Dr. Tatsuo Matsushima for his valuable discussions concerning the manuscript. We also thank Dr. Michael Schmerling for his aid with the electron microscope, and Diane Mumme and Gail Raven for their help in preparing the manuscript. Finally we thank Professors L. Schmidt and W. H. Weinberg for informing us of their results prior to publication. This work was supported in part by the National Science Foundation Grant CHE75-13732.

References and Notes

- (1) J. S. Close and J. M. White, *J. Catal.*, **36**, 185 (1975).
- (2) G. Ertl and J. Koch, "Adsorption-Desorption Phenomena", F. Ricca, Ed., Academic Press, New York, N.Y., 1972, p 345.
- (3) E. Raub and W. Plate, *Z. Metallkd.*, **48**, 529 (1968).
- (4) G. Bayer and H. G. Wildemann, *Thermochim. Acta*, **11**, 79 (1975).
- (5) J. C. Chaston, *Platinum Met. Rev.*, **9**, 126 (1965).
- (6) N. G. Schmahl and E. Minzl, *Z. Phys. Chem. (Frankfurt am Main)*, **47**, 142 (1965).
- (7) L. Wohler, *Z. Elektrochem.*, **12**, 781 (1906).
- (8) R. Schenck and F. Kurzen, *Z. Anorg. Chem.*, **220**, 97 (1934).
- (9) Y. L. Sandler and D. D. Durigon, *J. Phys. Chem.*, **73**, 2392 (1969).
- (10) L. Riekert and H. P. Schuchmann, *Ber. Bunsenges. Phys. Chem.*, **68**, 986 (1964).
- (11) S. Dushman and J. M. Lafferty, "Scientific Foundations of Vacuum Technique", 2nd ed, Wiley, New York, N.Y., 1962, p 741.
- (12) W. E. Bell, R. E. Inyard, and M. Tagami, *J. Phys. Chem.*, **70**, 3735 (1966).
- (13) J. S. Warner, *J. Electrochem. Soc.*, **114**(1), 68 (1967).
- (14) R. F. Baddour, M. Modell, and R. L. Goldsmith, *J. Phys. Chem.*, **74**, 1787 (1970).
- (15) R. F. Baddour, M. Modell, and U. K. Heusser, *J. Phys. Chem.*, **72**, 3621 (1968).
- (16) G. Ertl and J. Koch, *Proc. Int. Congr. Catal. 5th*, **67**, 969 (1972).
- (17) T. Matsushima, D. B. Almy, D. C. Foyt, J. S. Close, and J. M. White, *J. Catal.*, **39**, 277 (1975).
- (18) T. Matsushima and J. M. White, *J. Catal.*, **40**, 334 (1975).
- (19) T. Matsushima, C. J. Mussett, and J. M. White, *J. Catal.*, **41**, 397 (1976).
- (20) T. Matsushima and J. M. White, *J. Catal.*, **39**, 265 (1975).
- (21) R. W. McCabe and L. D. Schmidt, to be submitted for publication.
- (22) R. Ducros and R. P. Merrill, *Surf. Sci.*, **55**, 227 (1976).
- (23) V. P. Ivanov, G. K. Borekov, V. I. Savchenko, W. F. Egelhoff, Jr., and W. H. Weinberg *Surf. Sci.*, submitted for publication.
- (24) P. A. Zhdan, G. K. Borekov, A. I. Boronin, W. F. Egelhoff, Jr., and W. H. Weinberg, *Surf. Sci.*, submitted for publication.
- (25) D. B. Almy, private communication of unpublished results.
- (26) No penetration of oxygen into the bulk was observable below 250 °C: S. A. Isa and J. M. Saleh, *J. Phys. Chem.*, **76**, 2530 (1972).
- (27) A. Z. Ullman and R. J. Madix, *High Temp. Sci.*, **6**, 342 (1974).
- (28) G. Ertl and P. Rau, *Surf. Sci.*, **15**, 443 (1969).
- (29) G. Ertl and J. Koch, *Z. Phys. Chem. (Frankfurt am Main)*, **69**, 323 (1970).
- (30) R. B. Bird, W. E. Stewart, and E. N. Lightfoot, "Transport Phenomena", Wiley, New York, N.Y., 1960, p 596.
- (31) S. Nakamura and W. W. Muller, *J. Appl. Phys.*, **36**, 3634 (1965).
- (32) M. A. Chesters and G. A. Somorjai, *Surf. Sci.*, **52**, 21 (1975).

COMMUNICATIONS TO THE EDITOR

Temperature-Jump Study on the Aquation of the Iron(III) Complex by Dodecylpyridinium Chloride-Solubilized Water in Chloroform

Sir: In recent years reactions in reversed micelles have attracted much attention, especially with regard to their similarity to enzymatic functions.¹ Reversed micelles are formed in nonpolar and less polar solvents such as benzene and chloroform. It has seemed therefore impossible to apply the Joule heating temperature-jump (T-jump) technique to rapid reactions in these media, because this method has been thought to require high conductivity for the sample solution.²

In the present communication we obtained successfully detailed information regarding the dynamic properties of

metal ions solubilized in reversed micelles, that is, the aquation of the 1:1 complex (DP-FeCl₃) of anhydrous ferric chloride with dodecylpyridinium chloride (DPCI) by DPCI-solubilized water in chloroform by means of the T-jump technique.

Monomeric DPCI undergoes a 1:1 complex formation with FeCl₃ in chloroform below the critical micelle concentration (cmc) of DPCI; cmc = $(4.5 \pm 0.2) \times 10^{-4}$ M. The formula and dissociation constant for this complex were determined spectrophotometrically by the molar ratio method: $K_d = (6.6 \pm 4.0) \times 10^{-10}$ M at 20 °C.^{3,4} It was similarly confirmed that above the cmc, FeCl₃ also formed a 1:1 complex with DPCI.⁴

In order to interpret the observed water effects on (i) the absorption spectra, (ii) the relaxation time, and (iii) the relaxation amplitude of T-jump signals obtained above

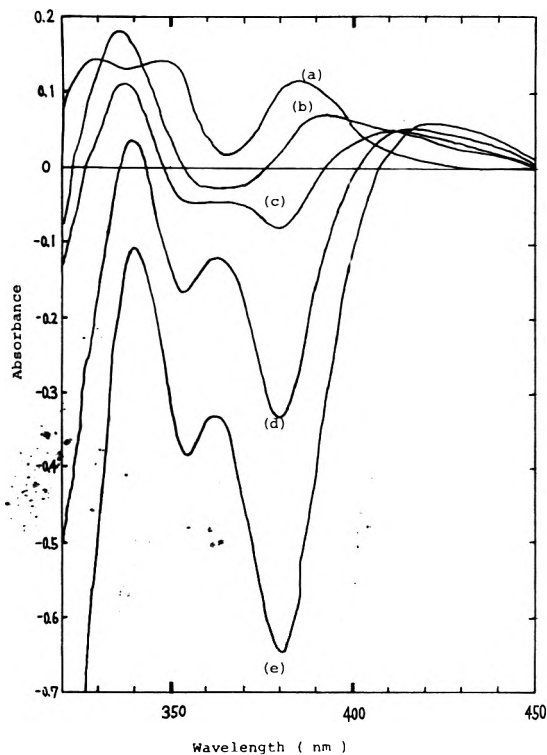
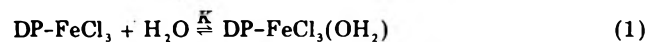


Figure 1. Water dependence of the difference spectra for the chloroform solution of 0.50 M DPCL and 3.0×10^{-3} M FeCl_3 at 20 °C, using a pair of cells with 0.2-cm pathlength. The concentrations of water, b , were as follows; (a) 0.02 M, (b) 1.1 M, (c) 1.7 M, (d) 2.2 M, and (e) 2.8 M.

the cmc of DPCL, the following simple mechanism was assumed:



$$K_{\text{eq}} = k_1 K / k_2 \quad (3)$$

(i) Figure 1 shows difference spectra taken from 320 to 450 nm at 20 °C, using a reference cell containing constant concentrations of FeCl_3 (3.0×10^{-3} M) and DPCL (0.50 M) in the absence of water and a sample cell containing the same amounts of FeCl_3 and DPCL and a variable amount of added water (1.0–2.8 M).⁵ The observed decrease of absorbance was essentially caused by the aequation of DP- FeCl_3 because adding water without FeCl_3 did not change the spectrum in this wavelength region.

The following equation was derived from mechanism 1–2:

$$-\frac{0.20}{\Delta A} = \frac{1}{\Delta \epsilon a} \left(\frac{1}{K_{\text{eq}} b^2} + 1 \right) \quad (4)$$

where ΔA is the measured difference absorbance with a cell of 0.20 cm pathlength, $\Delta \epsilon = \epsilon_{\text{DP-FeCl}_3} - \epsilon_{\text{DP-FeCl}_3(\text{OH}_2)_2}$, a and b are the analytical concentrations of FeCl_3 and H_2O ($a \ll b$), respectively.

A straight line was obtained from the plot of $-0.20/\Delta A$ at 380 nm vs. b^{-2} as shown in Figure 2, leading to $K_{\text{eq}}\Delta \epsilon = 6.2 \pm 0.6 \text{ M}^{-3} \text{ cm}^{-1}$ at 410 nm.

(ii) The T-jump measurements were performed with a Union Giken temperature-jump apparatus.⁶ Relaxations were observed at 410 nm for a solution containing 3.0×10^{-3} M of FeCl_3 , 0.50 M of DPCL, and 1.0–2.8 M of water. The solution was thermostated at 15 °C before temper-

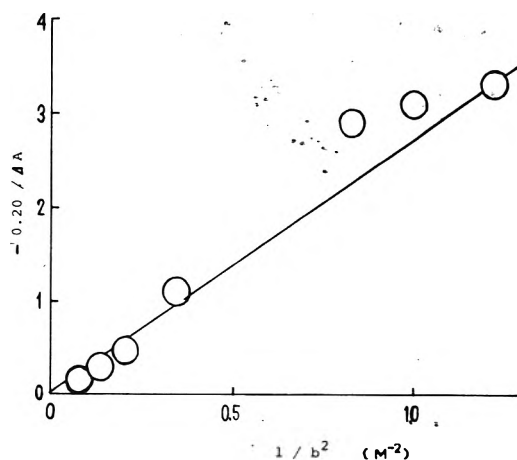


Figure 2. Plot of $-0.20/\Delta A$ at 380 nm against the reciprocal square of water concentration (b^{-2}).

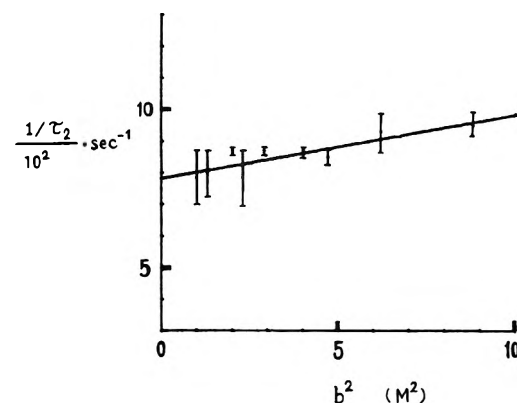


Figure 3. Plot of $1/\tau_2$ against the square of water concentration (b^2). The line is drawn by the least-squares fitting using Yokogawa Hewlett-Packard calculator. Sample solutions contain 3.0×10^{-3} M FeCl_3 , 0.50 M DPCL, and 1.0–2.8 M of H_2O in chloroform.

ature rise of 5.0 ± 0.5 °C. Two relaxation times (τ_1 and τ_2) were observed under this condition. The faster relaxation time (τ_1) coincided with the calculated rise time of the temperature of solution.^{6,7} This relaxation might arise from reversed micellation. It would be concluded that the relaxation due to reversed micellation is much faster than the observed one due to the temperature rise. $1/\tau_1$ was independent of the water concentration (1.0–2.8 M): $1/\tau_1 = (3.8\text{--}4.3) \times 10^4 \text{ s}^{-1}$.

Another slower relaxation time (τ_2) was due to the aequation of DP- FeCl_3 by DPCL-solubilized water. The following expression was derived for τ_2 , assuming that reaction 2 was the rate-determining step:

$$1/\tau_2 = k_1 K b^2 + k_2 \quad (5)$$

As shown in Figure 3, $1/\tau_2$ was linearly proportional to the square of the water concentration (b^2). From the intercept and the slope of the straight line constructed by least-squares analysis, we obtained $k_1 K = (2.0 \pm 0.3) \times 10 \text{ M}^{-2} \text{ s}^{-1}$ and $k_2 = (7.8 \pm 0.5) \times 10^2 \text{ s}^{-1}$. Using eq 3, K_{eq} was determined to be $(2.6 \pm 0.3) \times 10^{-2} \text{ M}^{-2}$. Inserting this value into $K_{\text{eq}}\Delta \epsilon = 6.2 \pm 0.6 \text{ M}^{-3} \text{ cm}^{-1}$, $\Delta \epsilon$ in eq 4 became $240 \pm 30 \text{ M}^{-1} \text{ cm}^{-1}$ at 410 nm.

(iii) The amplitude measurements of the slower relaxation could yield information on the reaction enthalpies.^{2,8} The following expression was derived for the overall equilibrium of eq 1 and 2:

$$\Delta A_{\text{m}}^{-1} = -(RT^2/2.30\Delta \epsilon \Delta H dT a)(1/K_{\text{eq}} b^2 + 2) \quad (6)$$

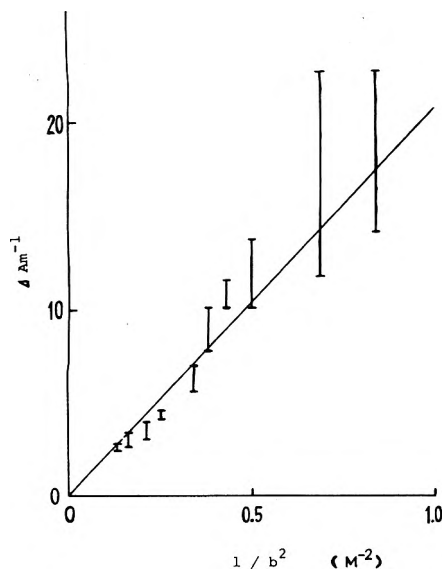


Figure 4. Plot of ΔA_m^{-1} at 410 nm against b^{-2} .

where ΔA_m is the measured relaxation amplitude at 410 nm, $\Delta H = H_{\text{DP-FeC}_3(\text{OH})_2} - 2H_{\text{H}_2\text{O}} - H_{\text{DP-FeCl}_3}$, $dT = 5.0 \pm 0.5$ K, and $T = 293$ K. It was noted that a plot of ΔA_m^{-1} against b^{-2} gave a straight line, as shown in Figure 4. Since $\Delta\epsilon$ and K_{eq} are already known, the enthalpy could be estimated from the slope: $\Delta H = -38 \pm 15$ kcal mol $^{-1}$. This value was in agreement with the enthalpy of the aequation of free Fe(III) ion evaluated by Bernal and Fowler.⁹

Acknowledgment. We are grateful to Professor M. Fujimoto for his encouragement and to Professors K. Yagi and S. Nishida for their permission to use the apparatus. We also wish to express our thanks to Professors T. Tsuji and T. Furukawa for their valuable discussions.

Supplementary Material Available: Appendices I, II, and III contain the three derivations for eq 4, 5, and 6 (3 pages). Ordering information is given on any current masthead page.

References and Notes

- J. H. Fendler and E. J. Fendler, "Catalysis in Micellar and Macromolecular Systems", Academic Press, New York, N.Y., 1975.
- M. Eigen and L. DeMaeyer in "Techniques of Organic Chemistry", Vol. VIII, 2nd ed, Part 2, S. L. Friess, E. S. Lewis, and A. Weissberger, Ed., Wiley, New York, N.Y., 1963, p 895.
- A. E. Harvey, Jr., and D. L. Manning, *J. Am. Chem. Soc.*, **72**, 4488 (1950).
- T. Masui, F. Watanabe, and A. Yamagishi, submitted for publication.
- The apparent aggregation number of DPCI (\bar{n}) in chloroform was determined by the vapor pressure depression method; $\bar{n} = 5-7$ at 0.50 M DPCI.
- The T-jump apparatus used has a coaxial cable of 157 m length as a capacitor. The characteristic impedance of the cable is 50 Ω .
- (a) F. Watanabe, Doctoral Thesis, Hokkaido University, Japan, 1976. (b) It was found that discharge of electrical energy stored in the cable into the sample solution is determined substantially by the resistance of the solution. Taking into account this finding, the rise time of the temperature was calculated. More detailed representation of the calculation will be given by F. Watanabe, T. Masui, and A. Yamagishi, to be published.
- F. Guillain and D. Thusius, *J. Am. Chem. Soc.*, **92**, 5534 (1970); D. Thusius, *ibid.*, **94**, 356 (1972).
- J. D. Bernal and R. H. Fowler, *J. Chem. Phys.*, **1**, 515 (1933).

Department of Chemistry
Faculty of Science
Hokkaido University
Kita-ku, Sapporo, Japan 060

Takeshi Masui
Fumiyuki Watanabe*
Akihiko Yamagishi

Received August 30, 1976

Solubility Product Constant of Calcium Fluoride

Publication costs assisted by the National Science Foundation

Sir: In a paper appearing recently in this journal, Stearns and Berndt¹ present evidence that the classical solubility product of calcium fluoride is not a constant at a given temperature and pressure but changes as a function of the composition of the solution phase. Some thermodynamic arguments in support of this finding were offered. The implications of this conclusion are so far-reaching as to demand further consideration.

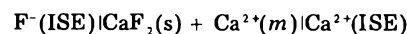
Stearns and Berndt used a fluoride-selective electrode to measure the concentration of free fluoride ion in a solution containing a known stoichiometric concentration of added calcium ion and excess solid calcium fluoride. In effect, the concentration solubility product constant K'_{sp} was calculated by

$$K'_{\text{sp}} = ([\text{Ca}^{2+} \text{ added}] + 1/2[\text{F}^-])[\text{F}^-]^2 \quad (1)$$

and was found to increase by a factor of 2 over a range of added calcium ion from 0 to 0.01 M, after which it decreased to near its original value with further additions of calcium ion. Anomalies in the value of K_{sp} derived from measurements with the fluoride-selective electrode have been reported before.²

We have now repeated the measurements of Stearns and Berndt (at 25 °C rather than at 20 °C) using the calcium ion-selective electrode as well as the fluoride electrode. Our measurements suggest that the activity solubility product is indeed a constant within the experimental error inherent in the electrode system. The results suggest that the variability observed by Stearns and Berndt (and confirmed by us when the fluoride electrode alone was used) may be due to adsorption of ions on the solid CaF_2 . Under these circumstances, the system can no longer be defined by measurements of the fluoride ion concentration alone.

The cell can be represented by



where m is molality and s represents a solid phase. If both electrodes respond in Nernstian fashion, one can write for the emf E of cell A

$$E = E_{\text{Ca}}^0 - E_{\text{F}}^0 + k \log (a_{\text{Ca}^{2+}} a_{\text{F}^{-2}}) \\ = \text{constant} - kpK_{\text{sp}} \quad (2)$$

where k is $(RT \ln 10)/2F$. The emf of the cell should thus be constant if the activity product is a constant. The measurements were made at an ionic strength of 1.0 mol kg $^{-1}$, maintained by addition of appropriate amounts of KCl. In this way it was hoped that the liquid-junction potentials would be stabilized and that changes in the activity coefficients of Ca^{2+} and F^- would be minimized. It was therefore possible to monitor independently the molalities (rather than the activities) of the two ions by measuring the potentials of the calcium-responsive and fluoride-responsive electrodes individually with respect to a saturated calomel reference electrode (SCE). By measurements in solutions of KF/KCl and in solutions of CaCl_2/KCl , the standard emf values for the cells SCE|ISE were found to be -177.9 and 108.0 mV for the fluoride and calcium electrodes, respectively, at 25 °C. The corresponding Nernst slopes were 59.42 and 29.74 mV per decade.

The salts used (KF, KCl, CaCl_2 , and CaF_2) were of reagent quality. Calcium fluoride was digested repeatedly under successive portions of boiling distilled water over a period of 2 days. Potassium fluoride was dried to constant weight, and a solution of recrystallized calcium

TABLE I: Equilibrium Data for Solutions of Calcium Chloride Saturated with Calcium Fluoride at 25 °C

Added CaCl ₂ , <i>m</i>	10 ³ <i>m</i> _{Ca²⁺}	10 ⁴ <i>m</i> _{F⁻}	10 ¹⁰ <i>K'</i> _{sp} (eq 1)	10 ¹⁰ <i>K'</i> _{sp} (eq 3)	<i>E</i> (cell A), mV
0	0.855	6.36			4.8
0.000 431	1.16	5.41	2.05	3.38	4.5
0.001 030	1.66	4.63	2.71	3.57	5.2
0.001 997	2.50	3.76	2.94	3.53	4.4
0.003 108	3.51	3.22	3.38	3.64	5.4
0.005 279	5.46	2.63	3.74	3.77	5.9
0.009 155	9.00	1.99	3.66	3.56	5.2
0.013 27	12.8	1.76	4.13	3.95	6.5
0.023 72	22.3	1.36	4.41	4.14	7.1
0.037 96	35.6	1.06	4.29	4.01	6.7
0.055 33	52.0	0.868	4.18	3.92	6.4
0.079 30	75.9	0.715	4.06	3.89	6.3
0.100 1	96.9	0.625	3.90	3.78	5.9
0.116 8	115	0.563	3.70	3.65	5.5
0.130 3	129	0.529	3.64	3.61	5.4

chloride was standardized. An Orion 96-09 lanthanum fluoride electrode was used. The calcium ion-selective electrode made use of a membrane incorporating a neutral ligand carrier.³ The electrodes were mounted, together with a commercial saturated calomel reference electrode, in the top of a water-jacketed titration cell provided with a magnetic stirrer and maintained at 25.0 °C. The cell was charged with a weighed quantity of 1 *m* KCl and known excess of calcium fluoride. After the emf (measured by a Corning Model 112 pH electrometer) between each indicator electrode and the SCE had reached a constant value, successive weighed portions of a CaCl₂/KCl solutions (ionic strength 1.0) were added and the measurements repeated. The ion-selective electrodes were calibrated on the molality (*m*) scale by emf measurements in solutions having the compositions CaCl₂(*m*), KCl (1 - 3*m*) or KF(*m*), KCl (1 - *m*), where *m* was varied over the range encountered in the reported experiments. Although as much as 12 h, with stirring, was sometimes required for equilibrium, the calibration remained essentially unchanged over the series of measurements.

The results of the measurements of ion molalities in solutions of calcium chloride saturated with CaF₂ are given in the first three columns of Table I. From these data, it is possible to calculate an apparent solubility product (*K'*_{sp} = *m*_{Ca²⁺}*m*_{F⁻}²) in three different ways. The first is by use of eq 1, as was done by Stearns and Berndt.¹ The others follow from the equations

$$K'_{sp} = m_{Ca^{2+}}(\text{measured})m_{F^{-}}^2(\text{measured}) \quad (3)$$

and

$$\log K'_{sp} = (E - E^0_{Ca} + E^0_{F})/k \quad (4)$$

The fourth column shows that our measurements of *m*_{F⁻} confirm the variability found by Stearns and Berndt. When *K'*_{sp} is calculated from the measured molalities of both Ca²⁺ and F⁻ ions, however, *K'*_{sp} is more nearly constant (fifth column).

The emf of cell A is listed in the last column of Table I. It is evident that the data are adequately represented by an emf of 5.5 ± 1 mV, leading to a value of 3.31 × 10⁻¹⁰ for *K'*_{sp} in 1 *m* KCl. When an estimate of γ_±(CaF₂) by the Brønsted-Guggenheim equation with interaction parameters appropriate to an ionic strength of 1.0 is applied, one finds 3.1 × 10⁻¹¹ for the thermodynamic activity product. This is in acceptable agreement with 4.9 × 10⁻¹¹, the literature value for this equilibrium constant.⁴

It is noteworthy that the residual liquid-junction potentials in the measurement of the calcium and fluoride

ion molalities cancel in the calculation of log *K'*_{sp} by eq 4. Although the fluoride electrode is very suitable for measurements of this type, the stability and reproducibility of the calcium ion-selective electrode leave something to be desired. For this reason, an uncertainty of 1 mV does not seem unreasonable for this design of the experiment. We therefore conclude that *K*_{sp} is in fact constant over a significant range of solution compositions but that the system cannot be completely defined by measurement of the fluoride ion molality alone.

A possible clue to the reasons why the system defies simple definition is to be found in the results given in Table I for the first solution, which contained no added Ca²⁺. For this solution, one should be able to calculate *K'*_{sp} from either of the experimental parameters, *m*_{Ca²⁺} or *m*_{F⁻}, as follows:

$$K'_{sp} = 4m_{Ca^{2+}}^3 \quad (5)$$

or

$$K'_{sp} = 0.5m_{F^{-}}^3 \quad (6)$$

The values of *m*_{Ca²⁺} and *m*_{F⁻} determined experimentally for this saturated solution are in fact 8.55 × 10⁻⁴ and 6.36 × 10⁻⁴ mol kg⁻¹, respectively, far removed from the anticipated stoichiometric ratio of 1:2, so that eq 5 and 6 would lead to highly disparate values for *K'*_{sp}. The product *m*_{Ca²⁺}*m*_{F⁻}² is nonetheless in reasonable accord with the main body of data, indicating that there is no serious experimental error. This observation suggests that F⁻ is being adsorbed on the surface of the solid phase.

Another illustration of this same effect is given by an experiment in which CaF₂ was added to a solution already in equilibrium with a known amount of the solid phase. In the absence of any surface effects, one would expect no change in the composition of the aqueous phase. Nevertheless, a rapid significant increase in *m*_{Ca²⁺}, with a compensating decrease in *m*_{F⁻}, was found, consistent with further surface adsorption of fluoride ions. The possibility that inclusion of soluble calcium in the CaF₂ was responsible for this result was minimized by repeated extraction and digestion of the CaF₂ added. Anion adsorption would explain an initially low apparent *K*_{sp} calculated from a measurement of the free fluoride ion concentration alone but cannot account for the decrease observed at higher molalities of calcium ion.

At the pH of our solutions (about 6.0), ion pairing between H⁺ and F⁻ is negligible and, furthermore, is relevant only to those calculations based on *m*_{F⁻} alone. Stearns and Berndt controlled both the ionic strength and the pH with an acetate buffer, thus introducing the further complication of Ca²⁺-Ac⁻ ion pairing. This may be expected to reduce their calcium ion concentrations by a factor of 5 but probably did not alter their conclusions. In both their study and ours, the existence of Ca²⁺-F⁻ ion pairs has been ignored. Again this simplification is irrelevant when both *m*_{Ca²⁺} and *m*_{F⁻} are measured independently. Although this equilibrium would alter the mass balance considerations necessary to the Stearns and Berndt method of calculating *K'*_{sp}, the effect is not serious.

Finally, Stearns and Berndt¹ give as their criterion for saturation equilibrium the relations

$$\mu_{Ca^{2+},aq} = \mu_{Ca^{2+},s} \quad (7)$$

and

$$\mu_{F^{-},aq} = \mu_{F^{-},s} \quad (8)$$

where μ is the chemical potential. We believe that these equalities apply only to the electrochemical potential or

when the potential difference between the two phases is zero. In the words of Guggenheim,⁵ "For the distribution of ionic species i between two phases α, β of different chemical composition the equilibrium condition is equality of the electrochemical potential...". On the other hand, the classical definition of the solubility equilibrium

$$\mu_{\text{Ca}^{2+}, \text{aq}} + \mu_{\text{F}^-} = \mu_{\text{CaF}_2, \text{s}} \quad (9)$$

is valid for both the chemical and electrochemical potentials. Furthermore, it is well established that activities of electrolytes derived from the emf of cells containing electrodes of the second kind (as, for example, Ag|AgCl or Pb|PbSO₄) agree with those calculated from vapor pressure measurements or other colligative properties. If the Gibbs energy of the solid varied appreciably with the ionic concentration of the solution, agreement would not be found. Equation 9 does not lend support to the idea that $a_{\text{CaF}_2, \text{s}}$ varies with the solution composition or that the activity product is merely an approximation to the true constant.

The study of Stearns and Berndt draws attention to the need for complete characterization of systems containing finely divided solids. Surface adsorption of ions in the calcium fluoride system, a function of both specific surface area and the ionic strength of the solution in equilibrium with the solid phase, can account for the apparent variability of the solubility product constant.

Note Added in Proof. Since this communication was

submitted, we have been able to make surface area measurements on the digested CaF₂ used in these experiments. The specific surface area was 5 m² g⁻¹, or probably large enough for surface energies to influence solubility and adsorption properties. Furthermore, electrophoresis measurements on colloidal CaF₂ suspensions with and without added Ca²⁺ and F⁻ showed the particles to be carrying significant charge. The authors are grateful to John Horn and James Adair of the Department of Materials Science and Engineering for cooperation in these measurements.

Acknowledgment. This work was supported in part by the National Science Foundation under Grant CHE73-05019 A02.

References and Notes

- (1) R. I. Stearns and A. F. Berndt, *J. Phys. Chem.*, **80**, 1060 (1976).
- (2) J. J. Lingane, *Anal. Chem.*, **39**, 881 (1967).
- (3) W. E. Morf, D. Ammann, E. Pretsch, and W. Simon, *Pure Appl. Chem.*, **36**, 421 (1973).
- (4) J. Bjerrum, G. Schwarzenbach, and L. G. Sillen, "Stability Constants of Metal Complexes", Part II, The Chemical Society, London, 1958.
- (5) E. A. Guggenheim, "Thermodynamics", North Holland Publishing Co., Amsterdam, 1949, p 332.

Department of Chemistry
University of Florida
Gainesville, Florida 32611

J. B. Macaskill
Roger G. Bates*

Received October 12, 1976

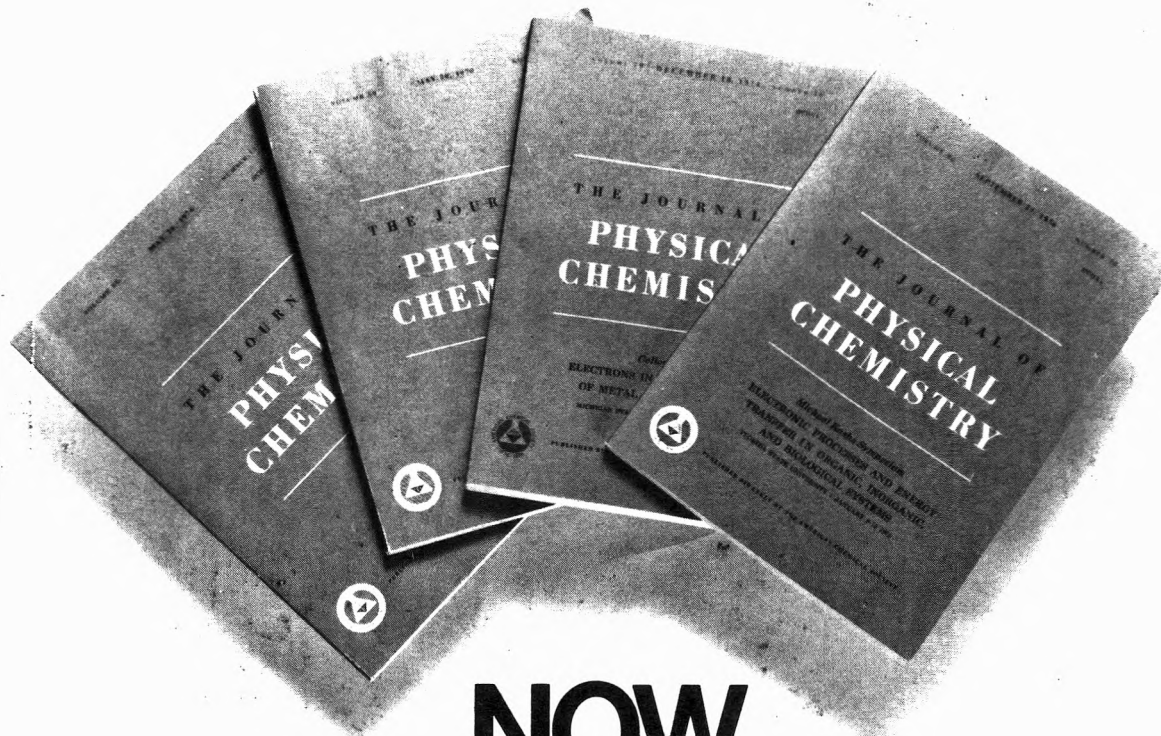
ADDITIONS AND CORRECTIONS

1977, Volume 81

R. A. Orwoll, R. H. Rhyne, Jr., S. D. Christesen, and S. N. Young: Volume Changes of Mixing for the System *p,p'*-Di-*n*-heptyloxyazoxybenzene + Xylene.

Page 181. The title on this page incorrectly mentions *p,p'*-Di-*n*-hexyloxyazoxybenzene, whereas the article is concerned only with *p,p*-Di-*n'*-heptyloxyazoxybenzene. The same error occurred in the table of contents for the issue.—R. A. Orwoll

V. Ph.
Corrected
28 June 1977



NOW you can buy all four special issues of The Journal of Physical Chemistry

and save money on three of them.

By buying the December 16, 1976 J. L. Franklin issue for the regular price of \$4.75, you can get the **three other special issues for only \$10.00!**

The Franklin issue consists of a collection of papers in theoretical and applied research, especially thermodynamics and energetics.

The other issues are:

- **Colloque Weyl IV.**
Electrons in Fluids—The Nature of Metal-Ammonia Solutions
- **Michael Kasha**
Symposium—Electronic Processes and Energy Transfer in Organic, Inorganic, and Biological Systems

- **Richard C. Lord**
Issue consists of contributions from colleagues, former students, and associates of Dr. Lord. Papers are on spectroscopy and related subjects

You can order just one or two of the issues instead of all three. In that case, the price is \$4.00 per issue. But please remember, it is necessary to buy the Franklin issue at the regular price before you can take advantage of the lower price.

Just fill out the form and mail it back to us today. We'll see that you receive the issue or issues of your choice just as soon as we can process your order.

MAIL WITH REMITTANCE TO:
Business Operations
American Chemical Society
1155 16th Street, N.W.
Washington, D.C. 20036

Please send me the following JOURNAL OF PHYSICAL CHEMISTRY SPECIAL ISSUES:

- J. L. Franklin issue** \$4.75
- Colloque Weyl IV. Issue** \$4.00*
- Michael Kasha Symposium** \$4.00*
- Richard C. Lord Issue** \$4.00*

*All three \$10.00

I am enclosing _____.

Check Money Order

Please print clearly.

NAME _____

ADDRESS _____

CITY _____

STATE/COUNTRY _____ ZIP _____



**TIRED of
searching through
dozens of
publications?**

WE CAN PUT AN END TO ALL THAT!

**As an ACS member,
you may now subscribe to the new,
semimonthly service called
ACS CUSTOMIZED ARTICLE SERVICE**

The **key feature** of this service will be a comprehensive selection of **articles of interest to you** from all the ACS journals except C&EN and CHEMISTRY. You'll receive the complete articles (on microfiche) and not a list of references. Along with these you'll receive monthly hard copies of ENVIRONMENTAL SCIENCE & TECHNOLOGY or the JOURNAL OF MEDICINAL CHEMISTRY depending on your choice of subject area. And in addition, we'll send you the semimonthly ACS SINGLE ARTICLE ANNOUNCEMENT.

The number of articles you receive is expected to **average** between 20 to 30 in each semimonthly package. All in all, you'll be getting a really significant amount of information for the modest sum of \$75 a year!

All you have to do to start this valuable service in **January 1977** is to fill out the form at the bottom of this ad and send it back to us today. The **IMPORTANT** thing is to make sure you are one of the charter subscribers to ACS CUSTOMIZED ARTICLE SERVICE. We'll take care of the rest.

American Chemical Society
1155 Sixteenth Street, N.W.
Washington, D.C. 20036

Yes . . . I would like to start the new service called ACS CUSTOMIZED ARTICLE SERVICE, in January 1977.

	U.S.	PUAS, Canada, Other Nations
One Year	\$75.00/per	\$100.00/per subject
ACS MEMBERS ONLY	subject area	area

Please indicate to which subject area(s) you want to subscribe:

Environmental Chemistry ()
Medicinal Chemistry ()

Please send me information on Microfiche Readers

NAME _____

ADDRESS _____

CITY _____ STATE _____ ZIP _____